

Copyright

By


Shawn Patrick Gross

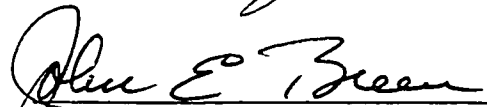
1998

**FIELD PERFORMANCE OF PRESTRESSED HIGH PERFORMANCE
CONCRETE HIGHWAY BRIDGES IN TEXAS**

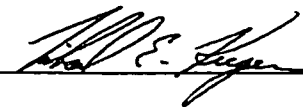
**Approved by
Dissertation Committee:**











**FIELD PERFORMANCE OF PRESTRESSED HIGH PERFORMANCE
CONCRETE HIGHWAY BRIDGES IN TEXAS**

by

Shawn Patrick Gross, B.S.E., M.S.E.

Dissertation

Presented to the Faculty of the Graduate School of

the University of Texas at Austin

in Partial Fulfillment

of the Requirements

for the Degree of

Doctor of Philosophy

The University of Texas at Austin

December 1998

*To Jennifer,
for your endless love and support*

ACKNOWLEDGEMENTS

A research program as extensive as the one discussed in this dissertation could not have been conducted successfully without the assistance and support of many individuals. Special thanks is expressed to the following people who have contributed greatly to the overall research effort:

Mary Lou Ralls, Texas Department of Transportation
Susan Lane, Federal Highway Administration
Paul Guthrie, Texas Concrete Company
Burson Patton, Texas Concrete Company
Bruce Williams, Texas Concrete Company
Craig Patton, Texas Concrete Company
John Jordan, Jascon, Inc.
Juan Bahena, Williams Brothers, Inc.
Thomas Nixon, Williams Brothers, Inc.

Special thanks is also extended to *all* individuals of the above listed organizations who have provided assistance throughout this research program.

The author also wishes to thank the following persons:

Dr. Ramon Carrasquillo, Dr. John Breen, Dr. Michael Kreger, and Dr. Eric Becker, for your valuable time, comments, and interest while serving on the author's doctoral committee.

The staff of the Construction Materials Research Group (CMRG) and the Ferguson Structural Engineering Laboratory (FSEL), including Carole Reese, Michael Rung, Rose Rung, Paul Walters, David Whitney, Joy Whitney, Wayne Fontenot, and Blake Stassney, for endless hours of technical assistance, support, and suggestions throughout the duration of this research program.

John Myers and Ken Byle, as well as the numerous other graduate and undergraduate students who contributed to this project, for their creativity, hard work, and dedication to the research program. I am sure that we will never forget those long hours travelling those lonely stretches of Texas highways, both early in the morning and late at night, but somehow it all seems worth while now.

Dr. Ned Burns, for your constant encouragement, interest, patience, suggestions, and incredible ability to put everything into perspective. I cannot express enough thanks for the numerous hours of time you have provided me as an advisor and mentor. It has been an honor to work alongside you.

To all of my friends, who have made my (our) stay in Texas memorable in so many ways. Thank you Dan and Rae-Ann, Denny and Mylene, Matt, Ron and Val, Danny, Kevin, and all of the others. I (we) will miss you all.

To my family, for your love, support, and understanding. Thank you, Mom, your encouragement came at just the right time and meant so much.

And finally, to my loving wife Jennifer, for you endless hours of optimism, support, patience, and love. You were my reader, my crutch, and my best friend during this incredible process. I thank you with all my heart. I love you.

Shawn Patrick Gross
Austin, Texas, 1998

FIELD PERFORMANCE OF PRESTRESSED HIGH PERFORMANCE CONCRETE HIGHWAY BRIDGES IN TEXAS

Publication No. _____

Shawn Patrick Gross, Ph.D.
The University of Texas at Austin, 1998

Supervisor: Ned H. Burns

Two prestressed high performance concrete (HPC) highway bridges were constructed in Texas utilizing concrete with 56 day design strengths of up to 97 MPa (14,000 psi). The utilization of HPC allowed for longer spans and larger girder spacing than typically used in conventional prestressed concrete bridges. An extensive research program, sponsored by the Federal Highway Administration and the Texas Department of Transportation, was conducted to monitor the short- and long-term structural behavior of these unique highway bridge structures.

The Louetta Road Overpass near Houston, Texas consists of two adjacent three-span simply-supported HPC highway bridges. The Louetta bridges utilize the Texas U-beam in conjunction with high performance concrete and 15 mm (0.6 in.) diameter prestressing strands, resulting in an efficient structural design. Span lengths for the Louetta bridges range from 37.0 to 41.3 m (121.5 to 135.5 ft.), with a maximum girder spacing of 5.07 m (16.6 ft.) on center.

The North Concho River/U.S. 87/S. O. R. R. Overpass in San Angelo, Texas consists of a 290 m (951 ft.) long eight-span HPC Eastbound bridge and an adjacent 292 m (958 ft.) long nine-span conventional concrete Westbound bridge. Both

bridges utilize the AASHTO Type IV beam cross-section in the main spans. HPC was used in conjunction with 15 mm (0.6 in.) diameter strands to increase span lengths and girder spacing in the Eastbound HPC bridge relative to the conventional concrete Westbound bridge. The maximum span length in the Eastbound HPC bridge was 47.9 m (157 ft.), compared to 39.9 m (131 ft.) in the Westbound conventional concrete bridge.

As part of the research program, instrumentation gauges were placed in selected structural components of the bridges. These gauges were monitored through the construction process and into the service lives of the completed bridges. Data were collected on prestress losses, beam deflection (camber), concrete strains, and concrete temperatures. These data were analyzed to examine the applicability of current standard design procedures and assumptions for highway bridges using HPC, and to compare the structural behavior of the two bridges, which represent similar yet different implementations of HPC in highway bridge structures.

TABLE OF CONTENTS

LIST OF TABLES.....	xviii
LIST OF FIGURES	xxiii
1 CHAPTER ONE: INTRODUCTION.....	1
1.1 General.....	1
1.2 Definitions of HPC	2
1.2.1 Definitions Based on Compressive Strength (HSC).....	2
1.2.2 Definitions Incorporating Strength and Durability Characteristics (HPC).....	3
1.2.3 Broad Definitions (HPC)	3
1.2.4 Proposed Definition of HPC	4
1.2.5 Terminology Used in this Dissertation: HPC vs. HSC.....	5
1.3 Applications of HPC.....	5
1.3.1 Tall Buildings	6
1.3.2 Long-Span Bridges.....	6
1.3.3 Short-to-Medium Span Bridges	7
1.3.4 FHWA Showcase Projects	10
1.4 Advantages of HPC for Highway Bridge Structures	10
1.4.1 General.....	10
1.4.2 Short-Term Benefits: Construction	11
1.4.3 Long-Term Benefits: Maintenance	13
1.5 Research Program.....	14
1.5.1 Research Team and Sponsors.....	14
1.5.2 Texas HPC Bridges	15
1.5.3 Research Objectives	16
1.6 Scope of This Dissertation.....	18
1.7 Organization of This Dissertation	19

2	CHAPTER TWO: PROJECT DETAILS	20
2.1	General.....	20
2.2	Louetta Road Overpass.....	20
2.2.1	General Project Description	20
2.2.2	Texas U54 Beam.....	32
2.2.3	Louetta Beam Design Details	39
2.2.4	Contractors, Fabricators, and Project Timeline.....	46
2.3	North Concho River/U.S. 87/S.O.R.R. Overpass	47
2.3.1	General Project Description	47
2.3.2	AASHTO Type IV Beam.....	56
2.3.3	San Angelo Beam Design Details	57
2.3.4	Contractors, Fabricators, and Project Timeline.....	65
3	CHAPTER THREE: INSTRUMENTATION PLANS AND PROCEDURES ...	67
3.1	Introduction.....	67
3.2	Measurements, Gauges, and Instrumentation Systems.....	68
3.2.1	Types of Measurements.....	68
3.2.1.1	Concrete Temperatures.....	69
3.2.1.2	Concrete Strains.....	69
3.2.1.3	Beam Camber/Deflection	70
3.2.2	Types of Gauges and Measurement Systems	70
3.2.2.1	Thermocouples.....	71
3.2.2.2	Thermistors.....	72
3.2.2.3	Vibrating Wire Strain Gauges	72
3.2.2.4	Resistance Strain Gauges.....	73
3.2.2.5	Surface Mechanical Strain Gauges (DEMEC)	74
3.2.2.6	Tensioned-Wire Deflection Measuring System	76
3.2.2.7	Precise Surveying Method.....	81
3.3	Data Acquisition.....	86
3.3.1	Description of Data Acquisition Systems	86
3.3.2	Programming and Collection of Data	93
3.3.3	Manipulation and Reduction of Data	95
3.4	Instrumentation Plans.....	95

3.4.1	Gauge Numbering and Identification	96
3.4.2	Typical Instrumentation Schemes for Components.....	97
3.4.2.1	Prestressed Beams	97
3.4.2.2	Precast Deck Panels	104
3.4.2.3	Cast-in-Place Bridge Decks	104
3.4.3	Summary of Instrumentation Plans	105
3.4.3.1	Louetta Road Overpass.....	105
3.4.3.2	North Concho River / U.S. 87 / S.O.R.R. Overpass (San Angelo)	106
3.5	Preparation and Field Installation of Instrumentation	113
3.5.1	Preparation of Instrumentation	113
3.5.1.1	Embedded Gauges.....	113
3.5.1.2	Tensioned-Wire Deflection System	114
3.5.2	Field Installation of Instrumentation.....	114
3.5.2.1	Prestressed Beams	114
3.5.2.2	Precast Deck Panels	118
3.5.2.3	Cast-in-Place Bridge Decks	118
3.5.3	Coordination of Efforts Between Researchers and Contractors	121
3.5.4	Travel.....	123
3.6	Problems Encountered	124
3.6.1	Lost Data	124
3.6.2	Damage to instrumentation	125
3.6.3	Cracking of Concrete.....	126
3.6.4	Mislabeling and Misplacement of Gauges and Beams	126
3.6.5	Other.....	126
3.7	Durability of Embedded Gauges.....	127
4	CHAPTER FOUR: MATERIAL PROPERTIES	129
4.1	Introduction	129
4.1.1	General.....	129
4.1.2	Classification of Concrete Mixes	129
4.2	Mix Proportions and Fresh Concrete Properties	131
4.3	Compressive Strength	136

4.3.1	Background	136
4.3.2	Method of Measurement.....	137
4.3.3	Measurements.....	138
4.3.4	Regression Analyses for Use in Time-Dependent Models.....	140
4.4	Modulus of Elasticity	144
4.4.1	Background	144
4.4.2	Method of Measurement.....	146
4.4.3	Measurements.....	148
4.4.4	Regression Analyses for Use in Time-Dependent Models.....	149
4.5	Creep.....	152
4.5.1	Background	152
4.5.2	Method of Measurement.....	158
4.5.3	Measurements.....	162
4.5.4	Regression Analyses for Use in Time-Dependent Models.....	167
4.6	Shrinkage.....	172
4.6.1	Background	172
4.6.2	Method of Measurement.....	177
4.6.3	Measurements.....	178
4.6.4	Regression Analyses for Use in Time-Dependent Models.....	186
4.7	Coefficient of Thermal Expansion.....	187
4.7.1	Background	187
4.7.2	Method of Measurement.....	188
4.7.3	Measurements.....	189
5	CHAPTER FIVE: TEMPERATURE MEASUREMENTS	191
5.1	Introduction	191
5.1.1	General.....	191
5.1.2	Climatic Descriptions for Jobsites	193
5.1.3	Ambient Temperature Data	193
5.2	Hydration Temperatures.....	194
5.2.1	Background	194
5.2.2	Measurements.....	197
5.2.3	Discussion	208

5.3	Mean Bridge Temperatures	210
5.3.1	Background	210
5.3.2	Measurements.....	214
5.3.3	Discussion	224
5.4	Thermal Gradients	228
5.4.1	Background	228
5.4.2	Measurements.....	236
5.4.3	Discussion	253
5.5	Summary and Conclusions.....	260
5.6	Recommendations.....	265
6	CHAPTER SIX: CONCRETE STRAIN MEASUREMENTS	267
6.1	Introduction.....	267
6.1.1	General.....	267
6.1.2	Interpretation of Gauge Readings	268
6.2	Concrete Strains Before Release	270
6.2.1	Background	270
6.2.2	Measurements.....	271
6.2.3	Discussion	273
6.3	Concrete Stresses at Release of Prestress (Pretensioning)	280
6.3.1	Background	280
6.3.2	Measurements.....	282
6.3.3	Discussion	288
6.4	Time-Dependent Growth of Strains in Beams During Storage.....	291
6.4.1	Background	291
6.4.2	Measurements.....	294
6.4.3	Discussion	295
6.5	Elastic Responses to Post-tensioning and Deck Loads	301
6.5.1	Background	301
6.5.1.1	Post-Tensioning.....	301
6.5.1.2	Deck Loads.....	304
6.5.2	Measurements.....	305
6.5.2.1	Post-Tensioning.....	305

6.5.2.2	Deck Loads.....	308
6.5.3	Discussion	310
6.5.3.1	Post-Tensioning.....	310
6.5.3.2	Deck Loads.....	312
6.6	Summary and Conclusions.....	313
6.7	Recommendations.....	318
7	CHAPTER SEVEN: PRESTRESS LOSSES	320
7.1	Introduction	320
7.1.1	General.....	320
7.1.2	Measurement of Prestress Losses Using Embedded Gauges	322
7.2	Prestress Losses Before Release	324
7.2.1	Background	324
7.2.2	Measurements.....	327
7.2.3	Discussion	337
7.3	Elastic Shortening at Release of Pretensioned Strands	342
7.3.1	Background	342
7.3.2	Measurements.....	344
7.3.3	Discussion	347
7.4	Total Losses	352
7.4.1	Background	352
7.4.2	Measurements.....	356
7.4.3	Discussion	364
7.5	Summary and Conclusions.....	370
7.6	Recommendations.....	373
8	CHAPTER EIGHT: CAMBER AND DEFLECTION	376
8.1	Introduction	376
8.1.1	General.....	376
8.1.2	Corrections to Field Measurements of Camber and Deflection	379
8.2	Camber at Release of Prestress (Pretensioning)	381
8.2.1	Background	381
8.2.2	Measurements.....	383

8.2.3	Discussion	391
8.3	Time-Dependent Camber Growth in Beams During Storage	400
8.3.1	Background	400
8.3.2	Measurements	401
8.3.3	Discussion	410
8.4	Elastic Deflection Responses to Post-Tensioning and Deck Loads	417
8.4.1	Background	417
8.4.1.1	Post-Tensioning	417
8.4.1.2	Deck Loads	418
8.4.2	Measurements	419
8.4.2.1	Post-Tensioning	419
8.4.2.2	Deck Loads	421
8.4.3	Discussion	427
8.4.3.1	Post-Tensioning	427
8.4.3.2	Deck Loads	428
8.5	Long-Term Deflection Behavior	430
8.5.1	Background	430
8.5.2	Measurements	433
8.5.3	Discussion	440
8.6	Summary and Conclusions	452
8.7	Recommendations	457
9	CHAPTER NINE: STATIC LIVE LOAD TESTS	460
9.1	Introduction	460
9.2	Loading Arrangements and Test Procedures	461
9.3	Measurements	464
9.3.1	San Angelo	464
9.3.2	Louetta	465
9.4	Discussion	472
9.4.1	General Magnitudes of the Deflection and Curvature Responses ..	479
9.4.2	Distribution of Loads	481
9.4.3	Continuity	482
9.5	Summary and Conclusions	485

9.6	Recommendations.....	486
10	CHAPTER TEN: COMPARISON OF THE BRIDGES	487
10.1	Introduction.....	487
10.2	Beam Fabrication Issues.....	488
10.3	Handling Issues.....	490
10.4	Project Costs.....	495
10.5	Ultimate Strength and Ductility.....	497
10.6	Summary and Recommendations.....	503
10.6.1	Texas U54 Beam vs. AASHTO Type IV Beam.....	504
10.6.2	Long Spans vs. Larger Girder Spacing.....	505
11	CHAPTER ELEVEN: SUMMARY AND CONCLUSIONS	507
11.1	General.....	507
11.2	Summary of Most Important Findings.....	507
11.3	Major Trends.....	510
11.4	Recommendations for Future Research.....	512
	APPENDIX A: SKETCHES DEPICTING GAUGE LOCATIONS FOR INSTRUMENTATION OF THE LOUETTA ROAD OVERPASS	513
	APPENDIX B: SKETCHES DEPICTING GAUGE LOCATIONS FOR INSTRUMENTATION OF THE N. CONCHO RIVER/U.S. 87/S.O.R.R. OVERPASS	536
	APPENDIX C: MEASURED CAST-IN-PLACE DECK GAUGE DEPTHS	560
	APPENDIX D: CREEP AND SHRINKAGE PLOTS	565
	APPENDIX E: EXTREME BRIDGE TEMPERATURE AND THERMAL GRADIENT PLOTS.....	577
	APPENDIX F: IMPORTANT PARAMETERS AND CONSTRUCTION SCHEDULES	594
	APPENDIX G: PLOTS OF LONG-TERM CAMBER AND PRESTRESS LOSS ...	636

APPENDIX H: PRESTRESS LOSS MEASUREMENTS AND CALCULATIONS FOR INDIVIDUAL BEAMS.....	666
BIBLIOGRAPHY	678
VITA.....	691

LIST OF TABLES

Table 1.1 - Categories of HPC Based on 1991 SHRP Definition [143]	4
Table 1.2 - Performance Characteristics in 1996 FHWA Definition of HPC [55]	4
Table 1.3 - Selected Structures Constructed With HPC	8
Table 2.1 - Design Concrete Strengths for the Louetta Road Overpass	28
Table 2.2 - Comparison of Section Properties and Guyon Efficiency for Selected 1370 mm (54 in.) Deep Girder Cross-Sections	32
Table 2.3 - Beam Design Details for the Northbound Louetta Road Overpass	41
Table 2.4 - Beam Design Details for the Southbound Louetta Road Overpass	42
Table 2.5 - Comparison of Eastbound and Westbound Bridge Designs	53
Table 2.6 - Joint Types at Bents in Main Spans (N. Concho River Overpass)	55
Table 2.7 - Design Concrete Strengths for the North Concho River Overpass	56
Table 2.8 - Beam Weights for Various Sections and Beam Lengths	58
Table 2.9 - Beam Design Details for Spans 1 through 6 of the Westbound North Concho River Overpass	59
Table 2.10 - Original Beam Design Details for Spans 1 through 5 of the Eastbound North Concho River Overpass	60
Table 2.11 - Details of Modified (Two-Stage) Beam Designs for Spans 1 through 5 of the Eastbound North Concho River Overpass	65
Table 3.1 - Types of Measurements and Data	68
Table 3.2 - Precise Surveying Measurement Systems	85
Table 3.3 - Capacities of DAS Systems by Gauge Type	91
Table 3.4 - Gauge Identification Designations	98
Table 3.5 - Summary of Instrumentation Plan for Beams in the Northbound Louetta Road Overpass	108
Table 3.6 - Summary of Instrumentation Plan for Beams in the Southbound Louetta Road Overpass	109

Table 3.7 - Summary of Instrumentation Plan for Beams in the Eastbound North Concho River Overpass (San Angelo)	111
Table 3.8 - Summary of Instrumentation Plan for Beams in the Westbound North Concho River Overpass (San Angelo)	112
Table 4.1 - HPC Classifications for Strength and Durability	131
Table 4.2 - Mix Properties for Prestressed Beams	132
Table 4.3 - Mix Properties for Precast Deck Panels	133
Table 4.4 - Mix Proportions for Louetta Cast-in-Place Decks	134
Table 4.5 - Mix Properties for San Angelo Cast-in-Place Decks	135
Table 4.6 - Curing Regimes Used for QC/QA Investigations	137
Table 4.7 - Summary of Compressive Strength Data for Precast Mixes	139
Table 4.8 - Summary of Compressive Strength Data for Cast-in-Place Mixes	140
Table 4.9 - Strength-Time Curve Parameters from Regression Analyses Using Measured Compressive Strength Data (Precast Mixes)	141
Table 4.10 - Strength-Time Curve Parameters from Regression Analyses Using Measured Compressive Strength Data (Cast-in-Place Mixes)	142
Table 4.11 - Measured Modulus of Elasticity for Precast Mixes	147
Table 4.12 - Measured Modulus of Elasticity for Cast-in-Place Mixes	148
Table 4.13 - Modulus-Strength Curve Parameters from Regression Analyses Using Measured Modulus of Elasticity Data	151
Table 4.14 - Measured Creep Coefficients	164
Table 4.15 - Measured Specific Creep	165
Table 4.16 - Percentage of Creep at 180 days Occurring at Various Ages	168
Table 4.17 - Creep-Time Regression Curve Parameters (General Form)	169
Table 4.18 - Creep-Time Regression Curve Parameters (Power Fixed)	170
Table 4.19 - Creep-Time Regression Curve Parameters (Parameters Fixed)	170
Table 4.20 - Measured Shrinkage Strains	181
Table 4.21 - Percentage of Shrinkage at 180 Days Occurring at Various Ages ...	182
Table 4.22 - Shrinkage-Time Regression Curve Parameters (General Form)	184
Table 4.23 - Shrinkage-Time Regression Curve Parameters (Power Fixed)	185
Table 4.24 - Shrinkage-Time Regression Curve Parameters (Parameters Fixed)	185
Table 4.25 - Measured Coefficients of Thermal Expansion	189

Table 5.1 - Summary of Measured Hydration Temperatures for Beams	202
Table 5.2 - Summary of Measured Hydration Temperatures for Panels	204
Table 5.3 - Summary of Measured Hydration Temperatures for CIP Decks	206
Table 5.4 - Deck Dimensions and Gauge Depths for Selected Composite Beams	215
Table 5.5 - Weights Used for Calculation of Average Bridge Temperature	216
Table 5.6 - Comparison of Maximum Measured Temperatures	221
Table 5.7 - Comparison of Minimum Measured Temperatures	222
Table 5.8 - Comparison of Measured Temperatures and Design Temperatures ..	225
Table 5.9 - Summary of Maximum Measured Gradients	243
Table 5.10 - Recommended Load Factors for Thermal Gradients	266
Table 6.1 - Measured Crack Widths and Spacing in Beams Just Before Release	279
Table 6.2 - Summary of Methods Used for Prediction of Midspan Release Stresses	283
Table 6.3 - Sensitivity of Release Stresses to Important Parameters	290
Table 7.1 - Measured and Calculated Prestress Losses Between Stressing and Casting	330
Table 7.2 - Prestress Losses Between Casting and Release Calculated Using Analytical Model	339
Table 7.3 - Measured Release Strains and Equivalent Elastic Shortening Losses	345
Table 7.4 - Summary of Methods Used for Prediction of Elastic Shortening Losses	346
Table 7.5 - Measured and Predicted Elastic Shortening Loss (Stress Change) ...	348
Table 7.6 - Measured and Predicted Elastic Shortening Losses (Percent Loss) ..	349
Table 7.7 - Summary of Equations Used In the Prediction of Total Losses by Components	357
Table 7.8 - Measured Total Prestress Losses in Individual Beams by Component	358
Table 7.9 - Comparison of Measured and Calculated Total Prestress Losses	359

Table 7.10 - Summary of Design and Measured Parameters Used in Calculations of Prestress Losses	360
Table 7.11 - Suggested Equations for Calculation of Total Losses by Components	369
Table 8.1 - Summary of Measured and Predicted Midspan Release Cambers	386
Table 8.2 - Summary of Methods Used for Prediction of Midspan Release Camber	387
Table 8.3 - Approximate Error in Prediction of Camber at Release	389
Table 8.4 - Measured Camber at Release Before and After Removal to Storage	398
Table 8.5 - Summary of Measured and Predicted Camber Growth in Beams During Storage at the Prestressing Plant.....	409
Table 8.6 - Sensitivity of Elastic and Time-Dependent Camber to Selected Parameters (Louetta HPC Beam N21)	415
Table 8.7 - Sensitivity of Elastic and Time-Dependent Camber to Selected Parameters (San Angelo Eastbound HPC Beam E35)	415
Table 8.8 - Sensitivity of Elastic and Time-Dependent Camber to Selected Parameters (San Angelo Westbound non-HPC Beam W17)	416
Table 8.9 - Measured and Predicted Elastic Camber Due to Post-Tensioning	420
Table 8.10 - Measured and Predicted Elastic Deflections Due to Placement of the Cast-in-Place Deck (Louetta)	422
Table 8.11 - Measured and Predicted Elastic Deflections Due to Placement of the Cast-in-Place Deck (San Angelo).....	424
Table 8.12 - Measured and Predicted Deflections Due to Total Deck Load.....	425
Table 8.13 - Measured and Predicted Camber at Erection	434
Table 8.14 - Measured and Predicted Long-Term Service Camber	435
Table 8.15 - Summary of Measured and Predicted Erection and Long-Term Cambers	438
Table 8.16 - Important Parameters of the Beam Designs Used in Sensitivity Analysis	442
Table 8.17 - Sensitivity Analysis for Net Camber at Erection and Long-Term Service (Camber Values)	443

Table 8.18 - Sensitivity Analysis for Net Camber at Erection and Long-Term Service (Differences from Base Predictions).....	444
Table 8.19 - Suggested Modifications to Parameters for Upper and Lower Bound Approach to Camber Calculations	459
Table 9.1 - Axle Weights for Dump Trucks Used in Live Load Tests	466
Table 9.2 - Description of Loading Arrangements	472
Table 9.3 - Main Live Load Test Measurements (Loading SE-A1).....	473
Table 9.4 - Main Live Load Test Measurements (Loading SE-A2).....	473
Table 9.5 - Main Live Load Test Measurements (Loading SE-B).....	474
Table 9.6 - Main Live Load Test Measurements (Loading SW-A).....	474
Table 9.7 - Main Live Load Test Measurements (Loading SE-C)	475
Table 9.8 - Main Live Load Test Measurements (Loading SE-D)	475
Table 9.9 - Main Live Load Test Measurements (Loading SE-E, Span 2)	476
Table 9.10 - Main Live Load Test Measurements (Loading SE-E, Span 3)	476
Table 9.11 - Main Live Load Test Measurements (Loading LS-A1)	477
Table 9.12 - Main Live Load Test Measurements (Loading LS-A2)	477
Table 9.13 - Main Live Load Test Measurements (Loading LS-B)	478
Table 9.14 - Main Live Load Test Measurements (Loading LS-C)	478
Table 9.15 - Main Live Load Test Measurements (Loading LS-D)	479
Table 10.1 - Cost Summary for Louetta and San Angelo Bridge Projects	496
Table 10.2 - Ultimate Strength and Ductility Comparison for a Louetta HPC Beam and a San Angelo HPC Beam	501

LIST OF FIGURES

Figure 1.1 - Allowable Stress Criteria for 7,000 psi (48 MPa) Design	9
Figure 1.2 - Allowable Stress Criteria for 12,000 psi (83 MPa) Design	9
Figure 1.3 - Summary of the Benefits of HPC in Prestressed Girder Design	14
Figure 1.4 - Locations of Texas HPC Bridges	16
Figure 2.1- Louetta Road Overpass	21
Figure 2.2 - Site of the Louetta Road Overpass in Northwest Houston, TX	21
Figure 2.3 - Plan of the Louetta Road Overpass	22
Figure 2.4 - Partial Roadway Cross-Section (Louetta Road Overpass)	23
Figure 2.5 - Erection of Precast Panels (Louetta Road Overpass)	26
Figure 2.6 - Placement of Louetta Cast-in-Place Deck Concrete	26
Figure 2.7 - Screeding of Louetta Cast-in-Place Deck Concrete.....	27
Figure 2.8 - Louetta Road Overpass Substructure	27
Figure 2.9 - Louetta Road Overpass Substructure	28
Figure 2.10 - Completed Original Louetta Bridges (Prior to Widening)	29
Figure 2.11 - Additional Beams and Panels for Louetta Bridge Widening	29
Figure 2.12 - Selected 1370 mm (54 in.) Deep Girder Cross-Sections	30
Figure 2.13 - Pretensioned Strand Patterns for Selected 1370 mm (54 in.) Deep Girder Cross-Sections	31
Figure 2.14 - Effective Bottom Fiber Moment Due to Prestress	36
Figure 2.15 - Effective Bottom Fiber Moment Due to Allowable Stress	36
Figure 2.16 - Moment Due to Girder Self-Weight	37
Figure 2.17 - Internal Diaphragms in Texas U-Beam	39
Figure 2.18 - Louetta U-Beam During Fabrication	43
Figure 2.19 - Reinforcement in the Skewed End Block of a Louetta Beam.....	43
Figure 2.20 - Skewed End Block in a Completed Louetta Beam	44
Figure 2.21 - Method Used to Determine Beam Spacing	44
Figure 2.22 - Timeline for Construction of the Louetta Road Overpass	45
Figure 2.23 - North Concho River/U.S. 87/S.O.R.R. Overpass	48
Figure 2.24 - Site of the N. Concho River Overpass in Central San Angelo, TX	48

Figure 2.25 - Plan of the Main Spans of the North Concho River Overpass	49
Figure 2.26 - Partial Roadway Cross-Section (North Concho River Overpass).....	50
Figure 2.27 - Erection of Precast Panels in the Westbound Bridge	51
Figure 2.28 - Pumping of Concrete During Deck Pour in the Eastbound Bridge	54
Figure 2.29 - Deck Placement in the Eastbound Bridge.....	54
Figure 2.30 - Pier Column in the North Concho River Overpass.....	55
Figure 2.31 - Pier Cap in the North Concho River Overpass	56
Figure 2.32 - Two-Stage Beam Fabrication Process.....	63
Figure 2.33 - Fabrication of Eastbound HPC Beam	63
Figure 2.34 - Post-tensioning of Eastbound HPC Beam	64
Figure 2.35 - Anchorage Reinforcement in Eastbound HPC Beam	64
Figure 2.36 - Timeline for Construction of the North Concho River Overpass	66
Figure 3.1 - Thermocouple	71
Figure 3.2 - Vibrating Wire Strain Gauge	72
Figure 3.3 - Bonded and Waterproofed Electrical Resistance Strain Gauges	75
Figure 3.4 - DEMEC Mechanical Strain Gauge and Target Disks	76
Figure 3.5 - Schematic of the Tensioned-Wire Deflection System	77
Figure 3.6 - Precision Scale Fixed to Girder at Midspan	78
Figure 3.7 - Dead (Anchorage) End of Tensioned-Wire Deflection System	78
Figure 3.8 - Live (Stressing) End of Tensioned-Wire Deflection System	79
Figure 3.9 - Reading the Tensioned-Wire Deflection System	79
Figure 3.10 - Measurement of Camber Using the Precise Surveying System	82
Figure 3.11 - Surveying Rod with Precision Scales Attached	83
Figure 3.12 - Use of Post Level with Surveying Rod	83
Figure 3.13 - Schematic of Relative and Absolute Precise Surveying Systems	84
Figure 3.14 - Use of a Man-Lift to Get Surveying Rod to the Level of the Beams in Spans 2, 3, and 4 of the Eastbound North Concho River Overpass	87
Figure 3.15 - Completed Data Acquisition System (DAS) Box.....	88
Figure 3.16 - Schematic of a Typical Data Acquisition System	90
Figure 3.17 - Gauges Connected to a DAS Box Shortly After Beam Casting	91
Figure 3.18 - Use of Construction Equipment to Access a DAS Box	92
Figure 3.19 - DAS Box with Companion Access Box (Louetta)	92

Figure 3.20 - DAS Box with Companion Access Box (San Angelo)	93
Figure 3.21 - Schematic of Program and Data Transfer Between Datalogger and Personal Computer Using Storage Modules	94
Figure 3.22 - Switching of Batteries and Storage Modules in the Field	94
Figure 3.23 - Typical Instrumentation Scheme for Prestressed Beams	100
Figure 3.24 - Typical Gauge Locations in Prestressed Beams	101
Figure 3.25 - Typical Instrumentation Scheme for Precast Deck Panels	102
Figure 3.26 - Typical Instrumentation Scheme for Cast-in-Place Bridge Decks ...	103
Figure 3.27 - Instrumented Areas of the Louetta Road Overpass	107
Figure 3.28 - Instrumented Areas of the North Concho River/U.S. 87/S.O.R.R. Overpass (San Angelo)	110
Figure 3.29 - Spooling of Leadwire for a Group of Gauges	115
Figure 3.30 - Placement of an Embedded Gauge in a Beam	116
Figure 3.31 - Complete Group of Gauges at Midspan of a Beam	116
Figure 3.32 - Leadwires Tied to Reinforcement in the Top Flange of a Beam	117
Figure 3.33 - Thermocouple Tied to Cast-in-Place Deck Reinforcement	119
Figure 3.34 - Vibrating Wire Gauges Placed in Cast-in-Place Bridge Deck	120
Figure 3.35 - Leadwires Tied to Reinforcement in Cast-in-Place Deck	120
Figure 3.36 - Leadwires Run Through Holes in Deck Formwork Near DAS Box ..	121
Figure 3.37 - Travel Distances from Austin to Jobsites and Precast Plants.....	123
Figure 3.38 - Durability of Embedded Gauges	128
Figure 4.1 - Strength-Time Regression Curve Fit for Louetta Panels	143
Figure 4.2 - Strength-Time Regression Curve for an HPC Beam Pour	144
Figure 4.3 - Modulus vs. Compressive Strength for Louetta HPC Beam Mix	150
Figure 4.4 - C/S/T Specimens Just After Casting at Jobsite	160
Figure 4.5 - Arrangement of DEMEC Gauge Points on C/S/T Specimens	161
Figure 4.6 - Creep Test Frames with Specimens Under Sustained Load	161
Figure 4.7 - Creep vs. 28-day (Member-Cured) Compressive Strength.....	166
Figure 4.8 - Creep vs. Water-to-Binder Ratio	166
Figure 4.9 - Creep vs. Quantity of Mix Water	167
Figure 4.10 - Typical Creep Coefficient Curve Fits from Regression Analyses	169
Figure 4.11 - Shrinkage (Unloaded) Specimens in Testing Room	180

Figure 4.12 - Correction to Measured Shrinkage Data to Account for Unmeasured Shrinkage Before First Reading	180
Figure 4.13 - Shrinkage vs. 28-day (Member-Cured) Compressive Strength	183
Figure 4.14 - Shrinkage vs. Water-to-Binder Ratio	183
Figure 4.15 - Shrinkage vs. Quantity of Mix Water	184
Figure 4.16 - Coefficient of Thermal Expansion by Aggregate Type and Source ..	190
Figure 5.1 - Heat Evolution and Concrete Temperature During Hydration	196
Figure 5.2 - Measured Hydration Temperatures in San Angelo HPC Beam E14 .	198
Figure 5.3 - Measured Hydration Temperatures in San Angelo HPC Beam E34 .	198
Figure 5.4 - Measured Hydration Temperatures in Louetta HPC Beam S16	199
Figure 5.5 - Measured Hydration Temperatures in Three Precast Panels	203
Figure 5.6 - Sections for Hydration Temperature Measurements in CIP Decks	205
Figure 5.7 - Measured Hydration Temperatures in Louetta SB Deck Span 1	207
Figure 5.8 - Measured Hydration Temperatures in San Angelo EB Deck Span 1	207
Figure 5.9 - Relationship Between Extreme Bridge Temperatures and Extreme Normal Daily Temperatures Suggested in NCHRP Report 276 [65]	213
Figure 5.10 - Gauge Locations and Layers Used for Calculation of Average Bridge Temperature	214
Figure 5.11 - Typical Temperature Behavior on a Sunny Summer Day	217
Figure 5.12 - Typical Temperature Behavior on an Overcast Winter Day	217
Figure 5.13 - Temperature Behavior Affected by a Cold Front	218
Figure 5.14 - Maximum Daily Temperatures for Composite Beam S14-E in 1997	218
Figure 5.15 - Minimum Daily Temperatures for Composite Beam S14-E in 1997	219
Figure 5.16 - Average Maximum Daily Temperatures by Month for Composite Beam S14-E in 1997	219
Figure 5.17 - Average Minimum Daily Temperatures by Month for Composite Beam S14-E in 1997	220
Figure 5.18 - Design Thermal Gradients Suggested in NCHRP Report 276 [65]..	230
Figure 5.19 - Design Thermal Gradients Specified in the <i>AASHTO LRFD Specifications</i> [1]	231
Figure 5.20 - Determination of Thermal Stresses and Strains in a Determinate Member Subjected to a Nonlinear Thermal Gradient	233

Figure 5.21 - Typical Heating Behavior in a Type IV Beam on a Sunny Summer Day	237
Figure 5.22 - Typical Cooling Behavior in a Type IV Beam Following a Sunny Summer Day	237
Figure 5.23 - Typical Heating Behavior in a U54 Beam on a Sunny Summer Day	238
Figure 5.24 - Typical Cooling Behavior in a U54 Beam Following a Sunny Summer Day	238
Figure 5.25 - Typical Thermal Behavior in a Type IV Beam On a Cloudy Day	239
Figure 5.26 - Thermal Behavior in a U54 Beam During Passage of a Cold Front	239
Figure 5.27 - Maximum Daily Positive Thermal Gradients During 1997 in the Louetta Northbound Bridge	241
Figure 5.28 - Maximum Daily Negative Thermal Gradients During 1997 in the Louetta Northbound Bridge	241
Figure 5.29 - Time of Maximum Positive and Negative Gradients Measured in Louetta Northbound Bridge During 1997	242
Figure 5.30 - Average Maximum Daily Gradients by Month in Louetta Northbound Bridge During 1997	242
Figure 5.31 - Comparison of Thermal Gradients in Interior and Exterior Beams of the San Angelo Westbound Bridge at Various Times	246
Figure 5.32 - Comparison of Thermal Gradients in Interior and Exterior Beams of the San Angelo Eastbound Bridge at Various Times	246
Figure 5.33 - Comparison of Thermal Gradients in Interior and Exterior Beams of the Louetta Southbound Bridge at Various Times	247
Figure 5.34 - Comparison of Thermal Gradients in Interior and Exterior Beams of the Louetta Northbound Bridge at Various Times	247
Figure 5.35 - Temperature Profiles at Sections of the Louetta Southbound Cast-in-Place Deck on a Sunny Summer Day	248
Figure 5.36 - Temperature Profiles at Sections of the Louetta Southbound Cast-in-Place Deck During the Night Following Sunny Summer Day	249
Figure 5.37 - Temperature Gradients in a U-Beam in Storage	250
Figure 5.38 - Temperature Gradients in a Type IV Beam in Storage	250
Figure 5.39 - Comparison of Maximum Measured Positive Gradients to Code Design Gradients	251

Figure 5.40 - Comparison of Maximum Measured Negative Gradients to Code Design Gradients.....	252
Figure 5.41 - Recommended Design Gradients for Concrete Highway Bridges in Texas (with No Topping)	255
Figure 5.42 - Response of Composite Beam E25 to Maximum Positive Gradient (Relative to 8:00 AM Same Morning)	256
Figure 5.43 - Thermal Stresses Calculated From Maximum Measured Gradients	257
Figure 5.44 - Thermal Moments and Deflections in a (Fictitious) Continuous Louetta Northbound Bridge	258
Figure 5.45 - Measured and Predicted Thermal Camber in Louetta Southbound Bridge on Day of Live Load Tests	258
Figure 6.1 - Measured Strains and Temperatures in Beam E35 Prior to Release	275
Figure 6.2 - Measured Strains and Temperatures in Beam E26 Prior to Release	276
Figure 6.3 - Idealized Strain Behavior in Beams Prior to Release	277
Figure 6.4 - Typical Cracking Pattern Observed in Beams Prior to Release	277
Figure 6.5 - Cracking in a San Angelo HPC Type IV Beam Prior to Release	278
Figure 6.6 - Measurement of Crack Widths Using a Crack Comparitor	278
Figure 6.7 - Measured Release Strains at Midspan in Beam E13.....	284
Figure 6.8 - Comparison of Predicted and Measured Release Stresses at Midspan in Beam E13	284
Figure 6.9 - Comparison of Predicted and Measured Midspan Stresses at Release of Pretensioning (Louetta)	285
Figure 6.10 - Comparison of Predicted and Measured Midspan Stresses at Release of Pretensioning (San Angelo)	286
Figure 6.11 - Effect of Error in Modulus of Elasticity on Measured Stress Profile ..	287
Figure 6.12 - Measured and Predicted Time Dependent Strains in Louetta HPC Beams (Predicted Based on Measured Parameters).....	298
Figure 6.13 - Measured and Predicted Time Dependent Strains in San Angelo Eastbound HPC Beams (Predicted Based on Measured Parameters)	299
Figure 6.14 - Predicted Time-Dependent Strains in Beams S15 and E14 Based on Design and Measured Parameters.....	300
Figure 6.15 - Typical Stress Profile After Friction and Anchorage Losses	303

Figure 6.16 - Measured and Predicted Beam Stresses Due to Post-Tensioning ..	307
Figure 6.17 - Measured and Predicted Beam Stresses Due to Post-Tensioning in Beam E13 (Including Stresses Computed for Actual Beam Design)	308
Figure 6.18 - Measured and Predicted Stresses in Beams Due to the Placement of Cast-in-Place Decks	311
Figure 7.1 - Setup for Measurement of Strand Stresses (Forces) and Temperatures Before Release	329
Figure 7.2 - Measured Strand Stress and Temperature Before Casting (Strand 4C)	331
Figure 7.3 - Measured Strand Stress and Temperature Before Casting (Strand 6C)	331
Figure 7.4 - Measured Strand Forces and Temperatures from Stressing Through Casting and Release (Strand 4C).....	332
Figure 7.5 - Analytical Model for Calculation of Estimated Prestress Losses Before Release	338
Figure 7.6 - Measured Strand Force at Bulkhead and Calculated Strand Forces Between Casting and Release (Strand 4C)	340
Figure 7.7 - Comparison of Measured and Predicted (Exact Method) Elastic Shortening Losses	350
Figure 7.8 - Components of Measured and Predicted Losses for Beam E24	366
Figure 8.1 - Measurement Location Correction for Camber and Deflection Readings	380
Figure 8.2 - Measured and Predicted Midspan Release Camber (Louetta)	385
Figure 8.3 - Measured and Predicted Midspan Release Camber (San Angelo) ...	385
Figure 8.4 - Difference in Measured and Predicted Midspan Release Camber	387
Figure 8.5 - Measured Release Camber and Predicted Release Camber Shown as Algebraic Sum of Two Components	388
Figure 8.6 - Ratio of Measured to Predicted Release Cambers at Midspan	390
Figure 8.7 - Influence of Unit Weight and Prestress Loss on Release Camber	394
Figure 8.8 - Camber Deficit as a Function of Span Length	398

Figure 8.9 - Effect of Analytical Corrections for Support Conditions and Thermal Gradients on Camber Measurements	402
Figure 8.10 - Measured and Predicted Time-Dependent Camber for Beams in Storage (Louetta HPC Northbound Span 2)	403
Figure 8.11 - Measured and Predicted Time-Dependent Camber for Beams in Storage (Louetta HPC Northbound Span 3)	403
Figure 8.12 - Measured and Predicted Time-Dependent Camber for Beams in Storage (Louetta HPC Southbound Span 1)	404
Figure 8.13 - Measured and Predicted Time-Dependent Camber for Beams in Storage (Louetta HPC Southbound Span 2)	404
Figure 8.14 - Measured and Predicted Time-Dependent Camber for Beams in Storage (San Angelo HPC Eastbound Span 1)	405
Figure 8.15 - Measured and Predicted Time-Dependent Camber for Beams in Storage (San Angelo HPC Eastbound Span 2)	405
Figure 8.16 - Measured and Predicted Time-Dependent Camber for Beams in Storage (San Angelo HPC Eastbound Span 3)	406
Figure 8.17 - Measured and Predicted Time-Dependent Camber for Beams in Storage (San Angelo HPC Eastbound Span 4)	406
Figure 8.18 - Measured and Predicted Time-Dependent Camber for Beams in Storage (San Angelo Non-HPC Westbound Span 1)	407
Figure 8.19 - Predicted Camber Based on Design and Measured Parameters for Selected Beams	414
Figure 8.20 - Difference in Predicted Camber Based on Design and Measured Parameters for Selected Beams	414
Figure 8.21 - Measured and Predicted Elastic Camber Due to Post-Tensioning ..	421
Figure 8.22 - Measured and Predicted Elastic Deflections Due to Placement of the Cast-in-Place Deck (Louetta)	423
Figure 8.23 - Measured and Predicted Elastic Deflections Due to Placement of the Cast-in-Place Deck (San Angelo)	423
Figure 8.24 - Typical Time-Dependent Camber and Deflection Behavior for a Louetta HPC Beam (Beam S15)	436
Figure 8.25 - Typical Time-Dependent Camber and Deflection Behavior for a San Angelo Eastbound HPC Beam (Beam E33)	436

Figure 8.26 - Typical Time-Dependent Camber and Deflection Behavior for a San Angelo Westbound non-HPC Beam (Beam W15).....	437
Figure 8.27 - Base Predicted Camber and Upper and Lower Bounds (Beam N21)	445
Figure 8.28 - Base Predicted Camber and Upper and Lower Bounds (Beam N33).....	445
Figure 8.29 - Base Predicted Camber and Upper and Lower Bounds (Beam E13)	446
Figure 8.30 - Base Predicted Camber and Upper and Lower Bounds (Beam E24).....	446
Figure 8.31 - Base Predicted Camber and Upper and Lower Bounds (Beam W14)	447
Figure 8.32 - Base Predicted Camber and Upper and Lower Bounds (Typical Conventional Concrete Beam)	447
Figure 9.1 - Test Trucks Being Positioned During San Angelo Live Load Tests...	463
Figure 9.2 - Test Trucks Positioned in Louetta Loading Arrangement LS-B	463
Figure 9.3 - AASHTO HS20-44 Truck and Dump Trucks Used in Live Load Tests	466
Figure 9.4 - Comparison of Shear and Moment Diagrams for Loading SE-C and an HS20-44 Truck Load (San Angelo Eastbound Bridge, Span 2)	467
Figure 9.5 - Loading Arrangements for San Angelo Live Load Tests.....	468
Figure 9.6 - Loading Arrangements for Louetta Live Load Tests	470
Figure 9.7 - Deck Strain Measurements Near "Poor-Boy" Continuous Bents	483
Figure 10.1 - Prestressed Beam at Roll Equilibrium.....	491
Figure 10.2 - Use of Rigid Lifting Frame for Handling of San Angelo Eastbound HPC Type IV Beams at Prestressing Plant	493
Figure 10.3 - Transportation of San Angelo Eastbound HPC Type IV Beams	493
Figure 10.4 - Erection of San Angelo Eastbound HPC Type IV Beams at Jobsite	494
Figure 10.5 - Composite Sections and Constitutive Relationships for Strain Compatibility Analyses	499
Figure 10.6 - Moment Curvature Relationship for Louetta Beam N21 Based on Strain Compatibility Analysis	500

Figure 10.7 - Moment Curvature Relationship for San Angelo Beam E24 Based on
Strain Compatibility Analysis 500

1 CHAPTER ONE: INTRODUCTION

1.1 General

High performance concrete, or HPC, can be used to provide economic benefits for the design and construction of several types of structures — with respect to both structural efficiency and maintenance requirements. In the 1990's, HPC has become more readily available, been produced with a higher degree of quality control, and been used more frequently by engineers in the design of structures throughout the world. As HPC is utilized more and more in the design of such structures, the limits of current design assumptions and construction practices are being stretched, and the adequacy of these existing procedures must be examined.

Prestressed concrete highway bridges represent one category of structure for which HPC can provide multiple benefits. Two prestressed concrete highway bridges have recently been constructed in Texas utilizing HPC. These bridges have been fitted with instrumentation in order to monitor selected aspects of structural performance throughout the construction process and early service lives. The observations made regarding the structural performance of these bridges will be used to assess current design and construction procedures, and to determine special requirements that the use of HPC may dictate.

This chapter includes background information regarding high performance concrete and its applications. First, HPC is defined and a brief overview of past applications of HPC is provided. The specific benefits of the use of HPC for prestressed concrete highway bridges are then discussed. Finally, the scope and organization of the research projects and this dissertation are presented.

1.2 Definitions of HPC

Though extensive research has been performed on this construction material over the past twenty to thirty years, and several structures have been constructed with it, the terms “high performance concrete” and “HPC” are relatively new. Until recently, the terms “high strength concrete” and “HSC” were commonly used to describe this material. Engineers have always tried to relate other characteristic properties of concrete to compressive strength, making it natural to describe these concretes in terms of this fundamental property.

The production of HSC generally requires the use of high quality materials, including mineral and chemical admixtures such as fly ash, silica fume, and high-range-water-reducers (superplasticizers). As a result, higher compressive strengths often mean concrete with improved overall characteristics. Engineers around the world have recognized this improved overall performance, and during this decade have adopted “high performance concrete” and “HPC” as more appropriate terms for this class of material. Today, with the consideration of both strength-related and durability-related performance characteristics, defining high performance concrete is an ongoing, ever changing process.

1.2.1 Definitions Based on Compressive Strength (HSC)

Few, if any, current definitions of high performance concrete are based on compressive strength alone. In fact, definitions based on compressive strength alone are truly definitions of HSC, not HPC. Still, it is often convenient to define high strength concrete in order to distinguish it from the range of conventional concretes on which most empirical relationships used in structural codes today are based. For example, ACI Committee 363 [10] defines HSC as concrete with compressive strengths of 41 MPa (6000 psi) or greater, and not made using exotic materials and techniques (high-range-water-reducers, silica fume, and fly ash are not considered exotic). The Texas Department of Transportation (TxDOT), in a recent addendum to its *Standard Specifications* [131], defines HSC as concrete with design compressive strengths of 62 MPa (9000 psi) and greater.

The European FIP/CEB [67] definitions specify a range of 60 to 130 MPa (8700 to 18,900 psi) for HSC. Interestingly, most countries other than the United States specify an

upper limit for compressive strength [141]. These upper limits range from 80 MPa (11,600 psi) in Japan to 115 MPa (16,700 psi) in Germany. Above these upper limits, special approval is generally required for use in design.

1.2.2 *Definitions Incorporating Strength and Durability Characteristics (HPC)*

Some definitions of high performance concrete incorporate criteria relating to both strength and durability. One of the first HPC definitions of this type was developed in 1991 by Zia, Leming, and Ahmad under a Strategic Highway Research Program (SHRP) study [143]. They classified HPC as concrete meeting one of three strength-related criteria, in addition to two durability-related criteria. The three strength classifications reflect different requirements for different applications, and include very high strength (VHS), high early strength (HES), and very early strength (VES) concretes. These strength-based classifications are summarized in Table 1.1. The durability criteria include a minimum durability factor of 80% based on freeze-thaw resistance, and a maximum water-cementitious ratio of 0.35.

In 1996, the Federal Highway Administration (FHWA) proposed a definition of HPC based on four strength-related and four durability-related performance characteristics. For each of the eight characteristics, one of four HPC performance grades can be specified, allowing the designer to tailor the definition to the design requirements and exposure conditions of each individual project. The eight characteristics are listed in Table 1.2, and are measured by a set of well-known standardized tests. Details of the grade classifications for each characteristic are presented by Goodspeed, Vanikar, and Cook [55]. The definition may be difficult to apply because of its length, but it does a very good job of defining eight important performance-based criteria related to both strength and durability.

1.2.3 *Broad Definitions (HPC)*

Several recently proposed definitions have taken a very broad approach in defining HPC. In a 1996 state-of-the-art report, Zia, Ahmad, and Leming define HPC as “any concrete which satisfies certain criteria proposed to overcome limitations of conventional

concretes" [142]. Similarly, ACI has defined HPC as "concrete which meets special performance and uniformity requirements that cannot always be achieved routinely by using only conventional materials and normal mixing, placing, and curing practices" [12]. ACI also recognizes that these special requirements may pertain to placement and compaction without segregation, long-term mechanical properties, early-age strength, volume stability, or service life in severe environments.

Table 1.1 - Categories of HPC Based on 1991 SHRP Definition [143]

Category	Minimum Comp. Strength	Age
Very Early Strength (VES)	2,000 psi (14 MPa)	6 hours
High Early Strength (HES)	5,000 psi (35 MPa)	24 hours
Very High Strength (VHS)	10,000 psi (70 MPa)	28 days

Table 1.2 - Performance Characteristics in 1996 FHWA Definition of HPC [55]

Strength Characteristics	Durability Characteristics
Compressive Strength	Freeze-Thaw Durability
Modulus of Elasticity	Scaling Resistance
Shrinkage	Abrasion Resistance
Creep	Chloride Penetration

1.2.4 Proposed Definition of HPC

Debate will continue as to exactly what defines HPC. Complex definitions today acknowledge that HPC benefits may be of both a strength and durability nature. The existence of the broad definitions discussed in the previous section, however, clearly illustrates that HPC is widely considered to be concrete which overcomes the limitations of conventional concretes. In many senses, HPC is truly an engineered concrete which is designed to perform under a specific application. The following definition of HPC is thus proposed:

HPC is an engineered concrete whose components are carefully selected and proportioned to produce a material with beneficial properties suitable for a specific application. Beneficial properties may be related to any of a number of strength and/or durability characteristics, dependent upon the given application.

1.2.5 Terminology Used in this Dissertation: HPC vs. HSC

The preceding sections have illustrated that there is no widely accepted definition for either HPC or HSC. The point has been made, however, that all HSC's are considered HPC's. On the contrary, not all HPC's are HSC's, as their primary beneficial properties may be durability-related.

For simplification, the terms "high strength concrete" and "HSC" are not used in this dissertation. Although the beneficial strength of HPC will be of primary interest for discussion of the structural performance, all HPC — whether related to strength, durability, or both — will simply be referred to as "HPC" in the text. Further clarification of the type of HPC used for each concrete mix is provided in Section 4.1.2.

1.3 Applications of HPC

Over the past thirty years, several types of structures have utilized the beneficial properties of HPC. The primary applications of HPC have been in tall buildings and bridges, and the following sections briefly describe a few structures of each type which have utilized HPC. These structures represent some of the more major and well-known applications of HPC, and are not intended to be a complete listing. Table 1.3 presents basic information pertaining to the structures mentioned in the following sections. Additional information on these and other structures utilizing HPC may be found in the references [10,117,121,142].

In addition to tall buildings and bridges, numerous other applications exist for high performance concrete. HPC has been or is currently being used in highway pavements, bridge deck overlays, prestressed concrete piles and poles, offshore structures, marine foundations, dams, grandstand roofs, and modular bank vaults [10,121].

1.3.1 Tall Buildings

Several tall building structures in the United States have utilized the strength-related benefits of HPC. The use of HPC can accommodate the high axial compressive forces in the columns of tall buildings, and at the same time provide a significant increase in structural stiffness. Many tall buildings in Chicago have been constructed using HPC, including Lake Point Tower (1966), Water Tower Place (1975), 311 South Wacker Drive (1988) [129], and 225 West Wacker Drive (1988) [85]. In fact, over 30 buildings in the Chicago area since 1972 have incorporated HPC with design compressive strengths of 62 MPa (9000 psi) and higher [10]. HPC has also been used in composite steel-concrete columns in the Texas Commerce Tower in Houston (1981) [42], Interfirst Plaza in Dallas (1983) [135], and Two Union Square in Seattle (1988) [110].

HPC is also being used in tall buildings around the world. Toronto, Canada has several tall buildings constructed using HPC. In Malaysia, the world's tallest buildings have recently been completed utilizing HPC. The twin Petronas Towers measure 452 m (1483 ft.) and were constructed using HPC with design compressive strengths of up to 80 MPa (11,600 psi) in its columns and central core structure [132].

1.3.2 Long-Span Bridges

A number of long-span bridges around the world have also utilized HPC. The high strength characteristics of HPC allow for a substantial reduction in dead load, which is typically the largest portion of the total load in long-span bridges. At the same time, the improved durability characteristics of HPC can be utilized to reduce the potential for corrosion of reinforcement and other maintenance problems. Most of the applications in this category are cable stayed bridges, where large axial compressive forces must be accommodated in the superstructure to equilibrate tension in the cables. HPC can also be used to carry the large axial forces in the substructures of long-span bridges.

The East Huntington Bridge (1984) [64], a cable-stayed bridge spanning the Ohio River between Ohio and West Virginia, represents an early use of HPC for a long-span bridge in

the United States. The bridge superstructure consists of post-tensioned segmental concrete box girders with 55 MPa (8000 psi) HPC. Long-span bridges in Canada and France have utilized HPC in combination with steel. The Annacis Bridge (1986) [124] in Vancouver, Canada was constructed using 55 MPa (8000 psi) HPC precast deck panels on top of deep steel I-beams. Composite action was achieved through shear studs welded to the girder flanges. The Normandy Bridge (1994) [137] in Normandy, France, the world's longest cable-stayed bridge, utilizes HPC with compressive strengths of 60 MPa (8700 psi) in concrete box sections that make up 232 m (761 ft.) of the 856 m (2808 ft.) main span and all of the side spans. Steel box girders were used for the central portion of the main span, and composite steel and concrete boxes were used for the pylons in the substructure.

The Northumberland Strait Crossing (1997) [74], also known as the Confederation Bridge, represents the largest use of HPC in a structure in North America. The 12.9 km (8 mi.) long bridge links Prince Edward Island and New Brunswick, Canada, and has 43 main spans of 250 m (820 ft.). Each span consists of variable-depth precast girders cantilevered 95 m (312 ft.) from the pier at each end of the span, and a 60 m (197 ft.) precast drop-in section. HPC was used to build a structure that was both efficient and durable, considering the total length of the bridge and the harsh environment in the Northumberland Strait. In the superstructure, 55 MPa (8000 psi) low permeability HPC was used, and 80 MPa (11,600 psi) HPC with high abrasion resistance was used in some of the piers.

1.3.3 Short-to-Medium Span Bridges

HPC has been used around the world for many short-to-medium span bridges. During the 1970's a number of HPC railway bridges were constructed in Japan, including the Iwahana Railway Bridge (1973), the Ootanabe Railway Bridge (1973), and the Akkagawa Railway Bridge (1975) [125]. These concrete truss bridges used HPC precast members with compressive strengths of 80 MPa (11,500 psi) and greater. Concrete was chosen over steel to reduce deflections, reduce maintenance costs, and eliminate noise and vibration problems [142]. In France, an externally prestressed double I-section with 60 MPa (8700 psi) HPC was utilized in the construction of the experimental Joigny Bridge (1988) [78]. This combination resulted in a reduction of the superstructure weight by about 25% over a design with conventional 35 MPa (5000 psi) concrete.

Table 1.3 - Selected Structures Constructed With HPC

Structure	Location	Type	Year	Strength ^a (MPa, psi)	
Tall Buildings					
Lake Point Tower	Chicago	70 story R/C	1966	52	7500
Water Tower Place	Chicago	76 story R/C	1975	62	9000
TX Commerce Tower	Houston	75 story composite	1981	52	7500
Interfirst Plaza	Dallas	72 story composite	1983	69	10000
Two Union Square	Seattle	58 story composite	1988	97 ^b	14000 ^b
311 S. Wacker Drive	Chicago	70 story R/C	1988	83	12000
225 W. Wacker Drive	Chicago	31 story R/C	1988	97	14000
Petronas Towers	Malaysia	95 story R/C & steel	1997	80	11600
Long-Span Bridges					
E. Huntington Bridge	WV / OH	cable-stayed (900 ft. main span)	1984	55	8000
Annacis Bridge	Canada	cable-stayed ^c (1526 ft. main span)	1986	55	8000
Normandy Bridge	France	cable-stayed ^d (2808 ft. main span)	1994	60	8700
Northumberland Strait Crossing	Canada	continuous precast (820 ft. main spans)	1997	55 ^e	8000 ^e
Short-to-Medium Span Bridges					
Iwahana Railway Br.	Japan	147 ft. max. span	1973	89	12800
Ootanabe Railway Br.	Japan	79 ft. max. span	1973	79	11400
Akkagawa Railway Br	Japan	150 ft. max. span	1976	79	11400
Tower Road Bridge	WA	161 ft. max. span	1981	62	9000
Mountain View Rd. Br	WA	138 ft. max. span	1984	48	7000
Braker Lane Bridge	TX	85 ft. max. span	1987	66	9600
Joigny Bridge	France	150 ft. max. span	1988	60	8700
1 ft. = 0.3048 m 1 psi = 0.006895 MPa					
^a Design compressive strength. Actual concrete strengths usually higher.					
^b 19,000 psi (131 MPa) actually specified to obtain desired modulus of elasticity.					
^c Composite structure using deep steel I-beams and HPC precast deck panels.					
^d Center 2047 ft. (624 m) of main span is steel box girder. Side spans use HPC.					
^e Strength for superstructure. 11,600 psi (80 MPa) used in some pier elements.					

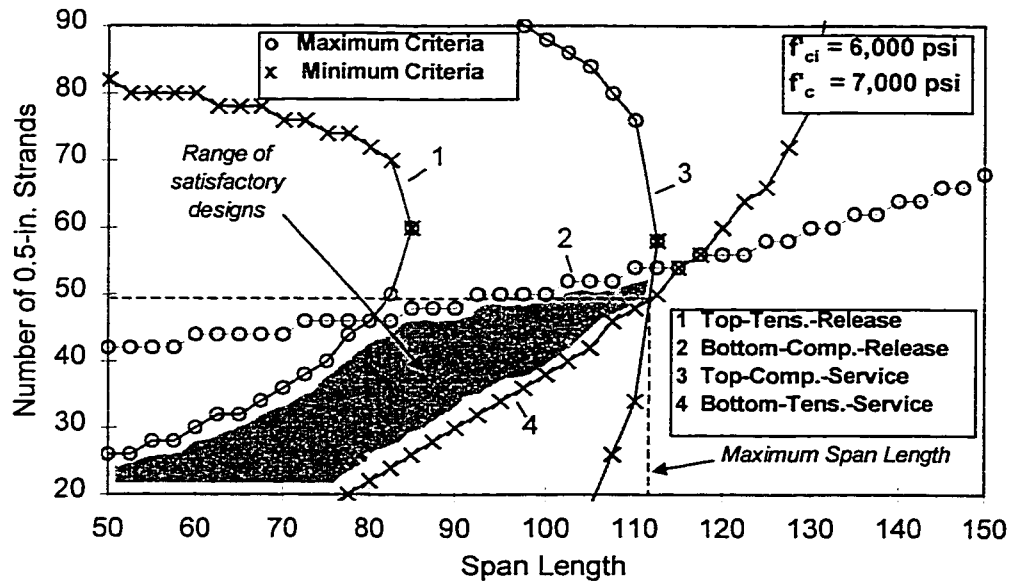


Figure 1.1 - Allowable Stress Criteria for 7,000 psi (48 MPa) Design

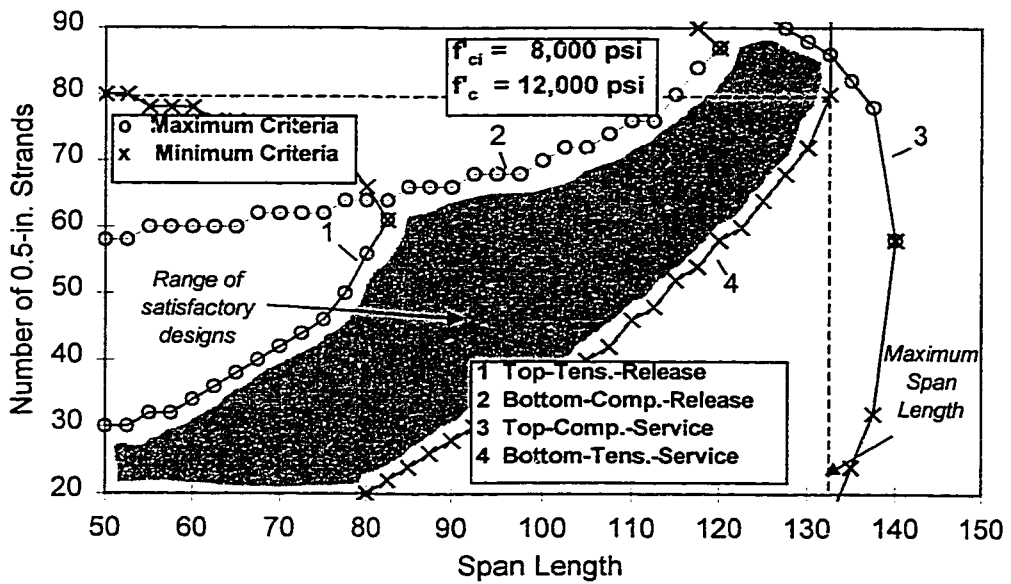


Figure 1.2 - Allowable Stress Criteria for 12,000 psi (83 MPa) Design

Highway bridges using standard girder sections have also been constructed using HPC, including several in the state of Washington since the early 1980's. The Tower Road Bridge (1981) [134] and the Mountain View Road Bridge (1984) [86] represent some of the first major applications of HPC in standard precast girder sections for highway bridges. The Braker Lane Bridge (1987) [48] in Austin, Texas similarly demonstrated the benefits of using HPC in standard girder cross-sections. In each of these structures, longer spans or larger girder spacings were accommodated using standard cross-sections, resulting in more efficient designs. The benefits of the use of HPC in this type of structure are discussed in detail in Section 1.4.

1.3.4 FHWA Showcase Projects

An FHWA program designed to advance the use of HPC in highway bridges has been underway since 1993. The focus of the program is the design and construction of actual bridge structures using HPC. As of early 1998, Alabama, Colorado, Georgia, Indiana, Nebraska, New Hampshire, North Carolina, Ohio, Texas, Virginia, Washington, and Wisconsin are currently involved in or have completed the design and construction of HPC highway bridges under the Showcase program. Several of the bridges constructed under this program are being instrumented to monitor long-term structural performance.

The two Texas bridges, on which the research program described in this dissertation is based, are part of the Showcase program. A brief description of the bridge projects is presented in Section 1.5.2. Structural details of the two bridges are presented in Chapter 2.

1.4 Advantages of HPC for Highway Bridge Structures

1.4.1 General

The use of high performance concrete in the design and construction of highway bridge structures is expected to lead to both short- and long- term cost savings. The

beneficial strength characteristics of HPC will lead to more efficient designs, resulting in direct cost savings if material costs can be kept to a reasonable level. Likewise, the beneficial durability characteristics of HPC are expected to result in lower life cycle costs due to longer service lives and reduced maintenance requirements. The following sections discuss these potential benefits, with emphasis placed on aspects of structural efficiency since the primary focus of this dissertation is structural performance.

1.4.2 Short-Term Benefits: Construction

Several authors [38,40,66,115,119,145] have performed parametric studies to investigate the impact of HPC on the design of prestressed, pretensioned highway bridge girders. These studies have shown that the use of HPC results in longer span and larger girder spacing capabilities for standard girder sections. The use of long spans and/or larger spacing should result in a direct economic benefit by reducing the number of beams and/or substructure elements required for a given design. Some authors have also suggested that shallower girder sections can be used instead of longer spans and larger girder spacing. For the replacement of existing bridges due to increased clearance requirements, the use of shallower sections would require less grade modification to existing approaches.

In the studies mentioned above, it has been noted that the benefits of using HPC in design are limited by the maximum available prestress force. Above a certain threshold, an increase in f_c does not result in a significant increase in span or spacing capabilities. Above this limit, more prestress force must be added to the section to make use of the higher concrete strength. Zia [145] found this limit to be in the range of 55 to 83 MPa (8,000 to 12,000 psi) for different cross-sections. Russell et. al. [119] found this limit to be around 69 MPa (10,000 psi) for most cross-sections. This principle of diminishing returns for higher compressive strengths is a result of the bottom fiber tension stress at midspan under service loads controlling the design.

Figure 1.1 and Figure 1.2 show plots of allowable stress criteria for typical girder designs with two different concrete strengths. In the figures, each data point represents the maximum or minimum number of 13 mm (0.5 in.) strands required to satisfy one of the four allowable stress criteria at a given span length. Maximum and minimum strand requirements were determined for each criterion at several span lengths, resulting in a

curve for each allowable stress criterion. The shaded area in each figure represents the range of designs meeting all four allowable stress criteria. For development of each figure, *AASHTO Standard Specifications* [3] allowable stress criteria and AASHTO Type IV girder sections were used. Release criteria were checked at the quarter points of the span, assuming straight strand patterns between the quarter points and midspan.

As shown in Figure 1.1, the efficiency of designs with lower concrete strengths are likely to be limited by top fiber compressive stresses at midspan under service loads. The limiting factor in this case is strand layout. As the number of strands is increased, strands become less efficient until the eccentricity of additional strands becomes so low that these additional strands would actually cause additional compressive stress at the top fiber. The diminishing efficiency of additional strands with respect to the top fiber stress eliminates any benefit to adding these strands.

As can be seen in Figure 1.2, designs with sufficiently high concrete strengths may be governed by the bottom fiber tensile stress at midspan under service loads. In this case, the limiting factor is again strand layout. Above a certain number of total strands, the negative eccentricity of additional strands becomes large enough to introduce tensile stresses at the bottom fiber. As with the top fiber compressive service stress for designs with lower concrete strengths, this loss in strand efficiency limits the maximum span length.

The two figures clearly show that the top fiber service stress criterion is greatly influenced by concrete strength. Higher compressive strengths increase the allowable compressive stress, resulting in a higher girder load capacity in the form of longer spans (or larger girder spacing). However, the bottom fiber service stress criterion is not affected much by an increase in compressive strength. This is due to the fact that the allowable tensile stress is proportional only to the square root of the compressive strength. Since designs with high compressive strengths are controlled by tension at the bottom fiber under service loads, additional prestress force must be introduced to make use of the higher compressive strengths. Additional prestress force would offset the higher loads resulting from longer span lengths and/or larger girder spacing. Of course, any additional prestress force must have enough positive eccentricity, or low enough negative eccentricity, to be effective.

Unfortunately, prestress force in pretensioned members is limited by the strand pattern, which is determined by the cross-section geometry. In most cases, the requirement for higher prestress forces must be accommodated by using larger diameter strands. For

example, 15 mm (0.6 in.) diameter strands have a 41 percent larger capacity than the industry-standard 13 mm (0.5 in.) diameter strand. Note that several recent studies [32,33,58,73,84,116] have examined the transfer and development length of larger diameter strands in HPC, which were not allowed in pretensioned applications by FHWA between 1988 and 1996 because of concerns over bond. Other methods of obtaining higher prestress forces include the use of smaller strand spacing, the use of post-tensioning, and the use of cross-sections with very efficient strand patterns compared to those of standard sections.

Of course, allowable stress criteria must also be satisfied at release for all designs. With most designs, adequately high release strengths and control of end stresses through draping or debonding of strands will be sufficient to meet these criteria. However, as more prestress force is introduced into the section to make use of higher concrete strengths, release criteria are more likely to control designs. It is possible that maximum obtainable release strengths may govern designs with HPC.

The use of high performance concrete in the design of prestressed girders is summarized in Figure 1.3. Concrete strength, strand size, and cross-section geometry can be controlled to implement higher prestress forces in each girder. These higher prestress forces, if efficient in terms of eccentricity, ultimately allow for higher service loads to be accommodated by each girder in the form of longer spans, larger girder spacing, or shallower sections.

The preceding discussion has focused on allowable stress criteria, but ultimate strength, shear, and serviceability (deflection) criteria must also be satisfied for every design. In most cases, ultimate strength is easily satisfied for HPC designs because of the increased compressive strength and large quantity of tensile reinforcement. Shear is a concern for prestressed highway bridge girders only in members with short span lengths or very thin webs. Deflection criteria will be discussed more extensively in Chapter 8.

1.4.3 Long-Term Benefits: Maintenance

The improved durability characteristics of HPC are expected to provide great economic benefits over the life cycle of highway bridge structures. For example, the reduced permeability of HPC is expected to provide better resistance to corrosion of

reinforcement over the life of the structure. Likewise, many HPC's have improved resistance to scaling, abrasion, and freeze-thaw damage. These beneficial durability properties of HPC should result in both longer service lives and reduced maintenance costs. A more detailed discussion of the durability-related benefits of HPC for highway bridges is presented by Myers and Carrasquillo [88].

1.5 Research Program

1.5.1 Research Team and Sponsors

The research program discussed in this dissertation was performed as part of three highway research projects administered by the Center for Transportation Research (CTR) at The University of Texas at Austin. CTR Project 9-580, "Design and Construction of Extra-High Strength Concrete Bridges", was a four-year study begun in 1993, and CTR Project 9-589, "High Performance Concrete for Bridges", is an ongoing five-year study begun in 1995. Both projects focus on the implementation and application of HPC, and each involved the actual construction of an HPC highway bridge. CTR Project 7-3993, "Long-Term Behavior of HPC Louetta Road Overpass", is a three-year continuation study started after the conclusion of CTR Project 9-580 in 1997.

Structural Benefits for a Given Prestressed Beam:

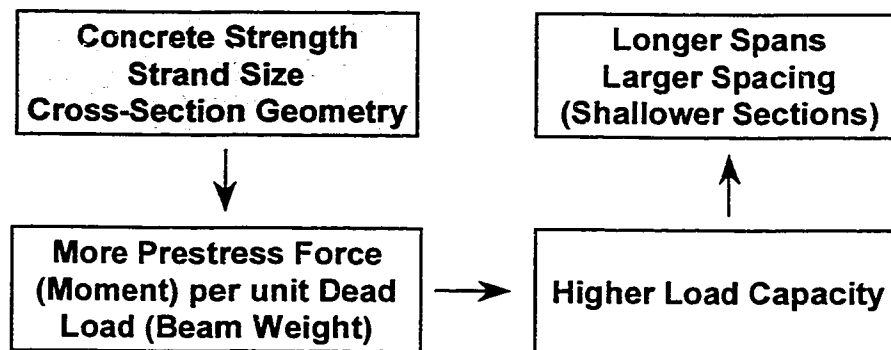


Figure 1.3 - Summary of the Benefits of HPC in Prestressed Girder Design

All three projects are jointly funded by the Federal Highway Administration (FHWA) and the Texas Department of Transportation (TxDOT), and are part of the FHWA HPC Showcase program discussed in Section 1.3.4. The TxDOT research director for all three projects is Mary Lou Ralls, P.E. The principal investigators are Ramon L. Carrasquillo, Ph.D., P.E., Ned H. Burns, Ph.D., P.E., and David W. Fowler, Ph.D., P.E.

Research under these projects was managed and conducted by the Construction Materials Research Group (CMRG) within the Department of Civil Engineering at The University of Texas at Austin. Additional testing was performed at and additional assistance provided by the Phil M. Ferguson Structural Engineering Laboratory (FSEL). Both the CMRG and FSEL laboratories are located at the J. J. Pickle Research Campus of the university, approximately ten miles north of the main campus in Austin, Texas.

1.5.2 Texas HPC Bridges

In conjunction with the research projects mentioned in the previous section, two high performance concrete highway bridges have been constructed in Texas. Construction was completed on the Louetta Road Overpass on State Highway 249 in Houston, Texas in April 1997, though the two adjacent bridges were widened during the following year. The bridges were opened to traffic in June 1998. The North Concho River/U.S. 87/S.O.R.R. Overpass on U.S. 67 in San Angelo, Texas was completed and opened to traffic in January 1998. The locations of the two bridges are shown in Figure 1.4.

Structural layout and design of the two projects is discussed in detail in Chapter 2, so only a brief overview is presented in this section. The Louetta Road Overpass in Houston, Texas consists of two adjacent three-span simply supported highway bridges utilizing concrete with compressive strengths of up to 90.3 MPa (13,100 psi). The use of 15 mm (0.6 in.) diameter prestressing strands, high performance concrete, and the recently developed 1372 mm (54 in.) deep Texas U54 beam [113] resulted in span lengths of 37.0 to 41.3 m (121.5 to 135.5 ft.) with girder spacings of 3.61 to 5.07 m (11.8 to 16.6 ft.) on center. All components of the two bridge structures, including prestressed beams, precast deck panels, cast-in-place bridge decks, and precast post-tensioned piers, were constructed with HPC.

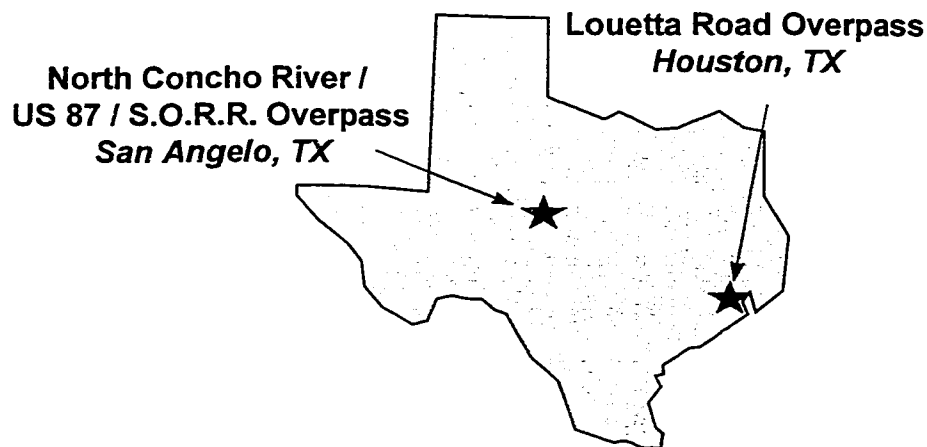


Figure 1.4 - Locations of Texas HPC Bridges

The North Concho River/U.S. 87/S.O.R.R. Overpass in San Angelo, Texas consists of a 290 m (951 ft.) long 8-span HPC Eastbound bridge, and an adjacent 9-span 292 m (958 ft.) long Westbound bridge constructed with conventional concrete. Both bridges utilized the standard 1372 mm (54 in.) deep AASHTO Type IV cross-section in the main spans. Span lengths in the main spans of the Eastbound HPC bridge range from 39.9 to 47.9 m (131 to 157 ft.). Concrete strengths of up to 96.5 MPa (14,000 psi), 15 mm (0.6 in.) diameter strands, and a two-stage (pretension/ post-tension) fabrication process were required to accommodate these long span lengths. Standard 13 mm (0.5 in.) strands and concrete strengths of up to 61 MPa (8,900 psi), which is commonly achieved at prestressing plants in Texas, were used in the Westbound bridge. All components of the Eastbound bridge were constructed with HPC, and the cast-in-place bridge deck of selected spans in the Westbound bridge was designated as HPC for improved durability performance.

1.5.3 Research Objectives

The overall research program has several objectives related to the practical field application of HPC in highway bridge structures. These objectives can generally be classified in terms of materials-related issues and issues related to structural performance.

The three research projects mentioned in Section 1.5.1 have essentially been treated as one major research effort by the researchers, with a materials subdivision and a structural subdivision. The major research objectives within each of these two subdivisions are discussed in the following paragraphs.

Responsibilities within the materials subdivision of the projects included the development of laboratory trial batches, assisting fabricators and contractors with mix design and placement issues as necessary, the development and execution of an extensive quality control/quality assurance program, and durability testing of field samples. Most of the materials-related research, including the objectives listed above, is discussed by Myers and Carrasquillo [88]. Additional materials-related research was performed under these projects and is summarized in three additional research reports. Cetin and Carrasquillo [41] examined the effect of accelerated heat curing and mix characteristics on the mechanical properties of a series of laboratory HPC trial batches. Carlton and Carrasquillo [37] studied the relationship between in-situ strengths and strengths measured from standard quality control specimens for HPC, and also examined the effects of curing and test methods on standard tests. Finally, Touma [133] examined the relationships between two standard methods of durability testing for HPC — the rapid chloride-ion permeability test and the chloride ponding test.

Research objectives and responsibilities related to structural performance of HPC highway bridges included design assistance as necessary, field and laboratory testing for transfer and development length, laboratory creep and shrinkage testing, and instrumentation of the bridges for the monitoring of short-term and long-term structural performance. The major focus of the structural research, the instrumentation and monitoring of the bridges, is discussed in this dissertation. As part of the instrumentation program, Byle and Burns [35] studied the time-dependent deformation behavior of the HPC beams in the Louetta Road Overpass. Barrios et. al. [23] discussed the design of the Louetta U-beams and examined the behavior of prototype U-beams at transfer of prestress. Gross and Burns [58], and Cordova et. al. [46] performed transfer and development length tests of 15 mm (0.6 in.) diameter strands at 50 mm (2 in.) spacing on full-scale test specimens. These tests were required by FHWA for approval of the designs for the actual HPC bridge girders, which utilized these larger strands at standard spacing. Finally, Farrington et. al. [51] performed an extensive study on the creep and shrinkage properties of the Louetta HPC beam concrete. (Although creep and shrinkage are material properties

of concrete, the creep and shrinkage test program was performed under the structural subdivision of the projects. The results were primarily used in time-dependent analyses of prestress losses and beam camber, not for quality control investigations.)

1.6 Scope of This Dissertation

The scope of this dissertation is the overall examination of the structural behavior of the two HPC bridges described in Section 1.5.2. The primary focus is on temperature measurements, concrete strains, loss of prestress, and beam camber (or deflection). Field measurements of prestress loss and camber at various stages of construction and service are compared to standard prediction methods and models used for design. Comparisons are performed using both measured material properties and assumed material properties for design, such that both the accuracy and sensitivity of standard prediction methods can be assessed.

Furthermore, the structural behavior of the two bridges relative to one another is considered here. The bridges represent two different implementations of HPC for highway bridge structures and thus present a unique opportunity for comparison. As appropriate, comparisons are based both on measurements and on practical observations that arose throughout the construction of the two bridges.

The work presented in this dissertation is the culmination of all of the structural research performed on these projects to date. Much of the research presented in the publications referenced in Section 1.5.3 is therefore incorporated into this dissertation. The work of Byle and Burns [35] regarding the time-dependent behavior of the Louetta HPC beams is expanded upon here and compared to the time-dependent behavior of the North Concho HPC and conventional concrete beams. Likewise, the work of Farrington et. al. [51] has been expanded to investigate the creep and shrinkage properties of not just the Louetta HPC beams, but of all eleven concrete mixes used in the superstructures of the two bridges. In many ways, this dissertation is intended to “tie together” all of the structural research on these projects to examine the overall structural performance.

1.7 Organization of This Dissertation

This dissertation consists of eleven chapters that together are intended to provide a complete examination of the short- and long-term structural performance of these unique highway bridges. Chapters 1 through 4 provide background information on HPC and its application for highway bridge structures, discuss details of the two bridge projects, present an overview of the instrumentation plans and procedures, and list the measured material properties for the many concrete mixes used in the two bridges. The results of the primary instrumentation program are presented in Chapters 5 through 8 in terms of temperature measurements, concrete strains, prestress losses, and beam camber (or deflection). Testing of the completed bridges under static live loads is discussed in Chapter 9. Non-measurement based observations regarding the practical construction of these two bridges are presented in Chapter 10, and Chapter 11 provides a summary and set of conclusions for the research program.

2 CHAPTER TWO: PROJECT DETAILS

2.1 General

Detailed information on the two Texas high performance concrete highway bridge projects which were the focus of this study is reported in this chapter. Details of the Louetta Road Overpass in Houston, Texas are presented first, followed by details of the North Concho River/U.S. 87/S.O.R.R. Overpass in San Angelo, Texas. Each of the two bridges has several unique features, some of which are a result of utilizing HPC in the design and construction processes. These unique features are discussed in this chapter, in addition to specific design parameters for the beams of each bridge, including span lengths, girder spacing, strand patterns, and design concrete strengths.

2.2 Louetta Road Overpass

2.2.1 *General Project Description*

The Louetta Road Overpass, shown in Figure 2.1, consists of a pair of three-span highway bridge structures on State Highway 249 in northwest Houston, Texas. The Northbound and Southbound bridges of the Louetta Road Overpass are part of a 4.8 km (3.0 mi.) improvement of S.H. 249 from a non-freeway facility to a freeway facility in northwest Harris County. A sketch of the site location may be found in Figure 2.2. The Northbound Overpass was designed to carry three lanes of traffic, while the Southbound Overpass was designed to carry three lanes of traffic with an additional exit lane. After construction was completed, but before the original structures were opened to traffic, the bridges were expanded by one lane in each direction to accommodate an increase in the projected usage for S.H. 249.

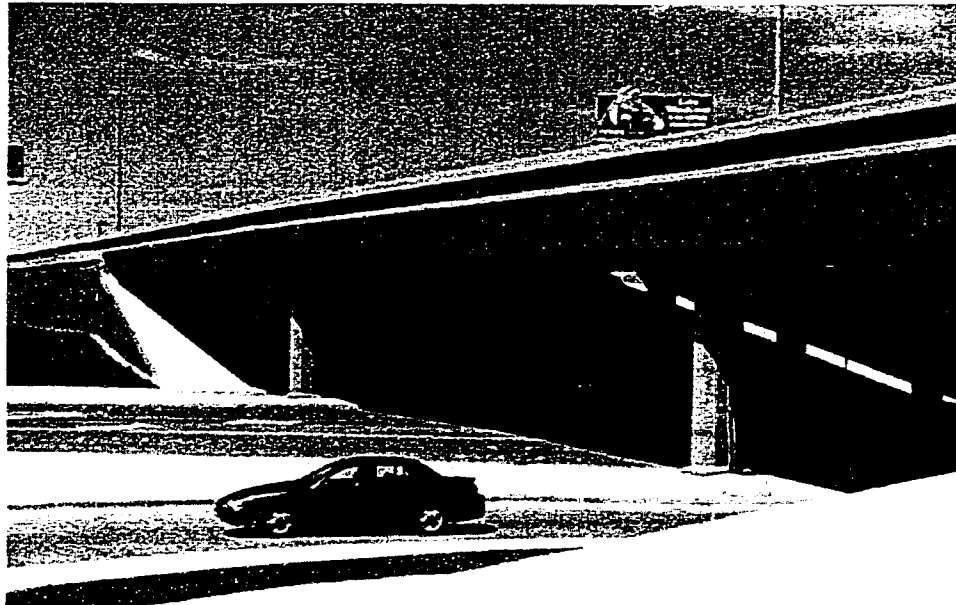


Figure 2.1- Louetta Road Overpass

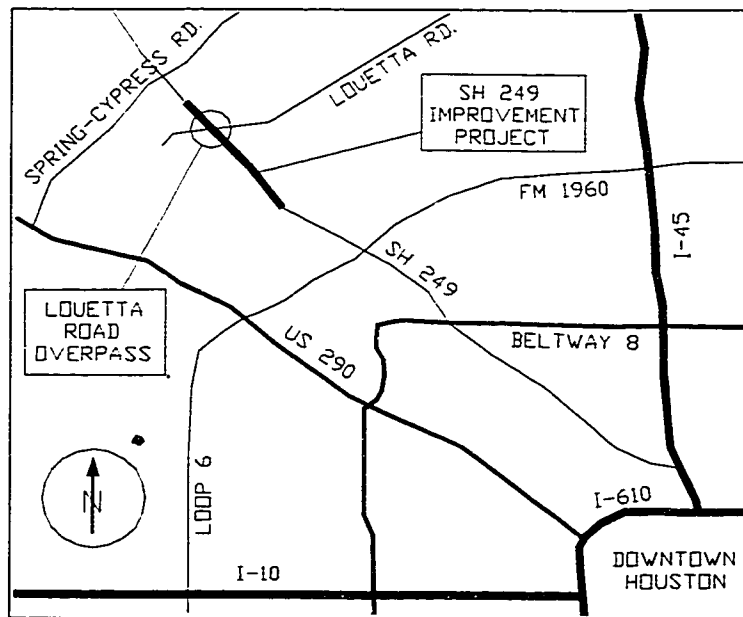
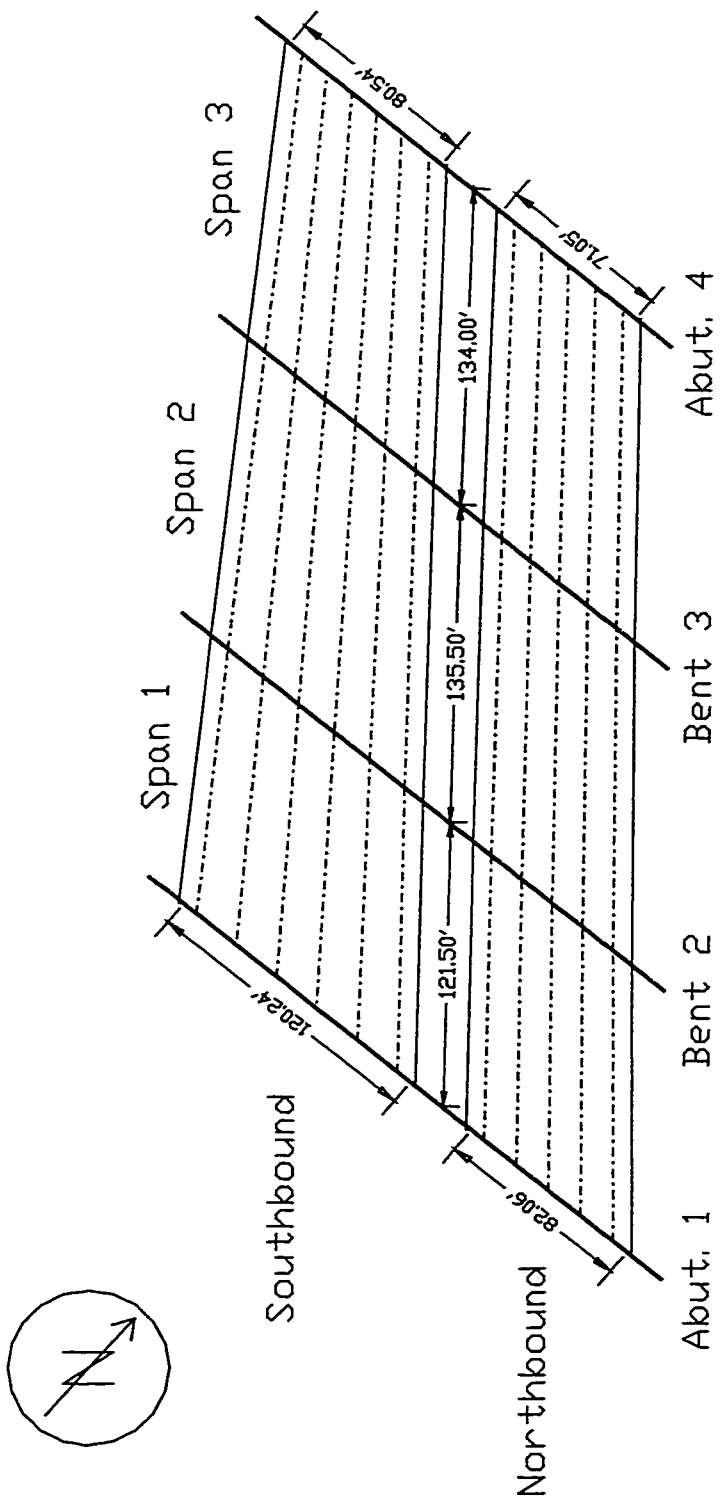


Figure 2.2 - Site of the Louetta Road Overpass in Northwest Houston, TX



LOUETTA ROAD OVERPASS (prior to widening)

1 ft. = 0.3048 m

Figure 2.3 - Plan of the Louetta Road Overpass

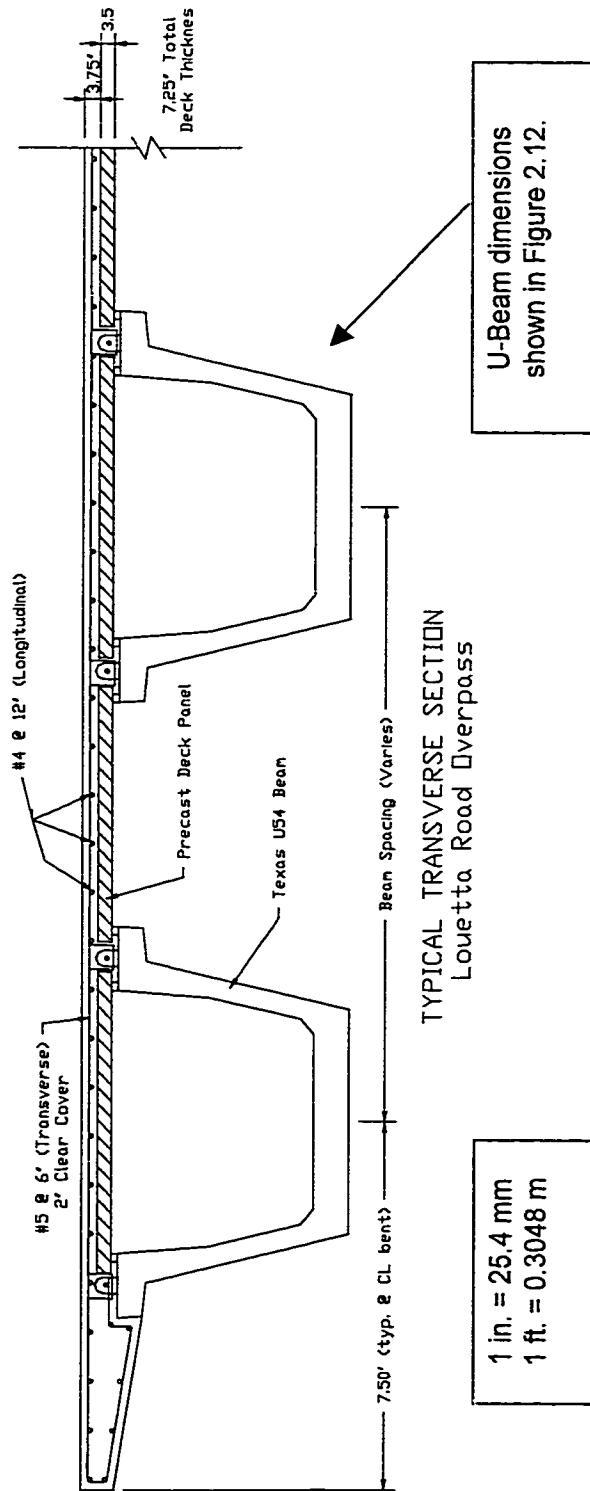


Figure 2.4 - Partial Roadway Cross-Section (Louetta Road Overpass)

A plan view of the original design of the Louetta Road Overpass (prior to widening of the bridges) is presented in Figure 2.3. Each of the bridges span Louetta Road, an eight-lane arterial roadway, and two U-turn lanes for the access roads of S.H. 249. The total length of the three-span structures is 119 m (391 ft.), with span lengths of 37.0, 41.3, and 40.8 m (121.5, 135.5, and 134.0 ft.) along the centerline of S.H. 249. Each span in the original Northbound bridge consists of five Texas U54 beams, and each span in the original Southbound bridge consists of six U54 beams.

A partial roadway cross-section is shown in Figure 2.4. The 184 mm (7.25 in.) bridge deck is designed to act compositely with the Texas U54 beams, and consists of a 95 mm (3.75 in.) reinforced concrete cast-in-place portion over 89 mm (3.50 in.) thick stay-in-place precast concrete panels. The use of stay-in-place precast concrete deck panels is preferred in Texas [113], as they are relatively inexpensive, can be easily erected, and provide a safe working area for the placement of cast-in-place concrete in the remaining portion of the deck. Panels are supported on fiberboard strips and span between adjacent top flanges of the U-beams (either over a single beam or between adjacent beams). The erection of precast panels at the jobsite is shown in Figure 2.5. Panels in the two Louetta bridges are generally 2.44 m (8.00 ft) long (dimension parallel to beams) and are of varying width (dimension perpendicular to beams) since the beam spacing is not constant. The beam spacing varies because the beams in the skewed bridges are not perfectly parallel.

Each precast panel is transversely prestressed (strands run perpendicular to beam lines) with 9.5 mm (0.38 in.) diameter strands spaced at 150 mm (6 in.). This prestress helps resist tensile stresses in the deck due to flexural action between beams. Each deck panel is also reinforced with welded wire fabric (WWF 12x4xW3.5xW7.5) at middepth of the 89 mm (3.50 in.) total panel thickness. Typical cast-in-place deck reinforcement consists of Grade 60 #4 steel reinforcing bars spaced longitudinally at 305 mm (12 in.) and Grade 60 #5 steel reinforcing bars spaced transversely at 153 mm (6 in.). Additional reinforcement is located between deck panels directly above beam flanges, and directly above piers and abutments where deck panels were terminated.

Deck concrete was placed using a concrete pump and compacted using internal vibrators and a rolling screed, as shown in Figure 2.6 and Figure 2.7, respectively. For each bridge, all three spans of the cast-in-place portion of the deck were placed in a single pour. Shortly after placement of the concrete, tooled control joints were placed at each interior bent to control cracking. Expansion joints are located only at the ends of the three-

span bridges. This method of deck construction is common in Texas, and this type of deck is often referred to as a “poor boy” slab. With a “poor boy” slab, some degree of continuity between adjacent spans is typically provided by the reinforcement running across the control joints. However, each span was assumed to be simply-supported for design.

Each beam is supported on an individual pier, as shown in Figure 2.8 and Figure 2.9. This provides an aesthetically pleasing alternative to the standard column and bent cap substructure widely used in Texas. Piers were constructed using precast reinforced concrete segments, which were post-tensioned at the jobsite. Each segment is 0.99 m (3.25 ft.) long, 0.99 m (3.25 ft.) wide, and either 1.2 or 1.5 m (4.0 or 5.0 ft.) tall. A 1.12 m (3.67 ft.) tall precast capital is located at the top of each pier.

All components of the Louetta Road Overpass were constructed using high performance concrete. Design concrete strengths for the beams, precast piers, precast deck panels, and cast-in-place decks are listed in Table 2.1. Mix proportions for each of these elements are presented in Section 4.2, and additional information on the classification of these mixes as strength-related or durability-related HPC may be found in Section 4.1.2.

As previously mentioned, both the Northbound and Southbound bridges were widened before they were opened to traffic. In anticipation of the widening, the original bridge deck on the widened side was poured only to the center of the top flange of the original exterior girder. That is, the overhang on the widened side of each bridge was not constructed during the original deck pour. The termination of the original bridge deck and the preparation for casting of the additional (widened) deck area can be seen in Figure 2.10 and Figure 2.11.



Figure 2.5 - Erection of Precast Panels (Louetta Road Overpass)



Figure 2.6 - Placement of Louetta Cast-in-Place Deck Concrete



Figure 2.7 - Screeding of Louetta Cast-in-Place Deck Concrete



Figure 2.8 - Louetta Road Overpass Substructure



Figure 2.9 - Louetta Road Overpass Substructure

Table 2.1 - Design Concrete Strengths for the Louetta Road Overpass

	Northbound Bridge	Southbound Bridge
Prestressed Beams	9,800 to 13,100 psi	9,800 to 13,100 psi
Precast Deck Panels	8,000 psi	8,000 psi
Cast-in-Place Decks	4,000 psi	8,000 psi
Precast Pier Segments	10,000 psi	10,000 psi
1 psi = 0.006895 MPa		



Figure 2.10 - Completed Original Louetta Bridges (Prior to Widening)

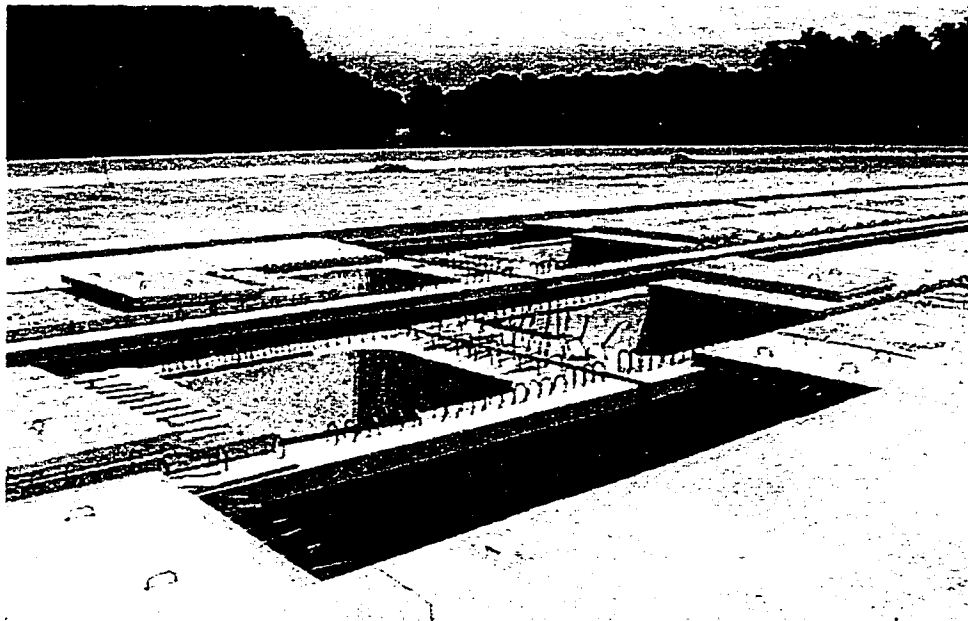


Figure 2.11 - Additional Beams and Panels for Louetta Bridge Widening

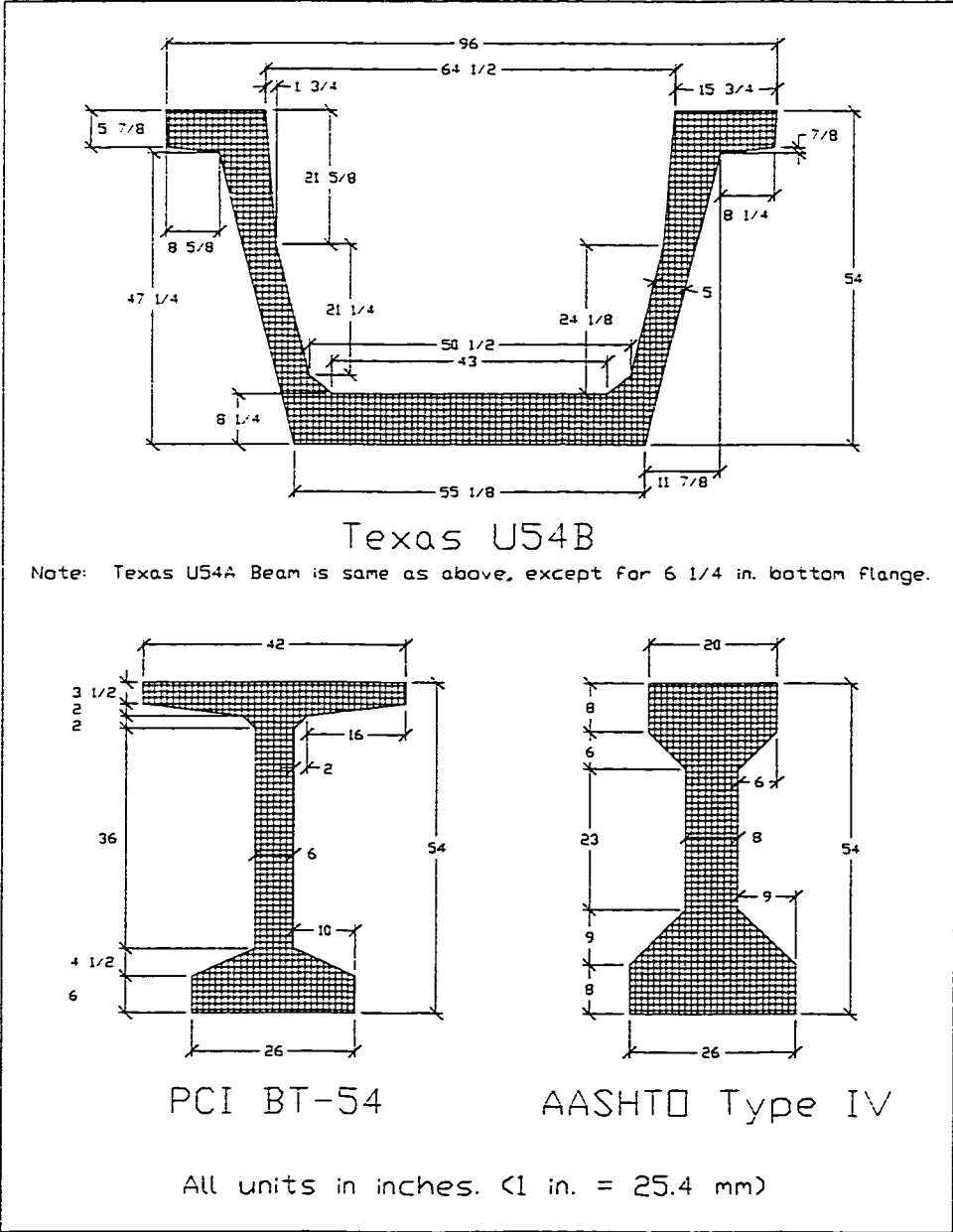


Figure 2.12 - Selected 1370 mm (54 in.) Deep Girder Cross-Sections

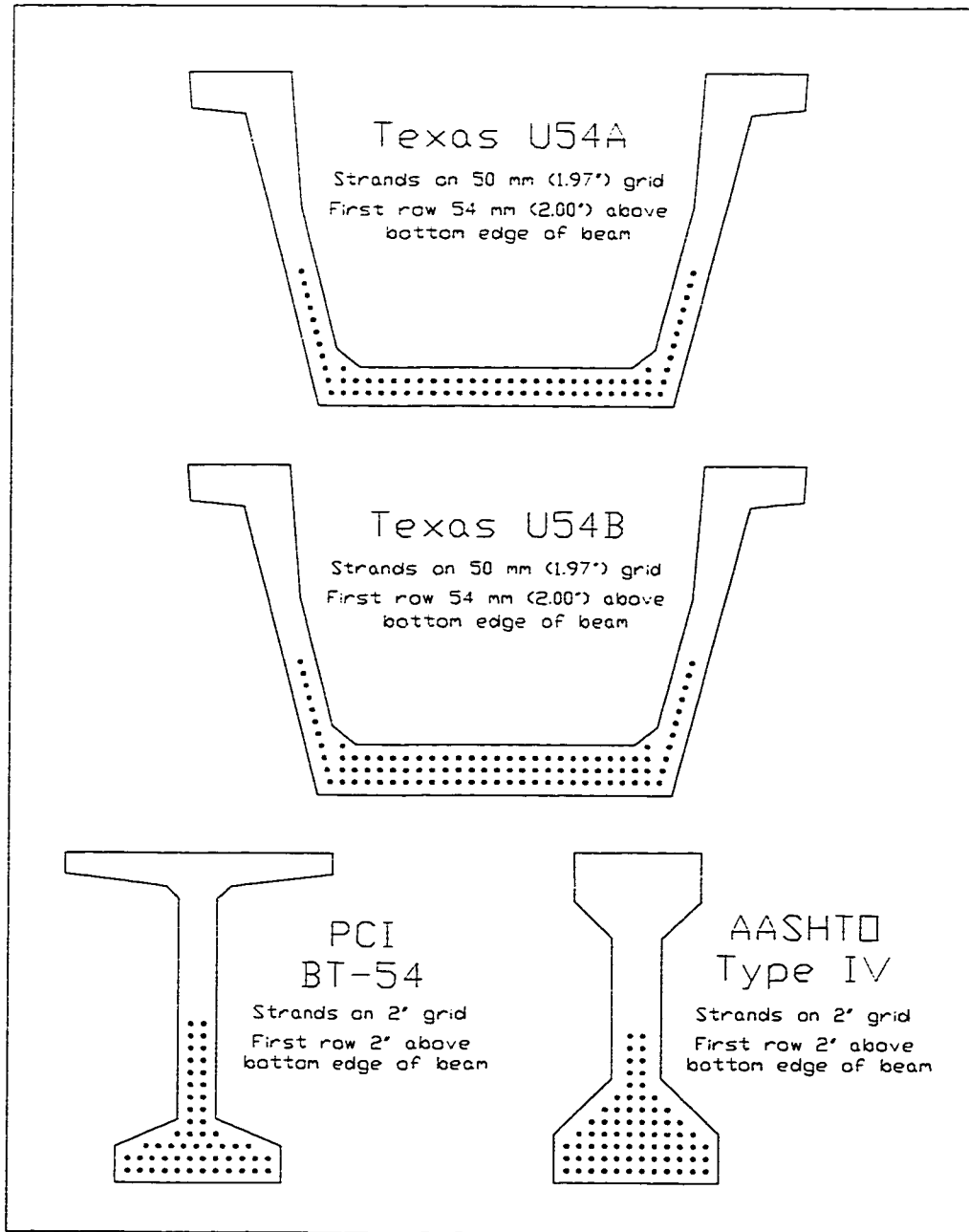


Figure 2.13 - Pretensioned Strand Patterns for Selected 1370 mm (54 in.) Deep Girder Cross-Sections

**Table 2.2 - Comparison of Section Properties and Guyon Efficiency for Selected
1370 mm (54 in.) Deep Girder Cross-Sections**

		PCI BT-54	AASHTO Type IV	Texas U54A	Texas U54B
<i>Cross-Section Properties</i>					
A	(in. ²)	659	789	1025	1121
I _x	(in. ⁴)	268,050	260,400	380,420	404,230
I _y	(in. ⁴)	37,310	24,370	897,800	917,080
r _x	(in.)	20.17	18.17	19.27	18.99
r _y	(in.)	7.52	5.56	29.60	28.60
y _{bot}	(in.)	27.63	24.73	23.88	22.48
y _{top}	(in.)	26.37	29.27	30.12	31.52
S _{bot}	(in. ³)	9,701	10,530	15,931	17,982
S _{top}	(in. ³)	10,165	8,897	12,630	12,825
Weight ¹	(kip/ft.)	0.686	0.822	1.068	1.168
ρ (Guyon Efficiency - Equation 2.1)		0.558	0.456	0.516	0.509
1 in. = 25.4 mm; 1 kip/ft. = 14.6 kN/m Note: Gross section properties shown.					
¹ Assumes unit weight of 150 pcf (2400 kg/m ³).					

2.2.2 Texas U54 Beam

As mentioned in Section 2.2, the Texas U-beam was used for the construction of the Louetta Road Overpass. The Texas U-Beam is an open-top trapezoidal cross-section developed by the Texas Department Transportation (TxDOT) during the late 1980's and early 1990's as an alternative to standard I-shaped and closed-box girders. As discussed by Ralls et. al. [113], the section was designed with both economy and aesthetics in mind. The section was developed in SI units in accordance with the federal metrication effort, and is fabricated in both 1016 and 1372 mm (40 and 54 in.) depths. Each of these depths is also produced with two different bottom flange thicknesses, resulting in four U-beam cross-sections: U40A, U40B, U54A, and U54B. The U40A and U54A sections have a 158 mm (6.2 in.) deep bottom flange which accommodates two rows of strands, while the U40B and U54B sections have a 208 mm (8.2 in.) deep bottom flange which accommodates three

rows of strands. The dimensions and strand patterns for the U54 cross-sections are presented in Figure 2.12 and Figure 2.13, respectively.

Also shown in Figure 2.12 and Figure 2.13 are dimensions and strand patterns for two other 1370 mm (54 in.) deep cross-sections, the American Association of State Highway and Transportation Officials (AASHTO) Type IV and the Precast/Prestressed Concrete Institute (PCI) BT-54. Section properties and efficiency parameters for the four 1370 mm (54 in.) deep sections shown in Figure 2.12 and Figure 2.13 are listed in Table 2.2. The AASHTO Type IV is a standard cross-section, developed in the late 1950's by AASHTO and PCI, which has been widely used in Texas and throughout the United States. The PCI BT-54 is a bulb-tee type cross-section developed by the PCI Committee on Concrete Bridges in the late 1980's. The BT-54 was designed to be a cross-section with increased efficiency that could still be constructed and handled with ease [119]. The BT-54 is currently used in several states around the country, and similar cross-sections have been developed by Washington, Florida, Nebraska, and other states.

According to Guyon [60], the structural efficiency of a prestressed cross-section is dependent on both the top and bottom fiber section moduli. By maximizing the section moduli for a given cross-sectional area, Guyon derived an expression for structural efficiency. The efficiency factor, ρ , is defined as:

$$\rho = \frac{I_x}{A y_{\text{bot}} y_{\text{top}}} = \frac{r_x^2}{y_{\text{bot}} y_{\text{top}}}$$

Equation 2.1

where

- ρ = structural efficiency of the cross-section
- I_x = cross-sectional moment of inertia about the horizontal centroidal axis
- A = area of the cross-section
- y_{bot} = distance from the centroid of the section to the extreme bottom fiber
- y_{top} = distance from the centroid of the section to the extreme top fiber
- r_x = radius of gyration about the horizontal centroidal axis = $(I_x / A)^{1/2}$

Of the four cross-sections being compared, the PCI-54 has the highest structural efficiency as computed by Guyon's formula. The PCI BT-54 has most of its area concentrated near the extreme fibers of the flanges, at a large distance from the centroid of the section. The U54A and U54B beams also have a substantial portion of their area concentrated near the extreme fibers, but lose some structural efficiency because they each have two webs. While less efficient than the PCI BT-54, the Texas U54 beams are clearly more efficient than the AASHTO Type IV. The Type IV has a relatively small portion of its flange area located near the extreme fibers, and also has a wide web.

For pretensioned girders, the layout of the strand pattern is also important in determining the design efficiency and capacity of a section. The importance of the strand pattern is illustrated by first converting the familiar allowable stress inequality for bottom fiber stress under service loads into an equivalent moment equation. The common allowable stress inequality is given in Equation 2.2:

$$-\frac{F}{A} - \frac{Fe}{S_{bot}} + \frac{M_{self-wt}}{S_{bot}} + \frac{M_{non-comp}}{S_{bot}} + \frac{M_{comp}}{S'_{bot}} \leq f_{allow_{bot}}$$

Equation 2.2

Multiplying through by the bottom fiber section modulus replaces each stress term with a moment term. The result is shown in Equation 2.3:

$$-\frac{FS_{bot}}{A} - Fe + M_{self-wt} + M_{non-comp} + \lambda_{bot}M_{comp} \leq f_{allow_{bot}}S_{bot}$$

where $\lambda_{bot} = S_{bot}/S'_{bot}$

Equation 2.3

Grouping and rearranging terms yields Equation 2.4, the equivalent moment inequality for a prestressed beam based on bottom fiber allowable service stresses:

$$- M^*_{\text{prestress}_{\text{bot}}} + M^*_{\text{allowable}_{\text{bot}}} - M^*_{\text{self-wt}_{\text{bot}}} \geq M^*_{\text{applied-loads}_{\text{bot}}}$$

where:

$$\begin{cases} M^*_{\text{prestress}_{\text{bot}}} = - \left[\frac{FS_{\text{bot}}}{A} + Fe \right] \\ M^*_{\text{allowable}_{\text{bot}}} = S_{\text{bot}} \cdot [6\sqrt{f'_c}] \\ M^*_{\text{self-wt}_{\text{bot}}} = M_{\text{self-wt}} = \frac{w_{\text{bm}}L^2}{8} \\ M^*_{\text{applied-loads}_{\text{bot}}} = M_{\text{non-comp}} + \lambda_{\text{bot}}M_{\text{comp}} = \frac{w_{\text{non-comp}}L^2}{8} + \lambda_{\text{bot}} \frac{w_{\text{comp}}L^2}{8} \end{cases}$$

Equation 2.4

The left-hand side of Equation 2.4 represents the moment capacity of a given beam section with respect to unfactored applied loads. Note that loads acting on the composite section may be reduced by the factor λ_{bot} , the ratio of the noncomposite and composite section moduli.

$M^*_{\text{prestress}_{\text{bot}}}$ plotted in Figure 2.14 for the four 1370 mm (54 in.) deep cross-sections, represents the effective negative moment acting on the section due to prestress. This effective moment causes the same bottom fiber stress as the sum of axial and flexural stress due to prestress, but combines the effects into a single term. The effective bottom fiber prestress moment is a function of the number of strands, as well as the layout of the strand pattern. In the figure, strands are assumed to be placed in order from the bottom of the section upward, and prestress losses at the time of service load application are assumed to be 20 percent.

From Figure 2.14, it is clear that the Texas U54 beams can provide a substantially larger effective bottom fiber prestress moment than the other 1370 mm (54 in.) deep sections. They can accommodate a significantly larger number of strands in their bottom flanges. Furthermore, most of these strands are in the bottom flange of the section, and have enough eccentricity to be very efficient. The PCI BT-54 in contrast, although very efficient in terms of Guyon eccentricity, is limited in terms of $M^*_{\text{prestress}_{\text{bot}}}$ by its relatively small bottom flange.

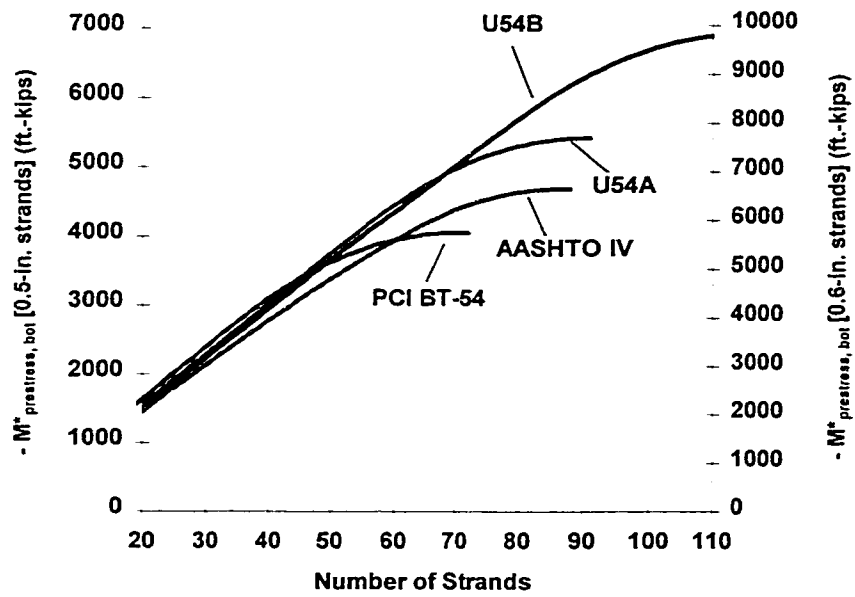


Figure 2.14 - Effective Bottom Fiber Moment Due to Prestress

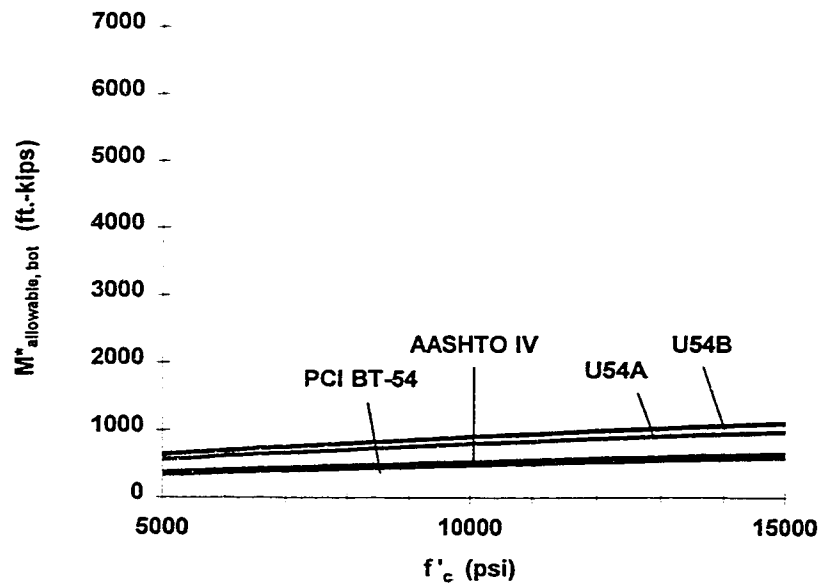


Figure 2.15 - Effective Bottom Fiber Moment Due to Allowable Stress

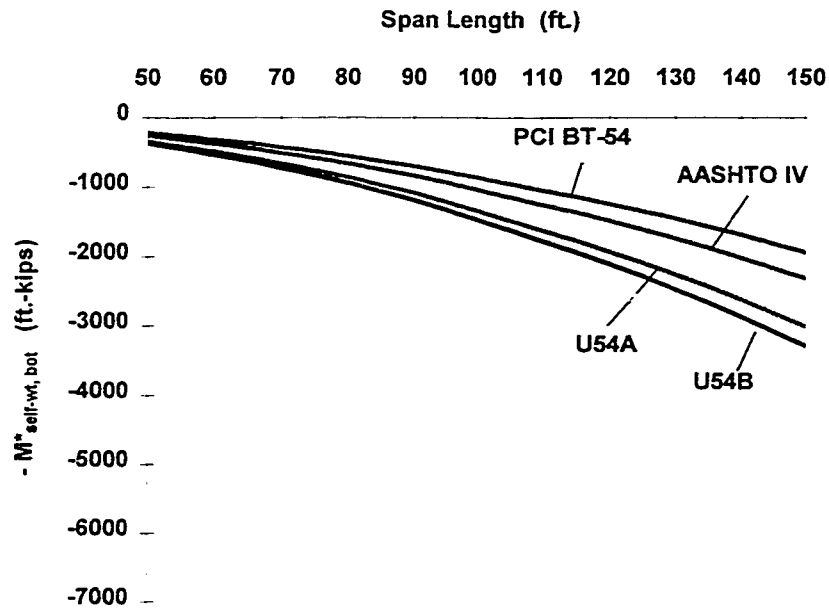


Figure 2.16 - Moment Due to Girder Self-Weight

$M_{\text{allowable, bot}}^*$ represents the acceptable net positive effective moment under all unfactored loads. When moved to the left hand side of Equation 2.4, it can be viewed as an additional effective moment offsetting the moments from applied loads. The magnitude of $M_{\text{allowable, bot}}^*$ is much lower than that of $M_{\text{prestress, bot}}^*$ and is shown as a function of concrete strength in Figure 2.15. The Texas U54 beams provide an advantage over the other 1370 mm (54 in.) deep sections because of their large section moduli.

The self-weight moment for the four sections is plotted in Figure 2.16 as a function of span length. $M_{\text{self-wt, bot}}^*$ is plotted as a negative value because this term reduces the total moment capacity in Equation 2.4. The high self-weight of the Texas U54 sections, as compared to the PCI Bt-54 and AASHTO Type IV sections, is clearly a disadvantage. Note that the magnitude of this term increases rapidly for long spans.

The net applied moment capacity, represented by the left hand side of Equation 2.4, is the algebraic sum of the ordinates shown in Figure 2.14, Figure 2.15, and Figure 2.16 for a given cross-section, concrete strength, and span length. Examination of the figures reveals that for designs with a relatively small number of strands, lower concrete strengths,

and shorter span lengths, the difference in capacity between the sections is small. However, for designs with a large number of strands, high concrete strengths, and long spans, the Texas U54 sections show a clear benefit. The U54 sections may provide as much as 22,000 to 29,000 kN/m (1500 to 2000 ft.-kips) more applied load capacity, especially if 15 mm (0.6 in.) diameter strands are used.

As discussed in Section 1.4.2, the bottom fiber tensile stress will govern most designs with HPC. Regardless, a similar analysis can be performed using top fiber stresses. In this case, the magnitude of $M_{\text{prestress, top}}^*$ will be small because the axial compression and flexural tension resulting from prestress counteract each other at the top fiber. $M_{\text{allowable, top}}^*$, however, will be substantially higher because it is based on allowable compressive stress rather than allowable tensile stress. In terms of net capacity, it can be shown that the U54 sections are again most efficient.

The preceding discussion shows the clear benefits of the Texas U54 sections for design with high performance concrete. These designs will typically require a high prestress force to offset increased moments from longer spans and/or larger spacing. The large bottom flange of the U54 sections can accommodate this high prestress force requirement, while their large section moduli help to offset the negative effects of the increased beam weight. It is estimated by Ralls et. al. [113] that depending on the overall roadway width, a single U-beam (U40 or U54) replaces 1.7 to 2.0 I-shaped beams of the same depth. However, a typical Texas U-beam weighs only about 40 percent more than a typical I-shaped girder of the same depth. A 20 to 40 percent reduction in beam weight can therefore be expected for a given span when I-shaped beams, including the Texas standard AASHTO Type IV beam, are replaced by U-beams of the same depth.

Another benefit of the Texas U54 beams is their high lateral stiffness. As can be seen in Table 2.2, the U54A and U54B actually have higher moments of inertia in the horizontal direction than the vertical direction. This high lateral stiffness eliminates any problems with stability of girders during transportation and handling, as well as the potential for "sweep", or horizontal deflection at release of prestress. Internal diaphragms are cast in the U-beams, as shown in Figure 2.17, to provide lateral stiffness to the individual webs of each beam. Stability issues will be discussed in more detail in Chapter 10.

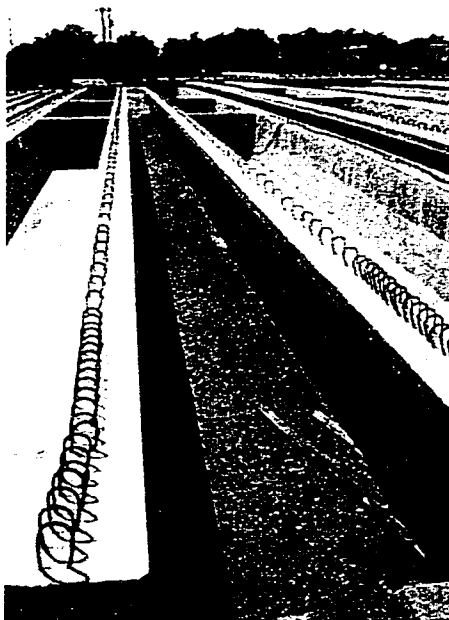


Figure 2.17 - Internal Diaphragms in Texas U-Beam

Two design details for the U-beams differ from those for typical I-shaped girders. Draping is not used to control end stresses with the U-beams because of the sloped webs. Instead, debonding is used to control stresses, and the same standard debonding criteria as used in Texas box girders is applied [113]. Also, U-beams are typically supported by three elastomeric bearing pads — two at one end of the span and one at the opposite end. This detail prevents the beams from rocking on the supports, as might occur with one support at each end or with two supports at each end.

2.2.3 Louetta Beam Design Details

The design of beams for the Louetta Road Overpass was performed by the Bridge Division of the Texas Department of Transportation. Beams were designed in accordance with the 1992 *AASHTO Standard Specifications* [4]. Simply-supported spans, unshored deck construction, and HS20-44 live load were assumed. Design and analysis of beams was performed with the assistance of PSTRS14 [130], a computer program developed by the Bridge Division in 1990.

The PSTRS14 computer program computes strand layout and concrete strengths required to satisfy allowable stress, ultimate strength, and shear strength criteria. Maximum beam camber is estimated based on the hyperbolic time-dependent functions proposed by Sinno [122]. Elastic deflections under each component of dead load are also computed, but neither maximum camber nor elastic deflection calculations are used as design criteria. Prestress losses are computed using the method described in the 1989 *AASHTO Standard Specifications* [5], with the initial prestress loss (at release) assumed to be equal to the elastic shortening loss plus half of the total relaxation loss.

A few special assumptions and allowances were used in the design of the HPC girders for the Louetta Road Overpass. Allowable tensile stresses at release and service were increased by 33% over those specified by the *AASHTO Standard Specifications* [4] to take advantage of the increased tensile strength of HPC [39]. Thus, allowable tensile stresses were $10\sqrt{f'_{ci}}$ and $8\sqrt{f'_c}$ at release and service, respectively, instead of $7.5\sqrt{f'_{ci}}$ and $6\sqrt{f'_c}$. Allowable compressive stresses were not modified, but were kept as $0.60(f'_c)$ at release and $0.40(f'_c)$ at service. In an attempt to control potentially excessive deflections, a minimum modulus of elasticity of 41.4 GPa (6.0×10^6 psi) was specified and used for all calculations. Note that there was no consideration of the generally improved creep and shrinkage properties of HPC in the original beam designs.

Specific design details for the beams in the Northbound and Southbound bridges are presented in Table 2.3 and Table 2.4, respectively. Although the span length and girder spacing are different for each of the 33 original beams, only seven unique beam designs were used for simplicity. Allowable stress criteria governed the beam designs in all cases. Either the U54A or U54B section was utilized for each beam, depending on the number of strands required. Grade 270 low-relaxation 15 mm (0.6 in.) diameter strands were used at 50 mm (2.0 in.) spacing on centers in all girders, except for the three interior girders in Span 1 of the Northbound bridge, which used 13 mm (0.5 in.) diameter strands. Laboratory and field testing to determine the transfer and development length of 15 mm (0.6 in.) strands in HPC was required for design approval, and results of the tests are discussed by Gross and Burns [58]. A maximum of 87 strands was required for a single girder. The strand layout in the bottom flange of a typical Louetta beam is shown in Figure 2.18.

Table 2.3 - Beam Design Details for the Northbound Louetta Road Overpass

Span / Beam ¹	Beam Length (ft.)	Length- CL to CL Bearings (ft.)	Beam Spacing ² (ft.)	Beam Type	No. of 0.6 in. Strands ³	Specified Release Strength (psi)	Specified 56-day Strength (psi)
N11	121.17	119.86	13.97 ⁺	U54B	68	7,700	11,600
N12	121.74	120.42	12.94	U54B	76 @	6,900	9,800
N13	122.30	120.98	12.88	U54B	76 @	6,900	9,800
N14	122.87	121.54	12.82	U54B	76 @	6,900	9,800
N15	123.44	122.11	13.91	U54B	68	7,700	11,600
# N21	135.26	134.17	13.66 ⁺	U54B	87	8,800	13,100
# N22	135.83	134.74	12.33	U54B	68	7,700	11,600
# N23	136.41	135.32	12.28	U54B	68	7,700	11,600
N24	136.99	135.89	12.22	U54B	68	7,700	11,600
N25	137.57	136.48	13.61	U54B	87	8,800	13,100
# N31	133.67	132.38	13.30 ⁺	U54B	80	8,800	13,100
# N32	134.18	132.89	11.61	U54A	64	7,700	11,600
# N33	134.70	133.40	11.56	U54A	64	7,700	11,600
N34	135.22	133.92	11.52	U54A	64	7,700	11,600
N35	135.74	134.43	13.26	U54B	80	8,800	13,100

1 ft. = 0.3048 m; 1 psi = 0.006895 MPa

Note: Table does not include three beams used in widening of bridge.

¹ Beam designation discussed in Section 3.4.1 (xyz: x=bridge, y=span, z=beam).
"#" denotes beam with instrumentation.

² Average of perpendicular distance to adjacent beams (or overhang) at midspan.

³ Debonding used to control end stresses. 24 to 34 strands debonded per beam.

@ 13 mm (0.5 in.) Strands

⁺ Based on original design with 2.29 m (7.5 ft.) overhang (does not consider widening of bridge).

Table 2.4 - Beam Design Details for the Southbound Louetta Road Overpass

Span / Beam ¹	Beam Length (ft.)	Length-CL to CL Bearings (ft.)	Beam Spacing ² (ft.)	Beam Type	No. of 0.6 in. Strands ³	Specified Release Strength (psi)	Specified 56-day Strength (psi)
S11	113.52	112.27	15.81	U54B	68	7,700	11,600
S12	114.94	113.68	16.62	U54A	64	7,700	11,600
S13	116.40	115.13	16.41	U54A	64	7,700	11,600
# S14	117.91	116.62	16.20	U54A	64	7,700	11,600
# S15	119.44	118.15	16.00	U54A	64	7,700	11,600
# S16	121.02	119.71	15.50 *	U54B	68	7,700	11,600
S21	127.04	125.95	14.72	U54B	87	8,800	13,100
S22	128.56	127.48	14.45	U54B	68	7,700	11,600
S23	130.14	129.05	14.27	U54B	68	7,700	11,600
# S24	131.75	130.66	14.10	U54B	68	7,700	11,600
# S25	133.40	132.31	13.92	U54B	68	7,700	11,600
# S26	135.09	134.00	14.46 *	U54B	87	8,800	13,100
S31	126.30	125.06	13.62	U54B	76	7,700	11,600
S32	127.67	126.43	12.25	U54A	60	6,900	9,800
S33	129.08	127.83	12.11	U54A	60	6,900	9,800
S34	130.52	129.26	11.98	U54A	60	6,900	9,800
S35	132.00	130.72	11.84	U54A	60	6,900	9,800
S36	133.50	132.22	13.42 *	U54B	76	7,700	11,600

1 ft. = 0.3048 m; 1 psi = 0.006895 MPa

Note: Table does not include three beams used in widening of bridge.

¹ Beam designation discussed in Section 3.4.1 (xyz: x=bridge, y=span, z=beam).
"#" denotes beam with instrumentation.

² Average of perpendicular distance to adjacent beams (or overhang) at midspan.

³ Debonding used to control end stresses. 24 to 34 strands debonded per beam.

* Based on original design with 2.29 m (7.5 ft.) overhang (does not consider widening of bridge).

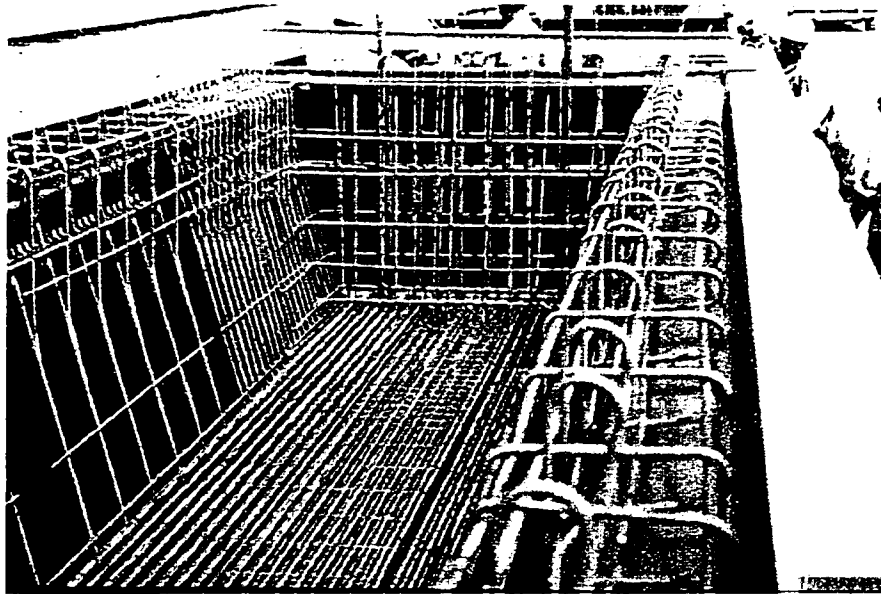


Figure 2.18 - Louetta U-Beam During Fabrication



Figure 2.19 - Reinforcement in the Skewed End Block of a Louetta Beam

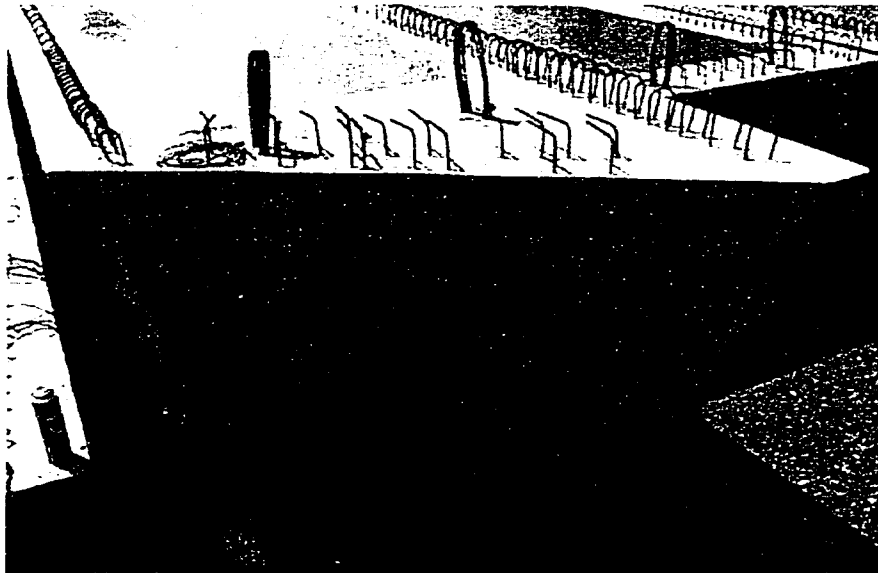


Figure 2.20 - Skewed End Block in a Completed Louetta Beam

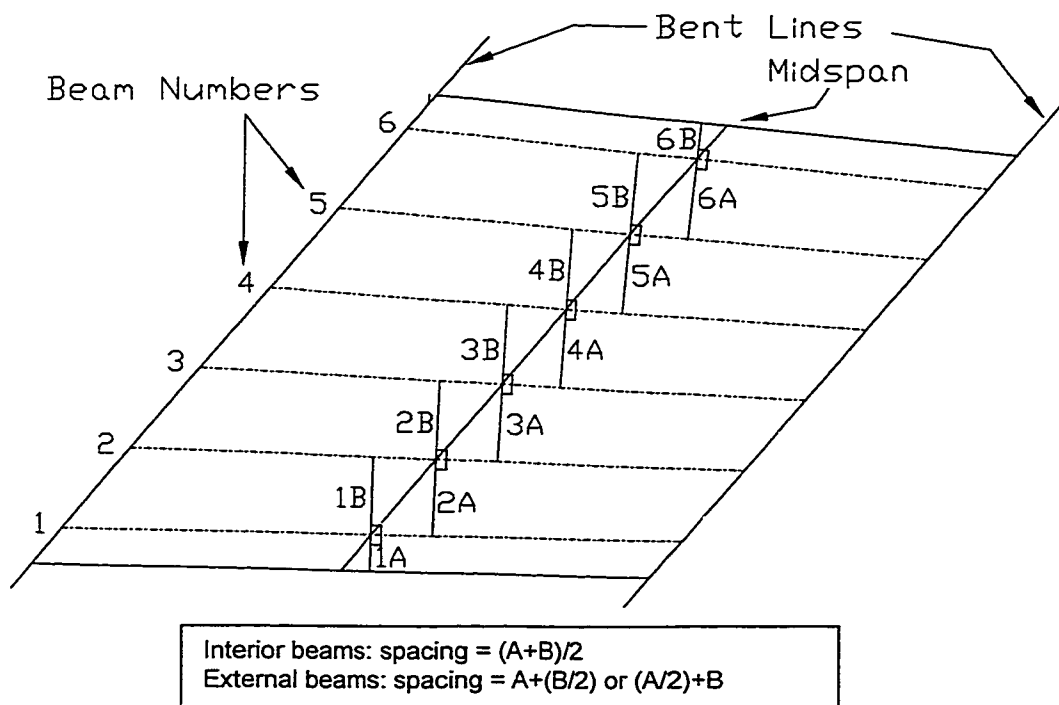


Figure 2.21 - Method Used to Determine Beam Spacing

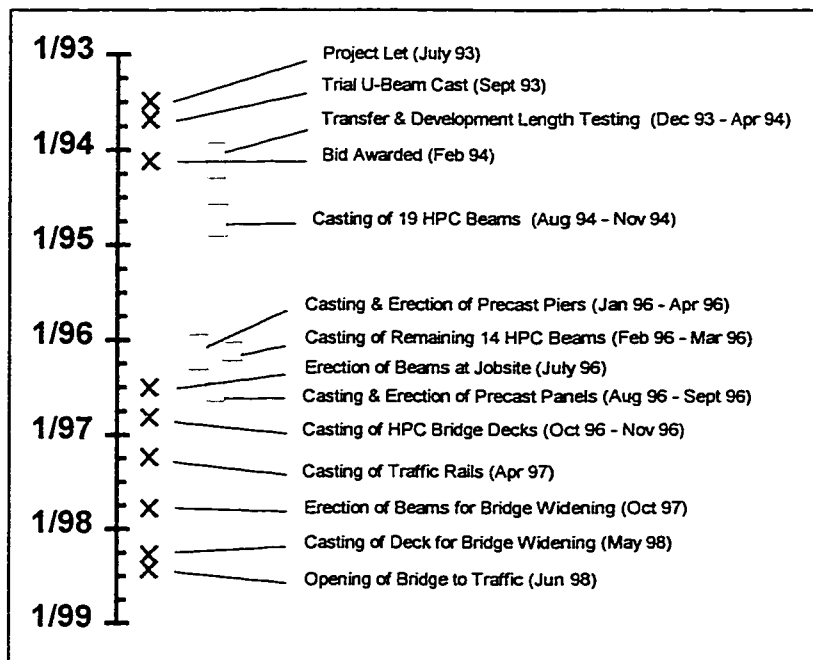


Figure 2.22 - Timeline for Construction of the Louetta Road Overpass

Shear reinforcement for a typical Louetta U-beam can also be seen in Figure 2.18. Shear reinforcement consists of vertical Grade 60 #4 steel reinforcing bars, assembled in welded wire fabric sheets to facilitate placement. These stirrups are located at 102 mm (4 in.) for the first 2.13 m (7.0 ft.), 305 mm (12 in.) for the next 1.83 m (6.0 ft.), and 457 mm (18 in.) thereafter. Anchorage zone reinforcement required to resist tensile stresses at the beam ends resulting from release of prestress consists of six Grade 60 #5 steel reinforcing bars at each beam end. More details related to the mild steel reinforcement, as well as a detailed discussion of the design methodology for the Louetta beams, may be found in the project report by Barrios et. al. [23].

As a consequence of the site layout, 22 of the 33 original beams were designed with skewed ends that would line up with the back wall of the abutments. The skew angle, relative to a line perpendicular to the beam axis, ranged from 32.6° to 39.4°. The fabricator was given two options for the skewed beam end, including casting a constant thickness end block parallel to the skew, or casting a large end block with one side perpendicular to the beam axis. The fabricator chose the second option, which called for a massive end block, so that standard void forms did not require modification. As can be seen in Figure 2.19, a

tremendous amount of reinforcement is located in these skewed end blocks. An end block in a completed beam is shown in Figure 2.20.

As previously mentioned, the spacing for each beam was unique because of the skewed layout of the bent lines and beam lines. Even across a single span, the beam spacing varied because girders were not parallel. The beam spacing reported for the beams in Table 2.3 and Table 2.4 was computed as shown schematically in Figure 2.21. The spacing was computed as the average of the perpendicular distance to adjacent beams at midspan of the beam in question. A 2.29 m (7.50 ft.) overhang was assumed for exterior girders. Beam spacing ranged from 3.61 m (11.84 ft.) to 5.07 m (16.62 ft.) for interior girders and 4.02 m (13.42 ft.) to 4.82 m (15.81 ft.) for exterior girders, with much more variation in the Southbound bridge than in the Northbound. These relatively large girder spacings are a direct result of the use of HPC in the Louetta bridges.

2.2.4 Contractors, Fabricators, and Project Timeline

Williams Brothers Construction Company, Inc. of Houston, Texas was the general contractor for the construction of the Louetta Road Overpass. Prestressed concrete beams were fabricated at Texas Concrete Company, which is located in Victoria, Texas, approximately 220 km (140 mi.) southwest of the Louetta jobsite in Houston. Precast pier segments and precast deck panels were fabricated at Houston Prestress Products in east Houston, about 50 km (30 mi.) from the Louetta jobsite. All ready-mixed concrete for the jobsite, including concrete for cast-in-place bridge decks, was supplied by Lopez-Gloria Ready-Mixed Concrete of Houston, Texas.

A timeline showing the stages of the construction of the Louetta Road Overpass is presented in Figure 2.22. The S.H. 249 improvement project, of which the Louetta Road Overpass is a part, was let in July 1993 and the bid was awarded in February 1994. Nineteen of the HPC beams were cast in the fall of 1994, but delays at the jobsite caused the fabricator to wait until the spring of 1996 to cast the remaining fourteen beams. Most of the jobsite construction took place during 1996, with the bridge decks cast in late October and early November. Work on the widening of the Louetta Road Overpass began in the fall of 1997, but progressed slowly. The bridge was finally opened to traffic in June 1998, almost five years after the project was originally let.

2.3 North Concho River/U.S. 87/S.O.R.R. Overpass

2.3.1 General Project Description

The North Concho River/U.S. Highway 87/South Orient Railroad Overpass in San Angelo, Texas, commonly referred to as the North Concho River Overpass, can be seen in Figure 2.23. The North Concho River Overpass is part of a multi-stage freeway construction project on U.S. Highway 67 in central San Angelo, Texas. The portion of the freeway construction which includes the North Concho River Overpass has been planned for more than 25 years, and is very important to the community of San Angelo. The location of the bridge in San Angelo is shown in Figure 2.24.

The North Concho River Overpass consists of two adjacent mainlanes bridge structures — each of which is designed to accommodate two lanes of traffic and a shoulder — as well as two ramp structures. The high performance concrete Eastbound Overpass is an eight span structure, 290 m (950 ft.) in length. The conventional concrete Westbound Overpass is a 292 m (958 ft.) -long structure with nine spans. All components of the Eastbound bridge, but only selected segments of the cast-in-place decks in the Westbound bridge, were constructed using HPC. Each bridge crosses the North Concho River and a park road which runs along the river, two U-turn lanes for the access roads of U.S. 67, the South Orient Railroad, and U.S. Highway 87. U.S. Highway 87 is an eight-lane main highway which runs through central San Angelo. The plan of the main spans of the two bridges is shown in Figure 2.25. Spans 1 through 5 of the Eastbound Overpass and Spans 1 through 6 of the Westbound Overpass are considered main spans. The design of the remaining spans in the bridge was controlled by the geometry and clearance requirements associated with the railroad. Note that the roadway in the main spans of the Westbound Overpass is slightly wider than the roadway in the main spans of the Eastbound Overpass due to the layout of the ramps.

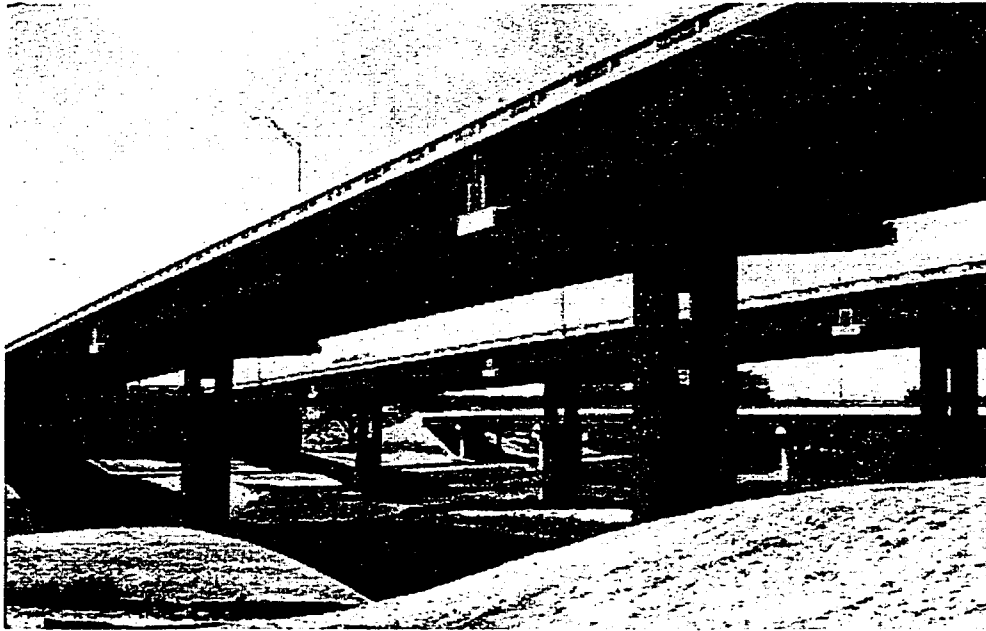


Figure 2.23 - North Concho River/U.S. 87/S.O.R.R. Overpass

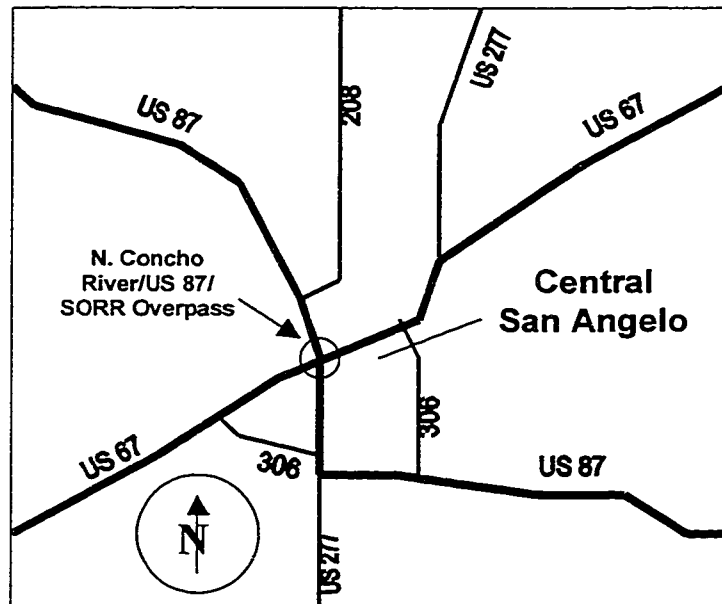
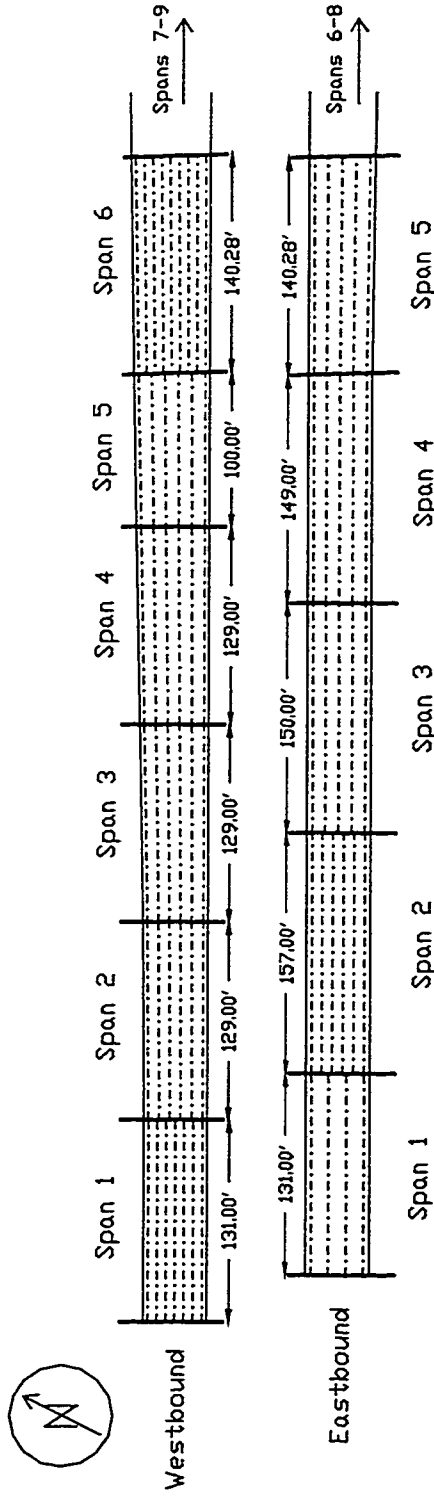


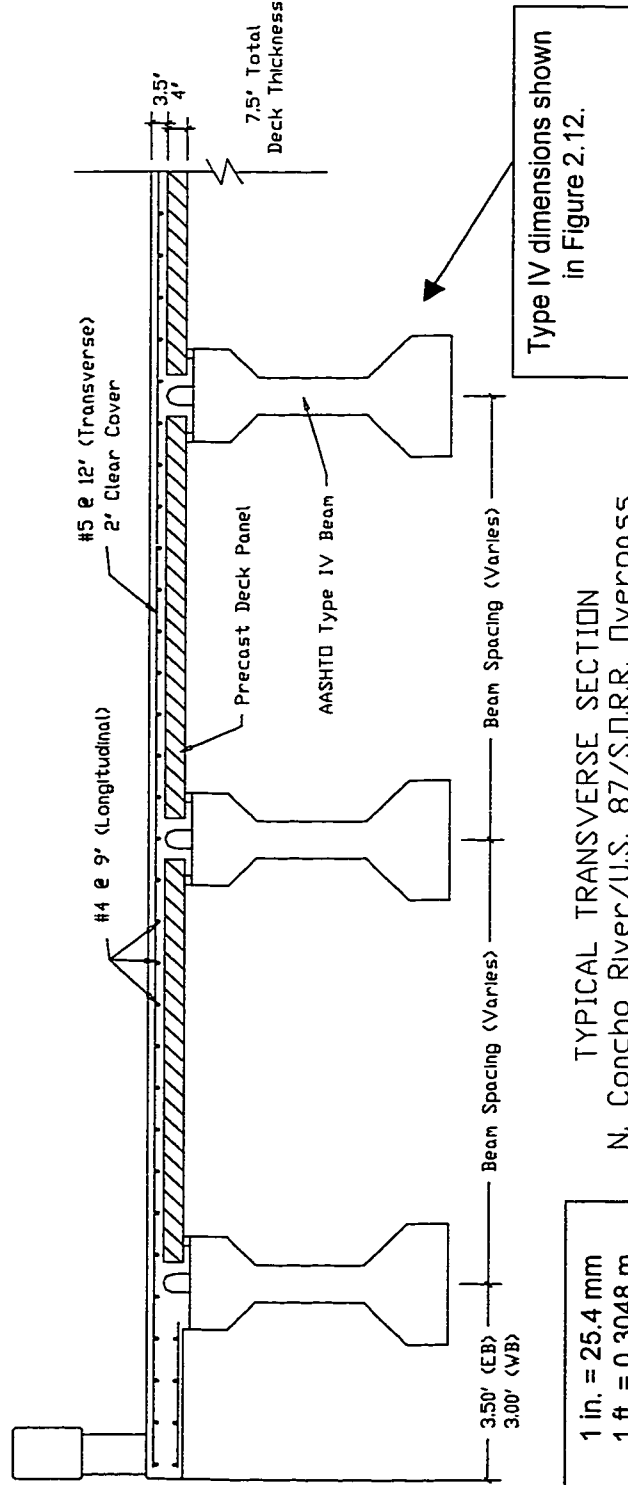
Figure 2.24 - Site of the N. Concho River Overpass in Central San Angelo, TX



NORTH CONCHO RIVER/U. S. 87/S. D. R. R. OVERPASS (San Angelo)
 (Only Main Spans Shown)

1 ft. = 0.3048 m

Figure 2.25 - Plan of the Main Spans of the North Concho River Overpass



TYPICAL TRANSVERSE SECTION
N. Concho River/U.S. 87/S.D.R.R. Overpass

Figure 2.26 - Partial Roadway Cross-Section (North Concho River Overpass)

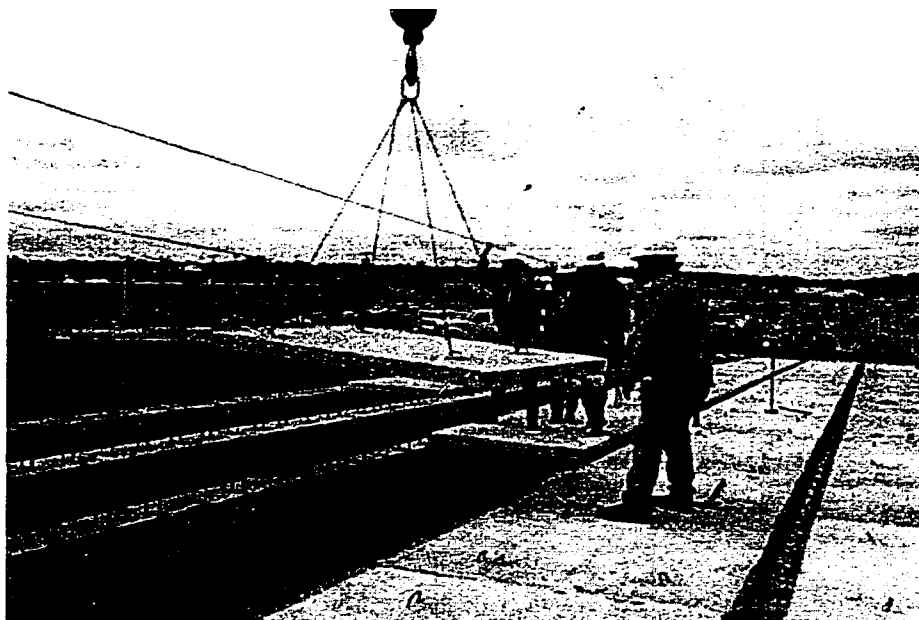


Figure 2.27 - Erection of Precast Panels in the Westbound Bridge

AASHTO Type IV girders were used for all beams in the main spans of each bridge. As can be seen in Figure 2.25, the Eastbound HPC bridge has significantly longer spans than the conventional concrete Westbound bridge. The maximum span length is 47.9 m (157 ft.) in Span 2 of the Eastbound bridge, which crosses the river. Note that Span 1 of each bridge has the same length and roadway width, providing a unique opportunity to compare the design and performance of identical spans with HPC and conventional concrete. Span 1 of the Westbound conventional concrete bridge required seven beams, while Span 1 of the Eastbound HPC bridge required only four beams.

A simple comparison of the design of the Eastbound and Westbound bridges is shown in Table 2.5. Note that this comparison is based strictly on efficiency, and does not consider the unit costs of conventional and high performance concrete. The relative costs of the two bridges are discussed in Chapter 10. Approximately 0.489 m of beams were required per square meter (0.149 ft. per sq. ft.) of bridge deck for the main spans of the Westbound bridge. However, only 0.404 m of beams were required per square meter (0.123 ft. per sq. ft.) of bridge deck in the main spans of the Eastbound HPC bridge. On the basis of this simple comparison, the Eastbound HPC bridge is about 17 percent more efficient than the Westbound bridge. In all, one less pier and fifteen fewer beams were

required for the main spans of the Eastbound bridge, despite a reduction in total deck area of only 13 percent.

A partial roadway cross-section for the bridges of the North Concho River Overpass is shown in Figure 2.26. The superstructure of each bridge consists of AASHTO Type IV girders with a 191 mm (7.5 in.) thick composite deck slab. The deck is composed of a layer of 102 mm (4.0 in.) thick precast deck panels and an 89 mm (3.5 in.) layer of cast-in-place concrete. Precast panels span between the top flanges of adjacent girders and are typically 2.44 m (8.00 ft.) in length (dimension parallel to beams). The width of precast panels is a function of the beam spacing and is constant within each span. The erection of precast panels in the Westbound bridge is shown in Figure 2.27.

As with the Louetta precast deck panels, each panel for the San Angelo bridge is transversely prestressed with 9.5 mm (0.38 in.) diameter strands spaced at 150 mm (6 in.) to resist flexural stresses in the deck between beams. A layer of welded wire fabric (WWF 12x4xW3.5xW7.5) reinforcement is also located at middepth of each panel. Typical longitudinal deck reinforcement in both the Eastbound and Westbound cast-in-place bridge decks consists of Grade 60 #4 steel reinforcing bars spaced at 229 mm (9 in.). Typical transverse cast-in-place deck reinforcement consists of Grade 60 #5 steel reinforcing bars spaced at 305 mm (12 in.), except that 254 mm (10 in.) spacing was used in Span 1 of the Eastbound bridge, where beam spacing was large. Additional deck reinforcement is located at the ends of each span where precast panels were terminated, and longitudinally above each barr.

Cast-in-place deck concrete was pumped to the level of the deck from below as shown in Figure 2.28. Concrete was compacted using internal vibrators and a rolling screed, as shown in Figure 2.29. The cast-in-place portion of the bridge deck for each of the main spans in the two bridges was placed in single-span segments. Thus, at each bent there is either an expansion joint or a cold construction joint with minimal continuous deck reinforcement between spans. Table 2.6 specifies the type of joint placed at each bent for the main spans of the two bridges. All spans were assumed to be simply-supported for design.

The substructure for the North Concho River Overpass bridges was designed with aesthetics in mind. As can be seen in Figure 2.30, single column reinforced concrete piers with windows are used to support the bridge at each interior bent. Pier columns are 2.44, 2.74, or 3.05 m (8.0, 9.0, or 10.0 ft.) wide and 1.37 m (4.5 ft.) deep. The height of pier

columns varies from 5.79 to 11.58 m (19.0 to 38.0 ft.). A reinforced concrete inverted-tee cap is located at the top of each pier column to support the beam and deck. An example of these pier caps, which are typically 2.06 m (6.75 ft.) wide at the base and 0.99 m (3.25 ft.) wide at the junction with the underside of the deck, is shown in Figure 2.31.

All components of the Eastbound bridge were constructed using high performance concrete. The only HPC components in the Westbound bridge are the cast-in-place deck in Spans 1 through 5, which are HPC for improved durability performance. Additional information regarding the classification of HPC mixes as strength-related or durability-related HPC is presented in Section 4.1.2. Design concrete strengths for the beams, piers, and decks of the two bridges are listed in Table 2.7. Proportions for the concrete mixes used in the two bridges may be found in Section 4.2.

Table 2.5 - Comparison of Eastbound and Westbound Bridge Designs

Span	Span Length (ft.)	Avg. Beam Length (ft.)	No. of Beams	Total Beam Length (ft.)	Deck Area (sq. ft.)	Total Beam Length per Square Ft. of Bridge Deck (ft. / sq. ft.)
Westbound Bridge (Conventional Concrete)						
1	131	128.95	7	903	5240	0.172
2	129	125.33	6	752	5192	0.145
3	129	125.32	6	752	5473	0.137
4	129	125.31	6	752	5805	0.130
5	100	96.05	6	576	4718	0.122
6	140	136.53	9	1229	6947	0.177
Total	758		40	4963	33,375	0.149
Eastbound Bridge (HPC)						
1	131	128.95	4	516	5240	0.098
2	157	153.34	6	920	6280	0.146
3	150	146.32	5	732	6000	0.122
4	149	145.39	5	727	5964	0.122
5	140	136.58	5	683	5641	0.121
Total	727		25	3577	29,125	0.123
1 ft. = 0.3048 m Note: All beams AASHTO Type IV.						

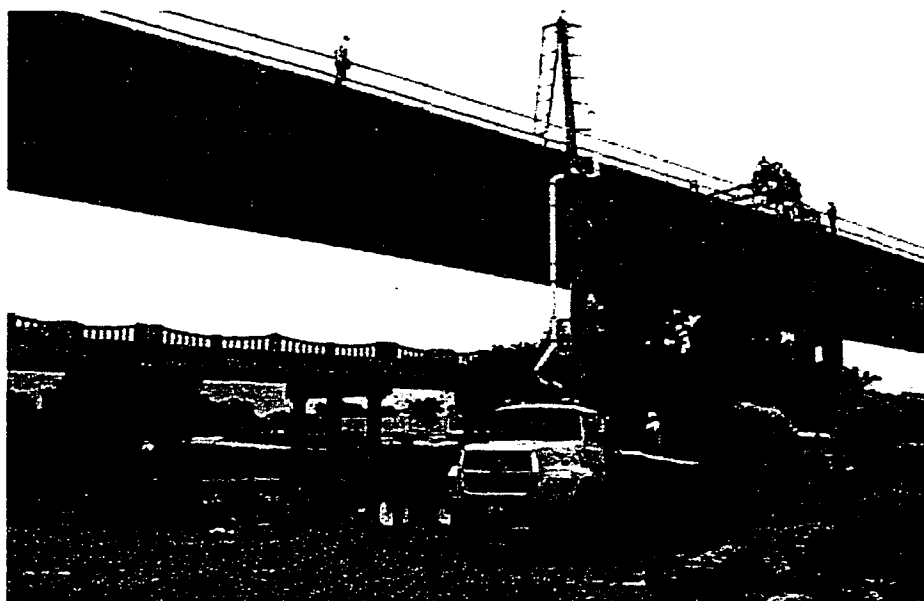


Figure 2.28 - Pumping of Concrete During Deck Pour in the Eastbound Bridge



Figure 2.29 - Deck Placement in the Eastbound Bridge

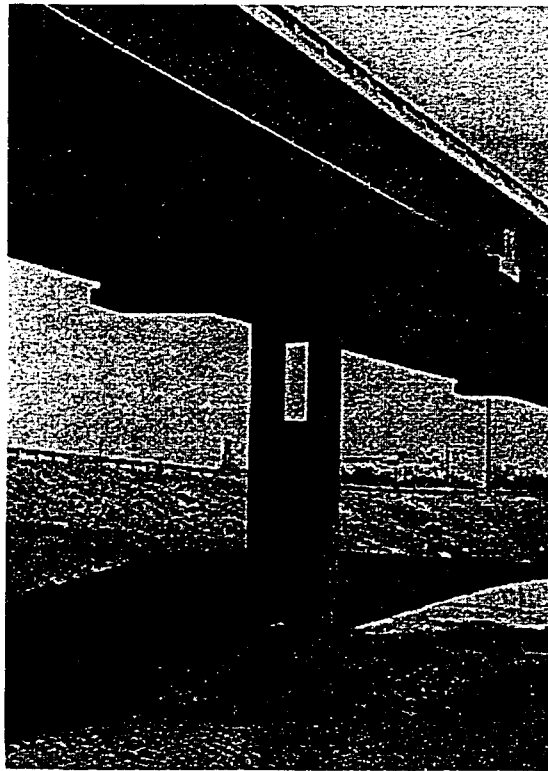


Figure 2.30 - Pier Column in the North Concho River Overpass

Table 2.6 - Joint Types at Bents in Main Spans (N. Concho River Overpass)

Bent Number	Eastbound Bridge	Westbound Bridge
Abutment 1	Expansion	Expansion
Bent 2	Expansion	Expansion
Bent 3	Construction	Construction
Bent 4	Expansion	Expansion
Bent 5	Construction	Construction
Bent 6	Expansion	Expansion
Bent 7		Construction

Note: Only main spans are listed.
Span 1 is between Abutment 1 and Bent 2, Span 2 between Bent 2 and Bent 3, etc.



Figure 2.31 - Pier Cap in the North Concho River Overpass

Table 2.7 - Design Concrete Strengths for the North Concho River Overpass

	Eastbound Bridge	Westbound Bridge
Prestressed Beams	12,500 to 14,000 psi #	5,000 to 8,900 psi
Precast Deck Panels	6,000 psi	5,000 psi
Cast-in-Place Decks	6,000 psi	4,000 psi
Pier Columns	6,000 psi	3,600 psi
Pier Caps	8,000 psi	6,000 psi
1 psi = 0.006895 MPa		
# For main spans (1-5), beam design strengths ranged from 12,500 to 14,000 psi. For other spans (6-8), range was 5,800 to 7,800 psi.		

2.3.2 AASHTO Type IV Beam

All beams in the main spans of the Eastbound and Westbound bridges of the North Concho River Overpass are 1372 mm (54 in.) deep AASHTO Type IV cross-sections. The Type IV was developed by AASHTO and PCI in the late 1950's and has been widely used throughout the United States ever since. The Type IV is still the primary 1372 mm (54 in.) deep section used in Texas. Dimensions for the AASHTO Type IV are shown in Figure

2.12, and section properties are listed in Table 2.2. The strand pattern for the Type IV beam may be found in Figure 2.13.

As discussed in Section 2.2.2, the Type IV is a relatively inefficient cross-section because very little of its flange area is concentrated near the extreme fibers, and because it has a very wide web. A more efficient modified AASHTO Type IV girder can be fabricated by reducing all width dimensions of the standard Type IV section by 50 mm (2 in.), but this modified section is not commonly produced in Texas. The standard Type IV also has very low lateral stiffness, making it highly susceptible to handling and transportation difficulties.

The AASHTO Type IV section does have some advantages, however, over other cross-sections of the same depth. Because the Type IV is a standard section which has been used for many years, fabricators have become very efficient in producing Type IV beams in a cost-effective manner. Furthermore, the cross-section can accommodate either draping or debonding of strands for control of end stresses, and the 200 mm (8 in.) wide web can accommodate ducts for post-tensioned strands. The section is also significantly lighter than the Texas U-beams of the same depth (U54A and U54B), resulting in lighter bridge girders as shown in Table 2.8. Thus, if stability concerns are adequately addressed, long-span Type IV girders can be fabricated and handled without limitations due to beam weight.

2.3.3 San Angelo Beam Design Details

The beams of the North Concho River Overpass were originally designed by the Bridge Division of TxDOT in accordance with the 1992 *AASHTO Standard Specifications* [4]. The beam design and analysis program PSTRS14 [130], which was discussed in Section 2.2.3, was used for design assistance. Simply-supported spans, unshored deck construction, and HS20-44 live load were assumed in the design of beams for both the Eastbound and Westbound Overpasses. As with the Louetta Road Overpass, a few special allowances and assumptions were used for the design of HPC beams: allowable tensile stresses at both release and service were increased 33%, and a modulus of elasticity of elasticity of 41.4 MPa (6.0×10^6 psi) was assumed. Allowable stress criteria governed the original beam designs for both the Eastbound and Westbound main spans.

Table 2.8 - Beam Weights for Various Sections and Beam Lengths

Beam Length	AASHTO Type IV	Texas U54A	Texas U54B
100 ft.	82 kips	107 kips	117 kips
125 ft.	103 kips	134 kips	146 kips
150 ft.	123 kips	160 kips	175 kips
1 kip = 4.45 kN			
Weights are approximate and assume concrete unit weight of 150 pcf (2400 kg/m ³)			

Specific details for the designs of the conventional concrete beams in the main spans of the Westbound Overpass are presented in Table 2.9. All main span Westbound beams are AASHTO Type IV sections, with Grade 270 low-relaxation 13 mm (0.5 in.) diameter strands at 50 mm (2.0 in.) spacing on centers. Draping of strands was used to control end stresses at release of prestress. A maximum of 64 strands was required, with a maximum design compressive strength of 61.5 MPa (8,920 psi). Although 61.5 MPa (8,920 psi) concrete would be considered HPC by some definitions, this concrete was not designated as HPC because it is representative of concrete routinely placed at several precast plants in Texas. Shear reinforcement for the Westbound beams generally consisted of Grade 60 #4 steel reinforcing bars spaced at 102 mm (4 in.) for the first 0.85 m (2.79 ft.), 203 mm (8 in.) for the next 1.22 m (4.00 ft.), 305 mm (12 in.) for the next 1.83 m (6.00 ft.), and 458 mm (18 in.) thereafter.

Details of the original designs for the HPC beams in the main spans of the Eastbound bridge are presented in Table 2.10. These beams were also AASHTO Type IV sections, but used Grade 270 low-relaxation 15 mm (0.6 in.) strands at 50 mm (2.0 in.) spacing instead of 13 mm (0.5 in.) strands. Field and laboratory transfer and development length tests were performed in order to obtain design approval from the Federal Highway Administration (FHWA) for use of the larger diameter strand in the actual bridge beams. Results of those tests are reported by Cordova et. al. [46]. The original HPC beam designs called for release strengths of 61.4 to 74.5 MPa (8,900 to 10,800 psi) and 56-day design strengths of 75.2 to 101.4 MPa (10,900 to 14,700 psi). A maximum of 84 15 mm (0.6 in.) strands was required, with up to 34 strands draped for the control of end stresses.

**Table 2.9 - Beam Design Details for Spans 1 through 6 of the Westbound
North Concho River Overpass**

Span / Beams		Beam Length ¹ (ft.)	Length-CL to CL Bearings ¹ (ft.)	Beam Spacing ² (ft.)	No. of 0.5 in. Strands ³	Specified Release Strength (psi)	Specified 56-day Strength (psi)
W1	1,7	128.96	127.79	5.84	52	5,770	7,850
	2-6			5.67			
W2	1,6	125.33	124.17	6.46	56	5,940	7,910
	2-5			6.91			
W3	1,6	125.32	124.17	6.65	58	6,160	8,150
	2-5			7.29			
W4	1,6	125.31	124.17	6.90	64	6,560	8,540
	2-5			7.80			
W5	1,6	96.05	94.94	7.13	34	4,020	5,000
	2-5			8.26			
W6	1,9	136.53	135.42	5.72	58	6,210	8,920
	2-8			5.43			

1 ft. = 0.3048 m; 1 psi = 0.006895 MPa. Note: All beams AASHTO Type IV.
Spans 7-9 were controlled by geometry and clearance.
Beams 4-7 of Westbound Span 1 (W14, W15, W16, W17) were instrumented.

¹ Represents average for span. Individual beam lengths may vary slightly.
² First value is for exterior beams (assuming 0.91 m [3.0 ft.] overhang). Second value is for interior beams.
³ Six to fourteen strands per beam are draped to control end stresses.

Table 2.10 - Original Beam Design Details for Spans 1 through 5 of the Eastbound North Concho River Overpass

Span / Beam ¹	Beam Length (ft.)	Length-CL to CL Bearings (ft.)	Beam Spacing (ft.)	No. of 0.6 in. Strands	No. of Draped Strands	Specified Release Strength (psi)	Specified 56-day Strength (psi)
E11	128.95	127.79	9.00	84	34	10,800	13,600
E12	128.95	127.79	11.00	84	34	10,800	13,600
# E13	128.95	127.79	11.00	84	34	10,800	13,600
# E14	128.95	127.79	9.00	84	34	10,800	13,600
E21	153.34	152.17	6.80	70	20	9,200	13,500
E22	153.34	152.17	6.60	66	16	9,200	12,800
E23	153.34	152.17	6.60	66	16	9,200	12,800
# E24	153.34	152.17	6.60	66	16	9,200	12,800
# E25	153.34	152.17	6.60	66	16	9,200	12,800
# E26	153.34	152.17	6.80	70	20	9,200	13,500
E31	146.32	145.17	7.63	84	34	10,300	14,700
E32	146.32	145.17	8.25	84	34	10,300	14,700
# E33	146.32	145.17	8.25	84	34	10,300	14,700
# E34	146.32	145.17	8.25	84	34	10,300	14,700
# E35	146.32	145.17	7.63	84	34	10,300	14,700
E41	144.84	143.69	7.63	80	30	9,800	14,000
E42	145.12	143.97	8.25	80	30	9,800	14,000
E43	145.39	144.24	8.25	80	30	9,800	14,000
# E44	145.67	144.52	8.25	80	30	9,800	14,000
# E45	145.94	144.79	7.63	80	30	9,800	14,000
E51	136.55	135.42	7.74	60	12	8,900	10,900
E52	136.57	135.44	8.47	60	12	8,900	10,900
E53	136.57	135.44	8.47	60	12	8,900	10,900
E54	136.60	135.47	8.47	60	12	8,900	10,900
E55	136.60	135.47	7.74	60	12	8,900	10,900

1 ft. = 0.3048 m; 1 psi = 0.006895 MPa. Note: All beams AASHTO Type IV.
Spans 6-8 were controlled by geometry and clearance and are not HPC.
¹ Beam designation discussed in Section 3.4.1 (xyz: x=bridge, y=span, z=beam).
"#" denotes beam with instrumentation.

The beam fabricator, Texas Concrete Company, had several concerns with the original beam designs for the Eastbound HPC beams. The high required prestress force — up to 165 GN (3,700 kips) — exceeded the fabricator's highest available bed capacity. Therefore, the fabricator would have had to modify existing prestressing beds in order to accommodate the required forces. In addition, the fabricator did not have experience draping 15 mm (0.6) diameter strands. There was concern over the safety of draping these large diameter strands, as well as the magnitude of hold-down forces required to drape a large number of these strands.

As a result of these concerns, the fabricator elected to use a two-stage (pretensioning/post-tensioning) fabrication process, which is shown in Figure 2.32. A maximum of 56 straight 15 mm (0.6 in.) diameter strands were pretensioned, eliminating the need for the fabricator to increase the capacity of existing beds. Debonding was used to control end stresses at release of pretensioning. Six of the pretensioned strands were located in the top flange and bonded only over the end 6.1 m (20 ft.) of each beam. These strands assisted with control of end stresses, and provided additional stability to the section during handling and transportation. The six top flange strands were then cut over the debonded length after erection of the beams at the jobsite. An additional 20 or 26 strands were post-tensioned seven to 28 days after casting to provide the total prestress force required for the section. These strands were grouted within 48 hours of post-tensioning. The interior of an HPC beam prior to placement of side forms is shown in Figure 2.33. The post-tensioning of an HPC beam is shown in Figure 2.34.

The redesigns of the Eastbound main span HPC beams required extensive time-dependent analyses because of the two-stage fabrication process. Lisa Carter Powell, P.E., of P.E. Structural Consultants, was hired by the fabricator to assist with the analyses and beam redesigns. The computer program ADAPT [13] was used for the time-dependent analyses. Measurements from creep and shrinkage tests, which were in progress at the Construction Materials Research Group (CMRG) laboratory, were supplied by the researchers and incorporated into the beam redesigns, which were actually deflection-critical. More strands were used in the redesigns than were necessary to satisfy allowable stress or ultimate strength criteria. The additional strands were intended to prevent a net downward deflection under full dead load.

Concerns related to the stability of such long and slender beams, which have a span-to-depth ratio of up to 34, during handling and transportation led the fabricator to cast

one HPC beam early in the construction process. This beam was shipped to the jobsite shortly after post-tensioning to investigate these stability concerns. The early casting of this girder also provided the researchers a chance to monitor the beam as part of the instrumentation program. The accuracy of the time-dependent analysis used for the redesigns with respect to deformations (strains and deflections) could then be assessed. Dubbed the “test beam”, this beam was originally designed as an exterior beam in Span 2 of the Eastbound bridge. However, it was subsequently moved to the interior of that span.

Camber measured on the test beam was significantly lower than predicted by the time-dependent analysis, leading to a few changes in the redesigns of the remaining HPC beams. The sensitivity of the deflection behavior for long spans was recognized, leading to an upper and lower bound approach considering possible differences in construction schedule and factors affecting creep and shrinkage. An allowance for prestress losses due to temperature changes in the strand between stressing and casting was also included in the redesigns. Finally, the unit weight of the beam concrete was increased slightly to account for the influence of the volume of embedded steel. These modifications resulted in a few more strands being utilized in the redesigns of the remaining beams.

Details of the redesigns of the Eastbound main span HPC beams are presented in Table 2.11. All HPC beams, except for the test beam, have 56 pretensioned Grade 270 low-relaxation 15 mm (0.6 in.) strands including the six strands in the top flange. Each beam has either 20 or 26 post-tensioned strands supplied in two ducts. Design concrete strengths for the redesigned HPC beams ranged from 86.2 to 96.5 MPa (12,500 to 14,000 psi). Release strengths were kept at approximately 55 MPa (8,000 psi), which typically allowed the fabricator to obtain release strengths in 24 hours. Shear reinforcement for the HPC girders is essentially the same as for the Westbound conventional concrete girders. Supplemental reinforcement in the post-tensioning anchorage regions is shown in Figure 2.35. Additional details of the design and fabrication processes are discussed by Powell [107] and Patton [102].

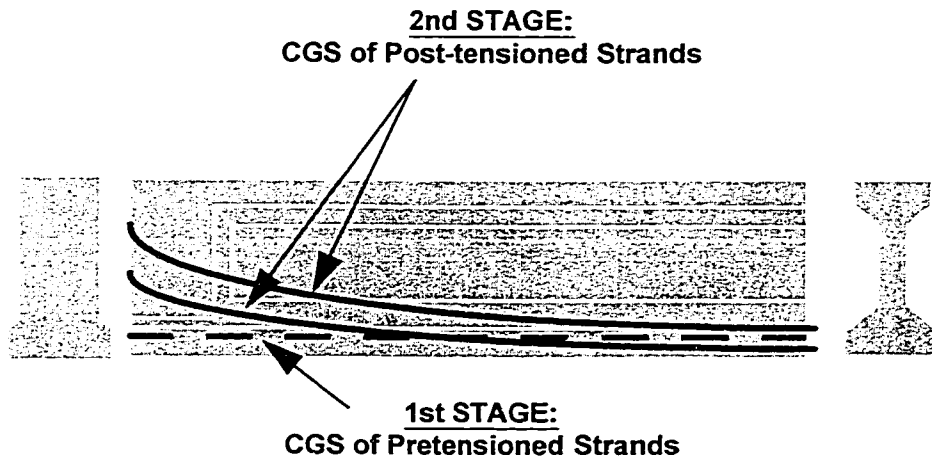


Figure 2.32 - Two-Stage Beam Fabrication Process



Figure 2.33 - Fabrication of Eastbound HPC Beam

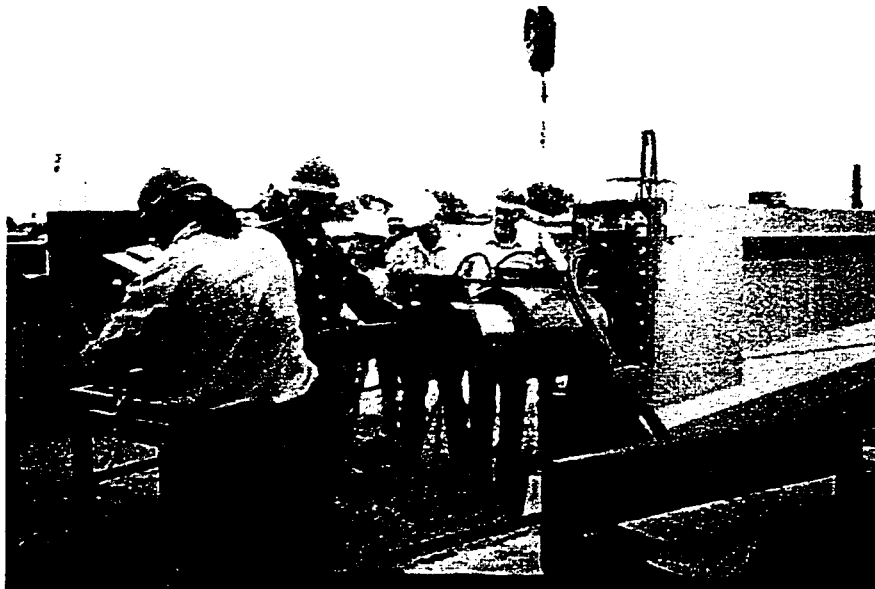


Figure 2.34 - Post-tensioning of Eastbound HPC Beam

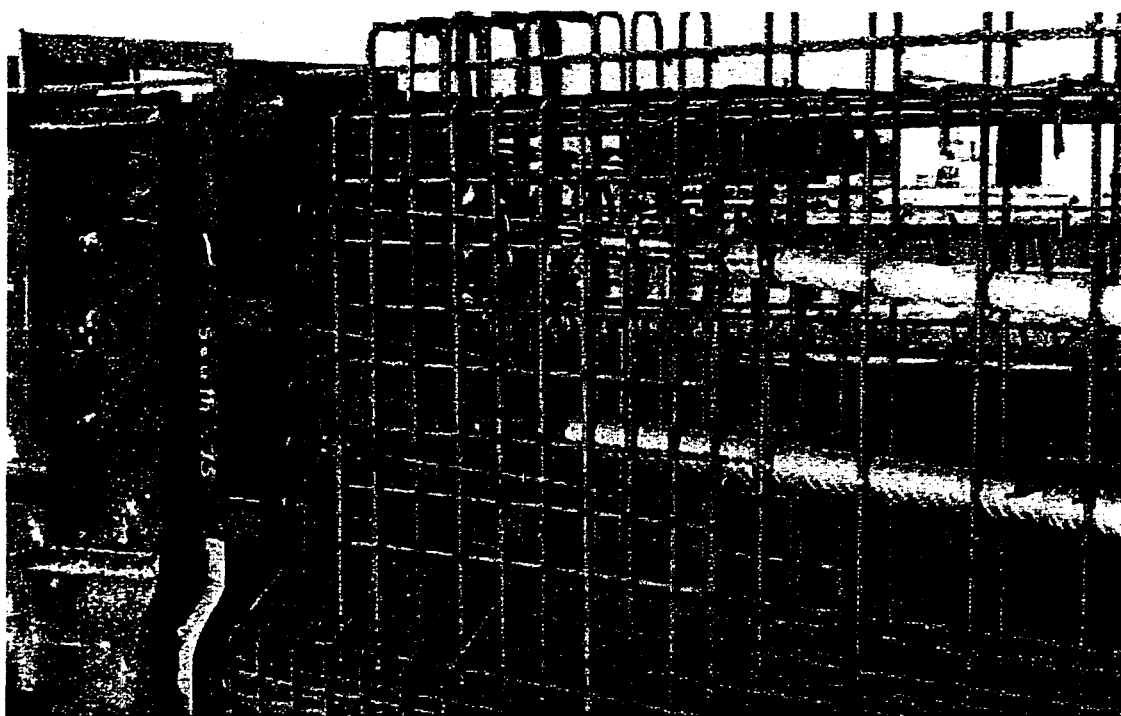


Figure 2.35 - Anchorage Reinforcement in Eastbound HPC Beam

Table 2.11 - Details of Modified (Two-Stage) Beam Designs for Spans 1 through 5 of the Eastbound North Concho River Overpass

Span / Beams		No. of 0.6 in. Pretensioned Strands ^{1,2}	No. of 0.6 in. Post-tensioned Strands ³	Specified Release Strength (psi)	Specified Post-tens. Strength (psi)	Specified 56-day Strength (psi)
E1	1-4	56	20	8,100	9,950	13,000
E2	1-6	56	26	8,000	9,800	14,000
E2	5 #	52	20	8,100	9,320	13,500
E3	1-5	56	26	8,000	10,400	13,800
E4	1-5	56	26	8,000	10,400	13,700
E5	1-5	56	20	8,000	9,800	12,500

1 psi = 0.006895 MPa. Note: All beams AASHTO Type IV.

¹ Includes six strands in top flange bonded over 20 ft. at each end of the beam. These strands were required to control end stresses and help with stability during handling and transportation. These strands were cut over unbonded length after erection of beams at the jobsite.

² Ten strands in bottom flange were debonded to help control end stresses.

³ Post-tensioned strands were placed in two parabolic ducts, with 13 strands in the bottom duct and either 7 or 13 strands in the top duct.

"Test beam". Cast early to investigate handling, transportation, and camber. Redesigns for other HPC beams were subsequently performed.

2.3.4 Contractors, Fabricators, and Project Timeline

Jascon, Inc. and Reese Albert, Inc. were joint general contractors for the construction of the North Concho River Overpass in San Angelo, with Jascon in charge of bridge and road construction and Reese Albert in charge of all earth moving and sitework. Prestressed concrete beams for both the Eastbound and Westbound Overpasses were fabricated at Texas Concrete Company in Victoria, Texas, approximately 500 km (310 mi.) southeast of San Angelo. All precast concrete deck panels were cast at Bexar Concrete Works in San Antonio, Texas, about 320 km (200 mi.) southeast of San Angelo. Ready-mixed concrete for the jobsite, including concrete for all piers and cast-in-place bridge decks, was supplied by Concho Concrete Company in San Angelo.

The stages of construction for the North Concho River Overpass are shown in a timeline in Figure 2.36. Note that the project was let in June 1995, almost two years after the Louetta Road Overpass was let, yet the bridges were opened to traffic in December 1997, approximately six months before the Louetta bridges were opened. Construction of the Westbound conventional concrete side was completed first, followed by construction of the Eastbound HPC side. For the most part, construction was continuous from the beginning of 1996 through the end of 1997, with the only minor delays due to inclement weather.

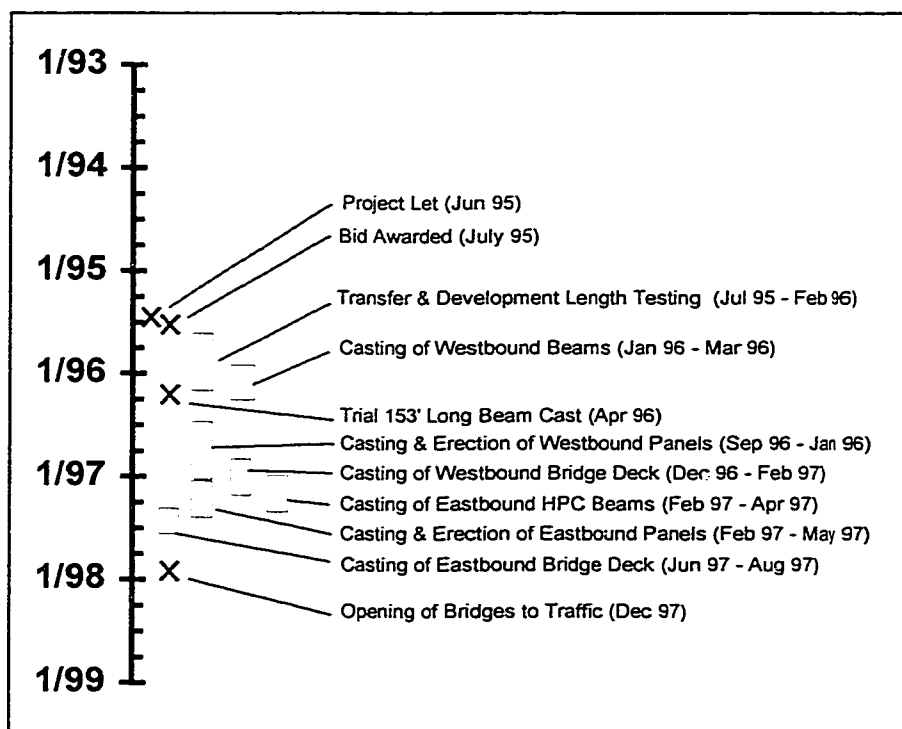


Figure 2.36 - Timeline for Construction of the North Concho River Overpass

3 CHAPTER THREE: INSTRUMENTATION PLANS AND PROCEDURES

3.1 Introduction

This chapter discusses the instrumentation of the two Texas HPC bridges. A brief overview of the types of measurements, gauges, and other instrumentation systems is presented first, followed by information on the data acquisition systems used for collection of data. A summary of the instrumentation for each bridge is then presented. Preparation and installation of gauges, as well as the travel requirements for the research program, are discussed next. Finally, a summary of problems encountered during the research program and an assessment of the durability of each type of gauge are presented. Due to the large amount of material presented in this chapter, detailed descriptions are not presented in some sections. Additional information on some of the instrumentation procedures discussed here, especially for the Louetta Road Overpass, may be found in the report by Byle and Burns [35].

It should be noted that there are some basic similarities and differences between the instrumentation plans and procedures used in this research program and the recommendations of the Federal Highway Administration for instrumentation of bridges in the High Performance Concrete Showcase program. The FHWA publication *Guidelines for Instrumentation of Bridges* [118] was actually published after the instrumentation program for the two Texas bridges was well underway. As a result, some of the experiences in the Texas program were incorporated into the guidelines. The guidelines also suggest some types of instrumentation not used in the Texas projects, and are intended to be a starting place for instrumentation projects rather than a rigid set of specifications for instrumentation. Because the instrumentation plan for the Texas bridges was developed independent from the guidelines, no comparison between the Texas plan and the FHWA guidelines will be made.

3.2 Measurements, Gauges, and Instrumentation Systems

3.2.1 Types of Measurements

Three basic types of measurements were made as part of the main instrumentation program: concrete temperatures, concrete strains, and camber or deflection of bridge girders. Each of these measurement types is discussed briefly below. The specific data monitored with each type of measurement are also listed. A summary of the types of measurements discussed in this section is presented in Table 3.1. Specific gauge types and instrumentation systems are discussed in the next subsection.

Table 3.1 - Types of Measurements and Data

Measurement Type	Gauge Type / Instrumentation System	Data from Measurements
Concrete Temperatures	<ul style="list-style-type: none"> • Thermocouples • Thermistors 	<ul style="list-style-type: none"> • Thermal Gradients • Extreme Seasonal Bridge Temperatures • Hydration Temperatures • Corrections for Strain and Deflection Measurements
Concrete Strains	<ul style="list-style-type: none"> • Vibrating Wire Gauges • Resistance Strain Gauges • Surface Mechanical Strain Gauges (DEMEC) 	<ul style="list-style-type: none"> • Beam Curvatures (Elastic and Time-Dependent Behavior of Beam and Composite Section) • Static Live Load Response • Prestress Losses
Beam Camber / Deflection	<ul style="list-style-type: none"> • Tensioned-Wire System • Precise Surveying 	<ul style="list-style-type: none"> • Elastic Responses to Prestress, Deck Loads, etc. • Time-Dependent Behavior due to Creep • Static Live Load Response

3.2.1.1 Concrete Temperatures

Concrete temperatures were measured in various components of the superstructures of the two bridges, including selected prestressed beams, selected precast deck panels, and portions of the cast-in-place bridge decks. Thermocouples were used for most concrete temperature measurements. However, temperature measurements were also recorded at each vibrating wire strain gauge location using thermistors, which were integrally attached to the vibrating wire gauges.

Measurement of concrete temperatures at various depths of the beams and within the composite bridge deck allowed for an investigation of thermal gradients in the completed bridges. Maximum and minimum seasonal bridge deck temperatures were also determined from collected data. Measurement of temperatures in beams, panels, and cast-in-place decks during casting and at very early-ages (within 24 hours of casting) provided information on the hydration behavior of the concrete mixes in the various structural elements. Finally, temperature data was used to correct for variations in strain and deflection measurements due to temperature effects. Discussion of all temperature measurements is presented in Chapter 5.

3.2.1.2 Concrete Strains

Like concrete temperatures, concrete strains were measured in selected prestressed beams, selected precast deck panels, and portions of the cast-in-place bridge decks. Internal concrete strains were measured using embedded vibrating wire gauges and bonded resistance strain gauges. In some cases, surface concrete strains were measured using mechanical strain gauges as a backup system.

Concrete strain measurements at various locations through the depth of selected girders and in the composite deck were used to examine the strain profile, or curvature, in the section at various stages of construction and loading. Both elastic curvature changes and time-dependent curvature changes resulting from creep and shrinkage were monitored using the measured concrete strains. The response of girders and deck to static live loads was also monitored using measured concrete strains. General concrete strain

measurements are presented in Chapter 6, and the static live load responses of the two bridges are discussed in Chapter 9.

Concrete strain measurements were also used to indirectly measure prestress losses in several beams. Assuming strain compatibility, measured changes in concrete strain at the level of the center-of-gravity of prestress are equal to strain changes in the steel strands at the same level. These strain changes can be then directly be converted to prestress losses due to elastic loads, shrinkage, and creep. More discussion of prestress losses, including a more detailed discussion of the measurement method, is presented in Chapter 7.

3.2.1.3 *Beam Camber/Deflection*

Deflection behavior for several beams of each bridge was monitored throughout construction and service. Stages at which beam camber (or deflection) were recorded include release of prestress, storage at the prestressing plant, erection at the jobsite, and casting of the bridge deck, as well as at several intervals between these specific stages. Prior to erection of the beams at the jobsite, the tensioned-wire method was used for camber measurements. For all stages after erection of the beams, the precise surveying method was used for measurement of camber or deflection.

Particular deflection behavior of interest includes elastic beam response due to prestress, deck loads, and other applied loads. Time-dependent camber or deflection due to creep was also monitored using recorded camber measurements. Discussion of these camber and deflection measurements is presented in Chapter 8. The deflection response of beams in the completed bridges under static live load is discussed in Chapter 9.

3.2.2 Types of Gauges and Measurement Systems

The specific types of gauges and measurement systems used for the long-term instrumentation of the two bridges are discussed in this subsection. Specific gauge types were selected on the basis of several criteria, including cost, reliability, accuracy, ease of installation, and compatibility with the data acquisition system. Although not necessarily

more important than the other three criteria, cost and ease of installation were of particular importance because of the magnitude of the instrumentation program. The advantages and disadvantages of each gauge type with respect to these five criteria are discussed below.

3.2.2.1 Thermocouples

Thermocouples are simple temperature measuring devices consisting of a junction of two metals, across which a voltage drop is inherently present. Since the magnitude of the voltage drop is proportional to the temperature of the junction, voltage measurements can be directly converted to temperatures using formulas or data tables developed for the specific combination of two metals. For the instrumentation of the two Texas bridges, thermocouples were created by tightly twisting thermocouple wire for a length of 13 to 25 mm (0.5 to 1.0 in.), as shown in Figure 3.1. The junction was then protected with electrical tape before being installed in the field. Twisted shielded Type T (copper-constantan) 20-gauge wire, manufactured by Omega Scientific, Inc., was used in both bridges. The accuracy of temperature measurements using this thermocouple wire is reported by the manufacturer to be ± 1.0 °C (± 1.8 °F). Thermocouples worked extremely well for field instrumentation, as they are inexpensive, reliable, easy to fabricate, and easy to install.

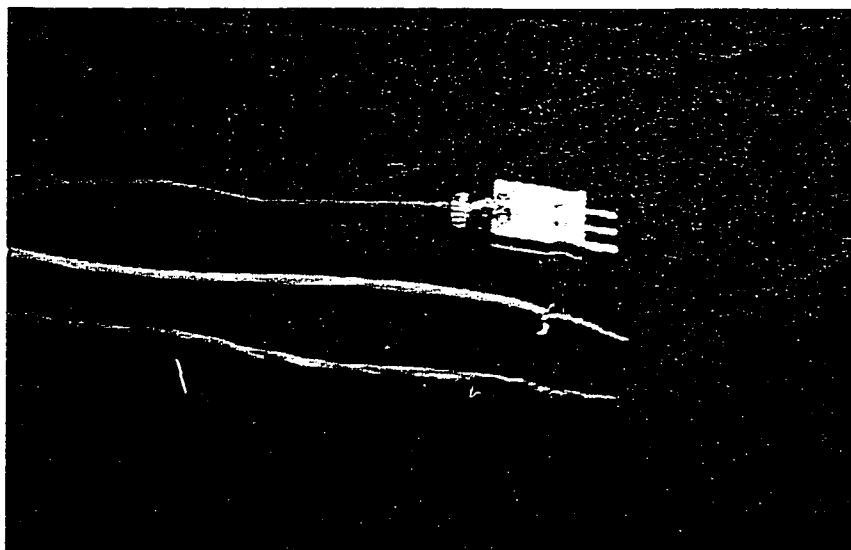


Figure 3.1 - Thermocouple

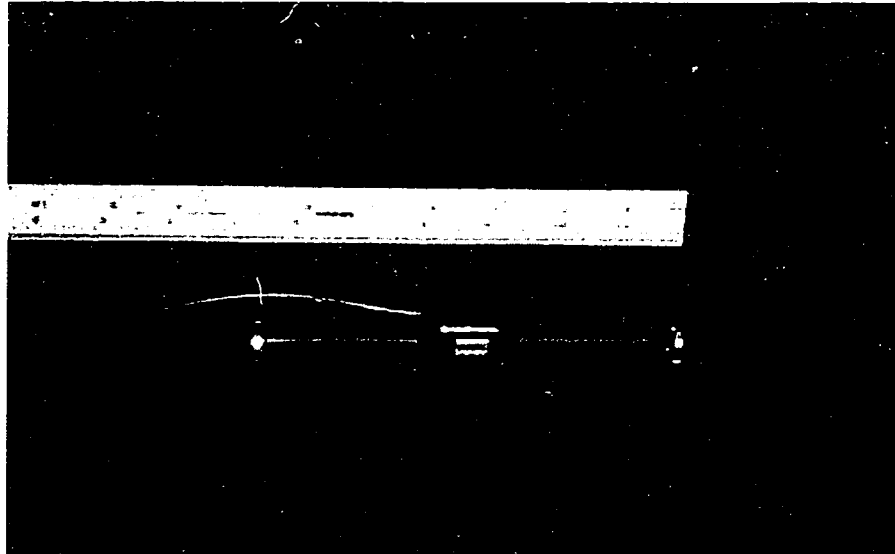


Figure 3.2 - Vibrating Wire Strain Gauge

3.2.2.2 Thermistors

Thermistors were used for temperature measurement at all vibrating wire gauge locations, since each gauge had a thermistor integrally attached. Thermistors are very sensitive temperature measuring devices made up of tiny resistors. Resistance changes due to temperature can be measured using standard bridge circuits, and converted to temperatures using equations developed for specific thermistors. Semiconductors are typically used in the fabrication of thermistors, making these gauges more expensive than thermocouples. Since they were integrally attached to the vibrating wire strain gauges, however, they did not add any additional cost to the instrumentation of the two bridges. Thermistors also offer a high level of accuracy, typically on the order of ± 0.1 °C (± 0.2 °F) [18].

3.2.2.3 Vibrating Wire Strain Gauges

Vibrating wire gauges are strain gauges operating on the principle that the resonant frequency of a tensioned wire changes as the tension in the wire changes. Strain can be

measured using vibrating wire gauges by electronically plucking the wire, determining the resonant frequency, and calculating the tension in the wire. This measurement can then be converted to strain by comparing the measured tension to a baseline tension in the unstressed condition. Vibrating wire gauges are extremely durable and can be expected to provide reliable readings for several years. They also have the benefit of having an integrally attached thermistor for measurement of temperature at the gauge location. Unfortunately, vibrating wire gauges are very expensive as compared to other types of gauges used for measuring internal concrete strains.

The specific gauge used for the instrumentation of both bridges was the Irad EM-5 gauge manufactured by RocTest, Inc. As can be seen in Figure 3.2, the gauge consists of a tensioned high-strength steel wire within a thin steel tube. Flanges at each end of the steel tube ensure that the gauge deforms with the concrete surrounding it. Each gauge is about 165 mm (6.5 in.) long, and is fabricated with the required length of 4-conductor 24-gauge leadwire attached. The range of these gauges is 3300 microstrain, with an accuracy of 1 microstrain.

3.2.2.4 Resistance Strain Gauges

Commonly used in laboratory applications, electrical resistance strain gauges (ERSG) are strain-measuring devices which operate on the principle that the resistance of a wire changes as the length of the wire itself changes. These gauges are typically composed of a length of tiny wire on a backing material. As the material to which the gauge has been bonded is strained, the length and resistance of the wire change. A common instrumentation bridge circuit can be used to measure the change in resistance, which can then be converted to strain.

For measurement of internal concrete strains in the Texas HPC bridges, ERSG gauges were bonded to lengths of #3 steel reinforcing bars. These bars were then tied into place prior to casting of concrete. Because the strain on the embedded reinforcing bar is being measured, rather than directly measuring the strain in the concrete, gauges of this type are often called "sister gauges". There must be strain compatibility between the bar and the concrete at the gauge location for an accurate measurement of concrete strain to be made.

To fabricate each “sister gauge”, bar deformations were smoothed down and gauges were bonded directly to the bar, as shown in Figure 3.3. The gauges were then waterproofed using a layer of butyl rubber, a layer of nitrile rubber, and a layer of electrical tape. Unlike vibrating wire gauges, resistance strain gauges cannot be purchased with long lengths of leadwire integrally attached, so for each gauge the appropriate length of leadwire (Belden #8771) was spliced to the short leads supplied by the gauge manufacturer. The leadwire splice for each gauge was waterproofed following the same technique used for the gauges themselves.

Gauges used for instrumentation of the two bridges were Model FLA-6-350-11-3LT gauges manufactured by Texas Measurements. These gauges use a three-leadwire setup that eliminates the effect of leadwire length on gauge resistance, and have a nominal resistance of 350 ohms to provide increased output over more common 120-ohm gauges. Each gauge is also temperature compensated such that the coefficient of thermal expansion of the gauge matches the coefficient of thermal expansion of the steel reinforcing bar to which it is bonded.

These gauges were used in the instrumentation of the Texas bridges because they are inexpensive compared to vibrating wire gauges. Unfortunately, they are not very durable or reliable for use in the field. There are simply too many places where a single gauge can be damaged during the construction process: at the gauge itself, at the leadwire splice, along the length of leadwire, and at the location where the leadwire exits the beam, panel, or bridge deck. This type of gauge also tends to become unstable over time and may not provide reliable long-term measurements. Measurement repeatability is difficult in the field because the resistance-based measurement is highly sensitive to the connection of leadwires to the data acquisition system. Finally, the preparation of these gauges for field instrumentation is very labor-intensive, since each gauge must be bonded, waterproofed, and connected to leadwire.

3.2.2.5 Surface Mechanical Strain Gauges (DEMEC)

During portions of the instrumentation program, surface mechanical strain gauges were used as a backup system for measurement of concrete strains. The Demountable Mechanical Gauge (DEMEC), manufactured by Mayes Instruments Limited, was used for

measurement of surface strains at locations corresponding to embedded instrumentation. Prior to release of prestress, stainless steel target discs were fixed to the concrete surface using a five-minute epoxy gel made by Devcon, Inc. Points were then allowed to set for 15 to 20 minutes before a set of initial readings was performed using the 200 mm (8 in.) DEMEC gauge. At later stages of the construction process, changes in distance (strain) between each set of points were determined by comparing later readings with the initial set of readings. The DEMEC gauge and target discs are shown in Figure 3.4.

Over the course of the instrumentation program, the DEMEC system was not found to be appropriate for long-term outdoor measurements. Durability of the system can be a problem if points fall off due to epoxy failure in adverse exposure conditions. Furthermore, substantial variation can arise from the differences in gauge-holding techniques used by different people. For a single reader, the accuracy of the DEMEC system is reported by Arrellaga [18] to be only about 16 microstrains. Readings are also extremely susceptible to temperature changes, especially when the beam is cooling quickly after form removal. Unfortunately, important baseline readings must be taken at this stage. Even with proper temperature correction, which requires both strain and temperature measurements on the concrete surface and on a standard reference bar, the accuracy of the system is reduced.

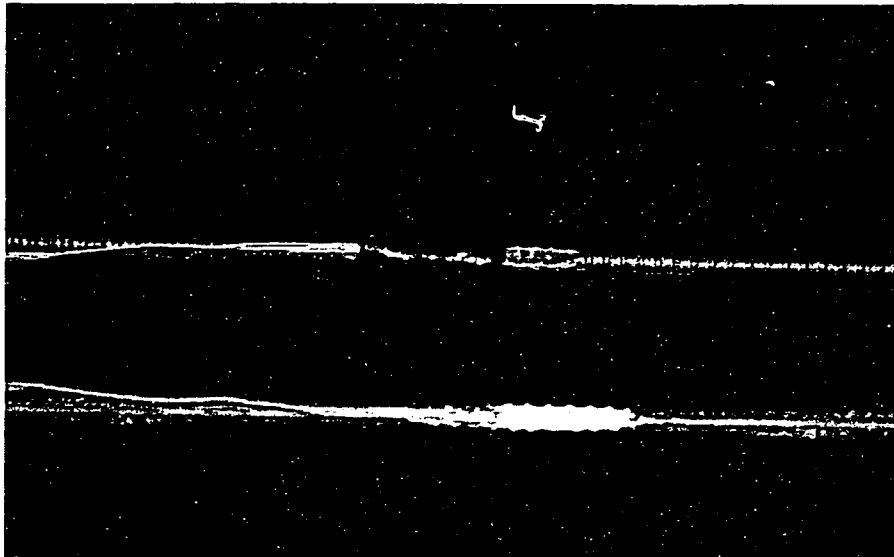


Figure 3.3 - Bonded and Waterproofed Electrical Resistance Strain Gauges

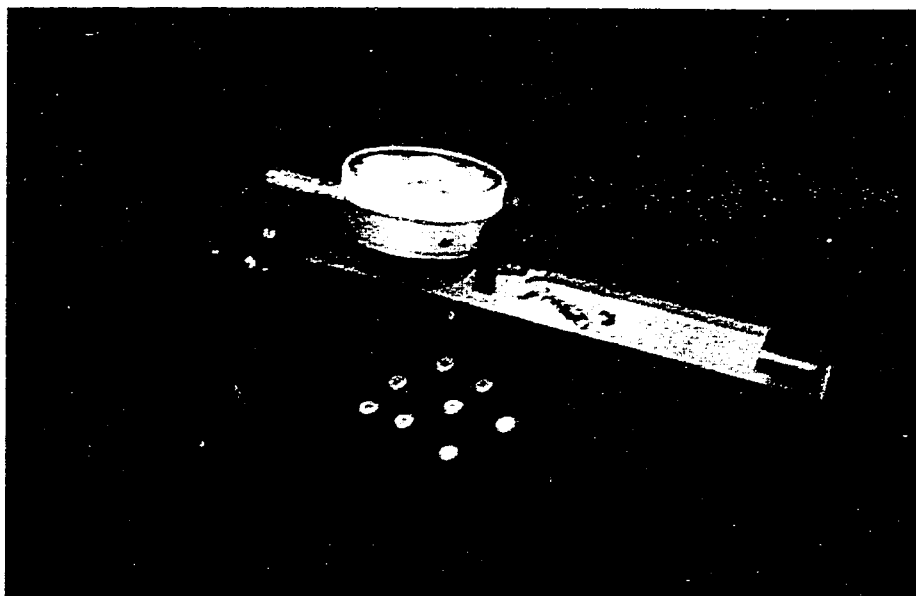


Figure 3.4 - DEMEC Mechanical Strain Gauge and Target Disks

Because the researchers ultimately felt that the benefits of the DEMEC system for long-term strain measurements did not outweigh the above concerns, the system was not used during later stages of the instrumentation program. Since the system was only intended as a backup anyway, this decision did not significantly alter the instrumentation plan. Note that the DEMEC mechanical strain gauge system was still used for the creep and shrinkage tests discussed in Chapter 4.

3.2.2.6 Tensioned-Wire Deflection Measuring System

The tensioned-wire system is a manual deflection measurement system that was used in the Texas instrumentation program for all camber readings at the precast plant. In this system, a precision scale is fixed to the girder at midspan, and movements of the girder (and scale) relative to a tensioned baseline are recorded. The system is both simple and reliable, and readings can be performed by one person. A schematic of the tensioned-wire deflection system is shown in Figure 3.5. The specific tensioned-wire system used in this instrumentation program is loosely based on the systems described by Kelly et. al. [69] and Arrellaga [18].

TENSIONED-WIRE DEFLECTION SYSTEM

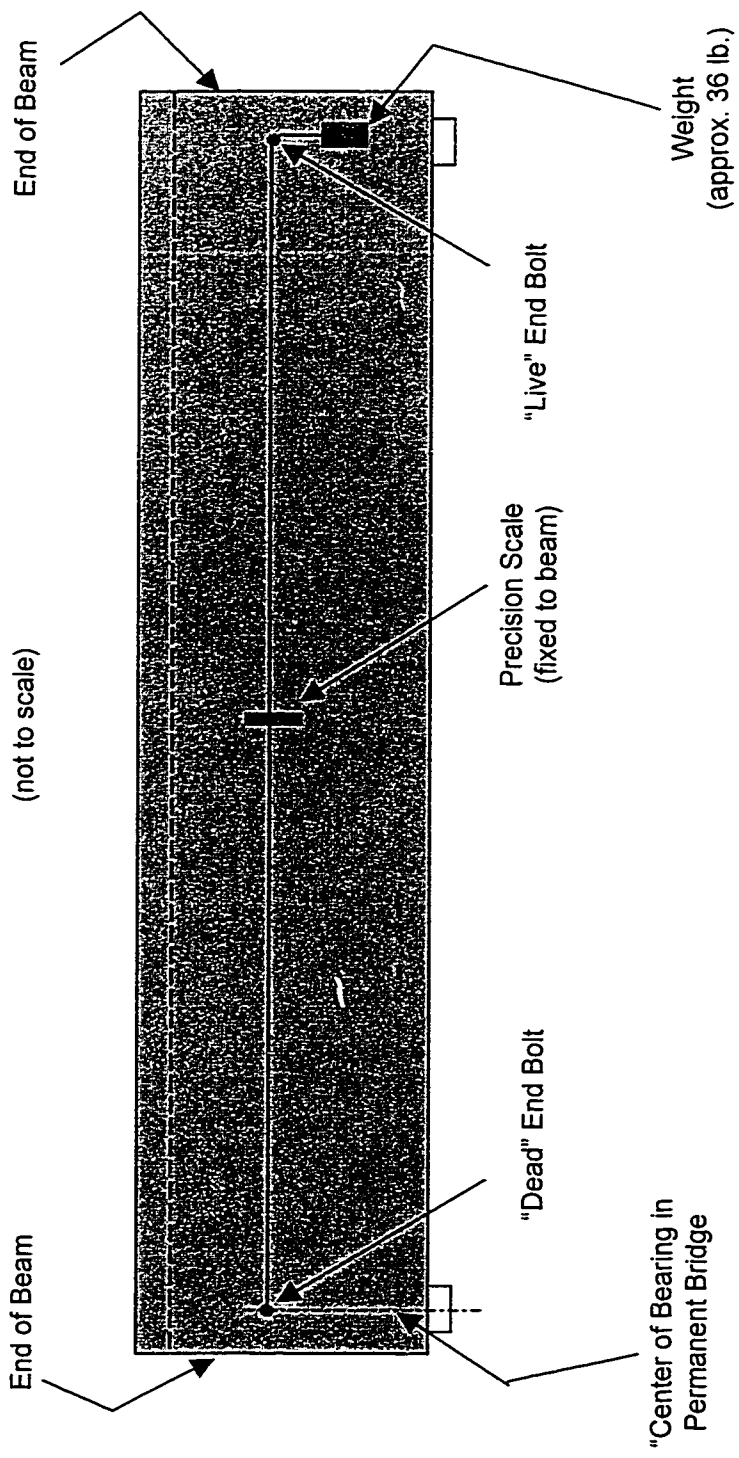


Figure 3.5 - Schematic of the Tensioned-Wire Deflection System

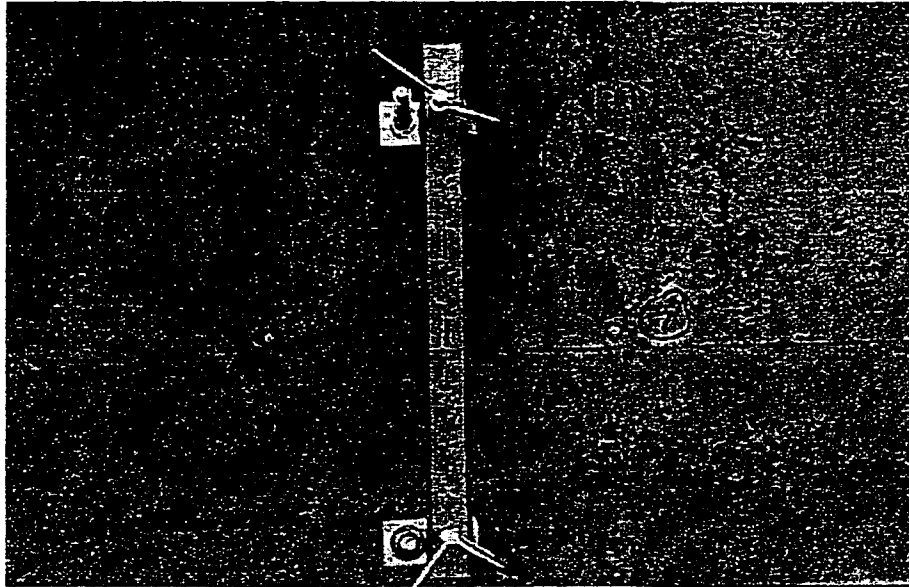


Figure 3.6 - Precision Scale Fixed to Girder at Midspan



Figure 3.7 - Dead (Anchorage) End of Tensioned-Wire Deflection System

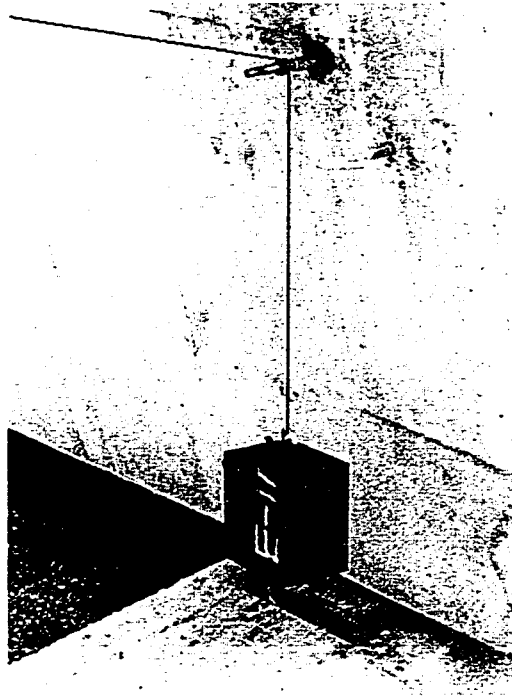


Figure 3.8 - Live (Stressing) End of Tensioned-Wire Deflection System



Figure 3.9 - Reading the Tensioned-Wire Deflection System

A precision scale with 0.25 mm (0.01 in.) divisions is fixed to midspan of the girder, as shown in Figure 3.6. Anchor bolts were retrofit into the girder for support of the scale, and small aluminum extension pieces were used to allow for adjustment of the scale to a level position. The scale was fixed to the aluminum extensions using a five-minute epoxy gel and clamps, which were left in place for added protection. Note that the scales were not directly epoxied to the sides of the girders because the Louetta U-beams had a sloped web, and because the San Angelo Type IV girders had recessed webs relative to their end blocks. A single vertical face running the entire length of the beam is required if scales are to be directly attached.

Size #6 piano-wire, with a diameter of 0.41 mm (0.016 in.), was used for the baseline (tensioned wire). As shown in Figure 3.7, the wire was anchored directly above the permanent bearing location at one end of the girder. A 16.6 kg (36.6 lb.) weight was used to tension the wire over a grooved bearing at the other end, as shown in Figure 3.8. The bearing was periodically lubricated with an all-purpose lubricant to minimize any friction between the bearing and the bolt. The tensioned wire can be read at the scale using a mirror to eliminate parallax, as shown in Figure 3.9. A baseline (zero camber or deflection) reading is taken just before release of prestress, with the assumption that the prestress bed is perfectly level. Measurements at later stages can be compared to the baseline reading to determine the beam camber at that stage.

As previously mentioned, the main advantage of the tensioned-wire system is that readings can easily be performed by one person in about two to three minutes per beam. The system also has a good level of repeatability, with the overall system accuracy estimated at about ± 0.50 mm (0.02 in.). Furthermore, the tensioned wire can be used to measure horizontal beam deflections at release of prestress and later stages. One of the main difficulties with the system is that wind can cause the wire to vibrate. This can result in a delay during the measurement process until the wind subsides. Also, the wires often corrode during storage of the girders, and thus must be replaced periodically. Note that the system was designed so that the replacement of a wire does not change the measurement.

The greatest drawback of the system is that it is entirely based on measurements relative to the baseline reading. Should the scale become unbonded for any reason, the system fails. New readings with a replaced scale cannot be properly tied in to the original baseline. Unfortunately, the scales were removed from a few beams during storage at the precast plant, and a few subsequent readings were lost.

Overall, the tensioned-wire system worked extremely well at the precast plant. The researchers felt, however, that the system would not work well for practical reasons once beams had been erected at the jobsite. For each set of readings, access to beams would have required the use of construction equipment. In some cases, the weight would have to have been hung over a river or very close to a roadway. Replacement of corroded wires would have been difficult, because it also would have involved crossing roadways and rivers. For these reasons, all camber and deflection measurements at the jobsite were performed using the precise surveying system.

3.2.2.7 Precise Surveying Method

The precise surveying method was used for all deflection measurements after erection of beams at the jobsite. This method is based on basic surveying principles, with modifications introduced to increase accuracy and reduce the potential for error. The system requires two people, one to use the instrument and one to hold the surveyor's rod, but overcomes many of the access difficulties associated with the tensioned-wire system. Measurement of beam camber using the precise surveying system is shown in Figure 3.10.

Three basic modifications to standard surveying procedures are used in the precise surveying method. First, sight distances between the instrument and rod are reduced to a maximum of about 12 m (40 ft.). This increases the level of accuracy for each shot. Second, precision scales are attached to the rod to increase the number of measurement divisions. A close-up of the rod with attached scales can be seen in Figure 3.11. Finally, a post level is used to ensure that the rod is perfectly vertical. A close-up of a post level in use with the surveying rod is shown in Figure 3.12. With these modifications, the precise surveying system generally provides good repeatability of measurements. The accuracy of the system is estimated to be approximately ± 0.50 mm (0.02 in.).

Either relative or absolute elevations can be used to make measurements of beam camber and deflection with the precise surveying system. The difference between these two approaches is shown schematically in Figure 3.13. In the relative system, only the differences in elevation between a point at midspan and points at each end of the beam are measured, and absolute elevations are not recorded. In the absolute system, the elevation of each point on the beam is determined using a set of established benchmarks. One

advantage of the absolute system is that elevations at beam ends do not need to be determined for every set of measurements if there is no reason to expect movement at the piers or abutments. The total measurement time is greatly reduced if this assumption is made.

Selection of the appropriate system for each span of the two bridges was dependent upon the conditions and restraints at each jobsite. Consideration was given to crossing roadways and rivers, clearance heights, and possible instrument setup locations. A summary of the type of system used in each bridge is presented in Table 3.2. For most measurements using the precise surveying system, elevations of the bottom surface of the beam were used. Points were marked with paint on the underside of the beams to ensure that the same point was measured each time. In other cases, the top of the bridge deck was used. These specific cases will be addressed in the following paragraphs.



Figure 3.10 - Measurement of Camber Using the Precise Surveying System

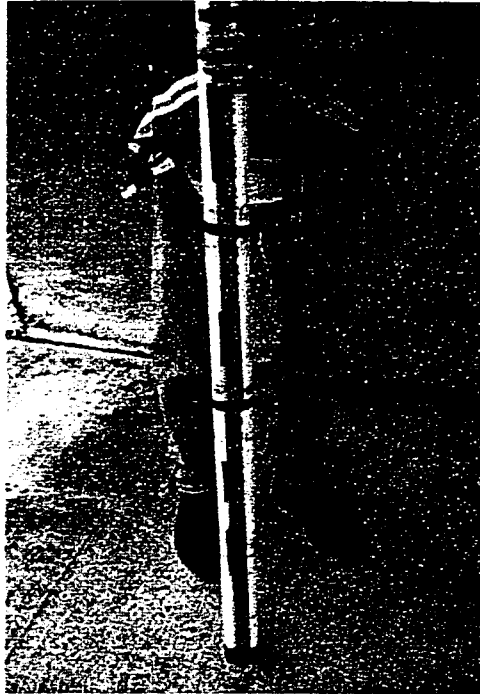


Figure 3.11 - Surveying Rod with Precision Scales Attached

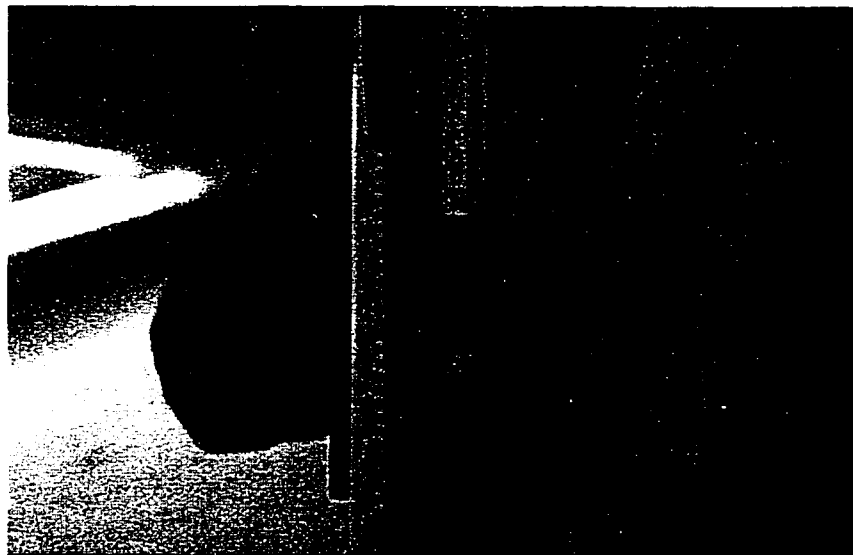


Figure 3.12 - Use of Post Level with Surveying Rod

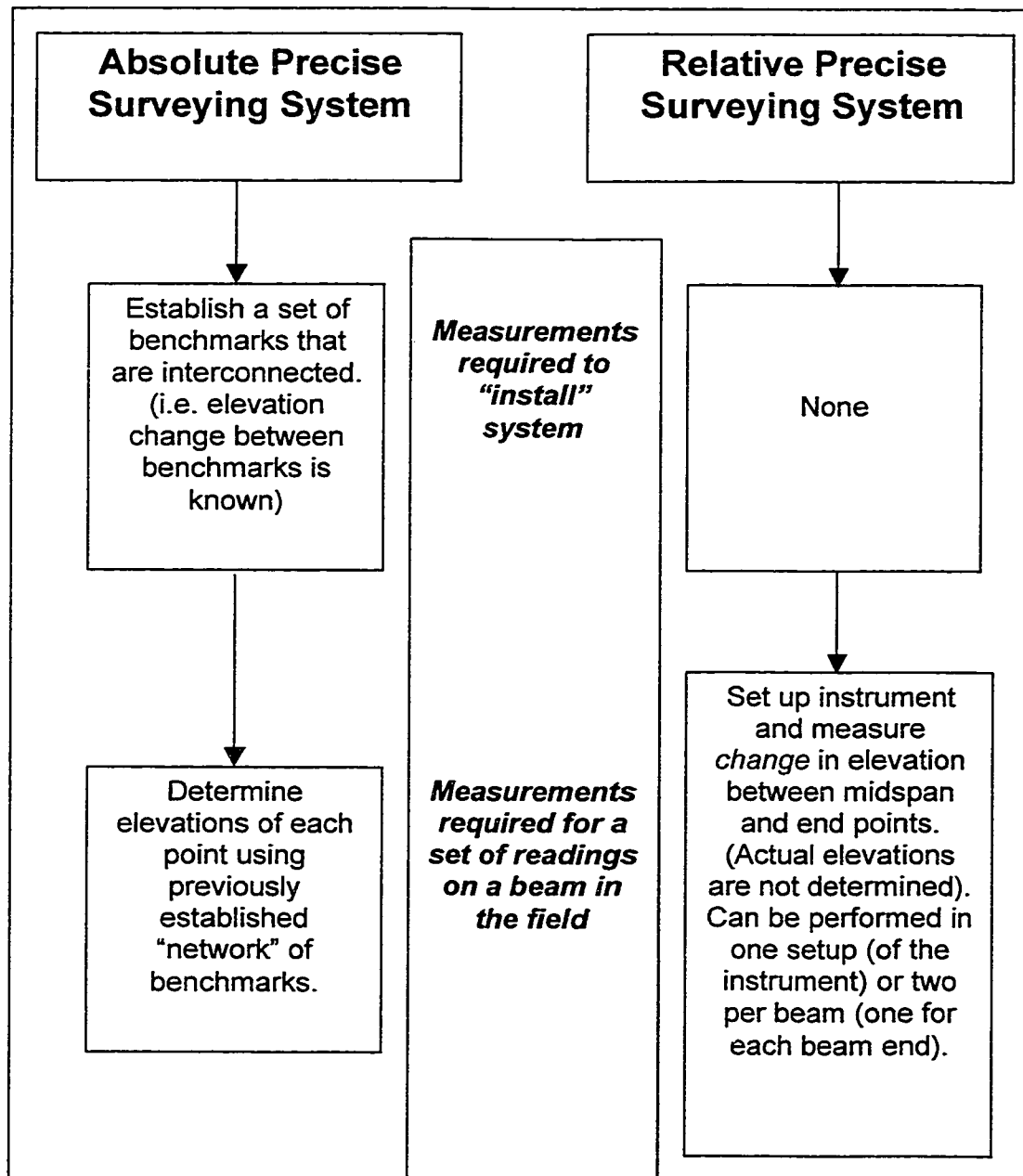


Figure 3.13 - Schematic of Relative and Absolute Precise Surveying Systems

Table 3.2 - Precise Surveying Measurement Systems

Camber or Deflection Measurement	System Type	Measurement Location
Louetta – all measurements before erection	Absolute	Bottom surface of beam
San Angelo – spans 1E,1W before deck casting	Absolute	Bottom surface of beam
San Angelo – spans 2E,3E,4E before deck casting	Relative	Bottom surface of beam
San Angelo – all spans after deck casting	Relative	Top surface of bridge deck

For all measurements of beam camber made at the Louetta jobsite, the precise surveying system was used with absolute elevation measurements. A set of benchmarks was installed with at least one benchmark near each group of instrumented beams, such that absolute elevations along the bottom surface of each beam could be determined. The same basic system was used for measurements on Span 1 of the Eastbound and Westbound San Angelo bridges. All of these beams were low enough that measurements could be made with the instrument at ground level.

Unfortunately, Spans 2, 3, and 4 of the Eastbound San Angelo bridge were too high to set up the instrument at ground level. Span 2 also crossed the North Concho River, leaving few setup options for the precise surveying system. These constraints required that the instrument be placed on the old San Angelo bridge, and that shots be taken from about 30 to 45 m (100 to 150 ft.) away. A relative elevation system was used, with all three shots (midspan and two ends) for each beam taken from a single instrument setup location. A man-lift was required to get the surveying rod to the level of the beams, as shown in Figure 3.14. Precision scales were not used on these spans because the divisions were too small to sight. As a result, the accuracy of the system was reduced to about 0.15 mm (0.06 in.).

After completion of the decks in the San Angelo bridges, measurements were performed using the relative system on the top surface of the bridge deck. The switch to the top surface eliminated the requirement for construction equipment used to access the

underside of the beams, although traffic control may be required for future periodic measurements. The original accuracy of the precise surveying system was also restored because site distances were kept short and the precision scales were used. Note that a full set of readings on the deck surface was taken within minutes of the final set of readings on the bottom surface of the beams, allowing all future readings to be correlated with previous readings.

The precise surveying system is extremely cheap if there is access to surveying equipment, since the precise scales and post level are the only pieces of equipment that must be purchased. The system is also highly flexible and can be adapted to a variety of jobsite constraints. Depending on the exact system used, measurements can be performed very quickly or may take a substantial length of time. The main difficulties associated with the system are due to wind and bridge slope. Wind can cause delays by vibrating the instrument and making it difficult to keep the rod vertical. Bridge slope, such as the 3% grade in some spans of the San Angelo bridges, can reduce accuracy because small changes in measurement locations can cause noticeable variations in measured elevations.

The greatest advantage of the precise surveying system is certainly its lack of a baseline measurement requirement. That is, each measurement is independent and does not need to be compared to a "zero deflection" measurement. The system cannot fail unless the painted measurement marks are removed. Fortunately, this was not a problem in this instrumentation program.

3.3 Data Acquisition

3.3.1 *Description of Data Acquisition Systems*

Five data acquisition systems (DAS) were custom-built by the researchers as part of the instrumentation program. Each DAS unit was constructed to be a stand-alone portable system that could later be installed in one of the completed bridges. Each system was also automated and contained its own power supply, allowing gauges to be read at time intervals programmed by the researchers. Equipment for the DAS units was carefully

selected to be sure that all types of gauges used in the research program – thermocouples, thermistors, vibrating wire gauges, and resistance strain gauges – could be read by the systems. The specific components used in the five DAS boxes were supplied by Campbell Scientific, Inc.

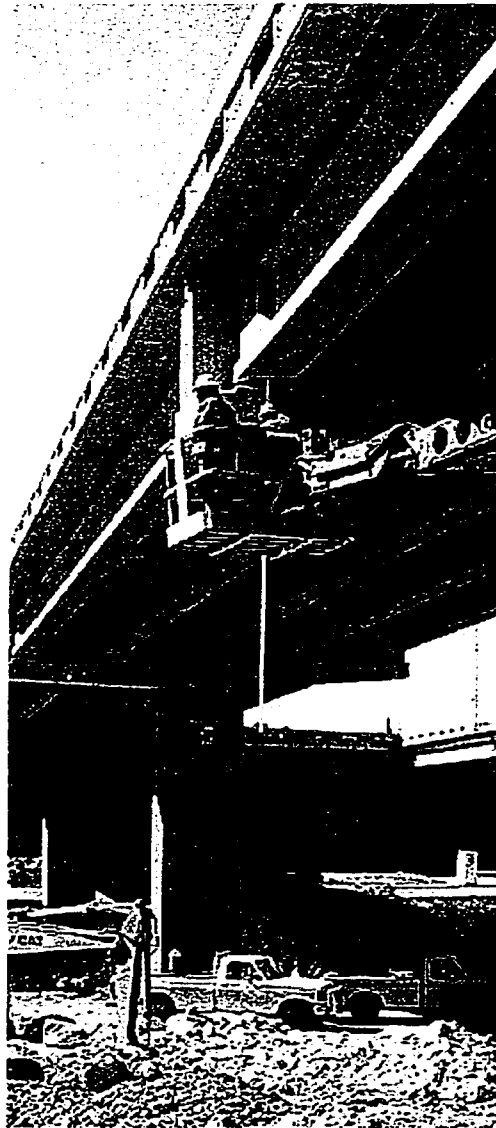


Figure 3.14 - Use of a Man-Lift to Get Surveying Rod to the Level of the Beams in Spans 2, 3, and 4 of the Eastbound North Concho River Overpass

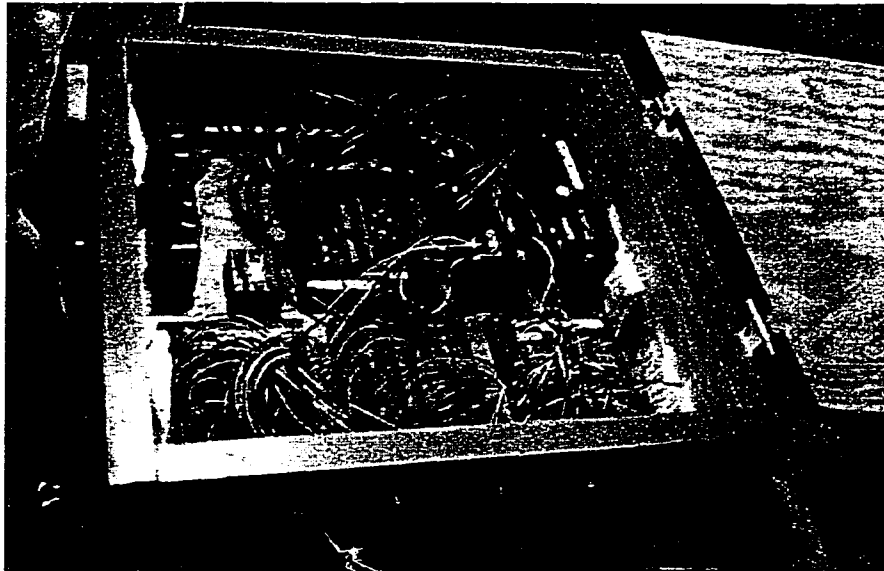


Figure 3.15 - Completed Data Acquisition System (DAS) Box

Each DAS box was fabricated at the Construction Materials Research Group (CMRG) laboratory. The boxes were constructed using 2x8 lumber for the sides and 19 mm (0.75 in.) thick plywood for the base and top. Each box measured approximately 690 mm (27 in.) long, 610 mm (24 in.) wide, and 230 mm (9 in.) deep. Female gauge connectors were installed on opposite sides of the DAS boxes to allow for connection of gauges in the field. Hinges and latches were attached to allow the boxes to open and close securely, and all joints were sealed with silicon to prevent moisture intrusion. A thin strip of foam weatherproofing along the edge of each box provided added protection. A completed DAS box can be seen in Figure 3.15.

A schematic of a typical data acquisition system constructed for the instrumentation program is presented in Figure 3.16. Because the CR10 datalogger has only six differential or twelve single-ended channels, AM416 relay multiplexers were used to allow up to 16 gauges of the same type to be scanned sequentially through a single differential channel. A total of 96 gauges could thus be read using a single datalogger. Note that each multiplexer could accommodate 16 or 32 gauges, depending on the type of gauge. A special vibrating wire interface was required between the multiplexer and datalogger for each group of 16 vibrating wire gauges. For each set of 16 resistance strain gauges, a quarter bridge completion circuit was installed between the multiplexer and datalogger.

Silver-plated Amphenol connectors were used to connect all resistance strain gauges and vibrating wire gauges to the DAS boxes. A special connector panel was purchased from Omega Scientific, Inc. for the connection of thermocouples. Each CR10 datalogger was powered by a 12 V power supply and charge regulator that used eight D-cell batteries. Each datalogger was also connected to a solid-state storage module, which had the capacity to store up to 150,000 data points. A portable numeric keypad could be connected to the datalogger and storage module to control the DAS.

As mentioned previously, five data acquisition system boxes were constructed for use in the instrumentation program. The capacities of each box by gauge type are listed in Table 3.3. Using the datalogger's unique programming language, each box was programmed to read all gauges at a specific time interval. The time interval could be adjusted easily using the numeric keypad. Programming and collection of data is discussed in more detail in Section 3.3.2.

All DAS boxes were designed to be portable so that a box could be connected to several beams in storage at the precast plant. During several beam castings, a DAS box was connected to the gauges of a beam, as shown in Figure 3.17. On many occasions, boxes were left connected to gauges overnight or for a period of several days. In these instances, boxes were typically protected using a sheet of plastic or polyethylene.

Once beams had been erected, DAS boxes were permanently moved to the jobsite. Initially, boxes were stored high on an abutment or attached directly to a beam or pier cap. A man-lift or other piece of construction equipment was usually required to access the DAS boxes, as shown in Figure 3.18. Eventually, all five boxes were modified slightly by moving the power supply and storage module to a second box, and extending the power and serial data cables between the original box and the companion box. This modified arrangement is shown in Figure 3.19 for a DAS box in the Louetta bridge, and in Figure 3.20 for a DAS box in the San Angelo bridge. The additional boxes were installed 3.0 to 3.7 m (10 to 12 ft.) above ground level, where they can be accessed by a step ladder. This arrangement proved to be very convenient, and eliminated the need for construction equipment.

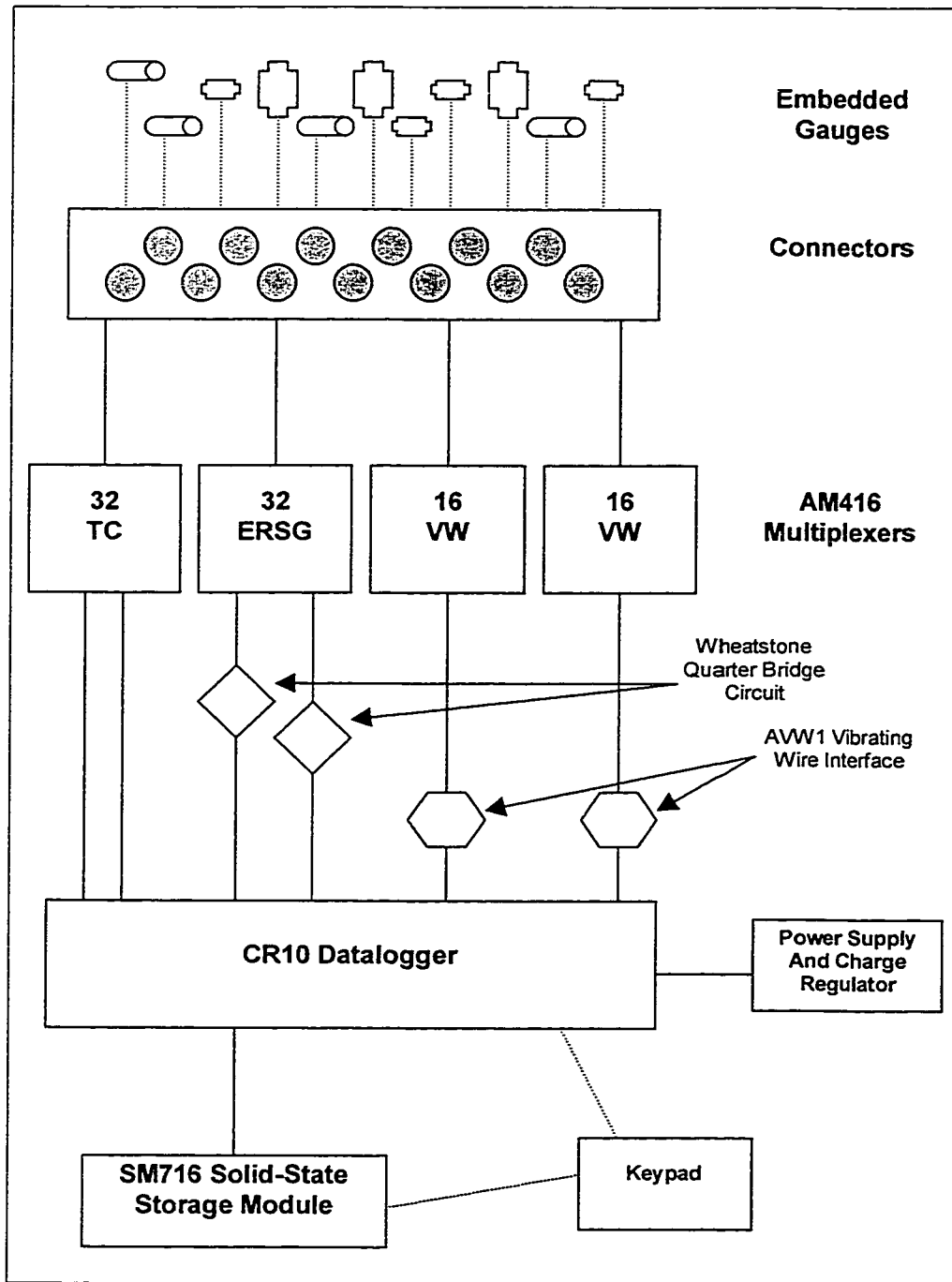


Figure 3.16 - Schematic of a Typical Data Acquisition System

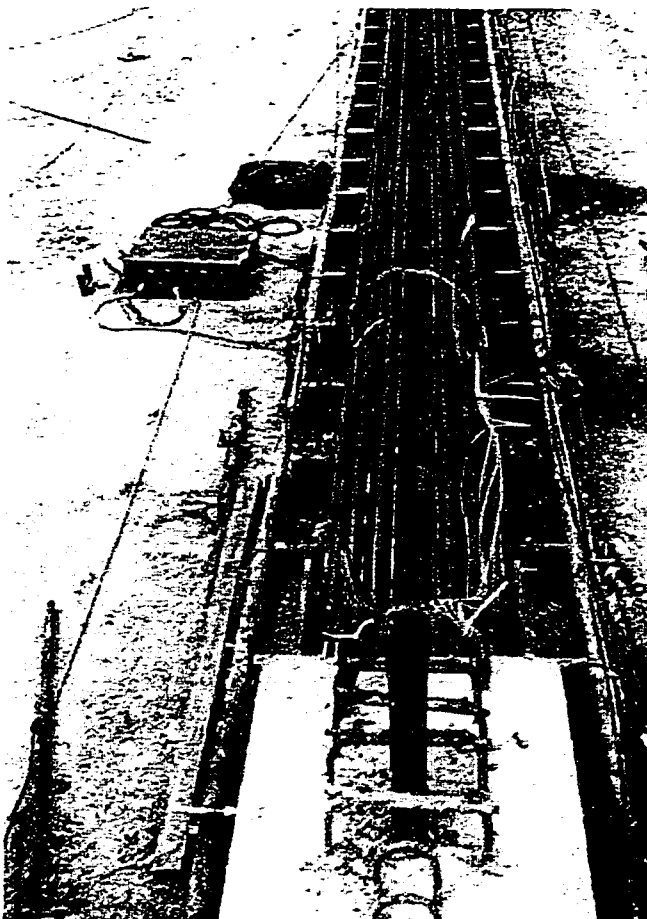


Figure 3.17 - Gauges Connected to a DAS Box Shortly After Beam Casting

Table 3.3 - Capacities of DAS Systems by Gauge Type

Box ID	Location/Spans	# ERSG Channels	# VW Channels ¹	# TC Channels
N	Louetta NB 2-3	64	16	16
S	Louetta SB 1-2	16	48	32
E	San Angelo EB 1-2	32	32	32
X	San Angelo EB 3-4	32	16	32
W	San Angelo WB 1	32	32	32

¹ For each vibrating wire channel, a companion thermistor channel exists

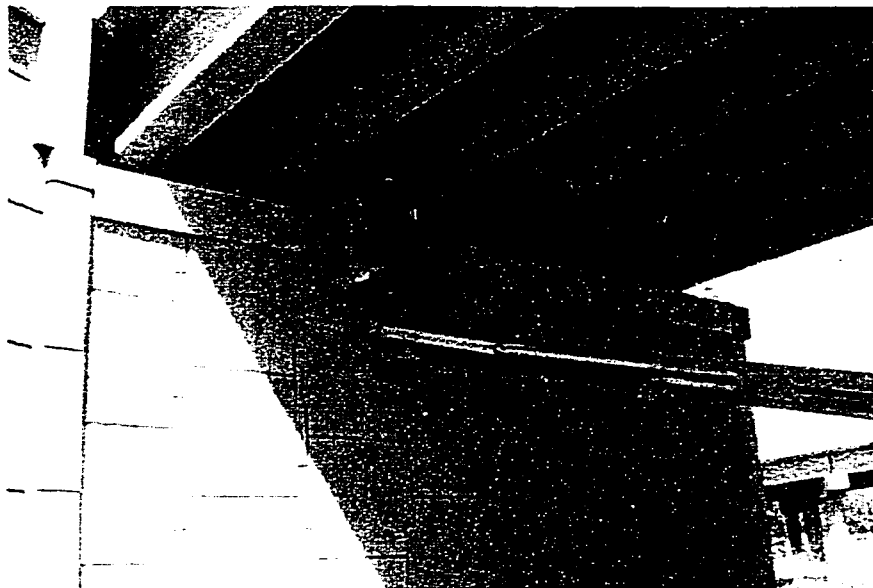


Figure 3.18 - Use of Construction Equipment to Access a DAS Box

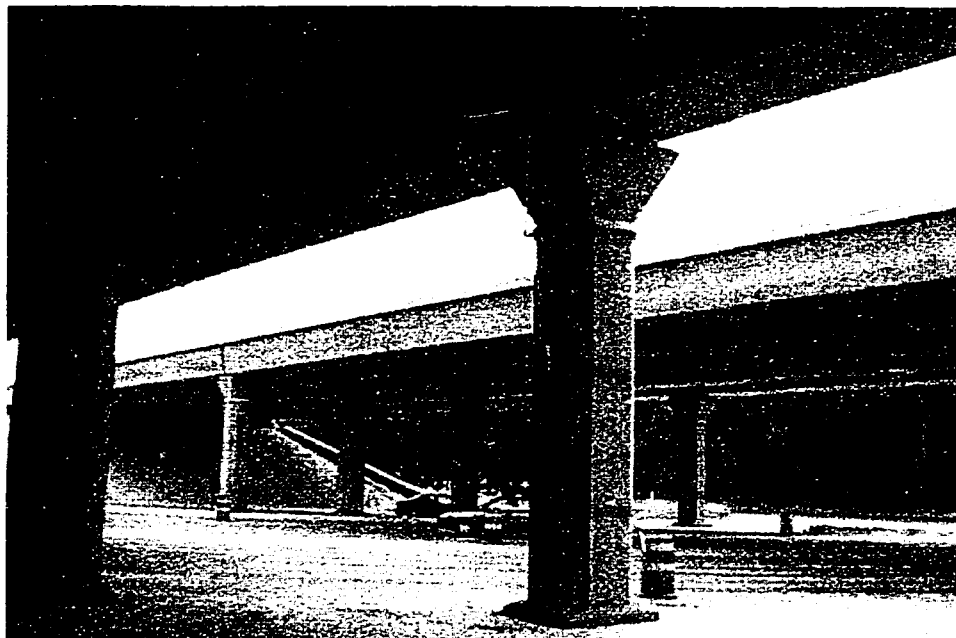


Figure 3.19 - DAS Box with Companion Access Box (Louetta)

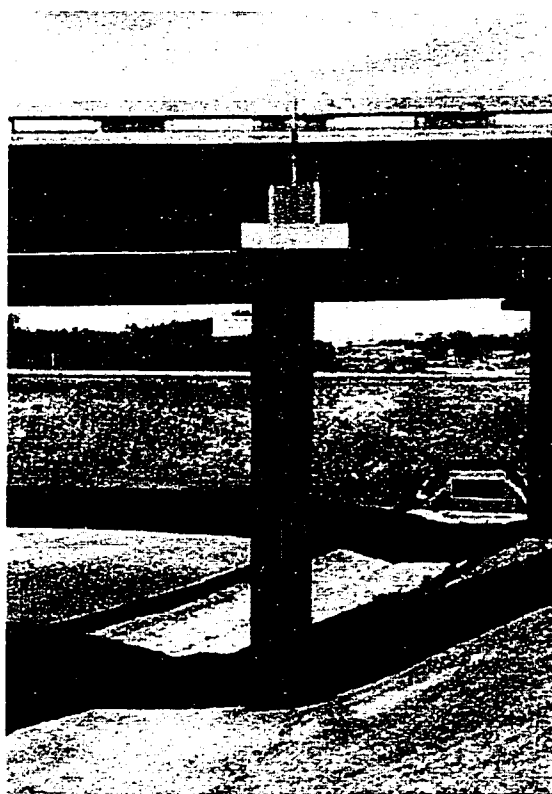


Figure 3.20 - DAS Box with Companion Access Box (San Angelo)

3.3.2 *Programming and Collection of Data*

Datalogger programming and collection of stored data was performed with the assistance of a personal computer and the PC208 [36] software package supplied with the datalogger. An optically-isolated RS232 interface allowed for communication between the computer and storage modules, as shown in the schematic diagram of Figure 3.21. The interchangeable storage modules were essentially used to transport programs and data between the datalogger in the field and the computer in the laboratory. Programs could be written and stored on the storage module at the CMRG laboratory, and then uploaded to the datalogger in the field using the keypad. Likewise, data stored on the storage module in the field could be downloaded into a computer text file at the laboratory. The purchase of extra storage modules allowed for constant rotation of modules between the field and the laboratory.

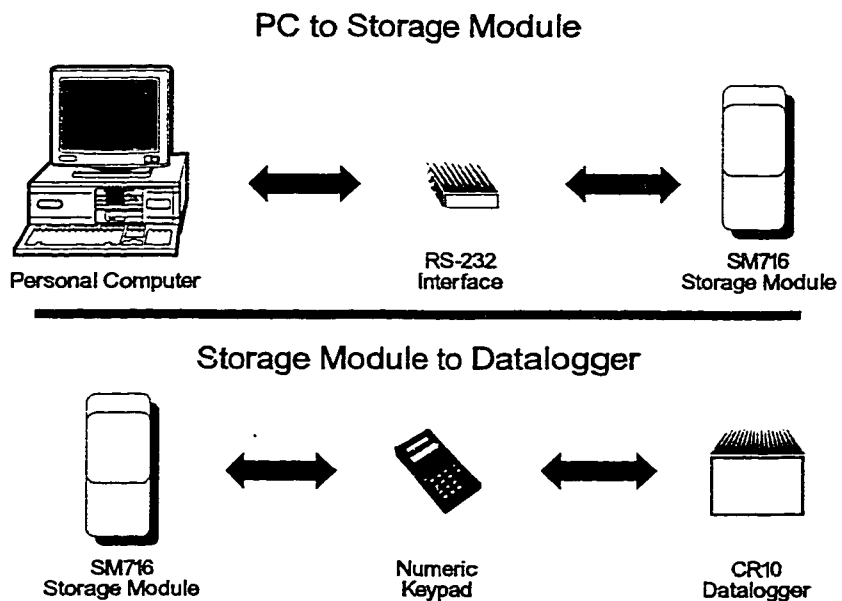


Figure 3.21 - Schematic of Program and Data Transfer Between Datalogger and Personal Computer Using Storage Modules



Figure 3.22 - Switching of Batteries and Storage Modules in the Field

In each DAS box, the datalogger batteries were periodically replaced and storage modules switched. For the long-term collection of data in the completed bridges, this process was typically performed every two to three months. The companion boxes discussed in Section 3.3.1 were accessed using a ladder, as shown in Figure 3.22. First, the storage modules were switched and batteries replaced. The datalogger clock was then checked and reset if necessary, and the correct program was loaded into the datalogger memory. Although travel to the jobsites was required for this box maintenance, the overall system worked very well.

3.3.3 *Manipulation and Reduction of Data*

Raw data values from the datalogger were stored in a CSV (comma-separated value) format in the order that gauges were scanned. Because this data consisted of raw voltages, frequencies, and temperatures in an order that was not useful, a short data manipulation program was written by the researchers. The SORTDTA1 [56] program was written in the PASCAL computer language, and serves two main functions. The data program rearranges the data into a useful order, and also performs mathematical conversion of voltages and frequencies into strain. The modified data file can then be incorporated into a spreadsheet and combined with other data for analysis.

3.4 Instrumentation Plans

The instrumentation plans for the Louetta Road Overpass in Houston and the North Concho River/U.S. 87/S.O.R.R. Overpass in San Angelo are discussed in this section. Emphasis is placed on numbering and identification, as well as presentation of general concepts for instrumented components. A summary of the specific Louetta and San Angelo instrumentation plans is presented at the end of this section. Sketches with gauge locations for every beam, panel, and cast-in-place deck span with instrumentation are presented in Appendix A and Appendix B for the Louetta and San Angelo bridges, respectively.

3.4.1 Gauge Numbering and Identification

Due to the size and complexity of the instrumentation program, complete identification of each embedded gauge required up to seven pieces of information. These pieces of identification are discussed briefly below and summarized in Table 3.4. While complete gauge designations are generally not used throughout this dissertation, they are discussed here because they were an important part of the instrumentation process. These designations were used by the researchers to minimize confusion during the fabrication and installation of gauges, as well as during data reduction and analysis.

Gauge Number - Each gauge was given a unique gauge number based on its location and type. These numbers were the primary form of gauge identification used during the instrumentation program.

Beam/Deck/Panel Designation - Each gauge was installed in or near a specific beam or precast deck panel, or in a certain cast-in-place deck span, which is identified by this designation. These same beam designations are used throughout this dissertation to identify beams for which camber and deflection measurements were made.

Gauge Depth - Each gauge was placed at a specific depth within the beam, panel, or cast-in-place portion of the deck. Some of the exact locations within beams were determined using transformed section properties for the beam. Locations in the cast-in-place deck are theoretical depths below the top of the deck, based on deck thicknesses specified in the project plans.

Gauge Orientation - For strain measurements, some gauges were oriented parallel to the beams, while other gauges were oriented perpendicular to the beams.

Transverse Location - Gauges placed in Louetta U-beams were placed in the web of the section specified by this designation. Gauges in the deck were placed in or above precast panels (between beams or directly over a single U-beam), or directly over the web of a beam.

Longitudinal Location - Gauges were generally placed at midspan or quarter-span of a given beam, or at the end of a span (at an abutment or bent). Additional gauges were placed in the girders near the beam ends.

Gauge Type - This designation identifies the type of each embedded gauge.

3.4.2 Typical Instrumentation Schemes for Components

3.4.2.1 Prestressed Beams

The basic components to the instrumentation scheme used for prestressed beams are shown in Figure 3.23. In nearly every instrumented beam, a strain gauge was placed at the center-of-gravity of pretensioned strands (CGS) for measurement of prestress loss. In most beams, especially during the later stages of the research program, a vibrating wire gauge was used at this location because of the necessity for long-term gauge durability. In selected beams, additional gauges were placed at the CGS at the quarter points of the span and near the beam ends. These gauges were intended to provide additional measurements of prestress loss along the girder. Gauges near the beam ends did not prove to be useful because the strain at these locations is greatly influenced by the transfer length and debonding of strands, and the exact locations of supports during girder storage.

In most beams, a vertical profile of six strain and six temperature gauges was placed at midspan. These gauges allowed for the investigation of the behavior of the complete cross-section, with respect to both strain and temperature. Additional gauges were typically placed in the deck above the beam (or beam web in the Louetta U-beams) to provide additional information about the behavior of the composite section. When vibrating wire gauges were used for this strain profile, temperature data was provided by the thermistors that were an integral part of each gauge. When resistance strain gauges were used for these strain measurements, temperature data was obtained using thermocouples placed at the same locations.

Table 3.4 - Gauge Identification Designations

Gauge Number	<p>001 to 299 Louetta Beam ERSG, VW, and TC</p> <p>301 to 599 Louetta Beam TR (=VW # + 300)</p> <p>601 to 699 Louetta Deck & Panel VW</p> <p>701 to 799 Louetta Deck & Panel ERSG</p> <p>801 to 899 Louetta Deck & Panel TC</p> <p>901 to 999 Louetta Deck & Panel TR (= VW # + 300)</p> <p>1001 to 1099 San Angelo Beam ERSG</p> <p>1101 to 1199 San Angelo Deck & Panel ERSG</p> <p>1201 to 1299 San Angelo Beam VW</p> <p>1301 to 1399 San Angelo Deck & Panel VW</p> <p>1401 to 1499 San Angelo Beam TR (= VW # + 200)</p> <p>1501 to 1599 San Angelo Deck & Panel TR (= VW # + 200)</p> <p>1601 to 1699 San Angelo Beam TC</p> <p>1701 to 1799 San Angelo Deck & Panel TC</p>
Beam / Panel / Deck Designation	<p>Beam:</p> <p>Xmn Where X = bridge, m = span #, and n = beam #</p> <p>Bridge designations:</p> <p>N: Louetta Northbound</p> <p>S: Louetta Southbound</p> <p>E: San Angelo Eastbound</p> <p>W: San Angelo Westbound</p> <p>Example: S25 designates Beam #5 in Span 2 of Louetta Southbound Overpass</p> <p>Panel:</p> <p>LPn Louetta (SB), Panel # n</p> <p>SNPn San Angelo Normal (WB), Panel # n</p> <p>SHPmn San Angelo HPC (EB), Span # m, Panel # n</p> <p>CIP Deck:</p> <p>LNm Louetta Northbound, Span m</p> <p>LSm Louetta Southbound, Span m</p> <p>SWm San Angelo Westbound, Span m</p> <p>SEm San Angelo Eastbound, Span m</p>

Table 3.4 (continued) - Gauge Identification Designation

Gauge Depth	BF	Bottom Flange (2 in. above bottom surface)
	CGS	c.g. of Pretensioned Strands
	CGU	c.g. of Noncomposite U-beam
	CGI	c.g. of Noncomposite I-shaped (Type IV) Beam
	CGC	c.g. of Composite Beam
	TW	Top of Web (at junction between web & flange)
	TF	Top Flange (2 in. below top surface)
	P- <i>n</i> D- <i>n</i>	In panel, <i>n</i> inches above bottom of panel In CIP deck, <i>n</i> inches below top of deck
Gauge Orientation	L	Longitudinal (along beams)
	T	Transverse (across beams)
Transverse Location	E	In or above east web (Louetta U-beams only)
	W	In or above west web (Louetta U-beams only)
	P	In or above center of panel (Beam designation will specify whether over a single U-beam or whether between beams. Center of panel unless noted otherwise.)
Longitudinal Location	M	Midspan
	xQ	Quarter-span (<i>x</i> denotes direction: E,W,N,S)
	4	4 ft. from end of beam
	B	Bearing (approx. 8 in. from beam end)
	ABUT m BENT m	At abutment m , approx. 1 ft. from backwall At bent m , approx. 1 ft. from centerline of bent
Gauge Type	ERSG	Bonded Electric Resistance Strain Gauge
	VW	Vibrating Wire Strain Gauge
	TC	Thermocouple
	TR	Thermistor (integral with Vibrating Wire Gauge)
1 in. = 25.4 mm; 1 ft. = 0.3048 m		

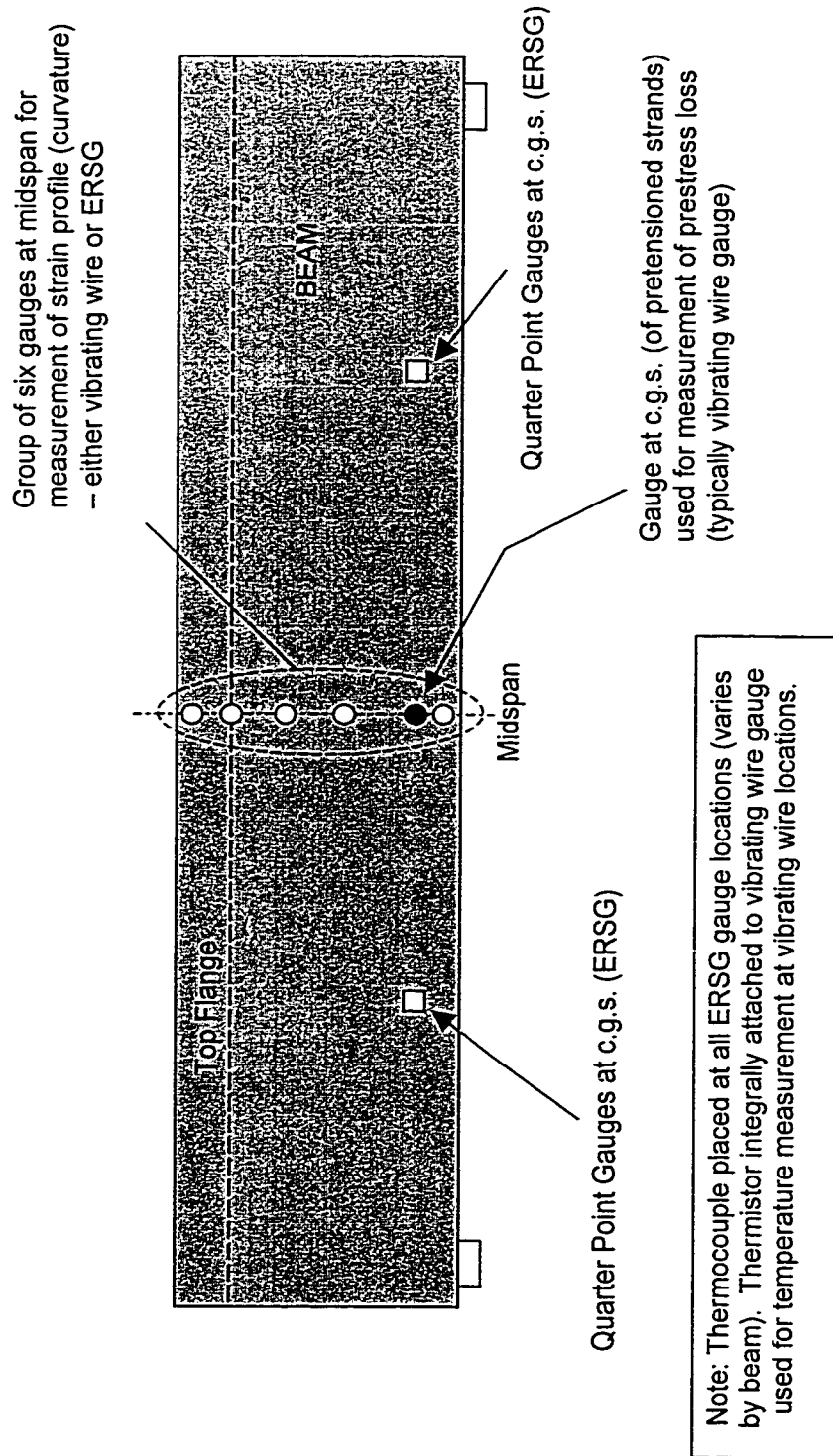


Figure 3.23 - Typical Instrumentation Scheme for Prestressed Beams

TF: Top Flange (2 in. Below Top Fiber)

TW: Top of Web

CGC: c.g. of Composite Beam Section

CGU/CGI: c.g. of Noncomposite Beam Section

CGS: c.g. of Pretensioned Strands

BF: Bottom Flange (2 in. Above Bottom Fiber)

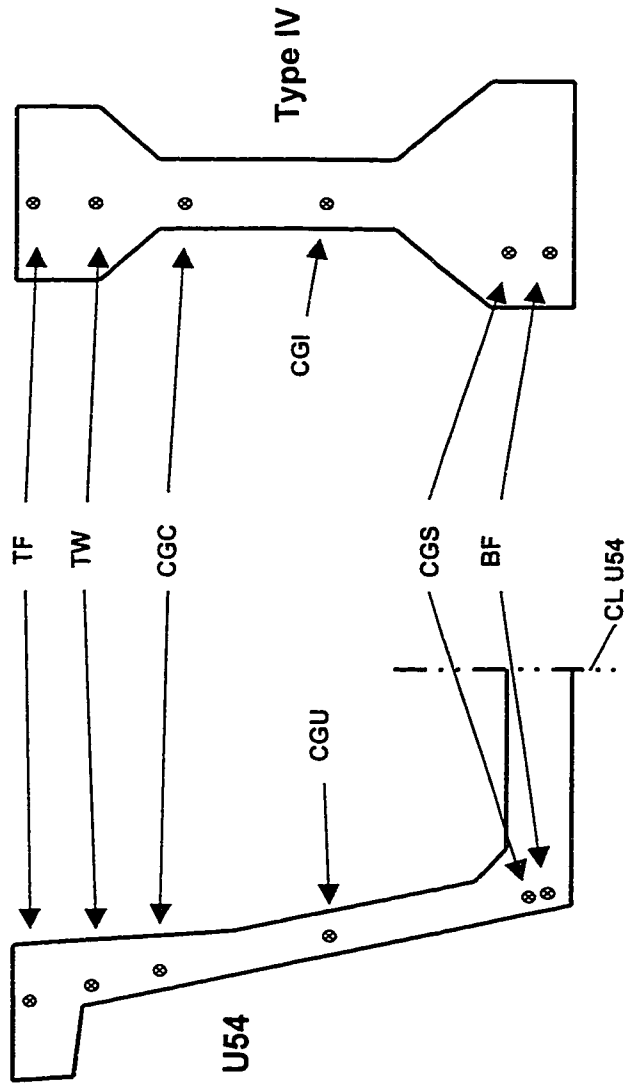


Figure 3.24 - Typical Gauge Locations in Prestressed Beams

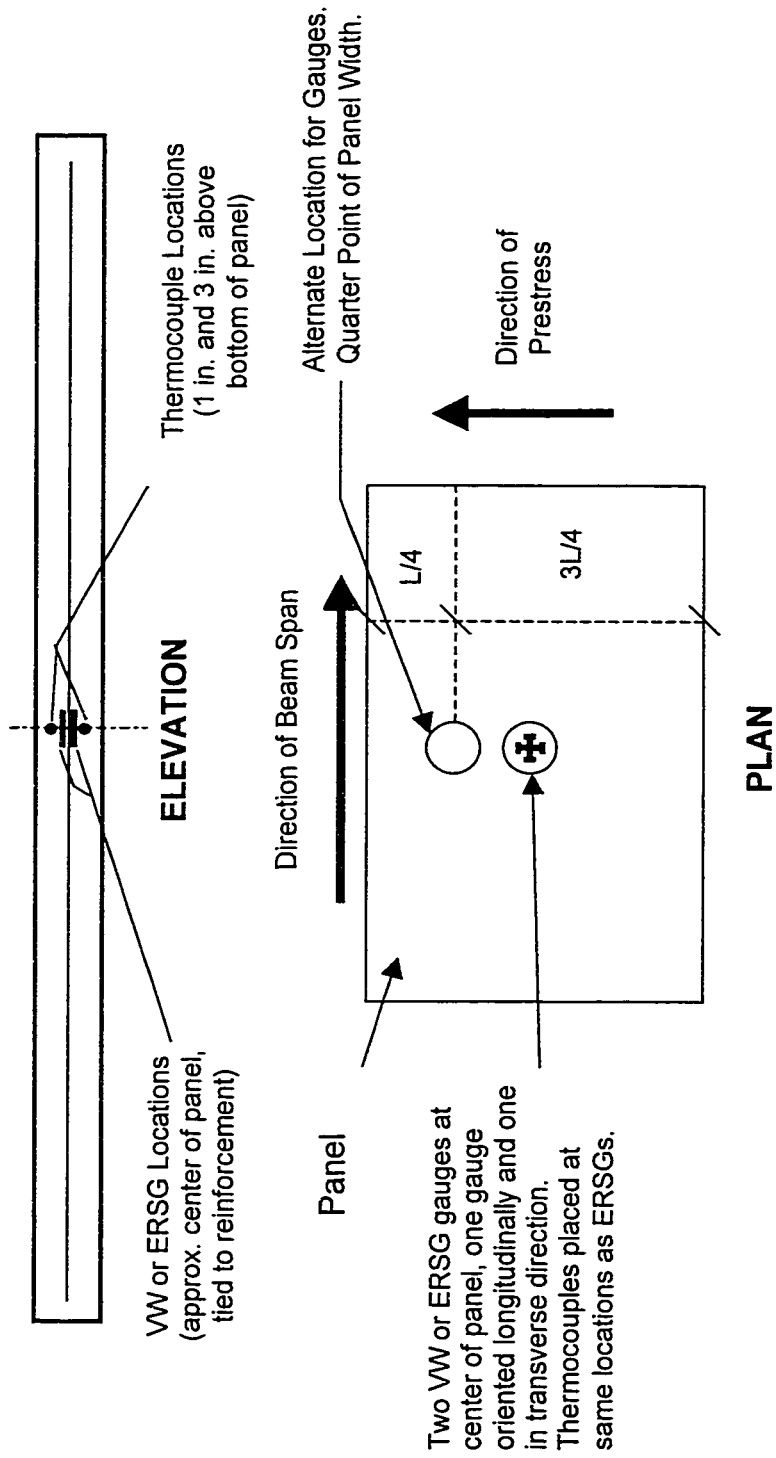


Figure 3.25 - Typical Instrumentation Scheme for Precast Deck Panels

Thermocouples placed in the deck, about 1.5 in. and 3 in. below top of deck to complete temperature profile through deck

In some cases, an ERSG or VW is located here and above beam webs, oriented transversely about 2 in. below top of deck, to investigate distribution of load during live load tests.

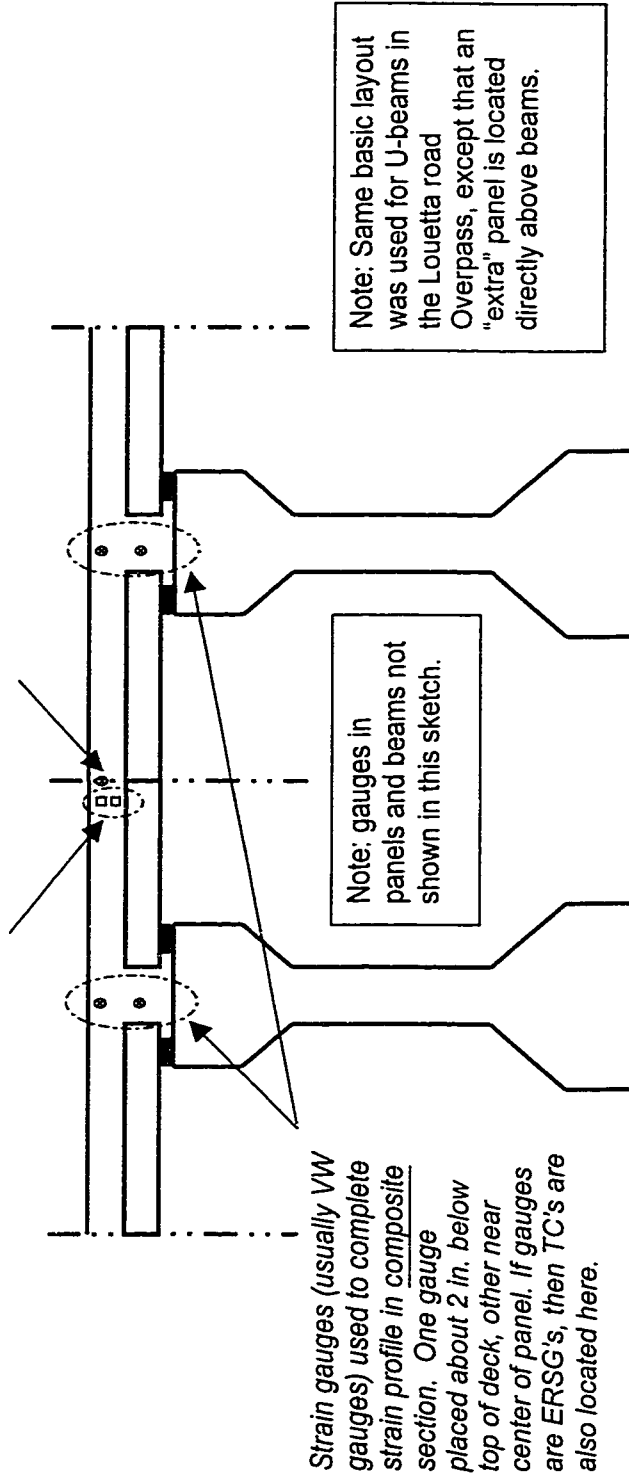


Figure 3.26 - Typical Instrumentation Scheme for Cast-in-Place Bridge Decks

The exact gauge locations used in the Texas U54 and AASHTO Type IV cross-sections are shown in Figure 3.24. In the web and top flange, gauges were typically placed on the inside of the plane of shear reinforcement. In the bottom flange, gauges were typically placed at the third strand from the outside. These gauges could not be placed any closer to the centerline of the section because gauges were always placed after all strands were tensioned. The post-tensioning ducts in the HPC AASHTO Type IV beams also prevented these gauges from being placed at the centerline of the section.

Since some components of the instrumentation scheme discussed in this section were not used in every instrumented beam, the specific instrumentation plans varied from beam to beam. A summary of instrumentation for each beam is presented in Section 3.4.3. The instrumentation of beams for camber and deflection measurements is also summarized in that section.

3.4.2.2 *Precast Deck Panels*

A sketch of the typical instrumentation layout used in precast deck panels is shown in Figure 3.25. Gauges were usually placed at the center of the panel, with one strain gauge oriented parallel to the strands (transverse to the beam in the completed bridge), and one strain gauge oriented perpendicular to the strands (parallel to the beam in the completed bridge). Each of these gauges was positioned as close to mid-depth of the panel as possible, with one gauge usually slightly above and one gauge slightly below. Most strain measurements were made using vibrating wire gauges, because of their improved long-term reliability over resistance strain gauges. In most panels, thermocouples were placed at 25 mm (1 in.) and 76 mm (3 in.) above the bottom of the panel to measure temperature at various depths in the panel.

3.4.2.3 *Cast-in-Place Bridge Decks*

The basic components of the instrumentation scheme used in the cast-in-place bridge decks can be seen in Figure 3.26. Longitudinal strain and temperature gauges were placed above the webs of several instrumented beams to complete the strain or

temperature profile through the composite section at midspan. In most cases, a vibrating wire gauge was used for strain and the integral thermistor was used to measure temperature. In some cases, a combination of resistance strain gauges and thermocouples were used. Additional temperature measurements were made using thermocouples placed directly above precast panels between adjacent beam flanges. In conjunction with thermocouples placed in the panels, these measurements provided a complete temperature profile through the deck between beams (or between the flanges of a single U-beam).

Additional strain instrumentation included gauges oriented transversely at midspan to monitor deck strains during static live load tests, and due to long-term shrinkage and thermal movements. These gauges were typically placed about 50 mm (2 in.) below the bottom surface of the deck, at locations above three or more adjacent beam webs and the deck panels between them. Longitudinal strain gauges were also sometimes placed above beam centerlines near abutments or interior bents. These gauges, which are not shown in Figure 3.26, were intended to provide information about deck continuity during static live load tests. Both vibrating wire gauges and resistance strain gauges were used for these transverse and longitudinal strain measurements.

3.4.3 Summary of Instrumentation Plans

3.4.3.1 Louetta Road Overpass

The basic plan for instrumentation of the Louetta Road Overpass was developed during the summer of 1994, shortly before the first Louetta U-beam was fabricated in August of the same year. Instrumentation was placed in specific regions of the Northbound and Southbound Overpasses, as shown in Figure 3.27. Gauges were then connected to a permanent data acquisition system box in the completed bridge. Note that all instrumented beams are labeled in Figure 3.27 using the designation described in Section 3.4.1.

Ten beams had some form of embedded instrumentation, and deflection behavior was monitored for twelve beams from casting through service. Deflections were monitored on two additional beams (N34 and N35) after erection at the jobsite to allow for investigation of deflection behavior across a full span. A summary of all instrumented beams is

presented in Table 3.5 and Table 3.6 for the Northbound and Southbound Overpasses, respectively. The instrumentation schemes listed in those tables were discussed in previous sections of this chapter. The Louetta instrumentation plan is somewhat complex, as several different arrangements of gauges were used for the prestressed beams. The plan is further complicated because each U-beam has two webs.

Additional instrumentation was placed in the cast-in-place deck of both the Northbound and Southbound Overpasses, in the same regions as instrumented beams. Gauges were also placed in three precast panels in Span 1 of the Southbound Overpass. Specific locations for gauges in beams, panels, and portions of the cast-in-place decks of the Louetta Road Overpass are presented in the sketches of Appendix A.

3.4.3.2 North Concho River / U.S. 87 / S.O.R.R. Overpass (San Angelo)

The original plan for instrumentation of the North Concho River/U.S. 87/S.O.R.R. Overpass in San Angelo was developed during the summer of 1995. The plan was modified during the winter of 1996, prior to fabrication of the first instrumented beams, based on experiences during the instrumentation of the Louetta Road Overpass. In general, the plan was simplified and more emphasis was placed on the use of vibrating wire gauges because of their improved durability. The instrumented areas of the San Angelo bridges can be seen in Figure 3.28. As in the Louetta Road Overpass, gauges were connected to permanent data acquisition system boxes in these regions of the completed bridges.

Ten beams in Spans 1 through 4 of the Eastbound HPC bridge and four beams in Span 1 of the Westbound conventional concrete bridge contained embedded instrumentation. Camber and deflection behavior was also monitored on these beams from casting through service. The deflection behavior of beams without embedded instrumentation in Span 1 of each bridge was monitored after beam erection, and the deflection behavior of all beams in Spans 1 through 4 of the Eastbound Overpass was monitored after the bridge decks were completed. The instrumentation plan for all San Angelo beams is summarized in Table 3.7 and Table 3.8 for the Eastbound and Westbound Overpasses, respectively.

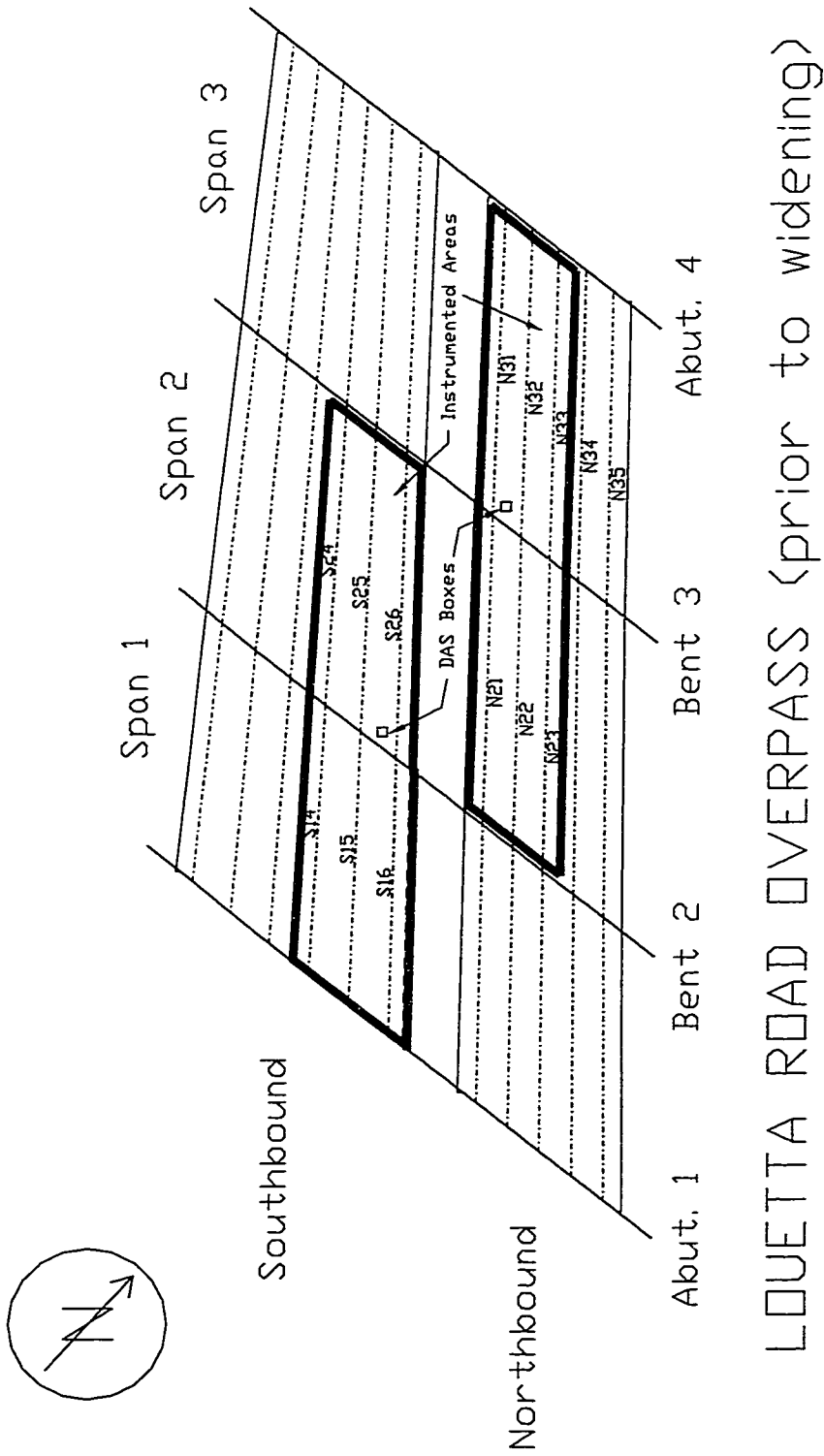


Figure 3.27 - Instrumented Areas of the Louetta Road Overpass

Table 3.5 - Summary of Instrumentation Plan for Beams in the Northbound Louetta Road Overpass

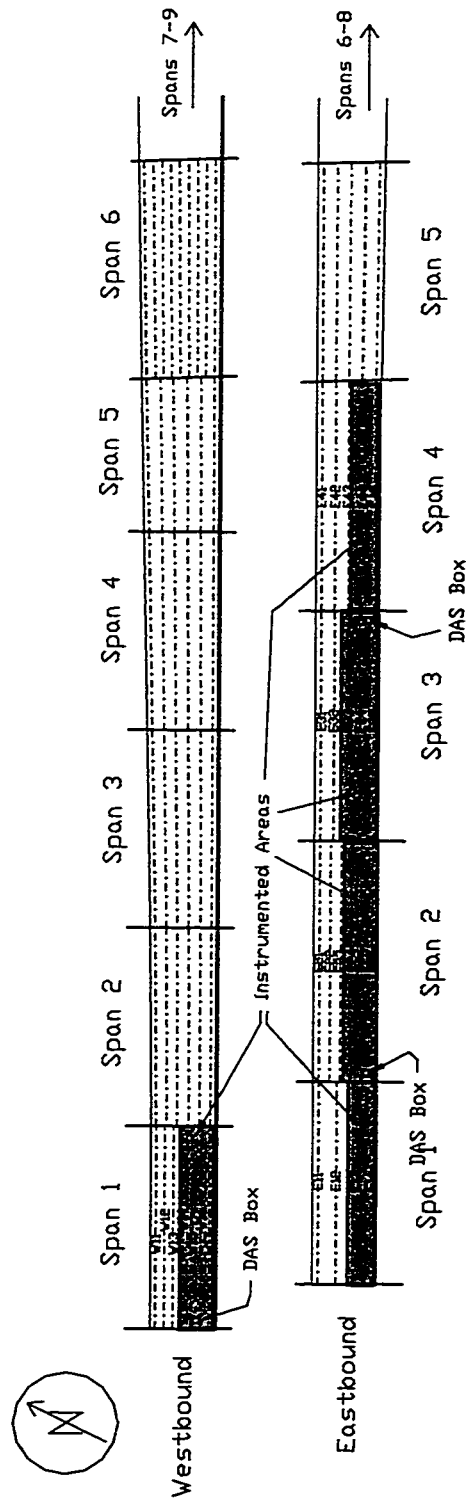
Beam	Side / Web	Strains			Temperatures		Camber/Deflection		
		Gauge at CGS Midspan	Gauges at CGS - Qtr. Point and Beam Ends	Gauges for Vertical Strain Profile at Midspan	Gauges for Vertical Temperature Profile at Midspan	Gauges for Temperature at CGS Along Beam	Before Beam Erection	After Beam Erection	After Deck Casting
N21	E	ERSG	ERSG		TC		TW	PS	PS
N21	W	ERSG	ERSG	ERSG	TC		TW	PS	PS
N22	E	ERSG	ERSG				TW	PS	PS
N22	W	ERSG	ERSG				TW	PS	PS
N23	E						TW	PS	PS
N23	W						TW	PS	PS
N31	E	ERSG	ERSG				TW	PS	PS
N31	W	ERSG	ERSG				TW	PS	PS
N32	E	VW		ERSG			TW	PS	PS
N32	W	VW		VW	TR		TW	PS	PS
N33	E	VW		ERSG			TW	PS	PS
N33	W	VW		VW	TR		TW	PS	PS
N34	E							PS	PS
N34	W							PS	PS
N35	E							PS	PS
N35	W							PS	PS

ERSG = Electrical Resistance Strain Gauge; VW = Vibrating Wire Strain Gauge
TC = Thermocouple; TR = Thermistor (Integral Part of Vibrating Wire Gauge)
TW = Tensioned-Wire Deflection System; PS = Precise Surveying Defl. System

Table 3.6 - Summary of Instrumentation Plan for Beams in the Southbound Louetta Road Overpass

Beam	Side / Web	Strains			Temperatures		Camber/Deflection		
		Gauge at CGS Midspan	Gauges at CGS - Qtr. Point and Beam Ends	Gauges for Vertical Strain Profile at Midspan	Gauges for Vertical Temperature Profile at Midspan	Gauges for Temperature at CGS Along Beam	Before Beam Erection	After Beam Erection	After Deck Casting
S14	E	ERSG		ERSG	TC		TW	PS	PS
S14	W						TW	PS	PS
S15	E	VW		VW	TR		TW	PS	PS
S15	W	VW		VW	TR		TW	PS	PS
S16	E	ERSG	ERSG	ERSG ¹	TC ¹		TW	PS	PS
S16	W	VW	ERSG				TW	PS	PS
S24	E						TW	PS	PS
S24	W						TW	PS	PS
S25	E	VW	ERSG	VW	TR	TC	TW	PS	PS
S25	W	VW	ERSG				TW	PS	PS
S26	E	ERSG	ERSG				TW	PS	PS
S26	W	VW	VW			TR	TW	PS	PS

¹ Additional vertical profile at U-beam diaphragm
ERSG = Electrical Resistance Strain Gauge; VW = Vibrating Wire Strain Gauge
TC = Thermocouple; TR = Thermistor (Integral Part of Vibrating Wire Gauge)
TW = Tensioned-Wire Deflection System; PS = Precise Surveying Defl. System



NORTH CONCHO RIVER/U. S. 87/S. O. R. R. OVERPASS (San Angelo)
 (Only Main Spans Shown)

Figure 3.28 - Instrumented Areas of the North Concho River/U.S. 87/S.O.R.R. Overpass (San Angelo)

**Table 3.7 - Summary of Instrumentation Plan for Beams in the Eastbound North
Concho River Overpass (San Angelo)**

Beam(s)	Strains			Temperatures	Camber/Deflection		
	Gauge at CGS Midspan	Gauges at CGS - Qtr. Point	Gauges for Vertical Strain Profile at Midspan	Gauges for Vertical Temperature Profile at Midspan	Before Beam Erection	After Beam Erection	After Deck Casting
E11,E12						PS	PS
E13	VW	ERSG	VW	TR	TW	PS	PS
E14	VW	ERSG	VW	TR	TW	PS	PS
E21,E22,E23							PS
E24	VW	ERSG	ERSG	TC	TW	PS	PS
E25	VW		VW	TR	TW	PS	PS
E26	VW	ERSG	ERSG	TC	TW	PS	PS
E31,E32							PS
E33	VW	ERSG	ERSG	TC	TW	PS	PS
E34	VW	ERSG	ERSG	TC	TW	PS	PS
E35	VW	ERSG	VW	TR	TW	PS	PS
E41,E42,E43							PS
E44	VW	ERSG	VW	TR	TW	PS	PS
E45	VW	ERSG	ERSG	TC	TW	PS	PS

ERSG = Electrical Resistance Strain Gauge; VW = Vibrating Wire Strain Gauge
TC = Thermocouple; TR = Thermistor (Integral Part of Vibrating Wire Gauge)
TW = Tensioned-Wire Deflection System; PS = Precise Surveying Defl. System

Table 3.8 - Summary of Instrumentation Plan for Beams in the Westbound North Concho River Overpass (San Angelo)

Beam	Strains			Temperatures	Camber/Deflection		
	Gauge at CGS Midspan	Gauges at CGS - Qtr. Point	Gauges for Vertical Strain Profile at Midspan	Gauges for Vertical Temperature Profile at Midspan	Before Beam Erection	After Beam Erection	After Deck Casting
W11						PS	PS
W12						PS	PS
W13						PS	PS
W14	VW	ERSG	ERSG	TC	TW	PS	PS
W15	VW	ERSG	ERSG	TC	TW	PS	PS
W16	VW	ERSG	VW	TR	TW	PS	PS
W17	VW	ERSG	VW	TR	TW	PS	PS
ERSG = Electrical Resistance Strain Gauge; VW = Vibrating Wire Strain Gauge TC = Thermocouple; TR = Thermistor (Integral Part of Vibrating Wire Gauge) TW = Tensioned-Wire Deflection System; PS = Precise Surveying Defl. System							

Instrumentation was also placed in precast panels and cast-in-place decks in the areas with instrumented beams. Six panels from the Eastbound Overpass and two panels from the Westbound Overpass were instrumented. Gauges were placed in the cast-in-place portions of the deck in Spans 1 through 3 of the Eastbound Overpass and Span 1 of the Westbound Overpass. The specific locations for gauges in all instrumented components of the San Angelo bridges are shown in the sketches of Appendix B.

3.5 Preparation and Field Installation of Instrumentation

This section summarizes the preparation required for instrumentation gauges and systems at the laboratory, as well as the procedures used to install instrumentation in the field. Emphasis is placed on the description of the overall process, rather than on specific details. More detailed descriptions for some of the procedures discussed in this section are presented by Byle and Burns [35]. Two major issues that heavily influenced the procedures used for field operations — communication with contractors and travel requirements for the researchers — are also discussed in this section.

3.5.1 Preparation of Instrumentation

3.5.1.1 Embedded Gauges

All gauges were prepared at the Construction Materials Research Group laboratory prior to installation in the field. Each type of gauge was prepared as discussed in Section 3.2.2. Vibrating wire gauges required no special preparation, but resistance strain gauges required extensive preparation. The pieces of steel reinforcing bars to which the gauges were to be bonded were first prepared by grinding, sanding, and cleaning a small area of the bar. Gauges were then bonded using a special adhesive epoxy, which was allowed to set overnight. Finally, each bonded gauge was waterproofed using layers of butyl rubber, nitrile rubber, and electrical tape as described in Section 3.2.2.4. Thermocouples were formed later, after leadwire was cut to length, by twisting thermocouple wire and protecting the connection with electrical tape as described in Section 3.2.2.1.

The second portion of the instrumentation preparation process involved the grouping of individual gauges. Leadwire was cut to a specific length for each individual gauge in a large field near the CMRG lab. After all leadwires for a gauge group were cut and labeled, the leadwires were spooled as shown in Figure 3.29. Any thermocouples in the gauge group were then formed, and resistance strain gauges were attached to appropriate leadwires. Finally, Amphenol or thermocouple connectors were placed on the other end of the leadwire group for attachment to the data acquisition system box. This

spooling system evolved over the course of the instrumentation process as the most efficient way to group and transport fully-prepared gauges. As discussed in Section 3.5.2, this grouping process also significantly reduced the installation time required at the precast plant or jobsite.

3.5.1.2 Tensioned-Wire Deflection System

The components of the tensioned-wire deflection system described in Section 3.2.2.6 were fabricated at the Construction Materials Research Group lab, with the assistance of the machine shop at the Ferguson Structural Engineering Laboratory. Fabrication of several systems was performed at once to save time. Bearings for the systems were first fabricated at the machine shop. Meanwhile, anchor bolts for each component of the system were cut to the proper length and checked for damage to threads. Bolts for the dead end of the system then had a 0.8 mm (0.03 in.) hole drilled through the cross-section to accommodate the tensioned wire, as shown in Figure 3.7. Using a lathe, bolts for the live end were smoothed to the match the inner diameter of the bearings. Finally, the extension pieces were cut from an aluminum strip using a band saw, and a hole was drilled into each piece to accommodate the anchor bolt using a drill press.

3.5.2 Field Installation of Instrumentation

3.5.2.1 Prestressed Beams

The complexity of the beams in both projects — including the skewed end blocks, post-tensioning ducts, extra anchorage zone reinforcement, and large number of debonded strands — increased the average beam fabrication cycle from two days to about one week. About three to four days before casting, strands were tensioned and debonding was applied to selected strands. Split plastic tubing and special tape were used for the debonding process. After all strands were tensioned and debonded, and usually about two days before casting, placement of the mild steel reinforcement would begin. The installation of

embedded instrumentation in prestressed beams was generally performed after this procedure was complete, since the steel reinforcement was used as a framework for the placement of gauges. The researchers found that this sequence minimized the potential for inadvertent damage to instrumentation during the beam fabrication process.

To begin the installation of embedded instrumentation, the group of gauge wires was unspooled alongside the beam and any major knots in the leadwire were untangled. Then, gauges were placed into the locations shown in Figure 3.24 using the strands and stirrups as framework. The process of placing a gauge is shown in Figure 3.30. Where necessary, short #3 steel reinforcing bars were tied to the stirrups at the correct depth. A complete set of gauges through the depth of a beam can be seen in Figure 3.31.

Nylon cable ties were then used to secure the leadwires to the steel framework. Wires were run up the stirrups, and then along the longitudinal reinforcement in the top flange to the beam ends, as shown in Figure 3.32. Although these wires may seem to be unprotected from damage due to internal vibrators, the researchers and fabricator made a conscious decision to run the wires in the top flange. There was a general feeling that a greater chance of damage was present if wires were run in the beam webs, since the wires would not be visible to workers during casting. At the beam ends, gauge wires were either connected to a data acquisition system box, or rolled up and protected in a plastic bag.

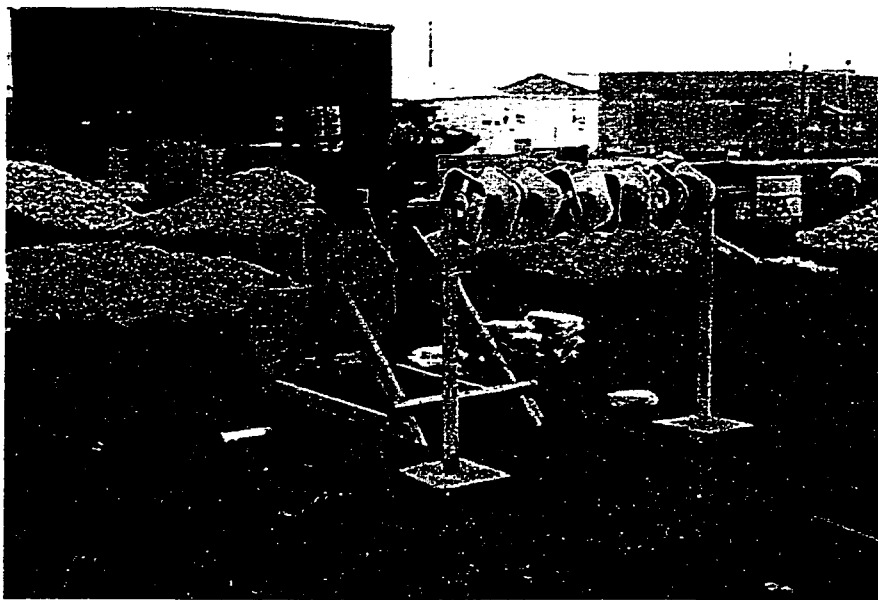


Figure 3.29 - Spooling of Leadwire for a Group of Gauges



Figure 3.30 - Placement of an Embedded Gauge in a Beam



Figure 3.31 - Complete Group of Gauges at Midspan of a Beam



Figure 3.32 - Leadwires Tied to Reinforcement in the Top Flange of a Beam

After the installation of embedded gauges was complete, the fabricator erected forms and prepared for casting the next day (or later the same day). The casting operation is not discussed in this dissertation, but is discussed by Myers and Carrasquillo [88]. Beams were cured overnight under tarps, and release strengths were generally obtained in about 18 to 24 hours. However, a few beams that were cast on Saturday were cured for two nights. During cool weather, steam was used to maintain a desirable ambient temperature under the tarps, but not to accelerate curing.

Forms were generally removed shortly after release strengths were obtained. External beam instrumentation was then installed, including the tensioned-wire deflection system and, in some cases, DEMEC mechanical strain gauge points. For the tensioned-wire deflection system, bolt holes were drilled using a hammer drill. Bolts were then installed and secured, and the precise scale was attached using the aluminum extensions, five-minute epoxy gel, and clamps. The piano wire was then strung between the beam ends. If the DEMEC system was used, other members of the research team would simultaneously fix points to the side of the beam using five-minute epoxy gel. These points were then allowed to set for at least 15 to 20 minutes.

A full set of readings on both internal and external instrumentation was taken just before release. Once these readings were complete, the fabricator gradually released the

tension in the strands by slowly reducing the hydraulic pressure in the stressing system, which is the procedure required by the Texas Department of Transportation for the release of all their pretensioned beams. When the pressure was completely released, the extensions of detensioned strands were flame cut near each beam end. A complete set of readings was taken immediately after this flame cutting procedure. Beams were removed from the bed and placed into storage after the readings were complete, or the next morning if it was late in the day.

3.5.2.2 *Precast Deck Panels*

A few precast prestressed deck panels from each bridge were fitted with embedded instrumentation. For convenience, all instrumented panels of each type — Louetta HPC, San Angelo HPC, and San Angelo non-HPC — were fabricated during a single pour. Vibrating wire or resistance strain gauges were tied to the strands and panel reinforcement as close to the center of the panel as possible. Thermocouples were placed at specific depths in the panel by pre-attaching them to a small piece of 6 mm (0.25 in.) diameter steel rod, and then tying the rod to the strands and panel reinforcement. Gauge wires were tied to the reinforcement using nylon cable ties, and run toward the edge of the panel.

Selected gauges were connected to the DAS box during casting, which was stored alongside the casting bed and wrapped in plastic for protection. Gauge wires that were not connected during casting were rolled up and stored in plastic bags. Panels were generally cured overnight and released the next morning. HPC panels for the Louetta bridge were cured under tarps, while all panels for the San Angelo bridge were cured by pooling water over the finished concrete panels. A full set of readings was taken on all embedded gauges just before and just after the release of prestress.

3.5.2.3 *Cast-in-Place Bridge Decks*

The same spooling system used for grouping beam gauges discussed in Section 3.5.1.1 was used to transport gauges for the cast-in-place decks. As with the prestressed beams, cast-in-place deck gauges were installed after all steel reinforcement was in place.

This allowed the reinforcement to act as a framework for the placement of gauges. Above deck panels, gauges were typically tied directly to the transverse deck reinforcement. A thermocouple installed directly on the reinforcement above a deck panel can be seen in Figure 3.33. Where necessary, small pieces of reinforcement were tied to existing reinforcement to support gauges. Gauges directly above beams were sometimes tied to stirrups or to the short lengths of strand protruding from precast deck panels. Two vibrating wire gauges installed directly above a beam can be seen in Figure 3.34.

Gauge wires were run along the top of the longitudinal reinforcement toward the location of a DAS box at the abutment or interior bent. Although it would have been desirable to run wires underneath the transverse reinforcement, this was not done because it would have required that each wire be fed under each transverse bar. Instead, wires were tied down every 0.6 to 0.9 m (2 to 3 ft.) using nylon cable ties, and marked using fluorescent orange spray paint. The paint was intended to make the wires stand out to assist workers in protecting them during the deck pour. An example of leadwires that have been tied down and marked is shown in Figure 3.35. At a location near the abutment or bent, the leadwires were run through holes cut into the deck formwork. As can be seen in Figure 3.36, this allowed the wires to be brought under the deck for hookup to the DAS box.

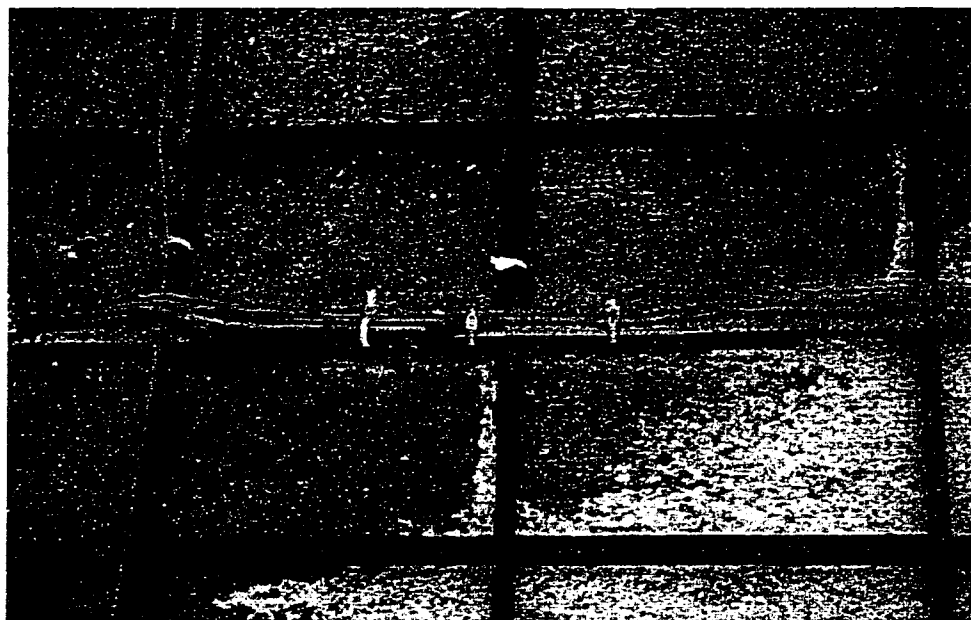


Figure 3.33 - Thermocouple Tied to Cast-in-Place Deck Reinforcement

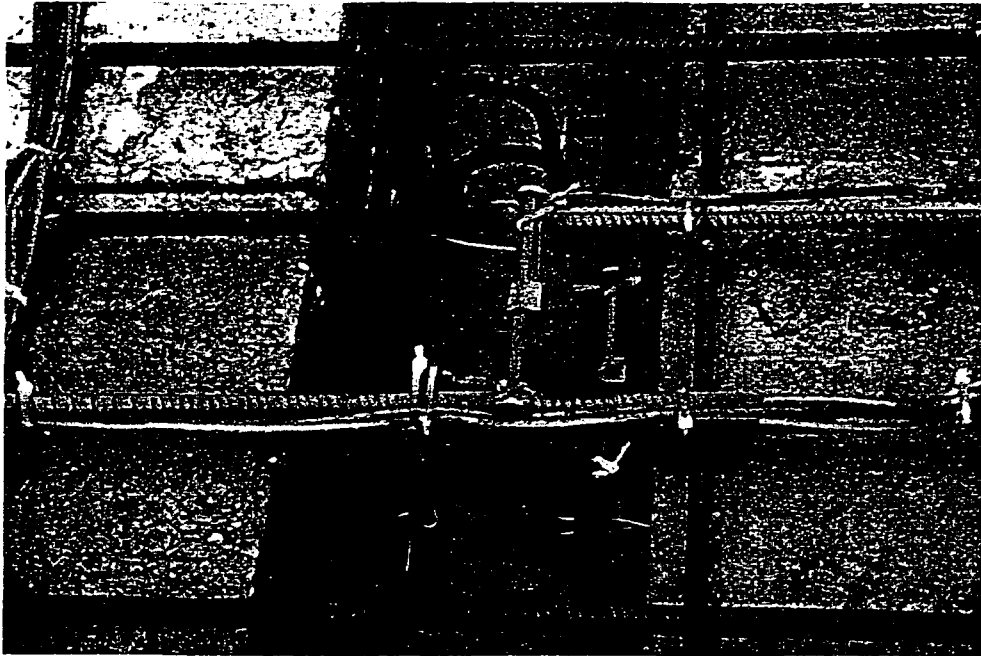


Figure 3.34 - Vibrating Wire Gauges Placed in Cast-in-Place Bridge Deck

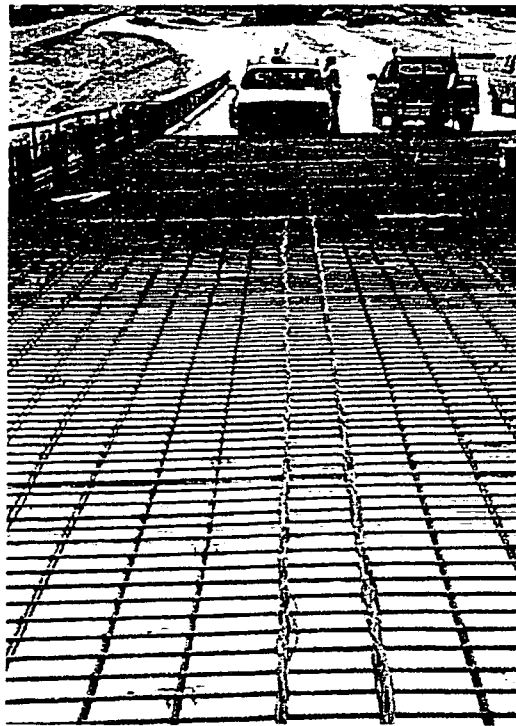


Figure 3.35 - Leadwires Tied to Reinforcement in Cast-in-Place Deck



Figure 3.36 - Leadwires Run Through Holes in Deck Formwork Near DAS Box

Since gauges were installed using the deck reinforcement as framework, and the exact depth of the reinforcement within the cast-in-place portion of the deck varies in each bridge, the distance of each gauge location above or below the top of the deck panels was measured and recorded. Measurements were also taken from the top surfaces of beams to the tops of the precast panels. Combined with measurements of average deck thicknesses provided by the TxDOT field engineers, the location of each gauge within the deck can be determined. Tables summarizing these measurements for all cast-in-place deck gauges may be found in Appendix C. These measurements were recorded for all cast-in-place deck pours with embedded instrumentation, except for the Northbound Louetta Road Overpass.

3.5.3 *Coordination of Efforts Between Researchers and Contractors*

In field research projects, communication and cooperation between the researchers and contractors is absolutely essential. Each party has its own interests: the researchers want to run a successful scientific research program, while the contractor wants to construct

a bridge in an efficient manner without costly delays. Scheduling thus becomes a key issue in satisfying the needs of both parties. Furthermore, the parties can work together to solve unexpected problems that arise with respect to the research needs. In both the Louetta and San Angelo projects, pre-bid and pre-construction partnering meetings, which also involved representatives of TxDOT, helped ensure a healthy relationship between all parties.

Scheduling was an extremely important issue in both projects because of the long distances that the researchers had to travel between Austin and the jobsites or precast plants. As discussed in Section 3.5.2, the researchers needed to install instrumentation at a specific stage of the construction process. Good communication with the contractor or fabricator enabled the researchers to plan travel as far in advance as reasonably possible. Still, the nature of the construction process does not lend itself to perfect scheduling, so flexibility on the part of both parties was essential. Scheduling issues were also dealt with in a practical manner, by arranging the beam and panel casting sequence such that delays due to instrumentation were minimized. For example, the beam casting sequence called for most pours with instrumentation to include two instrumented beams, rather than one or three beams. This allowed researchers to reduce the number of instrumented pours without significantly increasing the delay on each pour.

Every effort was made by the researchers to minimize the delays to the contractors' normal schedules caused by the instrumentation process, without sacrificing the quality of the research program. As discussed in Section 3.5.1 and Section 3.5.2, gauges were grouped at the laboratory using a spooling system. This significantly reduced the time required to install gauges in the field, thereby reducing delays to the contractor's schedule. A strong effort was also made to have enough members of the research team on hand for each step of the instrumentation process, although this was difficult to arrange in some cases because of the amount of travel involved.

Delays were also minimized by keeping the contractors and fabricators aware of the steps involved in each aspect of the instrumentation process, so that the contractors could make necessary arrangements. Contractors often helped the researchers by supplying construction equipment, such as man-lifts, generators, and hammer drills. When unexpected problems arose regarding the installation or reading of instrumentation, the researchers and contractors often worked together to come up with a satisfactory alternative. Through the duration of this research program, communication and cooperation between the researchers and the contractors proved to be a valuable asset.

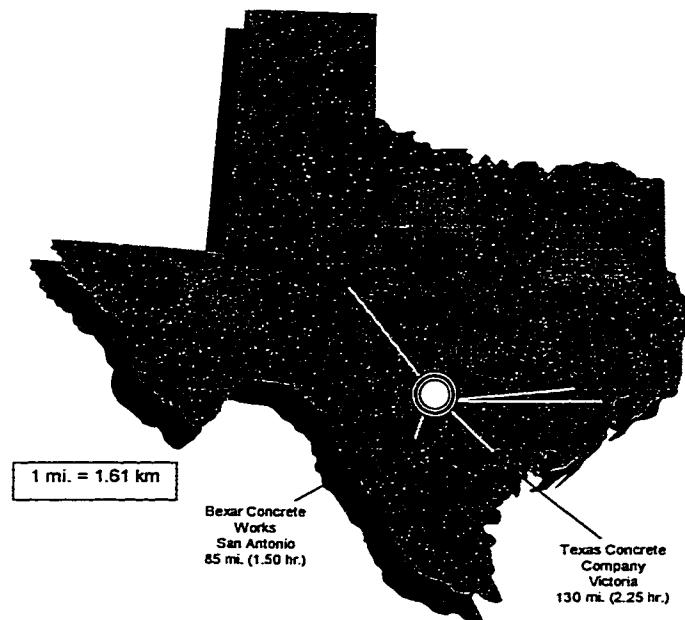


Figure 3.37 - Travel Distances from Austin to Jobsites and Precast Plants

3.5.4 *Travel*

One of the greatest difficulties associated with the research program was dealing with the many hours of travel required for implementation of the research plan. Long trips were required to install instrumentation or data acquisition system boxes, to make companion specimens during concrete pours, and to make measurements on the completed components or completed bridge. Several overnight trips were made, but most trips were day trips to accommodate the schedules of the different members of the research team, especially with respect to coursework. Therefore, trips usually involved leaving very early in the morning and returning late in the evening.

The mileage and typical travel times from Austin to the jobsites and precast plants are shown in Figure 3.37. Based on informal records kept by the researchers, it is estimated that 125 trips were made to the various sites as part of the instrumentation program. The total mileage traveled on such trips, which do not include trips for project meetings and presentations, was approximately 64,000 km (40,000 mi.). It is also estimated

that over 3500 man-hours were spent outside of Austin on the research program, and that approximately 45% of that time was spent just travelling to and from the various jobsites and precast plants. Simply put, travel requirements made execution of the instrumentation plan a monumental task.

3.6 Problems Encountered

Problems invariably arise during field research projects, in large part because the researchers do not control the environment in which the research is being conducted. Furthermore, measurements and readings may generally be taken only once, and if problems occur, data is usually lost. There is generally no practice run, and generally no second chance. Some of the problems inherent to the instrumentation systems used in this research program have been discussed throughout this chapter. Problems due to more specific occurrences are discussed below, and have been separated into five groups.

3.6.1 *Lost Data*

There were a few instances in which data was not collected by the data acquisition system boxes. It is assumed that either the datalogger program was not activated, or that there was a battery failure. The most notable and important occurrence of this type of problem was for the zero readings on a few beams just prior to release. On a few other occasions, data was collected by the datalogger, but the data for certain gauges was missing. This most likely occurred because the connectors between the leadwires and DAS box were not fully connected. These problems clearly show one of the biggest deficiencies of the data acquisition systems – the lack of real time data output.

A second type of problem with the DAS boxes occurred when data on the storage module was lost because it was overwritten by new data before it could be downloaded. This occurred because the storage modules have circular memory, and because an error was made in calculating the capacity of the storage module. Circular memory means that once the data storage capacity is reached, the oldest data is overwritten by new data. The

error in capacity was due to an oversight that the data was being stored in high-resolution format, which requires two data locations per measurement value. As a result, some data was lost in the Fall of 1996 from the casting of the Northbound Louetta and San Angelo Westbound Span 1 cast-in-place decks. This error was later corrected when it was discovered that the storage modules could be programmed to stop recording data when capacity has been reached, and this error did not occur again.

3.6.2 *Damage to instrumentation*

Unfortunately, some unexpected damage to instrumentation occurred in addition to the normal expected losses of some gauges during casting and over time. During transportation of the Louetta beams to the jobsite, the leadwires for two full groups of gauges were damaged by a chain or other piece of heavy equipment. One group of these wires were thermocouples, and were easily repaired in the field using thermocouple connectors, but the other group of vibrating wire gauges could not be repaired. There was also some difficulty during the first cast-in-place deck pour, that of the Northbound Louetta Overpass, in keeping deck gauges in place during the casting process. A modification was thus made to the installation process to make gauges more stable for the future deck pours. The modified procedure was discussed in Section 3.5.2.3, and involved using extra pieces of reinforcement where necessary for the support of gauges.

At several times during the storage of beams at the precast plant, pieces of the tensioned-wire system were stolen. Although this usually involved unimportant clamps that were not critical to the system, some rulers were removed between the last reading in storage and the arrival of beams at the jobsite. This problem was overcome by switching to the precise surveying system for the erected beams. Another problem occurred when water seeped into a DAS box that was set up to record readings on a beam in storage for several consecutive days. The box was wrapped and covered in plastic, but a strong storm damaged the plastic and allowed the box to get wet. Although no permanent damage to that particular DAS box was apparent, the box has exhibited erratic behavior at a few times in the completed bridge.

3.6.3 Cracking of Concrete

Cracking of concrete also presented a problem at certain stages of the instrumentation program. Cracks that form at or very close to a gauge significantly influence the output of that gauge by introducing apparent tensile strains due to the growth of the crack over the gauge length. Likewise, apparent compressive strains may be registered when a crack at or near a gauge closes. In several of the San Angelo beam pours, concrete cracking occurred while the beams sat on the casting bed prior to the release of prestress force. This cracking and its impacts are discussed in several later chapters of this dissertation, but it is important to note here that in some cases concrete cracking had a significant impact on the gauge readings.

3.6.4 Mislabeled and Misplacement of Gauges and Beams

In a few isolated cases, gauges for two beams were switched during the installation of instrumentation at the precast plant. Because this occurred only with identical sets of gauges, there was no significant impact other than that the leadwire lengths were too long or short as a result. There was also a case where two beams were switched during the erection process. Since the beams were identical except for embedded instrumentation gauges, the contractor had simply assumed that they could be placed in any spot within the span. A note of the switch was made by the researchers and data recorded appropriately, so there was no significant impact as a result of the switch.

3.6.5 Other

In general, the other problems encountered during this research program were a result of scheduling and communication difficulties. The Louetta precast pier segments were initially going to be fitted with instrumentation to measure long-term strains, but the fabricator did not notify the researchers of the casting date before segments were cast. Readings of camber and deflection just before beam erection were also missed on a few beams in the San Angelo project, because there was a miscommunication between the

contractor and the researchers about the schedule. It should be noted that these types of problems were not a common occurrence during the research program, since communication between the contractors and researchers was very good overall.

3.7 Durability of Embedded Gauges

An important part of the instrumentation process is the assessment of the reliability and durability of the types of instrumentation used in the research program. Throughout this chapter, comments on general durability trends have been made. Toward the end of the research program, a quantitative survey was performed to verify these trends. Data from all 518 embedded gauges used in the instrumentation program was examined to determine whether each gauge was providing reliable measurements at casting, 60 days after casting, one year after casting, and as of the date of the survey in March 1998. The results of this survey are shown graphically in Figure 3.38.

The overall performance of thermocouples and vibrating wire gauges was very good. Most of the damage to these gauges occurred during casting, or at later ages when the leadwires to an entire group of gauges were damaged or disconnected. For example, the leadwires for an entire set of six vibrating wire gauges in one of the Louetta U-beams were inadvertently cut during transportation of the beams to the jobsite. Also, a few beam thermocouples were consciously disconnected by the researchers to make room for additional vibrating wire gauges in the deck. These instances explain most of the decrease in durability for thermocouples and vibrating wire gauges after casting.

Resistance strain gauges, on the other hand, did not show good long-term durability. More gauges of this type were damaged during casting, as expected, because of they are susceptible to water damage and have an extra leadwire splice, as discussed in Section 3.2.2.4. Furthermore, these gauges tended to break down over time and provide unreliable readings. Only 36% of resistance strain gauges were providing reliable readings after one year, making these gauges inappropriate for long-term measurements. The use of resistance strain gauges in future field research projects is not recommended, especially where long-term data acquisition is desired.

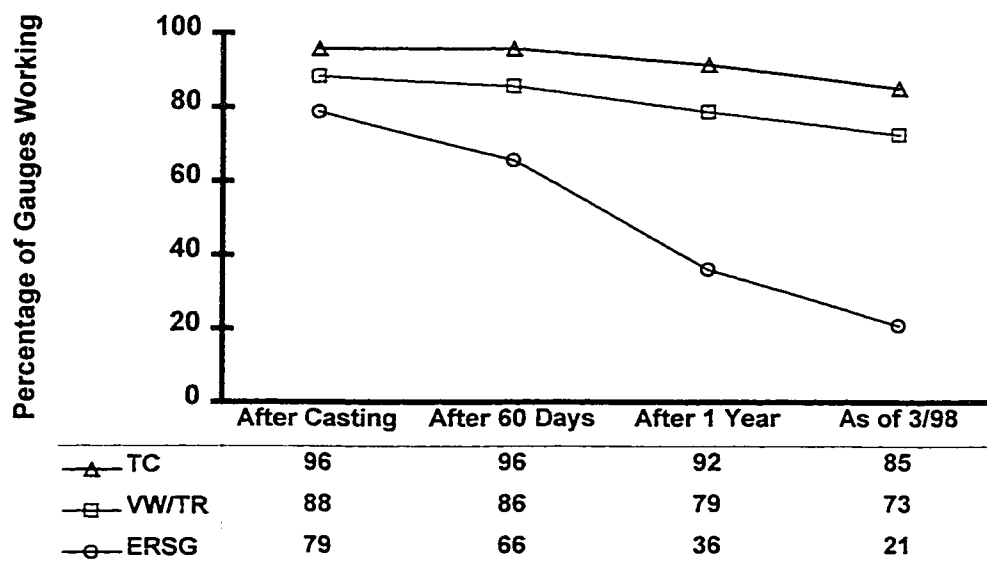


Figure 3.38 - Durability of Embedded Gauges

4 CHAPTER FOUR: MATERIAL PROPERTIES

4.1 Introduction

4.1.1 *General*

Measured material properties and concrete mix proportions are presented in this chapter for all superstructure components of the Louetta and San Angelo bridges. The purpose of this chapter is to summarize data collected on those material properties that were utilized in analyses of structural behavior. Myers and Carrasquillo [88] present a more elaborate discussion of the quality control/quality assurance program for the construction of the two bridges. For each material property, a summary of important measured values is given, followed by the results of regression analyses fit to the measured data. Both measured data values and regression curves developed from the measured data were used in the various analyses of structural behavior discussed throughout this dissertation.

Material properties discussed in this chapter include compressive strength, modulus of elasticity, creep, shrinkage, and coefficient of thermal expansion. Compressive strength and modulus of elasticity measurements were primarily performed within the materials subdivision of these research projects, and thus are only summarized here. The measurement program for those properties is discussed in detail by Myers and Carrasquillo [88]. The creep, shrinkage, and thermal expansion tests discussed in the later portions of this chapter were conducted primarily within the structures subdivision of these research projects, and are therefore discussed in more detail here.

4.1.2 *Classification of Concrete Mixes*

A total of eleven concrete mixes were used in the superstructures of the Texas HPC bridges, including four for the Louetta Road Overpass in Houston and seven for the North

Concho River Overpass in San Angelo. For purposes of discussion in this chapter, these eleven mixes are subdivided into two sets. Mixes corresponding to prestressed beams and precast prestressed deck panels are designated as “precast” mixes, while those corresponding to the various bridge decks cast at the jobsites are designated as “cast-in-place” mixes. The six precast mixes include the following:

- Louetta Northbound and Southbound HPC Prestressed Beams
- San Angelo Eastbound HPC Prestressed Beams
- San Angelo Westbound Non-HPC Prestressed Beams
- Louetta Northbound and Southbound HPC Precast Deck Panels
- San Angelo Eastbound HPC Precast Deck Panels
- San Angelo Westbound Non-HPC Precast Deck Panels

The five cast-in-place mixes include the following:

- Louetta Northbound HPC Bridge Deck
- Louetta Southbound HPC Bridge Deck
- San Angelo Eastbound HPC Class K Bridge Deck
- San Angelo Westbound (Spans 1-5) HPC Modified Class S Bridge Deck
- San Angelo Westbound (Spans 6-9) Non-HPC Standard Class S Bridge Deck

As discussed in Section 1.2, concrete may be classified as HPC based on both strength and durability properties, but the HPC designation does not always define whether it is strength (and) or durability properties that are of concern. Thus, some HPC concrete used in these two projects was HPC for strength, some was HPC for durability, and some was HPC for *both* strength and durability. For simplicity, the term HPC is used throughout this dissertation to refer to any of the these three combinations. The purpose of Table 4.1 is to further classify the eleven mixes discussed throughout this dissertation in terms of their strength and durability HPC designations.

Table 4.1 - HPC Classifications for Strength and Durability

	HPC for Strength	HPC for Durability
Precast Mixes		
Louetta NB/SB HPC Prestressed Beams	Yes	No
San Angelo EB HPC Prestressed Beams	Yes	No
San Angelo WB Non-HPC Prestressed Beams	No †	No
Louetta NB/SB HPC Precast Deck Panels	Yes	Yes
San Angelo EB HPC Precast Deck Panels	Yes	Yes
San Angelo WB Non-HPC Precast Deck Panels	No	No
Cast-in-Place Mixes		
Louetta NB HPC Deck	No	Yes
Louetta SB HPC Deck	Yes	Yes
San Angelo EB HPC Class K Deck	Yes	Yes
San Angelo WB HPC Modified Class S Deck	No	Yes
San Angelo WB Non-HPC Standard Class S Deck	No	No
† The Westbound San Angelo prestressed beam concrete was not designated as HPC because it is representative of standard concrete produced by the precast/prestressed industry in Texas. By some definitions, its design compressive strength (8900 psi [61.4 MPa]), would classify it as HPC.		

4.2 Mix Proportions and Fresh Concrete Properties

The concrete mix proportions for the eleven components listed in Section 4.1 are presented in Table 4.2, Table 4.3, Table 4.4, and Table 4.5. Fresh concrete properties, including water-to-binder ratio, slump, air content, and unit weight, may also be found in these tables. The listed release and design compressive strengths are those required for quality control acceptance by TxDOT. Design compressive strengths were specified at 28 days for non-HPC and at 56 days for HPC. The use of 56-day tests for HPC is intended to allow fabricators to make use of the strength gain that some HPC exhibits after 28 days.

Table 4.2 - Mix Properties for Prestressed Beams

	Louetta NB/SB HPC Beams	San Angelo EB HPC Beams	San Angelo WB Non-HPC Beams
Mix Proportions			
Coarse Aggregate, Type	Crushed Dolomitic Limestone, ½ in. max	Crushed Dolomitic Limestone, ½ in. max	Crushed River Gravel, ¾ in. max
Quantity	1919 lb/yd ³	1863 lb/yd ³	1998 lb/yd ³
Fine Aggregate	1086 lb/yd ³	1062 lb/yd ³	1160 lb/yd ³
Water	248 lb/yd ³	246 lb/yd ³	196 lb/yd ³
Cement, Type	Type III	Type III	Type III
Quantity	671 lb/yd ³	671 lb/yd ³	526 lb/yd ³
Fly Ash, ASTM Class C % Replacement by Weight	315 lb/yd ³ 32%	312 lb/yd ³ 32%	196 lb/yd ³ 27%
Retarder, ASTM Type D	27 oz/yd ³	28 oz/yd ³	16 oz/yd ³
HRWR, ASTM Type F	200 oz/yd ³	200 oz/yd ³	159 oz/yd ³
Air Entrainer, ASTM C260	None	None	None
Fresh Concrete Properties			
W/(C+FA), by weight	0.25	0.25	0.27
Slump	8 to 10 in.	6 to 9 in.	7 to 8 in.
Total Air	0.9% *	0.9% *	0.9% *
Unit Weight	153.9 lb/ft ³	152.9 lb/ft ³	149.3 lb/ft ³
Required Release and Design Compressive Strengths			
Release Strength (psi)	6900 - 8800	8000 - 8100	4000 - 6600
Design Strength (psi) **	9800 - 13100	13000 - 14000	5000 - 8900
* No entrained air			
** 28 days for non-HPC mixes, 56 days for HPC mixes			
1 lb/yd ³ = 27 lb/ft ³ = 0.593 kg/m ³ ; 1 oz/yd ³ = 0.0388 L/m ³			
1 in. = 25.4 mm; 1 psi = 0.006895 MPa			

Table 4.3 - Mix Properties for Precast Deck Panels

	Louetta NB/SB HPC Panels	San Angelo EB HPC Panels	San Angelo WB Non-HPC Panels
Mix Proportions			
Coarse Aggregate, Type	Crushed River Gravel, ¾ in. max	Crushed Limestone, 1 in. max	Crushed Limestone, 1 in. max
Quantity	1983 lb/yd ³	1844 lb/yd ³	1888 lb/yd ³
Fine Aggregate	1109 lb/yd ³	1356 lb/yd ³	1457 lb/yd ³
Water	228 lb/yd ³	251 lb/yd ³	275 lb/yd ³
Cement, Type	Type III	Type III	Type III
Quantity	565 lb/yd ³	658 lb/yd ³	563 lb/yd ³
Fly Ash, ASTM Class C % Replacement by Weight	164 lb/yd ³ 22%	None None	None None
Retarder, ASTM Type D	23 oz/yd ³	79 oz/yd ³	49 oz/yd ³
HRWR/WR	170 oz/yd ³ @	300 oz/yd ³ #	257 oz/yd ³ #
Air Entrainer, ASTM C260	None	None	None
Fresh Concrete Properties			
W/(C+FA), by weight	0.31	0.38	0.49
Slump	7 to 8 in.	5 to 6 in.	6 to 7 in.
Total Air	2.0% *	1.5% *	1.5% *
Unit Weight	149.9 lb/ft ³	150.9 lb/ft ³	150.7 lb/ft ³
Required Release and Design Compressive Strengths			
Release Strength (psi)	6000	4000	4000
Design Strength (psi) **	8000	6000	5000
* No entrained air ** 28 days for non-HPC mixes, 56 days for HPC mixes @ ASTM Type F HRWR; # ASTM Type D WR 1 lb/yd ³ = 27 lb/ft ³ = 0.593 kg/m ³ ; 1 oz/yd ³ = 0.0388 L/m ³ 1 in. = 25.4 mm; 1 psi = 0.006895 MPa			

Table 4.4 - Mix Proportions for Louetta Cast-in-Place Decks

	Louetta NB HPC Deck	Louetta SB HPC Deck
Mix Proportions		
Coarse Aggregate, Type	Crushed Limestone, 1 ½ in. max	Crushed Limestone, 1 in. max
Quantity	1856 lb/yd ³	1811 lb/yd ³
Fine Aggregate	1243 lb/yd ³	1303 lb/yd ³
Water	229 lb/yd ³	244 lb/yd ³
Cement, Type	Type I	Type I
Quantity	383 lb/yd ³	474 lb/yd ³
Fly Ash, ASTM Class C % Replacement by Weight	148 lb/yd ³ 28%	221 lb/yd ³ 32%
Retarder, ASTM Type D	45 oz/yd ³	22 oz/yd ²
HRWR, ASTM Type F	None	122 oz/yd ³
Air Entrainment, ASTM C260	2.1 oz/yd ³	None
Fresh Concrete Properties		
W/(C+FA), by weight	0.43	0.35
Slump	3 to 4 in.	8 to 9 ½ in.
Total Air	5.0%	0.9% *
Unit Weight	143.2 lb/ft ³	150.2 lb/ft ³
Required Design Compressive Strengths		
Design Strength (psi) **	4000	8000
* No entrained air		
** 28 days for non-HPC mixes, 56 days for HPC mixes		
1 lb/yd ³ = 27 lb/ft ³ = 0.593 kg/m ³ ; 1 oz/yd ³ = 0.0388 L/m ³		
1 in. = 25.4 mm; 1 psi = 0.006895 MPa		

Table 4.5 - Mix Properties for San Angelo Cast-in-Place Decks

	San Angelo EB HPC Class K Deck	San Angelo WB HPC Modified Class S Deck	San Angelo WB Non-HPC Standard Class S Deck
Mix Proportions			
Coarse Aggregate, Type	Crushed River Gravel, 1 ¼ in. max	Crushed River Gravel, 1 ¼ in. max	Crushed River Gravel, 1 ¼ in. max
Quantity	1900 lb/yd ³	1856 lb/yd ³	1856 lb/yd ³
Fine Aggregate	1366 lb/yd ³	1239 lb/yd ³	1243 lb/yd ³
Water	219 lb/yd ³	258 lb/yd ³	258 lb/yd ³
Cement, Type	Type II	Type II	Type II
Quantity	491 lb/yd ³	427 lb/yd ³	610 lb/yd ³
Fly Ash, ASTM Class C % Replacement by Weight	211 lb/yd ³ 30%	184 lb/yd ³ 30%	None None
Retarder, ASTM Type D	28 oz/yd ³	26 oz/yd ³	26 oz/yd ³
HRWR, ASTM Type F	156 oz/yd ³	None	None
Air Entrainer, ASTM C260	3.1 oz/yd ³	3.1 oz/yd ³	3.1 oz/yd ³
Fresh Concrete Properties			
W/(C+FA), by weight	0.31	0.42	0.42
Slump	7 to 9 in.	3 to 4 in.	3 to 4 in.
Total Air	6.0 %	6.0 %	6.0 %
Unit Weight	149.4 lb/ft ³	145.3 lb/ft ³	145.6 lb/ft ³
Required Design Compressive Strengths			
Design Strength (psi) **	6000	4000	4000
** 28 days for non-HPC mixes, 56 days for HPC mixes 1 lb/yd ³ = 27 lb/ft ³ = 0.593 kg/m ³ ; 1 oz/yd ³ = 0.0388 L/m ³ 1 in. = 25.4 mm; 1 psi = 0.006895 MPa			

4.3 Compressive Strength

4.3.1 Background

Compressive strength is probably the most fundamental strength-related property of hardened concrete. Numerous attempts have been made to correlate several other material properties to compressive strength, including modulus of elasticity, split-tensile strength, and modulus of rupture. Many, if not most, HPC's exhibit high compressive strengths. Concretes classified as HPC for strength are, by definition, high in compressive strength. Concretes classified as HPC for durability often indirectly exhibit high compressive strengths as a result of their mix composition and proportions.

The proper combination of conventional materials with mineral and chemical admixtures, including fly ash, silica fume, and high-range water reducers (HRWR), can result in concrete with high compressive strengths. Several references [9,10,71,94,121] discuss mix proportioning to obtain HPC with high compressive strengths. Myers and Carrasquillo [88] present a discussion of the material selection and mix proportioning for various components of the Texas HPC bridge projects discussed in this dissertation.

Based on the work of Branson et. al. [26,27], ACI Committee 209 [8] recommends the following expression for the prediction of compressive strength at any time t in days, as a function of the 28-day compressive strength:

$$(f'_c)_t = \frac{t}{a + bt} (f'_c)_{28}$$

Equation 4.1

The parameters a and b are dependent on the composition of the concrete and the method of curing, and can be determined from a nonlinear regression analysis of measured data. Typical values of a and b for various combinations of cement type and curing method may be found in the ACI 209 Committee Report [8]. These values were developed using a database of test results from the 1950's and 1960's on normal-weight, sand-lightweight, and all-lightweight concretes with compressive strengths of less than 42 MPa (6000 psi) [26,27].

Table 4.6 - Curing Regimes Used for QC/QA Investigations

Curing Regime (Abbreviation)	Before Release ¹	After Release
ASTM C31 (ASTM)	73 °F (23 °C) room (plastic molds)	water tank with lime
TxDOT official quality control cylinders (TxDOT)	alongside member (steel molds)	water tank with lime
Member-cured cylinders (MC)	alongside member (plastic molds)	alongside member
Sure-Cure brand match curing system (SC) ²	cured in special insulated molds to same temperature as member	alongside member
¹ For cast-in-place decks, "Before Release" corresponds to initial hydration period, usually overnight. ² Used for HPC prestressed beams only.		

4.3.2 Method of Measurement

Concrete compressive strength was monitored on all pours corresponding to bridge instrumentation as part of the quality control/quality assurance program conducted by Myers and Carrasquillo [88]. All measurements were made on 100 x 200 mm (4 ix 8 in.) companion cylinders according to the testing procedure outlined in ASTM C39 [20], except that neoprene pads and steel caps were used at the cylinder ends. Testing was performed with a 2720 kN (600 kip) capacity Forney testing machine at the CMRG laboratory in Austin, except for cylinders corresponding to the release of prestressed beams, which were tested at the precast plant in Victoria.

Four unique curing regimes were used for quality control investigations. Table 4.6 lists each curing regime with a brief description of the curing method used before and after release. For the purpose of the work in this dissertation, it was desirable to model the curing of the cylinders as closely as possible to the curing of the actual members (beam, panel, or deck). Therefore, compressive strengths presented in this dissertation are not based on ASTM C31 [19] cylinder curing standards (unless otherwise noted).

Generally, a match curing system best models the hydration of the actual member by controlling the curing temperature of the cylinders to match that of a thermocouple placed in the member. In the Texas HPC projects, the Sure-Cure brand match curing system was

used during the casting of most HPC prestressed beams. However, since a limited number of Sure-Cure molds were available and several locations in each member were being modeled for quality control purposes, there were usually not enough Sure-Cure cylinders available to perform testing at all desired ages. All compressive strength data presented and utilized in this dissertation is thus based on member-cured cylinders, with the exception of most data at release of HPC prestressed beams. The member-cured cylinders reasonably follow the long-term curing of the actual members since they are stored with the member at all times. However, the member-cured cylinders do not experience the early-age hydration effects related to the mass of the member itself. Because this mass-related hydration is extremely important in HPC members and because the data was available, Sure-Cure strengths were used for all HPC beams at release of prestress.

4.3.3 Measurements

In general, measurements of compressive strength were made at release of prestress (where applicable), and at ages of 7, 28, and 56 days. A summary of measured strengths at release of prestress and at 28 or 56 days is presented in Table 4.7 for precast mixes and Table 4.8 for cast-in-place mixes. Required release and design strengths for each mix are also listed in the tables. Note that for HPC mixes, the required design strength is specified at 56 days rather than the standard 28 days. This modification allows the fabricators and contractors to make use of the long-term strength gain after 28 days, which could be critical for HPC with high strengths.

For a few of the mixes in Table 4.7 and Table 4.8, the listed measured compressive strength is less than the required compressive strength. However, the required strengths are based on official TxDOT cylinders, while the measured strengths listed in the tables are for member-cured cylinders (in most cases). TxDOT cylinders typically exhibit higher strengths than member cured cylinders at release because they are cured in steel molds, which retain heat better than plastic molds. Furthermore, TxDOT cylinders exhibit higher long-term strengths than member-cured cylinders because they are cured in a water tank after the molds are stripped. For mixes corresponding to instrumented components, all official quality control tests using TxDOT cylinders resulted in measured strengths sufficiently higher than required strengths.

Table 4.7 - Summary of Compressive Strength Data for Precast Mixes

Component	Casting Date	Required f'_{ci} (psi)	Measured f'_{ci} (psi)	Test Age # (hr.)	Required f'_c @ (psi)	Measured f'_c @ (psi)
Louetta HPC Beams						
Beam N23	9/23/94	7700	11070 [†]	19	11600	11500*
Beams S16, N22	9/30/94	7700	8710 [‡]	24	11600	13290*
Beam S26	10/7/94	8800	11100 [†]	168 [§]	13100	13560*
Beams N21, N31	10/28/94	8800	10890 [†]	27	13100	14820
Beams S24, S25	11/10/94	7700	10320 [†]	24	11600	13410*
Beams N32, N33	2/15/96	7700	10470 [†]	27	11600	13630
Beams S14, S15	2/26/96	7700	10990 [†]	28	11600	14320
San Angelo EB HPC Beams						
Beam E25	4/1/96	8100	9790	27	13500	14830
Beams E13, E14	2/19/97	8100	10780 [†]	28	13000	13700
Beams E24, E26	3/8/97	8000	13070 [†]	50	14000	14240
Beams E33, E34	3/22/97	8000	12390 [†]	46	13800	13750*
Beam E35	3/29/97	8000	11340 [†]	46	13800	14490
Beams E44, E45	4/12/97	8000	9390 [†]	48	13700	14550
San Angelo WB Non-HPC Beams						
Beams W14, W15, W16	3/7/96	5770	8560	26	7850	10130
Beam W17	3/12/96	5770	8060	24	7850	10260
Louetta HPC Precast Deck Panels						
All Instrumented Panels	9/12/96	6000	6010	27	8000	9040
San Angelo EB HPC Precast Deck Panels						
All Instrumented Panels	2/5/97	4000	3140	24	6000	10100
San Angelo WB Non-HPC Precast Deck Panels						
All Instrumented Panels	9/4/96	4000	5310	24	5000	8250
1 psi = 0.006895 MPa						
Note: Data from member-cured cylinders unless otherwise noted (see Table 4.6).						
† Sure-cure data. ‡ TxDOT data. § Release at 7 days.						
# Test age for release cylinders; * 28-day value (56-day data unavailable)						
@ at 56 days for HPC mixes, at 28 days for non-HPC mixes						

Table 4.8 - Summary of Compressive Strength Data for Cast-in-Place Mixes

Component	Casting Date	Required $f_c^@$ (psi)	Measured $f_c^@$ (psi)
Louetta NB HPC Deck			
All Spans (1-3)	10/31/96	4000	5700
Louetta SB HPC Deck			
All Spans (1-3)	11/8/96	8000	9100
San Angelo EB HPC Deck			
Span 1	6/12/97	6000	7290
Span 2	6/25/97	6000	8420
Span 3	7/9/97	6000	9060
Span 4	7/23/97	6000	7550
San Angelo WB HPC Modified Class S Deck			
Span 1	12/3/96	4000	6120
Span 3 *	1/21/97	4000	4230
San Angelo WB Non-HPC Standard Class S Deck			
Spans 6-7 *	2/15/97	4000	5340
1 psi = 0.006895 MPa Note: Data from member-cured cylinders (see Table 4.6). * No instrumentation. Material testing only (incl. creep & shrinkage). @ at 56 days for HPC mixes, at 28 days for non-HPC mixes			

4.3.4 Regression Analyses for Use in Time-Dependent Models

Compressive strength was measured at several discrete ages, but a continuous strength-time relationship is more useful for time-dependent structural analyses. Thus, a nonlinear regression analysis was performed on measured values to determine the parameters of a strength-time curve for each casting. The form of each strength-time curve is the familiar ACI 209 [8] equation presented in Equation 4.1. The results of these analyses are summarized in Table 4.9 and Table 4.10 for precast and cast-in-place mixes, respectively. Although the regressions are only technically valid over the range of data to which they were fit, the resulting curves were used in time-dependent analyses to model concrete of all ages.

Table 4.9 - Strength-Time Curve Parameters from Regression Analyses Using Measured Compressive Strength Data (Precast Mixes)

Component	Casting Date	$f'_{c,28}$ [@] (psi)	a	b	R ²	# Tests
Louetta HPC Beams						
Beam N23	9/23/94	11500	.032	.999	N/A †	2
Beams S16, N22	9/30/94	13290	.545	.981	N/A †	2
Beam S26	10/7/94	12550	.438	.984	.895	3
Beams N21, N31	10/28/94	14820	.414	.993	N/A †	2
Beams S24, S25	11/10/94	13410	.311	.989	N/A †	2
Beams N32, N33	2/15/96	12760	.267	.990	.826	4
Beams S14, S15	2/26/96	13080	.244	.991	.705	4
San Angelo EB HPC Beams						
Beam E25	4/1/96	13700	.478	.983	.934	4
Beams E13, E14	2/19/97	12560	.224	.992	.493	4
Beams E24, E26	3/8/97	13670	.121	.996	.468	5
Beams E33, E34	3/22/97	13150	.172	.994	.350	3
Beam E35	3/29/97	13760	.512	.982	.755	4
Beams E44, E45	4/12/97	13720	1.028	.963	.978	5
San Angelo WB Non-HPC Beams						
Beams W14, W15, W16	3/7/96	10200	.231	.992	.637	4
Beam W17	3/12/96	10380	.305	.989	.921	4
Louetta HPC Precast Deck Panels						
All Instrumented Panels	9/12/96	8700	.525	.981	.988	4
San Angelo EB HPC Precast Deck Panels						
All Instrumented Panels	2/5/97	9550	2.125	.924	.998	4
San Angelo WB Non-HPC Precast Deck Panels						
All Instrumented Panels	9/4/96	7900	.523	.981	.882	4
1 psi = 0.006895 MPa						
Note: Curves based on member-cured cylinder data, except Sure-Cure data used for most prestressed beams at release (see Table 4.6).						
① This value is a parameter determined from regression analysis and does not represent the actual test data at 28 days shown in Table 4.7.						
† No R ² value computed for mixes with measured strengths at less than three different ages.						

Table 4.10 - Strength-Time Curve Parameters from Regression Analyses Using Measured Compressive Strength Data (Cast-in-Place Mixes)

Component	Casting Date	$f'_{c,28}$ @ (psi)	a	b	R ²	# Tests
Louetta NB HPC Deck						
All Spans (1-3)	10/31/96	5280	2.861	.898	.916	4
Louetta SB HPC Deck						
All Spans (1-3)	11/8/96	8940	2.415	.914	.971	4
San Angelo EB HPC Deck						
Span 1	6/12/97	6490	.938	.967	.755	5
Span 2	6/25/97	8350	1.688	.940	.895	4
Span 3	7/9/97	7820	5.373	.808	.770	4
Span 4	7/23/97	7460	.638	.977	.996	4
San Angelo WB HPC Modified Class S Deck						
Span 1	12/3/96	6140	2.730	.920	.961	4
Span 3 *	1/21/97	3850	1.887	.933	.752	4
San Angelo WB Non-HPC Standard Class S Deck						
Spans 6-7 *	2/15/97	5440	5.140	.816	.973	5
1 psi = 0.006895 MPa						
Note: Curves based on member-cured cylinder data (see Table 4.6).						
@ This value is a parameter determined from regression analysis and does not represent the actual test data at 28 days shown in Table 4.8.						

When the parameter b in Equation 4.1 is close to unity, the initial gain in strength at early-ages is very fast and the long-term strength gain is minimal. The fast strength gain of precast mixes, all of which use Type III cement, is thus evidenced by the relatively high values of b for those mixes. Likewise, the slower strength gain of cast-in-place mixes, which use Type I or Type II cement, is demonstrated by the relatively low values of b for those mixes.

For most pours, the regression curves provide a reasonably good fit to the measured data, as verified by the range of values for the coefficient of determination, R^2 , listed in the tables. An example of a regression curve with an excellent fit to the measured data is shown in Figure 4.1 for the Louetta precast deck panels cast on September 12,

1996. However, the regression curves for many HPC beam mixes do not perfectly model the measured strength data. For some of the Louetta HPC beams, only release and 28 or 56 day strengths were available, making it impossible to establish the accuracy of the regression curve for other ages. For other beam pours, the regression curve underestimates the long-term strength gain between 28 and 56 days. An example of this type of curve can be seen in Figure 4.2 for the San Angelo Eastbound HPC beam casting on February 29, 1997. Some of the error may be attributable to the use of Sure-Cure data for release strengths and member-cured data for strengths at other ages. In addition, the mathematical form of Equation 4.1 appears to have difficulty representing the high early-strengths resulting from the use of Type III cement *and* the later-age strength gain resulting from the use of substantial fly ash replacement. Despite these errors, the regression curves provide a reasonably good estimate of a continuous-strength time relationship. Measured data falls within 10 percent of the regression curves in all cases.

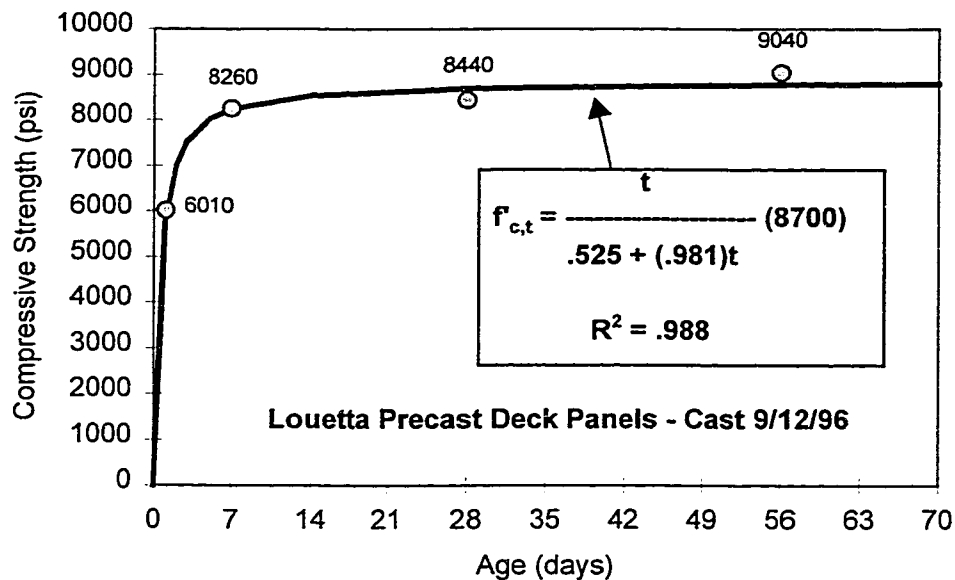


Figure 4.1 - Strength-Time Regression Curve Fit for Louetta Panels

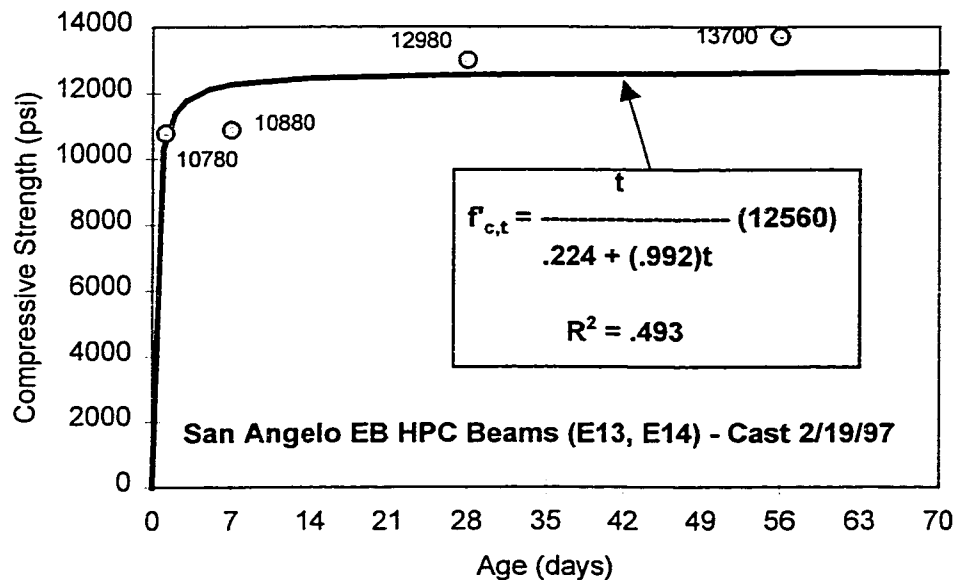


Figure 4.2 - Strength-Time Regression Curve for an HPC Beam Pour

4.4 Modulus of Elasticity

4.4.1 Background

The modulus of elasticity of any concrete is greatly affected by the size, shape, stiffness, and quantity of its coarse aggregate [83,95,121]. Concretes made with hard crushed aggregates such as limestone generally exhibit higher moduli of elasticity than concretes made from smooth river gravel and crushed granites [15,39]. This trend is generally attributed to a lower tensile bond strength at the paste-aggregate interface in gravel concretes. Moisture content also has an effect on the measured modulus of elasticity of concrete, with wet specimens generally exhibiting higher moduli than dry specimens [96,121]. The modulus of elasticity of concrete is a function of age, and increases at a much faster rate than compressive strength for most concrete [96].

Modulus of elasticity is commonly defined as the secant modulus at 45% of the compressive strength [7], and is often measured according to ASTM C469 [22] as the chord modulus between 40% of the compressive strength and a very small strain of 50 $\mu\epsilon$. An increase in compressive strength (for concretes with similar aggregate type and mix composition) generally results in an increased modulus of elasticity. Carrasquillo, Nilson, and Slate [39] attribute this trend to the lower water-to-cement (or water-to-binder) ratio of higher strength concretes, which leads to increased mortar stiffness and a higher tensile bond strength between the paste and the aggregate.

Several empirical relationships have been proposed to relate modulus of elasticity to compressive strength. Based on the work of Pauw [103] with normal-weight concretes of compressive strengths lower than 42 MPa (6000 psi), the AASHTO [1,3] and ACI 318 [7] specifications suggest the following empirical relationship, which includes the effect of the unit weight ρ :

$$E_c = 33 \cdot \rho^{1.5} \cdot \sqrt{f'_c}$$

Equation 4.2

Note that in this empirical relationship, the modulus of elasticity, E_c , and compressive strength, f'_c , are expressed in psi, while the unit weight, ρ , is expressed in pounds per cubic foot. Both the AASHTO and ACI specifications permit the use of a simplified form of Equation 4.2 for “normal-weight” concrete (with unit weight of 145 pounds per cubic foot):

$$E_c = 57,000 \cdot \sqrt{f'_c}$$

Equation 4.3

Carrasquillo et. al. [39] found that Equation 4.2 overestimated the modulus of elasticity for high strength concrete, and proposed a similar empirical relationship, where E_c and f'_c are expressed in psi:

$$E_c = 40,000 \cdot \sqrt{f'_c} + 1,000,000$$

Equation 4.4

Equation 4.4 was adopted by ACI Committee 363 [10] for use with normal-weight high strength concrete (and lower strength concretes) in the range of 21 to 83 MPa (3,000 to 12,000 psi). The equation was developed considering results from the original Pauw [103] study, Portland Cement Association tests [68,105], and tests performed at Cornell University on high strength concretes made with both gravel and crushed limestone aggregates and in the strength range of 34 to 77 MPa (4,900 to 11,100 psi). It was also noted in the Carrasquillo et. al. [39] study that the measured modulus of elasticity was much higher for concretes with crushed limestone than for concretes made with gravel.

Several other empirical equations have been suggested for modulus of elasticity in the literature [14,44,45,66], indicating the high degree of variability in modulus of elasticity among different concretes. Nearly all proposed empirical equations relate the modulus of elasticity to compressive strength and unit weight. Note that the CEB-FIP Model Code [44] relates the modulus of elasticity to the cube root of the compressive strength, rather than the square root.

4.4.2 Method of Measurement

Modulus of elasticity was measured on all pours corresponding to instrumented bridge components as part of the quality control/quality assurance program under the direction of Myers and Carrasquillo [88]. Measurements were made on the same 100 x 200 mm (4 x 8 in.) companion cylinders used for measurement of compressive strength. As for compressive strength, all modulus of elasticity data presented in this section is based on member-cured cylinders, except that data from match-cured (Sure-Cure) cylinders was used for HPC beams at release. These curing regimes are described in Section 4.3.2.

All modulus of elasticity testing was conducted using the general procedures specified in ASTM C469 [22]. Load was applied and measured using a 2720 kN (600 kip) capacity Forney testing machine. Displacement was measured with a digital spring-loaded displacement gauge, which was fixed to the specimen using a frame composed of steel rings and screw pins. The modulus of elasticity was calculated using the secant modulus between points on the stress-strain curve at 40% of the compressive strength (at time of testing) and at a strain of 50 $\mu\epsilon$.

Table 4.11 - Measured Modulus of Elasticity for Precast Mixes

Component	Casting Date	Measured E_{ci} (ksi)	Test Age # (hr.)	Measured E_c @ (ksi)
Louetta HPC Beams				
Beam N23	9/23/94	6420 [†]	19	5730*
Beams S16, N22	9/30/94	—	24	6930*
Beam S26	10/7/94	6380 [†]	168 [§]	7500*
Beams N21, N31	10/28/94	5800 [†]	27	6710
Beams S24, S25	11/10/94	5480 [†]	24	6460*
Beams N32, N33	2/15/96	6290 [†]	27	6760
Beams S14, S15	2/26/96	6020 [†]	28	6680*
San Angelo EB HPC Beams				
Beam E25	4/1/96	5950	27	6540
Beams E13, E14	2/19/97	6320 [†]	28	6460
Beams E24, E26	3/8/97	6970 [†]	50	5560
Beams E33, E34	3/22/97	6310 [†]	46	5680*
Beam E35	3/29/97	6690 [†]	46	6490
Beams E44, E45	4/12/97	5580 [†]	48	6110
San Angelo WB Non-HPC Beams				
Beams W14, W15, W16	3/7/96	5940	26	5630
Beam W17	3/12/96	5880	24	5360
Louetta HPC Precast Deck Panels				
All Instrumented Panels	9/12/96	5490	27	5640
San Angelo EB HPC Precast Deck Panels				
All Instrumented Panels	2/5/97	2990	24	4620
San Angelo WB Non-HPC Precast Deck Panels				
All Instrumented Panels	9/4/96	3990	24	4680
1 ksi = 1000 psi = 6.895 MPa = 0.006895 GPa				
Note: Listed values from member-cured cylinders unless otherwise noted (see Table 4.6). [†] Sure-cure data. [§] Release at 7 days.				
* Test age for release cylinders; * 28-day value (56-day data unavailable)				
@ at 56 days for HPC mixes; at 28 days for non-HPC mixes				

Table 4.12 - Measured Modulus of Elasticity for Cast-in-Place Mixes

Component	Casting Date	Measured E_c @ (ksi)
Louetta NB HPC Deck		
All Spans (1-3)	10/31/96	4380
Louetta SB HPC Deck		
All Spans (1-3)	11/8/96	4990
San Angelo EB HPC Deck		
Span 1	6/12/97	5500
Span 2	6/25/97	5230
Span 3	7/9/97	6060
Span 4	7/23/97	5790
San Angelo WB HPC Modified Class S Deck		
Span 1	12/3/96	5170
Span 3 *	1/21/97	4310
San Angelo WB Non-HPC Standard Class S Deck		
Spans 6-7 *	2/15/97	4930
1 ksi = 1000 psi = 6.895 MPa = 0.006895 GPa		
Note: Listed values from member-cured cylinders (see Table 4.6).		
* No instrumentation. Material testing only (incl. creep & shrinkage).		
@ at 56 days for HPC mixes, at 28 days for non-HPC mixes		

4.4.3 Measurements

Measured modulus of elasticity values for all pours with instrumentation are presented in Table 4.11 and Table 4.12 for precast and cast-in-place mixes, respectively. Measured moduli are listed at 28 days for non-HPC mixes and 56 days for HPC mixes. Release values are also listed for all precast mixes. Data listed in the tables is based on member-cured cylinders, except that the data for most prestressed beams at release is based on Sure-Cure cylinders.

For most mixes, a required modulus of elasticity was not specified and TxDOT did not conduct tests on official quality control companion cylinders. However, a minimum modulus of 41 GPa (6000 ksi) was specified on contract drawings for all HPC prestressed

beams. The intent of this requirement was to control deflections. As can be seen in Table 4.11, this requirement was met in all but a few cases with respect to the test results on member-cured cylinders. (No official TxDOT acceptance tests were performed for modulus of elasticity.)

Also note the high degree of variability in measured modulus values for member-cured cylinders. In some cases, the measured modulus at 28 or 56 days is significantly lower than the modulus at release. This variability may be attributed to a combination of varying moisture content for member-cured cylinders and a lack of accuracy inherent in the test method, or it may simply reflect the high degree of variability in the material property (modulus of elasticity) itself.

4.4.4 Regression Analyses for Use in Time-Dependent Models

For time-dependent analyses, it is essential to estimate the modulus of elasticity of concrete as a function of its age. Unfortunately, the large scatter in measured modulus of elasticity data made the development of continuous modulus-time curves impossible. A more effective approach was to determine the relationship between modulus of elasticity and compressive strength for each mix design. These equations could then be used in conjunction with the strength-time relationships developed for each individual pour in Section 4.3.4 to estimate the modulus of elasticity at any given concrete age.

The general form of the regression equation is similar to the equations discussed in Section 4.4.1 (E_c in ksi, f'_c in psi):

$$E_c = g \cdot \sqrt{f'_c} + h$$

Equation 4.5

The coefficients g and h were determined from a linear regression analysis between the measured modulus and the square root of the measured compressive strength. For each mix design, a regression equation was determined using member-cured and Sure-Cure (at release) data for all instrumented pours corresponding to the given mix. Note that the unit

weight is not considered as a variable in the regression analysis because the developed equations are mix specific. Although the regression equations are only truly valid over the range of data from which they were developed, they were assumed to be applicable for all concrete strengths in the time-dependent analyses discussed later in this dissertation.

An example of a regression curve developed for the Louetta HPC beam mix is shown in Figure 4.3. The AASHTO/ACI 318 equation (Equation 4.2) and ACI 363/Carrasquillo et. al. equation (Equation 4.4) are also plotted in the figure for comparison. Note that for the Louetta HPC beam mix, Equation 4.2 overestimated the modulus for all but one data point, while Equation 4.4 underestimated the modulus for all but one data point. While it is not the intention of the structures portion of this research program to compare prediction methods for material properties such as modulus of elasticity, this simple comparison does illustrate the need for the modulus regression equations developed in this section.

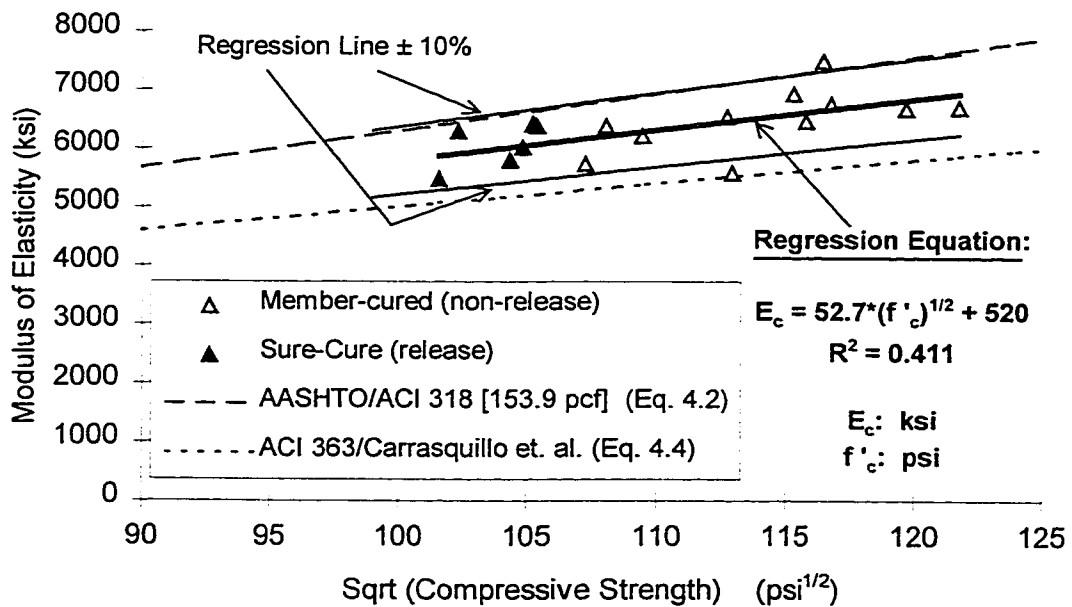


Figure 4.3 - Modulus vs. Compressive Strength for Louetta HPC Beam Mix

Table 4.13 - Modulus-Strength Curve Parameters from Regression Analyses Using Measured Modulus of Elasticity Data

Mix	g	h	R ²	# Tests
Louetta HPC Beams	52.7	520	.411	17
San Angelo EB HPC Beams	18.4	4,100	.079	25
San Angelo WB Non-HPC Beams	30.9	2,860	.168	8
Louetta HPC Precast Deck Panels	3.0	5,210	.024	4
San Angelo EB HPC Precast Panels	39.1	1,040	.722	4
San Angelo WB Non-HPC Precast Panels	47.0	520	.943	4
Louetta NB HPC Deck	68.2	- 660	.900	4
Louetta SB HPC Deck	- 9.9	5,860	.108	4
San Angelo EB HPC Deck	30.2	2,720	.332	17
San Angelo WB HPC Modified Class S Deck	53.7	920	.844	8
San Angelo WB Non-HPC Standard Class S Deck	45.4	1,720	.895	4
1 ksi = 1000 psi = 6.895 MPa = 0.006895 GPa				
Note: Regression analysis based on member-cured cylinder data, except Sure-Cure data used for most prestressed beams at release (see Table 4.6).				

A summary of the coefficients for the regression equations developed for each mix design is given in Table 4.13. All but one of the curves make physical sense by implying that the modulus increases with increasing compressive strength. The curve developed for the Louetta Southbound HPC bridge deck implies a very slight decrease in modulus for increasing compressive strengths. Because the decrease in modulus is only very slight (as evidenced by the coefficient g of -9.9), this regression equation essentially predicts a constant modulus. Note that for all mix designs, most of the measured modulus data points fell within 10 percent of the modulus predicted by the regression curve, as shown in Figure 4.3.

4.5 Creep

4.5.1 Background

Creep of concrete can broadly be defined as the time-dependent increase in strain under a sustained stress. Total creep actually consists of two components: basic creep and drying creep. Basic creep is the creep occurring with no moisture exchange between the concrete and its surroundings, while drying creep can be defined as the creep dependent on loss of moisture to the environment [75]. Basic creep is generally associated with the movement and rearrangement of adsorbed water layers, and drying creep is associated with the loss of evaporable water [98].

For most engineering applications, it is not necessary to distinguish between basic and drying creep. However, it is important to note that creep and shrinkage are not independent since drying creep is moisture-dependent, and thus influenced by shrinkage [97]. As a result, creep and shrinkage strains cannot truly be superimposed (i.e. the total time-dependent strain is not equal to the algebraic sum of the basic creep, drying creep, and shrinkage strains). For practical purposes, however, creep can be defined as the time-dependent change in strain of concrete under sustained load, less the shrinkage (and thermal) strain occurring on unstressed concrete in the same environmental conditions. This approach has been used by ACI Committee 209 [8] and in numerous past experimental studies, and allows for the superposition of creep and shrinkage strains in time-dependent analyses.

It is often useful to quantify creep of concrete in forms other than the total creep strain, ϵ_c . The two most common forms are specific creep, η_c , and creep coefficient, C_c . Specific creep is sometimes called the “unit creep strain”, and is defined as the creep strain per unit stress:

$$\eta_c = \frac{\epsilon_c}{\sigma}$$

Equation 4.6

The creep coefficient is defined as the ratio of the time-dependent creep strain to the initial elastic strain, ϵ_i :

$$C_c = \frac{\epsilon_c}{\epsilon_i}$$

Equation 4.7

Thus, a creep coefficient of 2.0 implies that the total strain due to initial elastic load response and time-dependent creep is three times the initial elastic strain. The specific creep and creep coefficient can be related by the following equation, where E_c is taken as the modulus of elasticity *at the time of loading*:

$$C_c = E_c \cdot \eta_c$$

Equation 4.8

Many factors have been shown to influence creep of concrete. These factors can generally be categorized as mix composition factors and other factors related to curing, service exposure conditions, loading conditions, and member geometry. Because so many factors influence creep, the magnitude of creep strains will vary greatly between different concretes under different conditions.

Creep essentially occurs in the paste of concrete, and the aggregate acts to restrain the creep of the paste [95]. As a result, the quantity and stiffness (modulus of elasticity) of the coarse aggregate will influence the creep behavior of the concrete to some extent [95]. Many attempts have been made in the literature to relate creep to water-to-cement (water-to-binder) ratio, cement content, cement type, water content, fine aggregate content, and other paste properties, but the interdependence of such properties has resulted in conflicting data concerning their effects [83]. Some authors argue that creep is essentially related to the stress-strength ratio (ratio of the applied stress to the concrete strength at time of loading), which encompasses the net effects of the previously mentioned interdependent paste properties [95,97].

However, it is generally agreed upon that concretes with lower water-to-cement (water-to-binder) ratios exhibit less creep than similar concretes with higher water-to-cement (water-to-binder) ratios [83,97]. Studies of experimental data have shown this trend to be especially true when corrections are made to account for differences in quantities of cement paste [97]. That is, concretes with lower water-to-cement (water-to-binder) ratios and the same paste content exhibit lower creep. This conclusion could also be interpreted as demonstrating the influence of water content. Concretes with less water tend to exhibit lower creep.

Loading factors that influence creep behavior include the age of the concrete at loading and magnitude of the applied load. Both of these factors contribute to the stress-strength ratio mentioned in preceding paragraphs. It has been well established that concrete creeps more when loaded at earlier ages [83,97]. Likewise, higher loads result in more creep strain for a given concrete. A linear relationship between creep strain and magnitude of applied stress is known to exist up to a given level of stress. The upper stress limit of the linear relationship is generally reported as about 50% to 60% of the compressive strength for most concretes [54,83,97]. Above this stress, microcracking may occur and the relationship may become nonlinear [54,95]. At stress levels approaching the ultimate strength of the concrete, creep can eventually lead to failure [95]. The stress level above which this occurs is commonly referred to as the sustained load strength.

Other factors that can influence creep of concrete include curing and service exposure conditions. Duration and type of curing can affect creep by influencing the concrete strength (and thus the stress-strength ratio) at the time of loading. Relative humidity can greatly affect creep, or more precisely, the magnitude of drying creep [95]. Lower relative humidity typically results in significantly increased creep [96]. Temperature also influences creep, although for most typical applications it is considered to be a less important environmental factor than relative humidity [97]. Over the range of temperatures applicable to most concrete structures (0 to 70°C [32 to 160°F]), creep increases with increasing temperature [95].

Tests have also shown that the size and shape of a concrete member or specimen can greatly influence its creep, both in terms of the rate of creep and magnitude of ultimate creep [61]. For larger members, the rate of creep and magnitude of ultimate creep are significantly smaller, and the magnitude of total creep approaches the magnitude of basic creep since very little moisture can be lost to the environment [61]. This member size and

shape influence has generally been expressed by relating creep to either volume-to-surface ratio, or to a minimum or average member thickness [8].

There is general agreement that creep is less for high strength concretes than for conventional or normal strength concretes. This trend would be expected given the generally low water-to-cement (water-to-binder) ratios of most high strength concretes. ACI Committee 363 [10] identifies several studies where less creep was measured for HSC than for comparable normal-strength concretes. Parrot [101] observed a 25 percent lower creep coefficient in high strength concrete under drying conditions, when compared to normal strength concrete loaded to a similar load ratio (30 percent of the concrete strength). Ngab et. al. [98] found that the specific creep and creep coefficient of high strength concrete with a water-to-cement ratio of 0.32 were respectively 20 to 25 percent and 50 to 75 percent that of normal strength concrete made with similar materials and a water-to-cement ratio of 0.64. Smadi et. al. [123] also observed substantially less creep for high strength concretes with compressive strengths of 59 to 69 MPa (8,500 to 10,000 psi) and a water-to-cement ratio of 0.32, when compared to low and medium strength concretes (compressive strengths less than 41 MPa [6,000 psi]) with water-to-cement ratios of 0.87 and 0.64, respectively.

The Smadi et. al. [123] study also noted that a higher limit exists for high strength concrete for the linear relationship between level of stress and creep strain. This limit was observed to be approximately 65 percent of the compressive strength for HSC, as compared to 45 percent for low and medium strength concretes. Similarly, it was observed that HSC has a higher sustained loading strength. The stress at which creep strains lead to failure was found to be 80 percent of the strength for HSC and 75 percent of the strength for low and medium strength concretes.

The effect on creep of mineral and chemical admixtures, which are commonly used in HPC, is somewhat unclear. Brooks and Neville [30] suggest that few generalizations can be made concerning their effects on creep, in part because available experimental data covers a wide range of test conditions. It is also important to recognize the indirect effect that admixtures have on creep with respect to the manner in which they influence other creep-influencing parameters (i.e. water-to-cement/water-to-binder ratio, slump/water content, strength, etc.). Nasser and Al-Manaseer [93] found that creep of 28 MPa (4000 psi) concrete with superplasticizer and 20% Class C fly ash replacement exhibited 72% more creep than the same concrete without admixtures. Sennour and Carrasquillo [120] observed a slight increase in creep for concretes with varying percentages of Class C fly

ash replacement, and a slight decrease in creep for concretes with Class F fly ash. The difference was attributed to the effect of the varying CaO contents between the two classes of fly ash.

Several models have been proposed for predicting creep as a function of time for a given concrete under a given set of load and exposure conditions. The most common method in use in the United States is probably the ACI 209 [8] method, which is based on the work of Branson et. al. [26,27]. This method allows for the determination of an ultimate creep coefficient, C_{cu} , either by experimental tests or by assuming and modifying a base value of 2.35. This base value was determined by analyzing the results of 120 specimens from several experimental studies conducted prior to 1970 on normal-weight, lightweight, and sand-lightweight concretes [26]. The assumed base value is meant to represent a general average for many concretes, and should be modified using a set of multipliers developed for various factors related to concrete composition. These factors include slump, fine aggregate percentage, cement content, and air content. The multipliers corresponding to these factors may be found in the ACI 209 Committee Report [8].

The corrected (assumed) or experimentally determined ultimate creep coefficient is then modified using multipliers corresponding to loading, curing, and environmental conditions. The multiplier for ambient relative humidity is given as:

$$\gamma_{rh} = 1.27 - (0.0067 \cdot H) \quad \text{for } H \geq 40$$

Equation 4.9

where H is the relative humidity in percent. The multiplier γ_{rh} defaults to 1.0 for a "standard" relative humidity of 40 percent. For relative humidity less than 40 percent, no equation is given, but γ_{rh} must be taken as greater than 1.0.

A multiplier for size and shape effects may be applied in one of two forms, one related to average member thickness and another related to volume-to-surface ratio. The multiplier corresponding to average member thickness is given as:

$$\gamma_{at} = 1.10 - (0.017 \cdot h)$$

Equation 4.10

for ultimate creep values, where h is specified as the average member thickness (in inches) of the part of the member under consideration. The constants 1.10 and 0.017 are replaced by 1.14 and 0.023, respectively, to correct creep values during the first year after loading. This modification is intended to reflect the greater influence of average member thickness during the first year after loading.

The multiplier for size and shape effects based on volume-to-surface ratio, v/s (in inches), is given by:

$$\gamma_{vs} = \frac{2}{3} \cdot \left[1 + 1.13 \cdot e^{(-.54 \cdot \frac{v}{s})} \right]$$

Equation 4.11

Note that this multiplier becomes 1.0 for the “standard” volume-to-surface ratio of 1.5 (in.).

A correction factor is also suggested to account for loading ages other than 7 days for moist-cured concrete and 1 to 3 days for steam-cured concrete. The equation for this multiplier may be found in the ACI 209 Committee Report [8].

Once all appropriate correction factors have been applied, the creep coefficient at any time t , C_{ct} , can be determined as a function of the corrected ultimate creep coefficient, C_{cu} . The following hyperbolic-power expression is used for the relationship, where t is the time in days after casting and t_0 is the time of loading:

$$C_{ct} = \frac{(t - t_0)^{0.6}}{10 + (t - t_0)^{0.6}} \cdot C_{cu}$$

Equation 4.12

The form of Equation 4.12 is based on the work of Branson et. al. [26,27]. The coefficients 10 and 0.6 were determined as average values from a set of 120 creep tests [26]. A suggested range of other possible values for these two coefficients, as well as for the ultimate creep coefficient, is provided in the ACI 209 Committee Report [8]. The general form of Equation 4.12 is given in Equation 4.13:

$$C_{ct} = \frac{(t - t_0)^c}{d + (t - t_0)^c} \cdot C_{cu}$$

Equation 4.13

Other well-known design-oriented prediction models for creep of concrete include the 1990 CEB model [44] and the simplified BP (Bazant-Panula) model [24]. The 1990 CEB model is very similar to the ACI 209 model, and allows for the prediction of creep as a function of loading age, loading duration, cement type, relative humidity, and member size and thickness. One of the primary differences between this model and the ACI 209 model is that concrete strength is also considered as a variable in the prediction of creep. A second major difference is that the effects of relative humidity and member size and thickness on the *rate* of creep are considered, in addition to the effect of these variables on the total or ultimate creep. The lack of consideration of the effects of these variables on the rate of creep is one of the major deficiencies of the ACI 209 model [82].

The simplified Bazant-Panula model [24] is a simplified form of a complex model for the prediction of creep. This model was developed using a large database of measured creep values from experimental tests. The interrelation of creep and shrinkage is considered in the BP model, and total creep is separated into terms representing basic creep and drying creep. One of the interesting features of this model is that concrete strength is the major variable in the model, and appears in the calculation of several parameters used in the model.

4.5.2 Method of Measurement

Creep tests were performed on the eleven mix designs discussed in Section 4.1 and Section 4.2. The ASTM C512 [21] test procedure was followed with a few basic modifications, including the use of 100 x 600 mm (4 x 24 in) cylinder specimens. This specimen diameter was consistent with that used for testing of compressive strength and modulus of elasticity, and assured that the applied loads required for testing were within the range of loads possible using equipment available to the researchers. The length of these specimens allowed for the measurement of surface strains during the test using a DEMEC

mechanical strain gauge with a 200 mm (8 in.) gauge length. In addition, the use of a single long specimen instead of stacking multiple short specimens, such as three 100 x 200 mm (4 x 8 in.) cylinders, eliminated difficulties with alignment between specimens during loading.

In general, a total of eight or nine test specimens were cast for each mix. Two of these specimens were loaded for measurement of creep strains. Three specimens were kept unloaded to monitor strains due to drying shrinkage and changes in the testing environment, and two specimens were used for determination of the coefficient of thermal expansion. One or two additional specimens were cast in case any of the specimens were damaged or poorly fabricated.

Specimens for each mix were cast alongside the member at the precast plant or alongside the structure at the jobsite. Precut segments of PVC pipe and specially fabricated aluminum end inserts were used to form the specimens. Concrete was placed in 100 to 150 mm (4 to 6 in.) layers and each layer was rodded 25 times. A set of creep/shrinkage/thermal (C/S/T) specimens, as well as a group of standard cylinders for testing of compressive strength and modulus of elasticity, is shown shortly after casting at the jobsite in Figure 4.4.

Specimens were capped to prevent moisture loss and were stored alongside the structure for 8 to 18 hours, at which time they were transported back to the CMRG laboratory in Austin. One set of lower strength specimens for a cast-in-place deck in San Angelo was transported back to Austin at too early an age, resulting in the failure of several specimens during transportation. These specimens were recast during the next deck pour, and extreme care was taken to prevent subsequent failure during transportation. No other problems were observed due to the transportation of specimens at early ages.

Approximately 24 hours after casting of the specimens, the PVC molds were removed and DEMEC mechanical strain gauge points were fixed to the surface of the specimen using a quick-set epoxy gel. Points were placed as shown in Figure 4.5, such that three surface strain measurements were taken on three "sides", 120° apart, for a total of nine strain measurements per specimen. The specimens were then sulfur capped to ensure smooth ends, and the DEMEC points allowed to set overnight.

Unfortunately, a controlled indoor environment was not available to the researchers for the entire duration of the tests. Thus, creep tests were performed in an uncontrolled indoor environment at the CMRG laboratory. Relative humidity in the room was monitored

throughout the test period, and found to average 55%. Concrete temperatures were recorded at the time of each reading in at least one specimen from each mix.

Creep specimens were loaded 2 days after casting if they were from a precast (beam or deck panel) mix and 28 days after loading if from a cast-in-place (deck) mix. These loading ages were selected as the best practical representations of the field loading conditions that could be routinely repeated for testing. For each mix, one specimen was loaded to 20% and one specimen to 40% of the nominal design compressive strength of the mix. Note that cast-in-place specimens were air cured in the testing room prior to being loaded at 28 days.

The applied load for each specimen was maintained throughout the tests using test frames, as shown in Figure 4.6. Stress was initially applied using a hydraulic pump and ram system, and a load cell was used to monitor the load. Once the required applied load was reached, the nuts were tightened and the ram removed. Load was maintained by the railroad springs at the base of the creep frame. The loss of load with time, due to the shortening of the specimens and consequential elongation of the springs, could be determined by monitoring the spring elongation since the stiffness of the springs was known. When 2% of the initial load was lost, the load was reapplied using the pump and ram.

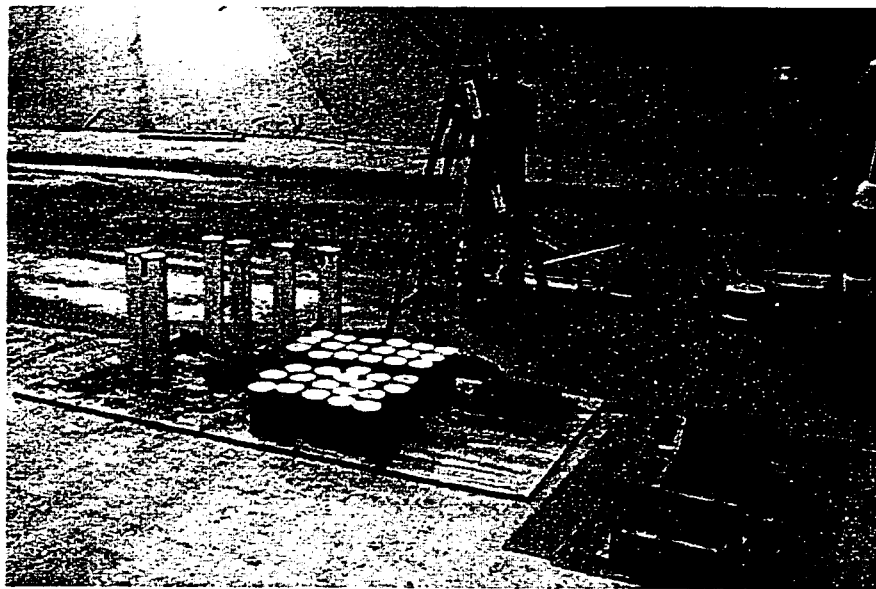


Figure 4.4 - C/S/T Specimens Just After Casting at Jobsite

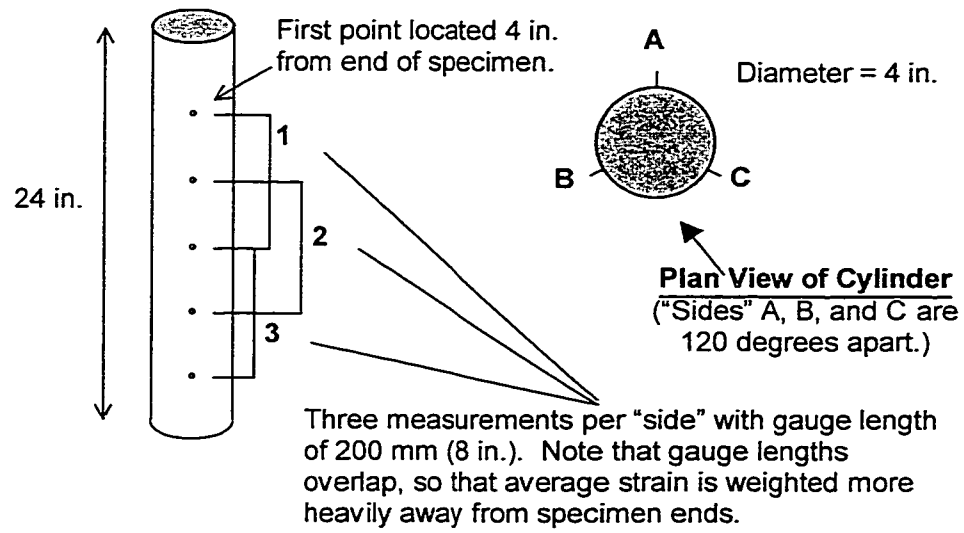


Figure 4.5 - Arrangement of DEMEC Gauge Points on C/S/T Specimens



Figure 4.6 - Creep Test Frames with Specimens Under Sustained Load

Strains were monitored on the two loaded specimens and three unloaded specimens for each mix. The creep strain for each loaded specimen was determined by subtracting the average strain on the unloaded specimens from the measured strain on the loaded specimen. Measurements were taken every few days for approximately the first 28 days, and every few weeks thereafter for a total duration of at least 180 days.

4.5.3 Measurements

Creep coefficient and specific creep were calculated from the measured creep strains and initial elastic (loading) strain for each specimen. Values were calculated at 7, 28, 56, and 180 days after loading using the strain measurements made at those time stages. When a measurement was not recorded *exactly* at a given time stage, an interpolation procedure was used to determine a value based on the measurements immediately before and after that time stage. The interpolation algorithm utilized a hyperbolic-power form for creep-time behavior like that discussed in Section 4.5.1.

The calculated values of creep coefficient and specific creep for each of the eleven concrete mixes tested are presented in Table 4.14 and Table 4.15, respectively. Except for the Louetta HPC beam mix, values listed in the table represent the average of two specimens, one loaded to 20% and one to 40% of the nominal design strength for the given mix. This averaging process is applicable because all tests were performed at stresses below the assumed limit of the linear relationship between stress and creep, which was discussed in Section 4.5.1. Creep data is plotted for each individual test specimen in Appendix D.

For the Louetta HPC beam mix, the data listed in Table 4.14 is based on the average of three specimens loaded to 8, 23, and 38 percent of the nominal design strength. These percentages correspond to stresses of 7, 21, and 35 MPa (1000, 3000, and 5000 psi), respectively. This data was taken from the work by Farrington and Burns [51] in an earlier portion of the research program, in which the creep and shrinkage properties of the Louetta beam mix were studied extensively.

The data shown in Table 4.14 and Table 4.15, as well as that in Appendix D, is based on test specimens with a volume-to-surface ratio of 1.0 (in.) and subjected to an average relative humidity in the testing room of 55%. It can be shown using the multipliers

given in Equation 4.9 and Equation 4.11 that, merely by coincidence, these data can be assumed to correlate directly to measurements under “standard” assumptions. For the test specimens, the relative humidity correction factor can be calculated as 0.902, while the volume-to-surface ratio correction factor can be calculated as 1.106. The product of these two correction factors is 1.00, *implying* that the same creep would have been measured on “standard” specimens ($v/s=1.5$ in.) under “standard” conditions (RH=40%). This coincidence is merely stated here because it allows for easier comparison of measurements in this study with experimental or recommended values specified at these “standard” conditions. The verification of these correction factors is beyond the scope of this research program. Note that for some purposes, adjustments for age at loading would still need to be applied to the measured data.

The primary objective of the creep testing program was to determine as accurately as possible the creep properties of the materials in the two Texas HPC bridges for use in data reduction and analysis. Still, it is useful to make small comparisons regarding similarities and differences in the creep behavior of the eleven mixes. The conclusions drawn from these comparisons are only intended to represent the concretes used in the two bridges, and are not meant to be extrapolated for use with other concretes. It is also important to note that the loading ages of the precast and cast-in-place mixes were different, although they are grouped together for comparison. However, the difference in loading age may not be overly significant since all precast mixes used Type III cement and were loaded at 2 days, while all cast-in-place mixes used Type I or Type II cement and were loaded at 28 days. The stress-strength ratios for each group of mixes were likely quite similar at their respective loading ages.

Measured creep coefficients at 180 days ranged from 0.85 to 2.23, as compared to a predicted value of 1.63 using the ACI 209 [8] method under “standard” conditions. Creep coefficients were also lower for most precast mixes, which were loaded at 2 days, than for cast-in-place mixes, which were loaded at 28 days. Note that measured creep coefficients at 180 days for the three beam mixes (Louetta HPC, San Angelo HPC, and San Angelo non-HPC) were 1.39, 1.25, and 0.85, respectively. These values are all substantially lower than the creep coefficient predicted by the ACI 209 method. These low creep coefficients can have a great impact on prestress losses, as is discussed in Chapter 7.

Table 4.14 - Measured Creep Coefficients

Days After Loading	CREEP COEFFICIENT			
	7	28	56	180
<i>Precast Mixes (Specimens Loaded at 2 days)</i>				
Louetta NB/SB HPC Prestressed Beams *	0.60	0.94	1.13	1.39
San Angelo EB HPC Prestressed Beams	0.73	0.92	1.06	1.25
San Angelo WB Non-HPC Prestressed Beams	0.47	0.71	0.75	0.85
Louetta NB/SB HPC Precast Deck Panels	0.54	0.77	0.92	1.16
San Angelo EB HPC Precast Deck Panels	0.58	1.12	1.41	1.95
San Angelo WB Non-HPC Precast Deck Panels	0.74	1.07	1.37	1.97
<i>Cast-in-Place Mixes (Specimens Loaded at 28 days)</i>				
Louetta NB HPC Deck	0.39	0.74	0.98	1.47
Louetta SB HPC Deck	0.46	0.80	1.09	1.69
San Angelo EB HPC Class K Deck	0.72	1.07	1.25	1.59
San Angelo WB HPC Modified Class S Deck	0.65	1.21	1.51	2.23
San Angelo WB Non-HPC Standard Class S Deck	0.53	0.94	1.43	1.96
Note: Values represent average of two specimens loaded to 20% and 40%, respectively, of design strength of the mix. Test specimens have a volume-to-surface ratio of 1.0 in., and average relative humidity in testing room was 55%. * Average of three specimens loaded to 8%, 23%, and 38% of design strength.				

It is difficult to make generalizations from the data regarding the behavior of HPC concretes versus non-HPC concretes. Simply put, some HPC concretes exhibited lower creep, while others exhibited higher creep. Since creep is generally regarded as a concrete property that is strength-dependent, it makes more sense to compare the creep behavior of the eleven concretes as classified by their compressive strengths. A plot of the measured creep at 180 days after loading versus the 28-day member-cured compressive strength is presented in Figure 4.7. In general, higher strength concretes exhibited less creep than lower strength concretes. Furthermore, the higher-strength, lower-creep concretes tended to be precast mixes rather than cast-in-place mixes.

There appears to be an even more direct relationship between water-to-binder ratio and measured creep, as shown in Figure 4.8. Regardless of the type of mix (i.e. precast or cast-in-place), concretes with lower water-to-binder ratios exhibited lower creep. This trend has been reported in the literature, and makes intuitive sense because creep is essentially a

behavior of the paste. Concretes with less porous pastes should, generally speaking, be expected to creep less.

Likewise, concrete with less mix water will have less potential to creep since creep is associated with the rearrangement and loss of water. A clear relationship between quantity of mix water and creep can be seen in Figure 4.9 for the eleven mixes in this study. This relationship may also explain why the San Angelo Westbound non-HPC beams exhibited the least creep of any mix, and less creep than the Louetta and San Angelo HPC beam mixes. Despite having a slightly higher water-to-binder ratio than the HPC beam mixes (0.27 vs. 0.25), this mix exhibited about 32 to 39 percent less creep (in terms of creep coefficient). Note that the Westbound non-HPC beam mix had about 20% less mix water than the HPC beam mixes (116 kg/m³ [196 pcy] vs. 146 to 147 kg/m³ [246 to 248 pcy]).

Table 4.15 - Measured Specific Creep

Days After Loading	SPECIFIC CREEP ($\mu\epsilon$ /psi)			
	7	28	56	180
<i>Precast Mixes (Specimens Loaded at 2 days)</i>				
Louetta NB/SB HPC Prestressed Beams *	.095	.151	.180	.222
San Angelo EB HPC Prestressed Beams	.120	.151	.174	.205
San Angelo WB Non-HPC Prestressed Beams	.079	.120	.126	.142
Louetta NB/SB HPC Precast Deck Panels	.085	.120	.143	.180
San Angelo EB HPC Precast Deck Panels	.133	.257	.324	.445
San Angelo WB Non-HPC Precast Deck Panels	.168	.244	.310	.444
<i>Cast-in-Place Mixes (Specimens Loaded at 28 days)</i>				
Louetta NB HPC Deck	.084	.160	.213	.317
Louetta SB HPC Deck	.087	.152	.206	.320
San Angelo EB HPC Class K Deck	.108	.161	.188	.240
San Angelo WB HPC Modified Class S Deck	.212	.390	.488	.722
San Angelo WB Non-HPC Standard Class S Deck	.106	.186	.284	.389
1 psi = 0.006895 MPa				
Note: Values represent average of two specimens loaded to 20% and 40%, respectively, of design strength of the mix. Test specimens have a volume-to-surface ratio of 1.0 in., and average relative humidity in testing room was 55%.				
* Average of three specimens loaded to 8%, 23%, and 38% of design strength.				

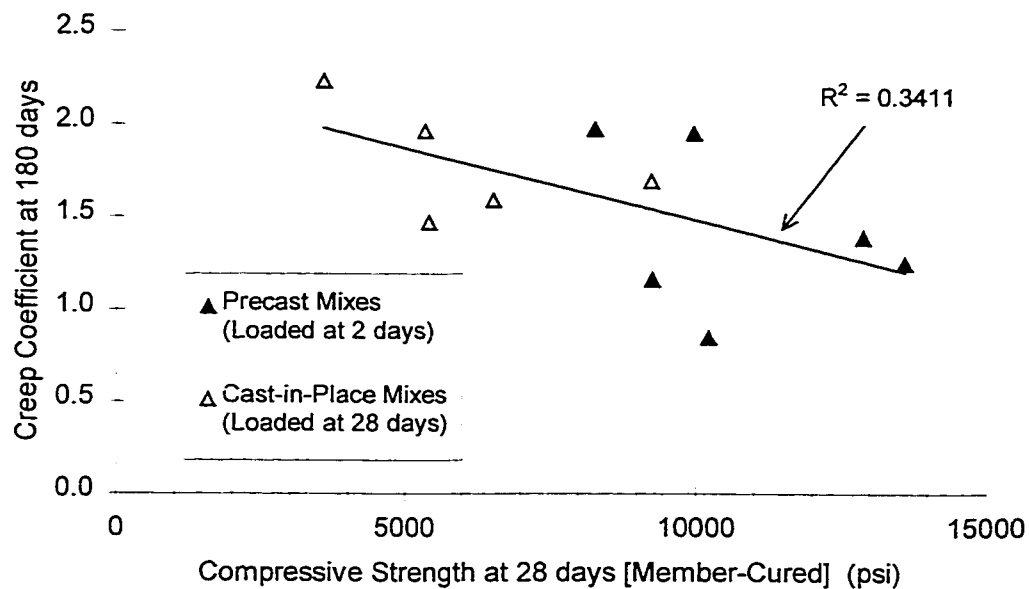


Figure 4.7 - Creep vs. 28-day (Member-Cured) Compressive Strength

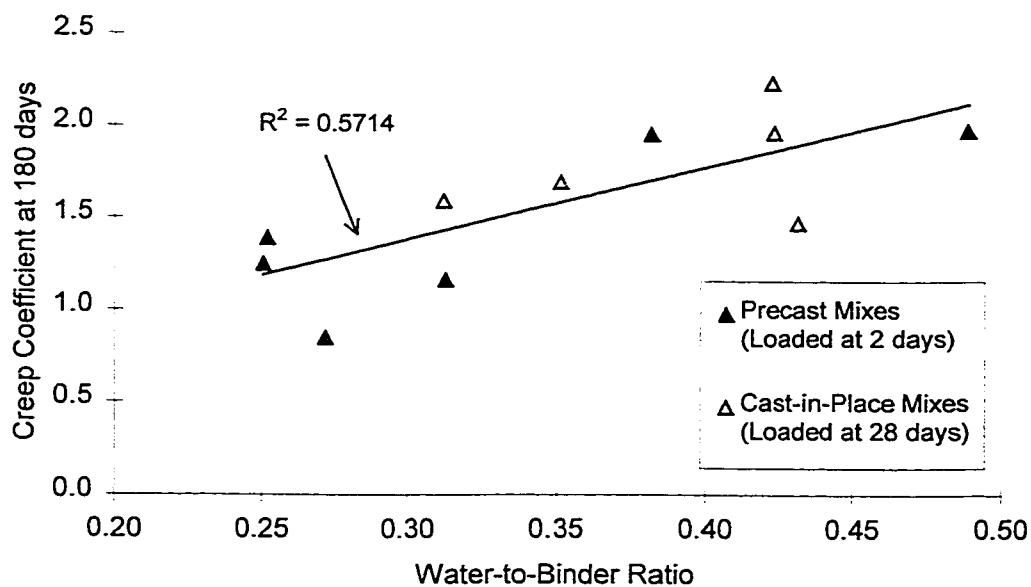


Figure 4.8 - Creep vs. Water-to-Binder Ratio

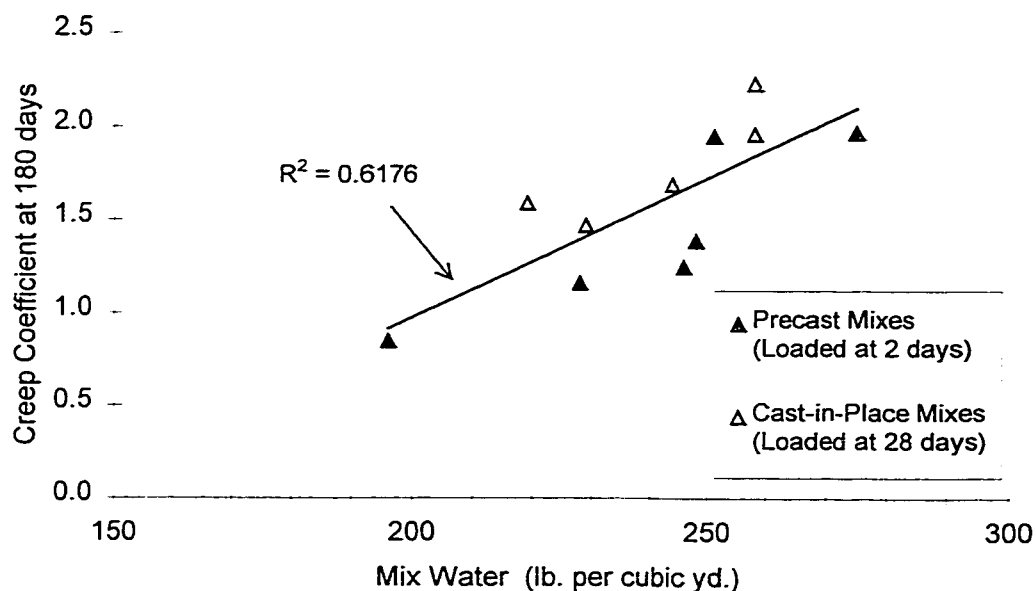


Figure 4.9 - Creep vs. Quantity of Mix Water

Finally, the rate of creep at early ages was seen to vary substantially between mixes. Percentages of the measured creep at 180 days that occurred 7, 28, and 56 days after loading are listed in Table 4.16 for each mix. The only clear trend is that creep occurred much more quickly in general in the precast mixes than in the cast-in-place mixes. It is unclear whether this is due to the earlier loading of the precast mixes, the higher strength of the precast mixes, or a combination of both.

4.5.4 Regression Analyses for Use in Time-Dependent Models

As for other material properties, continuous creep-time curves were necessary for use in modeling the time-dependent structural behavior of the two bridges. Thus, a nonlinear regression analysis was performed on the measured creep data for each of the eleven concrete mixes. Creep-time curves were fit to the form of Equation 4.13, the hyperbolic-power curve used in the ACI 209 [8] method. A regression analysis was performed on a linearized form of Equation 4.13 to determine the parameters d and C_{cw} , given a known value for the power c . This procedure was repeated for several values of c

(in increments of 0.1), and the best fit curve for each mix was selected as the curve that produced the highest coefficient of determination, R^2 . A summary of the parameters corresponding to the best-fit curves for each mix is presented in Table 4.17.

Note that in most cases, the parameter d for the best-fit curves falls approximately within the range of 6 to 30 recommended by ACI Committee 209 [8]. For a few of the precast mixes, this parameter is lower than 6, and the precast mixes as a group show significantly lower values for d than the cast-in-place mixes. This trend reflects the fact that the parameter d is a good indicator of the rate of creep at early ages. Low values of d , such as those seen for the precast mixes, imply that a large percentage of the total creep occurs at very early ages. This observation is consistent with the results discussed in Section 4.5.3.

Table 4.16 - Percentage of Creep at 180 days Occurring at Various Ages

Days After Loading	% of Creep at 180 days			
	7	28	56	180
<i>Precast Mixes (Specimens Loaded at 2 days)</i>				
Louetta NB/SB HPC Prestressed Beams *	43	68	81	100
San Angelo EB HPC Prestressed Beams	59	74	85	100
San Angelo WB Non-HPC Prestressed Beams	56	85	89	100
Louetta NB/SB HPC Precast Deck Panels	47	67	79	100
San Angelo EB HPC Precast Deck Panels	30	58	73	100
San Angelo WB Non-HPC Precast Deck Panels	38	55	70	100
<i>Cast-in-Place Mixes (Specimens Loaded at 28 days)</i>				
Louetta NB HPC Deck	26	50	67	100
Louetta SB HPC Deck	27	48	64	100
San Angelo EB HPC Class K Deck	45	67	78	100
San Angelo WB HPC Modified Class S Deck	29	54	68	100
San Angelo WB Non-HPC Standard Class S Deck	27	48	73	100
1 psi = 0.006895 MPa				
Note: Values represent average of two specimens loaded to 20% and 40%, respectively, of design strength of the mix. Test specimens have a volume-to-surface ratio of 1.0 in., and average relative humidity in testing room was 55%.				
* Average of three specimens loaded to 8%, 23%, and 38% of design strength.				

Table 4.17 - Creep-Time Regression Curve Parameters (General Form)

GENERAL FORM of Equation 4.13	c	d	C _{cu}	R ²
Precast Mixes (Loading Age = 2 Days)				
Louetta NB/SB HPC Prestressed Beams	0.6	6.5	1.78	.955
San Angelo EB HPC Prestressed Beams	0.3	3.9	2.26	.989
San Angelo WB Non-HPC Prestressed Beams	0.8	4.9	0.96	.913
Louetta NB/SB HPC Precast Deck Panels	0.7	4.5	1.16	.917
San Angelo EB HPC Precast Deck Panels	0.6	9.8	2.65	.862
San Angelo WB Non-HPC Precast Deck Panels	0.9	12.5	1.89	.865
Cast-in-Place Mixes (Loading Age = 28 Days)				
Louetta NB HPC Deck	0.7	16.7	2.03	.926
Louetta SB HPC Deck	0.7	14.4	2.16	.852
San Angelo EB HPC Class K Deck	0.4	6.3	2.79	.993
San Angelo WB HPC Modified Class S Deck	0.6	13.5	3.47	.967
San Angelo WB Non-HPC Standard Class S Deck	0.6	16.6	3.31	.815
Note: Values based on regression analysis using 180 days of measured data				

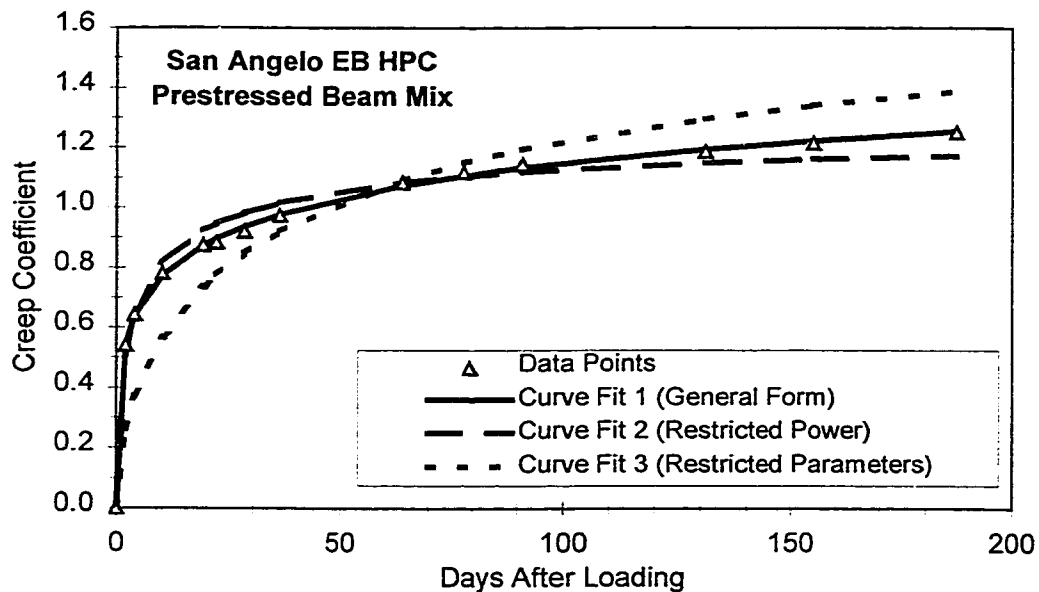


Figure 4.10 - Typical Creep Coefficient Curve Fits from Regression Analyses

Table 4.18 - Creep-Time Regression Curve Parameters (Power Fixed)

Equation 4.13, with $c=0.6$	c	d	C_{cu}	R^2
Precast Mixes (Loading Age = 2 Days)				
Louetta NB/SB HPC Prestressed Beams	0.6	6.5	1.78	.955
San Angelo EB HPC Prestressed Beams	0.6	2.3	1.29	.923
San Angelo WB Non-HPC Prestressed Beams	0.6	3.9	1.07	.873
Louetta NB/SB HPC Precast Deck Panels	0.6	4.3	1.25	.909
San Angelo EB HPC Precast Deck Panels	0.6	9.8	2.65	.862
San Angelo WB Non-HPC Precast Deck Panels	0.6	11.0	2.65	.637
Cast-in-Place Mixes (Loading Age = 28 Days)				
Louetta NB HPC Deck	0.6	21.1	2.85	.894
Louetta SB HPC Deck	0.6	18.1	2.96	.844
San Angelo EB HPC Class K Deck	0.6	4.9	1.83	.959
San Angelo WB HPC Modified Class S Deck	0.6	13.5	3.47	.967
San Angelo WB Non-HPC Standard Class S Deck	0.6	16.6	3.31	.815
Note: Values based on regression analysis using 180 days of measured data				

Table 4.19 - Creep-Time Regression Curve Parameters (Parameters Fixed)

Equation 4.13, with $c=0.6$ and $d=10$	c	d	C_{cu}	R^2
Precast Mixes (Loading Age = 2 Days)				
Louetta NB/SB HPC Prestressed Beams	0.6	10	2.12	.960
San Angelo EB HPC Prestressed Beams	0.6	10	1.99	.523
San Angelo WB Non-HPC Prestressed Beams	0.6	10	1.47	.571
Louetta NB/SB HPC Precast Deck Panels	0.6	10	1.68	.784
San Angelo EB HPC Precast Deck Panels	0.6	10	2.71	.990
San Angelo WB Non-HPC Precast Deck Panels	0.6	10	2.63	.973
Cast-in-Place Mixes (Loading Age = 28 Days)				
Louetta NB HPC Deck	0.6	10	1.97	.955
Louetta SB HPC Deck	0.6	10	2.25	.937
San Angelo EB HPC Class K Deck	0.6	10	2.39	.912
San Angelo WB HPC Modified Class S Deck	0.6	10	3.04	.979
San Angelo WB Non-HPC Standard Class S Deck	0.6	10	2.63	.930
Note: Values based on regression analysis using 180 days of measured data				

The power c , on the other hand, is a reasonably good indicator of the rate of creep at very late ages, such as several years from the time of loading. Lower values of c imply that there is a continual, albeit slow, gain in creep with time. Higher values of c (above 0.7 or so) indicate that the creep-time curve approaches its ultimate value within a few years. The range of c for the eleven mixes, 0.3 to 0.9, is approximately that recommended by ACI Committee 209 [8], 0.4 to 1.0.

Of course, the parameters c and d *together* determine the shape of the creep-time curve at all ages. Caution must be exercised in interpreting the value of C_{cu} for each mix. In some cases, this value is a good representation of the creep that might be expected to occur over the life of the structure. In other cases, however, C_{cu} represents nothing more than a mathematical asymptote to the creep-time curve that may never even be approached during the useful life of the structure. For example, the combination of c and d (0.3 and 3.9, respectively) for the San Angelo Eastbound HPC beams indicates that the creep coefficients at 10 and 50 years after loading will be only 75 and 83 percent, respectively, of C_{cu} . With this combination of parameters c and d , it would take almost 5000 years for the creep coefficient to reach 95 percent of C_{cu} . For this reason, the values of C_{cu} for the different mixes should not be arbitrarily compared without consideration of the other parameters.

Of course, the regression analyses are technically valid only over the range of data used for their development. There is an inherent danger in speculating on the long-term creep behavior of the mixes using only 180 days of data. Still, the regression analyses provide a reasonably sound method for the development of creep-time curves, and since they are based on measured data, should generally provide a great improvement over methods based entirely on assumptions developed empirically from measurements on other concrete mixes.

Since some time-dependent analysis programs utilize the ACI 209 creep curve but do not allow for input of all three parameters c , d , and C_{cu} , two other sets of regression curves were developed. The first type, the "power fixed" curve, determines the parameters d and C_{cu} where the power c is fixed to the ACI 209 value of 0.6. The second type, the "parameters fixed" curve, assumes that only C_{cu} may vary, and that the form of the creep-time relationship is given by Equation 4.11, with c and d fixed to 0.6 and 10, respectively. These curves are compared in Figure 4.10 for the San Angelo Eastbound HPC beam mix. Clearly, the restricted curves do not correlate as well with the measured data points. Again,

it is important to note that these curves were only developed for use where restrictions prohibit the use of the general form of Equation 4.13.

Summaries of the parameters developed for the restricted regression analyses are provided in Table 4.18 and Table 4.19. Note that the R^2 values for the case of the “parameters fixed” curves should not be compared to R^2 values for the other types of curves, because they represent different mathematical quantities. The “parameters fixed” analysis has only one degree of freedom, and is equivalent to a linear regression analysis where the intercept of the regression line is forced to equal zero.

4.6 Shrinkage

4.6.1 Background

Shrinkage can be broadly defined as the decrease in volume (not related to thermal effects) of hardened concrete with time. In this sense, shrinkage in hardened concrete is to be distinguished from plastic shrinkage, which occurs in concrete prior to setting. Three basic types of shrinkage are generally considered to contribute to the total time-dependent decrease in volume. Drying shrinkage is a result of the loss of moisture over time, carbonation shrinkage is due to the chemical reaction of hardened cement paste with atmospheric carbon dioxide, and autogenous shrinkage is due to a self-desiccating effect that occurs during hydration [83].

Drying shrinkage is generally considered to be the major component of the total shrinkage in concrete structures [75]. Still, carbonation shrinkage can greatly increase the total shrinkage under certain environmental conditions, namely the presence of high concentrations of CO_2 at intermediate relative humidities [95]. It is also suggested that many of the experimental data on drying shrinkage include the effects of carbonation shrinkage [95]. Autogenous shrinkage, on the other hand, is typically very small [75,96]. Fortunately, it is unnecessary to distinguish between these three types of shrinkage in structural design. Thus, the generic term shrinkage will be used throughout the rest of this dissertation, including portions related to the experimental tests conducted in this research program.

As with creep, a number of factors are known to affect shrinkage of concrete. These factors can generally be classified as factors related to mix composition, those related to curing and service exposure conditions, and those related to size and shape of the member.

Shrinkage is a property of the paste in concrete. Since the aggregate acts to restrain the shrinkage of the paste, it plays a major role in the determining the magnitude of concrete shrinkage. The proportion of aggregate in the mix, as well as the stiffness (modulus of elasticity) of the aggregate, are considered by many to be the most important mix composition factors influencing concrete shrinkage [83,95]. Water-to-cement (water-to-binder) ratio is also generally believed to be proportional to shrinkage, with lower ratios resulting in concrete with lower shrinkage. Water content itself is accepted to be proportional to shrinkage, but there is disagreement as to whether its influence is direct or indirect. Neville [95] suggests that water content only affects shrinkage in that it influences the proportion of aggregate in the mix. Nilson and Winter [100] suggest that the influence is more direct, and that the quantity of mix water is the chief mix-related factor influencing shrinkage. Their observations are based largely on the linear relationship between mix water and shrinkage strain shown by Troxell et. al. [136].

Curing and environmental exposure factors can greatly influence concrete shrinkage. Elevated curing temperatures have been shown to reduce long-term shrinkage in several studies [62,70,120]. Some studies [126] have also indicated that the duration of moist curing can influence long-term shrinkage, and ACI Committee 209 [8] suggests a modification factor that implies less shrinkage for longer moist curing periods. Ambient relative humidity under service conditions is known to greatly affect concrete shrinkage, primarily because it influences the rate of moisture exchange between the concrete and the surrounding atmosphere. Low relative humidities lead to increased shrinkage. It would similarly be expected that elevated temperatures would accelerate drying and thus increase the rate of shrinkage [54], but this effect is considered to be much less significant than the effect of relative humidity [8].

One of the most significant factors influencing concrete shrinkage is the size and shape of the member. Both the rate of shrinkage and the ultimate shrinkage tend to decrease as the member becomes larger [61]. In smaller (thinner) members, the shrinkage tends to occur rapidly and relatively uniformly. In larger (thicker) members, the rate of shrinkage will be fast near the surface, while shrinkage at the innermost parts of the

member may develop very slowly or even be nonexistent. Stresses may develop in large members as a result of this differential shrinkage [83]. The relationship between member geometry and shrinkage is generally modeled using the volume-to-surface ratio, or the average or minimum member thickness.

Experimental data has generally shown no clear trend with respect to shrinkage of high strength concrete, though it is often suggested that the shrinkage of high strength concrete is similar to the shrinkage of normal strength concretes [10]. Ngab et. al. [98] noted slightly higher shrinkage for high strength concrete when compared to normal strength concrete made with similar materials. Smadi et. al. [123] also observed higher shrinkage for high strength concrete (59 to 69 MPa [8,500 to 10,000 psi]) as opposed to normal strength concrete (35 to 41 MPa [5,000 to 6,000 psi]), but observed less shrinkage for HSC than for concretes with very low strengths concrete (21 to 24 MPa [3,000 to 3,500 psi]). Swamy and Anand [126] observed a high initial rate of shrinkage for high strength concrete made with finely ground portland cement, but noted that shrinkage strains after two years were approximately equal to values suggested in the CEB code [43].

There are also few conclusions regarding the shrinkage of high performance concrete (with or without high strengths), or regarding the effect of mineral and chemical admixtures on concrete shrinkage. Brooks and Neville [30] acknowledge that the effects of individual admixtures are difficult to identify, and that the small body of experimental data indicates varying results. Sennour and Carrasquillo [120] noted that the partial replacement of cement with both Class C and Class F fly ashes resulted in a slight increase in shrinkage, and that greater percentages of replacement led to greater increases in shrinkage. El Hindy et. al. [49] observed less shrinkage in HPC with a water-to-binder ratio of 0.22 and made using a blended cement (7 to 8 percent silica fume by weight) than in HPC with a water-to-binder ratio of 0.28 and no silica fume.

Several models have been proposed for the prediction of concrete shrinkage with time, most of which incorporate the effects of curing and environmental conditions and member geometry (size and shape). Some models also consider the effect of mix composition on shrinkage. The most widely used model in the United States is probably the ACI 209 [8] method, which was developed by Branson et. al. [26,27]. This method recommends an ultimate shrinkage strain of $780 \mu\epsilon$ based on an analysis of results from 356 experimental tests conducted on normal, lightweight, and sand-lightweight concretes [30]. This base value can be modified by a set of multipliers corresponding to mix

composition, or an ultimate shrinkage strain can be determined from experimental tests. Mix composition multipliers may be found in the ACI 209 Committee Report [8], and include considerations for slump, fine aggregate percentage, cement content, and air content.

The ultimate shrinkage strain is then modified using multipliers that account for relative humidity, member size and shape, and duration of moist curing. These multipliers are similar to those given for creep in Section 4.5.1, and the notation is consistent. The multiplier for average ambient relative humidity is given in Equation 4.14 and Equation 4.15:

$$\gamma_{rh} = 1.40 - (0.010 \cdot H) \quad \text{for } 40 \leq H \leq 80$$

Equation 4.14

$$\gamma_{rh} = 3.00 - (0.030 \cdot H) \quad \text{for } H > 80$$

Equation 4.15

Note that the multiplier becomes 1.0 for the “standard” relative humidity of 40 percent, and zero for a relative humidity of 100 percent (implying no shrinkage). No equation is given for relative humidities less than 40 percent, but the multiplier must be taken as greater than 1.0 in this case.

As for creep, the effect of size and shape effects may be considered by using a multiplier for *either* average member thickness *or* for volume-to-surface ratio. The multiplier for average member thickness is:

$$\gamma_{at} = 1.17 - (0.029 \cdot h)$$

Equation 4.16

for ultimate shrinkage values. The constants 1.17 and 0.029 are replaced by 1.23 and 0.038, respectively, to correct shrinkage values during the first year of drying. This modification reflects the greater influence of member thickness during the first year of drying.

The multiplier for size and shape effects based on volume-to-surface ratio v/s (in inches) is given by:

$$\gamma_{vs} = 1.2 \cdot e^{(-12 \cdot \frac{v}{s})}$$

Equation 4.17

Note that this multiplier is equal to 1.0 for the “standard” volume-to-surface ratio of 1.5 inches.

A loading factor to account for the duration of moist curing is given in tabular form in the ACI 209 Committee Report [8]. This factor allows for a reduction in shrinkage with moist curing periods greater than 7 days.

Following the application of all appropriate correction factors, the shrinkage strain $\epsilon_{sh,t}$ (at any time t after the time t_1 in which drying begins), can be determined as a function of the corrected ultimate shrinkage strain $\epsilon_{sh,u}$. The same hyperbolic-power expression used for the creep-time relationship is used, with a power of 1.0 and a time coefficient in the denominator of 35:

$$\epsilon_{sh,t} = \frac{(t - t_1)}{35 + (t - t_1)} \cdot \epsilon_{sh,u}$$

Equation 4.18

The coefficient 35 is intended for use with moist-cured concrete, and should be replaced with 55 for steam-cured concrete. The form of Equation 4.18 was suggested by Branson et al. [26,27], and the coefficients were determined as average values from a set of 95 experimental tests [26]. A suggested range of values for the general form of the shrinkage-time equation, given in Equation 4.19, is provided in the ACI 209 Committee Report [8]:

$$\epsilon_{sh,t} = \frac{(t - t_1)^e}{f + (t - t_1)^e} \cdot \epsilon_{sh,u}$$

Equation 4.19

Other design-oriented prediction models for shrinkage include the 1990 CEB model [44] and the simplified BP (Bazant-Panula) model [24]. The CEB model is similar to the ACI 209 approach, and includes considerations for the effects of concrete strength, cement type, relative humidity, and member size. Concrete strength is not meant to be a variable itself, but is included to represent the effects of water-to-cement (water-to-binder) ratio and water content, since most designers will not know these mix composition parameters [87]. Unlike the ACI 209 approach, the effects of member size on the *rate* of shrinkage are considered in the CEB model. The simplified Bazant-Panula model is a bit more complex, and considers several mix composition parameters, including sand-to-aggregate ratio, gravel-to-sand ratio, and water-to-cement (water-to-binder) ratio. The BP model also considers the interrelation of creep and shrinkage.

4.6.2 Method of Measurement

Shrinkage tests were performed on concrete from each of the eleven mixes described in Section 4.1 and 4.2. Tests were performed in parallel with the creep tests for each mix, and essentially involved the measurement of time-dependent strain on unloaded specimens. A description of the test specimens is provided in Section 4.5.2, along with details pertaining to the fabrication, transportation, and preparation of the specimens. Three specimens were typically used for each mix.

As discussed in Section 4.5.2, specimens were transported from the precast plant or jobsite at early ages. Cylinder molds were removed approximately 24 hours after the specimens were cast, and the first strain measurements were typically taken about 24 hours later. The 24 hours between stripping of the molds and the recording of the first strain measurement was necessary to allow adequate time for DEMEC points to be attached and bond to the cylinders. Specimens were air cured during this period.

Strain measurements were recorded on each specimen using a DEMEC mechanical strain gauge with a gauge length of 200 mm (8 in.). The arrangement of DEMEC gauge points on each specimen is shown in Figure 4.5. Measurements were performed simultaneously with measurements on creep (loaded) specimens, usually every

few days for the first 28 days and every few weeks thereafter. Readings were taken for a period of at least 180 days.

Shrinkage (unloaded) specimens can be seen in the testing room in Figure 4.11. Because the testing room was not a controlled environment, relative humidity was monitored and found to average 55%. The room temperature also fluctuated, so cylinder temperatures were recorded on selected specimens (at least one from each mix) at the time of each measurement. These temperatures were measured using thermocouples embedded in the specimens during casting.

For each specimen at each measurement interval, the average of the nine individual gauge readings was computed to determine the total strain on the specimen. This total strain represents the strain on the unloaded specimen due to both shrinkage and thermal effects. Temperature strains were then removed analytically using the measured cylinder temperatures and known coefficients of thermal expansion for each mix. In theory, the resulting strain represents the strain due to shrinkage alone.

A correction was also made to all shrinkage measurements to account for the fact that strains could not be measured beginning immediately after the removal of cylinder molds. The first measurements typically were recorded about 24 hours after drying commenced, as this period was required for the placement and bonding of DEMEC mechanical strain gauge points. The analytical correction was made by fitting a regression curve to the measured data, as described in Section 4.6.4, and projecting the curve back for the time period in which drying was occurring but measurements were not being recorded. This analytical correction procedure is shown in Figure 4.12 for a given set of readings.

4.6.3 Measurements

Shrinkage strains measured at 7, 28, 56, and 180 days after the stripping of cylinder molds are presented in Table 4.20. When a measurement was not recorded *exactly* at one of these time stages, strains were interpolated using the measurements recorded immediately before and after that time stage. The nonlinear hyperbolic-power relationship for shrinkage-time behavior discussed in Section 4.6.1 was used when interpolation was necessary. For most mixes, the shrinkage strains reported in Table 4.20 are based on an average of three specimens. One exception is the data from the Louetta HPC beam mix,

which was taken from the work by Farrington and Burns [51] in an earlier portion of this research program and includes six shrinkage specimens. Shrinkage data for individual specimens can be found in graphical form in Appendix D.

All shrinkage data reported in this study was collected on specimens with a volume-to-surface ratio of 1.0 and in an average ambient relative humidity of 55%. For these conditions, the multipliers given in Equation 4.14 and Equation 4.17 can be computed as 0.850 and 1.064, respectively. The product of these multipliers is 0.90, *implying* that the strains reported in Table 4.20 are approximately 90% of those that may be expected under “standard” conditions ($v/s=1.5$ in., $RH=40\%$). As stated in Section 4.5.3 for creep, the verification of these multipliers is beyond the scope of this research study, and the multipliers are only mentioned here to indicate that measured strains cannot directly be compared with recommended code values.

The range of measured shrinkage strains at 180 days was 265 to 528 $\mu\epsilon$. This is substantially less than predicted by the ACI 209 [8] method at 180 days (653 $\mu\epsilon$ under “standard” conditions), even when the correction factors mentioned in the preceding paragraph are applied. Note that there were no clear trends among the measured shrinkage strains at 180 days with respect to differences between precast mixes and cast-in-place mixes. Similarly, there was no obvious difference in the behavior of HPC mixes and non-HPC mixes.

There was also a wide range of behavior with respect to the rate of shrinkage. The percentages of measured shrinkage at 180 days occurring at various time stages is shown in Table 4.21. As a group, precast mixes exhibited a slightly faster rate of shrinkage than cast-in-place mixes, but the difference in rates was relatively small. No conclusion could be drawn with respect to the rate of shrinkage of HPC mixes versus non-HPC mixes.

Measured shrinkage strains at 180 days are plotted against 28-day (member-cured) compressive strength in Figure 4.13, and against water-to-binder ratio in Figure 4.14. There is clearly no relationship between shrinkage and compressive strength for the eleven mixes tested, and little or no relationship between shrinkage and water-to-binder ratio. It should be noted, however, that the effect of water-to-binder ratio is not truly isolated in this test program, since mixes were made with several different materials from several different sources. Most trends reported in the literature regarding the apparent relationship between shrinkage and water-to-binder ratio are based on mixes made from similar materials.

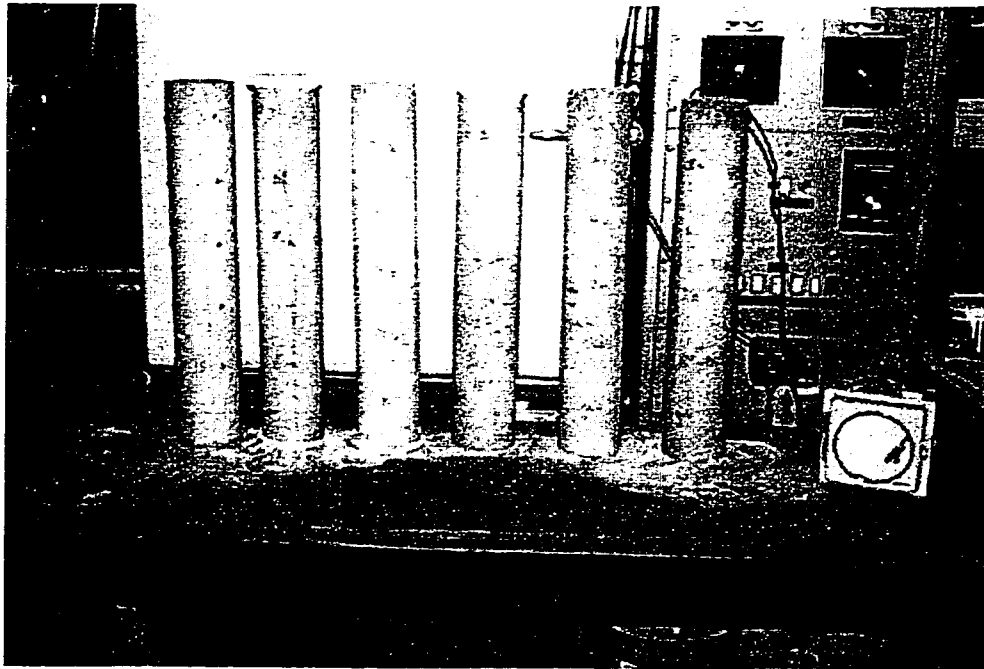


Figure 4.11 - Shrinkage (Unloaded) Specimens in Testing Room

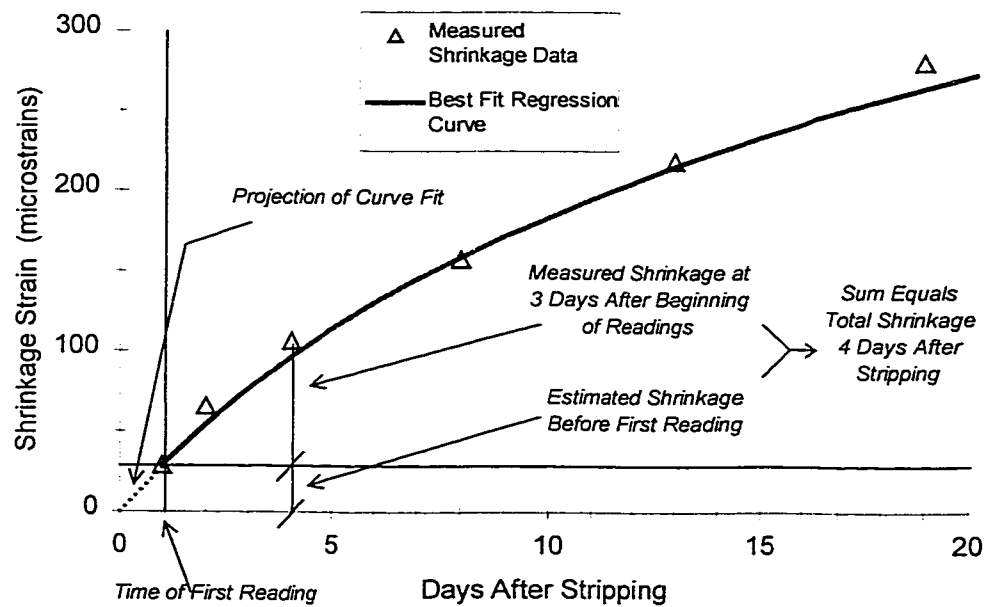


Figure 4.12 - Correction to Measured Shrinkage Data to Account for Unmeasured Shrinkage Before First Reading

Table 4.20 - Measured Shrinkage Strains

Days After Stripping	SHRINKAGE STRAIN ($\mu\epsilon$)			
	7	28	56	180
<i>Precast Mixes</i>				
Louetta NB/SB HPC Prestressed Beams	217	299	333	392
San Angelo EB HPC Prestressed Beams	223	307	353	382
San Angelo WB Non-HPC Prestressed Beams	98	242	269	298
Louetta NB/SB HPC Precast Deck Panels	80	198	233	268
San Angelo EB HPC Precast Deck Panels	135	330	404	528
San Angelo WB Non-HPC Precast Deck Panels	249	360	387	428
<i>Cast-in-Place Mixes</i>				
Louetta NB HPC Deck	66	178	240	296
Louetta SB HPC Deck	91	238	279	344
San Angelo EB HPC Class K Deck	138	251	285	265
San Angelo WB HPC Modified Class S Deck	125	269	371	462
San Angelo WB Non-HPC Standard Class S Deck	118	258	340	434
<p>Note: Values represent average of all unloaded specimens, corrected for thermal strains using measured temperatures and coefficients of thermal expansion for each mix. Estimated shrinkage prior to first measurement is also included in these values. Specimen molds were usually removed 24 hours after casting, and first measurement taken 24 hours later. Specimens were air cured during this period. Specimens have a volume-to-surface ratio of 1.0 in., and average humidity in testing room was 55%.</p>				

As can be seen in Figure 4.15, however, there does seem to be a clear relationship between shrinkage and the quantity of mixing water. For the eleven mixes in this study, the relationship was somewhat linear with lower water quantities resulting in lower shrinkage. As was discussed in Section 4.6.1, a linear relationship between shrinkage and water content has been suggested in the literature. This trend also makes physical sense because shrinkage is considered to be, to a large degree, a drying-related phenomenon.

Table 4.21 - Percentage of Shrinkage at 180 Days Occurring at Various Ages

Days After Stripping	% of Shrinkage at 180 days			
	7	28	56	180
Precast Mixes				
Louetta NB/SB HPC Prestressed Beams	55	76	85	100
San Angelo EB HPC Prestressed Beams	58	80	92	100
San Angelo WB Non-HPC Prestressed Beams	33	81	90	100
Louetta NB/SB HPC Precast Deck Panels	30	74	87	100
San Angelo EB HPC Precast Deck Panels	26	63	77	100
San Angelo WB Non-HPC Precast Deck Panels	58	84	90	100
Cast-in-Place Mixes				
Louetta NB HPC Deck	22	60	81	100
Louetta SB HPC Deck	26	69	81	100
San Angelo EB HPC Class K Deck	52	95	108	100
San Angelo WB HPC Modified Class S Deck	27	58	80	100
San Angelo WB Non-HPC Standard Class S Deck	27	59	78	100
<p>Note: Values represent average of all (usually three) unloaded specimens, corrected for thermal strains using measured temperatures and coefficients of thermal expansion for each mix. Estimated shrinkage prior to first measurement is also included in these values. Specimens molds were usually removed 24 hours after casting, and first measurement taken 24 hours later. Specimens were air cured during this period. Test specimens have a volume-to-surface ratio of 1.0 in., and average relative humidity in testing room was 55%.</p>				

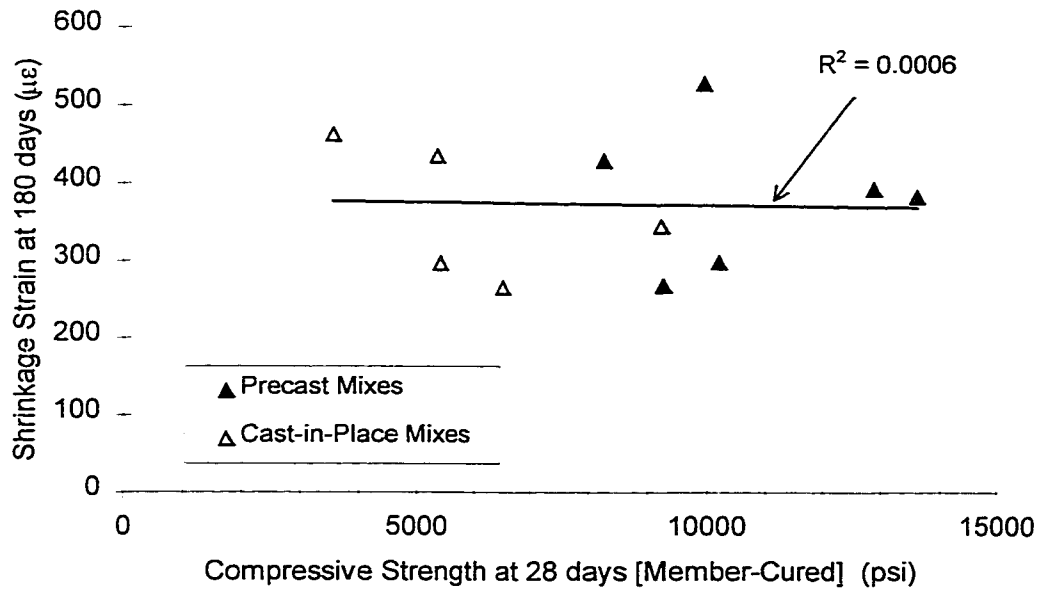


Figure 4.13 - Shrinkage vs. 28-day (Member-Cured) Compressive Strength

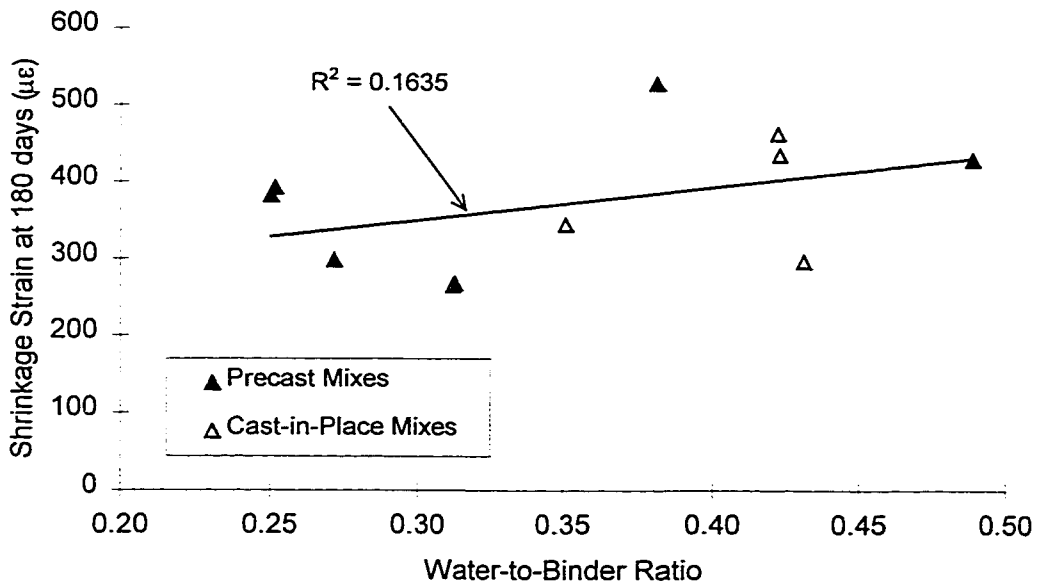


Figure 4.14 - Shrinkage vs. Water-to-Binder Ratio

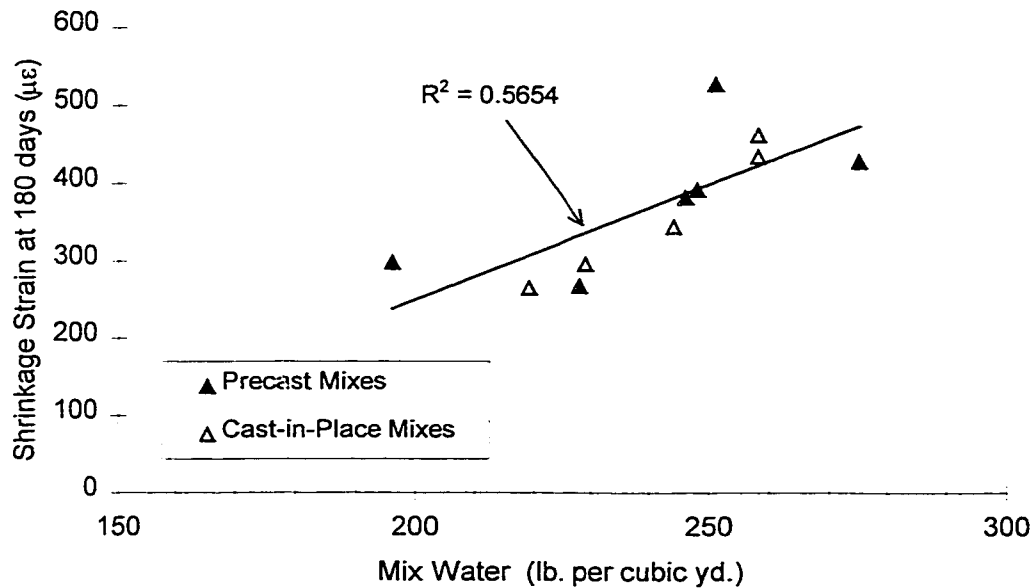


Figure 4.15 - Shrinkage vs. Quantity of Mix Water

Table 4.22 - Shrinkage-Time Regression Curve Parameters (General Form)

GENERAL FORM of Equation 4.19	e	f	$\epsilon_{sh,u}$	R ²
Precast Mixes				
Louetta NB/SB HPC Prestressed Beams	0.5	2.7	455	.878
San Angelo EB HPC Prestressed Beams	0.6	3.5	456	.962
San Angelo WB Non-HPC Prestressed Beams	1.6	42.4	284	.950
Louetta NB/SB HPC Precast Deck Panels	1.0	12.9	268	.817
San Angelo EB HPC Precast Deck Panels	0.9	17.5	600	.969
San Angelo WB Non-HPC Precast Deck Panels	0.7	3.4	470	.952
Cast-in-Place Mixes				
Louetta NB HPC Deck	1.1	25.8	293	.723
Louetta SB HPC Deck	1.0	16.6	359	.861
San Angelo EB HPC Class K Deck	1.2	9.6	295	.873
San Angelo WB HPC Modified Class S Deck	0.8	11.8	525	.798
San Angelo WB Non-HPC Standard Class S Deck	1.0	20.3	446	.903
Note: Values based on regression analysis using 180 days of measured data				

Table 4.23 - Shrinkage-Time Regression Curve Parameters (Power Fixed)

Equation 4.19, with $e=1.0$	e	f	$\epsilon_{sh,u}$	R^2
Precast Mixes				
Louetta NB/SB HPC Prestressed Beams	1.0	2.8	351	.740
San Angelo EB HPC Prestressed Beams	1.0	4.5	380	.893
San Angelo WB Non-HPC Prestressed Beams	1.0	12.4	318	.812
Louetta NB/SB HPC Precast Deck Panels	1.0	12.9	268	.817
San Angelo EB HPC Precast Deck Panels	1.0	18.0	546	.941
San Angelo WB Non-HPC Precast Deck Panels	1.0	4.1	417	.893
Cast-in-Place Mixes				
Louetta NB HPC Deck	1.0	22.8	313	.720
Louetta SB HPC Deck	1.0	16.6	359	.861
San Angelo EB HPC Class K Deck	1.0	7.3	310	.843
San Angelo WB HPC Modified Class S Deck	1.0	12.0	434	.713
San Angelo WB Non-HPC Standard Class S Deck	1.0	20.3	446	.903
Note: Values based on regression analysis using 180 days of measured data				

Table 4.24 - Shrinkage-Time Regression Curve Parameters (Parameters Fixed)

Equation 4.19, with $e=1.0$ and $f=35$	e	f	$\epsilon_{sh,u}$	R^2
Precast Mixes				
Louetta NB/SB HPC Prestressed Beams	1.0	35	546	-.383
San Angelo EB HPC Prestressed Beams	1.0	35	550	-.083
San Angelo WB Non-HPC Prestressed Beams	1.0	35	404	.423
Louetta NB/SB HPC Precast Deck Panels	1.0	35	343	.823
San Angelo EB HPC Precast Deck Panels	1.0	35	653	.971
San Angelo WB Non-HPC Precast Deck Panels	1.0	35	620	-.292
Cast-in-Place Mixes				
Louetta NB HPC Deck	1.0	35	365	.950
Louetta SB HPC Deck	1.0	35	444	.873
San Angelo EB HPC Class K Deck	1.0	35	436	-.429
San Angelo WB HPC Modified Class S Deck	1.0	35	589	.943
San Angelo WB Non-HPC Standard Class S Deck	1.0	35	521	.960
Note: Values based on regression analysis using 180 days of measured data				

4.6.4 Regression Analyses for Use in Time-Dependent Models

As for the other material properties discussed in this chapter, continuous shrinkage-time curves were necessary for use in modeling time-dependent structural behavior. A nonlinear regression analysis was thus performed to fit a curve of the form of Equation 4.19 to the measured shrinkage data for each mix. The method used was the same as for creep, and is discussed in Section 4.5.4. A summary of the parameters obtained from the regression analyses is presented in Table 4.22. Note that the regression analyses are technically valid only over the given range of data, but they will be used to estimate the shrinkage-time relationship for a given mix at all ages.

While the parameters e and f do not generally fall within the ranges suggested in the ACI 209 Committee Report [8] (0.9 to 1.1 for e , 20 to 130 for f), the intended effect of a “flat” shrinkage-time curve is reflected by the values listed in Table 4.22. Higher values for e (above about 0.7) generally result in shrinkage-time curves that become asymptotic to the ultimate strain at relatively early ages. Similarly, lower values of f imply a fast rate of shrinkage at very early ages. The few mixes whose regression analyses did not exhibit high values for e also exhibited low values of f , the net result being asymptotic behavior for all mixes. For example, the Louetta HPC Beam mix parameters (0.5 and 2.7 for e and f , respectively) imply that 88 percent of the ultimate shrinkage will occur within one year and 98 percent within 50 years. Parameters for the other ten mixes imply asymptotic behavior at even earlier ages. The mathematical value for the ultimate shrinkage strain, $\epsilon_{sh,u}$ is thus a reasonable representation of the ultimate strain that may be expected to occur over the useful lifetime of the structure. Recall that this was not necessarily the case for the ultimate creep coefficient, C_{cr} , as described in Section 4.5.4.

As for creep, two additional regression analyses were performed on restricted forms of Equation 4.19. These curves are intended for use only when the more general form is not permitted (such as in some time-dependent analyses). The parameters derived from these analyses are listed in Table 4.23 for the “power fixed” form and Table 4.24 for the “parameters fixed” form. Note that the negative values for the coefficient of determination, R^2 , listed in

Table 4.24 are a mathematical result of the restrictions imposed by fixing the parameters e and f . The negative values indicate essentially no relationship between the

least-squares regression line (whose intercept is fixed at the origin) and the data from a linearized form of Equation 4.19. Also note that for all eleven mixes, a fixed value of 35 for f resulted in a better-fitting regression curve than a value of 55. (ACI 209 [8] suggests the use of 35 for moist-cured concrete and 55 for steam-cured concrete.)

4.7 Coefficient of Thermal Expansion

4.7.1 Background

The coefficient of thermal expansion of concrete is a function of the coefficients of both the aggregate and paste. However, because aggregates generally make up the bulk of the concrete mix, the coefficient of thermal expansion of concrete is most influenced by the coefficient of the aggregate, as well as the quantity of aggregate in the mix [83,95]. The coefficients of individual aggregates vary greatly with mineralogical composition, but range from about 4 to 13 $\mu\epsilon/^\circ\text{C}$ (2.2 to 7.2 $\mu\epsilon/^\circ\text{F}$). Values for various aggregates are given by Mindess and Young [83]. The coefficient of thermal expansion for cement paste is substantially higher than for aggregates, such that the resulting coefficients of expansion for concrete will be higher than for the aggregate alone [83,95].

Mindess and Young [83] report a range of coefficients of thermal expansion for concrete of 7.4 to 13 $\mu\epsilon/^\circ\text{C}$ (4.1 to 7.3 $\mu\epsilon/^\circ\text{F}$). ACI Committee 209 [8] suggests a range of 8.5 to 11.7 $\mu\epsilon/^\circ\text{C}$ (4.7 to 6.5 $\mu\epsilon/^\circ\text{F}$) be used for ordinary thermal stress calculations in the absence of known data, with an average value of 10.0 $\mu\epsilon/^\circ\text{C}$ (5.5 $\mu\epsilon/^\circ\text{F}$). An average coefficient of 11 $\mu\epsilon/^\circ\text{C}$ (6 $\mu\epsilon/^\circ\text{F}$) is specified by AASHTO for use in all calculations [1,3].

There is little data available on the coefficient of thermal expansion for high strength or high performance concretes. It is suggested, however, that the thermal properties of high strength concretes are similar to those of conventional concretes [10].

Moisture content is also known to have a significant effect on the coefficient of thermal expansion for concrete [83,95]. The coefficient is minimum in the unsaturated or fully saturated conditions, and is maximum at intermediate moisture conditions. The influence of moisture content is a result of the internal rearrangement of water molecules between capillary and gel pores as temperature increases [83]. This rearrangement of

water adds an additional component of expansion under increasing temperatures, leading to a higher coefficient of thermal expansion. Since the rearrangement of water molecules is not possible in the unsaturated and fully saturated conditions, the coefficient of thermal expansion is minimized in these cases.

4.7.2 Method of Measurement

Coefficient of thermal expansion was measured on two specimens for each of the eleven mixes described in Section 4.1 and 4.2. As for the creep and shrinkage tests, specimens were 100 x 600 mm (4 x 24 in.) cylinders that were cast at the precast plant or jobsite using concrete from the actual bridge structures. Cylinder molds were stripped approximately 24 hours after casting, and specimens were air cured in the room used for creep and shrinkage tests (average RH=55%). Specimens were cured for a minimum of 56 days before testing. This minimized the potential for shrinkage to occur during the actual thermal tests.

Prior to testing, DEMEC mechanical strain gauge points were epoxied to the surface of each specimen as shown in Figure 4.5. Specimens were then pre-cycled to ensure that the specimens had reached the extreme test temperatures at least once prior to actual testing. During testing, specimens were cycled between extreme temperatures of 4.4 °C (40 °F) and 48.9 °C (120 °F). For each set of specimens, two cycles were performed with decreasing temperatures and two cycles with increasing temperatures. Thermocouples placed in the center of the specimens during casting were used to determine when the specimens had stabilized at the extreme temperatures. A Standard Environmental Systems Model RZ/40 environmental chamber was used to control temperature and relative humidity during each test cycle. The relative humidity in the environmental chamber was maintained at a 60% throughout the testing.

A set of DEMEC mechanical strain gauge readings was recorded during cycle after specimens stabilized at the extreme temperatures. The internal specimen temperatures were also recorded at the time of each strain measurement. The coefficient of thermal expansion was then determined for each specimen cycle by dividing the change in strain by the change in temperature over the cycle.

Table 4.25 - Measured Coefficients of Thermal Expansion

	$\mu\epsilon / ^\circ\text{F}$	$\mu\epsilon / ^\circ\text{C}$
<i>Precast Mixes</i>		
Louetta NB/SB HPC Prestressed Beams	6.1	10.9
San Angelo EB HPC Prestressed Beams	6.3	11.4
San Angelo WB Non-HPC Prestressed Beams	7.3	13.1
Louetta NB/SB HPC Precast Deck Panels	7.3	13.1
San Angelo EB HPC Precast Deck Panels	4.7	8.5
San Angelo WB Non-HPC Precast Deck Panels	4.6	8.3
<i>Cast-in-Place Mixes</i>		
Louetta NB HPC Deck	4.0	7.1
Louetta SB HPC Deck	4.2	7.6
San Angelo EB HPC Class K Deck	4.6	8.4
San Angelo WB HPC Modified Class S Deck	4.4	7.9
San Angelo WB Non-HPC Standard Class S Deck	4.9	8.8
Note: Values represent average of four cycles (two with increasing temperatures and two with decreasing temperatures) on two specimens for each mix. Each cycle had extreme temperatures of 40 °F (4.4 °C) and 120 °F (48.8 °C) and was performed at constant relative humidity of 60%.		

4.7.3 Measurements

Measured coefficients of thermal expansion for the eleven mixes are presented in Table 4.25. The listed values represent an average of four cycles with extreme temperatures of 4.4 °C (40 °F) and 48.9 °C (120 °F). Measured coefficients fell within the range of 7.1 to 13.1 $\mu\epsilon / ^\circ\text{C}$ (4.0 to 7.3 $\mu\epsilon / ^\circ\text{F}$), which is similar to the range of values suggested by Mindess and Young [83] for all concretes. Mixes with the same type and source of aggregate exhibited very similar coefficients of thermal expansion. This trend can be seen graphically in Figure 4.16. Note that the variation in coefficients of thermal expansion among mixes with crushed gravel aggregate is probably due to the differing mineralogical compositions of gravels from different sources.

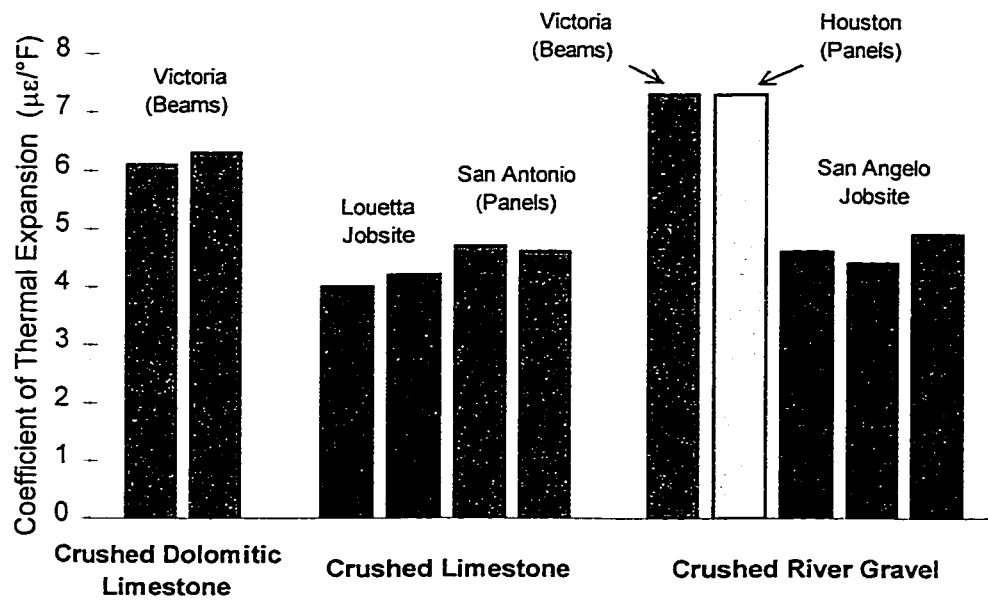


Figure 4.16 - Coefficient of Thermal Expansion by Aggregate Type and Source

5 CHAPTER FIVE: TEMPERATURE MEASUREMENTS

5.1 Introduction

5.1.1 General

Temperature can have a significant impact on concrete highway bridge structures. Large stresses and strains may result as a structure heats or cools, depending on the distribution of temperature and level of restraint present in the structure. In a determinate structure, large movements (strains and deflections) may result from the heating or cooling of the structure. In an indeterminate structure, large forces (and stresses) may result from the restraint of movement. A combination of strain and stress is usually present because a structure is rarely completely free to move or completely restrained from movement [114]. Depending on the magnitude of such strains and stresses, and their locations in the structure, thermal cracking may result. While the ultimate strength of the bridge or bridge member is not generally affected by thermal cracking, the serviceability of the structure may be significantly reduced.

High hydration temperatures are often developed in members using high-strength HPC because of the large quantities of cementitious materials are typically utilized in such mix designs. High temperatures can especially be expected during the hydration of precast members, where Type III cement is used to gain sufficient strength for the release of prestress at early ages. From a materials perspective, this high temperature during hydration can have a significant impact on the early-age and long-term strength gain of the concrete. In terms of structural behavior, high hydration temperatures can result in permanent deformations as the structure cools. Furthermore, if the cooling of a member shortly after hydration is restrained, thermal cracking may result.

There is continual transfer of heat between a bridge structure and the surrounding environment. Radiation, conduction, and convection all contribute to this transfer of heat energy, but radiation is generally considered to be the most important of these three

mechanisms [65]. The heating of the superstructure is thus influenced by several factors, including solar radiation, ambient temperature, wind speed, material properties, surface characteristics, and section geometry [109]. Variations in environmental conditions lead to two basic thermal cycles for any bridge structure: the seasonal (or annual) cycle, and the diurnal (or daily) cycle.

The seasonal cycle is governed mainly by the earth's orientation and orbit about the sun, which drives the seasonal weather cycle at any given location on the earth's surface. Except at the equator, ambient temperatures are highest during the summer months and lowest during the winter months. Average bridge temperatures follow the same basic trend. Bridge structures must be designed to accommodate the axial movements associated with this seasonal cycle (or stresses resulting from the restraint of these movements).

The diurnal (or daily) temperature cycle is governed by the path of the sun in the sky at the bridge location, as well as the changes in ambient conditions during the course of the day and night. During a typical morning and afternoon, the surface of the bridge deck heats up rapidly from the direct exposure to solar radiation and the increase in ambient temperature. The lower portions of the superstructure are shaded from direct sunlight, and thus warm much more slowly. This uneven heating produces a non-uniform temperature distribution, or temperature gradient, through the depth of the superstructure. A similar, but opposite, gradient may also exist around sunrise, when the surface of the deck has cooled to a lower temperature than the remaining superstructure. Thermal gradients produce a combination of axial and flexural stresses and strains through the depth of the structure. Although these stresses and strains are temporary in nature, their magnitude can exceed those resulting from live loads in certain cases [111].

While the consideration of high hydration temperatures is somewhat specific to members constructed with high strength HPC, the effects of the seasonal and daily temperature cycles are relevant to all concrete bridges. In many cases, the movements or stresses will be more pronounced for designs with HPC because of the longer span lengths and larger girder spacing often associated with such designs. This chapter examines the behavior of all bridges and structural components instrumented in this research program, whether HPC or conventional concrete. Differences in behavior resulting directly or indirectly from the use of HPC are then noted.

5.1.2 Climatic Descriptions for Jobsites

As described on the National Oceanic and Atmospheric Administration (NOAA) Internet site [92], Houston has a predominantly marine climate. Temperatures are moderated by the influence of the Gulf of Mexico, resulting in mild winters. Rainfall is generally abundant, and polar air penetrates the area frequently enough to provide variability in the weather. About one-quarter of days are clear, and sunshine averages nearly 60 percent of the potential amount for the year. Cloudy days are frequent from December to May, partly cloudy days are common from June through September, and a high number of clear days occur in October and November.

The climate in San Angelo is classified as semi-arid with some humid temperate characteristics [92]. Warm, dry weather predominates, but the passage of cold fronts and northers results in frequent rapid changes. High temperatures and low humidity predominate during the summer, with rapid temperature drops after sunset. During the winter, temperature drops of 11 to 17 °C (20 to 30 °F) in a short time may be expected when cold polar air invades the region. Much of the annual rainfall occurs from thunderstorm activity, and wide variations in annual rainfall occur from year to year. The heaviest rainfall typically occurs from April through June, and in September and October. The prevailing wind direction is from the south, and winds are frequently high and persistent for several days.

5.1.3 Ambient Temperature Data

Ambient temperature at the jobsites and precast plants was not measured as part of the instrumentation program because proper measurement of ambient temperature requires several considerations. Ambient temperature measurements should be recorded in an instrument shelter which is well-ventilated and protects the temperature measuring device from any exposure to radiation, whether from direct rays of sunlight or from nearby surfaces that radiate and reflect heat [77]. Since there was no convenient location at either jobsite to properly measure ambient temperature in an automated fashion (i.e. by connecting to existing data acquisition system boxes), official weather records were used for all ambient temperature measurements.

As necessary, ambient temperature data was obtained from the National Climatic Data Center (NCDC) via the Internet [108]. Ambient temperature data for the Louetta Road Overpass was taken from data for the National Weather Service (NWS) measurement station at the Houston Intercontinental Airport, which is located about 24 km (15 mi.) east of the Louetta Road Overpass. For the North Concho River Overpass, ambient temperature data was taken from the NWS measurement station at San Angelo Mathis Field, which is located approximately 8 km (5 mi.) south of the North Concho jobsite. Although these measurements do not represent *exact* jobsite conditions, the differences are slight.

5.2 Hydration Temperatures

5.2.1 Background

The hydration of portland cement is highly exothermic and can be summarized as a process occurring in five phases [72,83]. Phase 1 consists of a short period in which heat is rapidly evolved during initial mixing, and is followed by a dormant period (Phase 2) of several hours during which the concrete remains plastic. As the dormant period ends, the calcium silicate in the cement begins to react vigorously with water, until a maximum rate of heat evolution is reached. Final set occurs during this acceleration phase (Phase 3) [83]. The rate of heat evolution then slows, but the generated heat continues to raise the concrete temperature until the peak hydration temperature occurs at the end of Phase 4. During the final phase (Phase 5), heat generation is minimal and the concrete loses heat until a state of equilibrium is reached with the surrounding environment.

Concrete temperature and rate of heat evolution are shown in Figure 5.1 for a typical concrete member. The plot of concrete temperature in Figure 5.1 assumes adiabatic conditions for the first four phases of the hydration process. Adiabatic conditions exist only when there is no gain or loss of heat from the concrete member to the surrounding environment. For a real member such as a prestressed concrete beam or cast-in-place deck segment, the shape and magnitude of the hydration temperature plot during all five phases are significantly influenced by the ambient conditions. In general, the heat gain

during hydration is dependent on the cement content, water-to-cement (water-to-binder) ratio, size of the member, ambient temperature, and environmental conditions [10].

Because of their high cementitious contents, most high strength HPC's exhibit relatively high hydration temperatures. ACI Committee 363 [10] suggests that temperature rise during hydration for high strength concretes ranges from 6 to 8 °C per 59 kg/m³ of cement (11 to 15 °F per 100 lb/yd³ of cement). Various researchers have recorded peak hydration temperatures in massive high-strength HPC columns and footings in the range of 66 to 95 °C (150 to 203 °F) [16,47,121,140]. Little data exists on field measurements of hydration temperatures in actual HPC bridge structures, however.

There is a clear correlation between hydration temperature and compressive strength, both at early and long-term ages. A high temperature during placing and setting tends to increase the early-age strength, but may adversely affect the strength after about seven days [95]. The increase in early-age strength with increased hydration temperatures is simply a result of the more rapid hydration of the cement particles. Lower long-term strengths likely occur because the faster initial hydration results in a poorer matrix structure [95]. The effects of hydration temperature on measured compressive strengths in the Texas HPC bridge projects is discussed by Myers and Carrasquillo [88]. Use of the maturity method for prediction of compressive strength as a function of concrete temperature and age is also discussed by Myers and Carrasquillo.

High hydration temperatures can lead to cracking in structural members when restraint is present. Both external and internal restraint may lead to cracking when members are exposed to ambient conditions during hydration [96]. External restraint exists when the expansion or contraction of the member as a whole is prevented. The temperature within a concrete member during the hydration process will generally be significantly higher than the ambient temperature, unless the least dimension of the member is small. When a restrained member heats up, compressive stresses develop from the restraint against expansion. These stresses are relieved to some extent by creep of concrete at early ages [96]. As the member cools toward the ambient temperature, restraint against contraction causes tensile stresses. Creep also acts to relieve these stresses, but the creep is less because the concrete is more mature. If large enough in magnitude, these tensile stresses will lead to cracking.

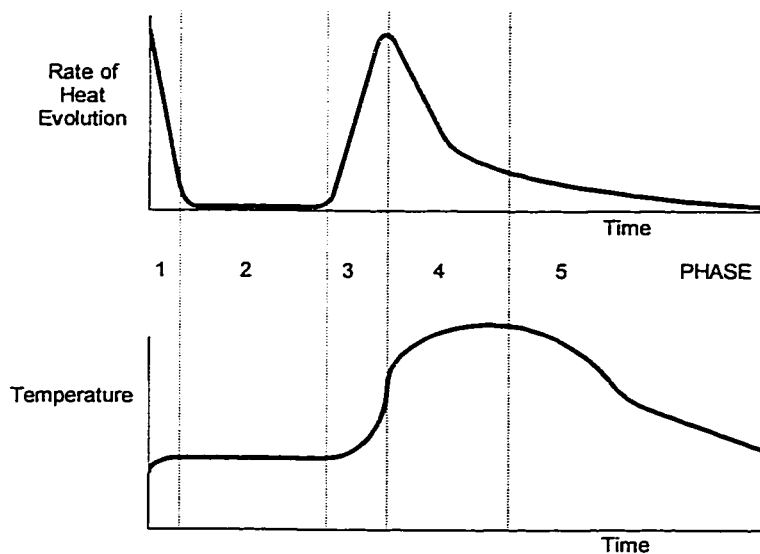


Figure 5.1 - Heat Evolution and Concrete Temperature During Hydration

Internal restraint exists when a nonuniform temperature gradient is present in the member. During hydration, the innermost portion of the member heats up to a higher temperature than the surface, which is influenced by the ambient temperature. The degree of influence of the ambient conditions depends on the curing conditions and type of formwork. Tensile stresses will develop at the surface and compressive stresses in the interior as the concrete there tries to expand more than the concrete at the surface. Creep helps relieve these stresses to some degree, but surface cracking may occur if the net tensile stress exceeds the tensile strength of the young concrete. Likewise, as the member cools from the peak hydration temperatures toward the ambient temperature, the interior of the member must cool more than the exterior. There are resulting tensile stresses in the interior of the member and compressive stresses at the surface. Although they are also relieved to some degree by creep, the resulting tensile stresses may lead to internal cracking in the member [96].

In most members with sufficient mass, some combination of internal and external restraint will be present. Members are rarely completely free to expand, such that some degree of external restraint is almost always present. Likewise, a temperature gradient will be present in most members during hydration. Exceptions would include very thin members cast on days where ambient conditions remain relatively constant.

5.2.2 Measurements

Hydration temperatures were measured in beams, panels, and sections of the cast-in-place bridge decks using thermocouples and thermistors, as described in Chapter 3. Specific gauge locations used in this study are discussed in detail in Section 3.4.2. For measurement of hydration temperatures, data acquisition systems were connected to embedded gauges shortly before placement of fresh concrete, and left connected for the duration of the main hydration cycle. Temperatures were generally recorded every 5 or 10 minutes, although in a few cases 15 or 20 minute intervals were used. Note that hydration temperatures discussed in this section correspond to embedded instrumentation gauges, and not to thermocouples installed as part of the match-curing system (Sure-Cure) used for quality control investigations. The role of hydration temperatures with respect to material properties, including compressive strength, in the Texas HPC bridge projects is discussed by Myers and Carrasquillo [88].

A typical hydration curve for a San Angelo HPC Type IV beam is shown in Figure 5.2. The beam on which this data was collected, Beam E14, was cast on February 19, 1997, and release of prestress occurred the following day. Note that both February 19 and 20 were cloudy days, and that 14 mm (0.54 in.) of rain fell on the February 20. Because of the relatively stable ambient conditions, as shown by the relatively constant ambient temperature, the hydration curve is similar in shape to what might be expected under adiabatic conditions. For this beam, the average placement temperature was 28°C (83°F), and the average temperature at the end of the dormant phase was 31°C (88°F). A maximum temperature of 62°C (144°F), corresponding to a gain of 30°C (54°F) from the end of the dormant phase, was measured at the TW gauge. This gauge is located 150 mm (6 in.) below the top surface of the beam, and very close to the centroid of the top flange.

It can also be seen in Figure 5.2 that a significant gradient develops over the depth of the cross-section during hydration. In general, the top portions of the section become significantly hotter than the lower portions. In Beam E14, a maximum gradient of 12°C (21°F) was observed between the TW and BF gauges. This maximum gradient was recorded shortly after the removal of forms, although the maximum gradient for most beams occurred at about the same time as the peak hydration temperatures.

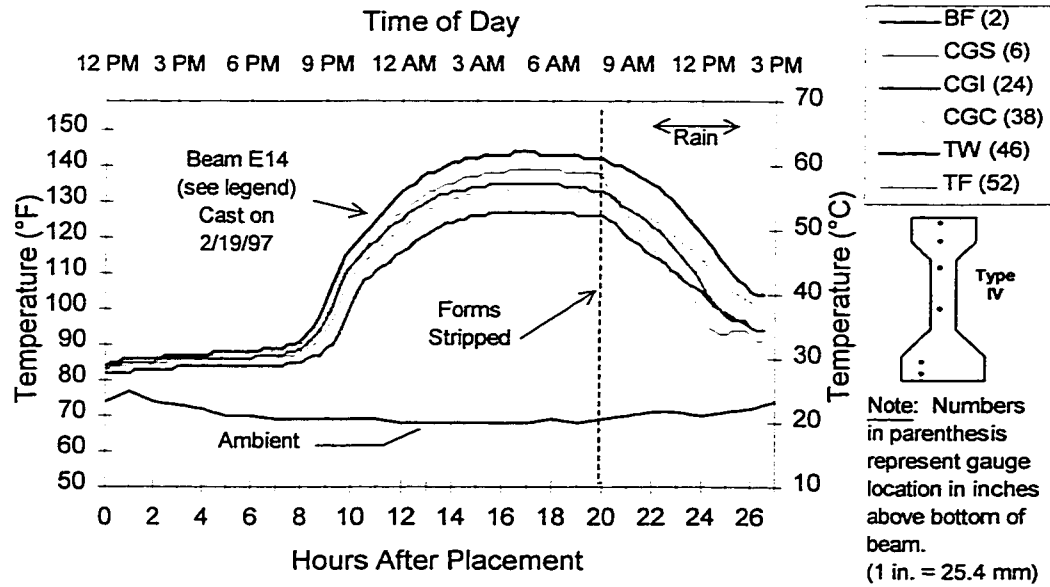


Figure 5.2 - Measured Hydration Temperatures in San Angelo HPC Beam E14

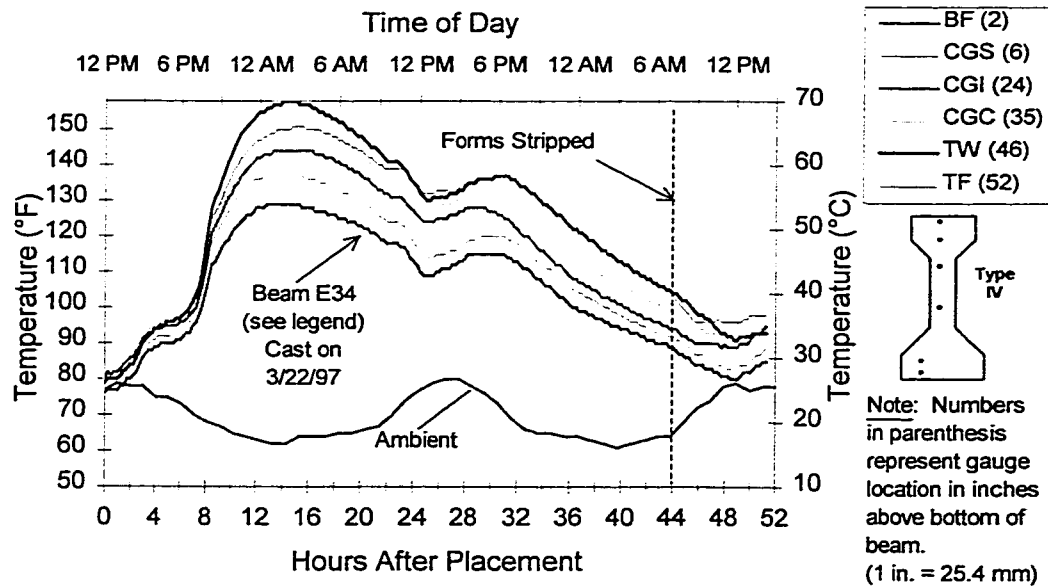


Figure 5.3 - Measured Hydration Temperatures in San Angelo HPC Beam E34

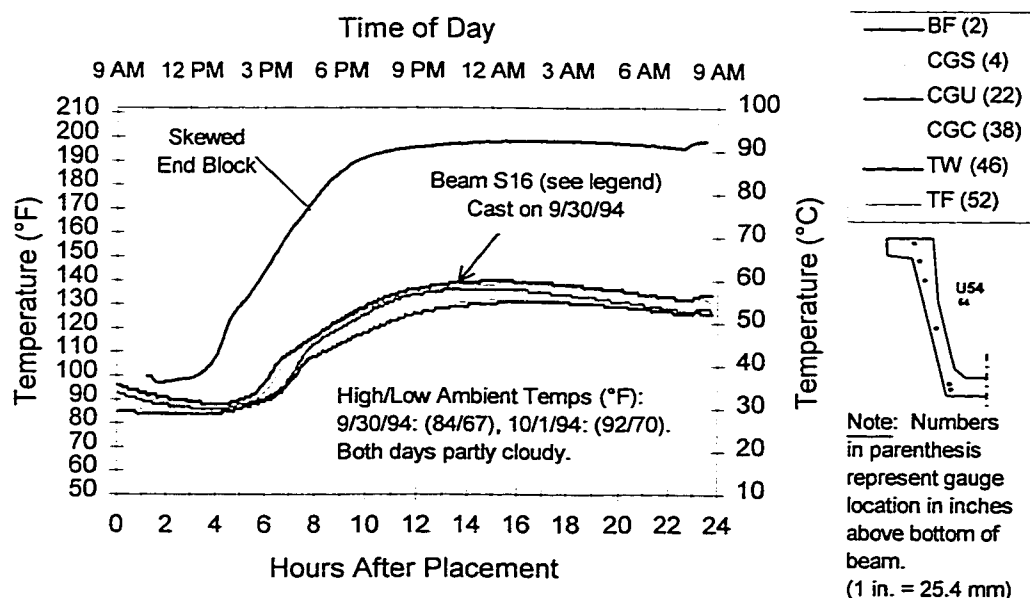


Figure 5.4 - Measured Hydration Temperatures in Louetta HPC Beam S16

The effect of the removal of curing tarps and side forms is also apparent in Figure 5.2. A sharp temperature drop occurs across the depth of the section, as the beams are suddenly fully exposed to ambient conditions. In the case of Beam E14, the temperature at the TF gauge, which is located 50 mm (2 in.) below the top surface, dropped substantially faster than in the rest of the section. This drop can be attributed to the proximity of the gauge to the surface, and to the cloudy and rainy weather conditions. This situation was not typical of all beams, because sunny or partly cloudy conditions usually prevailed after form removal.

A second hydration curve is shown in Figure 5.3 for Beam E34. This San Angelo HPC Type IV beam was cast on Saturday, March 22, 1997, but was not released until Monday, March 24. Sunny and partly cloudy skies prevailed during this three day period, and no rainfall was recorded. The effect of ambient conditions, particularly solar radiation, on temperatures during the dormant phase of the hydration cycle is apparent. The average measured concrete temperature was 26°C (79°F) at placement, but had risen to 36°C (96°F) at the end of the dormant phase.

The maximum hydration temperature in Beam E34 occurred at the TW gauge, and was measured as 70°C (158°F). This temperature represents the maximum hydration

temperature recorded during this study at any location other than the end blocks of beams. The corresponding temperature rise after the dormant period was 33°C (60°F). A maximum gradient of 16°C (29°F) occurred between the TW and BF gauges, which also represents the maximum measured gradient observed during hydration in any beam.

The two day curing cycle for Beam E34 resulted in a second peak hydration temperature occurring during the afternoon of the day after casting. This temperature rise is again directly attributable to solar radiation, as the black tarps under which beams were cured likely heated up and raised the air temperature underneath. Cooling occurred slowly during the two-day cycle such that by the morning of the third day, there was a smaller difference between the concrete and ambient temperatures than for Beam E14 shown in Figure 5.2. As a result, a dramatic temperature drop did not occur upon the removal of tarps. In fact, concrete temperatures in Beam E34 began to rise again shortly after form removal as a result of exposure to solar radiation.

A plot of hydration temperatures for Beam S16, a Louetta HPC U-beam cast on September 30, 1994 is shown in Figure 5.4. The shape of the hydration curve is very similar to what would be expected under adiabatic conditions, even though the day of casting and following day were both warm, partly cloudy days. The maximum hydration temperature recorded was 60°C (140°F), at both the TW and CGC gauges, and a maximum temperature rise of 28°C (50°F) was observed. Both of these values are slightly lower, but within the same general order of magnitude as those observed for the San Angelo HPC Type IV beams shown in Figure 5.2 and Figure 5.3. The maximum measured gradient during hydration of 8°C (14°F), however, is significantly less. Temperatures after the removal of forms and curing tarps were not recorded for Beam S16, but recorded temperatures on another Louetta HPC U-beam, Beam S25, show that a fast cooling period commences when forms are removed.

The measured hydration temperature in the center of the massive skewed end block of Beam S16 is also shown in Figure 5.4. The temperature in the skewed end block reached a maximum of 8°C (198°F), which is 53°C (96°F) higher than the concrete temperature of 39°C (102°F) at the end of the dormant phase. Skewed end block temperatures of up to 95°C (203°F) were measured in other beams as part of the quality control portion of the Louetta research project [37]. Because of their large mass, these end blocks also took several days to cool to ambient conditions. High temperatures were also

observed in the square end blocks of the Louetta U-beams, although temperatures were typically on the order of 6 to 11°C (10 to 20°F) less than in the massive skewed end blocks.

Hydration temperatures were monitored for a total of 10 beams, including two Louetta HPC U-beams, seven San Angelo HPC Type IV beams, and one San Angelo conventional concrete Type IV beam. Results of the hydration temperature measurements for these ten beams are summarized in Table 5.1. Collectively, these data include measurements from seven of the fourteen pours with instrumented beams. Hydration temperatures were not monitored on most of the other seven beam pours, and in a few cases data was incomplete as a result of broken gauges or a malfunctioning data acquisition system.

Maximum hydration temperatures in the nine monitored HPC beams ranged from 55 to 70°C (131 to 158°F), and maximum temperature rise after the end of the dormant period ranged from 28 to 33°C (50 to 60°F). In general, the maximum hydration temperature was recorded at the TW gauge. Exceptions included non-HPC Beam W17, in which the temperature at the CGC gauge (located near the top of the web) was just slightly higher than at the TW gauge, and HPC Beam S25, in which maximum temperatures were reached in the bottom flange of the U-beam. Note that both of these beams were steam cured in order to maintain a favorable ambient temperature under the tarp (but not to accelerate hydration per se). The maximum gradient was also significantly lower for the two Louetta U-beams that were monitored than for the San Angelo Type IV beams.

Hydration temperature plots for three instrumented precast panels are shown together in Figure 5.5. For each panel, temperatures were measured at 25 mm (1 in.) and 75 mm (3 in.) above the bottom surface of the panel. Clear differences exist between the hydration curves for the three panels shown in Figure 5.5. These differences can primarily be attributed to ambient conditions and method of curing, and to some extent the mix proportions for each panel type.

Louetta HPC panel LP2, cast on a sunny day, September 12, 1996, reached a peak hydration temperature of 54°C (130°F), with a temperature rise of 17°C (30°F) after the dormant period. Panel SNP2, a conventional concrete San Angelo Westbound panel, was also cast on a sunny day, September 4, 1996, but exhibited a much smaller temperature rise. Both panels were cured under tarps, but panel SNP2 was puddled with water before being covered. It is believed that this puddling helped cool the panel against ambient and radiant heating.

Table 5.1 - Summary of Measured Hydration Temperatures for Beams

Beam	Casting Date	Placement Time	Avg. Placement Temperature ¹	Avg. Temp. at End of Dormant Phase ¹	Peak Hydration Temperature ²	Location of Peak Hydration Temperature	Maximum Temp. Rise (After Dormant Period) ²	Max. Gradient ³
Louetta HPC Beams								
S16	9/30/94	9:00 AM	91	89	140	TW,CGC	50	14
S25 *	11/10/94	11:00 AM	77	82	131	BF,CGS	50	10
San Angelo EB HPC Beams								
E13	2/19/97	11:30 AM	83	87	141	TW	54	19
E14	2/19/97	12:00 PM	83	88	144	TW	54	21
E24	3/8/97	9:00 AM	81	82	139	TW	55	20
E26	3/8/97	9:30 AM	83	83	139	TW	54	26
E33	3/22/97	12:30 PM	83	96	157	TW	59	27
E34	3/22/97	11:45 AM	79	96	158	TW	60	29
E35	3/29/97	12:30 PM	87	92	150	TW	56	28
San Angelo WB Non-HPC Beams								
W17 *	3/12/96	1:30 PM	80	90	155	CGC	66	26
<p>All temperatures in °F. [Temp.: °F=(1.8*(°C))+32; Temp. Change: °F=1.8*(°C)]</p> <p>Note: Temperatures measured at six locations through depth of each beam. See Figure 3.25 for sketch of gauge locations.</p> <p>* Steam-cured to maintain a favorable ambient temperature under tarp.</p> <p>¹ Average for all gauge locations. ² At a single gauge location.</p> <p>³ Between two gauge locations (typically TW and BF gauges).</p>								

Furthermore, panels LP2 and SNP2 contained approximately the same amount of cement, but panel SNP2 contained more than twice the dosage of retarder as panel LP2. Panel SNP2 was also cast about an hour and a half later in the day. These two factors likely resulted in the dormant period for panel SNP2 lasting into the early evening, so that the main acceleration phase of the hydration cycle was offset to some extent by ambient cooling after sunset.

San Angelo Eastbound HPC panel SHP21 was cast on a cold, rainy day, February 5, 1997, and was cured in the same manner as panel SNP2 – by puddling water and covering with a tarp. Although this HPC panel had 17 percent more cement than the conventional concrete panels, it also contained 61 percent more retarder. The cold ambient conditions, the insulating effect of the puddled water, and the high dosage of retarder resulted in panel SHP21 exhibiting almost no temperature rise during hydration. In fact, the peak hydration temperature measured in this panel was only 22°C (71°F). Early-age compressive strengths measured on companion specimens for the February 5, 1997 panel pour were also very low, as can be seen in Table 4.7.

Hydration temperature measurements for all instrumented panels that were continually monitored during casting and curing are summarized in Table 5.2. Data is presented for the three panels shown in Figure 5.5, as well as additional instrumented panels on the same casting dates. Note that very small temperature gradients were observed during the hydration cycles of all instrumented panels, and that the maximum temperature always occurred at the gauge located closer to the bottom of the panel.

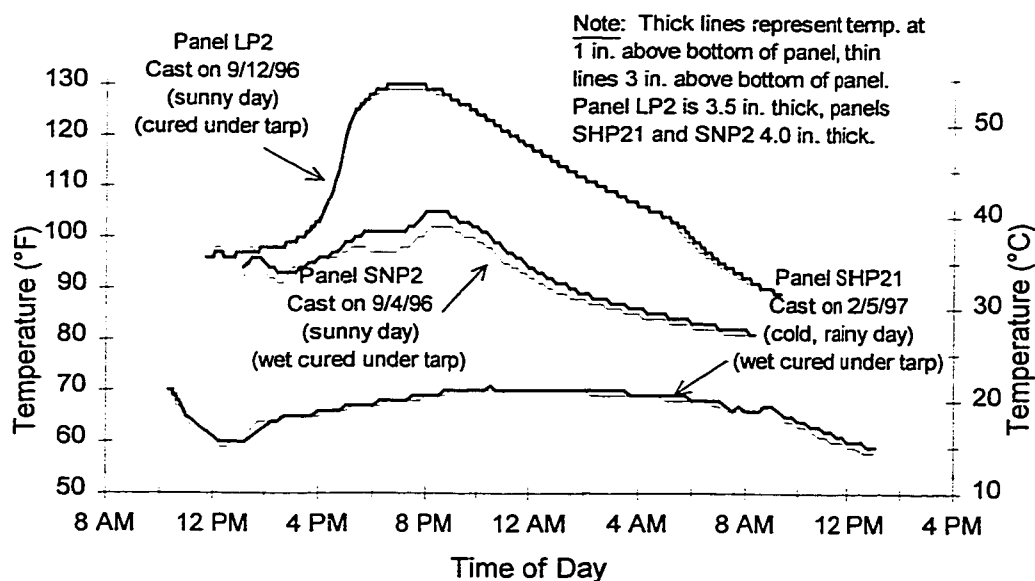


Figure 5.5 - Measured Hydration Temperatures in Three Precast Panels

Table 5.2 - Summary of Measured Hydration Temperatures for Panels

Panel	Casting Date	Placement Time	Avg. Placement Temperature ¹	Avg. Temp. at End of Dormant Phase ¹	Peak Hydration Temperature ²	Location of Peak Hydration Temperature	Maximum Temp. Rise (After Dormant Period) ²	Maximum Gradient ³
Louetta HPC Panels								
LP2	9/12/96	11:45 AM	95	100	130	P-1	30	2
San Angelo EB HPC Panels								
SHP11	2/5/97	10:20 AM	67	66	68	P-1	2	2
SHP21	2/5/97	10:20 AM	70	68	71	P-1	3	1
SHP22	2/5/97	10:20 AM	67	65	67	P-1	2	1
SHP31	2/5/97	10:20 AM	69	68	72	P-1	4	1
SHP41	2/5/97	10:20 AM	67	68	71	P-1	3	1
San Angelo WB Non-HPC Panels								
SNP1	9/4/96	1:10 PM	93	99	106	P-1	6	5
SNP2	9/4/96	1:10 PM	93	99	105	P-1	5	4
All temperatures in °F. [Temp.: °F=(1.8*(°C))+32; Temp. Change: °F=1.8*(°C)]								
Note: Temperatures measured at two depths within panel.								
P-1 corresponds to gauge located 1 in. (25 mm) above bottom of panel.								
P-3 corresponds to gauge located 3 in. (75 mm) above bottom of panel.								
¹ Average for both gauge locations.								
² At a single gauge location.								
³ Between two gauge locations.								

Hydration temperatures were measured in the instrumented cast-in-place bridge decks at the vertical sections shown in Figure 5.6. Temperatures were measured during hydration in all instrumented spans, but the data for the Northbound Louetta and Westbound San Angelo cast-in-place deck pours was overwritten on the storage module as discussed in Section 3.6.1. Data from selected spans of the Louetta Southbound and San Angelo Eastbound bridges is shown in Figure 5.7 and Figure 5.8, respectively. A summary of all data from these two bridges is presented in Table 5.3.

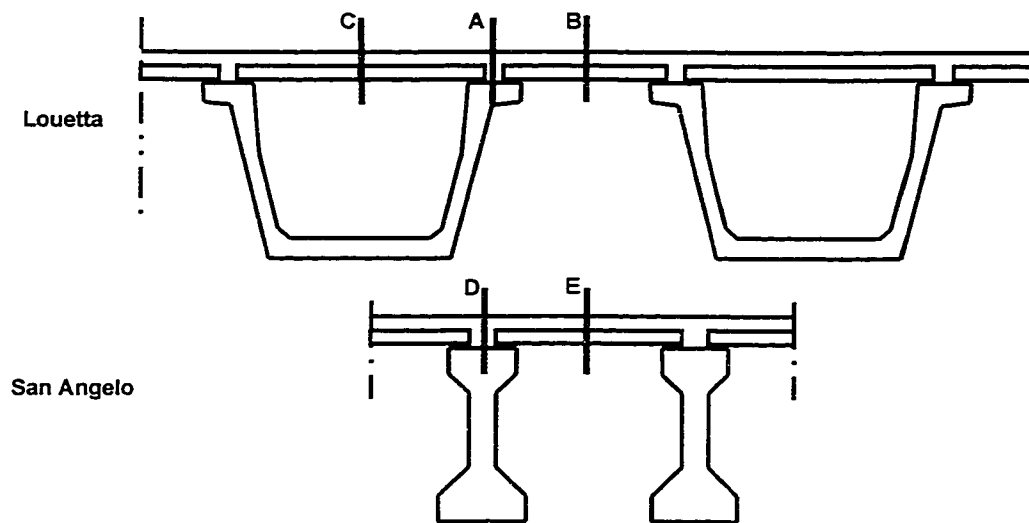


Figure 5.6 - Sections for Hydration Temperature Measurements in CIP Decks

Span 1 of the Louetta Southbound HPC bridge was cast on November 8, 1996, a sunny, cool day following a very cool night. As shown in Figure 5.7, very little temperature gain occurred during hydration at any of the vertical sections through the depth of the deck where measurements were recorded. A maximum hydration temperature of 23 °C (74 °F) was recorded directly above the beam, at a gauge located approximately 140 mm (5.5 in.) below the top surface of the deck. Because of the cool ambient temperatures during the night before casting, the average beam temperature at the time of concrete placement was only 13 °C (55 °F). The beams therefore acted as a heat sink, and the cool ambient temperatures during the day did not contribute to heat development. Note however, that the deck temperatures did not drop severely over the first night despite an ambient low temperature of only 6 °C (43 °F), indicating that heat was being generated by the hydration of the deck, but was offset by the drop in ambient temperature.

The hydration behavior observed in Span 1 of the San Angelo Eastbound HPC cast-in-place deck was drastically different from that observed in the Southbound Louetta bridge. This deck was cast on a sunny summer day, June 12, 1997. As can be seen in Figure 5.8, a large temperature rise occurred at sections both directly above beams and between beams, with a maximum measured hydration temperature of 49°C (121°F) directly above the beam. Radiant heating of the deck is apparent in this case from three observations. First, temperatures began to rise shortly after the placement of concrete.

Secondly, peak hydration temperatures at every section were measured at the gauge location closest to the deck surface, typically 57 mm (2.25 in.) below the top surface. Finally, the section between beams cools to a lower temperature at night than the section directly above the beams. Also note that the beams did not act as a heat sink initially, since the average beam temperature at the time of placement was 26°C (79°F). This temperature was equal to the temperature of the fresh deck concrete.

Table 5.3 - Summary of Measured Hydration Temperatures for CIP Decks

Span	Section ¹	Casting Date	Placement Time	Avg. Placement Temperature ²	Avg. Temp. at End of Dormant Phase ²	Peak Hydration Temperature ³	Location of Peak Hydration Temperature ¹	Maximum Temp. Rise (After Dormant Period) ³	Maximum Gradient ⁴
Louetta Southbound HPC Deck									
LS1	A	11/8/97	10:10 AM	74	70	74	D-5.50	5	2
	B	11/8/97	10:10 AM	72	71	74	D-2.25	3	1
	C	11/8/97	10:00 AM	73	69	71	D-3.75	2	2
LS2	A	11/8/97	2:10 PM	74	66	68	D-6.00	0	5
San Angelo EB HPC Deck									
SE1	D	6/12/97	8:10 AM	79	85	121	D-2.25	34	7
	E	6/12/97	8:10 AM	78	86	118	D-2.25	31	4
SE2	D	6/25/97	8:20 AM	78	82	108	D-2.25	25	6
	E	6/25/97	8:20 AM	76	82	101	D-2.25	20	1
SE3	D	7/9/97	8:40 AM	85	94	121	D-1.75	28	17
All temperatures in °F. [Temp.: °F=(1.8*(°C))+32; Temp. Change: °F=1.8*(°C)]									
¹ See Figure 5.10. D-x denotes a gauge approximately x in. below top surface.									
² Average for both gauge locations.									
³ At a single gauge location.									
⁴ Between two gauge locations.									

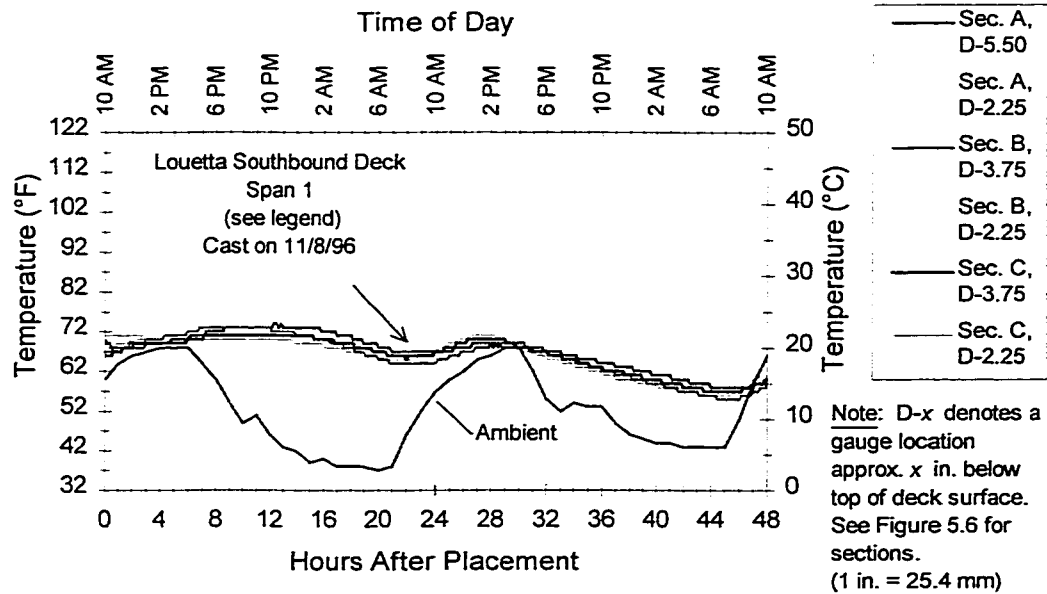


Figure 5.7 - Measured Hydration Temperatures in Louetta SB Deck Span 1

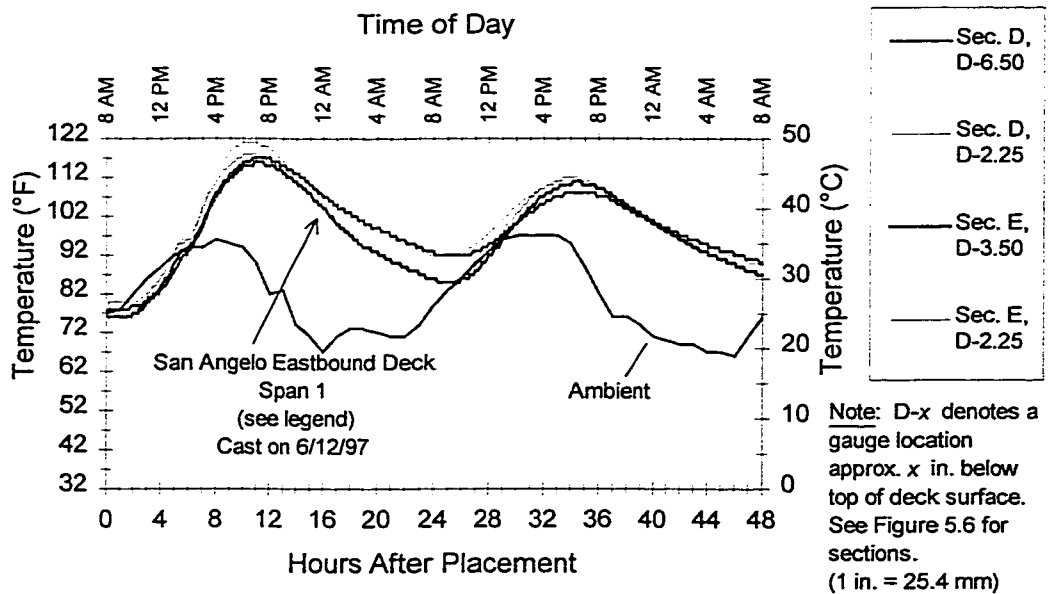


Figure 5.8 - Measured Hydration Temperatures in San Angelo EB Deck Span 1

The observations from Figure 5.7 and Figure 5.8 hold true for all spans summarized in Table 5.3, as the decks in Spans 2 and 3 of the Eastbound San Angelo HPC bridges were also cast on sunny summer days. Note that cement and retarder quantities were comparable for the Louetta Southbound and San Angelo Eastbound mix designs, such that mix proportions do not account for the differences in hydration temperatures. Also note that measured gradients were generally small in both bridges, with the exception of the gradient measured in Span 3 of the Eastbound San Angelo bridge. This large measured gradient of 9°C (17°F) is probably at least partially due to the fact that the top gauge location at this section was located closer to the deck surface than at other sections.

5.2.3 Discussion

Although not typically considered by designers, hydration temperatures can have a significant impact on several aspects of structural behavior. Both the magnitudes of the hydration temperatures and their distribution are of importance. High hydration temperatures in prestressed beams can lead to cracking if movement is restrained by the prestressing bed prior to release. A loss of prestress in pretensioned members may also occur if hydration temperatures are significantly higher than the ambient temperature at stressing. Furthermore, the development of hydration temperature gradients within a section can lead to internal cracking, and may cause a residual camber or deflection in long members.

Because this chapter is concerned primarily with measurements of temperature, and because each one of these topics merits extensive discussion, the impact of hydration temperatures on structural behavior is discussed in sections of subsequent chapters. Concrete strains in beams during hydration are discussed in Chapter 6. Loss of prestress associated with high hydration temperatures is discussed in Chapter 7. Residual camber and deflection resulting from hydration temperature gradients is discussed in Chapter 8.

Of course, hydration temperatures also affect several important material properties. Most notably, hydration temperatures affect the development of compressive strength, both at early ages and in the long term. The impact of hydration temperatures on material properties in the Texas HPC bridge projects is beyond the scope of this dissertation, but is discussed extensively by Myers and Carrasquillo [88].

With respect to the magnitude of hydration temperatures measured in this study, it does not appear that hydration temperatures in HPC members are excessive. The maximum measured hydration temperature in HPC prestressed beams, other than in massive end blocks, was 70 °C (158 °F), and the measured temperature gains after the end of the dormant period ranged from 28 to 33 °C (50 to 60 °F). Equivalent maximum temperature rises ranged from 4.2 to 4.9 °C per 59 kg/m³ (7.5 to 8.9 °F per 100 lb/yd³) of cement, or 2.8 to 3.4 °C per 59 kg/m³ (5.1 to 6.1 °F per 100 lb/yd³) of total cementitious material (cement and fly ash), both of which are well below values suggested by ACI Committee 363 [10]. Furthermore, the maximum temperature rise observed on the only monitored non-HPC San Angelo Westbound beam was actually higher than for any monitored HPC beam.

High hydration temperatures in the massive skewed end blocks of the Louetta U-beams could be a problem, however. Differences in hydration temperatures between the skewed end blocks and adjacent "standard" U-beam cross-section of the Louetta HPC beams led to cracking on several occasions. Transverse cracks typically formed across the entire cross-section at the location where the massive end blocks joined the standard U-beam cross-section. The cracks closed upon release of prestress and are probably of no structural significance, but they could pose a potential long-term durability problem. There is also a strong possibility that microcracking occurred in the massive end blocks as a result of the extremely high hydration temperatures observed in these areas. Consequently, the use of such end blocks should be discouraged.

Note that similar transverse cracking was observed away from the beam ends in most instrumented beams prior to release of prestress. This cracking is partially due to hydration temperatures, but can also be attributed to the fabrication methods and time sequence (including the indirect effect of the delays caused by researchers). This cracking is discussed in much more detail in Section 6.2.

5.3 Mean Bridge Temperatures

5.3.1 Background

Knowledge of mean bridge temperatures is important for the prediction of axial bridge movements during the seasonal temperature cycle. In many parts of the United States, including Texas, axial movements are accommodated by the use of expansion joints and/or flexible supports, such as sliding plates and elastomeric bearing pads. Alternatively, the superstructure and end supports can be designed to resist the forces and stresses resulting from the restraint against expansion or contraction of the structure. In either case, analysis of expected forces and/or deformations requires that approximate values of the extreme average bridge temperatures be known, as well as the approximate average temperatures of the structure at the time of beam erection and deck casting.

The current *AASHTO Standard Specifications* [3] do not directly specify the extreme mean bridge temperatures for which a structure should be designed, nor is it specified exactly how seasonal thermal effects should be considered in the design of concrete bridge structures. Instead, the specifications take a general approach to uniform temperature effects and specify a temperature rise or temperature fall that should be assumed for concrete structures. Within the chapter of the *Standard Specifications* dealing with loads, Section 3.16 reads:

3.16 THERMAL FORCES

Provision shall be made for stresses or movements resulting from variations in temperature. The rise and fall in temperature shall be fixed for the locality in which the structure is to be constructed and shall be computed from an assumed temperature at the time of erection. Due consideration shall be given to the lag between air temperature and the interior temperature of massive concrete members or structures.

The range of temperatures shall generally be as follows:

Metal Structures

Moderate climate, from 0 to 120°F.

Cold climate, from -30 to 120°F.

Concrete Structures

	<u>Temperature Rise</u>	<u>Temperature Fall</u>
Moderate climate	35°F	45°F
Cold climate	35°F	45°F

Note that the moderate and cold climate designations are not defined in either the code or the commentary.

Thermal load is to be considered in three service load combinations, as specified in Section 3.22 of the *Standard Specifications*:

Group IV: $D + (L+I)_n + CF + \beta EE + B + SF + (R+S+T)$ @ 125% (of allowable stresses)
 Group V: $D + E + B + SF + W + (R+S+T)$ @ 140%
 Group VI: $D + (L+I)_n + CF + \beta EE + B + SF + 0.3W + WL + LF + (R+S+T)$ @ 140%

where:

D = dead load
 L = live load
 I = live load impact
 βEE = earth pressure
 B = buoyancy
 W = wind load on structure
 WL = wind load on live load – 100 pounds per linear foot
 LF = longitudinal force from live load
 CF = centrifugal force
 R = rib shortening
 S = shrinkage
 T = temperature
 SF = stream flow pressure

Note that temperature loads are not considered in the basic service load Group I case.

Design for axial temperature effects is also mentioned briefly in the chapter of the *Standard Specifications* dealing with prestressed concrete. Section 9.5.1 reads:

9.5 EXPANSION AND CONTRACTION

9.5.1 In all bridges, provisions shall be made in the design to resist thermal stresses induced, or means shall be provided for movement caused by temperature changes.

The *AASHTO LRFD Specifications* [1] address design for uniform temperature changes in Section 3.12:

3.12.2 Uniform Temperature

3.12.2.1 TEMPERATURE RANGES

In the absence of more precise information, the ranges of temperature shall be as specified in Table 1. The difference between the extended upper or lower boundary and the base construction temperature assumed in the design shall be used to calculate thermal deformation effects.

Table 3.12.2.1-1 - Temperature Ranges

CLIMATE	STEEL OR ALUMINUM	CONCRETE	WOOD
Moderate	0 to 120 °F	10 to 80 °F	10 to 75 °F
Cold	-30 to 120 °F	0 to 80°F	0 to 75 °F

3.12.2.2 SETTING TEMPERATURE

The setting temperature of the bridge, or any component thereof, shall be taken as the actual air temperature averaged over the 24 hour period immediately preceding the setting event.

The *LRFD Specifications* [1] represent an improvement over the *Standard Specifications* [3] in the sense that the concept of a setting temperature is introduced, and because a moderate climate is defined in the commentary. A moderate climate is one in which there are less than 14 days per year where the average temperature is less than 0°C (32°F). The *LRFD Specifications* also clearly state that the temperature ranges are intended only to be a general guide in the absence of more precise information, whereas the *Standard Specifications* do not.

While the exact method of analysis by which uniform temperature changes should be considered is not specified, the commentary to Section 4.6.6 of the *LRFD Specifications* includes the effect of a uniform temperature increase in the analysis for thermal gradient effects. This analysis method is discussed in more detail in Section 5.4.1 of this dissertation.

Uniform temperature effects are to be considered in all strength and service load combinations specified in Section 3.4.1 of the *LRFD Specifications*. A load factor of 1.20 is specified for deformation considerations and 1.00 for all other effects in the service limit states. In the strength limit states, load factors of 1.20 for deformation considerations and 0.50 for all other effects are specified. These load combinations and factors represent the fact that temperature effects are always present in a structure, but reflects the low probability that maximum loading of all types, including uniform temperature loading, will act on a structure simultaneously. The lower load factors for the strength limit states reflect the fact that temperature effects will generally cause serviceability damage to a structure, but not significantly reduce the ultimate strength.

National Cooperative Highway Research Program (NCHRP) Report 276 [65], published in 1985, examined the effects of thermal effects in concrete bridge superstructures. Appendix A of this report presents recommended guidelines for design. In Section 2 of Appendix A, the report recommends that:

All concrete bridges shall be designed to accommodate the stresses and movements resulting from a fluctuation in the effective bridge temperature. The values for the anticipated minimum and maximum effective bridge temperatures are dependent on the type of construction and on the minimum and maximum normal air temperatures at the bridge site...

The report then presents a set of tables relating the minimum and maximum effective bridge temperatures to normal daily minimum and maximum temperatures, respectively. The data from these tables is shown graphically in Figure 5.9. If more precise climatic data is unavailable, the normal daily minimum temperature for January and the normal daily maximum temperature for July can be estimated at a given location in the United States using two isotherm maps provided in the guidelines.

The relationships between normal daily extreme temperatures and extreme effective bridge temperatures are based on the work by Emerson for bridge and shade (ambient) temperatures in England [50]. Emerson defined the effective bridge temperature as the temperature that governs the design of the bridge deck. According to Emerson, the effective temperature is derived by performing a calculation that includes the product of the areas between isotherms and their mean temperatures divided by the total area of the cross-section of the deck. Because the range of ambient temperatures in the United States is much greater than in England, Emerson's relationships were extrapolated to the range of values found in the United States for use in the NCHRP report.

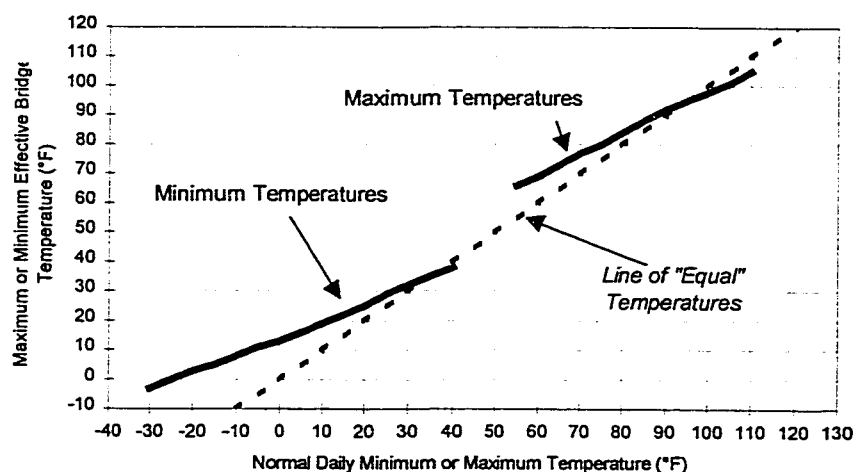


Figure 5.9 - Relationship Between Extreme Bridge Temperatures and Extreme Normal Daily Temperatures Suggested in NCHRP Report 276 [65]

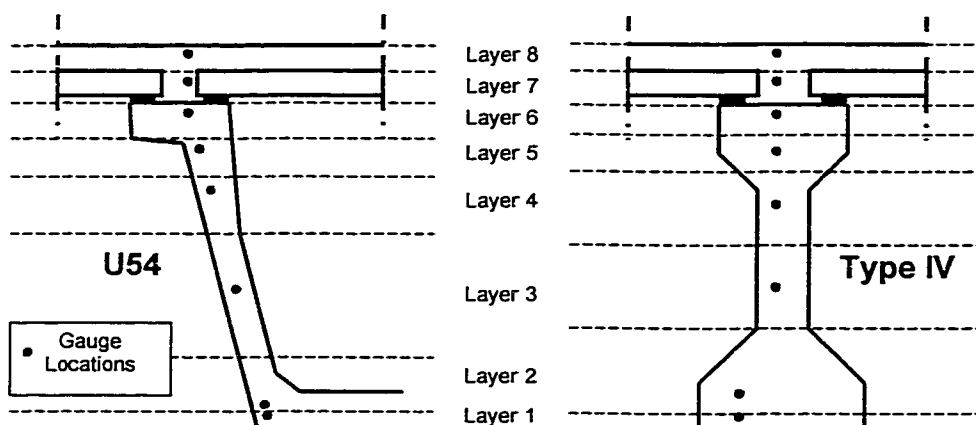


Figure 5.10 - Gauge Locations and Layers Used for Calculation of Average Bridge Temperature

5.3.2 Measurements

As discussed in Section 3.4, numerous thermocouples and thermistors were placed in beams, panels, and cast-in-place bridge decks for measurement of temperatures in the completed composite bridges. Six temperature gauges were placed in each instrumented beam, and two gauges were placed in the portion of the cast-in-place deck directly above each instrumented beam. This typical arrangement of temperature gauges can be seen in Figure 5.10. Temperatures were then recorded by the automated data acquisition systems at one or two hour intervals in the completed bridges.

Temperatures in several composite beams of each bridge were monitored in this manner. Data were collected on three of the four bridges for the full 1997 calendar year. For the San Angelo Eastbound HPC bridge, which was completed in June 1997 (for Spans 1 and 2), data were collected for nine months beginning in July 1997. Results from one composite beam of each bridge are compared in this section. Beams were selected for comparison on the basis of their location within the span, the location of gauges placed in the deck above the beam (determined as discussed in Section 3.5.2.3), and completeness of data. All beams selected are interior beams with eight reliable temperature gauges. The depth of the top deck gauge above each beam is approximately 57 mm (2.25 in.) below the deck surface, except for Beam W15 from the Westbound San Angelo bridge, in which the

gauge is located approximately 51 mm (2.00 in.) below the top surface. Deck dimensions for each of the composite beams discussed in this section are listed in Table 5.4. Complete temperature plots for each of the composite beams discussed in this section may be found in Appendix E.

For each set of readings (i.e. each one or two hour interval), an *average bridge temperature* was calculated. The average bridge temperature can be defined as a weighted mean of the temperatures at different depths of the composite cross-section, and is computed as the sum of the products of each measured temperature within the cross-section and its given weight. Weights were computed for each layer using the proportion of the total transformed area present in the given layer. Note that transformed areas were used because it is more the axial elongation or contraction corresponding to a given set of temperatures that is ultimately of interest, not the actual set of temperatures. Weights for each layer of the composite beams examined in this section are given in Table 5.5. Layers are identified in Figure 5.10. The total contribution of the deck temperatures to the average bridge temperatures ranges from 39 to 52 percent, depending on the beam cross-section, deck thickness, beam spacing, and moduli of elasticity of the various concretes.

Table 5.4 - Deck Dimensions and Gauge Depths for Selected Composite Beams

	Louetta NB	Louetta SB	S. Ang. WB	S. Ang. EB
Beam / Web ¹	N33-W	S14-E	W15	E25
Beam Type	U54A	U54A	IV	IV
Depth of CIP Deck Gauge Below Surface	2.25	2.25	2.00	2.25
CIP Deck Thickness	3.75	4.00	4.75	4.00
Precast Panel Thickness	3.50	3.50	4.00	4.00
Haunch Thickness	1.50	1.50	1.50	3.50
Total Deck Thickness Above Beam Flange	8.75	9.00	10.25	11.50
Total Deck Thickness Between Beams	7.25	7.50	8.75	8.00
Beam Spacing (Width of Tributary Deck)	150.36	194.40	68.00	79.20
Gap Between Precast Panels	14.63 [#]	14.63 [#]	9.00	9.00
Width of Haunch	23.50 [#]	23.50 [#]	16.00	16.00
All dimensions in inches. (1 in. = 25.4 mm)				
¹ See Section 3.4.1 for notation. [#] Total for top flanges above both webs.				

Table 5.5 - Weights Used for Calculation of Average Bridge Temperature

	Louetta NB	Louetta SB	San Angelo WB	San Angelo EB
Beam / Web	N33-W	S14-E	W15	E25
Weight, Layer 1	.090	.078	.060	.057
Weight, Layer 2	.138	.119	.218	.208
Weight, Layer 3	.112	.096	.086	.082
Weight, Layer 4	.060	.052	.081	.077
Weight, Layer 5	.054	.046	.086	.081
Weight, Layer 6	.100	.086	.077	.073
Weight, Layer 7	.242	.264	.183	.220
Weight, Layer 8	.205	.260	.208	.201

Temperature behavior on a typical sunny summer day is shown in Figure 5.11 for composite beam W15 in the Westbound San Angelo Overpass. During the early morning hours, the average bridge temperature is similar to or slightly warmer than the deck temperature, and substantially warmer than the ambient temperature. Later in the day, the deck heats up dramatically from the increase in ambient temperature, and more importantly solar radiation. The average bridge temperature increases during the day as well, but at a much slower rate because the beam is shaded and not exposed to solar radiation. Note that during the summer months, the daily maximum average bridge temperature is almost always greater than the daily maximum ambient temperature, and less than the daily maximum deck temperature.

Temperatures are plotted for an overcast winter day in Figure 5.12 for composite beam N33 (west web) in the Northbound Louetta bridge. Deck temperatures, and thus average bridge temperatures, tend to be more stable during a winter day than during a summer day because there is less solar radiation hitting the deck surface. Thus, the maximum average bridge temperature on an overcast winter day may be approximately equal to the maximum ambient temperature. The average bridge temperature is also very likely to remain warmer than the ambient temperature during typical winter nights (in Texas), unless the preceding few days have been cloudy and cold.

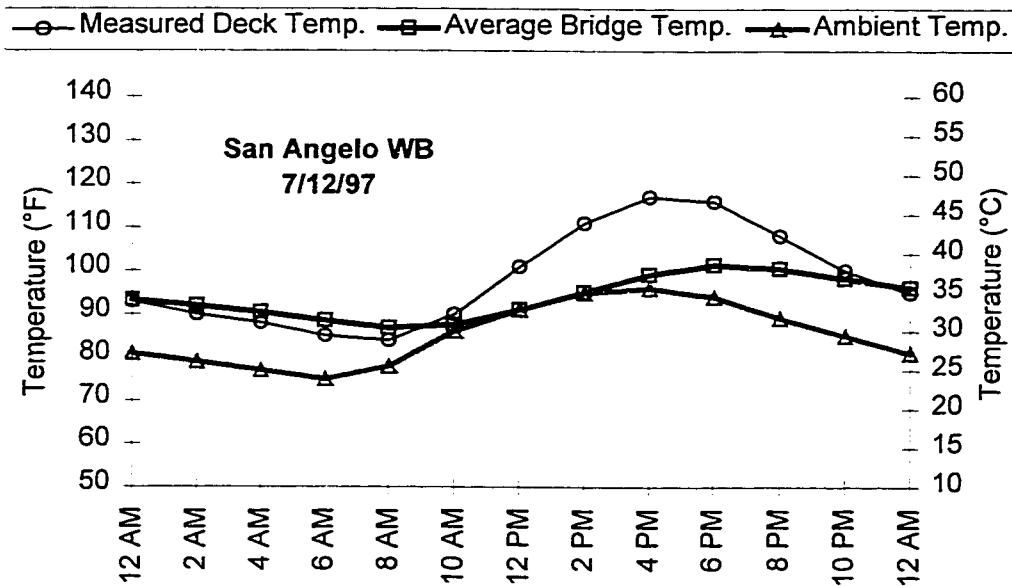


Figure 5.11 - Typical Temperature Behavior on a Sunny Summer Day

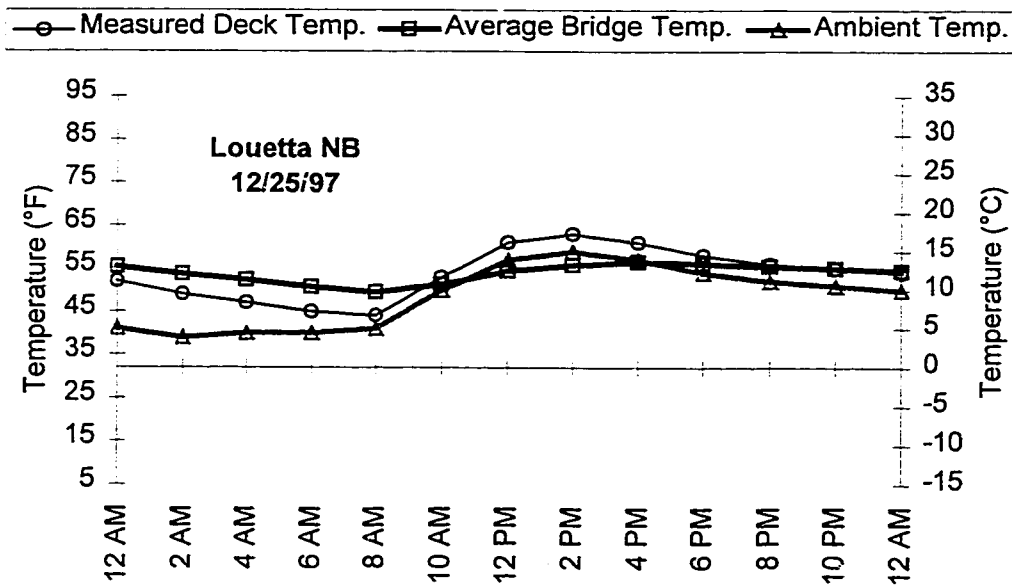


Figure 5.12 - Typical Temperature Behavior on an Overcast Winter Day

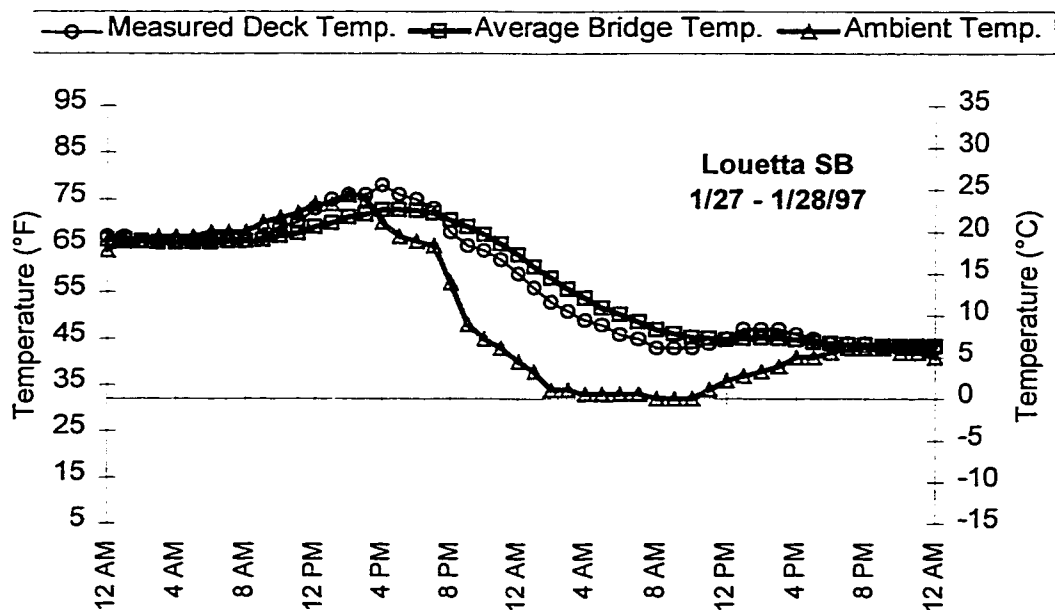


Figure 5.13 - Temperature Behavior Affected by a Cold Front

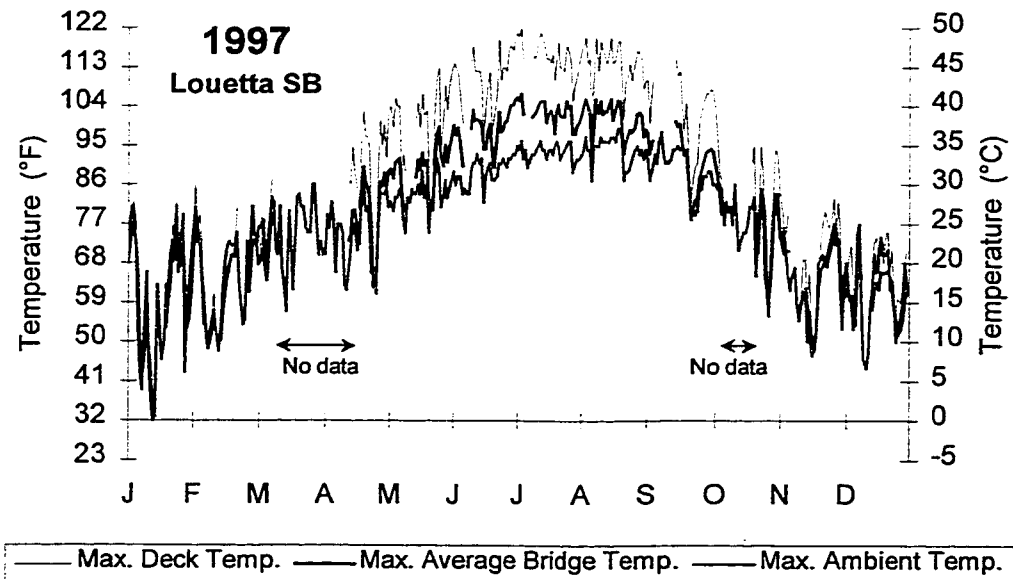


Figure 5.14 - Maximum Daily Temperatures for Composite Beam S14-E in 1997

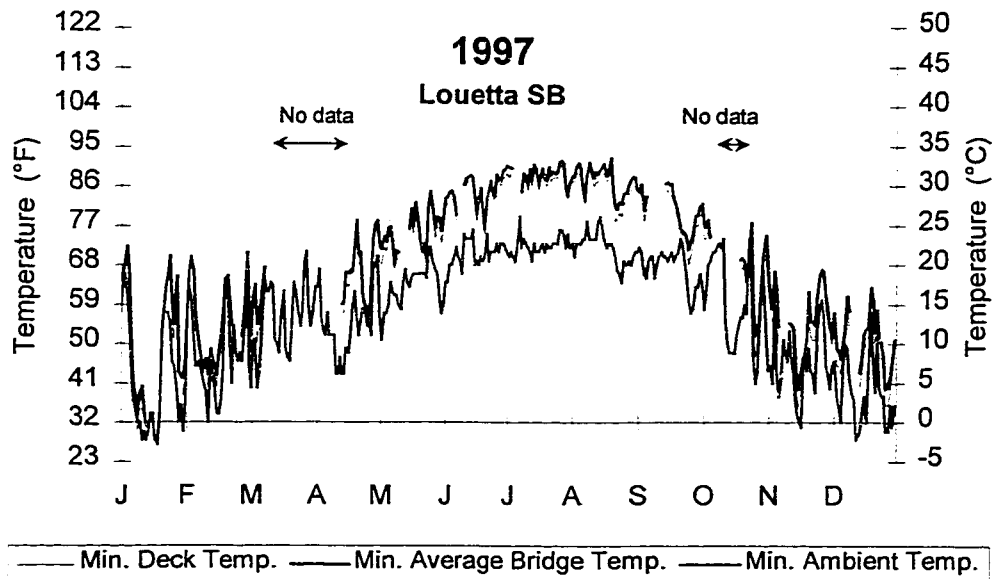


Figure 5.15 - Minimum Daily Temperatures for Composite Beam S14-E in 1997

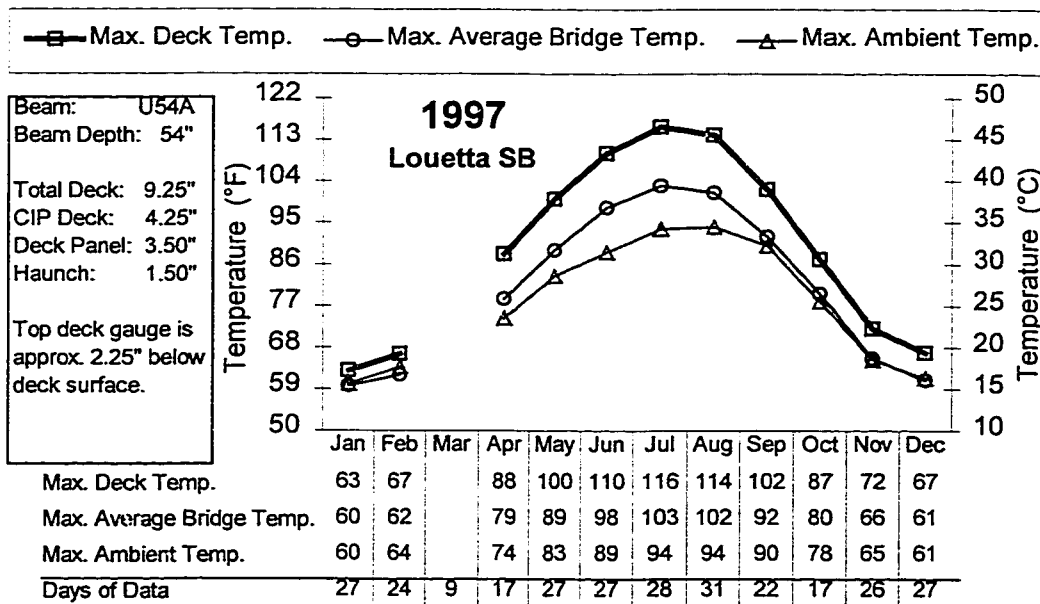


Figure 5.16 - Average Maximum Daily Temperatures by Month for Composite Beam S14-E in 1997

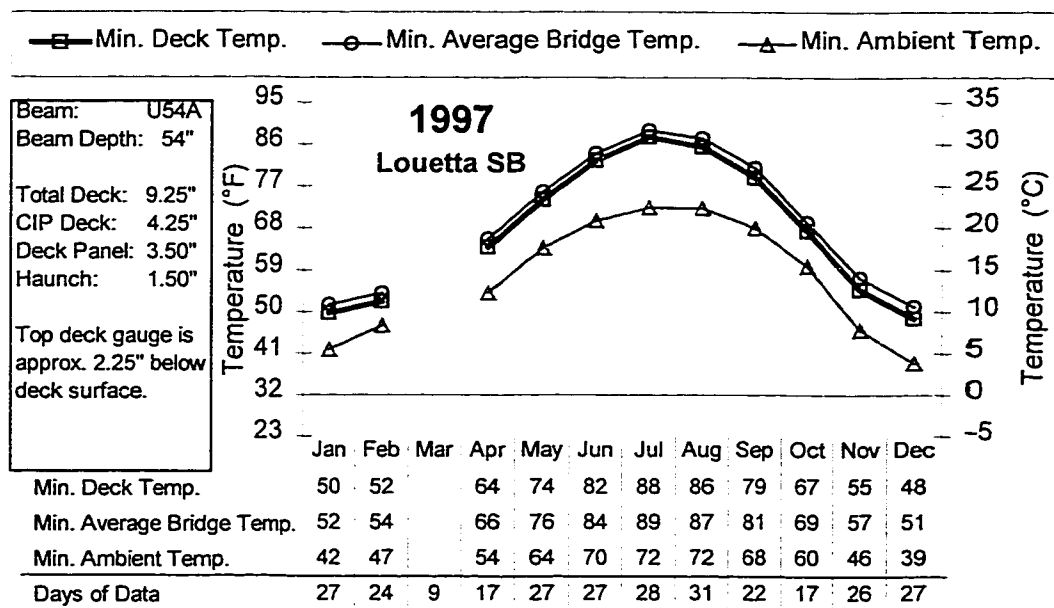


Figure 5.17 - Average Minimum Daily Temperatures by Month for Composite Beam S14-E in 1997

An excellent example of the "thermal inertia" exhibited by a completed composite bridge can be seen in Figure 5.13, in which temperatures are plotted for Beam S14 (east web) of the Louetta Southbound bridge before and after a cold front passes through Houston. Prior to the arrival of the cold front, ambient, deck, and average bridge temperatures are approximately equal, indicating several consecutive days of cool to mild, cloudy conditions. As the cold front hits at approximately 4:00 PM, a sharp drop occurs in the ambient temperature. Overnight, the ambient temperature dips to the freezing mark, but it takes about 30 hours for a state of equilibrium to be reached between the ambient and bridge temperatures. Note that during the period of cooling the night after the cold front hits, the deck temperature drops more quickly than the average bridge temperature, indicating a lag between cooling of the deck and cooling of the rest of the section.

Daily maximum and minimum temperatures for Beam S14 (east web) of the Louetta Southbound bridge are plotted in Figure 5.14 and Figure 5.15, respectively, for the entire 1997 calendar year. General trends can be seen in these plots, especially the difference in maximum and minimum deck, average bridge, and ambient temperatures during the

summer. However, the daily variations in temperatures make some trends difficult to visualize, so the average daily maximum and minimum temperatures were computed for each calendar month. These values can be seen in the plots of Figure 5.16 and Figure 5.17 for maximum and minimum data, respectively.

Table 5.6 - Comparison of Maximum Measured Temperatures

	Louetta NB	Louetta SB	San Angelo WB	San Angelo EB
<i>Absolute Maximum Temperatures</i>				
Measured Deck Temperature	121	122	123	113
Calculated Average Bridge Temperature	105	107	104	99
Ambient Temperature	99	99	101	101
<i>Lowest Daily Maximum Temperatures</i>				
Measured Deck Temperature	32	32	21	41
Calculated Average Bridge Temperature	33	33	21	41
Ambient Temperature	32	32	19	37
<i>Highest Average Daily Maximum Temperatures for a Calendar Month</i>				
Measured Deck Temperature	114 (7/97)	116 (7/97)	115 (7/97)	108 (7/97)
Calculated Average Bridge Temperature	101 (7/97)	103 (7/97)	100 (7/97)	96 (7/97)
Ambient Temperature	94 (8/97)	94 (8/97)	96 (7/97)	96 (7/97)
<i>Lowest Average Daily Maximum Temperatures for a Calendar Month</i>				
Measured Deck Temperature	61 (1/97)	63 (1/97)	54 (1/97)	58 (12/97)
Calculated Average Bridge Temperature	58 (1/97)	60 (1/97)	52 (1/97)	52 (12/97)
Ambient Temperature	60 (1/97)	60 (1/97)	56 (1/97)	57 (12/97)
All temperatures in °F. [$^{\circ}\text{C} = (5/9) * (^{\circ}\text{F} - 32)$]				

Table 5.7 - Comparison of Minimum Measured Temperatures

	Louetta NB	Louetta SB	San Angelo WB	San Angelo EB
Absolute Minimum Temperatures				
Measured Deck Temperature	30	30	18	25
Calculated Average Bridge Temperature	31	31	19	30
Ambient Temperature	27	27	16	19
Highest Daily Minimum Temperatures				
Measured Deck Temperature	89	91	88	86
Calculated Average Bridge Temperature	93	92	92	87
Ambient Temperature	79	79	78	78
Lowest Average Daily Minimum Temperatures for a Calendar Month				
Measured Deck Temperature	45 (12/97)	48 (12/97)	38 (1/97)	39 (12/97)
Calculated Average Bridge Temperature	49 (12/97)	51 (12/97)	41 (1/97)	42 (12/97)
Ambient Temperature	39 (12/97)	39 (12/97)	31 (12/97)	31 (12/97)
Highest Average Daily Minimum Temperatures for a Calendar Month				
Measured Deck Temperature	86 (7/97)	88 (7/97)	85 (7/97)	83 (7/97)
Calculated Average Bridge Temperature	88 (7/97)	89 (7/97)	88 (7/97)	84 (7/97)
Ambient Temperature	72 (7/97)	72 (7/97)	71 (7/97)	71 (7/97)
All temperatures in °F. [$^{\circ}\text{C} = (5/9)(^{\circ}\text{F} - 32)$]				

It is clear from Figure 5.16 that the maximum temperatures tend to occur during the middle of the summer, typically in July. During this period, the maximum average bridge temperature in composite beam S14 tended to be approximately 5 °C (9 °F) warmer than the maximum ambient temperatures. During the winter months of December and January, however, there was essentially no difference, on average, between the maximum average bridge temperatures and the maximum ambient temperatures. Similar observations can be made for minimum temperatures in composite beam S14 from Figure 5.17. Throughout the

entire year, the average daily minimum temperature tended to remain higher than the minimum ambient temperature. On average, the difference was about 9 °C (17 °F) during the peak summer month of July, and about 6 °C (10 °F) during the peak winter month of January.

Daily and average monthly extreme temperature plots for composite girders from all four bridges may be found in Appendix E. Note that monthly averages were not computed for any month with data available from less than half of the number of days in the month. Comparisons of the temperature behavior of the composite beams selected from each of the four bridges are presented in Table 5.6 and Table 5.7, for maximum and minimum temperatures, respectively. The extreme temperatures observed on any single day during the study period are also listed in these tables.

In general, behavior was similar for each of the three bridges in which data was collected during the full 1997 calendar year (Louetta Northbound, Louetta Southbound, and San Angelo Westbound). Maximum average bridge temperatures measured (and calculated) on any single day in 1997 were 41, 42, and 40 °C (105, 107, and 104 °F) for the Louetta Northbound, Louetta Southbound, and San Angelo Westbound bridges, respectively. These extreme temperatures were 3, 4, and 2 °C (6, 8, and 3 °F) above the highest ambient temperatures recorded at nearby official weather stations. Differences between the maximum average bridge temperatures and the maximum ambient temperatures calculated as monthly averages (for July) were approximately the same as for the extreme daily data. In all three bridges, the maximum average bridge temperature recorded for a single day exceed the July average maximum bridge temperature by 2 °C (4 °F). Note that the maximum temperatures recorded in the decks corresponding to these three bridges at any time during 1997 ranged from 49 to 51 °C (121 to 123 °F).

Minimum average bridge temperatures for a single day in 1997 were -1 °C (31 °F) for the Louetta Northbound and Southbound bridges, and -7 °C (19 °F) for the San Angelo Westbound bridge. These extreme single day temperatures are 10, 11, and 12 °C (18, 20, and 22 °F) lower than the minimum average bridge temperatures calculated by month (for either January or December), which were 9, 11, and 5 °C (49, 51, and 41 °F) for the Louetta Northbound, Louetta Southbound, and San Angelo Westbound bridges, respectively. The minimum average bridge temperature was 2 °C (3 to 4 °F) warmer than the minimum

ambient temperature for the single-day extreme measurements, and 6 to 7 °C (10 to 12 °F) warmer when calculated on the basis of monthly averages.

Data from the San Angelo Eastbound bridge showed different trends than data from the other three bridges, especially with respect to maximum temperatures. Maximum average bridge temperatures in the Eastbound bridge during the summer (of 1997) were approximately equal to maximum ambient temperatures. During the winter, maximum average bridge temperatures were generally less than maximum ambient temperatures. Maximum deck temperatures recorded in July 1997 also tended to be about 3 to 6 °C (5 to 10 °F) lower in the San Angelo Eastbound bridge than in the San Angelo Westbound bridge. By the following winter, however, deck temperatures in the Eastbound and Westbound bridges tended to be approximately equal.

Specific reasons for the different thermal behavior in the Eastbound bridge are unknown. Material (thermal) properties and bridge geometry (i.e. deck thickness, beam spacing, etc.) may be factors, as could concrete age and moisture content. It is important to note that during the period where the thermal behavior of the Eastbound and Westbound bridges has been compared, the Eastbound bridge was less than six months old while the Westbound bridge was much older. Future measurements on the Eastbound and Westbound San Angelo bridges should help to clarify some of these early observations.

5.3.3 Discussion

The average bridge temperature, defined in Section 5.3.2, is the best representation of the temperature associated with uniform axial movements of the bridge. Temperatures in both the deck and beams are used in the calculation of the average bridge temperature, such that the uniform movement of the entire bridge section can be modeled as a whole. The use of deck temperatures alone, or beam temperatures alone, does not consider the interaction between the beam and composite deck with respect to axial movements. Likewise, ambient temperatures alone do not consider the effect of solar radiation on bridge temperatures nor the thermal inertia associated with bridge temperatures.

Table 5.8 - Comparison of Measured Temperatures and Design Temperatures

	Maximum Temperatures		Minimum Temperatures	
	Louetta (Houston)	San Angelo	Louetta (Houston)	San Angelo
Historical Climate Data (Ambient Temperatures) ¹				
Extreme Ambient Temp. Ever Recorded	107	111	5	-4
Avg. Daily Extreme Ambient Temp. for Peak Month (January/July)	93	95	41	32
Measured Average Bridge Temperatures for 1997 ²				
Extreme Avg. Br. Temp.	106	105	31	19
Avg. Daily Extreme Avg. Br. Temp. for Peak Month (January/July)	102	101	50	41
Temperature Changes Relative to Setting Temperature				
Setting Temperature ^{3,4}	65/54	49/70	65/54	49/70
Extreme Avg. Br. Temp. ⁴	41/52	56/35	-34/-23	-30/-51
Avg. Daily Extreme Avg. Br. Temp. for Peak Month (January/July)	102	101	50	41
Design Temperatures				
AASHTO Standard Specifications [3] ⁵	ST+35	ST+35	ST-45	ST-45
AASHTO LRFD Specifications [1]	80	80	10	10
NCHRP Report 276 [65]	94	95	38	33
Suggested (Equations 5.1 and 5.2)	105	108	23	14
All temperatures in °F. [°C = (5/9)*(°F - 32)]				
¹ Obtained from <i>The USA Today Weather Almanac, 1995</i> [138]				
² Average measured temperatures for both bridges at each jobsite, except that minimum temperatures for San Angelo bridge are taken from Westbound bridge only since extreme data was collected during January 1997 (prior to completion of the San Angelo Eastbound bridge).				
³ Setting temperature as defined in <i>AASHTO LRFD Specifications</i> [1]				
⁴ For Louetta bridges, first number corresponds to NB bridge, second to SB bridge. For San Angelo bridges, first number corresponds to WB bridge, second to EB bridge.				
⁵ These values represent offsets to "base" or "setting" temperature. Values should be compared to temperature changes listed above, not to actual measured temperatures.				

In Table 5.8, the measured average bridge temperatures in this study are compared to the design temperatures suggested by the three methods discussed in Section 5.3.1. The design temperature increases suggested in the *AASHTO Standard Specifications* [3] underestimated the maximum increases that were observed in three of the four bridges. Meanwhile, the design temperature decreases suggested in the *Standard Specifications* overestimated the measured decreases observed in three of the four bridges. The magnitude of these underestimations and overestimations are clearly a function of the base setting temperature. Since the extreme temperatures themselves are not dependent on the base or setting temperature, the philosophy of these code provisions must be questioned. In cases where the base or setting temperature is very high or very low, this method could grossly underestimate the corresponding temperature increase or decrease.

The temperatures suggested in the *LRFD Specifications* [1] are also clearly inappropriate for the bridge locations monitored in this study. Both the maximum and minimum design temperatures were significantly lower than the extreme bridge temperatures observed during 1997. While the form of the *LRFD* code provisions are good, the temperatures suggested for use (in the absence of more specific data) are simply not general enough for use in warmer climates such as Texas.

The design temperatures suggested in NCHRP Report 276 [65] are, of course, more site specific. They are determined as a function of the average daily extreme ambient temperatures in January and July at the location of the given jobsite. Still, the temperatures observed in this study indicate that the NCHRP design temperatures are quite unconservative. Maximum design temperatures were 6 to 7 °C (10 to 12 °F) lower, and minimum design temperatures 4 to 8 °C (7 to 14 °F) higher, than the extreme values observed during 1997 in the bridges monitored in this study.

Few major problems have been observed in prestressed concrete highway bridges as a result of seasonal axial bridge movements, and creep acts to relieve stresses that do develop. Still, the general lack of conservatism of the design temperatures specified in the *LRFD Specifications* and NCHRP Report 276 compared to *only a single year of data* from this study raises questions about the applicability of the design temperatures specified by these methods. There are sure to be more extreme bridge temperatures during the lifetimes of the Louetta and San Angelo bridges than were observed during 1997.

Thus, a more general, yet simple approach is suggested for the determination of maximum and minimum design temperatures for the analysis of uniform axial effects in

prestressed concrete highway bridges. This approach is only intended to provide more realistic site-specific design temperatures than the current methods previously discussed. Like the methods discussed above, the suggested approach is not intended to exactly predict the extreme average bridge temperatures that may occur during the design life of a bridge structure. Experimental data (from bridges other than those monitored in this research program) is necessary to determine the validity of this approach.

The design maximum temperature can be calculated as:

$$T_{\text{design,max}} = \frac{1}{2}(T_{\text{July,max}} + T_{\text{all-time,max}}) + 5^{\circ}\text{F}$$

Equation 5.1

where $T_{\text{July,max}}$ is the average daily maximum ambient temperature in July at the bridge location, and $T_{\text{all-time,max}}$ is the maximum ambient temperature ever recorded at the bridge location. The averaging of these two temperatures is based on the idea that designing for the average ambient temperature in July is somewhat unconservative, and that designing for the all-time maximum ambient temperature is excessive. The additional term of 3 °C (5 °F) represents the trend observed in this study that maximum average bridge temperatures are usually greater than maximum ambient temperatures during the summer.

Similarly, the minimum design temperature can be computed as:

$$T_{\text{design,min}} = \frac{1}{2}(T_{\text{Jan,min}} + T_{\text{all-time,min}})$$

Equation 5.2

Note that although minimum average bridge temperatures were generally observed to be greater than minimum ambient temperatures in this study, no temperature is added to the average of the first two terms (as there was in Equation 5.1). This conservative approach reflects the fact that in extended periods of cold, it is quite possible for minimum ambient and minimum average bridge temperatures to be approximately equal. This situation is not possible for maximum temperatures because they are always dependent on solar radiation. Design temperatures computed for the bridge locations in this study using Equation 5.1 and Equation 5.2 are listed in Table 5.8.

The base construction or setting temperature is, of course, very important for design and must be used in the calculation of uniform axial bridge movements. Unfortunately, the setting temperature can vary tremendously over the course of the year at a given location. The method for calculation of setting temperature provided in Section 3.12.2.2 of the *AASHTO LRFD Specifications* is straightforward and should usually provide a reasonable estimate of the average bridge temperature at the time of the setting event. This method is therefore recommended for use, although other methods may also provide reasonable estimates.

Differences in thermal behavior resulting directly from the use of HPC were not observed in this study. However, the use of HPC can indirectly lead to slightly more extreme average bridge temperatures. If the use of HPC in a bridge results in larger girder spacing, the influence of the deck temperature on the average bridge temperature will be increased. Because the deck temperature fluctuates as a result of solar radiation and reradiation, maximum and minimum average bridge temperatures can be expected to fluctuate more. This impact is probably somewhat insignificant, however, and should not require significant changes in design.

5.4 Thermal Gradients

5.4.1 Background

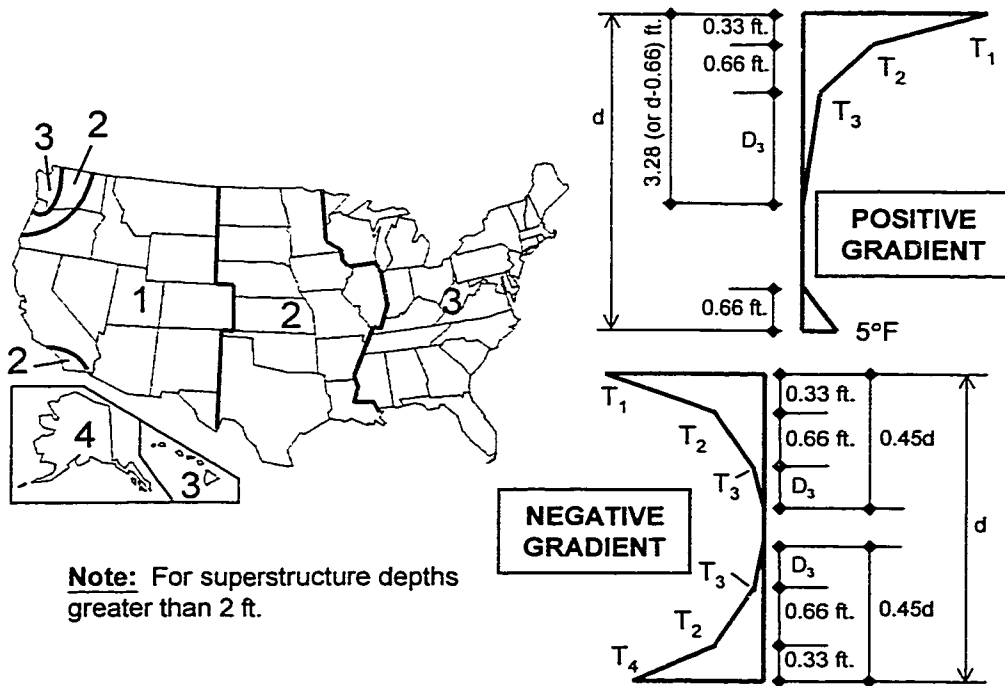
Consideration of the temperature distribution in a bridge is important in predicting the occurrence of internal thermal strains and stresses due to temperature gradients. As briefly discussed in Section 5.1.1, thermal gradients occur as a result of the diurnal (daily) temperature cycle that the bridge undergoes. During a sunny day, the exposed bridge deck heats up much more quickly than the underside of the bridge, which is shaded from direct sunlight. Since concrete has relatively low conductivity, heat is transferred very slowly from the deck to the underside of the bridge, and a positive (deck warmer than underside) thermal gradient results [65]. The magnitude of this gradient is highly dependent on the amount of radiation absorbed by the deck, which is a function of the absorptivity of the

concrete at the deck surface. A darker, rougher surface generally has a higher absorptivity than a lighter, smoother surface [111]. Positive gradients are typically much more significant during the summer, when the amount of solar radiation is at a maximum [65].

A negative (deck cooler than underside) gradient may develop when a bridge superstructure that had obtained a high temperature during the day experiences a reduction in temperature caused by a cool night [65]. The surface area of the bridge deck is typically much larger than for the rest of the superstructure, causing it to lose heat much more quickly. As the deck reradiates heat to the atmosphere, its temperature may drop below the temperature of the rest of the superstructure, resulting in a negative gradient. Since the negative gradient is dependent on the temperature distribution in the structure at the time when cooling begins, as well as the difference between concrete and ambient temperatures, its magnitude is highly variable.

NCHRP Report 276 presents a set of thermal gradients for use as part of the design guidelines provided in Appendix A of the report. The positive gradient, shown in Figure 5.18, follows a trilinear form over the top 1.0 m (3.28 ft.) of the superstructure depth. Temperature differentials are specified at 100 mm (4 in.), 200 mm (8 in.) and 1000 mm (39.4 in.) below the top of the superstructure in a set of tables. A 3°C (5°F) increase is also stipulated over the bottom 200 mm (8 in.) of the structure. The specified temperature differentials vary as a function of the blacktop thickness and location within the United States. For purposes of classification, the United States is separated into four zones based on maximum solar radiation. The recommended positive gradient is based on a one-dimensional heat flow model developed by Potgieter and Gamble [106].

A negative design gradient is also provided in the NCHRP report, and is also shown in Figure 5.18. The negative design gradient specifies temperature differentials at six locations through the depth. For convenience, some of the locations coincide with the locations of temperature differentials specified for the positive design gradient. The United States is divided into four zones based on maximum solar radiation, as for the positive gradient, and the depth of blacktop is considered in determination of the magnitude of temperature differentials. The shape of the gradient is based on negative gradient proposed in the 1978 British Standard BS5400 [29].



Note: For superstructure depths greater than 2 ft.

POSITIVE GRADIENT

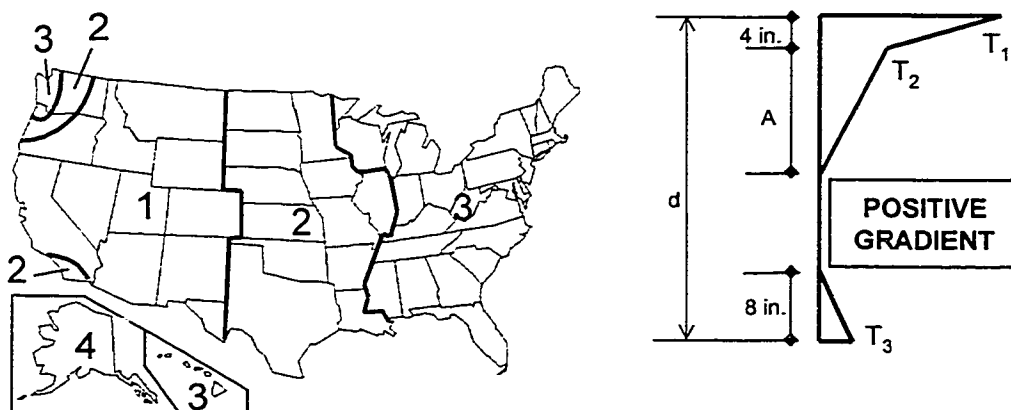
Zone	Plain Concrete Surface			2 in. Blacktop			4 in. Blacktop		
	T ₁	T ₂	T ₃	T ₁	T ₂	T ₃	T ₁	T ₂	T ₃
1	54	14	5	43	14	4	31	9	3
2	46	12	4	36	12	4	25	10	3
3	41	11	4	33	11	3	23	11	2
4	38	9	3	29	9	2	22	11	2

Note: All temperatures in degrees Fahrenheit.

NEGATIVE GRADIENT

Zone	Plain Concrete Surface				2 in. Blacktop				4 in. Blacktop			
	T ₁	T ₂	T ₃	T ₄	T ₁	T ₂	T ₃	T ₄	T ₁	T ₂	T ₃	T ₄
1	27	7	2	14	22	7	2	15	16	5	1	12
2	23	6	2	10	18	6	2	11	13	5	1	9
3	21	6	2	8	17	6	2	10	12	6	1	8
4	19	5	2	6	15	5	1	8	11	6	1	8

Figure 5.18 - Design Thermal Gradients Suggested in NCHRP Report 276 [65]



All temperatures in degrees Fahrenheit.

Notes:

The dimension "A" shall be taken as:

- 12.0 in. for concrete superstructures that are 16.0 in. or more in depth
- (d - 4) in. for concrete superstructures that are less than 16.0 in. in depth

The temperature value T_3 shall be taken as 0.0, unless a site-specific study is made to determine an appropriate value, but shall not exceed 5°F.

POSITIVE GRADIENT

Zone	Plain Concrete Surface		2 in. Blacktop		4 in. Blacktop	
	T_1	T_2	T_1	T_2	T_1	T_2
1	54	14	43	14	31	9
2	46	12	36	12	25	10
3	41	11	33	11	23	11
4	38	9	29	9	22	11

NEGATIVE GRADIENT values may be obtained by multiplying positive gradient values by -0.5.

Figure 5.19 - Design Thermal Gradients Specified in the AASHTO LRFD Specifications [1]

Thermal gradients are not mentioned in the *AASHTO Standard Specifications* [3], but are addressed in detail in the *AASHTO LRFD Specifications* [1]. The form of the design positive gradient found in Section 3.12.3 of the *LRFD Specifications* is a modified version of the positive gradient suggested in the NCHRP report, and is shown in Figure 5.19. The design gradient is simplified from the NCHRP gradient by eliminating the third specified temperature differential, and by eliminating the differential at the bottom of the section unless it is supported by site-specific data. The same classifications for geographical location and blacktop thickness used in the NCHRP report are used in the *LRFD Specifications*. The design negative gradient is simplified greatly over the negative gradient suggested in the NCHRP specifications, and is simply taken as a multiple of the positive gradient.

Note that a small change has been made to the 1994 *AASHTO LRFD* negative design gradient in the 1998 *AASHTO Guide Specifications for Segmental Bridges* [2]. The 1998 *Guide Specifications* recommend that the negative design gradient be taken as a multiple of -0.3 times the positive gradient, rather than a multiple of -0.5 as suggested in the 1994 *LRFD Specifications*. Other proposed design gradients include the New Zealand approach, in which a fifth-order parabola is used to approximate the temperature distribution (for positive gradients) over the top 1200 mm (47.2 in.) of the section [109].

Thermal gradients are specified in most of the load combinations listed in Section 3.4.1 of the *LRFD Specifications*. As discussed in Sections 3.4.1 and 3.12.3 of the commentary, there is strong agreement on the presence of thermal gradients in bridges, but little agreement relating to their impact. For instance, creep and cracking tend to relieve stresses that develop as a result of restrained movement. The load factor for thermal gradients is therefore determined on a project-specific basis. In many cases, a load factor of less than 1.0, and in some cases a load factor of 0.0 (implying that thermal gradients need not be considered), may be appropriate. The specific text of Sections 3.4.1 and 3.12.3 of the commentary read as follows:

(excerpt from C3.4.1)

The load factor for temperature gradient should be determined based on:

- the type of structure, and
- the limit state being investigated.

At this writing (1994), there is general agreement that the in situ measurements of temperature gradients have yielded a realistic distribution of temperatures through the depths of some types of bridges, most notably concrete box girders. There is very little agreement on the significance of the effect of that distribution. It is generally acknowledged that cracking, yielding, creep, and other non-linear responses diminish the effects. Therefore, load factors of less than 1.0 should be considered, and there is some basis for lower load factors at the strength and extreme event limit states than at the service limit state.

Similarly, open girder construction and multiple steel box girders have traditionally, but perhaps not necessarily correctly, been designed without consideration of temperature gradient, i.e., $\gamma_{TG} = 0.0$.

(excerpt from C3.12.3)

Temperature gradient is included in the various load combinations in Table 3.4.1-1. This does not mean that it need be investigated for all types of structures. If experience has shown that neglecting temperature gradient in the design of a given type of structure has not lead to structural distress, the Owner may choose to exclude temperature gradient. Multi-beam bridges are an example of a type of structure for which judgement and past experience should be considered.

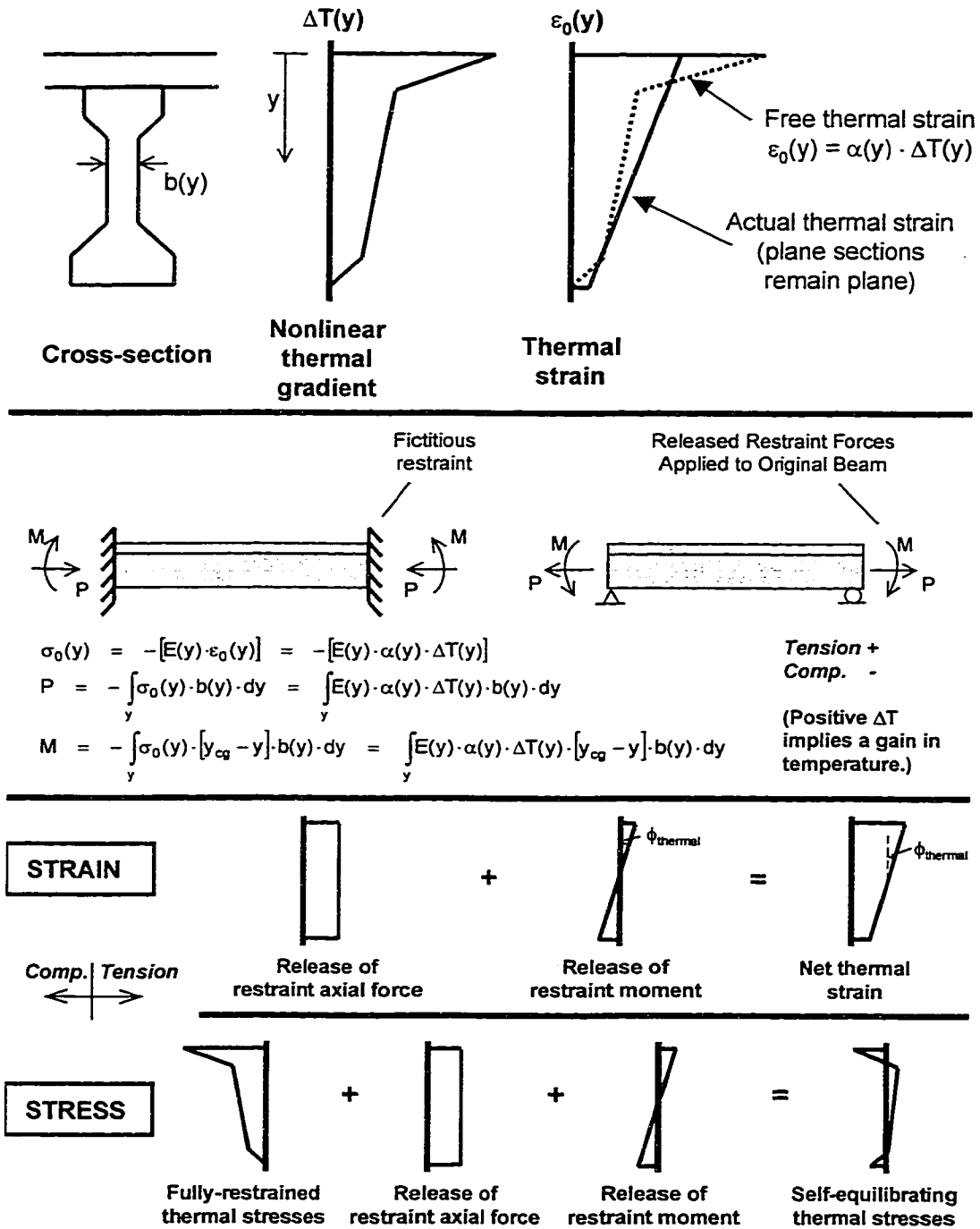


Figure 5.20 - Determination of Thermal Stresses and Strains in a Determinate Member Subjected to a Nonlinear Thermal Gradient

While there is little agreement on the net impact of thermal gradients in bridges, there is a widely accepted mechanics-based analysis method by which the elastic stresses and strains resulting from thermal gradients may be determined. This method is discussed briefly in Section 4.6.6 of the commentary of the *LRFD Specifications* [1]. A detailed discussion of the method is provided in Chapter Three of the NCHRP report [65] and by other authors [59,75].

When a homogeneous determinate structure is subjected to a linear temperature gradient, a linear strain profile is developed through the depth of the structure. The strain at any depth in such a structure is equal to the product of the coefficient of thermal expansion and the temperature differential at the given depth. This strain can be termed the free thermal strain, and is representative of the strain that would occur at any depth in the structure if the deformation of fibers at adjacent depths did not influence the deformation at the depth being considered.

When the structure is subjected to a nonlinear gradient as shown in Figure 5.20, or is non-homogeneous (i.e. the coefficient of thermal expansion varies with the depth), the resulting free thermal strain profile is nonlinear, and would not satisfy the hypothesis that plane sections remain plane. In order to satisfy the hypothesis, internal stresses must be developed through the depth of the cross-section. These stresses must also be self-equilibrating, since there is no external load acting on the structure.

These self-equilibrating stresses and the net thermal strain can be determined by applying fictitious axial and flexural restraints at the ends of the member, determining the stress distribution and restraint forces, and then releasing the fictitious restraints on the original member. The magnitude of the restraining axial force is determined by summing the fully-restrained thermal stresses, which are by definition the product of the free thermal strain and modulus of elasticity at a given depth, across the cross-section. The magnitude of the restraining moment is similarly computed by considering the distance from the center of gravity of the section to each differential stress element. For the sign convention where tensile stresses and strains are positive, and compressive stresses and strains are negative:

$$\sigma_0(y) = -[E(y) \cdot \varepsilon_0(y)] = -[E(y) \cdot \alpha(y) \cdot \Delta T(y)]$$

Equation 5.3

$$P = - \int_y \sigma_0(y) \cdot b(y) \cdot dy = \int_y E(y) \cdot \alpha(y) \cdot \Delta T(y) \cdot b(y) \cdot dy$$

Equation 5.4

$$M = - \int_y \sigma_0(y) \cdot [y_{cg} - y] \cdot b(y) \cdot dy = \int_y E(y) \cdot \alpha(y) \cdot \Delta T(y) \cdot [y_{cg} - y] \cdot b(y) \cdot dy$$

Equation 5.5

Once the magnitude of the restraining forces are known, the self-equilibrating stresses and net thermal strain can be determined. The self-equilibrating stress distribution is determined by summing the fully-restrained thermal stress distribution and the stress distributions resulting from the release of the restraint forces. At any depth, the self-equilibrating thermal stress is thus (tension positive, compression negative):

$$\sigma(y) = \sigma_0(y) + \frac{P}{A} + \frac{M(y_{cg} - y)}{I}$$

Equation 5.6

The net thermal strain at any depth can similarly be computed as the sum of the stresses resulting from the release of restraint forces, divided by the modulus of elasticity:

$$\varepsilon(y) = \frac{P}{EA} + \frac{M(y_{cg} - y)}{EI} = \varepsilon_{\text{uniform thermal}} + \phi_{\text{thermal}}(y_{cg} - y)$$

Equation 5.7

The first term in Equation 5.7 represents the uniform axial elongation or contraction of the member, and can be estimated for homogeneous sections using changes in the average bridge temperature. The second term represents the flexural thermal deformation, and can be used to calculate the thermal camber or deflection of the member. For a simply-

supported beam of length L , having the same vertical thermal gradient at any section along the length of the member, the midspan thermal camber or deflection would be calculated as (positive upward):

$$\Delta_{\text{thermal}} = -\frac{\phi_{\text{thermal}} \cdot L^2}{8}$$

Equation 5.8

Standard analysis techniques can be used to analyze thermal gradient effects in indeterminate members. For example, the structure can first be analyzed as a determinate structure by removing redundant supports, and the forces required for compatibility of deformations determined. For a continuous beam, this requirement would typically be zero deflection at internal redundant supports. The total stress distribution in an indeterminate structure is the sum of stresses in the determinate structure and the continuity stresses. Strains and deflections can be calculated in a similar manner.

5.4.2 Measurements

Thermal gradients were monitored in the same manner as average bridge temperatures discussed in Section 5.3.2. Temperatures from selected composite beams of each bridge are compared in this section. Deck dimensions for each of the composite beams compared in this section are listed in Table 5.4, and gauge layouts used for temperature measurements in the completed bridges are shown in Figure 5.10. Temperatures were recorded at one or two hour intervals using the automated data acquisition systems permanently installed in the bridges. Data from the Louetta Northbound, Louetta Southbound, and San Angelo Westbound bridges was collected for the entire 1997 calendar year, while data for the San Angelo Eastbound bridge was collected for a year after its completion, from July 1997 through March 1998.

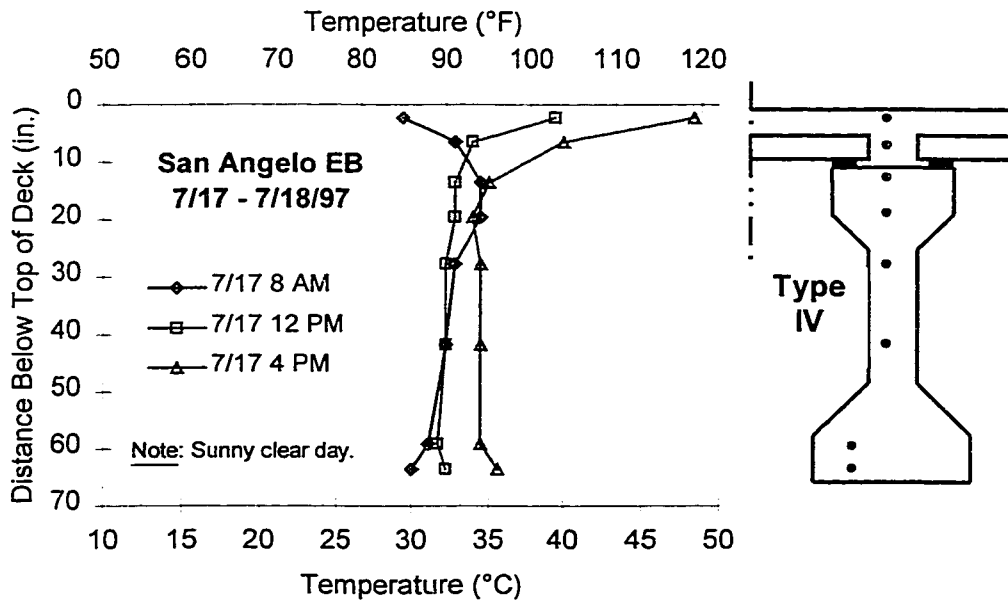


Figure 5.21 - Typical Heating Behavior in a Type IV Beam on a Sunny Summer Day

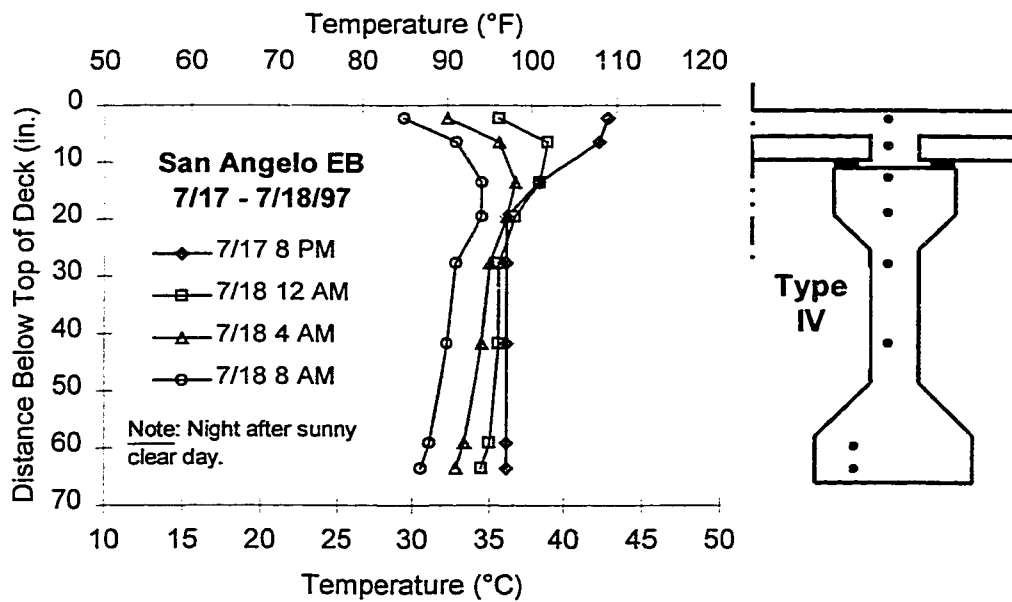


Figure 5.22 - Typical Cooling Behavior in a Type IV Beam Following a Sunny Summer Day

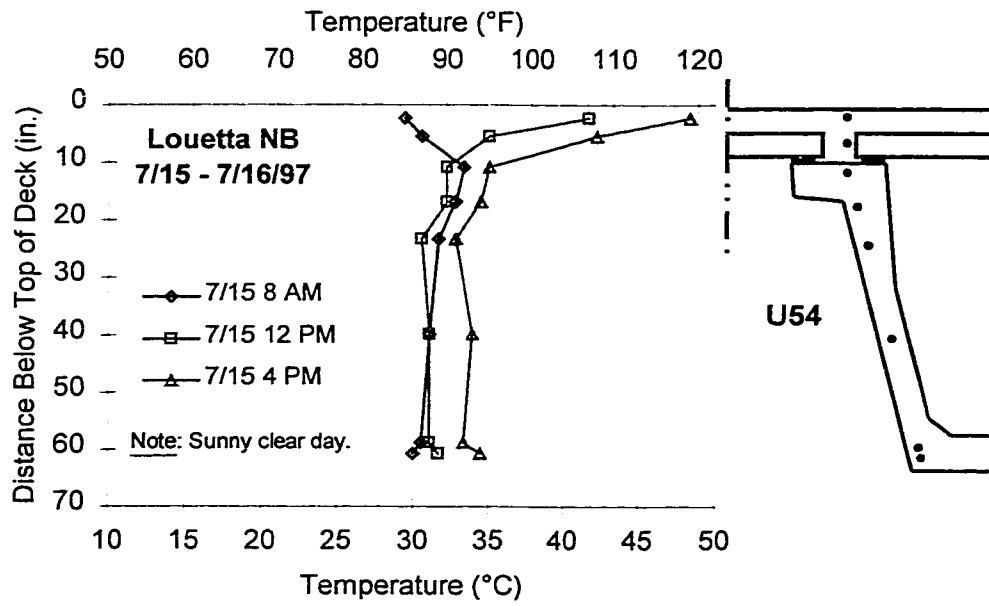


Figure 5.23 - Typical Heating Behavior in a U54 Beam on a Sunny Summer Day

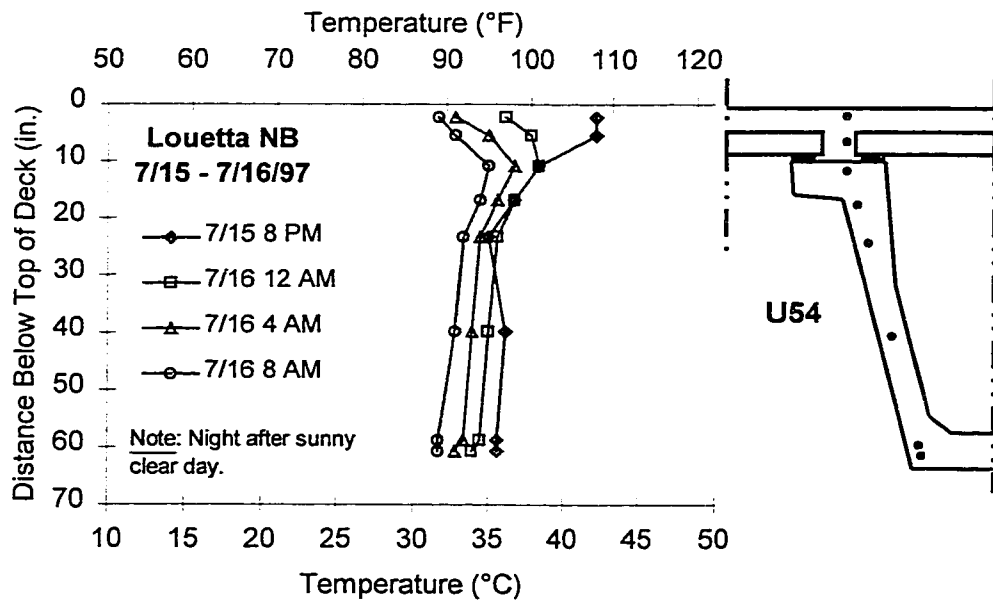


Figure 5.24 - Typical Cooling Behavior in a U54 Beam Following a Sunny Summer Day

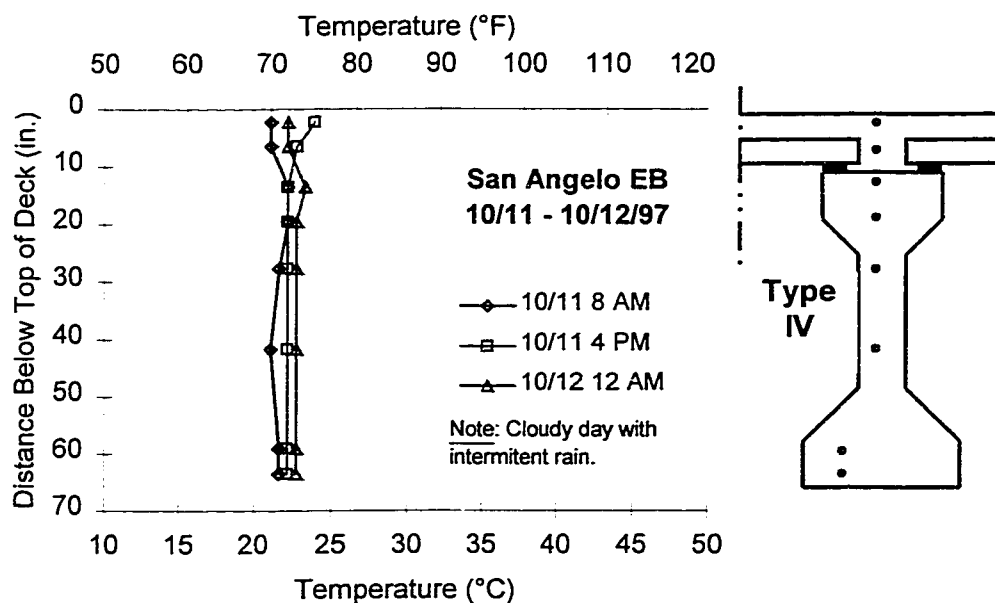


Figure 5.25 - Typical Thermal Behavior in a Type IV Beam On a Cloudy Day

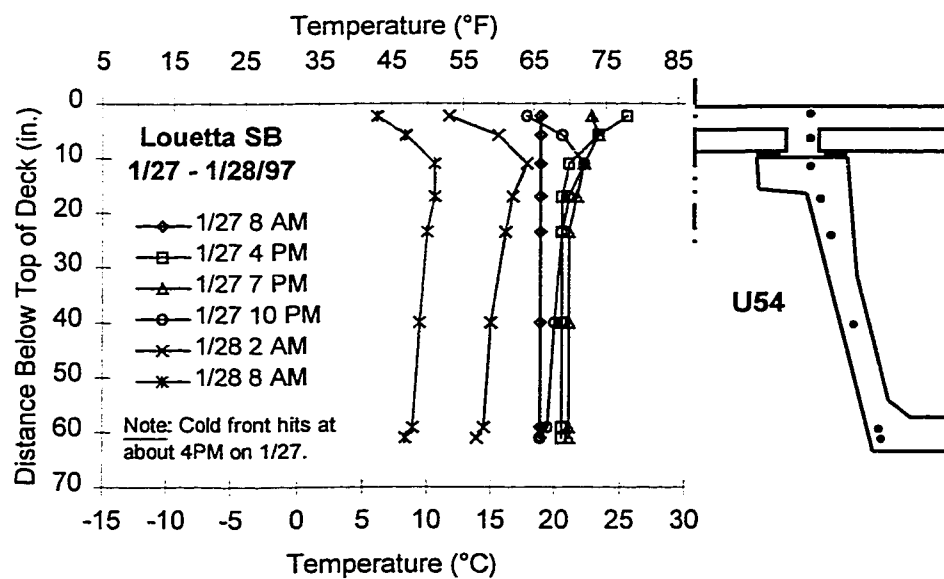


Figure 5.26 - Thermal Behavior in a U54 Beam During Passage of a Cold Front

Typical heating behavior on a sunny summer day and cooling behavior during the subsequent night are shown in Figure 5.21 and Figure 5.22, respectively, for a Type IV section. A negative (deck cooler than beam) gradient exists shortly after sunrise with fairly uniform beam temperatures. During the morning, the deck heats up quickly from solar radiation but temperatures in the beam change little, resulting in a positive (deck warmer than beam) thermal gradient. The beam heats up somewhat uniformly during the afternoon hours, but the deck continues to heat at a faster rate than the beam, and the magnitude of the positive gradient increases. During the late afternoon and early evening hours, the temperature toward the top of the deck begins to fall quickly, as heat is reradiated to the atmosphere. The beam cools more slowly and uniformly, until the deck temperature falls below the beam temperature, and by early morning a negative gradient has been reestablished.

Heating and cooling behavior for a U-beam in the Louetta Northbound bridge during a sunny summer day and subsequent night can be seen in Figure 5.23 and Figure 5.24, respectively. The behavior is clearly very similar to that observed for Type IV beams in Figure 5.21 and Figure 5.22.

Thermal behavior for a Type IV beam during a cloudy day with intermittent rain is shown in Figure 5.25. The effect of solar radiation, or lack thereof, on temperature gradients is evident, as the temperature throughout the entire depth of the section remains relatively constant during the day. The impact of a cold front, on the other hand, can be seen in Figure 5.26 for a Louetta U-beam. During the late afternoon, and just prior to the arrival of the cold front, a relatively small positive gradient exists. As the cold front passes, the temperature throughout the entire section drops dramatically, but the fastest and largest drop occurs near the exposed deck surface. As a result, a very large negative gradient develops by the early morning.

A plot of the maximum daily positive and negative thermal gradients measured in the Louetta Northbound bridge during 1997 may be found in Figure 5.27 and Figure 5.28, respectively. For purposes of computation, a positive thermal gradient was defined as a gradient in which the maximum temperature occurred at a location (typically in the deck) higher than the location of the minimum temperature. Similarly, a negative gradient was defined as a gradient in which the maximum temperature occurs at a location lower than the minimum temperature (typically in the deck). The magnitude of either gradient was defined as the difference between the maximum and minimum temperatures.

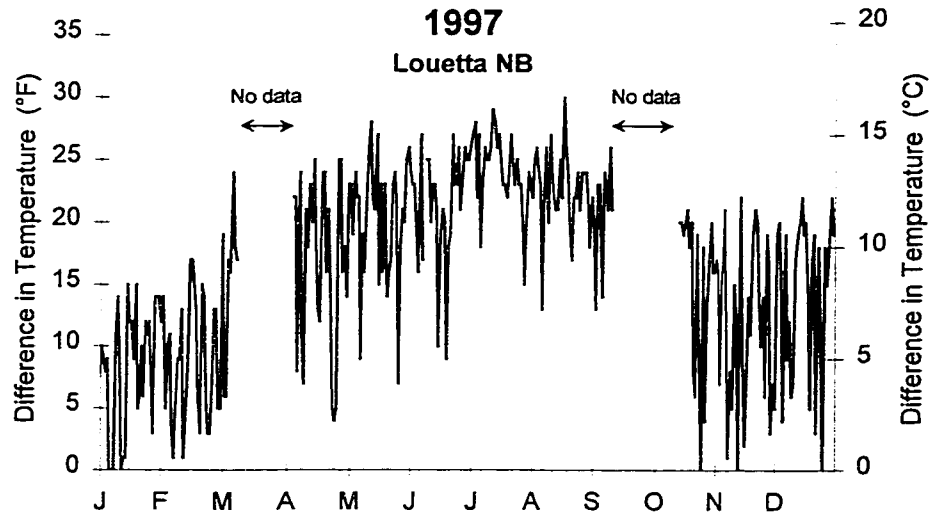


Figure 5.27 - Maximum Daily Positive Thermal Gradients During 1997 in the Louetta Northbound Bridge

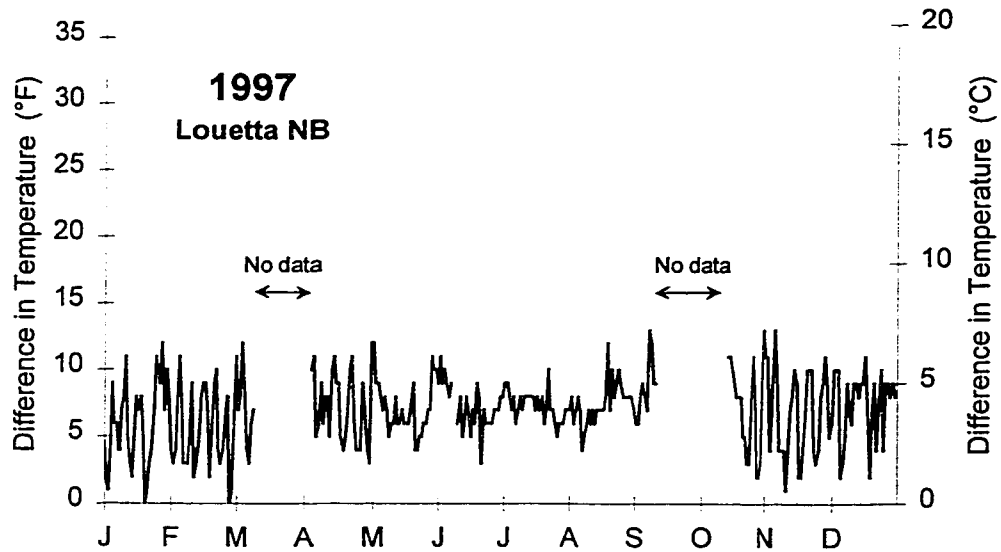


Figure 5.28 - Maximum Daily Negative Thermal Gradients During 1997 in the Louetta Northbound Bridge

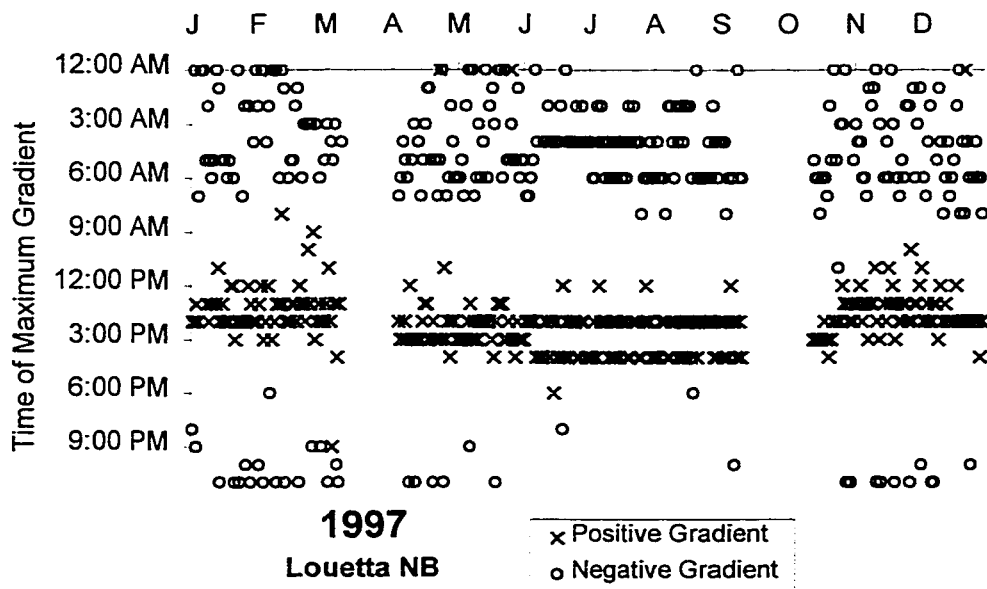


Figure 5.29 - Time of Maximum Positive and Negative Gradients Measured in Louetta Northbound Bridge During 1997

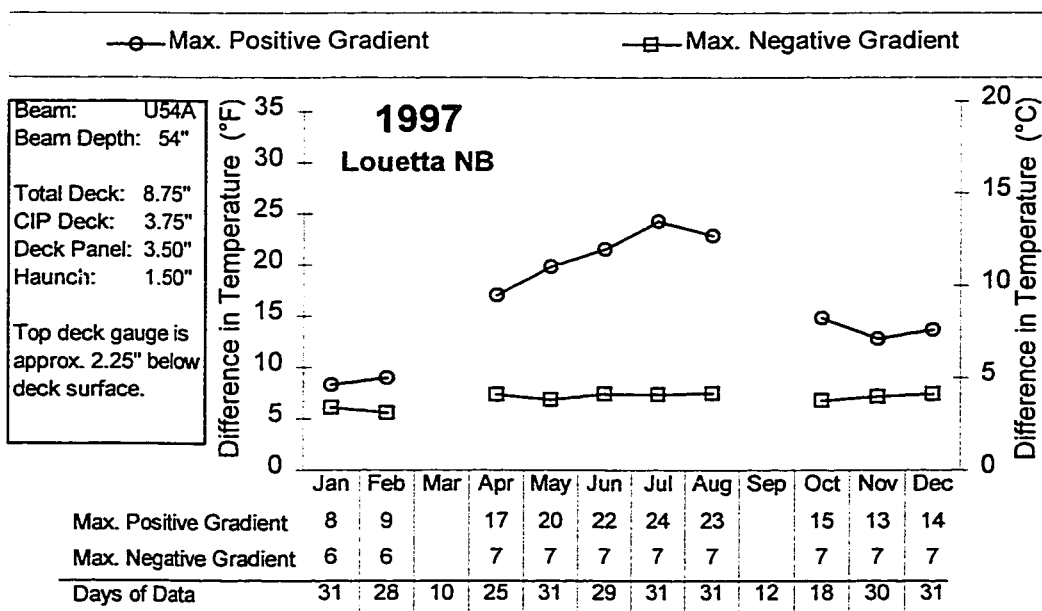


Figure 5.30 - Average Maximum Daily Gradients by Month in Louetta Northbound Bridge During 1997

As can be seen in Figure 5.27, the magnitude of the maximum positive gradient varies substantially from day to day. Maximum gradients clearly tended to be higher during the summer months, when solar radiation is most intense and ambient temperatures are highest. During the late fall and winter months, maximum positive gradients could be either high or low, depending on exact ambient conditions. Note that on a few winter days, no positive gradient was observed at any point during the day. From Figure 5.29, it can be seen that the maximum positive gradient almost always occurred between 12:00 PM and 2:00 PM during the winter, and between 2:00 PM and 4:00 PM (daylight time) during the summer.

Maximum daily negative gradients, as shown in Figure 5.28, also varied substantially from day to day. The magnitude of negative gradients tended to be more predictable during the summer months, but negative gradients were generally not higher during any part of the year. Note that the highest negative gradients typically coincided with the passage of cold fronts. As can be seen in Figure 5.29, the maximum negative gradient usually occurred sometime during the early morning, but the exact time varied substantially from day to day.

Table 5.9 - Summary of Maximum Measured Gradients

	Louetta NB	Louetta SB	San Angelo WB	San Angelo EB
<i>Maximum Measured Thermal Gradients</i>				
Positive Gradient	30	31	36	28
Negative Gradient	13	11	13	12
<i>Highest Average Measured Gradients for a Calendar Month</i>				
Positive Gradient	24 (7/97)	25 (7/97)	25 (6/97)	21 (3/98)
Negative Gradient	7 (M.M.)	6 (M.M.)	8 (M.M.)	7 (M.M.)
All values in °F. [°C = (5/9)*(°F)] M.M. = Multiple months				

A plot of the average daily maximum gradients by month is shown in Figure 5.30 for the Louetta Northbound bridge in 1997. Similar plots may be found for the other three monitored bridges in Appendix E, along with plots of daily maximum gradients. Clearly, the average maximum positive gradients are highest during the summer months and lowest during the winter months. The average maximum negative gradients are substantially smaller than the average maximum positive gradients, and remain relatively constant year round.

Magnitudes of the maximum measured gradients are compared for the four bridges in Table 5.9. The peak positive gradients recorded at any time during the measurement period ranged from 16 to 20 °C (28 to 36 °F), and the peak negative gradients ranged from 6 to 7 °C (11 to 13 °F). It is important to note that these gradients are temperature differences between the beam and the location of the top deck gauge, not the deck surface. The location of the top deck gauges ranged from 51 to 57 mm (2.00 to 2.25 in.) below the deck surface in the composite sections discussed here, and are listed in Table 5.4. The shape of the peak measured gradients is discussed in Section 5.4.3.

The thermal gradients in interior and adjacent exterior beams can be quite different in certain cases. In Figure 5.31, thermal gradients in an interior and exterior beam of the San Angelo Westbound bridge are compared at various times. The temperature profile in interior and exterior beams was nearly identical in June, when the angle between the path of the sun and the horizon is large. However, as the sun's path through the sky becomes low in October, and even lower in December, the temperatures in the exterior beam on the south side of the Westbound span are affected more and more. In general, temperatures are affected in the lower portions of the beam, where the deck overhang does not shade the beam surface. Note that for the exterior beam shown in Figure 5.31, the gauges in the bottom flange were located on the *interior* side of the span, explaining the lack of a difference in temperature (between the interior and exterior beam) at these locations.

Thermal gradients in interior and exterior beams are compared for the San Angelo Eastbound bridge in Figure 5.32. The same basic trends can be seen as for the Westbound bridge, with two exceptions. First, the temperature gauges in the bottom flange of the Eastbound exterior beam are on the *exterior* (exposed) side of the span, and are thus affected as the sun angle becomes low. This observation, combined with observations from the Westbound bridge, clearly indicate the presence of horizontal thermal gradients across the width of the bottom flanges of the exterior Type IV girders in the San Angelo bridges.

There is also a clear difference in deck temperatures between the exterior and interior composite beams in the Eastbound bridge. The differences in this case are thought to be due to differing deck thicknesses, but could also be due to more pronounced shading from the guardrail than was observed in the Westbound bridge.

The influence of beam orientation can be seen in the plots of Figure 5.33 and Figure 5.34, in which interior and exterior girders are compared in the Southbound and Northbound Louetta bridges, respectively. Note that the times of comparison are identical for the two figures, and that the deck did not overhang the exterior beam web in either bridge at the time of measurements (see Figure 2.10). In both bridges during March and June, the temperatures in the exterior beam web are greater than in the interior beam web, indicating additional heating in the exterior beam webs from exposure to the sun. During January, however, the interior and exterior beam (web) temperatures are approximately equal in the Southbound bridge. At the same time, differences between interior and exterior beam temperatures are maximum in the Northbound bridge. This behavior is clearly controlled by the fact that the Northbound exterior beam faces southwest, while the Southbound exterior beam faces northeast (see plan of the Louetta bridges in Figure 2.3.). The Northbound exterior beam web is exposed to significant sunlight during the winter while the Southbound exterior beam web is completely shaded.

The thermal behavior at different sections of the Louetta Southbound bridge deck during a sunny summer day is shown in Figure 5.35 and Figure 5.36. There appear to be few differences in the heating and cooling of the different sections of the deck, except that the section between beams cools to a slightly lower temperature overnight. The section of the deck located directly above a U-beam is insulated somewhat by the air trapped in the void between the U-beam and the deck. Likewise, the deck directly above a beam web is insulated by the beam itself. These insulating effects tend to keep these sections of the deck slightly warmer during the early morning hours, but the temperature differences tend to be small. The *horizontal* thermal gradient appears to be on the order of 2 to 3 °C (3 to 5 °F). Similar small horizontal thermal gradients were observed in the San Angelo bridges, between deck sections directly above beams and deck sections between beams.

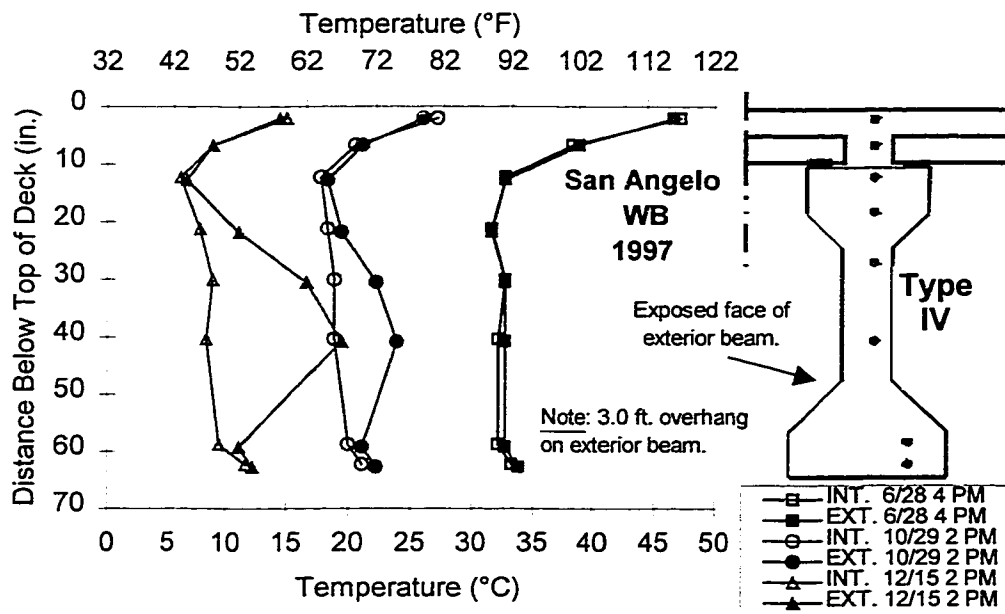


Figure 5.31 - Comparison of Thermal Gradients in Interior and Exterior Beams of the San Angelo Westbound Bridge at Various Times

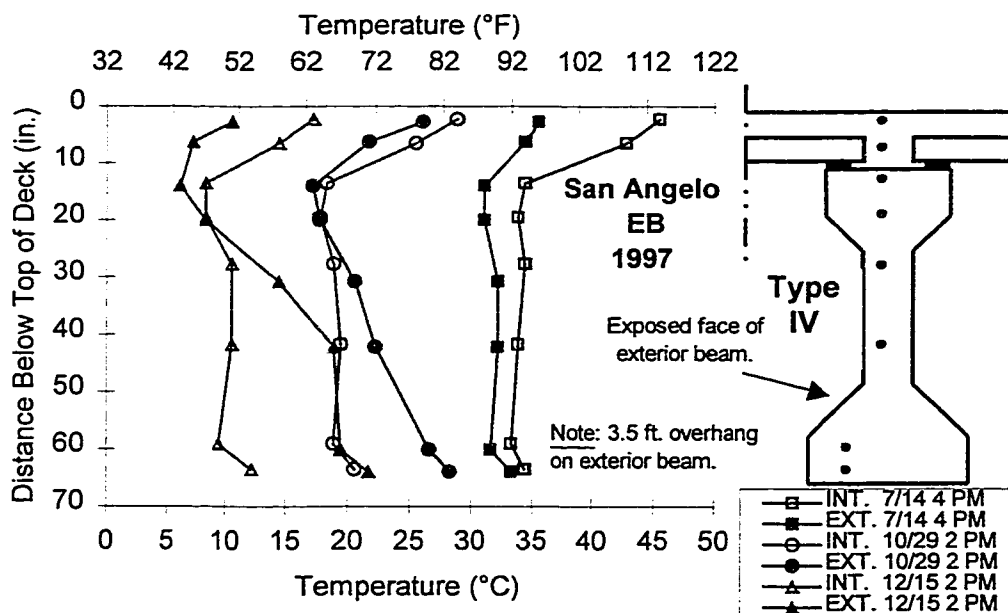


Figure 5.32 - Comparison of Thermal Gradients in Interior and Exterior Beams of the San Angelo Eastbound Bridge at Various Times

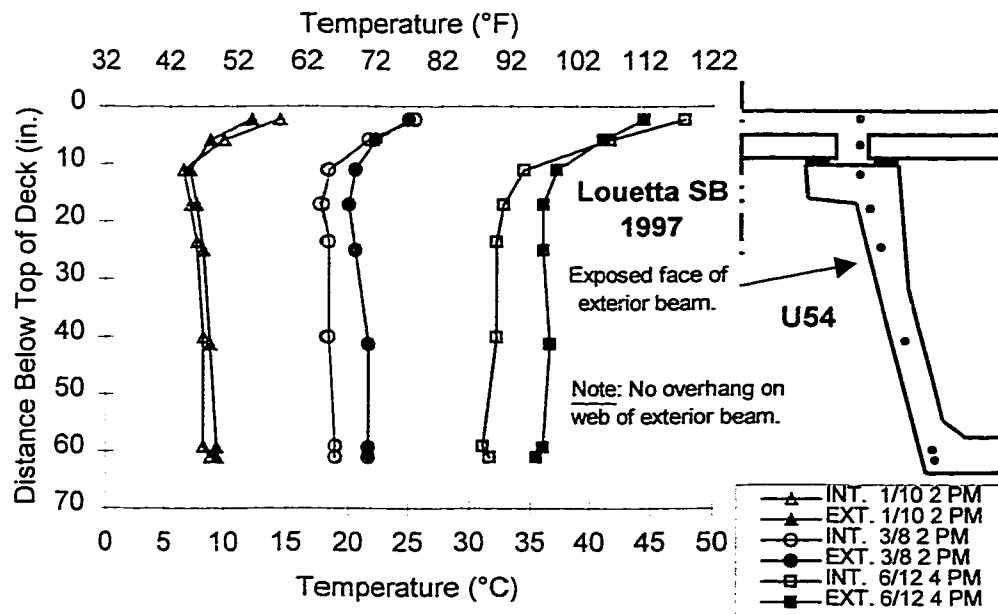


Figure 5.33 - Comparison of Thermal Gradients in Interior and Exterior Beams of the Louetta Southbound Bridge at Various Times

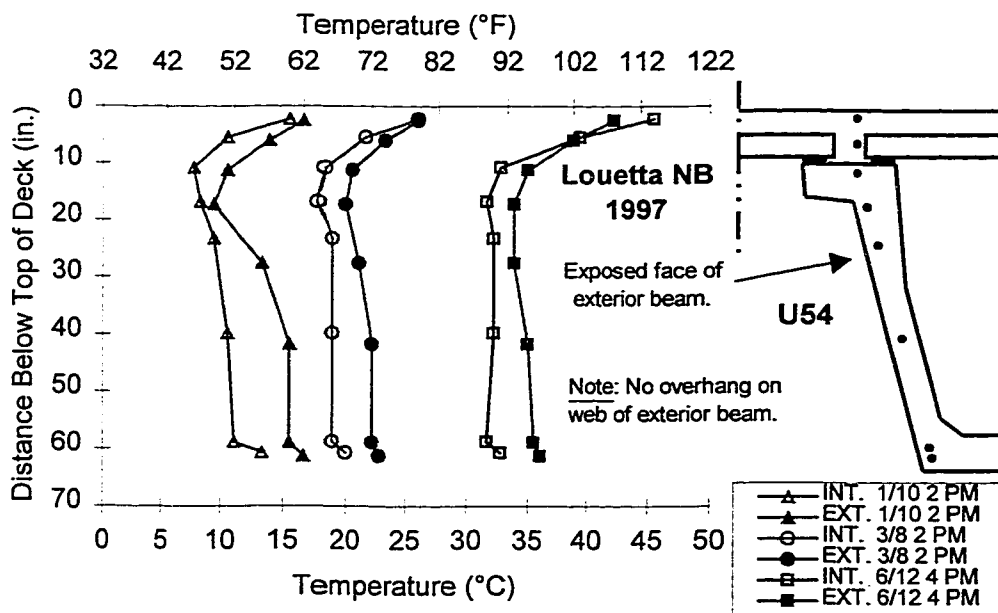


Figure 5.34 - Comparison of Thermal Gradients in Interior and Exterior Beams of the Louetta Northbound Bridge at Various Times

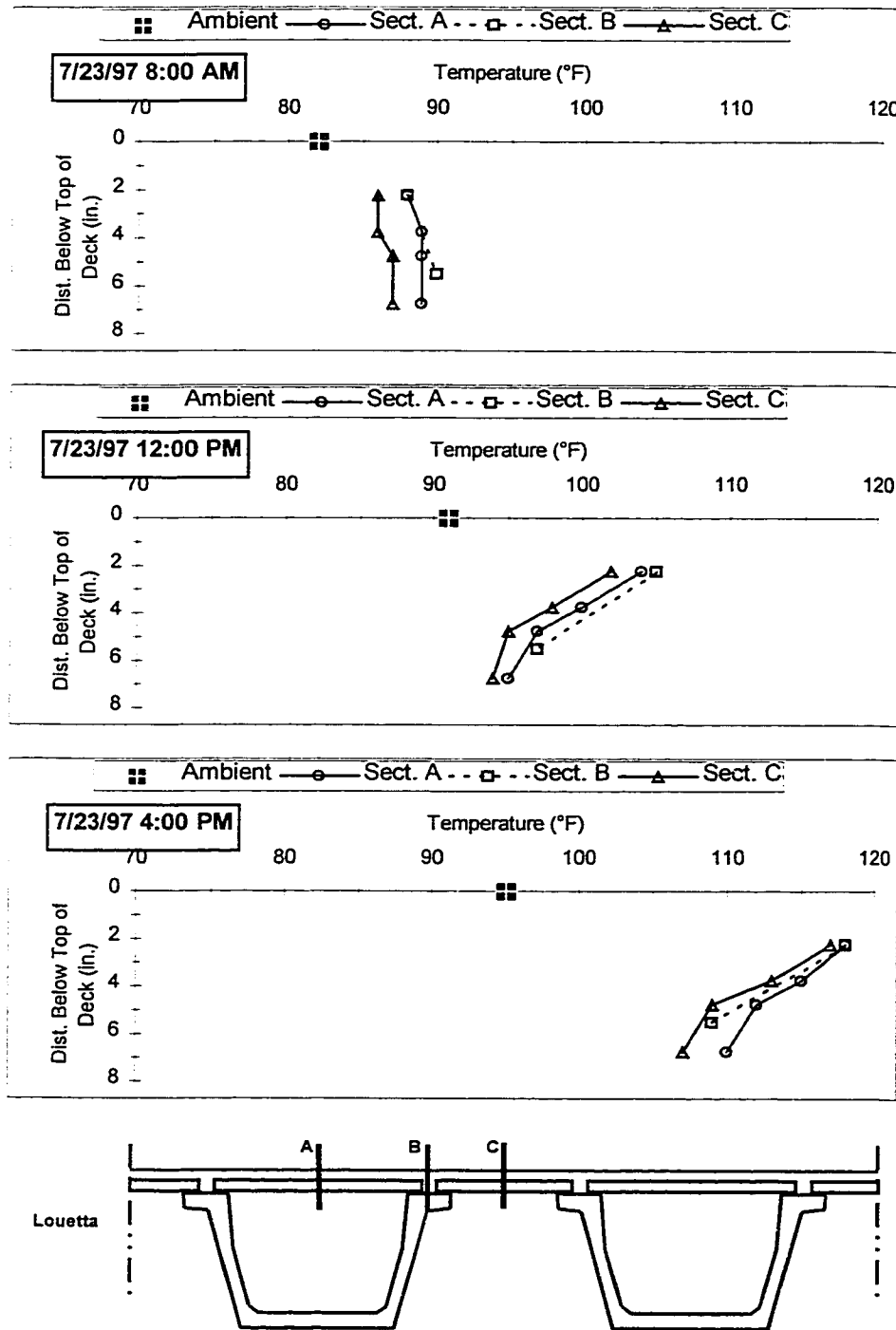


Figure 5.35 - Temperature Profiles at Sections of the Louetta Southbound Cast-in-Place Deck on a Sunny Summer Day

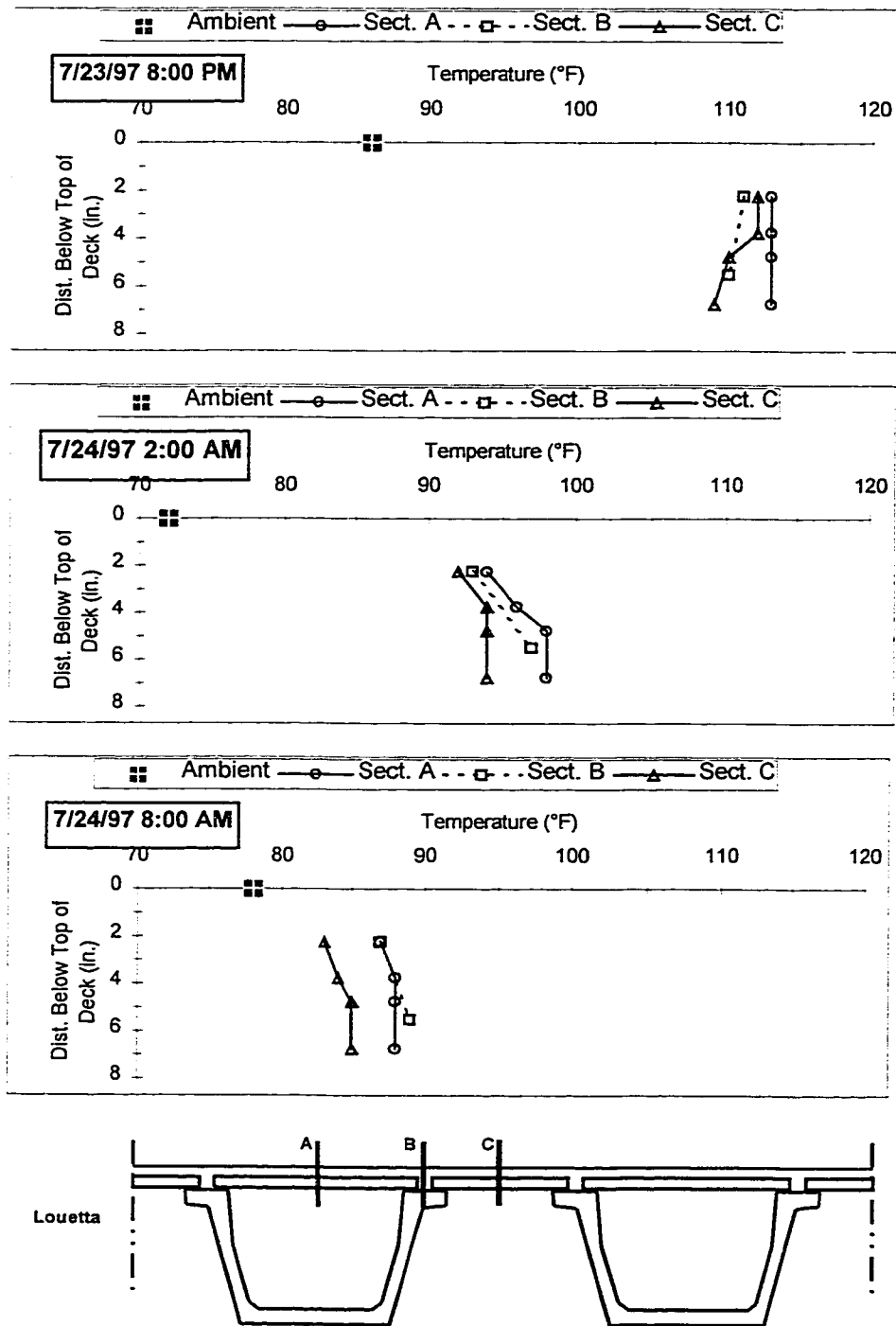


Figure 5.36 - Temperature Profiles at Sections of the Louetta Southbound Cast-in-Place Deck During the Night Following Sunny Summer Day

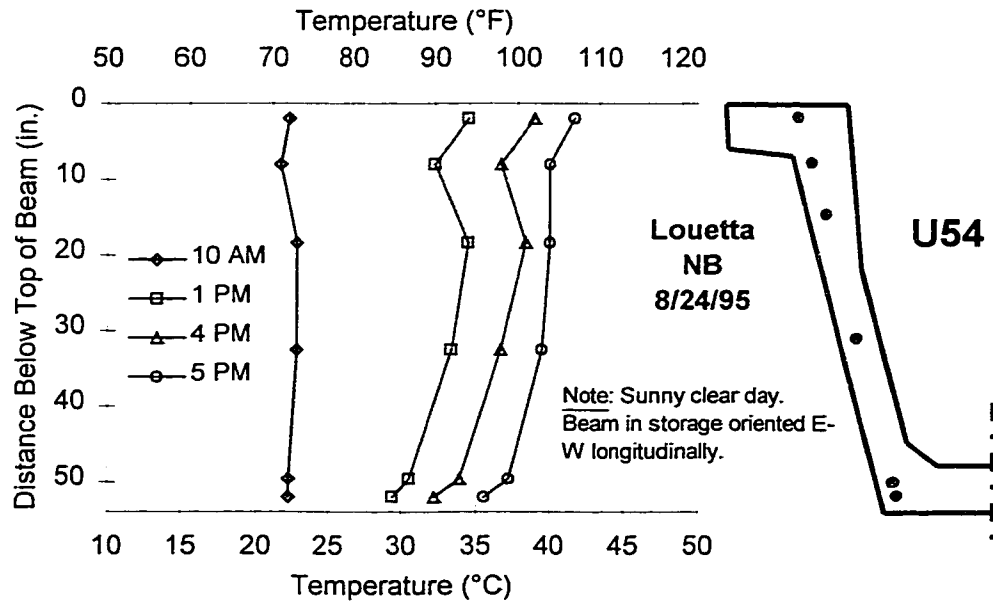


Figure 5.37 - Temperature Gradients in a U-Beam in Storage

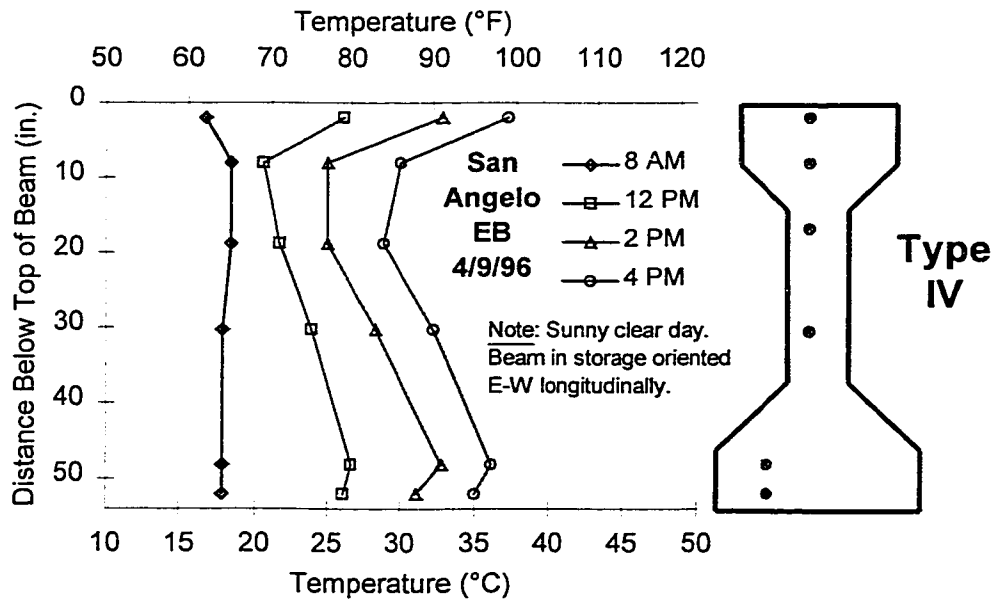


Figure 5.38 - Temperature Gradients in a Type IV Beam in Storage

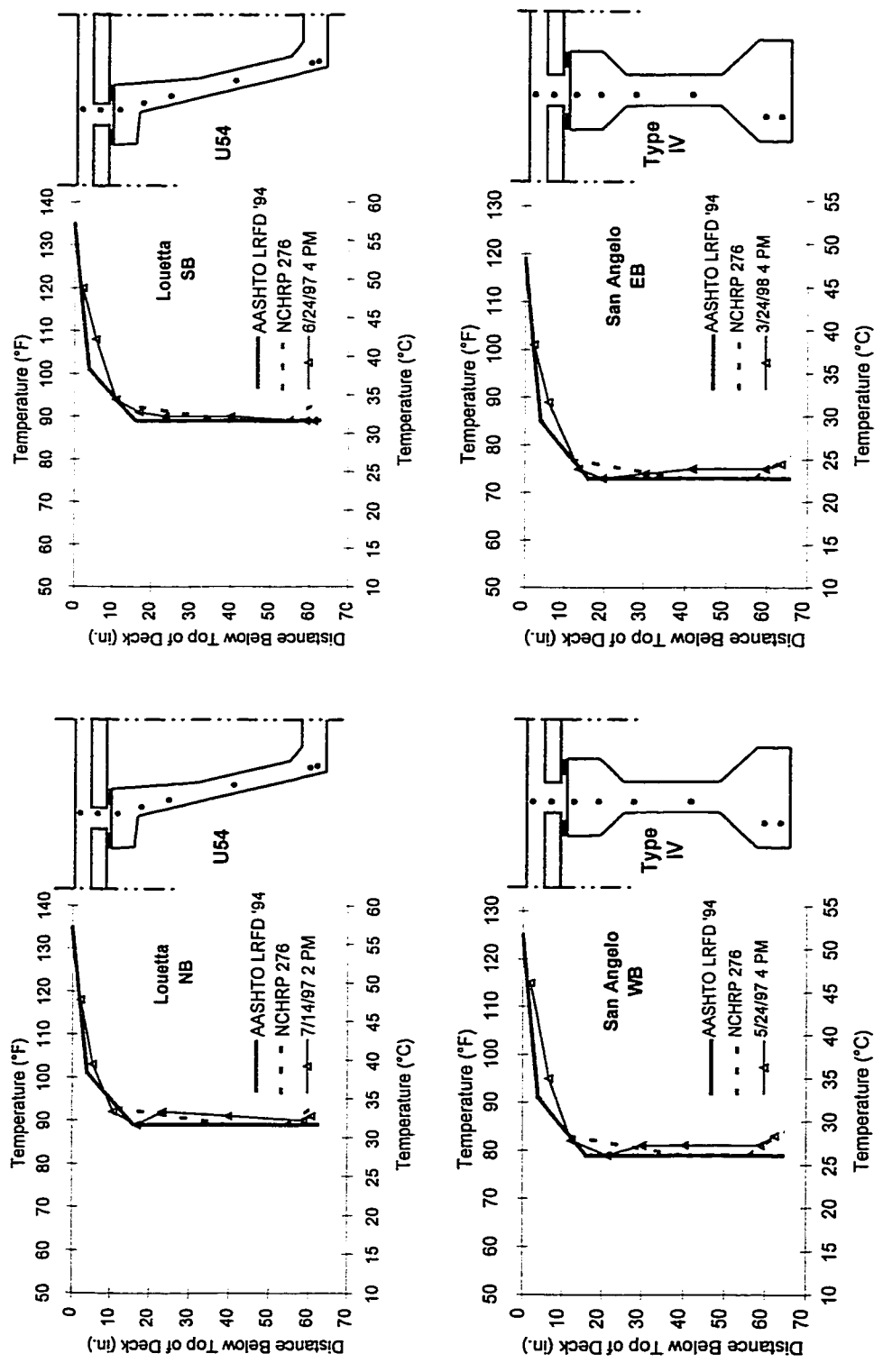


Figure 5.39 - Comparison of Maximum Measured Positive Gradients to Code Design Gradients

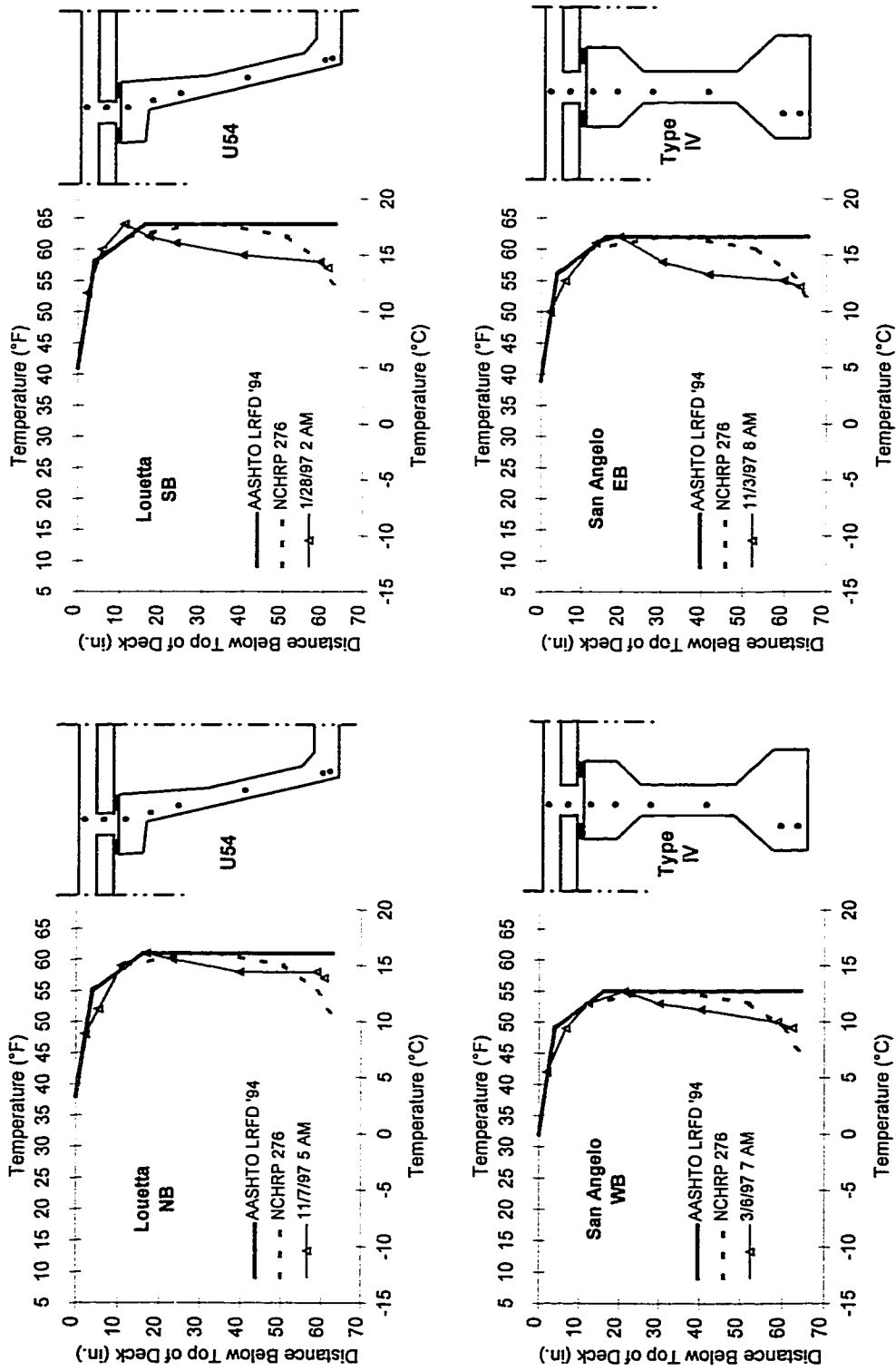


Figure 5.40 - Comparison of Maximum Measured Negative Gradients to Code Design Gradients

Finally, it is important to note that thermal gradients are also present within beams in storage at the precast plant. Typical thermal gradients in beams alone are shown in Figure 5.37 for a Louetta U-beam, and Figure 5.38 for a San Angelo Type IV beam. These gradients are primarily of concern in this research program because they can affect strain and camber measurements in beams in storage. However, it should also be noted that thermal gradients in beams alone can affect grade measurements on erected beams. The effects of thermal gradients in beams alone is discussed in various parts of Chapters 6, 7, and 8.

5.4.3 Discussion

Maximum and minimum gradients measured in each of the four bridges are compared in Figure 5.39 and Figure 5.40, respectively, to the NCHRP 276 [65] and AASHTO LRFD [1] design gradients described in Section 5.4.1. For positive gradients, the “base” temperature for the design gradients was arbitrarily taken as the minimum measured temperature at the time of the peak gradient. Similarly, the “base” temperature for the design negative gradients was taken as the maximum measured temperature at the time of the peak gradient.

It can clearly be seen in Figure 5.39 that the maximum measured positive gradients are reasonably similar in shape to the design positive gradients specified by NCHRP and AASHTO. The main difference is that the temperature at the lower deck gauge (located 146 to 171 mm [5.75 to 6.75 in.] below the deck surface) was underestimated by the design gradients in all cases. This difference ranged from 2 to 5 °C (4 to 9 °F) for the four bridges. Temperatures at the top gauge (located 51 to 57 mm [2.00 to 2.25 in.] below the deck surface) were also underestimated, although the difference was generally less than at the lower deck gauge. Differences at the top deck gauge ranged from 1 to 4 °C (1 to 7 °F). Unfortunately, temperatures at the deck surface could not be compared because measurements were not made at the actual deck surface.

As can be seen in Figure 5.40, the shape of the negative measured gradients in each of the four bridges were somewhat different from the design negative gradients. The measured maximum negative gradients included a relatively linear temperature decrease between the top flange of the beam and the bottom flange. The difference in temperature

between the top and bottom flanges ranged from 2 to 4 °C (4 to 8 °F). The measured temperature differences in the deck, on the other hand, showed good correlation with the temperatures computed using the design gradients. In only one case did the difference between these temperatures exceed 1 °C (1 °F).

In light of the observations discussed in the preceding paragraphs, slight modifications to the *AASHTO LRFD* design gradients can be suggested. These changes are suggested only for pretensioned concrete slab-and-girder highway bridges in Texas with standard cross-sections and no topping, and are merely intended to be refinements to the existing design gradients. Of course, data from other bridges is needed to verify these slight changes, and the many variables discussed in Section 5.4.1 may lead to quite different gradients.

The recommended design gradients are shown in Figure 5.41. Note that the negative gradient includes a linear temperature change through the lower portion of the section. The temperature at a depth of 100 mm (4 in.) has also been changed in the recommended positive gradient. From the results of this study alone, there is not a sufficient basis for changing the temperatures at the deck surface, especially since temperatures were not actually measured at the deck surface. If the temperature in the deck is assumed to vary linearly with depth, then the “projected” temperature at the deck surface (based on measured temperatures) might be slightly lower than the temperature specified by the code design gradients. However, if the temperature varies nonlinearly through the depth of the deck, then the “projected” temperature might actually be equal to or greater than the temperature specified by the code design gradients.

The theoretical thermal stresses and strains resulting from the maximum measured positive gradient in composite beam E25 are shown in Figure 5.42. The method used in this analysis was described in Section 5.4.1. Temperature differences were taken between the 8:00 AM reading on the day of the maximum positive gradient (representing the most uniform temperature distribution measured that day) and the 4:00 PM reading (time of the maximum gradient). The measured strains over this time period in Beam E25 are also shown in Figure 5.42, and can be seen to correlate reasonably well with the calculated strains. A positive curvature clearly develops in the section as a result of the positive gradient, and causes a theoretical upward (simply-supported) camber of 15 mm (0.60 in.). The self-equilibrating thermal stresses computed for the maximum positive gradient in Beam E25 consist of compressive stresses at the bottom fiber of the beam and top of the

deck slab, and tensile stresses at the top fiber of the beam. This situation is typical and is a direct result of the shape of the fully-restrained stress profile, which itself is dependent on the shape of the positive gradient.

The theoretical self-equilibrating thermal stresses calculated from the maximum measured gradients in each bridge can be seen in Figure 5.43. Stresses resulting from unfactored live load (plus impact) are also shown for comparison. In the case of the positive gradient, the thermal stresses actually offset the live load stresses at the extreme fibers of the beam. While the thermal stresses may be additive to the existing dead load stresses in the absence of live load, they are relatively small in magnitude and unlikely to cause any distress. This is especially true in unshored construction, where the dead load stresses resulting from the deck loads are acting on the beam alone and are relatively large. Thermal stresses resulting from the positive gradient may also induce additional compression at the top of the slab, but this location is rarely critical in design if unshored construction is used. Thermal stresses resulting from negative gradients are additive to live load stresses at the extreme beam fibers, but these stresses also tend to be very small in magnitude. Tension was developed at the top of the slab as a result of negative gradients, but in no case did this stress exceed 1.7 MPa (250 psi).

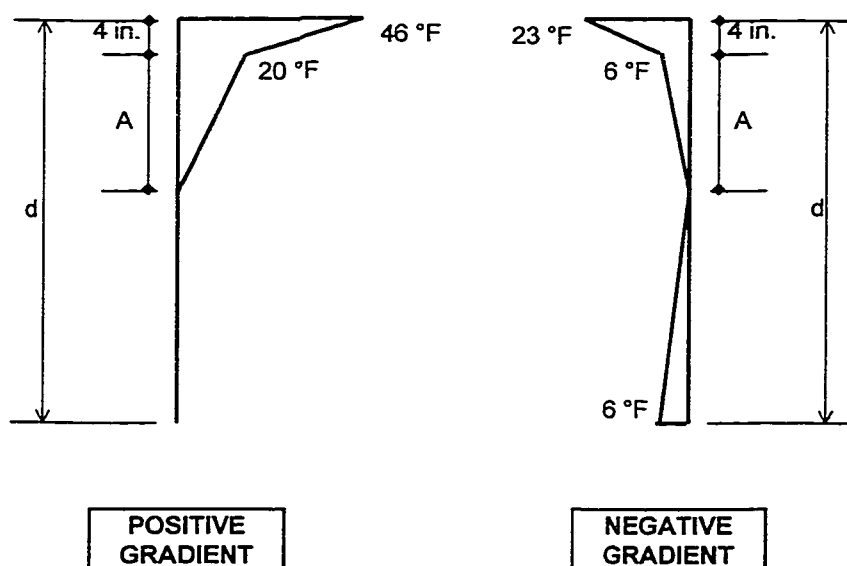


Figure 5.41 - Recommended Design Gradients for Concrete Highway Bridges in Texas (with No Topping)

P = 617 kips
M = 536 ft.-kips
 $\delta = 0.60$ in.

Composite Beam E25 - 3/24/98 (8:00 AM to 4:00 PM)
 Note: Compressive stresses and strains positive, tensile stresses and strains negative.

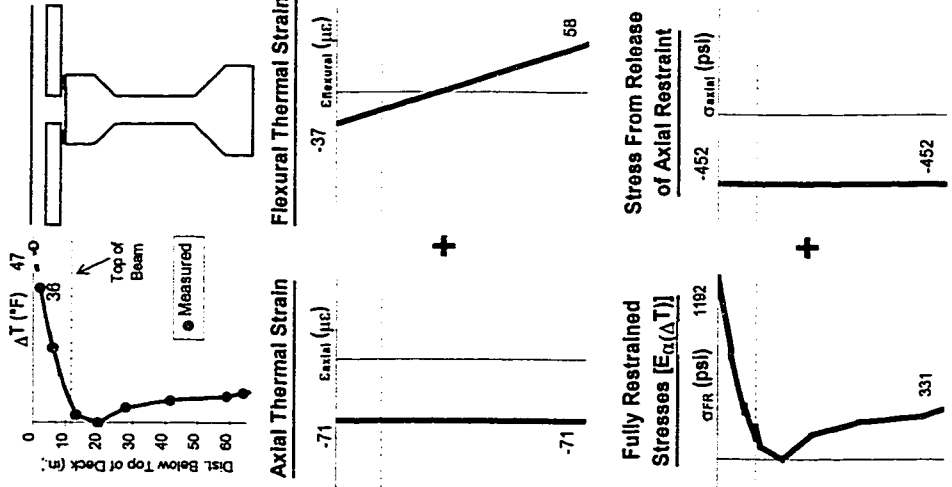


Figure 5.42 - Response of Composite Beam E25 to Maximum Positive Gradient (Relative to 8:00 AM Same Morning)

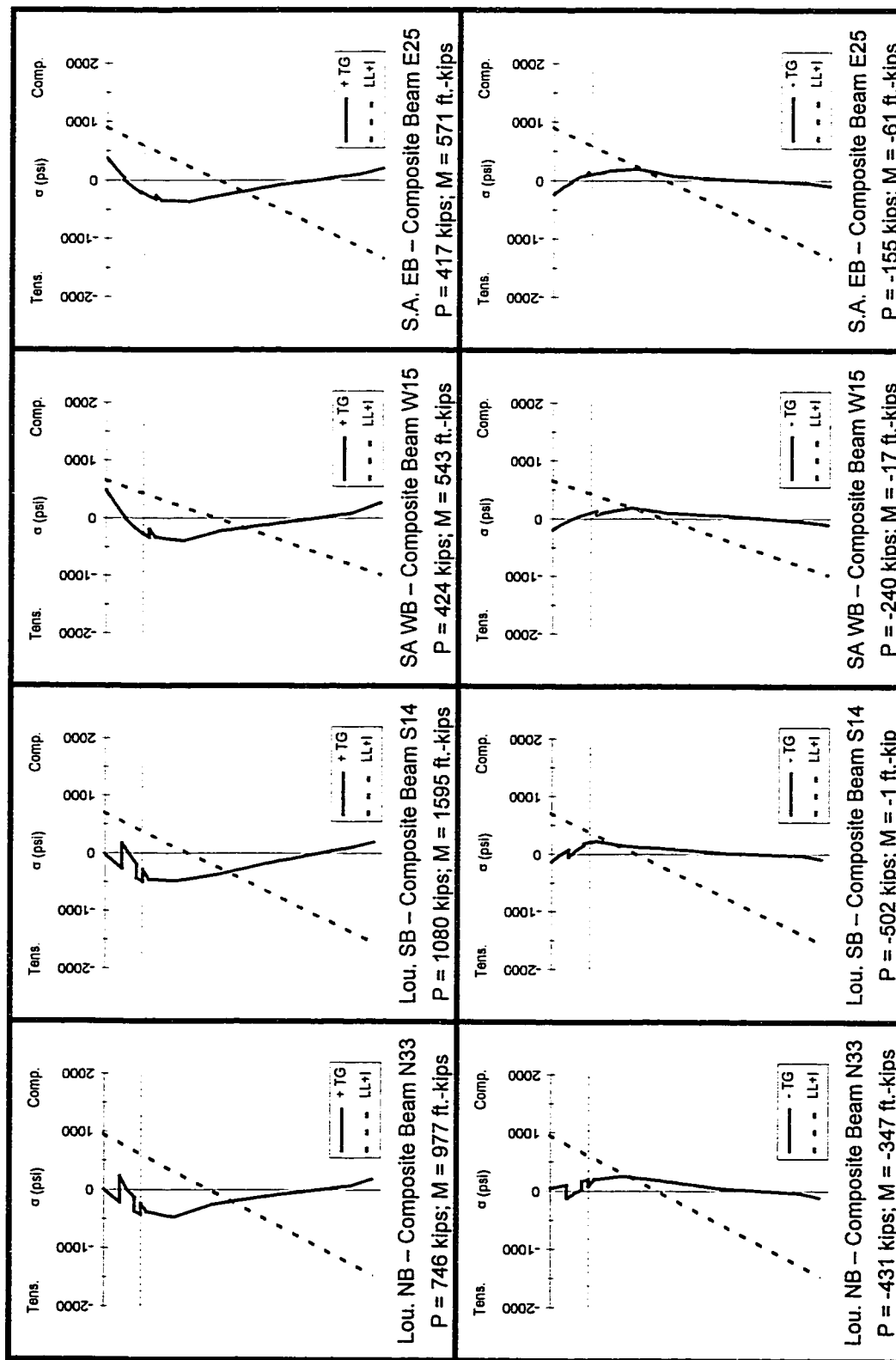


Figure 5.43 - Thermal Stresses Calculated From Maximum Measured Gradients

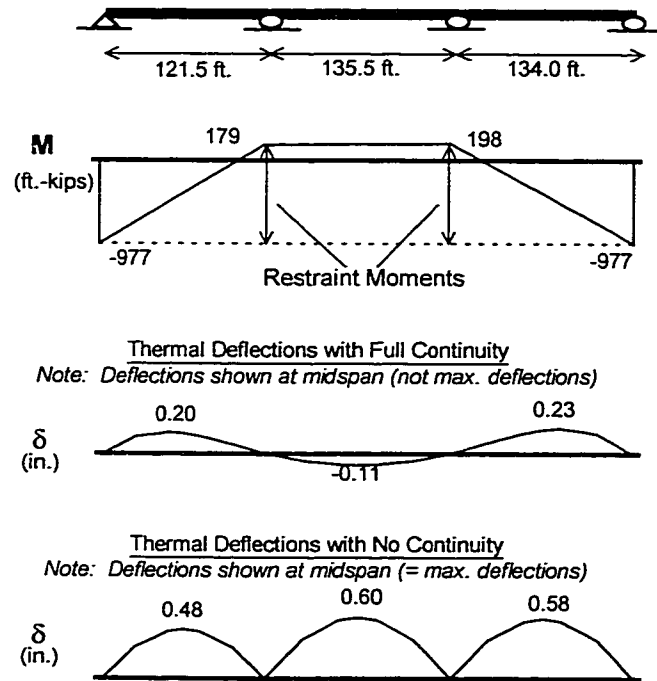


Figure 5.44 - Thermal Moments and Deflections in a (Fictitious) Continuous Louetta Northbound Bridge

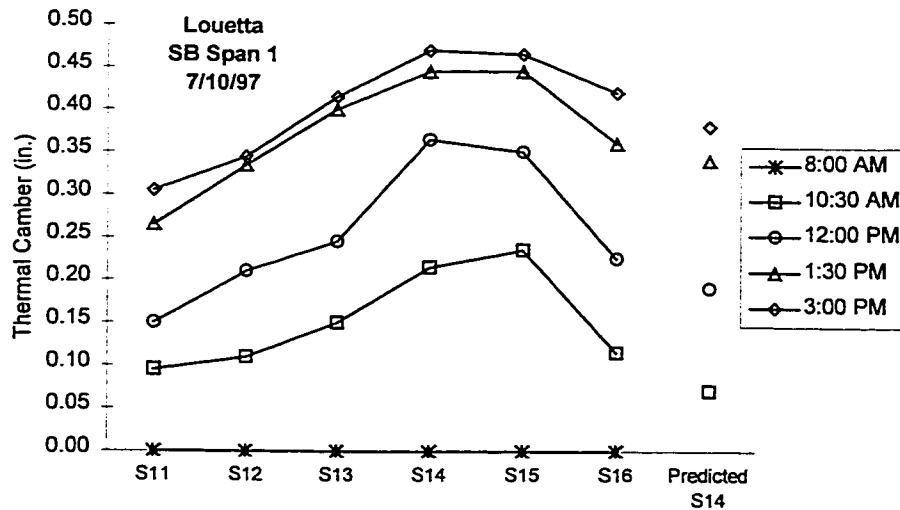


Figure 5.45 - Measured and Predicted Thermal Camber in Louetta Southbound Bridge on Day of Live Load Tests

Self-equilibrating thermal stresses are more likely to be of significance in shored construction. In this situation, the top fiber of the deck will be in compression from dead load, and there is a greater possibility that the stress at the top fiber of the deck will govern design. The compressive stress resulting from the positive gradient is thus more likely to cause the total stress at the top fiber of the deck to be greater than the allowable compressive stress. This is one case where the compressive strength of HPC, or high-strength concrete to be more precise, may be of some use in bridge decks.

In a continuous bridge structure, secondary moments will also be developed as a result of thermal gradients. Measured deflections and strains clearly indicated that none of the bridges in this study behaved as continuous structures, despite the poor-boy continuity used in the Louetta bridges and discussed in Section 2.2.1. Still, it is useful to examine the secondary moments that would be developed in continuous structures based on the measured maximum gradients. Moments and deflections that would occur in a continuous Louetta Northbound bridge are shown in Figure 5.44. The large positive restraint moment in the interior span is quite large in magnitude, and should be considered in design because it is additive to the positive live-load moment. The impact of continuity on thermal deflections is also quite significant, and can be seen in Figure 5.44

The basic thermal deflection behavior of Span 1 of the Louetta Southbound bridge, as measured at various times on the day of live load testing, can be seen in Figure 5.45. All camber measurements shown in the figure are relative to baseline measurements taken at approximately 8:00 AM. The bridge clearly cambers longitudinally as the deck heats up, but differences in camber were also observed across the span at each set of measurements. These differences are probably attributable to the changes in beam length across the span (see Table 2.4), as well as a transverse camber developed in the deck as it heats up. Longer beams (S14, S15, S16) would tend to camber more longitudinally, and a transverse camber would cause more camber in the interior beams. Note that in general, the predicted (simply-supported) camber for Beam S14 based on the method discussed in preceding paragraphs is reasonably close to the average camber across the span. The effects of thermal gradients on camber and deflection are also addressed in Chapter 8.

Some cracking was observed in the decks of the completed Louetta bridges, especially the Southbound bridge, and it is *possible* that thermal effects played some role. It is not thought that the magnitude of the thermal stresses associated with the maximum gradient were excessive. However, a (theoretical) stress discontinuity in the deck for the

Louetta bridges can be seen in Figure 5.42. This discontinuity results from the layered construction of the deck, and the fact that there was a significant difference in the coefficient of thermal expansion of the precast deck panels and cast-in-place deck (see Table 4.25). The coefficient of thermal expansion of the precast panels is substantially higher, such that as the panels try to expand they are restrained by the cast-in-place portion of the deck. If the difference in expansion is sufficient, the cast-in-place layer of the deck may be in enough tension that cracking develops.

Despite the prevailing feeling among designers that thermal gradients are irrelevant in the design of pretensioned concrete bridges, thermal gradients should probably be considered in the design of *all* concrete highway bridge structures. The specific effects of thermal gradients vary greatly depending on the construction technique. Thermal stresses are likely to be small when simply-supported, unshored construction is utilized. However, corresponding deformations in such structures may be quite large, especially if longer spans and larger girder spacings are used in conjunction with HPC. If unshored construction is used, stresses resulting from positive thermal gradients should be examined at the top of the deck. Secondary moments resulting from thermal gradients in continuous bridges should always be considered in the design process. In all cases, the effects of thermal gradients are largely related to serviceability issues, and not strength issues. Load factors of 1.0 for serviceability and 0.5 for strength are therefore recommended for continuous and/or unshored construction in pretensioned bridges. Lower load factors are more appropriate for simply-supported, unshored construction.

5.5 Summary and Conclusions

The following observations were made in this chapter regarding Hydration Temperatures:

- 1) Ambient conditions, especially ambient temperature and solar radiation, have a significant effect on the hydration temperature behavior of prestressed beams, precast deck panels, and cast-in-place bridge decks. The shape of all phases of the hydration temperature curve, including the dormant and cooling period, can be affected.

- 2) The maximum hydration temperatures recorded in nine HPC beams monitored during this study ranged from 55 to 70 °C (131 to 158 °F). The corresponding maximum temperature rise after the end of the dormant period ranged from 28 to 33 °C (50 to 60 °F).
- 3) The maximum temperature in Type IV beams was typically recorded at a gauge located near the centroid of the top flange. A maximum temperature location could not be identified in U-beams, although it is believed that the maximum temperature typically occurs in the upper portions of the section.
- 4) The temperature rise of 4.2 to 4.9 °C per 59 kg/m³ (7.5 to 8.9 °F per 100 lb/yd³) of cement (or 2.8 to 3.4 °C per 59 kg/m³ [5.1 to 6.1 °F per 100 lb/yd³] of total cementitious material) observed in HPC beams is significantly less than the temperature rise suggested by ACI Committee 363 [10] for high strength concrete.
- 5) A significant gradient developed in HPC beams during hydration, with the top of the section warmer than the bottom. The magnitude of the gradient ranged from 11 to 16 °C (19 to 29 °F) for Type IV beams and 6 to 8 °C (10 to 14 °F) for U-beams.
- 6) Hydration temperatures of up to 95 °C (203 °F) were measured in the skewed end blocks of Louetta HPC U-beams. Cracks were observed across the full cross-section in most U-beams at the location where the skewed end block meets the standard U-shaped cross-section, although these cracks closed after release.
- 7) Ambient conditions, time of placement, retarder dosage, and curing method affected measured hydration temperatures in HPC and non-HPC precast deck panels.
- 8) Ambient conditions before and during hydration were observed to have a significant influence on the hydration behavior of cast-in-place bridge decks. In particular, the ambient temperature, solar radiation, and temperature of the beams prior to placement of deck concrete can have a significant impact.
- 9) Where non-HPC components were monitored, large differences between the hydration temperature behavior of HPC and non-HPC components were not observed. In general, ambient conditions and other factors appeared to have as much influence as concrete composition.

The following observations were made in this chapter regarding Average Bridge Temperatures:

- 1) Bridge temperatures were recorded continuously for a one year period in each of the four bridges. Maximum temperatures are summarized in Table 5.6, and minimum temperatures are summarized in Table 5.7.
- 2) In three of the four bridges studied, the daily maximum average bridge temperature during summer months was observed to be greater than the daily maximum ambient temperature by up to 5 °C (9 °F). During the winter months, the difference between these temperatures was found to be negligible.
- 3) Trends regarding maximum temperatures in the Eastbound San Angelo bridge were observed to be different than for the other three bridges. Daily maximum average bridge temperatures were found to be lower than daily maximum ambient temperatures during the winter, and about equal during the summer. It is unclear whether this is a result of different material (thermal) properties, concrete age, moisture content, structural layout, or other factors.
- 4) Daily minimum average bridge temperatures were observed to be up to 7 °C (12 °F) greater than the minimum ambient temperatures in winter, and up to 9 °C (17 °F) greater during the summer. During periods of extended cold, these temperatures were approximately equal.
- 5) The absolute maximum average bridge temperature recorded for each bridge during the study was typically about 2 °C (4 °F) higher than the maximum monthly average (recorded during July). The absolute minimum average bridge temperatures were observed to be up to 12 °C (22 °F) lower than the minimum monthly average bridge temperatures (typically recorded during December or January).
- 6) Direct differences in behavior resulting from the use of HPC could not be identified in this study. It should be noted however, that the larger girder spacings resulting indirectly from the use of HPC can result in higher maximum average bridge temperatures. This can be attributed to the higher contribution of the deck temperature in calculation of the average bridge temperature.

- 7) The extreme temperatures (or temperature changes) specified in the *AASHTO Standard Specifications* [3] and *AASHTO LRFD Specifications* [1] did not accurately reflect the extreme temperatures measured in this study. The site-specific extreme temperatures recommended in the NCHRP Report 276 [65] were more accurate, but still quite unconservative.

The following observations were made in this chapter regarding Thermal Gradients:

- 1) Thermal gradients were measured for a one year period in each of the four bridges. Maximum positive thermal gradients in the four bridges ranged from 16 to 20 °C (28 to 36 °F). Maximum negative thermal gradients in the four bridges ranged from 6 to 7 °C (11 to 13 °F). These measurements are based on top deck gauges located between 51 and 57 mm (2.00 and 2.25 in.) below the deck surface.
- 2) Maximum positive gradients varied day to day, but were generally highest during the summer months. The maximum positive gradient typically occurred between 12:00 PM and 2:00 PM during the winter, and between 2:00 PM and 4:00 PM (daylight time) during the summer.
- 3) Maximum negative gradients varied day to day throughout the entire year, and were not highest during any particular season. The maximum negative gradients observed over the study period tended to be associated with the passage of cold fronts. Maximum negative gradients typically occurred during the early morning hours, but the exact time was highly variable.
- 4) The design positive gradients suggested by NCHRP 276 [65] and *AASHTO LRFD* [1] underestimated the temperatures measured at two depths of the deck. Otherwise, the shapes of the measured and design positive gradients were similar. No specific conclusions can be made about the magnitude of the gradient at the very top of the deck, because measurements were not actually made at the deck surface.
- 5) The shape of the measured and design negative gradients differed in that the temperature in the beam was found to be approximately linear rather than uniform. With respect to temperatures through the depth of the deck, the design and measured negative gradients correlated very well. No specific conclusions can be made about the

magnitude of the gradient at the very top of the deck, because measurements were not actually made at the deck surface.

- 6) At the extreme fibers of beams, self-equilibrating stresses calculated from maximum positive gradients were found to act opposite in sign to live load stresses. Negative gradients were found to cause stresses that are additive to live load stresses, but these stresses were very small in magnitude.
- 7) At the top of the deck slab, compressive stresses of less than 3.5 MPa (500 psi) were calculated based on maximum positive gradients. Tensile stresses of less than 1.7 MPa (250 psi) were calculated based on the maximum negative gradients.
- 8) Large secondary moments would result in typical continuous bridge structures as a result of the maximum gradients observed in this study.
- 9) Measured strains and beam cambers agreed reasonably well with predicted values based on analyses using the thermal gradients measured in this study.
- 10) Deck cracking observed in the completed Louetta bridges may be due in part to the different coefficients of thermal expansion for the deck panels and cast-in-place deck segments. In this case, differential expansion would lead to tensile stresses in the cast-in-place portion of the deck, and possibly, cracking.
- 11) The temperature profile and thermal gradients in exterior beams were observed to be quite different from those in interior beams under certain conditions. Bridge orientation, the angle of the sun in the sky (i.e. time of year), and width of deck overhang can all have a significant influence on thermal behavior in exterior beams.
- 12) Small horizontal temperature gradients were observed between deck sections located directly above beams and sections located between beams. Sections between beams typically cooled to lower temperatures overnight, but the temperature difference between sections was generally no more than 3 °C (5 °F).
- 13) Significant thermal gradients were also found to be present within beams in storage at the precast plant.

5.6 Recommendations

The following recommendation is made on the basis of the information presented in this chapter regarding Hydration Temperatures:

The use of massive skewed end blocks, such as those in the Louetta U-beams, is discouraged, especially with the use of HPC. Temperatures in these end blocks can become very high during hydration, and heat dissipation is quite slow. Cracks have been observed, and are likely to develop in future beams using these end blocks, at the location where the end block meets the regular U-shaped section. Microcracking is also a strong possibility in these end blocks. Where bridge geometry calls for skewed beam ends and U-beams are being utilized, the use of Styrofoam voids and a constant-thickness end block should be considered.

The following recommendations are made on the basis of the information presented in this chapter regarding Average Bridge Temperatures:

In general, the recommendations of Section 3.12.2 of the *AASHTO LRFD Specifications* [1] should be considered in the design of highway bridges for uniform axial movements associated with changes in temperature. However, the design extreme temperatures specified in Table 3.12.2.1-1 of the *LRFD Specifications* for concrete bridges should be replaced by Equation 5.1 and Equation 5.2, which allow for calculation of extreme design temperatures on a site-specific basis.

$$T_{\text{design,max}} = \frac{1}{2}(T_{\text{July,max}} + T_{\text{all-time,max}}) + 5^{\circ}\text{F}$$

Equation 5.1

$$T_{\text{design,min}} = \frac{1}{2}(T_{\text{Jan,min}} + T_{\text{all-time,min}})$$

Equation 5.2

Setting temperature should be estimated in accordance with Section 3.12.2.2 of the *LRFD Specifications* [1], or by another appropriate method, and should always be considered in determination of uniform axial bridge movements.

The following recommendations are made on the basis of the information presented in this chapter regarding Thermal Gradients:

Slight modifications are recommended to the NCHRP 276 [65] and *AASHTO LRFD* [1] design gradients based on the measurements made in this study, as shown in Figure 5.41. These gradients are only intended to be used for pretensioned concrete slab-and-girder highway bridges in Texas with standard cross-sections and no topping, and have not been verified by measurements other than those in this study. Many variables, including material properties and exposure conditions, may lead to different thermal gradients.

Thermal gradients should be considered in the design of all concrete highway bridge structures. The specific impact of thermal gradients will depend largely on the construction method. Thermal gradients are also considered to be more important in the service limit states than in the strength limit states. Load combinations found in Section 3.4.1 of the *AASHTO LRFD Specifications* should be considered when designing for the effect of thermal gradients. The following load factors are suggested:

Table 5.10 - Recommended Load Factors for Thermal Gradients

	Service Limit States	Strength Limit States
Continuous bridges and bridges utilizing shored construction	1.0 for deformations 1.0 for stresses	1.0 for deformations 0.5 for stresses
Simply-supported bridges utilizing unshored construction ¹	1.0 for deformations ≤ 1.0 for stresses	1.0 for deformations ≤ 0.5 for stresses
¹ Load factors to be determined on a project-specific basis, but may be taken as less than or equal to load factors specified for stresses in continuous and shored bridges.		

6 CHAPTER SIX: CONCRETE STRAIN MEASUREMENTS

6.1 Introduction

6.1.1 General

This chapter discusses a variety of concrete strain measurements made during this research program. Emphasis is placed on types of measurements related to design calculations, as well as measurements that have a significant influence on the overall structural behavior of the bridges and their components. For the most part, measurements discussed in this chapter are related to prestressed beams at several stages of the construction process. The strain behavior in beams prior to release of prestress is considered first, followed by the elastic response to the release of pretensioning. Next, the time-dependent strain behavior of beams after release, due to creep and shrinkage effects, is discussed. Finally, other elastic responses are examined, including the post-tensioning of the San Angelo Eastbound HPC Type IV beams and the placement of the deck components in the various bridges. Note that the live load response of the composite bridges is not considered in this chapter, but is discussed in Chapter 9.

In certain cases, comparisons are made to predicted concrete *stresses*, because these quantities are of more design importance than concrete *strains*. Since concrete stresses were not measured directly in this instrumentation program, stresses were often estimated by multiplying measured strains by the measured modulus of elasticity. This method is, of course, approximate, and some error is surely introduced as a result of this process. However, this method is clearly the most logical way to make certain comparisons in the absence of direct stress data.

In some sections of this chapter, measured stresses or strains are compared with predicted stresses and strains obtained by two methods. The first method involves the prediction based on standard *design* assumptions, while the second method is a refined method based on *measured* properties. For example, the design method uses a modulus of

elasticity predicted from a design concrete strength using a code equation, while the measured method utilizes the modulus of elasticity determined from tests on companion specimens. Differences between the two methods primarily include the consideration of material properties and section properties, but in some cases the refined method may include the consideration of factors not typically considered in design. The concept of using these two approaches is to examine both the applicability of the design or analysis method, as well as to examine the effects of standard design assumptions. Comparisons using the prediction method based on measured parameters also help to identify certain aspects of structural behavior. Throughout the sections of this chapter, important differences between the two prediction methods are discussed as appropriate. Specific properties for all beams based on both methods can be found in Appendix F.

6.1.2 Interpretation of Gauge Readings

Interpretation of raw strain readings is an important part of the overall data analysis process, and only in a few specific cases can strain readings be used without some correction. Generally speaking, temperature effects on the gauge reading must always be accounted for, even if thermal strains are the primary effect being studied. Thus, a temperature reading at the gauge location is essential for each strain reading. As discussed in Chapter 3, vibrating wire gauges used in this study had a thermistor integrally attached for this purpose. Similarly, when bonded resistance strain gauges were used in this study, a thermocouple was usually placed at the same gauge location for measurement of temperature.

If compressive strains are positive, the following relationship exists between the reported strain ϵ_{gauge} , and the actual strain at the gauge location ϵ_{actual} :

$$\epsilon_{\text{gauge}} = \epsilon_{\text{actual}} + (\alpha_{\text{gauge}} \cdot (T - T_0))$$

Equation 6.1

The second term on the right hand side of Equation 6.1 represents the strain not reported by the gauge. If the gauge itself heats up by a temperature change $(T - T_0)$, then the gauge

wire expands a corresponding amount and reduces the tension in the gauge wire. This appears as an apparent additional compressive strain, hence the *addition* rather than the subtraction of this term in Equation 6.1. This equation can be rearranged to a more useful form, which is shown in Equation 6.2:

$$\varepsilon_{\text{actual}} = \varepsilon_{\text{gauge}} - (\alpha_{\text{gauge}} \cdot (T - T_0))$$

Equation 6.2

Note that Equation 6.1 and Equation 6.2 are technically only correct for vibrating wire gauges, or gauges where the gauge wire itself is free to move and not restricted by the surrounding concrete. However, with a few minor adjustments these equations are also applicable for bonded resistance strain gauges (“sister gauges”). For this type of gauge, this correction method is not perfect in that it does not consider the interrelation of the gauge bar and surrounding concrete. The actual thermal expansion of both the gauge and concrete at the gauge location is equal to the product of the temperature increase and a coefficient of thermal expansion somewhere *between* that of the gauge and the concrete. If the concrete is considered to provide much more resistance to the gauge than vice versa, the coefficient of thermal expansion of the concrete should be used in Equation 6.1 and Equation 6.2.

Fortunately, the gauges used in this research program were thermally compensated, and had coefficients of thermal expansion very similar to those of the various concretes in the beams. The coefficients of thermal expansion of the vibrating wire gauges and bonded resistance strain gauges used in this research program were 11.5 and 11.0 $\mu\varepsilon/^\circ\text{C}$ (6.4 and 6.1 $\mu\varepsilon/^\circ\text{F}$), respectively. Coefficients of thermal expansion for the various concretes used in the two bridges are listed in Table 4.25.

If thermal effects are to be removed, then Equation 6.3 or Equation 6.4 can be used, where ε_{TER} is the strain with *Thermal Effects Removed*:

$$\varepsilon_{\text{TER}} = \varepsilon_{\text{actual}} - (\varepsilon_{\text{thermal,axial}} + \varepsilon_{\text{thermal,flexural}})$$

Equation 6.3

$$\epsilon_{\text{TER}} = \epsilon_{\text{gauge}} - (\alpha_{\text{gauge}} \cdot (T - T_0)) - (\epsilon_{\text{thermal,axial}} + \epsilon_{\text{thermal,flexural}})$$

Equation 6.4

Note that both axial and flexural thermal strains, computed as described in Section 5.4.1, must be subtracted from the actual strain. In other words, the removal of thermal strains must consider the temperature distribution through the entire cross-section, rather than just the temperature at the gauge location. Since even thermally compensated gauges only account for temperature changes at the individual gauge location, strains reported from such gauges should still be corrected using this method.

6.2 Concrete Strains Before Release

6.2.1 Background

Concrete strain behavior before release is generally very complex. Autogenous shrinkage during hydration may cause a small contraction, while increasing (hydration) temperatures lead to concrete expansion. The concrete then begins to contract as it cools from the peak hydration temperatures. In addition, drying shrinkage can also lead to significant contraction after forms are stripped. The magnitude of this expansion and contraction (i.e. tensile and compressive strain) is highly variable in a structural member, and is dependent on several factors including hydration temperature distribution in the member and level of restraint provided by the formwork. These factors are, of course, dependent on several other factors including (but not limited to) mix proportions, curing method, ambient conditions, and size and shape of the member.

Although rarely considered in design, concrete strain behavior prior to release can have a large impact on several aspects of behavior for prestressed beams. Strains and strain gradients may cause temporary or permanent deformations in a structural member. Depending on the time at which bond between the strand and the concrete occurs, prestress force in pretensioned members may also be affected by these strains. Finally, if

the contraction of a concrete member is restrained prior to release, cracking may develop through the cross-section at points along the length of the member.

6.2.2 *Measurements*

Concrete strains were measured prior to release for several beams. Strains were measured using either vibrating wire gauges or bonded resistance strain gauges, and were recorded at 5 to 20 minute intervals from the placement of concrete to just before release. In general, measurements were recorded for the same beams in which hydration temperatures were monitored. Measurements of hydration temperatures in beams are discussed in Section 5.2.2, and summarized in Table 5.1. Gauges were typically placed at six different depths in each beam for both strain and temperature measurements. These six gauge locations are discussed in detail in Section 3.4.2.

Early-age strain behavior was quite variable in the nine beams for which measurements were recorded, but some basic trends can be identified. Most aspects of the behavior for Beam E35, which is shown in Figure 6.1, are typical of the behavior observed in all monitored beams. Strains shown in Figure 6.1 are relative to "baseline" strain readings taken just after placement of concrete. Note that Beam E35 was one of the San Angelo HPC beams which was released two days after casting as opposed to the standard one day casting-release cycle.

During the dormant period of hydration, for approximately 6 hours after the concrete is placed, there appears to be a slight expansion of the beam concrete (i.e. increase in tensile strain). As the main hydration cycle occurs and temperatures increase over the next several hours, the beam concrete also expands. However, the expansion is substantially less than the free thermal strain ($E\alpha\Delta T$) corresponding to the increase in temperature. This would imply some restraint from the formwork against expansion of the beam concrete, and perhaps some autogenous shrinkage offsetting the expansion. It is also important to note that the expansion is greatest at the top of the beam, where temperature increases are highest (as described in Section 5.2).

As can be seen in Figure 6.1, there is a contraction corresponding to the cooling of the beam from the peak of hydration. This contraction continues as the beam cools slowly on the bed, and is probably increased by drying shrinkage of the hardened concrete. Note

that in the upper portions of the member, there is a net compressive strain relative to the time of placement of concrete. The net compressive strain is reasonably large in the case of Beam E35, which was not released until two days after casting. The contraction at the bottom of the member is clearly much smaller than at the top, indicating the presence of restraint. The bed liner probably provides much of the restraint at these lower levels, since the weight of the beam leads to a high frictional force between the beam and the liner. Of course, the side forms (prior to their removal) and unreleased strands provide additional restraint.

Similar early-age strain behavior can be seen in Figure 6.2 for Beam E26. Note that for this beam, which was also released two days after casting, a temperature peak also occurred during the second day. As can be seen in the figure, this second temperature increase tended to offset any contraction due to shrinkage. As the beam began to cool after this second temperature peak, a crack developed through the depth of the beam at the location of the gauges. This cracking is evidenced by the sudden apparent increase in tensile strain shown by the gauges in Figure 6.2, and indicates the presence of restraint against shortening of the entire cross-section. Note that the cracks were found to extend through the full depth of the section, but were very small in width at the bottom flange. This cracking is discussed in more detail in Section 6.2.3.

The early-age strain behavior observed on other monitored beams was similar in that the top of the beam usually expanded more (i.e. showed a higher tensile strain) than the lower portions of the beam during hydration. The magnitude of tensile strains developed during hydration was highly variable, but was always substantially less than the free thermal strain ($E\alpha\Delta T$) corresponding to the appropriate temperature increase. Most beams showed a net shortening in the upper portions of the beam, and evidence of significant restraint in the lower portions of the beam. Cracking was observed to affect strain measurements in four monitored beams, but cracking was observed on almost all beams. In many beams, the cracking simply did not coincide with the longitudinal location of the embedded gauges such that a large discontinuity did not occur in the strain measurements.

6.2.3 Discussion

An idealized model of the strain behavior in beams before release, in terms of strain profile over the depth of the beam, is shown in Figure 6.3. This simple model is based on the strain-time profiles similar to those shown in Section 6.2.2, and is only intended to describe general behavior patterns. The model is applicable to all types of prestressed beams examined in this research program (U-beams and I-beams, HPC and non-HPC), although the magnitudes of strain may vary among these beam groups.

A small tension may or may not develop in the beam during the initial (dormant) period of hydration, depending on ambient conditions at placement. The temperature in the beam then increases during hydration, more toward the top of the beam than toward the bottom, and a similar strain gradient is developed. The magnitude of these strains is substantially less than the free thermal strains ($E\alpha\Delta T$), because the formwork provides restraint against the expansion. Autogenous shrinkage also tends to offset this expansion somewhat. The concrete then contracts as it cools, although the magnitude of this contraction is also affected by restraint from the formwork. As the beam cools, a slight net compressive strain may exist, although the exact strain through the depth of the cross-section is dependent on many factors. Either a net positive or net negative curvature may exist at this stage. If the beam is not released at this point, it continues to contract as it cools. Drying shrinkage also adds to the compressive strain in the hardened beam, especially after forms are removed. The bottom portions of the beam typically do not exhibit as much strain as the top portions because of restraint from the bed liner and unreleased strands. However, restraint may exist through the entire depth of the beam, and if substantial enough, may cause cracking.

There are several consequences resulting from this idealized strain behavior before release, especially with respect to measurements made in this research program. These consequences will be discussed in later sections of this chapter and in other chapters as appropriate, but are mentioned briefly here. First, the presence of restraint on the beam prior to release means that the set of "zero" or "baseline" readings for strain measurements is not taken at a stress-free condition. The readings taken just after release thus include the effects of prestressing, member self-weight, and release of restraint. Second, depending on when bond between the concrete and the strand occurs, prestress losses may be affected

by the concrete strains during hydration. Finally, the development of strain gradients (i.e. curvatures) during hydration and before release may affect the camber and deflection behavior of beams.

As mentioned in Section 6.2.2, cracking was observed on almost all instrumented beams as a result of the restraint provided by the bed against contraction due to cooling and drying shrinkage. A sketch of the typical cracking pattern can be seen in Figure 6.4, and an actual crack can be seen in Figure 6.5. This type of cracking was observed on all types of beams, including Louetta HPC U-beams, San Angelo HPC Type IV beams, and San Angelo non-HPC Type IV beams.

Crack width and spacing (just prior to release) were recorded on the nine San Angelo HPC Type IV beams that were cast in the spring of 1997. These measurements are summarized in Table 6.1. Crack widths were recorded at three vertical locations for each crack using a crack comparator, as shown in Figure 6.6. The three locations were 25 mm (1 in.) below the top of the beam, mid-depth of the web, and 150 mm (6 in.) above the bottom surface of the beam (approximately c.g. of pretensioned strands). Note that crack width and spacing was not recorded for Louetta HPC U-beams or San Angelo non-HPC Type IV beams, but this type of cracking was observed in these beams as well.

It is clear from the measurements presented in Table 6.1 that cracks were much larger at the top of the beams than at the bottom. This implies that restraint was probably not relieved at the bottom of the beam by the cracking, where the bed liner and strands both provide restraint even after removal of side forms. It should also be noted that cracking still developed in Beams E13 and E14, which were the only San Angelo HPC beams (cast in the spring of 1997) that were released at one day after casting. Furthermore, cracks in these beams were much larger, although the spacing between cracks in these beams was also much greater. This indicates that there is sufficient restraint developed during the initial cooling period such that cracking may occur during the first day, and that *additional* cracking may develop if the beam is left on the bed for a longer period of time before release.

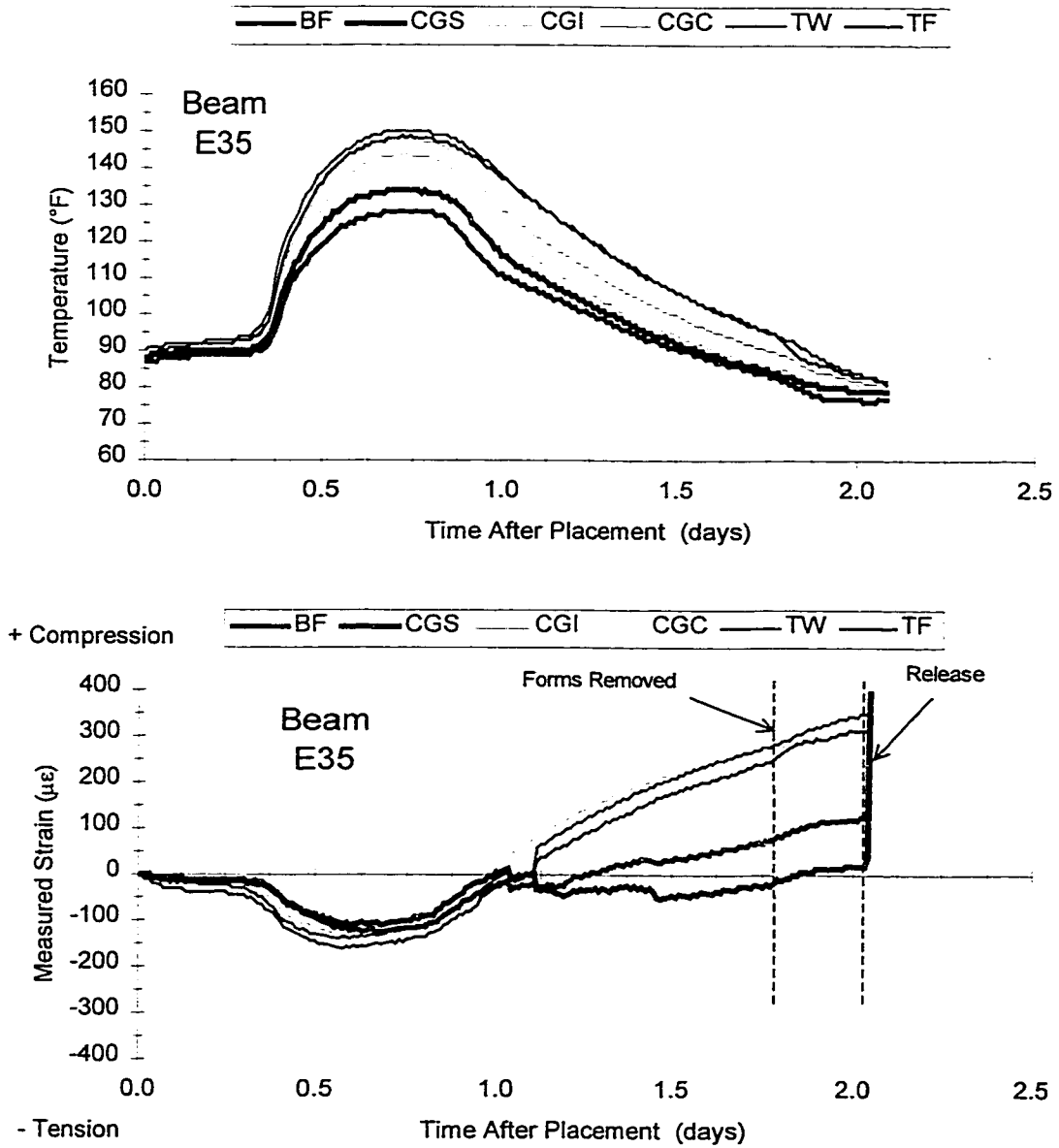


Figure 6.1 - Measured Strains and Temperatures in Beam E35 Prior to Release

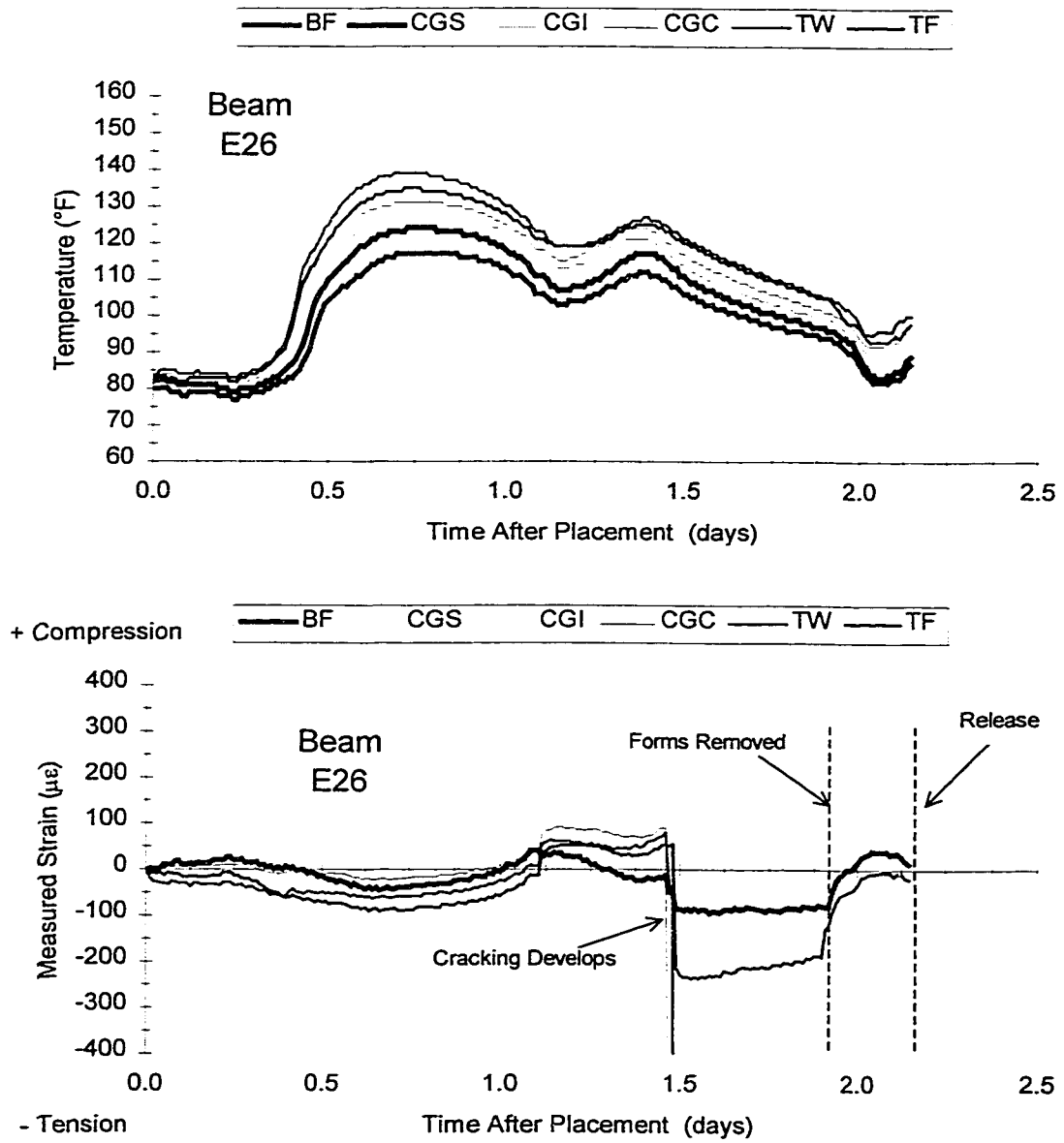


Figure 6.2 - Measured Strains and Temperatures in Beam E26 Prior to Release

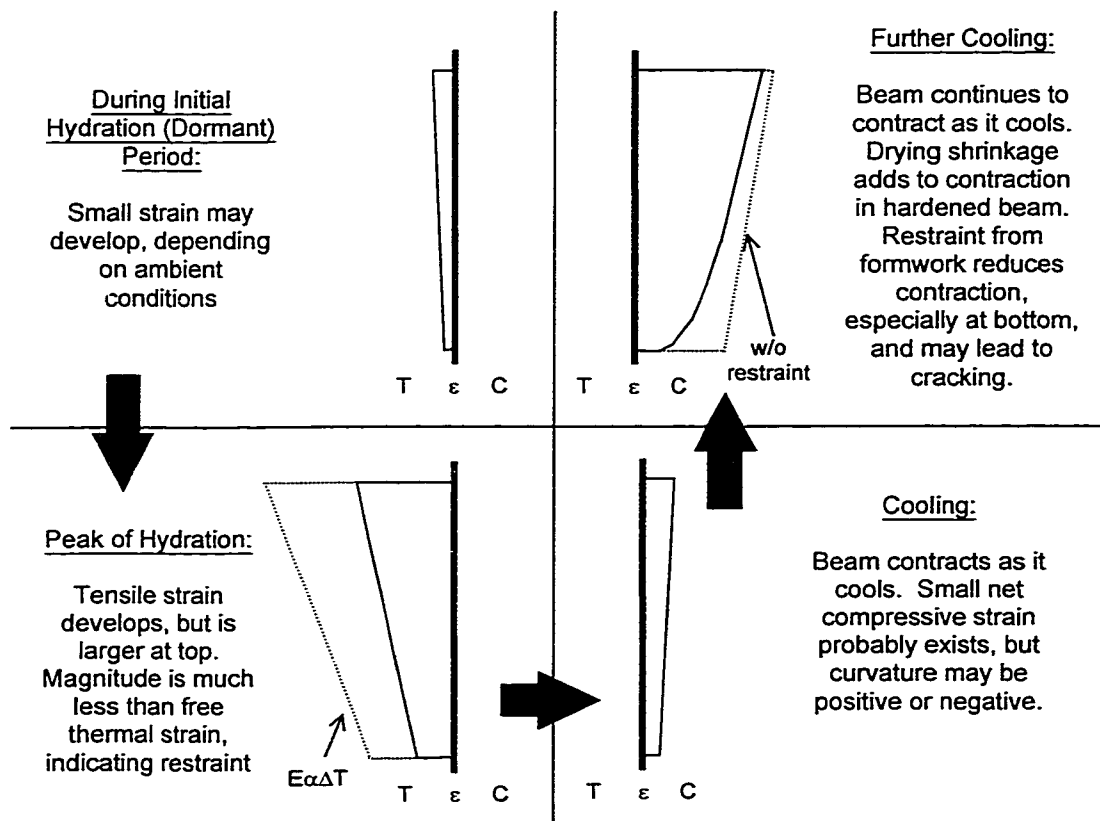


Figure 6.3 - Idealized Strain Behavior in Beams Prior to Release

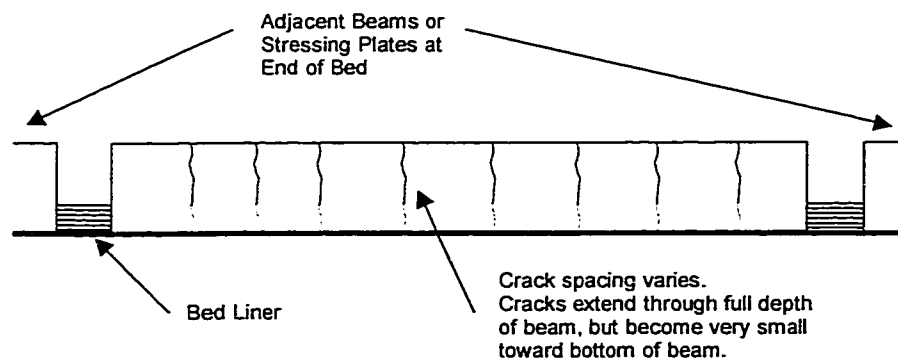


Figure 6.4 - Typical Cracking Pattern Observed in Beams Prior to Release

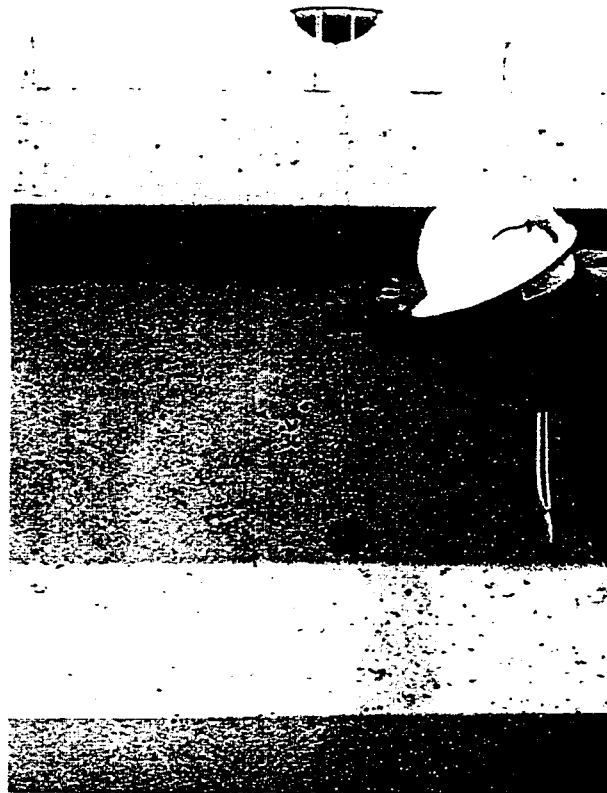


Figure 6.5 - Cracking in a San Angelo HPC Type IV Beam Prior to Release

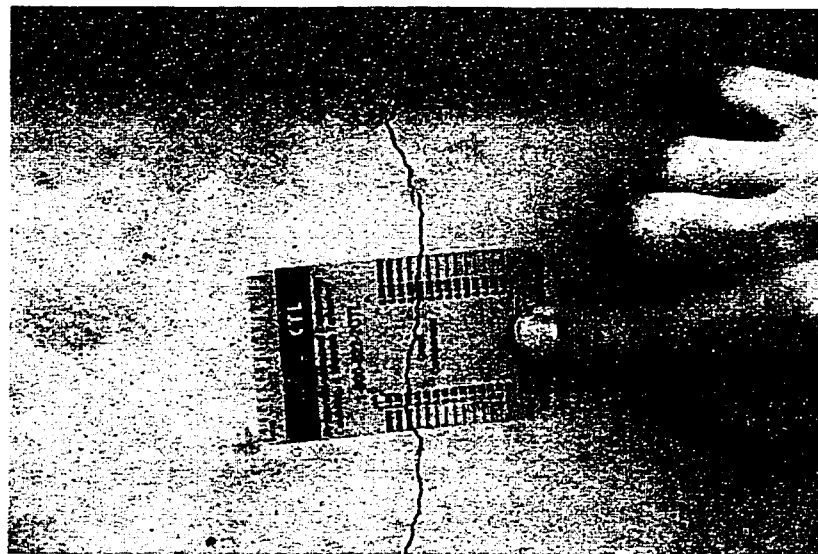


Figure 6.6 - Measurement of Crack Widths Using a Crack Comparitor

Table 6.1 - Measured Crack Widths and Spacing in Beams Just Before Release

Beam	Average Crack Width (in.)			Number of Cracks	Avg. Crack Spacing (ft.)
	1 in. Below Top of Beam	Mid-depth of Web	6" Above Bottom of Beam (approx. cgs)		
E13	.029	.016	.002	4	25.8
E14	.029	.020	.003	5	21.5
E24	.012	.008	.002	12	11.8
E26	.014	.009	.002	12	11.8
E33	.014	.010	.003	9	14.6
E34	.013	.010	.003	16	8.6
E35	.013	.009	.003	19	7.3
E44	.015	.009	.002	9	14.6
E45	.013	.009	.003	9	14.6

1 in. = 25.4 mm; 1 ft. = 0.3048 m

In fact, the exact timing of this cracking is very questionable and was observed to be highly variable. There is no doubt that the research process itself contributed to the development of cracking. In many cases, cracks were seen (or heard) forming as the researchers installed surface instrumentation (tensioned-wire deflection systems and DEMEC mechanical strain gauge points) prior to release. Cracking almost surely would have been less extensive if the strands had been released immediately after the removal of side forms. The question of whether cracking could have been avoided entirely is more difficult to answer. On many beams, some cracking was observed immediately upon removal of side forms.

It is important to note that these cracks closed entirely upon release of prestress, and were often impossible to find thereafter. No structural impact (i.e. on stiffness, deflections, etc.) was observed in this research program as a result of this cracking, and none should be expected. Still, cracks could pose a durability problem should they ever reopen, and should thus be avoided if possible.

In any event, it seems that timing during the construction process is the key controllable factor in avoiding such cracking. The high temperatures during hydration are essential for early concrete strength development, and only indirectly contribute to the

cracking. Furthermore, it is important to note that these cracks (and high hydration temperatures) were observed on all monitored beams, whether HPC or non-HPC. Thus, it can simply be concluded here that in order to avoid this type of cracking, beams should be released as soon as possible after required concrete strengths are obtained. Where possible, it would also be helpful to control ambient conditions to prevent rapid cooling and shrinkage before release.

6.3 Concrete Stresses at Release of Prestress (Pretensioning)

6.3.1 Background

The check of concrete stresses at release is one of the most fundamental calculations typically performed in the design of prestressed concrete girders. This check is necessary to ensure that the concrete is not overstressed immediately after release. If tensile stresses exceed the modulus of rupture of the concrete, flexural cracking may cause the serviceability of the structure to be reduced. If compressive stresses are too high, creep may eventually lead to a sustained-load failure.

The standard design calculations for stresses at release involve comparing extreme fiber stresses to stipulated allowable stresses. The extreme fiber stresses are calculated as the algebraic sum of three components: the axial stress resulting from prestressing, the flexural stress resulting from the eccentricity of the prestress, and the flexural stress resulting from the self-weight of the member. Standard equations are given in Equation 6.5 and Equation 6.6 (assuming compressive stresses are positive) for the extreme bottom and top fibers, respectively:

$$\sigma_{\text{rel,bot}} = \frac{P}{A} + \frac{Pe_{y_{\text{bot}}}}{I} - \frac{M_{\text{self-wt.}} y_{\text{bot}}}{I} \leq \sigma_{\text{allowable,rel,comp.}}$$

Equation 6.5

$$\sigma_{rel,top} = \frac{P}{A} - \frac{Pe y_{top}}{I} + \frac{M_{self-wt.} y_{top}}{I} \geq -\sigma_{allowable,rel,tens.}$$

Equation 6.6

The value to be used for the prestress force P in Equation 6.5 and Equation 6.6 is dependent on the section properties being used. The true theoretical solution requires that the full initial prestress force just prior to release P_i be used along with the transformed section properties [76]. If elastic shortening losses are computed exactly, then this solution is equivalent to a calculation of stresses using the initial prestress force P_o (after elastic shortening loss) with net concrete section properties. While either of these solutions provide theoretically correct results, it is common practice in design to estimate elastic shortening losses and compute stresses at release using the estimated initial stress and gross section properties.

Stresses should, of course, be checked at all critical locations where the stresses are maximized. In most pretensioned beams, the critical location does not occur at midspan, but rather at a drupe point or a termination of debonding. Specified allowable stresses differ among various codes, but the *AASHTO Standard Specifications* [3] allow compressive stresses of $0.60(f'_c)$ (f'_c in psi) and tensile stresses of $7.5\sqrt{f'_c}$ (in areas with bonded reinforcement) at release in pretensioned beams. The *AASHTO LRFD Specifications* [1] specify approximately the same allowable stresses, but in units of ksi rather than psi. Note that for designs involving HPC, it may be permissible to increase the allowable tensile stress. This was done in the design of the Louetta and San Angelo HPC bridges, as discussed in Chapter 2.

Elastic concrete strains at release, prior to time-dependent effects such as creep and shrinkage, can be calculated at the extreme fibers by dividing each term in Equation 6.5 or Equation 6.6 by the concrete modulus of elasticity. The release curvature (strain gradient) at any section can be predicted by considering only the flexural strain components, as shown in Equation 6.7:

$$\phi_{rel} = -\frac{Pe}{EI} + \frac{M_{self-wt.}}{EI}$$

Equation 6.7

The sign convention used in Equation 6.7 assumes that positive curvatures cause downward deflections. The primary importance of the curvature at release is that it is a measure of the deformation behavior at the given section. Consideration of the curvature along the member yields a prediction of the camber or deflection behavior of the beam. The same considerations regarding prestress force and section properties that were discussed for Equation 6.5 and Equation 6.6 apply for the calculation of curvature.

6.3.2 Measurements

As described in Section 3.4, strain gauges were placed at six different depths in several beams from each bridge, allowing for measurement of concrete strains through the depth of the cross-section. In some beams, strains were measured using vibrating wire gauges, and in other beams bonded resistance strain gauges were used. A “zero” or “baseline” strain reading was recorded for each instrumented beam just prior to release of prestress, and another set of readings was taken on each beam just after release of pretensioning. Strains resulting from release of prestress were successfully recorded in this manner for five Louetta U-beams (including two beams with measurements on both webs), five San Angelo Eastbound HPC Type IV beams, and one San Angelo Westbound non-HPC Type IV beam. Measurements were made on other beams, but problems with concrete cracking and damaged or inoperable gauges rendered these data unusable.

An example of measured midspan strain data at release can be seen in Figure 6.7 for San Angelo Eastbound HPC Beam E13. For the most part, plane sections were observed to remain plane. However, strain measurements were not *perfectly* linear over the depth of the beam in all cases, so a regression line was fit to the measured release strains for each beam. Measured stresses at release were then estimated using the regression line by multiplying strain values by the measured modulus of elasticity, and comparisons were made with predictions based on design properties and measured properties, as discussed in Section 6.1.1. An example of this comparison for Beam E13 can be seen in Figure 6.8.

Both *design* and *measured* predictions are based on the standard stress equations given in Equation 6.5 and Equation 6.6. The main difference between the two prediction methods is that gross section properties were used in the *design* prediction, while transformed section properties were used in the *measured* prediction. Other differences

include the treatment of modulus of elasticity and concrete unit weight, and assumptions regarding prestress losses before release. The methods used for determining key parameters in each analysis are summarized in Table 6.2, and values for many of the specific parameters are listed for each beam in Appendix F.

Measured and predicted midspan stresses at release are shown in Figure 6.9 and Figure 6.10 for the Louetta and San Angelo bridges, respectively. Overall, there was reasonable correlation between measured and predicted stresses, but some general trends were apparent. In about two-thirds of the beams, including five of the six San Angelo beams, the measured bottom fiber stresses were greater than predicted. Meanwhile, in every beam except San Angelo Beams E24 and E35, the measured top fiber stresses were greater than predicted.

There were also distinct differences in several beams regarding the slopes of the measured and predicted stress profiles (i.e. stress gradients). For almost all of the Louetta beams, the slope of the measured stress profile was steeper than the slope of the predicted stress profile. That is, there was less stress gradient for measured stresses than for predicted stresses. The opposite trend was generally true for the San Angelo beams, in which the slope of the predicted stress profile was steeper than the slope of the measured stress profile. In other words, there was a larger stress gradient for measured stresses than for predicted stresses in the San Angelo beams.

Table 6.2 - Summary of Methods Used for Prediction of Midspan Release Stresses

Parameter(s)	“Design” Analysis	“Measured” Analysis
Section Properties	Gross section properties	Transformed section properties
Prestress Force / Loss	No loss assumed before release. Elastic shortening loss calculated by approximate method given in <i>AASHTO LRFD Specifications</i> [1] (see Section 7.2).	3.5 to 4.5% loss assumed before release based on measurements in Section 7.2. Elastic shortening loss not added because exact analysis using transformed section properties was used.
Beam Self-Weight	Based on gross beam area and assumed 150 pcf (3.29 kg/m ³).	Based on gross beam area and measured unit weight, with approx. weight of steel included.
Modulus of Elasticity	Eq. 4.2 (non-HPC) or Eq. 4.4 (HPC).	Based on tests of companion specimens.

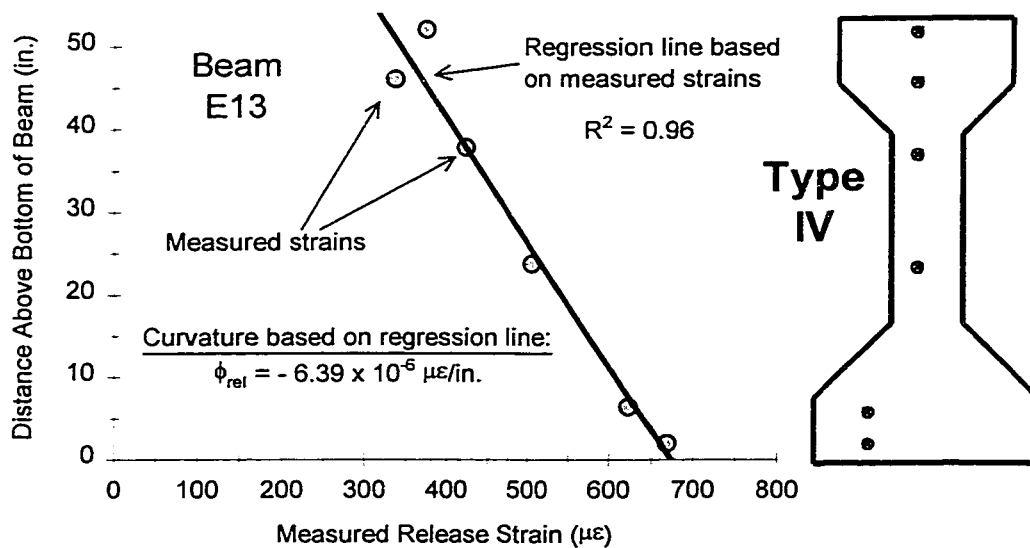


Figure 6.7 - Measured Release Strains at Midspan in Beam E13

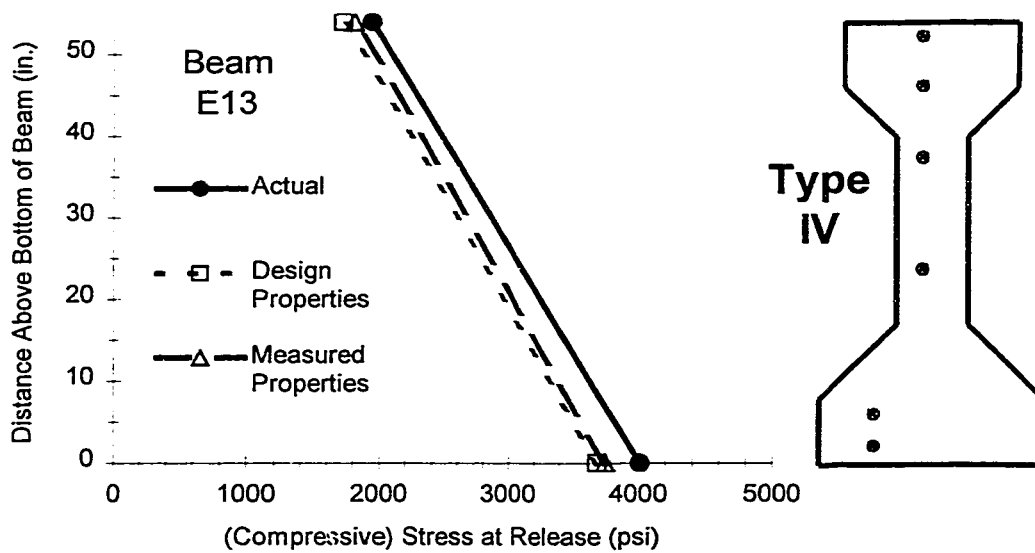


Figure 6.8 - Comparison of Predicted and Measured Release Stresses at Midspan in Beam E13

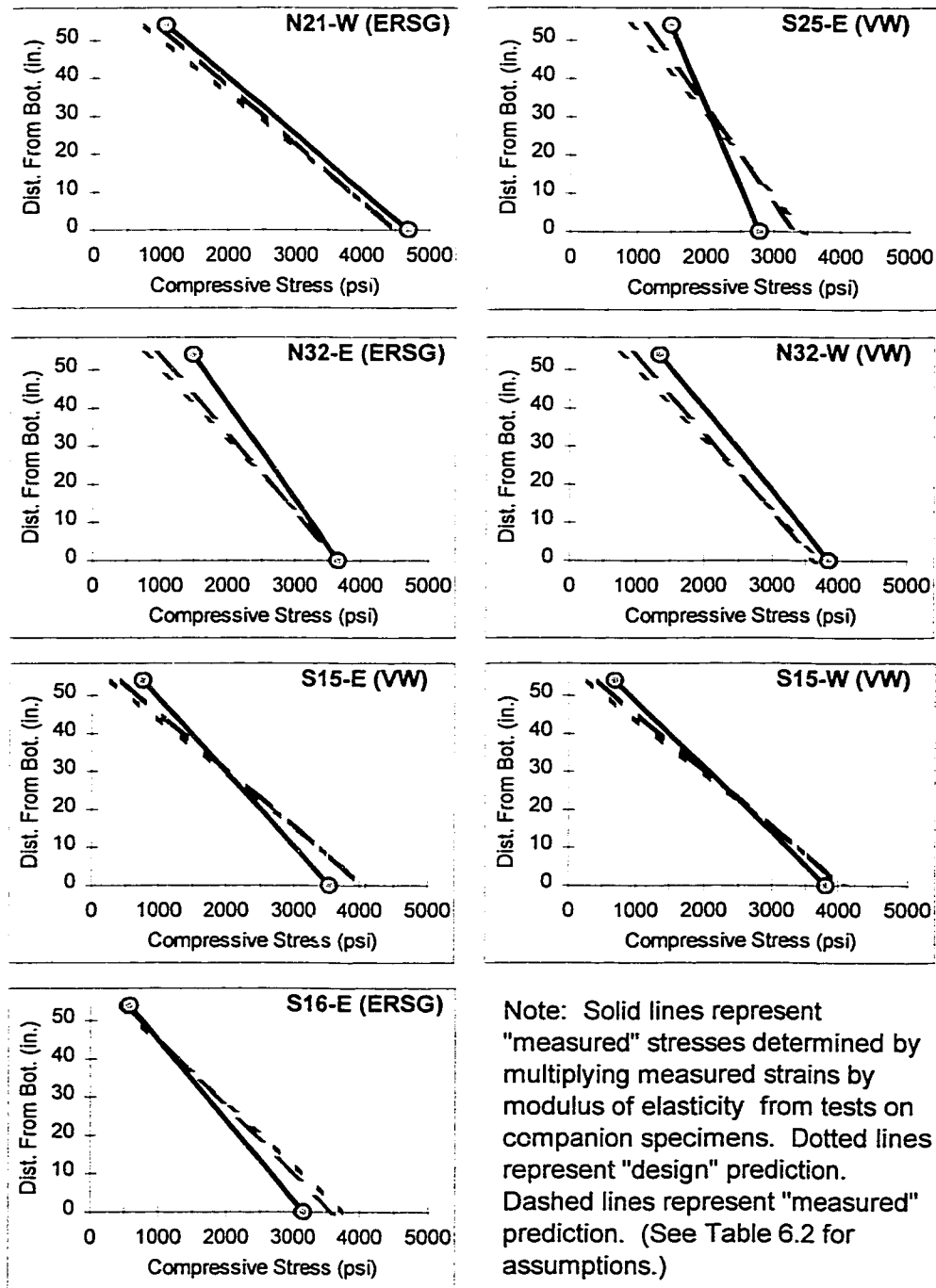
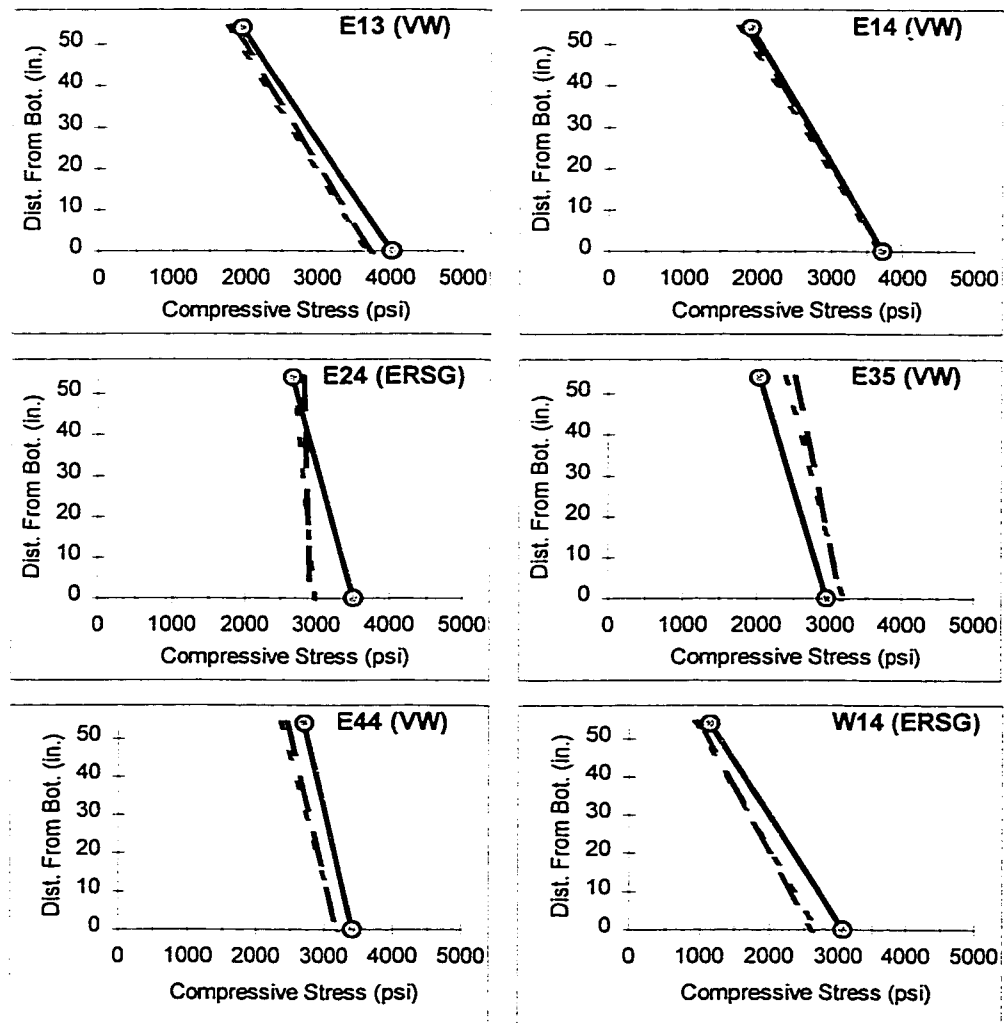


Figure 6.9 - Comparison of Predicted and Measured Midspan Stresses at Release of Pretensioning (Louetta)



Note: Solid lines represent "measured" stresses determined by multiplying measured strains by modulus of elasticity from tests on companion specimens. Dotted lines represent "design" prediction. Dashed lines represent "measured" prediction. (See Table 6.2 for assumptions.)

Figure 6.10 - Comparison of Predicted and Measured Midspan Stresses at Release of Pretensioning (San Angelo)

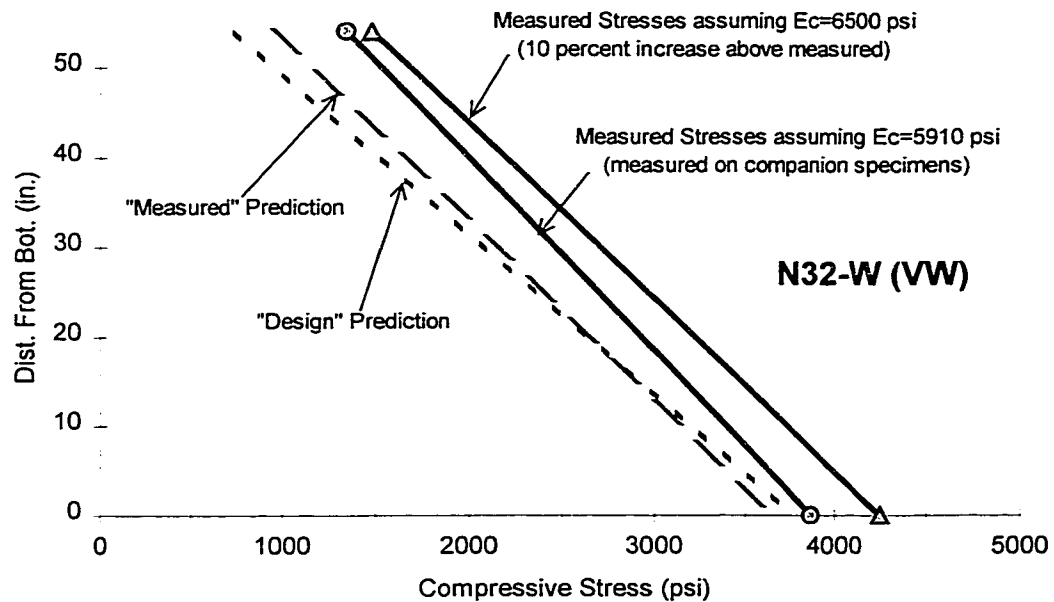


Figure 6.11 - Effect of Error in Modulus of Elasticity on Measured Stress Profile

Also note that the behavior with respect to measured release stresses was generally similar for companion beams cast on the same day, or within each web of the same Louetta U-beam. Examples of similar behavior can be seen for the measured stress profiles in Beam N32 (East and West webs), S15 (East and West web), and companion Beams E13 and E14. Measured midspan stresses were in compression through the entire depth of every beam, and were less than the allowable stresses. Of course, this conceptually makes sense because the critical section for release stresses is not at midspan. Relatively small stress gradients were observed in the San Angelo Eastbound HPC beams, although these beams have six strands in the top flange and have not been fully prestressed using pretensioning. Approximately 30 percent of the prestress force in these beams was applied through post-tensioning at a later date.

It is clear from the stress profiles plotted in Figure 6.9 and Figure 6.10 that there was little difference between predicted stresses based on design properties and those based on measured properties. This trend will be examined further in Section 6.3.3.

6.3.3 Discussion

Clearly, it is difficult to draw specific conclusions regarding extreme fiber stresses at release, considering the impact of the modulus of elasticity in the conversion of measured strains to stresses. As discussed in Section 4.4, modulus of elasticity can be highly variable, and it is quite possible that values for modulus of elasticity used in the conversion of measured strains to stresses differed from the actual modulus by 10 percent or more. The impact of an underestimation of the actual modulus of elasticity can be seen in Figure 6.11 for Beam N32 (west web). Note that the "measured" stresses increase if the modulus is actually higher, and that the measured stress gradient increases slightly as well.

Other observations made during this research program, including lower than predicted camber and deflection, indicate that the actual modulus of elasticity may be higher than the modulus determined from tests on companion specimens. The general trend that measured midspan release stresses were greater than predicted at both extreme fibers (for the majority of beams) contradicts this conclusion, since it implies that the actual modulus of elasticity may be lower than determined from companion specimen tests.

A more likely explanation for the high measured stresses is the presence of restraint from the bed liner prior to release, as described in Section 6.2.3. If shortening due to cooling and shrinkage is restrained, then there will be a tensile stress acting on the concrete at the time of the "zero" or "baseline" reading. Upon release of prestress, this stress would be released and would appear as an apparent *additional* compressive stress. It is important to note that this additional stress is only an apparent stress affecting measurements, and is not a true stress acting on the member.

In some beams, the measured stress gradients are also inconsistent with regard to other measurements. Low camber was observed for *all* beams prior to release, which implies that a lower stress gradient (i.e. steeper slope to the stress profile) should have been observed on all beams. The Louetta beams do, in fact, exhibit this behavior, but the opposite is true for most of the San Angelo beams. Again, the presence of restraint before release may be the cause, especially if the restraint were greater toward the bottom of the beam. The cracking observed prior to release on beams seems to verify a difference in restraint across the depth of the beam, as discussed in Section 6.2.3.

Despite the relative simplicity of Equation 6.5 and Equation 6.6, the prediction and measurement of stresses (strains) at release is clearly quite complex. The degree of accuracy for the predictions in this study is difficult to determine because of the effects of bed restraint and differences in modulus of elasticity on the interpretation of measured data. Considering these factors, it appears that predictions are at least reasonably accurate. Maximum differences between measured and predicted stresses based on design assumptions were 4.70 MPa (681 psi) and 5.07 MPa (735 psi) at the bottom and top fibers, respectively. Maximum differences with respect to predictions based on measured parameters were 4.12 MPa (598 psi) and 3.69 MPa (535 psi) at the bottom and top fibers, respectively.

It should be noted that the similarity between *design* and *measured* predictions for almost all beams is somewhat coincidental. The modulus of elasticity used in the design prediction, which was based on either Equation 4.2 or Equation 4.4, was 15 to 25 percent lower than the modulus determined from companion tests. As discussed in Section 7.3.3, this resulted in a high overprediction of elastic shortening loss and a lower prestress force, which balanced out the effects of underestimating the beam self-weight.

Still, it can be shown that the computation of stresses is not overly sensitive to the assumptions regarding prestress force, self-weight, and modulus of elasticity, even for the HPC beams in this study. Calculated midspan release stresses are shown in Table 6.3 for a Louetta and a San Angelo HPC beam. Stresses were computed using a base case corresponding to the known modulus of elasticity (from companion tests), an assumed beam weight of 3.29 kg/m³ (150 lb/ft.³), and no loss of prestress before release. Stresses were then computed for the individual modifications to these assumptions. Note that in each case, the stresses were computed using the exact (transformed section) and approximate (gross section) methods described in Section 6.3.1.

Clearly, the sensitivity of release stresses is very small due to these parameters, as shown in Table 6.3. Of the individual modifications examined, a 5 percent change in prestress force had the most significant effect on the bottom fiber stresses and a 5 percent change in self-weight had the most impact on top fiber stresses. Even if all three modifications are combined, there should be no more than a 3.45 MPa (500 psi) difference at the bottom fiber and a 1.72 MPa (250 psi) difference at the top fiber. Furthermore, the base case is generally conservative in terms of the bottom fiber stress, which is likely to govern the design of HPC members at release because of the large prestress forces

associated with these designs. Note that the data presented in the table also shows that the approximate gross-section method is adequate for computation of stresses.

Since the computation of release stresses is not overly sensitive to key parameters, even for HPC designs, no adjustments to standard design procedures are recommended. The use of gross-section properties is acceptable for computation of release stresses, and the use of assumed or calculated values for modulus of elasticity, beam self-weight, and prestress force immediately prior to release is permissible. Still, if any of these parameters are known from trial batching or previous experience, calculations should be performed using the refined values. Note that these statements apply only to concrete *stresses* at release, and not to deformation behavior.

Table 6.3 - Sensitivity of Release Stresses to Important Parameters

	Approximate (Gross Section Properties)		Exact (Transformed Section Properties)	
	Bot. Fiber	Top Fiber	Bot. Fiber	Top Fiber
<i>Louetta Beam N32 (HPC)</i>				
Base Case ¹	3928	695	4049	662
+5% Self-Weight	3850	804	3968	772
+5% Prestress Loss	3615	780	3765	739
+10% Modulus of Elasticity	3979	681	4094	650
<i>San Angelo Beam E44 (HPC)</i>				
Base Case ¹	3347	2341	3613	2236
+5% Self-Weight	3235	2484	3485	2392
+5% Prestress Loss	3034	2371	3304	2281
+10% Modulus of Elasticity	3389	2337	3613	2290
Note: all stresses in psi (1 psi = 0.006895 MPa)				
¹ Base case corresponds to known modulus of elasticity, 3.29 kg/m ³ (150 lb/ft. ³) beam self-weight, and zero prestress loss before release.				

6.4 Time-Dependent Growth of Strains in Beams During Storage

6.4.1 Background

Prestressed concrete beams deform over time as a result of creep and shrinkage of concrete. Time-dependent concrete strains are generally not considered explicitly in design, but are considered implicitly in the prediction of prestress losses and beam camber or deflection. In this section, strain behavior is examined directly since it provides insight into the time-dependent behavior at a particular cross-section. In particular, the growth of compressive strains during the storage of beams is considered, where only the initial forces (pretensioning and self-weight) are acting on the member. More complex time-dependent analyses including the effects of additional forces (post-tensioning, deck weight, and other superimposed dead loads) are discussed in Section 7.4 and 8.5, in terms of prestress loss and beam camber, respectively.

The theoretical time-dependent strains at a given section can be computed as a function of the initial elastic strains using the approximate step-function equations developed by Branson [25] and adopted by ACI Committee 435 [11]. (Note that this method was developed for computation of time-dependent prestress losses and deflections, and has been adapted here to the more general computation of strains.) This method provides a single equation that approximates the results of more laborious incremental time-step procedures. The initial elastic strain corresponding to each stress component (axial prestress, eccentric prestress, and beam self-weight) at release is magnified to account for the effects of creep, and the additional strain due to shrinkage is added. Recall that the elastic strain corresponding to each stress component is computed by dividing the stress by E_{ci} , the modulus of elasticity at release. The time-dependent strain $\epsilon(y,t)$ at a distance y from the centroid can thus be computed as:

$$\epsilon(y,t) = \left(\frac{1+S_t}{E_{ci}} \right) \cdot \left(\frac{P_0}{A} \right) + \left(\frac{1+S_t}{E_{ci}} \right) \cdot \left(\frac{P_0 e y}{I} \right) - \left(\frac{1+C_{ct}}{E_{ci}} \right) \cdot \left(\frac{M_{\text{self-wt.}y}}{I} \right) + \epsilon_{sh,t}$$

Equation 6.8

Note that the sign convention used in Equation 6.8 assumes y to be positive below the centroid. Compressive strains are assumed to be positive and tensile stresses negative.

The parameter S_t is used in the first two terms of Equation 6.8 to represent not only the effects of creep, but the effects of prestress loss and the *interrelation* between creep and prestress loss. The strain resulting from the axial and flexural (eccentric) components of prestress will increase over time as a result of creep, but will also be reduced to some extent as prestress is lost (from creep, shrinkage, and relaxation). The primary difficulty in determining the parameter S_t is that the magnitude of the creep strain associated with prestress is dependent on the magnitude of the prestress force. In other words, the parameter S_t must account for the creep strain under a *variable stress history*. Branson [25] and ACI Committee 435 [11] suggest that the strain associated with creep under prestress can be adequately approximated by considering the *average* prestress force over the interval between release and the time at which strains are being computed. Since the “elastic” change in strain resulting from the loss of prestress must also be considered, the parameter S_t is estimated as:

$$S_t = -\frac{\Delta P}{P_0} + \left(1 - \frac{\Delta P}{2P_0}\right) \cdot C_{ct}$$

where $\Delta P = P_0 - P_e$

P_0 = prestress force at release (after initial losses)

P_e = effective prestress force at time when strain is being computed (after losses)

Equation 6.9

With the introduction of the parameter S_t , an approximation regarding prestress loss must be used in the calculation of time-dependent strain by Equation 6.8. That is, the time-dependent strain is a function of the time-dependent prestress loss, but the time-dependent prestress loss is also a function of the time-dependent strain. Sufficient accuracy can usually be obtained if the prestress loss (relative to the prestress immediately after transfer) is assumed based on past experience, and the validity of any assumption can be checked by comparing the assumed loss with the calculated strain at the c.g. of the prestressing strands. It should also be noted that Equation 6.8 does not explicitly account for changes in modulus of elasticity with time. However, if the creep coefficient is based on measured

tests as described in Section 4.5 for this research program, the change in modulus of elasticity is inherently embedded in the creep coefficient. Recall that the creep coefficient was defined as the ratio of total time-dependent strain (not including initial elastic strain) to initial elastic strain. As such, no distinction is made between the increase in strain actually resulting from creep and the decrease in "elastic" strain resulting from an increase in modulus of elasticity. If the effects of time on the modulus of elasticity are not directly accounted for in the creep coefficient, then the age-adjusted modulus approach can be used [11].

It is also acknowledged that shrinkage strains are generally not uniform over the depth of the cross-section, as implied in Equation 6.8. The steel reinforcement (especially the strands) will internally resist shrinkage deformations, such that a strain gradient is developed through the depth of the cross-section. This effect can be approximated by a number of empirical methods, or a simple analysis can be performed by the equivalent tensile force method [11]. It can be shown that the reduction in shrinkage strain at the level of the strands and corresponding curvature are relatively small for prestressed beams, including those in this study, and this effect is thus neglected in the calculations discussed in the following sections. Differential shrinkage through the depth of the concrete member itself will also result in non-uniform shrinkage strains, but this effect is also neglected in Equation 6.8.

To be technically correct, Equation 6.8 as stated should be used with the net concrete section properties. An approximate solution can be developed using gross section properties, and this is usually sufficient for most purposes. An alternative exact solution can be found by using the transformed section, and replacing P_0 in Equation 6.8 and Equation 6.9 with P_1 , the prestress force just before release. If the transformed section is used, then the calculation of ΔP in Equation 6.9 should also ignore the loss due to elastic shortening, since it is directly accounted for by using the transformed section.

Note that Equation 6.8 is not intended to provide an exact model, but rather an approximate procedure for calculation of time-dependent strains. Values obtained from this equation will be used in Section 6.4.2 to allow for comparisons with measured strains. Although approximate in nature, the equation should still provide a reasonably sound basis for such comparisons. At the very least, its use allows for easier identification of behavior trends for the beams in this study.

6.4.2 Measurements

Strain profiles were recorded at several stages during storage of beams at the prestressing plant. Measurements were successfully recorded for eight beams (four Louetta HPC beams and four San Angelo HPC beams) using vibrating wire gauges. Strain profiles were measured in a few other beams using vibrating wire gauges, but concrete cracking at the gauge location prior to release affected the baseline strain readings in these gauges. Strains were also monitored using resistance strain gauges in other beams, but these gauges did not perform well enough over time to render such data useful.

Time-dependent strain measurements reported in this section are relative to baseline readings obtained just before release on each beam. All strains have been corrected for thermal effects (including thermal gradients) in beams using the procedure described in Section 6.1.2. The effects of small changes in the location of beam supports during storage have also been considered. As for the concrete strain data at release described in Section 6.3.2, regression lines have been fit to the measured time-dependent strain data to account for small inconsistencies in the measured data through the depth of the cross-section. An example of this approach can be seen in Figure 6.7.

In this section, measured strain profiles are compared to time-dependent strain profiles predicted using Equation 6.8. Some of the assumptions regarding the use of Equation 6.8 were detailed in Section 6.4.2. Transformed section properties and measured concrete moduli of elasticity and unit weights were used in the predictions. Parameters used for the analysis on each beam are listed in Appendix F. Creep-time and shrinkage-time equations based on measured data, which are given in Section 4.5 and Section 4.6, were also used with appropriate corrections for relative humidity and volume-to-surface ratio. Note that a design-based prediction method was not used in this section, since the computation of time-dependent strain is not a typical design calculation. A prediction based on design values will be used in Section 6.4.3, however, to illustrate the sensitivity of time-dependent strains to material properties.

Measured and predicted time-dependent strains are shown for three Louetta beams (four beam webs) in Figure 6.12. For each beam, strains are plotted at release, approximately one week after release, and at a later age during storage (129 to 221 days after release). The general time-dependent strain behavior is as expected. Compressive

strains increase with time, with larger strain increases toward the bottom of each beam where the compressive stress is highest. However, at both the top and bottom of each beam, the magnitude of the strain growth is substantially lower than predicted. In general, the long-term strain growth is on the order of 100 to 250 $\mu\epsilon$ less than predicted. Note that the curvature growth over time is slightly lower than the predicted curvature growth in the four Louetta beams.

Time-dependent strains are plotted in Figure 6.13 for four San Angelo Eastbound HPC beams. Measured and predicted strains are plotted at release, a few days after release, and approximately one month after release. Note that strains are not shown after post-tensioning of these beams because prediction of the time-dependent strain behavior becomes quite complex at that stage, and time-dependent effects cannot be isolated. As for the Louetta beams, the strain growth over time is substantially less than predicted. In fact, three of the San Angelo Eastbound HPC beams (Beams E13, E14, and E35) exhibited almost no strain growth over time at the top of the beam. Strain growth at the bottom of the beam was on the order of 150 to 200 $\mu\epsilon$ less than predicted at about one month after release, and curvature growth was actually greater than predicted in all four of these beams.

6.4.3 Discussion

As with measured strains at release, the cumulative time-dependent strains are dependent on the baseline reading taken just before release. Therefore, these measurements may also include the effect of the release of restraint against shortening of the beam (prior to release). As discussed in Section 6.3.3, these measurements may thus be artificially high because the release of restraint appears as an apparent additional compressive strain. This effect does not influence the time-dependent *growth* of strain, however, and for this reason the following discussion concentrates on the time-dependent changes in strain rather than the cumulative strain.

There are a few potential reasons that time-dependent strain growth was substantially lower than predicted. First, the moduli of elasticity may have been substantially higher in the actual beams than as measured by tests on companion specimens. Second, the creep coefficient measured on companion specimens may have been higher than the creep coefficient in the actual beams. It is also possible that the

correction factors (for average relative humidity and volume-to-surface ratio) applied to the creep coefficient in the prediction equation were in error. Any of these situations might cause the time-dependent strain to be substantially overpredicted.

It is important to note that the observations regarding curvature growth during storage are in general agreement with observations regarding camber growth during storage, which is discussed in Section 8.3. Measured midspan curvature growth and measured midspan camber growth were both slightly less than predicted in the Louetta HPC beams, and approximately equal to or slightly greater than predicted in the San Angelo Eastbound HPC and San Angelo Westbound non-HPC beams. These trends are consistent with probable errors in the measured modulus of elasticity or creep coefficient for the Louetta beams, but not for the San Angelo beams. In other words, if the actual modulus of elasticity were substantially underestimated or the actual creep was substantially overestimated, as implied by the lower than predicted time-dependent strains, then the growth in curvature and camber should also have been lower than predicted.

It is more likely that differences between the measured and predicted shrinkage behavior contributed to the lower than predicted time-dependent strain growth. Shrinkage in the actual beams may have been substantially lower (or slower) than predicted based on the measurements on companion specimens, or correction factors for average relative humidity and volume-to-surface ratio may have been in error. It is also very possible that a large portion of the shrinkage occurred *before* release (and thus before the “baseline” or “zero” strain reading), such that this shrinkage was not measured. Any of these scenarios would have resulted in significantly less time-dependent strain growth than predicted.

The relative lack of increase in top fiber strain observed in the San Angelo Eastbound HPC beams, and the corresponding higher than predicted curvature increase, also seem to be consistent with other observed aspects of structural behavior in these beams. The possibility of differential shrinkage across the depth of the beams (prior to release) was mentioned in Section 6.2 regarding strains before release, and in Section 8.2 regarding measured camber at release. This differential shrinkage would cause lower camber at release, since the top of the beam has shortened more than the bottom at that stage. After release, the bottom of the beam would shrink more than the top (since much of the shrinkage at the top has already occurred), and an increase in (negative) curvature and corresponding camber would result. As mentioned previously, a higher than predicted increase in time-dependent camber was observed in the San Angelo Eastbound beams but

not in the Louetta beams, which is consistent with the observations regarding curvatures in this section. This may also suggest that differential shrinkage prior to release is more prevalent in the San Angelo Eastbound HPC beams than in the Louetta HPC beams.

The above theory represents one possible explanation of the behavior observed in beams at release and during storage that is consistent with both strain and camber measurements. Still, it is impossible to precisely identify a single cause of the lower than expected time-dependent strain growth, especially when the sensitivity to actual material and section properties is considered. An example of this sensitivity is shown in Figure 6.14, where time-dependent strain growth predicted using Equation 6.8 is shown for a Louetta HPC beam and a San Angelo HPC beam.

Each plot shows predicted growth for design-based parameters and for measured parameters. Design parameters are based on standard equations and assumptions for the estimation of modulus of elasticity, unit weight, creep, and shrinkage. In particular, creep and shrinkage parameters for the design-based prediction utilize the "standard" equations recommended by ACI Committee 209 [8], with corrections for average relative humidity and volume-to-surface ratio, and modulus of elasticity was estimated using Equation 4.4. Measured parameters are based on tests on companion specimens for modulus of elasticity, unit weight, creep, and shrinkage. Each of these measured parameters may be found in the appropriate sections of Chapter 4 and in Appendix F. Note that actual measured strains are not plotted in Figure 6.14 for clarity, but are shown in Figure 6.12 and Figure 6.13 along with the predictions based on measured parameters.

It is clear from the plots in Figure 6.14 that the prediction based on design assumptions is grossly in error. Predicted strains and curvatures are much higher than for the prediction based on measured parameters, and thus will be truly excessive in comparison to actual measured strains. The combined effects of underestimating the modulus of elasticity and overestimating the creep and shrinkage are evident. In fact, errors regarding any one of these properties are likely to result in significant errors regarding the prediction of time-dependent strains in HPC beams. Such errors can have a significant impact on the prediction of prestress loss and camber, as discussed in Chapter 7 and Chapter 8, respectively.

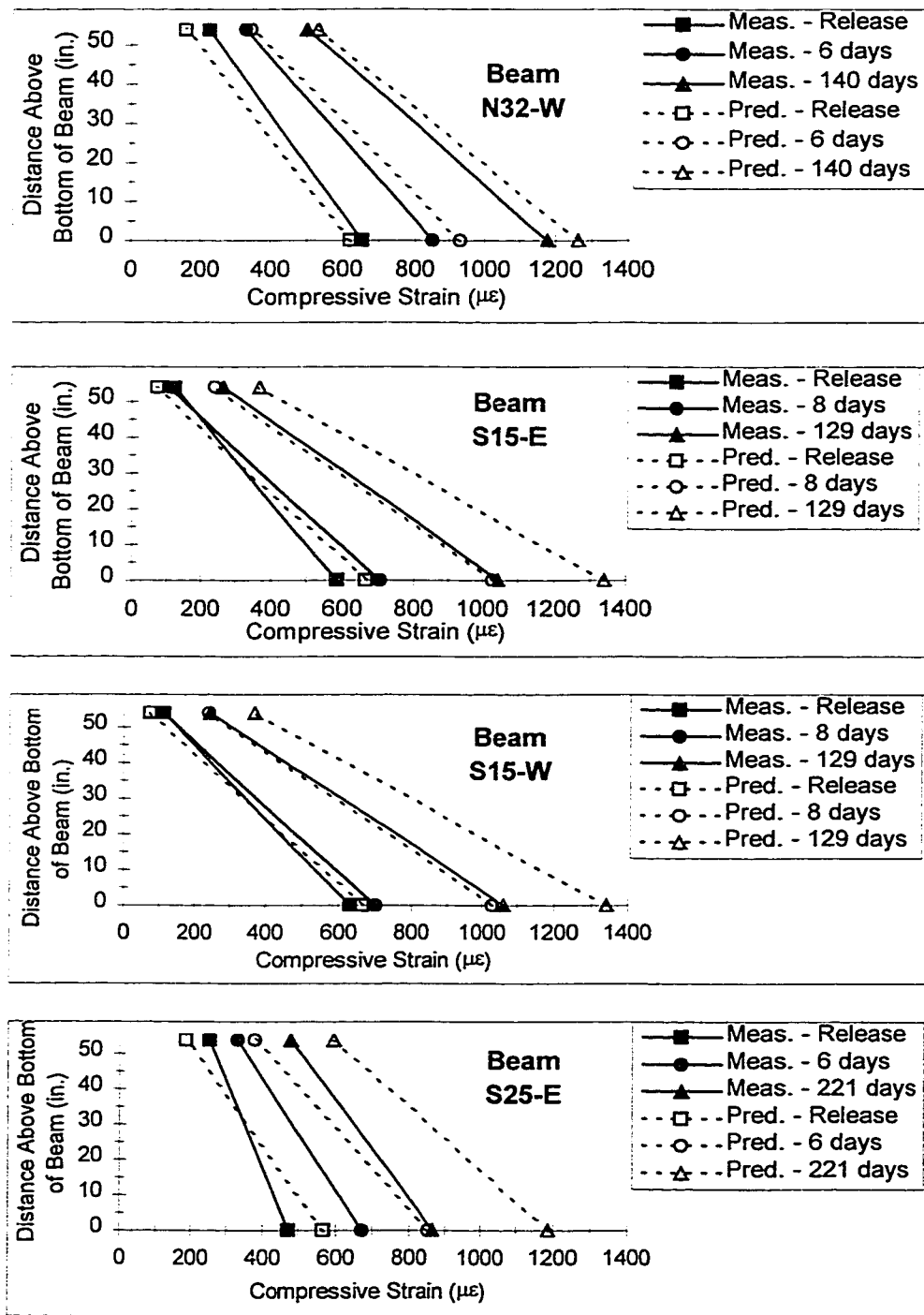


Figure 6.12 - Measured and Predicted Time Dependent Strains in Louetta HPC Beams (Predicted Based on Measured Parameters)

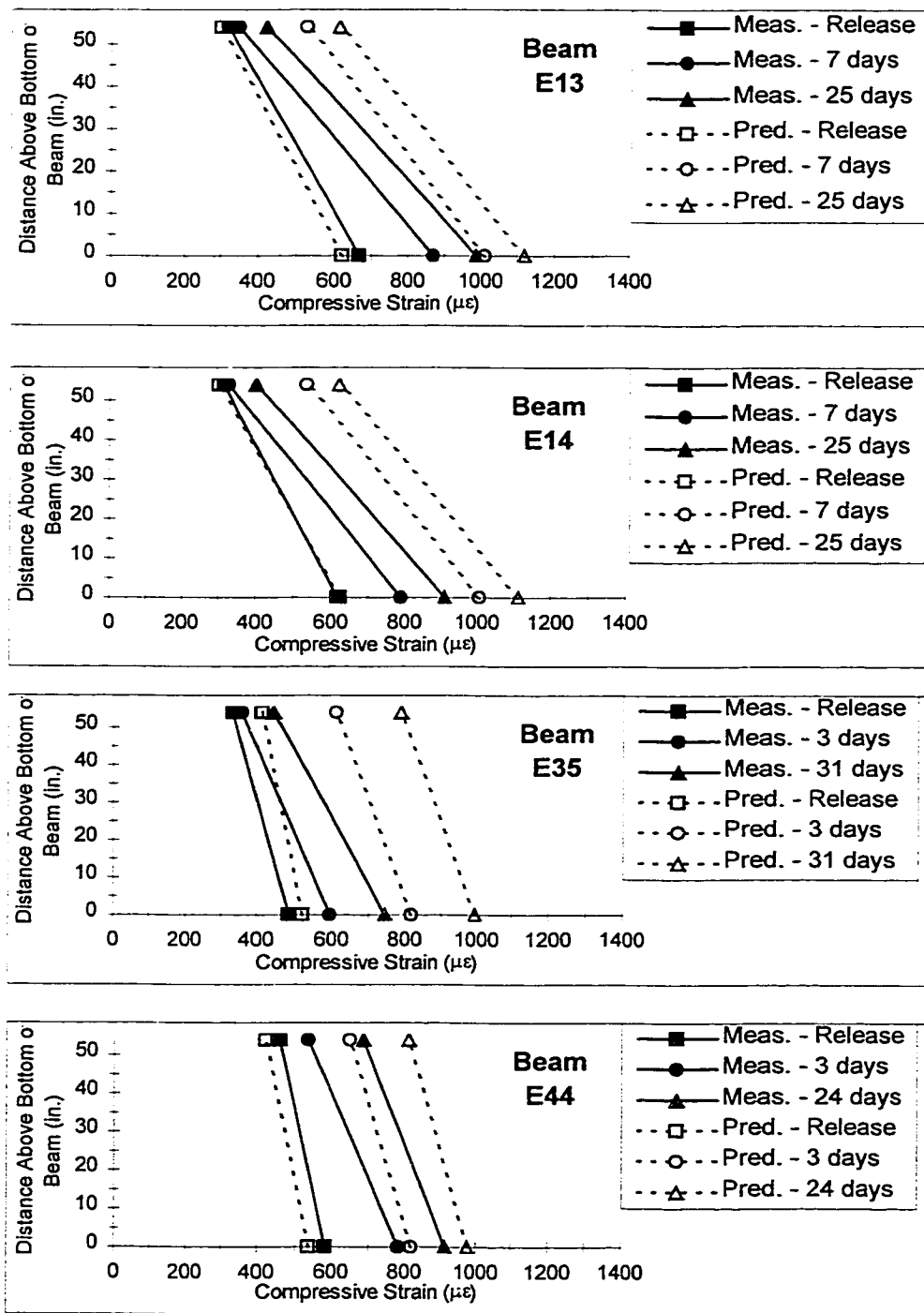


Figure 6.13 - Measured and Predicted Time Dependent Strains in San Angelo Eastbound HPC Beams (Predicted Based on Measured Parameters)

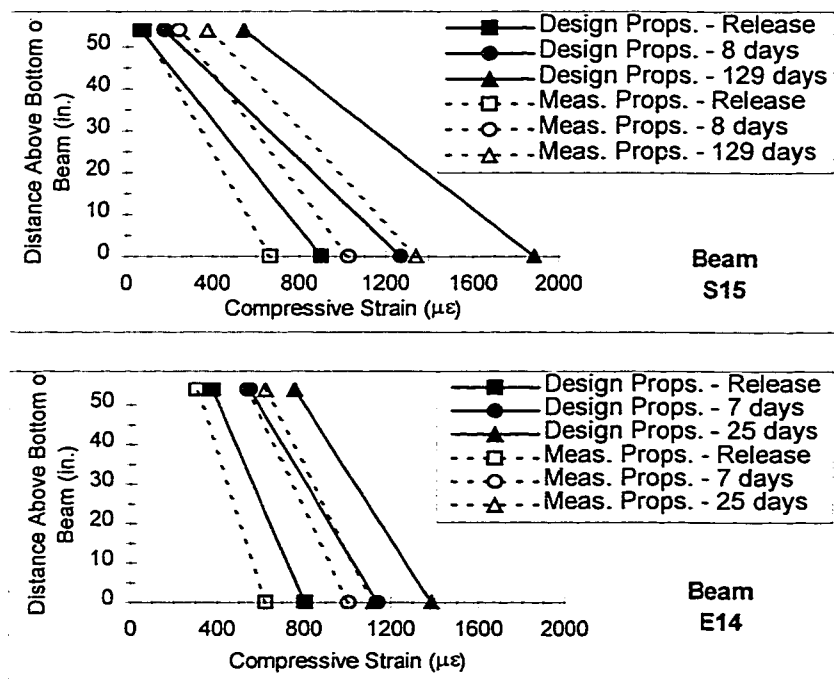


Figure 6.14 - Predicted Time-Dependent Strains in Beams S15 and E14 Based on Design and Measured Parameters

It is clear that the time-dependent strain behavior in prestressed concrete beams is very sensitive to material properties. Specifically, variations in modulus of elasticity, creep, and shrinkage properties can result in large variations in the time-dependent strains. The importance of these parameters is addressed more appropriately in Section 7.4 and 8.5, in terms of total prestress losses and time-dependent deflection behavior under full dead load. Unfortunately, the results presented in this section have shown that even if these material properties are measured on companion specimens, the precise prediction of time-dependent strains is difficult. Time-dependent strains are dependent on not just the material properties of the concrete, but the elastic strain distribution, ambient conditions, and the effects of differential shrinkage. Because these effects are difficult to predict precisely, and because of possible variations in material properties, it is clearly unreasonable to expect predictions of time-dependent strains to be more than estimations.

6.5 Elastic Responses to Post-tensioning and Deck Loads

6.5.1 Background

The prediction of *elastic* stresses from applied loads or forces acting on prestressed highway bridge beams is an important step in the determination of the net stresses under service load. Accurate (or at least conservative) prediction of such stresses is essential for the design of highway bridges under service loads, in which it is generally desired to prevent cracking. Casting of the bridge deck and the placement of precast deck panels are obvious examples of applied loads added to prestressed concrete beams that produce elastic stresses. Post-tensioning of pretensioned beams can be considered either as an additional prestress or as an applied load, but in either case the addition of post-tensioning produces elastic stresses in the beam. Elastic stresses due to both post-tensioning and deck loads are considered in this section.

6.5.1.1 Post-Tensioning

Prediction of concrete stresses due to post-tensioning requires consideration of several factors, including tendon layout and losses in the post-tensioning force along the length of the tendons during post-tensioning. In particular, losses due to friction, anchorage, and elastic shortening (if multiple tendons are used) must be considered. A full discussion of the calculation of each of these components of loss is presented by Lin and Burns [76], and a brief summary is provided here.

The friction loss between the tendon and duct at any point along the length of the tendon can be approximated by Equation 6.10, which can be found in both the *AASHTO Standard Specifications* [3] and *AASHTO LRFD Specifications* [1]:

$$T_0 = T_x e^{(KL + \mu\alpha)}$$

where T_0 = tendon stress at jacking end

T_x = tendon stress at any point x along the tendon

K = wobble coefficient per foot of tendon

L = length from the jacking end to the point x along the tendon

μ = friction curvature coefficient

α = total angle change of tendon profile from jacking end to point x (radians)

Equation 6.10

Friction accumulates along the length of the tendon during tensioning, such that the tendon stress changes along the length of the member. Tendon stress will be highest at the jacking end and may be substantially lower at the non-jacking (dead) end. Friction loss can be considered to be the sum of two components, one related to the friction that would be expected to occur if the duct were straight, and one related to the effect of the curvature of the tendon (and duct) along the length of the member. The wobble coefficient K and the friction curvature coefficient μ in Equation 6.10 are intended to account for these effects, respectively. These coefficients are usually experimentally determined, and are often provided to the fabricator or contractor by the post-tensioning supplier. Note that the derivation of Equation 6.10 is presented by Lin and Burns [76].

Anchorage loss occurs as the anchorage device at the jacking end seats or “wedges” itself into the tendon. This loss is computed by considering that the tendon slips over a certain length as the seating occurs. The slip can be treated as a reverse-friction loss, since the slip occurs in a direction opposite to the initial tension. The anchorage loss is thus greatest at the jacking end of the beam and decreases over the tendon length as shown in Figure 6.15, where the (calculated) tendon stress after friction loss and after anchorage is plotted for a tendon from a San Angelo Eastbound HPC beam. As with the wobble and curvature coefficients, the anchorage (given as a length of seating at the anchorage) is usually specified by the post-tensioning supplier.

Because of their relative complexity, and the fact that losses must be computed at several sections along the length of the tendon, friction and anchorage losses are typically computed with the assistance of a computer program. Once they are known, the concrete stresses at each section can be determined using the simple formula given in Equation 6.11:

$$\sigma_{PT}(y) = \frac{T_x}{A} + \frac{T_x e_{PT} y}{I}$$

Equation 6.11

Note that T_x refers to the tendon stress at the section after friction and anchorage losses, and e_{PT} refers to the eccentricity of the tendon about the centroid of the beam. Both e_{PT} and y are assumed to be positive below the centroid, and compressive stresses are assumed to be positive.

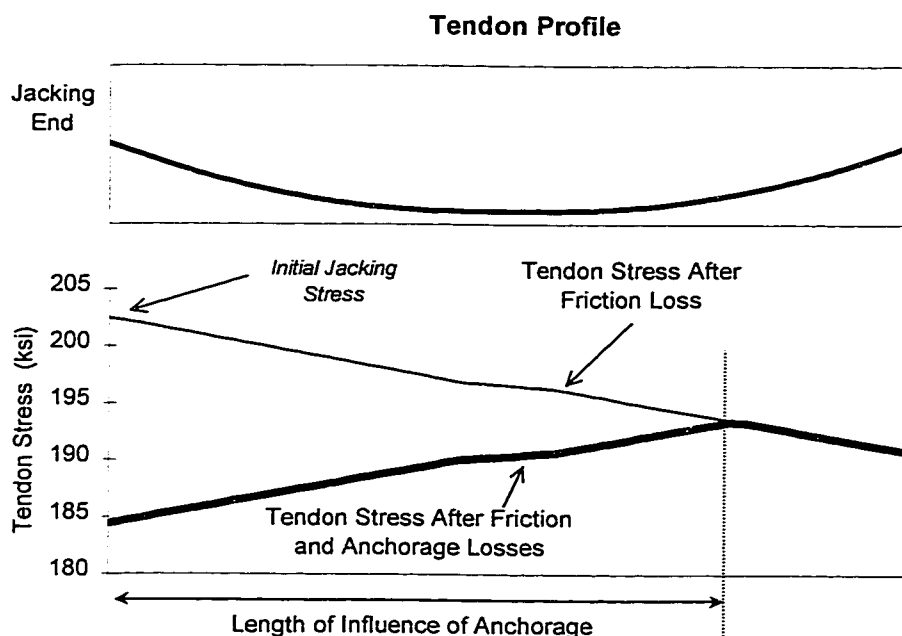


Figure 6.15 - Typical Stress Profile After Friction and Anchorage Losses

The calculation of stresses resulting from post-tensioning is slightly more complicated when multiple tendons are used, or when pretensioned strands are present. The effects of subsequent post-tensioning on previously tensioned tendons must be considered, since sequential stressing will cause the tendons stressed first to shorten. Similarly, post-tensioning will cause a change in stress in bonded pretensioned strands. These effects can be accounted for by treating the stress changes in any of the previously

stressed tendons or pretensioned strands as elastic shortening losses (or gain). The secondary effects on the cross-section can then be analyzed by applying the change in prestress force to the section at the location of the tendon or strands.

Alternatively, the transformed section may be used to account for the effects of changes in the *bonded* pretensioned strands [76]. If the post-tensioning force is applied to the transformed section, then elastic shortening losses need not be computed for the bonded pretensioned strands. The stress in such strands *will* change, but with this method the change in stress does not need to be considered a loss.

6.5.1.2 Deck Loads

Stresses resulting from deck loads are generally computed using a classical mechanics approach. The moment acting at a section is first computed and the stresses at an individual section resulting from the moment are then calculated. For a uniformly distributed load w , the resulting stress at midspan in a simply-supported beam would be computed using Equation 6.12:

$$\sigma(y) = -\frac{My}{I} = -\frac{\left(\frac{wL^2}{8}\right) \cdot y}{I}$$

Equation 6.12

Note that y is defined as positive below the centroid of the beam for Equation 6.12, and that compressive stresses are assumed to be positive. A positive moment is defined as one causing downward deflection in a simply-supported member.

Equation 6.12 can be applied to deck loads by computing the uniformly distributed weight of the deck per unit length of beam. For accurate estimation of this weight, several parameters must be known including thickness of the deck, spacing of the beams (i.e. tributary width of the deck per beam), and unit weight of the deck concrete. Unfortunately, the exact deck thickness is seldom known, and may vary substantially along the length of the beam or between beams. The exact unit weight of the deck concrete is also usually

unknown in design, and is often assumed to be 3.18 to 3.29 kg/m³ (145 or 150 lb./ft.³) for normal-weight concrete.

If the deck is unshored during construction, then the beam alone is assumed to resist the full deck load and the precast beam section properties should be used. If the deck is shored, then its weight is applied to the composite section and the section properties of the composite beam should be used. In either case, Equation 6.12 should be used with transformed section properties to be correct, but gross section properties are often used in design and are usually sufficient.

For bonded pretensioned strands or bonded post-tensioned tendons, the stress in the strands or tendons will change as a result of bending under the deck load (unless the prestress is concentric). If the transformed section is used, then the change in stress of the strands or tendons need not be considered as a "loss" [76]. However, if the gross or net concrete sections are used, the loss or gain in prestress should be applied to the section as a force, and secondary stresses in the beam calculated.

6.5.2 Measurements

6.5.2.1 Post-Tensioning

Concrete strains were measured immediately before and immediately after the post-tensioning of each San Angelo Eastbound HPC Type IV beam. Measurements were recorded at six locations across the depth of each beam using either vibrating wire or bonded resistance strain gauges. Strains were successfully recorded on six of the ten beams, including all five beams with vibrating wire gauges across the full depth, and one beam with bonded resistance gauges across the depth. Bonded resistance gauges in the other four beams did not yield useful data because of the deterioration of many of these gauges.

Strain readings were corrected for thermal effects, including thermal gradients, as discussed in Section 6.1.2. Because post-tensioning operations usually only required about one hour per beam, these corrections were typically very small. Strain readings were then converted to "measured" stresses by multiplying each strain by the modulus of elasticity

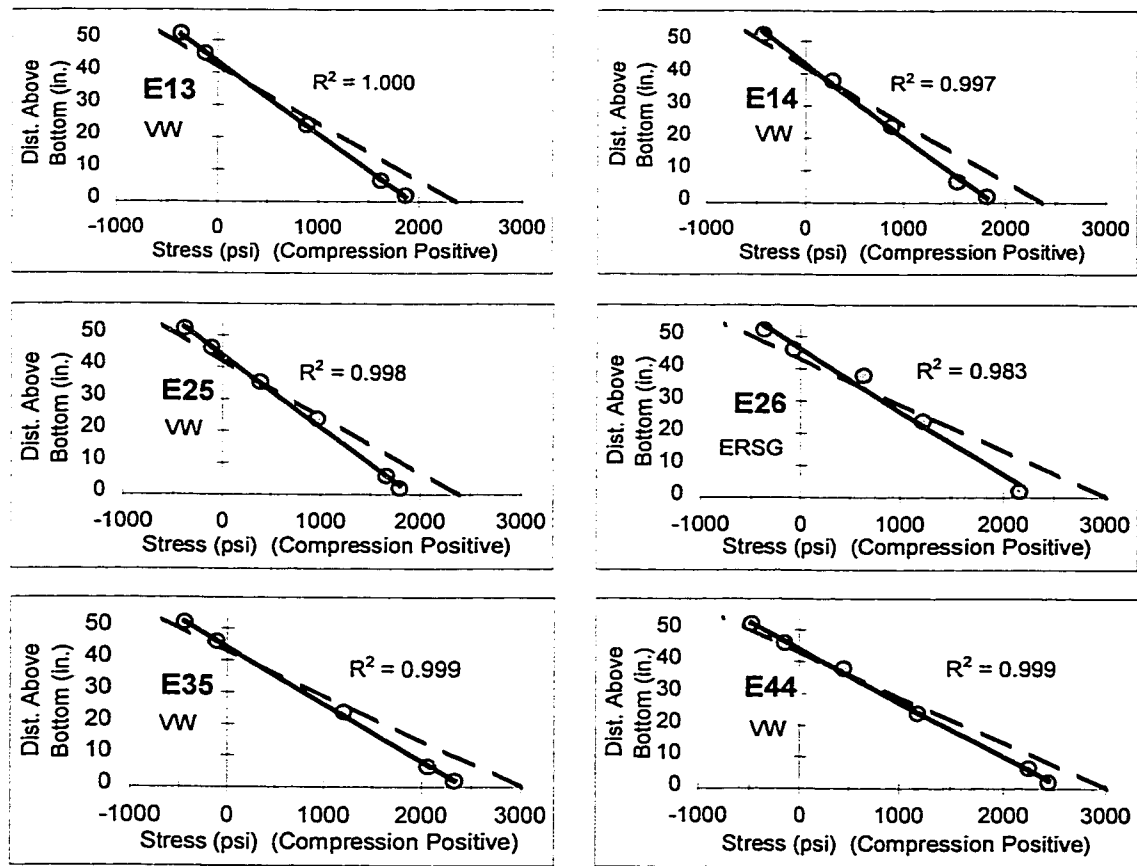
measured on companion specimens. Alternatively, the measured modulus could have been used to convert predicted stresses to strains for comparison with the actual measured strains. Stresses are compared in this section because they are the quantity that is generally more useful for design. In either case, the modulus of elasticity must be known exactly if correct comparisons are to be made between measured and predicted data. Differences between the actual and measured moduli of elasticity will introduce some degree of unavoidable error into the comparisons.

Measured elastic stresses in beams due to post-tensioning are shown in Figure 6.16 for six of the ten San Angelo Eastbound HPC beams. Once the measured stresses had been determined at each gauge in a beam, a regression line was fit to the data points through the depth of the section. These regression lines, which are also shown in Figure 6.16, were used primarily to determine the approximate curvature and value of M/I (the stress equivalent to curvature, or slope of the stress diagram) for each beam. Note that the plots clearly show that plane sections remained plane in all beams, and that slight inconsistencies in the measured data were only observed for Beam E26, in which data was collected using bonded resistance strain gauges.

Also shown in Figure 6.16 are predicted concrete stresses corresponding to an analysis based on measured parameters. The analyses are based on the method described in Section 6.5.1.1, and use transformed section properties and the measured modulus of elasticity for each beam. Post-tensioning tendon layouts were specified on the plans, and values for the wobble coefficient, curvature coefficient, and anchorage seating were specified by the post-tensioning supplier. These parameters were taken as 0.00066 /m (0.0002 /ft.), 0.25, and 9.5 mm (0.375 in.), respectively. The analyses also included the consideration of elastic shortening losses in the first (top) tendon due to the stressing of the second (bottom) tendon, although these losses were typically small.

For all six beams, measured stresses were substantially less than predicted stresses. Measured stresses at the bottom fiber were an average of 3.33 MPa (484 psi) or 18 percent less than predicted, and top fiber stresses were an average of 1.47 MPa (213 psi) or 30 percent less than predicted. The measured stress gradients were also less than predicted by an average of 21 percent. It should also be noted that the location of zero stress (i.e. neutral axis due to post-tensioning stresses) was slightly higher than predicted in all six beams, although the differences were generally small (about 25 mm [1 in.]).

Midspan stresses computed as part of the actual beam design (using the ADAPT computer program) are not plotted in Figure 6.16 for clarity. These computed stresses were very similar to the stresses predicted by the analysis using measured parameters, as can be seen in Figure 6.17 for Beam E13. Stresses computed by these two approaches differed by no more than 1.38 MPa (200 psi) at the bottom fiber and 0.79 MPa (115 psi) at the top fiber, and the slopes of the stress profiles differed by no more than 8 percent for any beam. Thus, the measured stresses were also less than the stresses computed during the actual beam designs by a significant amount.



Note: Points represent measured stresses (strains multiplied by measured modulus of elasticity). Solid lines represent regression lines fit to measured data (coefficient of determination given on each chart). Dashed lines represent predicted stresses based on analysis using measured modulus of elasticity and net transformed section properties.

Figure 6.16 - Measured and Predicted Beam Stresses Due to Post-Tensioning

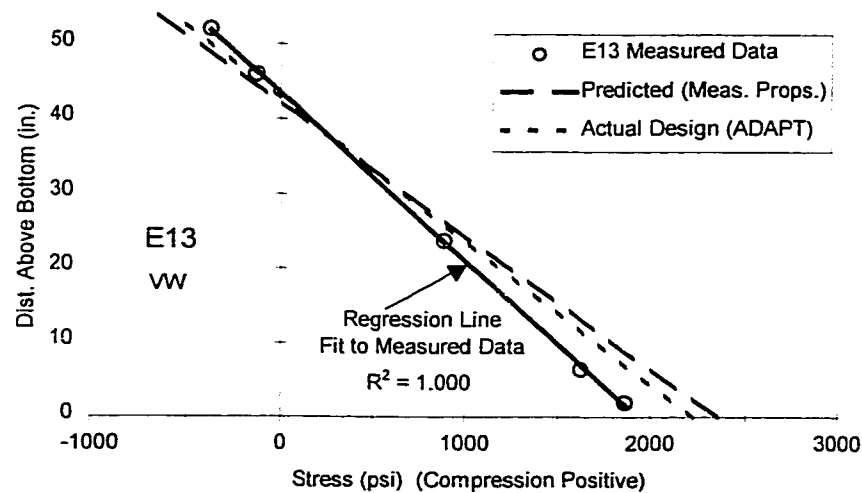


Figure 6.17 - Measured and Predicted Beam Stresses Due to Post-Tensioning in Beam E13 (Including Stresses Computed for Actual Beam Design)

6.5.2.2 Deck Loads

Strains resulting from the placement of the cast-in-place deck were measured in several beams. For each beam, measurements were taken prior to the placement of any concrete in the corresponding span and after all concrete in the span had been placed. As for other strain measurements, strains were recorded at six locations through the depth of each beam using vibrating wire gauges or bonded resistance strain gauges. Strains were successfully recorded in this manner for five San Angelo Eastbound HPC beams and for (both webs of) one Louetta Southbound HPC beam. Measurements were unsuccessful in other beams of these two bridges because bonded resistance strain gauges had deteriorated over time, or because in one case leadwires were damaged during casting of the deck. As discussed in Section 3.6.1, strains were measured for beams in the Louetta Northbound HPC and San Angelo Westbound non-HPC bridges, but these data were overwritten on the storage modules before being downloaded. It should also be noted that strain readings were not obtained for most beams immediately before and after placement of the precast deck panels, because panels were usually placed over a period of several days (or even weeks).

Strain readings were corrected for thermal effects using the procedure discussed in Section 6.1.2, although these corrections were typically small because the decks (panels and cast-in-place portion) kept the beams shaded from direct sunlight. Strain readings were then converted to “measured” stresses using the measured modulus of elasticity, and a regression line was fit to the measured data for each beam. Both of these procedures are discussed briefly in Section 6.5.2.1.

Measured elastic stresses in beams due to cast-in-place deck loads are shown in Figure 6.18 for six San Angelo Eastbound HPC beams and both webs of one Louetta Southbound HPC beam. It can clearly be seen that plane sections remained plane in all cases. Predicted stresses using measured parameters are also shown in Figure 6.18 for each beam. These predictions are based on transformed section properties, deck thicknesses measured by state inspectors during the pours, and the measured unit weights of the respective deck concretes.

For all six San Angelo Eastbound HPC beams, measured stresses were lower than predicted stresses. Compressive stresses at the top fiber were an average of 3.34 MPa (484 psi) or 27 percent less than predicted. Tensile stresses at the bottom fiber were an average of 2.37 MPa (344 psi) or 25 percent less than predicted. The location of the neutral axis for measured stresses almost exactly coincided with the predicted location (as computed using transformed section properties), and the stress gradient (M/I) was an average of 26 percent less than predicted.

Similar behavior was observed in Louetta HPC Beam S15, and excellent agreement was shown between the measurements in the east and west webs. Measured stresses were lower than predicted at the top fiber by 2.53 MPa (367 psi) or 24 percent, and by 1.27 MPa (184 psi) or 16 percent at the bottom fiber. The measured stress gradient was about 20 percent lower than predicted, and the location of the neutral axis for measured stresses was found to be slightly higher than the predicted location by about 33 mm (1.3 in.).

Stresses computed from actual beam designs are not plotted in Figure 6.18 because the beam designs did not separate the loads from precast deck panels and those from the cast-in-place portion of the deck. In design, stresses due to deck placement are usually based on an assumed unit weight for the deck concrete, and on theoretical deck thicknesses that may vary substantially from actual thicknesses. Furthermore, all beams in a single span (interior and exterior) were assumed to resist deck loads evenly in the design of the San Angelo Eastbound HPC beams, and Louetta beams were designed in groups

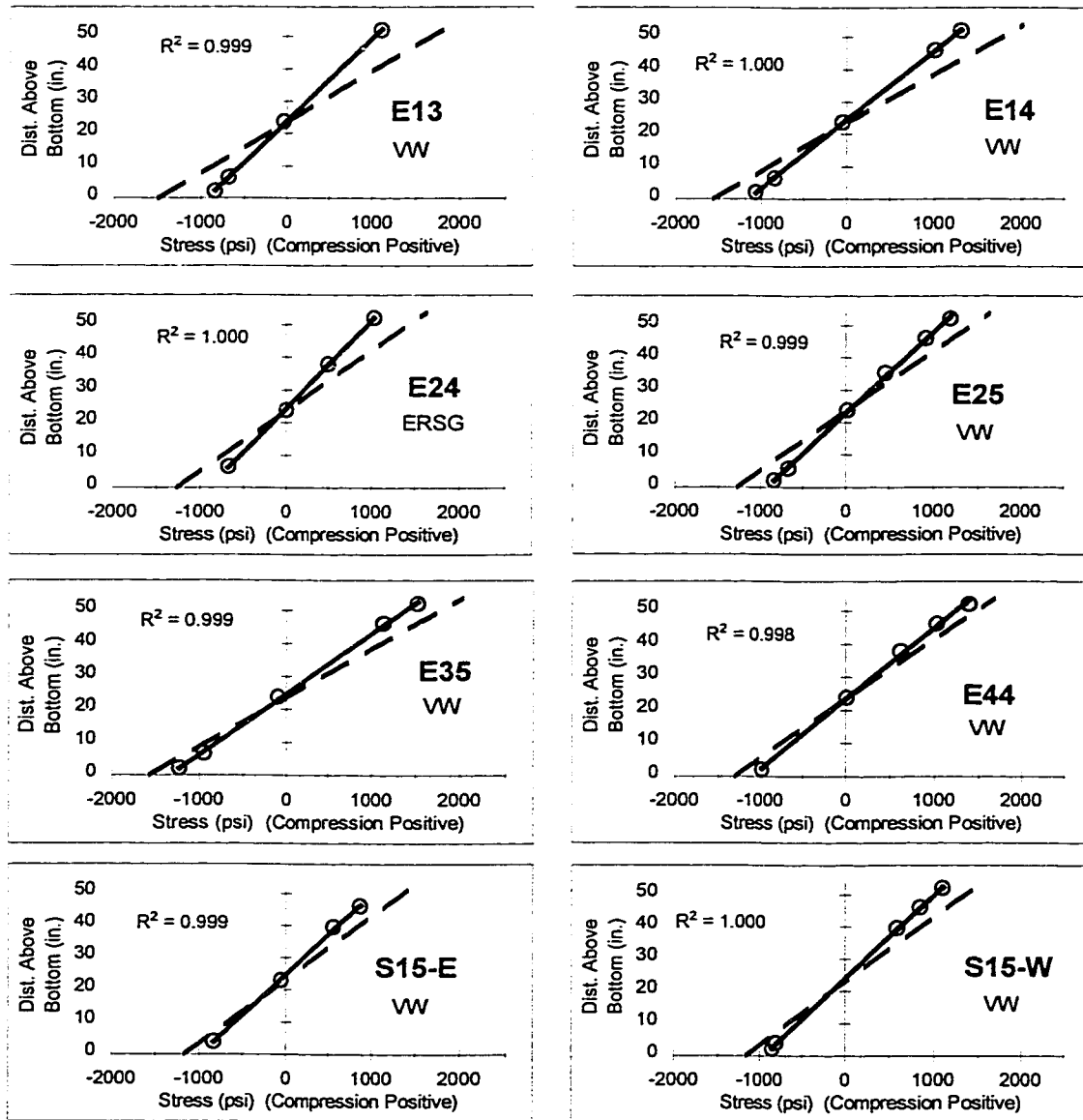
rather than individually to simplify fabrication. Because of these assumptions and simplifications, a large degree of inaccuracy might be expected for the design-based calculation of stresses due to cast-in-place deck loads. These assumptions are not examined in detail in this section, but are discussed with respect to the deflection of beams under the full deck load in Section 8.4. The effect on stresses and deflections should be similar in this case.

6.5.3 Discussion

6.5.3.1 Post-Tensioning

Observations regarding measured and predicted stress gradients (or curvatures) are relatively consistent with the observations discussed in Section 8.4.2.1 regarding camber due to post-tensioning. On average, the beam curvatures (measured on six beams) were less than predicted curvatures by 20 percent, while the beam cambers (measured on all ten San Angelo Eastbound HPC beams) were less than predicted by 28 percent. This consistency serves to validate each type of measurement.

There are two potential reasons why the measured stresses were substantially less than predicted. First, the modulus of elasticity in the actual beams may have been higher than the values obtained from measurements on companion specimens. Secondly, the friction and anchorage losses may have been underestimated, such that the actual post-tensioning force was lower than predicted. Because the stresses are directly related to both the modulus of elasticity (in the conversion of actual measured strains to stresses) and the post-tensioning force (as shown in Equation 6.11), it is impossible to determine the individual effects of each. Based on observations regarding other types of measurements in this research program, it is very probable that the actual modulus was higher than the measured modulus, but the extent of the difference is not clear. The magnitude of the difference between measured and predicted post-tensioning stresses is quite large, and it is probably reasonable to conclude that errors in estimation of the modulus and post-tensioning force *both* contributed to the lower than predicted stresses.



Note: Points represent measured stresses (strains multiplied by measured modulus of elasticity). Solid lines represent regression lines fit to measured data (coefficient of determination given on each chart). Dashed lines represent predicted stresses based on analysis using measured modulus of elasticity, measured deck thickness, and transformed section properties.

Figure 6.18 - Measured and Predicted Stresses in Beams Due to the Placement of Cast-in-Place Decks

Reasons for the slight observed difference in the measured and predicted neutral axis location are not clear, but the implication is a slight error in determination of beam section properties. Changes in any of the section properties affect the ratio of the magnitudes of the axial and flexural stresses given by the terms in Equation 6.11. If the actual (net transformed) area were lower, or the (net transformed) moment of inertia higher, then the neutral axis due to post-tensioning stresses would shift upward. Similarly, if the actual (net transformed) centroid were lower, or if the location of the tendons were slightly higher, then the neutral axis would shift upward. Because the measured neutral axis location was observed to coincide almost exactly with the predicted neutral axis location for stresses due to the placement of deck concrete, as discussed in Section 6.5.2.2, it is probably most likely that the location of the tendons was slightly different than anticipated. Any slight misplacement of the duct or movement of the duct during casting of the beam could have caused a slight change in the eccentricity of the tendons, and resulted in a shift of the neutral axis. Because the observed change was rather small, it should not be considered as significant. It is roughly equivalent to the differences in stress resulting from the use of gross section properties.

No specific adjustments to standard design procedures are recommended based on the observations in this section. Most importantly, the difficulty in exact prediction of post-tensioning stresses has been illustrated. Such stresses can be predicted accurately if all necessary parameters are known precisely, but since this is almost never the case, calculation of stresses should be regarded as approximate in nature.

6.5.3.2 Deck Loads

There is strong agreement between observations related to stress gradients (curvatures) due to cast-in-place deck loads and observations related to beam deflections under the same loads, which are presented in Section 8.4.2.2. In general, measured curvatures and deflections are significantly lower than predicted. For the San Angelo Eastbound HPC beams, curvatures were 26 percent lower than predicted and deflections were 25 percent lower than predicted. For the Louetta HPC beams, curvatures (measured only in each web of Beam S15) were 20 percent lower than predicted and deflections were

22 percent lower than predicted. The correlation between the two measurements serves as a verification or validation of the measured data.

There are two main potential reasons that measured stresses due to cast-in-place deck loads were less than predicted. First, the actual modulus of elasticity in the beams may have been higher than the values obtained from tests on companion specimens. This possibility is supported by observations regarding several other types of measurements in this research program, but it is unlikely that differences in the modulus could have accounted for the entire discrepancy. If the modulus of elasticity were the only cause, then the actual modulus would need to be 20 to 25 percent higher than for companion specimens, and the actual moduli would have to be in the range of 52 to 59 GPa (7500 to 8500 ksi).

It is also very possible that variations in the actual deck thickness contributed to the differences between measured and predicted stresses. Even though the deck thickness measured at point locations by state inspectors was used in the predictions, the actual deck thickness will undoubtedly vary throughout the span. Furthermore, small variations can lead to large differences in loads and stresses. A 13 mm (0.5 in.) difference in a 102 to 127 mm (4 to 5 in.) thick cast-in-place deck can cause a 10 to 13 percent difference in load or stress. Considering the magnitude of the difference between measured and predicted stresses, it is very likely that errors in estimation of *both* modulus of elasticity and deck thickness contributed to the stress difference.

As for stresses due to post-tensioning, no specific design adjustments are recommended on the basis of the measurements in this section. It should simply be noted that beam stresses under deck loads can be no more than estimates, as the parameters required for computation will almost never be known precisely.

6.6 Summary and Conclusions

The following observations were made in this chapter regarding Concrete Strains Before Release:

- 1) Concrete strain behavior prior to release appeared to be influenced to a great extent by restraint from formwork and the bed liner, hydration temperatures, and shrinkage (autogenous and drying).
- 2) With respect to concrete strains before release, some general patterns of behavior were identified in beams where measurements were recorded. These patterns are summarized in the idealized behavior model shown in Figure 6.3.
- 3) Strain gradients developed in beams during hydration in a manner that was consistent with observed temperature gradients. However, measured strains were substantially less than the free thermal strains ($E\alpha\Delta T$) corresponding to measured temperatures.
- 4) Cracking was observed on all instrumented beams prior to release as a result of restraint against shortening due to cooling and drying shrinkage. Cracks extended through the entire depth of the member at several longitudinal sections, as shown in the sketch of Figure 6.4.
- 5) Measurements in San Angelo Eastbound HPC beams just prior to release verified that these cracks were much larger at the tops of the beams than at the bottoms, indicating the presence of more restraint at the bottom. Cracks closed up completely upon release. Similar behavior was observed on Louetta HPC beams and San Angelo Westbound non-HPC beams.
- 6) The exact timing of the observed cracking is not known. Delays caused by the installation of instrumentation (for research) contributed to additional cracking, but a few cracks were generally present upon removal of side forms or shortly thereafter.

The following observations were made in this chapter regarding Concrete Stresses at Release of Prestress (Pretensioning):

- 1) Midspan concrete stresses at release of prestress (determined from strain measurements) were generally greater than predicted. Bottom fiber stresses were higher than predicted in about two-thirds of the beams, and top fiber stresses were higher than predicted in eleven of the thirteen beams (beam webs) for which measurements were successfully recorded.

- 2) High measured stresses are probably due in part to an unavoidable measurement error related to the restraint against shortening of the beam prior to release. The removal of this restraint would have caused an additional compressive stress (strain) to appear as part of the difference between baseline measurements (just before release) and measurements immediately after release.
- 3) Differences between actual modulus of elasticity and values obtained from tests on companion specimens also may have affected the conversion of measured strains to stresses. However, this error probably would have caused even larger differences between measured and predicted stresses.
- 4) For most of the Louetta HPC beams, a smaller stress gradient (i.e. more uniform stress) than predicted was observed over the depth of the beam at release. The opposite trend was generally observed to be true for the San Angelo Eastbound HPC beams, which contradicts the low camber measurements at release observed for these beams. This may be a result of restraint before release being more significant at the bottom of the beam.
- 5) Considering these factors, predicted stresses were at least reasonably accurate. Maximum differences between measured and predicted stresses at the bottom and top fibers were 4.70 and 5.07 MPa (681 and 735 psi) for design-based predictions. Respective maximum differences for predictions based on measured parameters were 4.12 and 3.69 MPa (598 and 535 psi).
- 6) The computation of release stresses for HPC beam designs was not found to be overly sensitive to assumptions related to prestress loss (force), self-weight, and modulus of elasticity. For most cases, errors in estimation of these properties will result in changes of no more than 1.72 and 3.45 MPa (250 and 500 psi) at the top and bottom fibers, respectively.
- 7) The use of gross section properties for computation of release stresses is an acceptable approximation for designs using HPC.

The following observations were made in this chapter regarding Time-Dependent Growth of Strains in Beams During Storage:

- 1) In the Louetta HPC beams, time-dependent strain growth during storage was substantially lower than predicted using an analysis based on measured properties. At both the top and bottom fibers, strain growth was on the order of 100 to 250 $\mu\epsilon$ lower than predicted at 120 to 650 days after release.
- 2) In the San Angelo Eastbound HPC beams, time-dependent strain growth at the bottom of the beam was about 150 to 200 $\mu\epsilon$ less than predicted at about one month after release. Almost no strain growth was observed at the top fiber in three of the four beams of this type where measurements were successfully recorded.
- 3) Curvature growth over time was slightly lower than predicted in the Louetta HPC beams, and slightly higher than predicted in the San Angelo Eastbound HPC beams. Both of these observations are consistent with the observations regarding time-dependent camber growth discussed in Section 8.3.
- 4) Differences between the actual moduli of elasticity, creep coefficients, and shrinkage strains and the parameters determined by tests on companion specimens may have contributed to the lower than expected strain growth observed in all beams. Errors in the creep and shrinkage correction factors for volume-to-surface ratio and relative humidity may also have affected these results.
- 5) Differential shrinkage may be responsible for the lack of strain growth at the top fiber of the majority of San Angelo Eastbound HPC beams, and may also explain the higher than predicted curvature growth in these beams. These observations also imply that if differential shrinkage is a factor, it is more prevalent in the San Angelo Eastbound HPC beams than in the Louetta HPC beams.
- 6) Predictions of time-dependent strains based on typical design assumptions, including the ACI 209 [8] "standard" creep and shrinkage parameters and Equation 4.4 for modulus of elasticity, grossly overestimated the actual time-dependent strains for the HPC beams in this study. Time-dependent strain behavior for HPC beams is clearly very sensitive to material properties.

The following observations were made in this chapter regarding the Elastic Responses of Beams to Post-Tensioning and Deck Loads:

- 1) Measured elastic stresses due to post-tensioning were significantly less than predicted in the San Angelo Eastbound HPC beams. Measured stresses were an average of 3.33 MPa (484 psi) or 18 percent less than predicted at the bottom fiber, and an average of 1.47 MPa (213 psi) or 21 percent less than predicted at the top fiber.
- 2) Measured stress gradients due to post-tensioning in the San Angelo Eastbound HPC beams an average of 21 percent less than predicted. This trend is consistent with observations regarding measured camber due to post-tensioning.
- 3) Differences between the actual and measured modulus of elasticity may have contributed to the difference between measured and predicted stresses due to post-tensioning by affecting the conversion of measured strains to “measured” stresses. Errors in the prediction of friction and anchorage losses may also have contributed. Based on the magnitude of the difference between measured and predicted stresses, it is likely that both of these factors contributed to some degree.
- 4) The location of the neutral axis due to post-tensioning stresses in the San Angelo Eastbound HPC beams was slightly higher than predicted according to the measured stresses. This may indicate a slight difference between the actual and intended tendon locations, or a difference between the actual and theoretical section properties. This neutral axis shift is not considered to be significant.
- 5) Measured elastic beam stresses due to placement of the cast-in-place deck were significantly less than predicted in the San Angelo Eastbound HPC beams. Measured stresses were an average of 3.34 MPa (484 psi) or 27 percent less than predicted at the top fiber, and an average of 2.37 MPa (344 psi) or 25 percent less than predicted at the bottom fiber.
- 6) In both webs of the one Louetta HPC beam where elastic beam stresses due to placement of the cast-in-place deck were recorded, measured stresses were significantly less than predicted. Measured stresses were an average of 2.53 MPa (367 psi) or 24 percent less than predicted at the top fiber, and an average of 1.27 MPa (184 psi) or 16 percent less than predicted at the bottom fiber.
- 7) Measured stress gradients due to placement of the cast-in-place deck an average of 26 percent less than predicted were in the San Angelo Eastbound HPC beams. For Louetta HPC Beam S15, the measured stress gradients (in both webs) were an average

of 20 percent lower than predicted. These trend are consistent with observations regarding measured camber due to post-tensioning.

- 8) Differences between the actual and measured modulus of elasticity may have contributed to the difference between measured and predicted stresses due to cast-in-place deck loads by affecting the conversion of measured strains to “measured” stresses. Variations in the actual deck thickness may also have contributed. Based on the magnitude of the difference between measured and predicted stresses, it is likely that both of these factors contributed to some extent.

6.7 Recommendations

The following recommendations are made on the basis of the information presented in this chapter regarding Concrete Strains Before Release:

Cracking in beams as a result of restraint against cooling and drying shrinkage prior to release should be avoided if possible. It is acknowledged that relatively high hydration temperatures are essential for the development of sufficient release strengths in HPC members at an early age. Furthermore, suppression of maximum hydration temperatures could result in the production of HPC prestressed highway beams becoming economically unfeasible. It is therefore recommended that cracking be deterred by releasing prestress in beams as soon as possible after release strengths are obtained. In general, beams should not be permitted to remain on the prestressing bed for extended periods if required concrete strengths have been obtained. Where possible, exposure conditions should also be controlled to prevent *rapid* cooling and shrinkage prior to release.

The following recommendations are made on the basis of the information presented in this chapter regarding Concrete Stresses at Release:

No adjustments to standard design procedures and approximations are necessary for designs with HPC. The use of gross section properties and assumed or calculated

values for modulus of elasticity, beam self-weight, and loss of prestress are acceptable. However, if any of these parameters are known more precisely from past experience or from trial batching, correct values should be used in calculations.

The following recommendations are made on the basis of the information presented in this chapter regarding Time-Dependent Growth of Strains in Beams During Storage:

Predictions of time-dependent strains, and elements of structural behavior directly related to time-dependent strains (i.e. prestress losses and camber or deflection), are clearly very sensitive to material properties for HPC beams. In particular, time-dependent strains are affected significantly by modulus of elasticity and creep. For a reasonable prediction of time-dependent strain behavior, these properties must be known to a good degree of accuracy.

Even if these parameters are estimated from companion specimen tests, however, actual time-dependent strain behavior can differ substantially from predicted behavior. The actual time-dependent strain behavior for members can be affected by variations in material properties, the elastic strain distribution, ambient conditions, and the effects of differential shrinkage. Since these effects are difficult to predict precisely, predictions of time-dependent strain behavior should never be taken as more than estimations of actual behavior.

The following recommendations are made on the basis of the information presented in this chapter regarding the Elastic Response to Post-Tensioning and Deck Loads:

The exact prediction of elastic beam stresses resulting from post-tensioning and the placement of cast-in-place deck concrete is difficult. These stresses can only be predicted accurately if all parameters are known precisely. These parameters include friction and anchorage losses for post-tensioning tendons, as well as the exact location of the tendon. For the placement of cast-in-place decks, the deck thickness will almost surely be highly variable. Because these parameters are typically not known to great precision, computations of elastic beam stresses due to these events should never be considered to be more than a good estimate. No specific changes to standard design methods are recommended for the calculation of these stresses.

7 CHAPTER SEVEN: PRESTRESS LOSSES

7.1 Introduction

7.1.1 General

Prestress losses are an important factor related to serviceability conditions for prestressed concrete highway bridge beams. The effective level of prestress in beams is related to the magnitude of prestress losses. As a result, losses have a direct impact on concrete stresses and deflection behavior. A poor estimate of losses can result in a structure where allowable stresses are exceeded or camber and deflection behavior is poorly predicted, such that the serviceability of a structure may be adversely impacted. It should be noted that for bonded members, prestress losses do not impact the ultimate strength of a member.

There are several sources of loss in prestressed concrete highway bridge beams. These losses are summarized below, although more extensive descriptions of each type of loss may be found in several texts [75,76,99]. The following discussion also focuses on losses in bonded members, although similar (yet slightly different) concepts apply to unbonded members.

Elastic shortening loss is related to the decrease in tension in the strand as the member to which it is bonded (or anchored) shortens under the transfer of prestress force. Similar effects occur when elastic loads are applied to a member with bonded strands. Bending under an applied load will result in a change in strand stress, which may be thought of as a loss or gain in prestress. It is extremely important to note, however, that any elastic change in strand stress should only be treated as a loss or gain of prestress if calculations are based on the net concrete section (or approximated by the gross concrete section). When calculations are based on the transformed section, these elastic effects need not and should not be treated as changes in prestress. These concepts are explained further by Lin and Burns [76].

There are other losses of prestress related to time-dependent effects in beams. *Creep* of concrete causes an time-dependent change in strain throughout the depth of the member. Where the cross-section is in compression under elastic effects, an additional compressive strain will develop over time. Any strand bonded to the concrete section in these compressive regions will shorten along with the concrete such that the tension in the strand is reduced. Concrete *shrinkage* will result in a similar time-dependent compressive strain (i.e. shortening), and will also cause a loss of tension in the strand. Strand *relaxation*, which is defined as the slight reduction in strand stress under a sustained deformation, also results in a time-dependent change in the strand stress. Since the changes in strand stress related to these time-dependent effects are related to internal effects within the cross-section, they should always be considered as losses of prestress.

In post-tensioned members, additional losses occur during stressing operations. These losses are related to *friction* between the duct and tendon, and to the loss of stress as the *anchorage* devices seat themselves into the tendon. Each of these losses are discussed in more detail in Section 6.5.1.1. Anchorage losses also occur during the stressing of pretensioned strands, but are often compensated for by a slight overstressing during fabrication. When this approach is used, anchorage losses are not considered in design for pretensioned members.

Finally, there is an additional potential loss in pretensioned members related to *thermal effects*. Because pretensioned strands anchored between two bulkheads during stressing are indeterminate structures, any change in temperature of the strands before they are bonded will not result in a change in the total length of the strand. Instead, there will be a change in strand stress as a result of temperature variations. Increases in temperature will result in a decrease in (tensile) strand stress associated with the prevention of elongation, while an decrease in temperature will result in an increase in (tensile) stress associated with the prevention of shortening. It should be noted that this potential loss is rarely considered in design, partly because it is difficult to predict temperature variations in the strand.

There are few documented measurements related to prestress losses in actual HPC highway bridge beams in the literature, although measurements are currently being recorded on HPC bridges in several states as part of the Federal Highway Administration HPC Bridge Showcase program. The improved stiffness and reduced creep of most HPC concretes, especially those exhibiting higher compressive strengths, will clearly have a

beneficial effect on prestress losses. However, the higher prestress forces associated with HPC designs result in larger compressive stresses. Common thought in the industry is therefore that losses in HPC members should be of the same order of magnitude as for conventional concrete members [10]. Unfortunately, many of the current methods used to predict losses do not account for the reduced creep and improved stiffness of HPC, such that extremely high losses may be calculated for these members. These methods will be discussed further in Section 7.4.

This chapter discusses measurements of prestress loss in the instrumented beams of this research program. Prestress losses before the release of pretensioning are discussed first. Measurements of elastic shortening loss at the release of pretensioned strands are examined next. Finally, total prestress loss in service is discussed, including time-dependent losses due to creep, shrinkage, and relaxation. Total measured losses are compared to losses predicted using a variety of current methods, and simple recommendations for the calculation of losses in HPC beams are presented.

7.1.2 Measurement of Prestress Losses Using Embedded Gauges

In Section 7.3 and Section 7.4, measurements of prestressed losses in actual bridge beams are presented. Technically, these measurements are indirect in the sense that changes in stress were not actually measured. Instead, changes in concrete strain at the level of the c.g. of pretensioned strands were measured using embedded gauges, and these results were converted to prestress losses. This method assumes that strain compatibility exists between the concrete and the steel (strands), such that the change in strain of the concrete is equal to the change in strain of the steel (at the level of the c.g.s.). This strain can then be multiplied by the modulus of elasticity of the prestressed steel in order to compute the change in steel stress, as shown in Equation 7.1:

$$\Delta f_{ps,measured} = E_{ps} \cdot \varepsilon_{cgs,measured}$$

Equation 7.1

Note that in Equation 7.1, the modulus of elasticity of the prestressed steel was taken as 193 GPa (28,000 ksi).

This method of measurement does not account for losses due to relaxation of the strand, since these losses do not cause a direct change in strain in the concrete at the level of the strand. Instead, these losses must be added analytically using an established relaxation-time relationship for the strand. If the low relaxation strand is used, as was the case for the beams in this research program, then the magnitude of the relaxation loss is very small, and little error should result from the use of this analytical correction.

Losses before the baseline strain readings are also not recorded using this measurement method. For the beams in this study, these baseline measurements were recorded just before release of pretensioning. There are certainly some unrecorded prestress losses prior to this time as a result of relaxation, early-age shrinkage, and thermal effects. These losses, which are discussed in Section 7.2, must also be added analytically to the total measurements of prestress loss. Of course, relaxation losses before release should be added in one analytical correction or the other, but should not be accounted for twice. The corrected measured prestress loss is thus given by Equation 7.2:

$$\Delta f_{ps, \text{total measured}} = E_{ps} \cdot \varepsilon_{cgs, \text{measured}} + \Delta f_{ps, \text{relaxation}} + \Delta f_{ps, \text{pre--release}}$$

Equation 7.2

Because measurements of prestress loss in this study are based on measurements using embedded concrete strain gauges, consideration must also be given to the effect of thermal variations on the measurements. Ideally, all concrete strains reported by the gauges should be corrected by removing the effects of uniform temperature changes and thermal gradients, as suggested in Equation 6.4. However, temperature measurements through the entire depth of the cross-section (noncomposite or composite) were not available for every single strain measurement, making it difficult to correct for thermal gradient effects in all cases. These effects were thus reduced by using early-to-mid morning readings for all prestress loss measurements, since the thermal gradients are typically very small at this time. In particular, 8:00 AM readings were used for measurements whenever possible. Fortunately, there was a concrete temperature measurement at the gauge location for every strain reading, such that adjustments for uniform temperature effects could be applied in all cases. This adjustment allows for readings at any time of the year to be directly compared, and minimizes (or theoretically eliminates) the effects of seasonal variations in bridge temperatures.

7.2 Prestress Losses Before Release

7.2.1 Background

In pretensioned concrete beams, there is some loss of prestress before release of the pretensioned strands. There are three main sources of loss at this stage – relaxation of the strand, temperature effects, and concrete shrinkage. Consideration of these potential losses is important because they directly affect the level of prestress applied to the member. Some components of loss that may occur before release, such as relaxation and shrinkage, are typically calculated as part of the total loss of prestress during design. However, consideration of these losses at the appropriate time stage (i.e. before release) should yield a more accurate assessment of stresses in the member. Furthermore, the magnitude of elastic shortening losses and long-term losses due to creep are directly dependent on the initial prestress *after* any losses that may occur before release. Thermal losses are also often ignored during the design process, especially since it is impossible to know the temperature at the time of stressing during the design stage.

Before the placement of concrete, each strand is essentially a simple indeterminate structure and computation of losses is theoretically straightforward. The strand is anchored between the bulkheads at each end of the bed and neglecting frictional effects at the temporary bulkheads along the bed (used to form up the beam ends), the stress in the strand should be uniform along its length. The entire length of the strand is free and has a uniform axial stiffness, such that the effect of temperature changes along the strand can be computed using a simple mechanics equation. For any temperature change, there will be an axial stress (or force) developed in the strand such that the total length of the strand does not change. This stress is given by the simple relationship shown in Equation 7.3, and can be considered directly as a loss (or gain) of prestress:

$$\Delta f_{ps,thermal(pre-casting)} = E_{ps} \cdot \alpha_{ps} \cdot \Delta T$$

Equation 7.3

Compressive stresses (or losses of tensile stress) are assumed to be positive. Since an increase in strand temperature will cause a decrease in tension, a positive ΔT represents an increase in temperature. For the computation of losses relative to the jacking stress, changes in temperature should be computed relative to the strand temperature at jacking.

Relaxation losses can also be computed fairly easily if the relaxation-time relationship is known. This relationship is sometimes supplied by the strand manufacturer, or a well known equation is typically used to compute this stress change:

$$\Delta f_{ps,relaxation} = f_{jack} \cdot \left(\frac{\log_{10} t}{45} \right) \cdot \left(\frac{f_{jack}}{f_{py}} - 0.55 \right)$$

Equation 7.4

The time t is the time after initial stressing and must be taken in hours. The yield stress of the strand f_{py} is typically assumed to be 90 percent of the nominal ultimate strength of the strand f_{pu} . Note that the relationship suggested in Equation 7.4 is for low-relaxation strands, which are typically used in the fabrication of prestressed highway beams today. If stress-relieved strands are used, then the stress change will be significantly higher, and may be predicted using Equation 7.4 by replacing the coefficient of 45 in the denominator with a value of 10.

Once concrete is placed during casting of the beam(s), the situation becomes much more complex. The strand is no longer free, but is instead restrained to varying degrees along its length. Even before bond actually occurs, there is a significant amount of frictional restraint between the fresh concrete and the strand. The level of restraint is then constantly changing as bond occurs and the concrete gains stiffness. The situation is further complicated by the fact that the concrete in which the strand is embedded is restrained by the formwork and bed liner. Considering the complexity of the situation, there is even some question at this stage regarding what is and is not a loss of prestress. A simplified approach considers the time periods before and after bond separately. For purposes of discussion, bond is assumed to occur at an instant rather than over an extended period of time.

Any thermal and relaxation losses before bond can be assumed to be "locked in" as bond occurs. Relaxation losses after bond can be computed in the same manner as before bond, although the rate of relaxation may increase slightly during hydration. Such an

increase would occur because the magnitude of relaxation is temperature-dependent [75]. Thermal effects after bond would cause strain changes in the strand and the concrete to which it is bonded, except that the total length of the strand between the bulkheads cannot change. Therefore, an additional stress in the strand must develop to accommodate this compatibility requirement. The magnitude of the change in stress will vary along the length of the strand because the effective axial stiffness of the strand is different in the sections of strand bonded to concrete and the free sections of strand. The stress change in the bonded areas, which can be deemed a loss (or gain) of prestress, will generally be much smaller than the stress changes in the free sections of strand. Upon release, any thermal losses that occurred between bond and release will essentially be “locked in”, as the external indeterminacy of the strand is eliminated.

If the two materials have the same coefficient of thermal expansion, then there is no relative movement between the two and no additional stresses are induced. But if the coefficients of thermal expansion differ significantly, then additional stresses may be induced in the bonded lengths of strand. These additional stresses can also be treated as a loss or gain of prestress, depending on which material has the higher coefficient of thermal expansion. However, the magnitude of these losses due to differing coefficients of thermal expansion will fluctuate over time as the temperatures in the beam fluctuate. In this sense, such losses are of a more temporary nature than those associated with temperature variations along the strand itself before release.

Drying shrinkage from a loss of moisture may occur after stripping of the formwork, causing a shortening of the concrete. Because this shortening occurs in the concrete alone, it will induce a compressive stress in the strand. In other words, there will be a loss of tensile stress in the bonded strand in order to maintain strain compatibility. This loss of tensile stress can be treated directly as a loss of prestress. Although the effect of shrinkage before release should theoretically consider the indeterminacy of the strand at that stage, an approximate solution would treat this shrinkage loss as in the completed (and released) beam. The loss due to shrinkage will be smaller before release when considering the strand indeterminacy, since the shortening of the strand along its bonded lengths will cause a secondary increase in tension along the length of the strand.

The approach described above is an extreme simplification of what is actually a very complex behavior process before release. However, this behavior is very difficult to model and the above approach is structured in a manner that at least allows for estimation

of losses before release. There are also many questions about when bond actually does occur in prestressed concrete beams, although there is little doubt that it does not occur instantaneously but rather over a period of time. As mentioned in Section 5.2.1, it is suggested by Mindess and Young [83] that final set occurs during the acceleration phase of the hydration cycle. This certainly implies that bond occurs before peak hydration temperatures are reached, but it does not necessarily suggest that bond occurs by the end of the dormant phase of hydration. Indeed, bond probably occurs at some point (or period of time) *during* the acceleration phase. As a result, the high hydration temperatures typically exhibited by HPC members, including those in this study discussed in Section 5.2.3, may have a legitimate impact on the magnitude of thermal losses before release.

7.2.2 Measurements

In an effort to measure prestress losses before release, a 445 kN (100 kip) capacity calibrated load cell was placed at the bulkhead during stressing operations. Forces in selected strands were monitored from stressing through release for five of the beam pours corresponding to the San Angelo Eastbound HPC beams. Typically, forces in two strands were monitored for each casting sequence. For each instrumented strand, the load cell was placed between the strand chuck and the bulkhead at the dead (non-stressing) end of the bed, as shown in Figure 7.1. Spacers composed of strand chucks with the wedges removed were used to maintain clearance between the load cell and the chucks of surrounding strands. Measurements were always taken at the dead end in order to not complicate the stressing process itself, and measurements at both ends would have required an additional data acquisition system or an excessive length of leadwire. Note that strands for these beams were stressed individually using a hydraulic jack.

Thermocouples were also placed on the instrumented strands in order to measure temperatures at the same instances when strand forces were measured. These thermocouples were attached directly to the underside of the strands using electrical tape, such that the thermocouples themselves were not exposed to direct sunlight. Two thermocouples were placed on each instrumented strand – one outside the beam (on the free strand) and one at least 3 m (10 ft.) into the beam. These locations are shown in Figure 7.1. Strand forces and temperatures were recorded every 15 minutes using a small

automated data acquisition system. This temporary data acquisition system was similar to the data acquisition systems described in Section 3.3.1, and was actually constructed using parts of those future systems.

Strand stresses (forces) were measured directly *before* casting using the load cells. As discussed in Section 7.2.1, each strand is a simple indeterminate system. Neglecting friction at the bulkheads, the stress should be uniform along the length of the strand. The stress measured using the load cell at the dead end of the bed should be representative of the stress at any point along the strand. Theoretical thermal losses between stressing and casting were also calculated analytically using Equation 7.3 and the measured strand temperatures. Similarly, theoretical relaxation losses were calculated analytically as a function of time using Equation 7.4. A measured stress loss and calculated stress loss were obtained for each instrumented strand in this manner, and the results are summarized in Table 7.1.

As expected, measured losses fluctuated as a function of the time between stressing and casting and the temperature variation during that period. Measured losses ranged from - 9.5 to 33.0 MPa (- 1.38 to 4.79 ksi), with an average of 9.9 MPa (1.43 ksi) or 0.71 percent of the nominal 1396 MPa (202.5 ksi) jacking stress. Total calculated losses before casting ranged from 14.7 to 41.9 MPa (2.13 to 6.07 ksi), with an average of 25.7 MPa (3.73 ksi) or 1.84 percent. For eight of the nine strands that were instrumented, the measured loss was less than the calculated loss.

An example of the measured and calculated stress changes and measured temperatures over the time period between stressing and casting can be seen in Figure 7.2 and Figure 7.3 for Strand 4C and Strand 6C, respectively. Strand 4C is a bottom layer strand in the fourth San Angelo Eastbound HPC beam pour, and was stressed on March 6, 1997. Strand 6C is a bottom layer strand in the sixth pour, and was stressed on March 19, 1997. Strand stresses clearly follow the variations in strand temperature, with increases in temperature causing a decrease in strand stress. However, fluctuations in the measured stress do not seem to be as great as the calculated fluctuations in stress, which may be a sign of friction at the intermediate bulkheads. Note that large fluctuations in temperature were observed for some strands, such as Strand 6C in Figure 7.3, while the temperature history was more stable for other strands, such as Strand 4C shown in Figure 7.2.

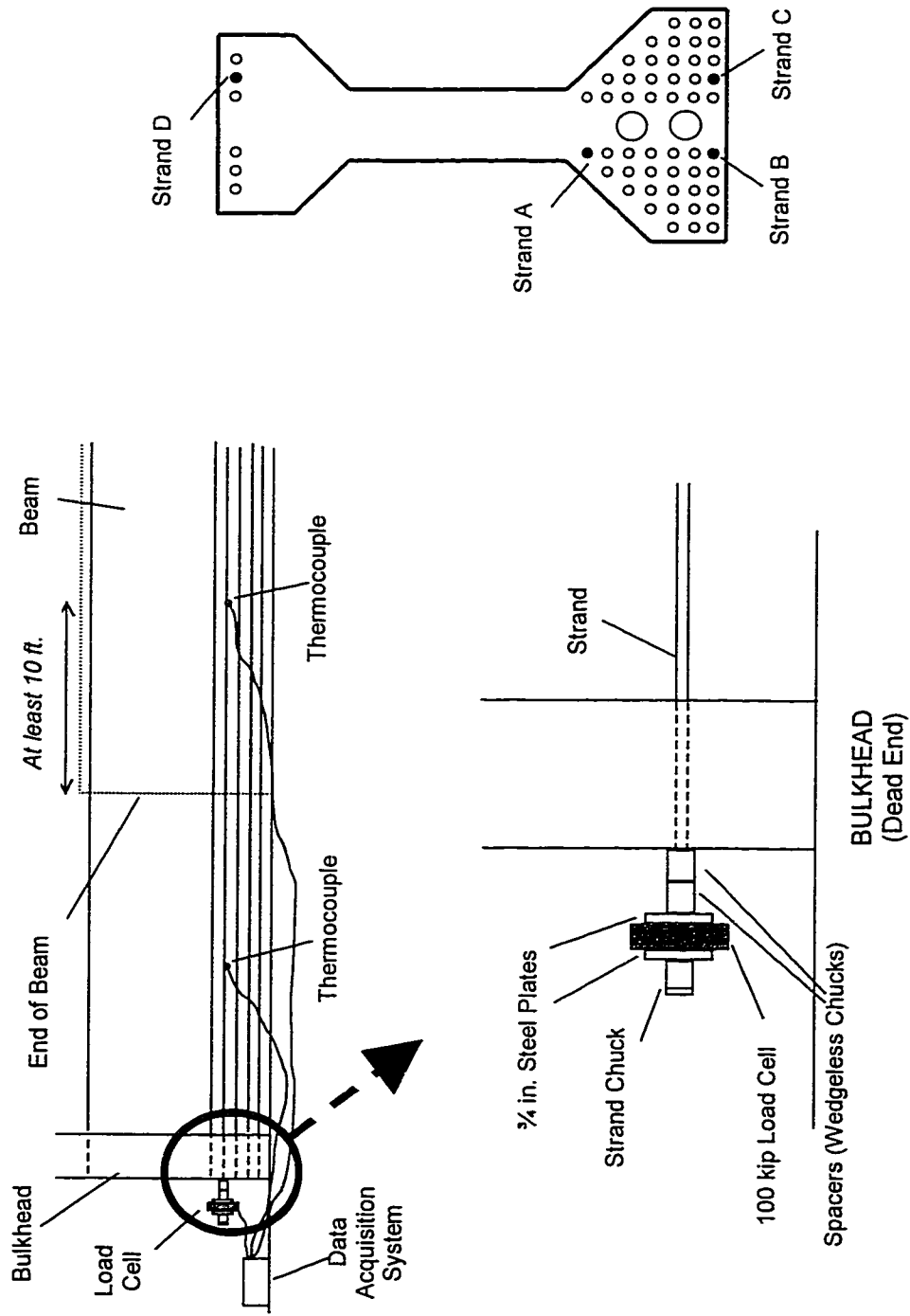


Figure 7.1 - Setup for Measurement of Strand Stresses (Forces) and Temperatures Before Release

Table 7.1 - Measured and Calculated Prestress Losses Between Stressing and Casting

Pour/Strand	Stressing Date	Time Between Stressing and Casting (days)	Measured Strand Temperatures (° F)		Measured Strand Forces (kips)		Measured Prestress Loss (ksi)	Calculated Prestress Loss (ksi)		
			At Stressing	Just Before Casting	At Stressing ¹	Just Before Casting		Total	Thermal	Relaxation
1-A	2/13/97	5.87	57.7	72.8	43.52	42.48	4.79	6.07	2.69	3.38
3-A	2/28/97	3.06	72.1	79.7	43.10	42.39	3.27	4.20	1.28	2.92
3-B	2/28/97	3.06	70.3	78.3	45.02	44.84	0.83	4.80	1.34	3.46
4-A	3/6/97	1.92	61.6	66.6	41.54	41.71	-0.78	3.13	0.84	2.29
4-C	3/6/97	1.92	57.1	66.0	43.80	43.64	0.74	4.35	1.50	2.85
6-C	3/19/97	2.69	68.1	65.3	42.22	42.36	-0.65	2.13	-0.49	2.62
6-D	3/19/97	2.69	69.6	69.1	41.46	41.76	-1.38	2.38	-0.04	2.42
7-C	3/27/97	1.93	69.5	73.9	41.81	41.40	1.89	3.09	0.73	2.36
7-D	3/27/97	1.93	69.8	75.2	42.39	41.49	4.15	3.40	0.90	2.50
Average²		2.79	66.2	71.9	42.76	42.45	1.43	3.73	0.97	2.76
			97.3 %	96.6 %			0.71 %	1.84 %	0.48 %	1.36 %

° F = ° C*(1.8) + 32 1 kip = 4.448 kN 1 ksi = 6.895 MPa = 0.006895 GPa

¹ Recorded within 15 minutes after strand was stressed.

² Percentages represent loss as percentage of 1396 MPa (202.5 ksi) nominal jacking stress (= .75*f_{pu})

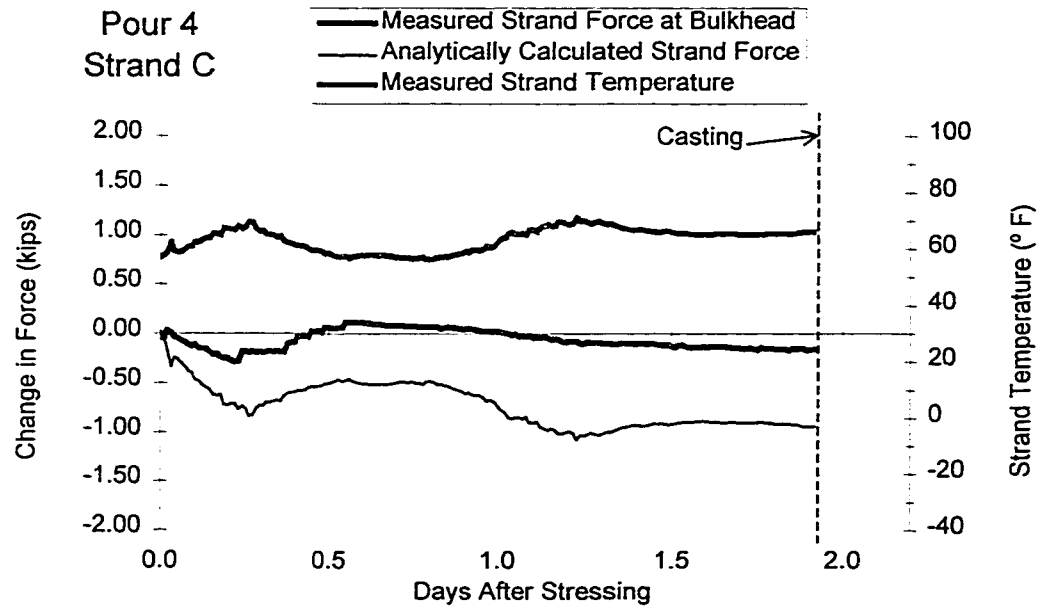


Figure 7.2 - Measured Strand Stress and Temperature Before Casting (Strand 4C)

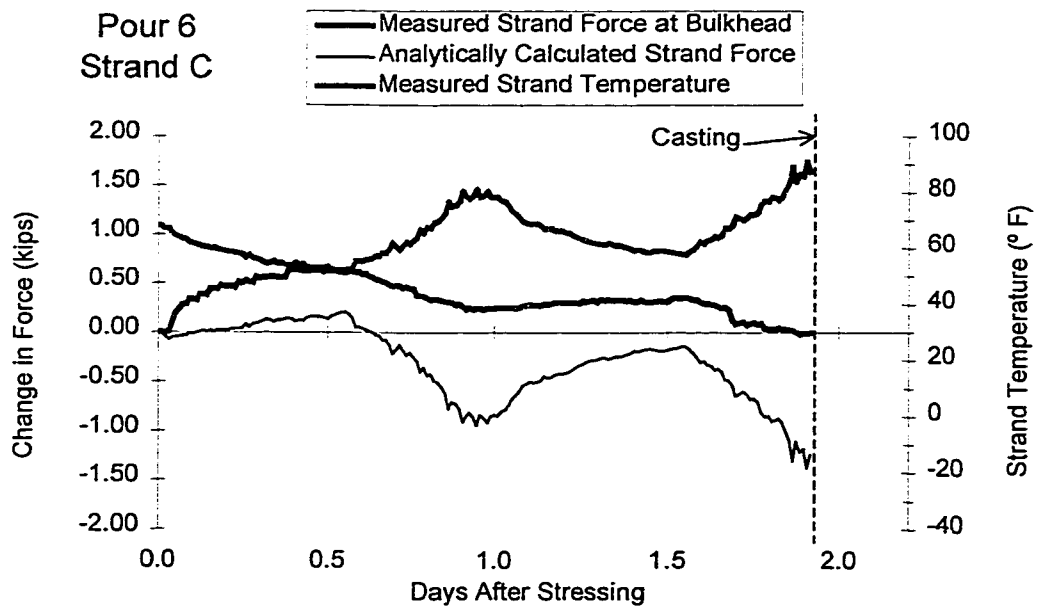


Figure 7.3 - Measured Strand Stress and Temperature Before Casting (Strand 6C)

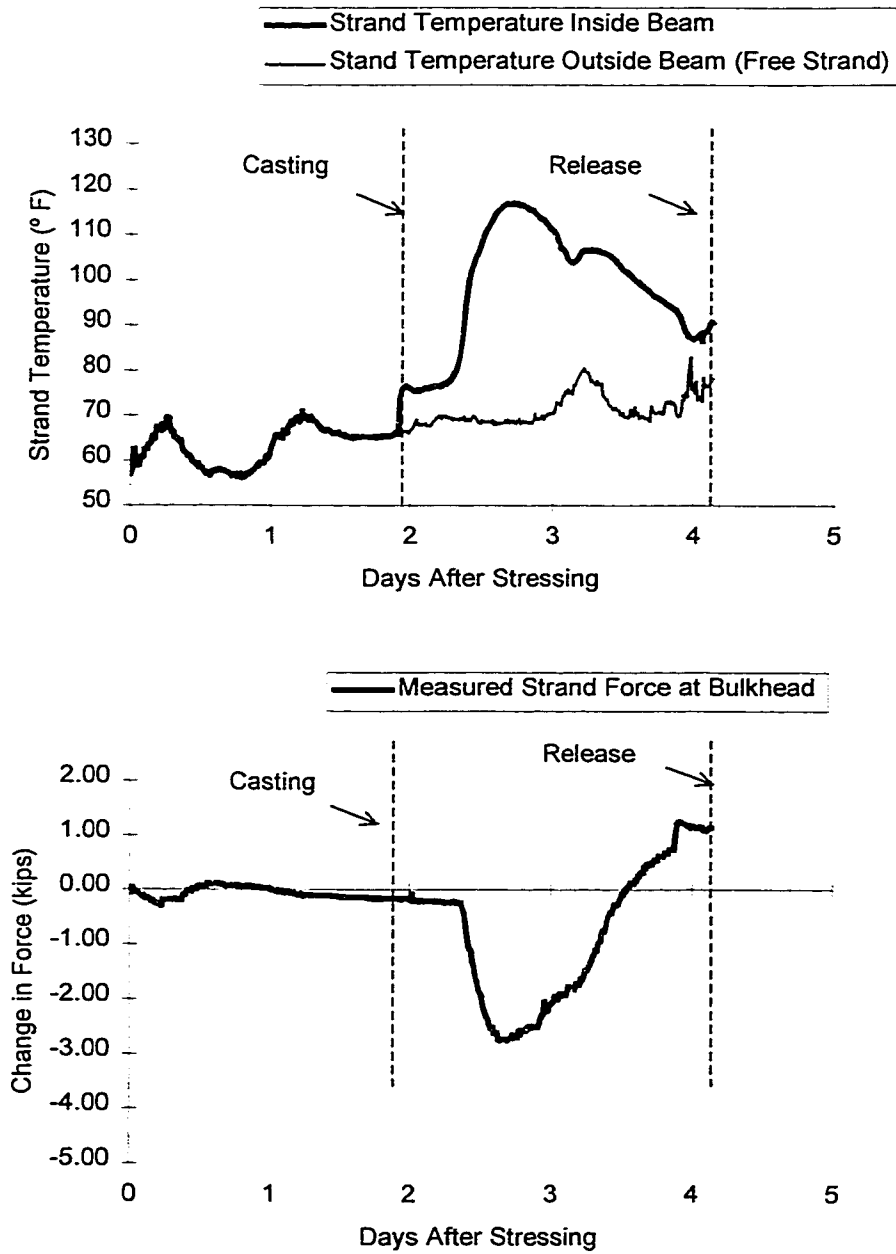


Figure 7.4 - Measured Strand Forces and Temperatures from Stressing Through Casting and Release (Strand 4C)

The initial measured stresses (forces) at stressing were also lower than expected. On average, initial measured stresses were lower than the nominal jacking stress of 1396 MPa (202.5 ksi) by an average of 2.7 percent. The average initial force per strand was measured to be 190.2 kN (42.76 kips) for these 15 mm (0.6 in.) diameter strands, which is equivalent to an initial stress of 1358 MPa (197.05 ksi). Possible reasons for these low initial stresses, and the low measured losses, are discussed in Section 7.2.3.

Prestress losses *after* casting are much more complex, as discussed in Section 7.2.1, and cannot be measured by simply placing a load cell on the strand at the bulkhead. Unlike the situation before casting, in which the strand is a simple indeterminate structure, the strand after casting is a very complex, highly indeterminate structure. The stress will not necessarily be uniform along the length of the strand because of the stiffness and restraint effects of the surrounding concrete and formwork. There is really no simple way to measure the stress in the bonded strand at this stage, although attaching strain gauges directly to the strand would provide additional information related to the strain behavior in these regions. For accurate measurements, stresses would have to be measured directly at several points along the bonded portion of the strand.

Still, the use of a load cell placed at the bulkhead does offer some benefit. In particular, the shape of the measured stress curve (at the bulkhead) can provide some insight into the behavior during this stage. An example of a measured stress curve is shown in Figure 7.4 for Strand 4C, which was stressed on March 6, 1997. Measured strand temperatures inside and outside of the beam are also plotted in Figure 7.4. Decreases in the strand force (stress) at the bulkhead are indicative that the strand is trying to lengthen at some point or points along the member. Similarly, increases in the strand force (stress) at the bulkhead indicate that the strand is trying to shorten. Clearly, there is a large degree of symmetry between the temperature history inside of the beam and the measured force in the strand at the bulkhead. Although little can be said quantitatively about the magnitude of the stress in the strand along its length on the basis of the measured force (stress) at the bulkhead alone, the variations in force at the bulkhead do confirm that stress is changing to some degree along the entire length of the strand.

In an effort to *estimate* the magnitude of losses in the bonded strand between casting and release, a simple analytical model was developed. The model, which is summarized in Figure 7.5, assumes that the highly indeterminate system can be replaced with a simpler indeterminate system. The simpler system essentially consists of a strand

anchored at each end, with an increased axial stiffness over a portion of its length. This increased stiffness is intended to model the effects of fresh concrete, bonded concrete, and formwork on the free movement of the strand, and is represented by the coefficient β . The coefficient β is essentially a multiplier on the axial stiffness of the free strand.

For simplification, β is taken to be constant over distinct intervals between significant events. These events are also summarized in Figure 7.5. A more elaborate approach might consider variations in β in a more continuous sense. For obvious reasons, β should generally increase with time and always be greater than unity. It should be noted, however, that β may actually decrease upon the removal of the side forms for the beam, since this allows a more unrestricted deformation of the concrete to which the strand is bonded.

Another important assumption related to the simplified model is that the strand forces at each bulkhead (i.e. at each end of the bed) are equivalent. In reality, friction along the bed may cause these forces to differ. If the friction acts symmetrically along the length of each beam, then this may be a valid assumption. An equally important assumption is that the individual lengths of bonded and free strand have the same stress and may be combined. This assumption is somewhat similar to the previous assumption in that if friction develops symmetrically along each beam, the assumption may hold true.

In the simplified analytical model, temperature changes are assumed to occur uniformly along the bonded and free lengths of strand, respectively. The coefficient of thermal expansion is also assumed to be the same for both sections of strand. As the respective lengths of strand try to deform, a force will be developed at the bulkheads in order to satisfy the compatibility requirement of no change in the total strand length. The following compatibility equation can thus be developed:

$$\alpha \cdot \Delta T_f \cdot L_f + \alpha \cdot \Delta T_b \cdot L_b - \frac{F \cdot L_f}{EA} - \frac{F \cdot L_b}{\beta EA} = 0$$

Equation 7.5

The change in force at the bulkhead, F , can be solved by rearranging Equation 7.5. Note that the change in force in the free strand, F_f , is equal to the change in force at the bulkhead, F . These (changes in) forces can be computed using Equation 7.6:

$$F = F_f = \frac{\alpha \cdot \beta EA \cdot (L_f \cdot \Delta T_f + L_b \cdot \Delta T_b)}{\beta \cdot L_f + L_b}$$

Equation 7.6

The change in force in the bonded strand will be less than the change in force at the bulkhead because of the increased effective axial stiffness. The prestress loss due to thermal effects between casting and release can thus be computed using Equation 7.7:

$$\Delta f_{ps,thermal} = \frac{F_b}{A} = \frac{F}{\beta A}$$

Equation 7.7

Note that the force in the *system* is assumed to be constant along the length, but the force in the *bonded strand* is assumed to be smaller. This is somewhat analogous to saying that a portion of the force is taken by the concrete surrounding the strand, and perhaps by any formwork restraining the concrete.

Relaxation losses in the time period between casting and release can be computed in the same manner as before casting using Equation 7.4. The effects of shrinkage after the stripping of formwork can be treated in a similar manner as thermal effects. A compressive shrinkage strain can be applied to the bonded length of strand, and the force necessary to satisfy compatibility requirements can be computed. Note that only the axial stiffness of the strand is considered to resist the application of this shrinkage strain, since it is applied to the strand by the concrete through bond. However, the effective axial stiffness is assumed to resist the compatibility force. As for thermal effects, a compatibility equation is developed and the forces at the bulkhead, in the free strand, and in the bonded strand (as well as the prestress loss in the bonded strand) can be computed:

$$- \epsilon_{sh} \cdot L_b + \frac{F \cdot L_f}{EA} + \frac{F \cdot L_b}{\beta EA} = 0$$

Equation 7.8

$$F = F_f = \frac{\varepsilon_{sh} \cdot \beta EA \cdot L_b}{\beta \cdot L_f + L_b}$$

Equation 7.9

$$\Delta f_{ps,shrinkage} = \frac{F_b}{A} = \varepsilon_{sh} \cdot E - \frac{F}{\beta A}$$

Equation 7.10

The main difficulty in applying the model is in the determination of the stiffness multipliers β_i . A trial-and-error type approach was thus used to apply the simplified model to the data collected in this study. Appropriate values of β were essentially determined for each set of strand force (at the bulkhead) and temperature measurements using a curve matching process. The appropriate values of β were defined as those that resulted in analytical curves for force at the bulkhead that showed the most agreement with the shape of the curves corresponding to the measured force at the bulkhead. An example can be seen in Figure 7.6 for Strand 4C, where the best match between curves was found for $\beta_1=1$, $\beta_2=5.5$, and $\beta_3=50$. Note that a simplifying assumption was also made that $\beta_4=\beta_3$, which is acceptable because these values of β were generally found to be very large in magnitude.

Once the appropriate values of β were determined as well as possible, changes in the force within the *bonded* length of strand were computed using the equations developed in this section. Temperatures used in the model were based on the actual measurements, and shrinkage was assumed to occur at a rate described by the shrinkage-time relationship for the beam concrete listed in Table 4.22. Appropriate correction factors for volume-to-surface ratio of the beams and average relative humidity were also assumed. Relaxation losses were calculated using Equation 7.4.

Losses calculated analytically using the measured force and temperature data are summarized in Table 7.2. The total losses calculated between casting and release ranged from 17.9 to 58.7 MPa (2.59 to 8.52 ksi), with an average of 33.1 MPa (4.80 ksi). This average loss corresponds to a 2.37 percent loss relative to the nominal jacking stress of 1396 MPa (202.5 ksi). About 64 percent of this average loss could be attributed to thermal loss, about 30 percent to shrinkage, and about 5 percent to relaxation. The magnitude of

thermal losses computed using the analytical model did show some correlation with the measured temperature increases during hydration, but the magnitude was not nearly as well defined as expected. This can probably be attributed to the variation in the parameter β_2 observed among the beams. This parameter was determined by the curve-matching technique described above, and is largely a measure of the level of restraint on the strand.

7.2.3 Discussion

There are a few possible reasons that measured losses between stressing and casting were lower than losses calculated using the measured times and temperatures. First, it is possible that some of the relaxation losses were not measured. The data acquisition system was automated to collect stress (force) and temperature data every 15 minutes, so the initial reading could have been recorded anytime within the first 15 minutes after the stressing of the strand was actually completed. Second, it is quite possible that friction between the strands and intermediate bulkheads (used to form the beam ends) contributed to the lower measured than calculated losses before casting. The shapes of the measured strand force curves, such as those shown in Figure 7.2 and Figure 7.3, generally support both of these possible causes. The difference between the measured and calculated loss tends to grow with time, very quickly at first, implying a difference in relaxation loss. The measured strand force curves also show much less variation due to temperatures than the calculated curves, indicating the possibility of frictional restraint.

The same two sources of error may contribute to the low measured initial stresses. The initial stress was measured within the first 15 minutes after the strands were stressed, but some relaxation will have occurred during this time period. In addition, the stresses (forces) were measured at the dead-end bulkhead. Any friction between the strand and intermediate bulkheads during stressing would reduce the stress at the dead-end, but not at the stressing end. Together, these factors may have combined to account for the average 2.7 percent difference between the measured initial stress and the nominal 1396 MPa (202.5 ksi) jacking stress.

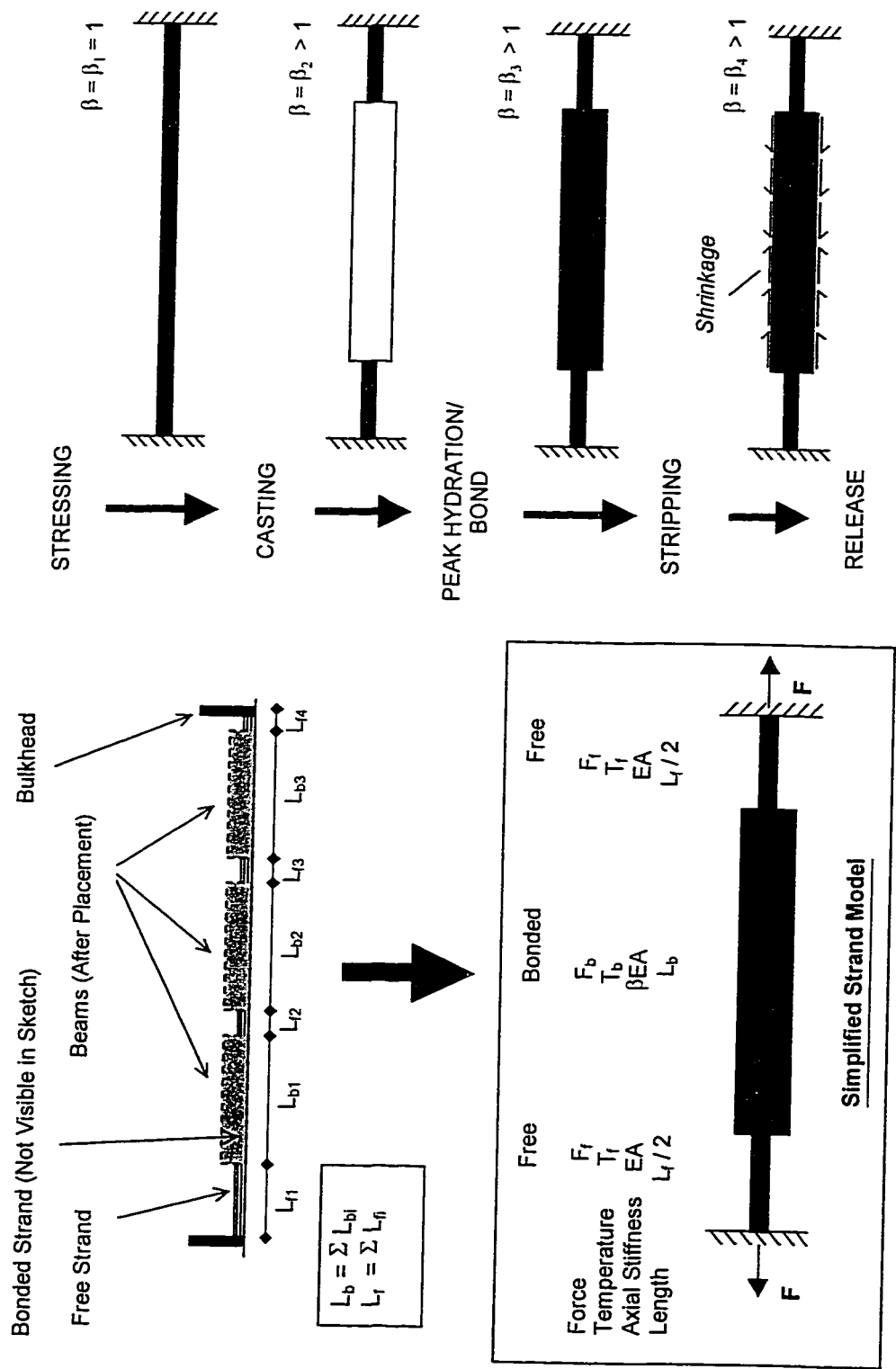


Figure 7.5 - Analytical Model for Calculation of Estimated Prestress Losses Before Release

Table 7.2 - Prestress Losses Between Casting and Release Calculated Using Analytical Model

Pour/Strand	Stressing Date	Time Between Casting and Release (days)	Measured Strand Temperatures ¹		Stiffness Parameters ¹		Calculated Prestress Losses			
			At Stressing (° F)	Just Before Casting (° F)	β_2 (kips)	$\beta_3 = \beta_4$ (kips)	Total (ksi)	Relaxation (ksi)	Shrinkage (ksi)	Thermal (ksi)
1-A	2/13/97	1.14	72.8	127.5	1.7	5.4	4.90	0.09	0.44	4.37
3-A	2/28/97	0.89	79.7	133.7	9	12	2.74	0.14	0.74	1.86
3-B	2/28/97	0.89	78.3	123.6	7.5	12	2.59	0.14	0.74	1.71
4-A	3/6/97	2.21	66.6	124.5	5	50	5.38	0.34	1.92	3.12
4-C	3/6/97	2.21	66.0	116.9	5.5	50	4.92	0.43	1.92	2.57
6-C	3/19/97	2.15	65.3	129.5	3.3	50	6.82	0.28	1.83	4.71
6-D	3/19/97	2.15	69.1	147.2	3.3	50	8.52	0.26	1.83	6.43
7-C	3/27/97	1.83	73.9	124.6	6	50	4.06	0.31	1.87	1.88
7-D	3/27/97	1.83	75.2	137.8	14	40	3.30	0.33	1.87	1.10
Average ²		1.70	71.9	129.5			4.80	0.26	1.46	3.08
							2.37 %	0.13 %	0.72 %	1.52 %

° F = ° C*(1.8) + 32 1 kip = 4.448 kN 1 ksi = 6.895 MPa = 0.006895 GPa

¹ Determined by matching curves for change in force at bulkhead (see discussion).

² Percentages represent loss as percentage of 1396 MPa (202.5 ksi) nominal jacking stress (= .75*f_{pu})

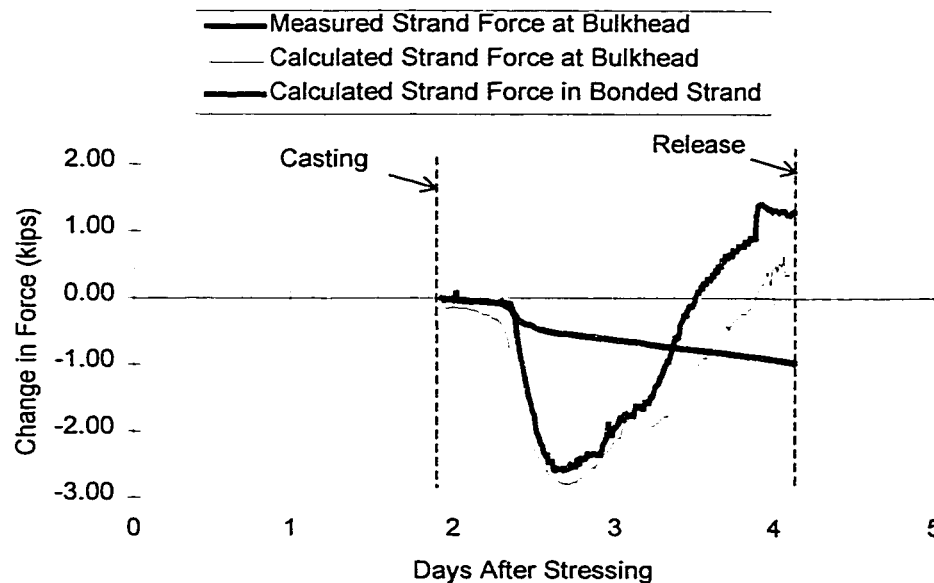


Figure 7.6 - Measured Strand Force at Bulkhead and Calculated Strand Forces Between Casting and Release (Strand 4C)

It is clear from the shape of the measured force curves between casting and release that there is some change in the strand stress during the period between casting and release. The magnitude of the total actual losses (i.e. change in stress in the *bonded* strand) during this time period were estimated to be in the range of about 17 to 59 MPa (2.5 to 8.5 ksi). However, the analytical model used for these calculations is only intended to provide a rough estimate. Aside from the fact that the model is an extreme simplification of a highly complex indeterminate situation, a few effects that may influence losses between casting and release are not considered in the model. Differences between the coefficients of thermal expansion of the strand and concrete would lead to a loss or gain of prestress. The coefficient of thermal expansion of concrete is a function of moisture content and age [95], so the actual coefficient of thermal expansion of the concrete during this stage may be very different from the values obtained on test specimens several months later. The actual coefficient of thermal expansion of the young concrete may therefore differ significantly from the coefficient for the strand. As mentioned in Section 7.2.2, it is also quite possible that the loss due to relaxation increases under the high hydration temperatures exhibited in HPC beams.

Clearly, much more research is needed on prestress losses before release. A good analytical or empirical approach needs to be developed that is simple enough to apply in design yet representative of the complex circumstances during fabrication. The analytical model presented in Section 7.2.2 may or may not meet these requirements. Additional research is especially important considering the high hydration temperatures often developed in HPC beams. Thermal losses for HPC beams may or may not be significant, but the simple model used in this study at the very least indicates that thermal loss is present to some degree. As a rough average estimate based on the measurements in this study, the thermal losses between casting and release appear to be approximately equal to the strain change corresponding to about one-third of the temperature increase during hydration. For these HPC beams, this is roughly equivalent to the strain change corresponding to a temperature increase of 11 °C (20 °F). It is recommended that thermal losses of approximately this magnitude be considered in future HPC designs, until further research is conducted in this area.

No broad conclusions should be made regarding total losses before release using only the measurements on the nine strands instrumented in this study. Still, some estimate of the total pre-release losses was necessary for other calculations in this research program. Based on the measured initial stresses, the measured losses before casting, the analytically-calculated losses between casting and release, and the potential errors in each of these measurements, pre-release losses were estimated for the beams in this study. Pre-release losses for the San Angelo Eastbound HPC beams were assumed to be approximately 4.5 percent of the nominal jacking stress, except for those beams which were released only one day after casting. For HPC beams released one day after casting, including all Louetta HPC beams, a slightly smaller 4.0 percent pre-release loss was assumed. Finally, a 3.5 percent loss was assumed for the San Angelo Westbound non-HPC beams on the basis of a much faster production schedule. As necessary, these estimates were used for calculations throughout this research program.

7.3 Elastic Shortening at Release of Pretensioned Strands

7.3.1 Background

Elastic shortening is the loss of prestress associated with shortening of the strand or tendon when the concrete member to which it is bonded or anchored is compressed. In pretensioned members, the stress in the strands is reduced during the transfer of prestress force to the concrete. In post-tensioned members, tendons do not lose stress due to elastic shortening during stressing because the concrete member is compressed prior to anchorage of the tendon. However, elastic shortening loss does occur during the sequential stressing of post-tensioned tendons, with tendons stressed earliest losing stress as subsequent tendons are stressed. Note that this section will only be concerned with elastic shortening losses in pretensioned strands.

For pretensioned members, elastic shortening losses can be computed exactly using the transformed section [76]. The full prestress force immediately before release P_i is applied, and stresses in the transformed section due to prestress and self-weight of the member (if it is not shored) are computed. In particular, stresses are computed at the c.g. of the pretensioned strands, as in Equation 7.11:

$$f_{cgs} = \frac{P_i}{A_t} + \frac{P_i e_t^2}{I_t} - \frac{M_{self-wt} e_t}{I_t}$$

Equation 7.11

Note that compressive stresses are assumed to be positive in Equation 7.11, and the eccentricity of the strands (based on transformed section properties) e_t is assumed to be positive when the c.g. of the strands is below the centroid of the section.

Once the stress at the c.g. of the strands in the transformed section has been calculated, the change in stress in the pretensioned reinforcement can be computed using the principles of strain compatibility. Since the strands are bonded, the strains in the concrete and steel must be equal. The change in stress in the two materials is thus proportional by the modular ratio at release, as shown in Equation 7.12:

$$\Delta f_{ES,steel} = n \cdot f_{cgs} = \frac{E_{ps}}{E_{ci}} \cdot f_{cgs}$$

Equation 7.12

It can be shown [76] that exact computation using the transformed section method is equivalent to computation using the net concrete area and reduced prestress force P_0 (after elastic shortening loss), as given by Equation 7.13:

$$f_{cgs} = \frac{P_0}{A_c} + \frac{P_0 e_c^2}{I_c} - \frac{M_{self-wt.} e_c}{I_c}$$

Equation 7.13

In other words, elastic shortening can be calculated by applying the full prestress force before release P_1 to the transformed section, or by applying the effective prestress force P_0 (after elastic shortening loss) to the net concrete section. The difficulty in using Equation 7.11 is that transformed section properties must be computed. The difference in using Equation 7.13 is that the effective force P_0 is dependent on the elastic shortening loss, such that an exact solution can only be obtained by iteration (or by combining Equation 7.12 and Equation 7.13 and solving symbolically for the change in prestress force).

For design purposes, it is usually considered sufficient to estimate the elastic shortening loss by using gross section properties and an assumed value for P_0 . This calculation is shown in Equation 7.14:

$$f_{cgs} = \frac{P_0}{A_g} + \frac{P_0 e_g^2}{I_g} - \frac{M_{self-wt.} e_g}{I_g}$$

Equation 7.14

The *AASHTO LRFD Specifications* [1] suggest that the effective prestress force be taken as 70 percent of the force corresponding to the ultimate strength of the strands or tendons

($f_{s0}=(.70)*f_{su}$). Similarly, the *AASHTO Standard Specifications* [3] suggest using 69 percent of the ultimate strength ($f_{s0}=(.69)*f_{su}$). The *PCI Design Handbook* [108] recommends that the effective prestress force be taken as 90 percent of the initial prestress force before elastic shortening ($P_0=(.90)*P_i$).

It should be noted that elastic shortening varies along the length of the member, as a function of the self-weight moment and prestressing layout at each section. Technically, elastic shortening should thus be calculated at each section critical for design. Furthermore, the magnitude of elastic shortening losses are highly dependent on the modulus of elasticity of the concrete at release, since losses in the steel are directly related to the stress in the concrete by the modular ratio.

7.3.2 Measurements

Elastic shortening losses were measured indirectly using the principles of strain compatibility, as described in Section 7.1.2. Elastic shortening measurements were obtained by comparing strain readings immediately after release to baseline strain measurements recorded just before release. In most instrumented beams, measurements were made using vibrating wire gauges embedded in the concrete at the level of the c.g. of the strands. In some beams however (mostly Louetta HPC U-beams), bonded resistance strain gauges were used. Measurements were successfully recorded on twenty beams, including nine Louetta HPC U-beams, seven San Angelo Eastbound HPC Type IV beams, and four San Angelo Westbound non-HPC Type IV beams. In five other beams, measurements were not successfully recorded because of concrete cracking before release, damaged gauges, or missed baseline readings. (In one beam, Louetta Beam S24, no embedded gauges were installed.)

Measured elastic shortening losses are reported for all beams in Table 7.3, in terms of both change in stress and percent loss relative to a nominal jacking stress of 1396 MPa (202.5 ksi). Note that for several beams, especially Louetta U-beams (which have two webs), release strains at c.g.s. were measured using more than one gauge. For these beams, strains were averaged. It can be seen in Table 7.3 that there was usually good agreement between gauges in the same beam.

Table 7.3 - Measured Release Strains and Equivalent Elastic Shortening Losses

Beam	Strain Measurements From Embedded Gauges [†]				Elastic Shortening Loss		
	VW Gauges		ERSG Gauges		Avg.	(ksi)	(% of f_i) [#]
Louetta HPC Beams							
N21			677	731	704	19.71	9.73%
N22			454		454	12.71	6.28%
N23							
N31			670		670	18.76	9.26%
N32	560	634	629		608	17.01	8.40%
N33							
S14			875		875	24.50	12.10%
S15	588	582			585	16.38	8.09%
S16	613		552		583	16.31	8.05%
S24							
S25	463	674			569	15.92	7.86%
S26	727				727	20.36	10.05%
San Angelo Eastbound HPC Beams							
E13	633				633	17.72	8.75%
E14	595				595	16.66	8.23%
E24	533				533	14.92	7.37%
E25	535		507		521	14.59	7.20%
E26							
E33							
E34	773				773	21.64	10.69%
E35	759				759	21.25	10.49%
E44	581				581	16.27	8.03%
E45							
San Angelo Westbound Non-HPC Beams							
W14	498				498	13.94	6.89%
W15	526				526	14.73	7.27%
W16	435				435	12.18	6.01%
W17	457				457	12.80	6.32%
1 ksi = 6.895 MPa							
† All strain measurements in microstrains (10^{-6} in./in.)							
# Relative to nominal jacking stress of 202.5 ksi (1396 MPa).							

Table 7.4 - Summary of Methods Used for Prediction of Elastic Shortening Losses

Parameter(s)	Exact Analysis (Equation 7.11)	Approximate (Equation 7.14)	Known Modulus (Equation 7.14)
Section Properties	Transformed section properties	Gross section properties	Gross section properties
Prestress Force	3.5 to 4.5% loss assumed before release based on measurements in Section 7.2. Full prestress (less above loss) used for calculations.	No loss assumed before release. Effective prestress force after losses assumed to be 70 percent of force corresponding to ultimate strength of strands, as suggested by <i>AASHTO LRFD</i> [1].	No loss assumed before release. Effective prestress force after losses assumed to be 70 percent of force corresponding to ultimate strength of strands, as suggested by <i>AASHTO LRFD</i> [1].
Beam Self-Weight	Based on gross beam area and measured unit weight, with approx. weight of steel included.	Based on gross beam area and assumed 150 pcf (3.29 kg/m ³) unit weight.	Based on gross beam area and assumed 150 pcf (3.29 kg/m ³) unit weight.
Modulus of Elasticity	Based on tests of companion specimens.	Eq. 4.2 (non-HPC) or Eq. 4.4 (HPC).	Based on tests of companion specimens.

Measured losses were compared to predicted elastic shortening losses, as computed by three methods. These methods are summarized in Table 7.4. The exact method involved computation of loss by Equation 7.11, using transformed section properties and the modulus of elasticity measured on companion specimens. The approximate method involved computation by Equation 7.14 using gross section properties and a modulus of elasticity computed by Equation 4.2 or Equation 4.4 (using specified release concrete strengths). The third method involved approximate computation using gross section properties, but with the modulus of elasticity measured from tests on companion specimens.

Measured elastic shortening losses are compared to predicted losses in Table 7.5 and Table 7.6 in terms of stress change and percent loss, respectively. Measured losses were highest in the Louetta HPC beams, with an average measured loss of 123.8 MPa (17.96 ksi) or 8.87 percent. Measured losses were also substantial in the San Angelo

Eastbound HPC beams, with an average loss of 121.2 MPa (17.58 ksi) or 8.68 percent. In the San Angelo Westbound non-HPC beams, the average measured loss was only 92.5 MPa (13.41 ksi) or 6.62 percent.

Measured elastic shortening losses were typically higher than losses predicted by the exact method, as can be seen in Figure 7.7 and from the average values listed in Table 7.5 and Table 7.6. This was especially true for the San Angelo Eastbound HPC beams, in which the average ratio of measured losses to losses predicted by the exact method was 1.25. For the Louetta HPC and San Angelo Westbound non-HPC beams, the ratios of measured loss to loss predicted by the exact method were 1.02 and 1.11, respectively. Note that for three individual beams (S14, E34, and E35), this ratio exceeded 1.38.

In general, measured losses were substantially lower than predicted losses computed by the approximate method. Using this method, average ratios of measured to predicted losses were 0.72, 0.91, and 0.86 for the Louetta HPC, San Angelo Eastbound HPC, and San Angelo Westbound non-HPC beams, respectively. Ratios were closer to unity when losses were predicted by the approximate method using the measured modulus of elasticity, and these predicted losses were typically close in magnitude to predicted losses based on the exact method. For the approximate method with the measured modulus of elasticity, the ratios of measured to predicted losses averaged 0.93, 1.20, and 1.07 for the Louetta HPC, San Angelo Eastbound HPC, and San Angelo Westbound non-HPC beams, respectively.

7.3.3 Discussion

The measured elastic shortening losses show the expected trend with regard to the influence of HPC. Measured losses in the Louetta HPC and San Angelo Eastbound HPC beams were generally substantially higher than in the San Angelo Westbound non-HPC beams. The influence of higher prestress forces for the HPC designs is clearly evident, especially considering that the moduli of elasticity for the HPC and non-HPC concretes were similar in tests of companion specimens.

Table 7.5 - Measured and Predicted Elastic Shortening Loss (Stress Change)

Beam	Measured Loss	Predicted Losses			Ratio (Meas. / Pred.)		
		Exact	Approx.	Known E	Exact	Approx.	Known E
Louetta HPC Beams							
N21	19.71	19.48	27.44	21.65	1.012	0.718	0.911
N22	12.71	15.98	21.36	17.70	0.796	0.595	0.718
N23		14.46	21.28	15.84			
N31	18.76	18.77	26.33	20.76	0.999	0.713	0.904
N32	17.01	16.40	23.73	18.10	1.037	0.717	0.940
N33		16.32	23.65	18.04			
S14	24.50	17.66	25.84	19.30	1.387	0.948	1.270
S15	16.38	17.46	25.66	19.16	0.938	0.638	0.855
S16	16.31	17.52	23.29	19.30	0.931	0.700	0.845
S24		15.35	21.91	16.83			
S25	15.92	15.13	21.85	16.67	1.052	0.729	0.955
S26	20.36	19.34	27.46	21.49	1.053	0.741	0.947
AVG	17.96	16.99	24.15	18.73	1.023	0.722	0.927
San Angelo Eastbound HPC Beams							
E13	17.72	15.59	21.10	16.14	1.137	0.840	1.098
E14	16.66	15.59	21.10	16.14	1.068	0.790	1.032
E24	14.92	13.06	18.53	13.69	1.143	0.805	1.090
E25	14.59	12.39	16.58	12.88	1.177	0.880	1.133
E26		13.06	18.53	13.69			
E33		13.77	19.34	14.40			
E34	21.64	13.77	19.34	14.40	1.572	1.119	1.503
E35	21.25	13.97	19.34	14.62	1.521	1.099	1.454
E44	16.27	14.40	19.42	15.13	1.130	0.838	1.075
E45		14.38	19.38	15.11			
AVG	17.58	14.00	19.27	14.62	1.250	0.910	1.198
San Angelo Westbound Non-HPC Beams							
W14	13.94	12.05	15.55	12.53	1.157	0.897	1.112
W15	14.73	12.05	15.55	12.53	1.222	0.947	1.175
W16	12.18	12.05	15.55	12.53	1.011	0.783	0.972
W17	12.80	12.21	15.55	12.74	1.048	0.823	1.005
AVG	13.41	12.09	15.55	12.59	1.110	0.862	1.066
Note: All losses reported in ksi. 1 ksi = 6.895 MPa							

Table 7.6 - Measured and Predicted Elastic Shortening Losses (Percent Loss)

Beam	Measured Loss	Predicted Losses			Ratio (Meas. / Pred.)		
		Exact	Approx.	Known E	Exact	Approx.	Known E
<i>Louetta HPC Beams</i>							
N21	9.73	9.62	13.55	10.69	1.012	0.718	0.911
N22	6.28	7.89	10.55	8.74	0.796	0.595	0.718
N23		7.14	10.51	7.82			
N31	9.26	9.27	13.00	10.25	0.999	0.713	0.904
N32	8.40	8.10	11.72	8.94	1.037	0.717	0.940
N33		8.06	11.68	8.91			
S14	12.10	8.72	12.76	9.53	1.387	0.948	1.270
S15	8.09	8.62	12.67	9.46	0.938	0.638	0.855
S16	8.05	8.65	11.50	9.53	0.931	0.700	0.845
S24		7.58	10.82	8.31			
S25	7.86	7.47	10.79	8.23	1.052	0.729	0.955
S26	10.05	9.55	13.56	10.61	1.053	0.741	0.947
AVG	8.87	8.39	11.93	9.25	1.023	0.722	0.927
<i>San Angelo Eastbound HPC Beams</i>							
E13	8.75	7.70	10.42	7.97	1.137	0.840	1.098
E14	8.23	7.70	10.42	7.97	1.068	0.790	1.032
E24	7.37	6.45	9.15	6.76	1.143	0.805	1.090
E25	7.20	6.12	8.19	6.36	1.177	0.880	1.133
E26		6.45	9.15	6.76			
E33		6.80	9.55	7.11			
E34	10.69	6.80	9.55	7.11	1.572	1.119	1.503
E35	10.49	6.90	9.55	7.22	1.521	1.099	1.454
E44	8.03	7.11	9.59	7.47	1.130	0.838	1.075
E45		7.10	9.57	7.46			
AVG	8.68	6.91	9.51	7.22	1.250	0.910	1.198
<i>San Angelo Westbound Non-HPC Beams</i>							
W14	6.89	5.95	7.68	6.19	1.157	0.897	1.112
W15	7.27	5.95	7.68	6.19	1.222	0.947	1.175
W16	6.01	5.95	7.68	6.19	1.011	0.783	0.972
W17	6.32	6.03	7.68	6.29	1.048	0.823	1.005
AVG	6.62	5.97	7.68	6.22	1.110	0.862	1.066
Note: All losses reported as percentage of 202.5 ksi (1396 MPa) jacking stress.							

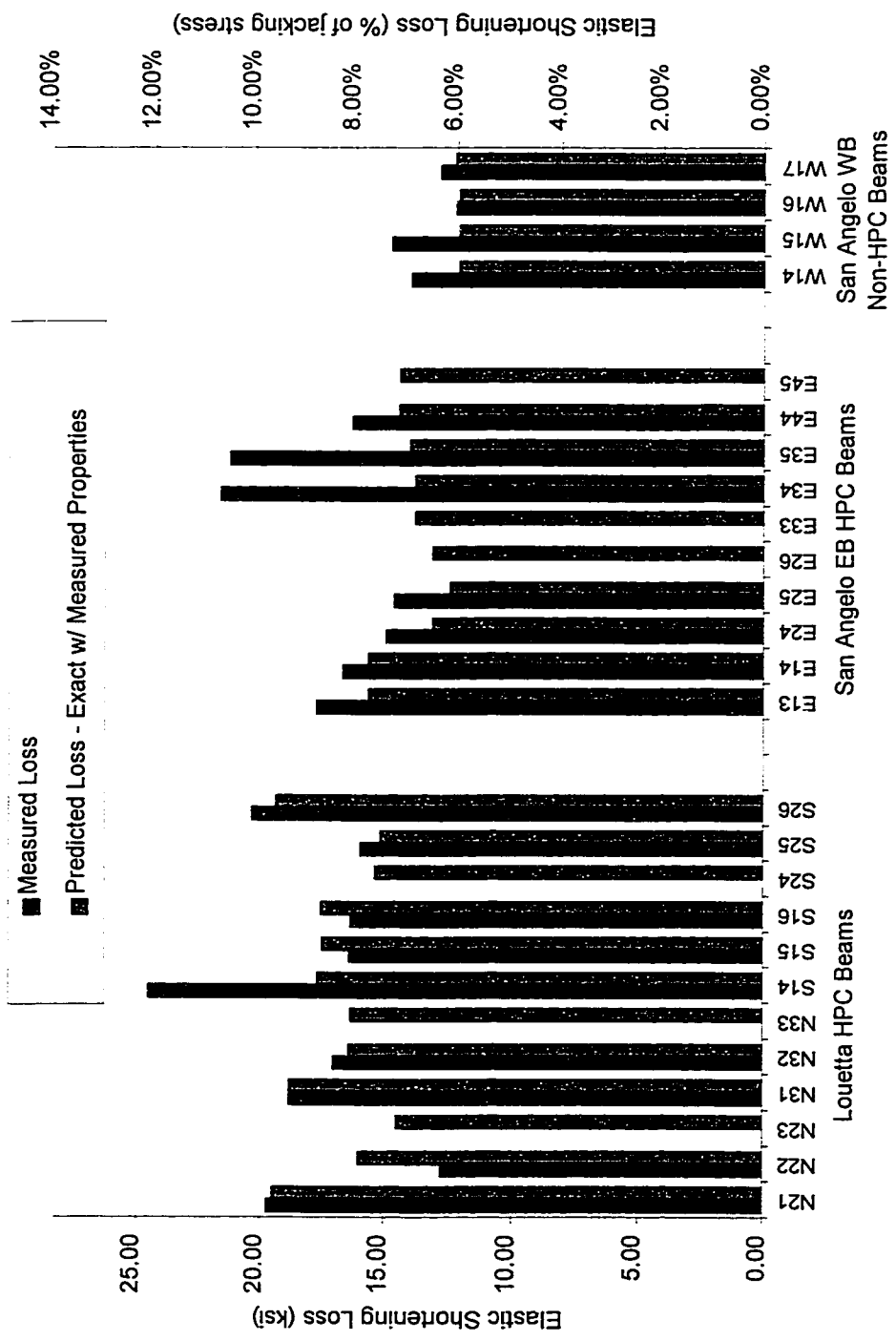


Figure 7.7 - Comparison of Measured and Predicted (Exact Method) Elastic Shortening Losses

The reasons for higher than predicted losses (by the exact method) should be the same as for the high measured strains at release discussed in Section 6.3.3, especially considering that they are essentially based on the same measurements. Restraint against shortening of the member prior to release would have affected the measurements, and caused the measured losses to be artificially high. Differences between the actual modulus of elasticity and the values obtained from tests on companion specimens also may have affected the measurements. However, other measurements in this research program, including lower than predicted camber at release, imply that the actual modulus may have been higher than companion specimen tests indicate. This error would tend to cause the measured elastic shortening losses to be lower than predicted rather than higher (as was observed). Considering the potential impacts of restraint and differences in modulus of elasticity, the measured losses seem to be in reasonable agreement with the exact predicted losses for the majority of beams in this study.

The small differences between the predicted losses based on the approximate method with the known modulus and the exact method imply that this approximate method is acceptable for design. The importance of modulus of elasticity is clearly evident, however, when the magnitudes of approximate losses computed without the known modulus of elasticity are examined. These predictions showed poor correlation with measured losses and losses predicted by the exact method, and were excessively high. This is clearly a result of fact that the modulus of elasticity predicted by Equation 4.2 or Equation 4.4 was 15 to 25 percent lower than the modulus measured on companion specimens (and perhaps even lower with respect to the actual modulus). The high magnitudes of these predicted losses, especially for the Louetta beams, also illustrates that excessive elastic shortening can be expected for HPC beam designs if large prestress forces are used in conjunction with concrete that does not have sufficient stiffness.

It is thus recommended that the approximate method (based on gross section properties) is permissible for the calculation of elastic shortening losses in HPC designs if the modulus of elasticity can be sufficiently estimated. Because of the importance of modulus of elasticity, with respect to both prediction of losses and control of the magnitude of losses, trial batching should be performed whenever possible to determine this parameter. If trial batching cannot be performed prior to design, then knowledge based on past experience with similar concretes, especially concretes with the same aggregate, should be utilized. It should not be assumed that code equations such as Equation 4.2 and

Equation 4.4 will provide sufficiently accurate estimates of the modulus of elasticity. Designers must also be aware that high elastic shortening losses (and higher time-dependent losses) can be expected if the modulus of elasticity is not sufficiently high. When necessary, a minimum modulus of elasticity should be specified as part of contract documents to ensure that concrete with adequate stiffness is actually used.

7.4 Total Losses

7.4.1 Background

In prestressed concrete highway bridge beams, the total loss of prestress due to all effects must be predicted so that the effective level of prestress in service can be estimated. The total loss consists of losses before release, elastic losses, and the time-dependent losses associated with creep, shrinkage, and relaxation. While these losses generally do not affect the ultimate strength of a member (with bonded strands), they do have a significant impact on serviceability, including concrete stresses and deflections. With regard to stresses, an underestimation of the total losses may result in cracking under service loads. For deflection behavior, losses must be reasonably estimated since either an underestimation or overestimation of the losses may lead to a poor prediction of service camber and deflection. Note that this section is concerned with the total loss in pretensioned bonded strands, as the measurements in this research program focus on these losses in particular.

Several different methods for estimating total prestress losses have been suggested throughout the literature and in common specifications. These methods exhibit varying levels of complexity and ease of use. The simplest methods are basic lump-sum estimates, in which the magnitude of the total loss is assumed to be a certain value. Perhaps the most popular methods are the component lump-sum estimates, in which the magnitude of the loss due to each source is estimated separately and the total loss is taken as the sum of the individual components. Finally, there are more advanced procedures including approximate and incremental time-step methods, which are often used in conjunction with a personal computer.

Basic lump-sum estimates of total prestress loss are provided in the *AASHTO Standard Specifications* [3] and the *PCI Design Handbook* [108]. These methods were not intended to be utilized for such complex and efficient beam designs as those in this research program, but a mention of these lump-sum estimates serves to broadly define a range of typical or expected losses. The *AASHTO Standard Specifications* [3] suggest a total loss of 310 MPa (45 ksi) for all pretensioned members based on an average design concrete strength of 34 MPa (5000 psi). The *PCI Design Handbook* [108] specifies a range of total losses for typical members constructed with normal-weight concrete. For low-relaxation strand, the maximum and minimum total losses are suggested as 207 and 276 MPa (30 and 40 ksi), respectively, although it is implied that the minimum loss may actually be lower.

The *AASHTO LRFD Specifications* [1] provide a more refined lump-sum estimate of total losses, which recognizes the inverse relationship typically displayed between creep and concrete strength and the effects of non-prestressed reinforcement. The estimates are based on a parametric study by Naaman and Hamza [90] using a computer time-step analysis, and consider a common range of values for creep, shrinkage, and exposure conditions. For I-shaped girders, the average time-dependent loss is taken as:

$$\Delta f_{ps,TD} \text{ (ksi)} = 33.0 \cdot \left[1.0 - 0.15 \cdot \frac{f'_c - 6.0}{f'_c} \right] + 6.0 \cdot \text{PPR}$$

Equation 7.15

For box girders, the concrete strength was found to have little effect and the average time-dependent loss can be taken as:

$$\Delta f_{ps,TD} \text{ (ksi)} = 19.0 + 4.0 \cdot \text{PPR}$$

Equation 7.16

For both Equation 7.15 and Equation 7.16, the partial prestressing ratio PPR is the ratio of prestressed reinforcement to total (prestressed plus nonprestressed) reinforcement. The lump-sum time-dependent losses should also be reduced by 28 MPa (4 ksi) for box girders and by 41 MPa (6 ksi) for I-shaped girders if low-relaxation strands are used. These

lump-sum estimates must be added to the elastic shortening loss in order to determine the total estimated loss in service.

Many authors and specifications have presented a set of equations allowing for the lump-sum estimation of losses by individual components. The losses due to elastic shortening, shrinkage, creep, and relaxation are computed individually and added to determine the total loss, as shown in Equation 7.17:

$$\Delta f_{ps,total} = \Delta f_{ps,ES} + \Delta f_{ps,SH} + \Delta f_{ps,CR} + \Delta f_{ps,RE}$$

Equation 7.17

Three of the most common component methods used by designers are those found in the *AASHTO Standard Specifications* [3], the *AASHTO LRFD Specifications* [1], and the *PCI Design Handbook* [108,144]. The equations for each component of loss used in these methods are summarized in Table 7.7. Note that the notation used in some of the equations has been modified to allow for easier comparison of the three methods.

For each method, elastic shortening is predicted as the product of the modular ratio at release and the concrete stress at the c.g. of the prestressed reinforcement due to prestress and member self-weight. The only difference between the methods is in the estimation of the initial prestress force acting just after release, and the expressions generally result in very similar values. Elastic shortening losses are discussed further in Section 7.3.

Creep is computed similarly to elastic shortening, as a function of the concrete stress at the c.g. of prestressed reinforcement just after release and the concrete stress at the c.g. of prestressed reinforcement due to dead loads applied after release. In the *AASHTO Standard* and *AASHTO LRFD* methods, multipliers of 12 and 7 are applied to these stresses, respectively. In a general sense, these multipliers represent the product of the ultimate creep coefficient for the concrete in the member and the modular ratio between the strand and the concrete. A lower multiplier for the applied dead loads is used to consider the effect of the age of loading on creep. A similar yet more transparent approach is used in the *PCI Design Handbook*, as the creep coefficient and modular ratio are separated in the expression. However, a value of 2.0 is specified for the creep coefficient with normal-weight concrete, and the same multiplier is used for the stress at release and stress due to dead loads applied at later ages.

In the *AASHTO Standard* and *AASHTO LRFD* methods, shrinkage loss is estimated with a very simple expression that considers only the average relative humidity as a variable. A more lengthy expression is utilized in the *PCI Design Handbook* method, as the effect of the volume-to-surface ratio of the member is also considered. Both approaches are essentially based on the same body of data [6,144] and can be shown to give similar results. Both expressions are based on an ultimate shrinkage strain of $550 \mu\epsilon$, but the *AASHTO* approach makes several simplifying assumptions. The *PCI Design Handbook* method is obviously more transparent.

With each method, relaxation losses are computed using an empirical expression containing terms related to the other components of loss. This approach is meant to consider the interdependence between the different components of loss. The methods differ only in the coefficients used in each expression, although it can be seen in Table 7.7 that the coefficients are similar for all three methods. These differences generally result in only a small variation in the computed loss because the magnitude of the relaxation loss is usually very small. Only the *AASHTO LRFD* method suggests computation of the relaxation loss *before* release, which should also be included in the estimation of total losses. Note that differences in the expressions used for relaxation loss are the only real difference between the computation of component lump-sum losses in the *AASHTO Standard Specifications* [3] and the *AASHTO LRFD Specifications* [1].

The *elastic* change in stress due to superimposed dead loads at the c.g. of the prestressed reinforcement can be interpreted as a "gain" in prestress under certain conditions, but it is typically not considered in the equations presented for losses in the literature. Neither the *AASHTO Standard Specifications* [3], the *AASHTO LRFD Specifications* [1], nor the *PCI Design Handbook* [108] consider this elastic change in stress. Neglecting this effect can be considered conservative for the computation of service stresses because losses will be overestimated.

Other expressions for the estimation of prestress losses have been developed and are suggested in the literature [63,104,128]. More advanced procedures for the computation of losses include the approximate time-step method of Branson [25,27] and the incremental time-step method proposed by many [28,53,75,89,99,104]. These methods consider the deformation (strain) history of the member in several small time intervals, and allow for better consideration of the interdependence of the different components of loss. They are generally considered to be much more accurate than empirical lump sum

estimations, but require a significant amount of information on specific material properties and a large amount of calculation. They are generally not well suited to hand calculation and are usually implemented with the assistance of a personal computer. These methods are often used for the computation of camber and deflection as well as prestress losses.

Few measurements of long-term prestress losses in actual HPC prestressed highway bridge beams have been documented in the literature, although measurements are currently being recorded on beams in several states as part of the Federal Highway Administration (FHWA) HPC Showcase program. Measurements of long-term prestress losses have been recorded for a few full-scale laboratory test beams at the University of Minnesota [52] and by Tulane University/Construction Technology Laboratories (CTL) [31]. However, these beams were not actual bridge beams and were not subjected to field conditions. Long-term losses in two Minnesota beams, which used 77 to 83 MPa (11,000 to 12,000 psi) concrete and had beam depths of 1140 mm (45 in.) with a noncomposite span-to-depth ratio of 35, were 20.2 and 25.6 percent of the nominal jacking stress. These measured losses were underpredicted at release and overpredicted in the long-term by standard *AASHTO* [3] and *PCI* [108] component loss equations. Long-term losses in a 1372 mm (54 in.) deep and 21.3 m (70 ft.) long Bulb-Tee beam were measured to be approximately 159 MPa (23 ksi) in the Tulane/CTL study. These losses were approximately one-half of the losses predicted using the *AASHTO* [3] component equations. The concrete strength for that beam was approximately 69 MPa (10,000 psi).

7.4.2 Measurements

Long-term prestress losses were successfully measured (from release through service) using vibrating wire gauges in fifteen of the twenty beams in which these gauges were installed at the c.g. of pretensioned strands at midspan. Measurements were obtained for four Louetta HPC beams, seven San Angelo Eastbound HPC beams, and four San Angelo Westbound non-HPC beams. Long-term losses were measured using the procedure outlined in Section 7.1.2, and were corrected for temperature changes as described in that section. Measured long-term losses are summarized in Table 7.8 for each individual beam, and are plotted over time for each beam in Appendix G.

Table 7.7 - Summary of Equations Used in the Prediction of Total Losses by Components

	AASHTO Standard [3]	AASHTO LRFD [1]	PCI Design Handbook [108]
$\Delta f_{ps,ES}$ El. Shortening	$\frac{E_{ps}}{E_{cl}} \cdot f_{cgp}$ ($f_{s0} = .69 \cdot f_{su}$)	$\frac{E_{ps}}{E_{cl}} \cdot f_{cgp}$ ($f_{s0} = .70 \cdot f_{su}$)	$\frac{E_{ps}}{E_{cl}} \cdot f_{cgp}$ ($f_{s0} = .90 \cdot f_{su}$)
$\Delta f_{ps,SH}$ Shrinkage	17.0 - 1.5 · RH	17.0 - 1.5 · RH	$(8.2 \times 10^{-6}) K_{sh} E_{ps} (1 - .06 \frac{V}{S})(100 - RH)$ ($K_{sh} = 1.0$)
$\Delta f_{ps,CR}$ Creep	$12.0 \cdot f_{cgp} - 7.0 \cdot f_{cdp}$	$12.0 \cdot f_{cgp} - 7.0 \cdot f_{cdp}$	$K_{cr} \cdot \left(\frac{E_{ps}}{E_c} \right) \cdot (f_{cgp} - f_{cdp})$ ($K_{cr} = 2.0$)
$\Delta f_{ps,RE}$ Relaxation	$5.0 - 0.10 \cdot \Delta f_{ps,ES}$ $- 0.05 \cdot \Delta f_{ps,SH} - 0.05 \cdot \Delta f_{ps,CR}$	$\frac{\log(24 \cdot t_0)}{40} \cdot \left[\frac{f_{sj}}{f_{sy}} - 0.55 \right] \cdot f_{sj}$ + $6.0 - 0.12 \cdot \Delta f_{ps,ES}$ $- 0.06 \cdot \Delta f_{ps,SH} - 0.06 \cdot \Delta f_{ps,CR}$	$[K_{re} - J \cdot (\Delta f_{ps,ES} + \Delta f_{ps,SH} + \Delta f_{ps,CR})]$ ($K_{re} = 5.0, J = 0.04, C = 1.00$)

All losses in units of ksi. 1 ksi = 6.895 MPa 1 in. = 25.4 mm

Note: Expressions listed above are for pretensioned, low-relaxation strands. Values for constants listed are for Grade 270 strands initially stressed to $0.75 \cdot f_{pu}$.

f_{cgp} = stress in concrete at c.g. of pretensioned strands at release (due to prestress and self-weight), ksi; f_{cdp} = stress in concrete at c.g. of pretensioned strands due to applied loads (not acting at release), ksi; E_{ps} = modulus of elasticity of prestressing steel, ksi; E_c = modulus of elasticity of concrete at release, ksi; f_{s0} = strand stress just after release, ksi; f_{su} = ultimate strength of the strand, ksi; f_{sj} = yield strength of the strand, ksi; RH = relative humidity in percent; t_0 = time in days between jacking and release; V/S = volume-to-surface ratio, in.

Table 7.8 - Measured Total Prestress Losses in Individual Beams by Component

Beam	Days After Release	Loss Components (ksi)				Total Loss (ksi)	Total Loss (% of f_{jack})
		PR	ES	CR+SH *	RE		
Louetta HPC Beams							
N32	761	8.10	17.75	14.47	2.78	43.11	21.29
S15	748	8.10	16.38	10.61	2.77	37.86	18.70
S16	1262	8.10	17.16	11.93	3.06	40.26	19.88
S25	1221	8.10	12.96	9.70	3.04	33.81	16.70
Average		8.10	16.07	11.68	2.92	38.76	19.14
San Angelo Eastbound HPC Beams							
E13	422	8.10	25.03	15.02	2.46	50.61	24.99
E14	422	8.10	24.58	22.10	2.46	57.24	28.27
E24	404	9.11	20.19	19.78	2.43	51.51	25.44
E25	746	8.10	22.46	18.63	2.77	51.95	25.66
E34	316	9.11	30.86	15.17	2.30	57.43	28.36
E35	309	9.11	30.52	16.26	2.28	58.17	28.73
E44	305	9.11	26.15	18.09	2.28	55.63	27.47
Average		8.68	25.68	17.86	2.42	54.65	26.99
San Angelo Westbound Non-HPC Beams							
W14	771	7.09	13.94	10.84	2.79	34.67	17.12
W15	771	7.09	14.73	9.81	2.79	34.41	16.99
W16	771	7.09	12.18	10.62	2.79	32.68	16.14
W17	766	7.09	12.80	7.84	2.79	30.51	15.07
Average		7.09	13.41	9.78	2.79	33.07	16.33
1 ksi = 6.895 MPa							
* Includes compensation for measured elastic change in stress due to superimposed dead load							
See general notes at beginning of Appendix H.							
PR: Pre-release (See Section 7.2); ES: Elastic Shortening; CR: Creep; SH: Shrinkage; RE: Relaxation							

Table 7.9 - Comparison of Measured and Calculated Total Prestress Losses

	Total Prestress Losses (ksi)								
	Measured #	Incremental Time-Step (Meas. Parameters) #	Actual Beam Designs (PSTRS14 or ADAPT) #	AASHTO LRFD Time-Dependent Lump-Sum (Design Parameters) ##	AASHTO LRFD Components (Design Parameters) ##	AASHTO LRFD Components (Meas. Parameters) ##	PCI Design Handbook Components (Design Parameters)	PCI Design Handbook Components (Meas. Parameters)	Suggested Method - Table 7.11 (Meas. Parameters) #
Louetta HPC Beams									
N32	43.11	42.30	57.79	38.72	67.05	57.71	50.57	38.79	40.02
S15	37.86	44.36	57.79	40.65	72.53	61.25	55.99	40.85	41.60
S16	40.26	46.32	52.99	38.29	69.92	59.88	55.78	41.64	41.65
S25	33.81	40.99	52.99	36.68	62.12	52.46	46.27	34.27	36.83
Avg.	38.76	43.49	55.39	38.59	67.91	57.83	52.15	38.89	40.03
San Angelo Eastbound HPC Beams									
E13	50.61	54.48	49.36	57.21	102.35	88.19	81.73	63.81	55.51
E14	57.24	54.76	49.36	57.21	104.46	89.40	84.84	65.40	56.27
E24	51.51	54.17	49.83	56.43	103.96	89.09	83.02	65.16	55.67
E25	51.95	49.74	42.26	51.50	89.31	77.32	70.00	55.23	49.63
E34	57.43	54.79	50.85	57.67	105.45	90.91	83.87	66.48	56.80
E35	58.17	54.73	50.85	57.67	106.27	90.69	85.06	65.93	56.71
E44	55.63	55.70	51.01	57.85	105.83	91.90	84.40	67.32	57.75
Avg.	54.65	54.05	49.07	56.51	102.52	88.21	81.85	64.19	55.48
San Angelo Westbound Non-HPC Beams									
W14	34.67	30.52	47.91	41.02	51.91	45.54	39.18	31.76	28.68
W15	34.41	30.52	47.91	41.02	51.91	45.54	39.18	31.76	28.68
W16	32.68	30.52	47.91	41.02	51.91	45.54	39.18	31.76	28.68
W17	30.51	30.49	47.91	41.02	51.71	43.98	38.87	29.55	28.15
Avg.	33.07	30.51	47.91	41.02	51.86	45.15	39.10	31.21	28.55
1 ksi = 6.895 MPa For individual loss components, see Appendix H.									
# Includes pre-release losses. ## Includes pre-release relaxation losses only.									

Table 7.10 - Summary of Design and Measured Parameters Used in Calculations of Prestress Losses

Parameter(s)	“Design” Parameters	“Measured” Parameters
Section Properties	Gross section properties	Transformed section properties
Concrete Unit Weights / Dead Loads	Based on assumed deck dimensions and 150 pcf (3.29 kg/m ³) for all concrete.	Based on measured deck thickness and measured unit weights, with approx. weight of steel included for beams.
Concrete Strength	Nominal design concrete strength	Based on tests of companion specimens.
Modulus of Elasticity	Eq. 4.2 (non-HPC) or Eq. 4.4 (HPC), using nominal design strengths.	Based on tests of companion specimens.

Losses listed in Table 7.8 are taken from measurements recorded during the Spring of 1998, well after the completion of construction at each jobsite. As can be seen in the plots of Appendix G, measured losses were very stable at this time. Measured losses listed in the table have also been separated into components. Pre-release losses (PR) were estimated as described in Section 7.2 and added to the total measurements. Elastic shortening losses (ES) were measured using the vibrating wire gauges and are discussed in Section 7.3. Time-dependent creep and shrinkage losses (CR+SH) were also measured using the vibrating wire gauges, but cannot be separated and are thus listed together. The relaxation losses (RE) listed in the table are those estimated analytically *after* release as discussed in Section 7.1.2. Estimated relaxation losses *before* release are included in the estimated pre-release losses.

Total measured losses in the Louetta HPC beams averaged 267.3 MPa (38.76 ksi). These losses are relatively high but are clearly not excessive compared to many lump-sum estimates of total losses found in the literature, and are equal to 19.14 percent of the nominal jacking stress of 1396 MPa (202.5 ksi). Elastic shortening accounted for the largest portion of the total loss, and the time-dependent loss due to both creep and shrinkage was less than the elastic shortening loss for all beams. Note that the estimated 56 MPa (8.10 ksi) average loss before release accounted for about 20 to 25 percent of the total measured losses. Total long-term losses were not successfully measured in the most highly stressed

Louetta HPC U-beams that contained 87 15 mm (0.6 in.) diameter strands, but the incremental time-step predictions shown in Appendix G do not imply that a substantially larger total loss will occur in these beams.

Total measured losses in the San Angelo Eastbound HPC beams were higher than in the Louetta HPC beams. Total measured losses in these beams averaged 376.8 MPa (54.65 ksi). These total losses correspond to 26.99 percent of the nominal jacking stress and are higher than the range of typical maximum losses for ordinary members suggested by several lump-sum estimates in the literature. As for the Louetta HPC beams, the largest component of loss was elastic shortening, which accounted for approximately one-half of the total loss. (Note that the elastic effect of post-tensioning on the bonded pretensioned strands was considered to be part of the elastic shortening loss for these beams.) Time-dependent creep and shrinkage losses were less than the elastic shortening loss for all beams. On average, the pre-release losses accounted for about 16 to 18 percent of the total losses.

Total measured losses were lowest for the San Angelo Westbound non-HPC beams. The average measured total loss for these beams was 228.0 MPa (33.07 ksi), which is equal to 16.33 percent of the nominal jacking stress. The largest component of loss in these beams was also elastic shortening, which accounted for approximately 40 to 50 percent of the total losses, and time-dependent losses due to creep and shrinkage were less than elastic shortening losses for all San Angelo Westbound non-HPC beams. The estimated pre-release losses accounted for about 20 to 25 percent of the total losses in these beams.

Total long-term losses computed during the actual beam designs are listed in Table 7.9 along with losses calculated for the instrumented beams using several common methods. Where appropriate, the individual components of loss calculated as part of these total loss predictions are listed in Appendix H for each beam. Note that for several of the methods, losses were computed on the basis of both design and measured parameters. As summarized in Table 7.10, differences in these parameters are primarily related to material and section properties. Parameters used in the specific computations for each beam may be found in Appendix F.

Many of the methods used for computation of losses cannot be directly applied to the complex dual-stage (pretensioned/post-tensioned) San Angelo Eastbound HPC beams without a few assumptions and simplifications. For these beams, the effects of post-

tensioning (on the bonded pretensioned strands) were incorporated into the elastic shortening component of loss. In addition, the six unbonded top strands which were cut just after erection of the beams were ignored at all stages. These assumptions should not have a major effect on the calculated losses, except in the slight differences in creep resulting from the simplifications regarding loading ages. Most importantly, they allow these methods for computation of losses to be applied directly to these complex beams.

Losses were also calculated for all beams using an incremental time-step procedure based on measured parameters and the actual construction schedules. Details of this incremental time-step analysis, which was implemented using a computer spreadsheet program, are discussed in Appendix G. Plots of losses predicted for each beam using the incremental time-step method are also shown in Appendix G along with the measured losses. For almost all beams, the total prestress losses predicted by the incremental time-step procedure showed reasonable agreement with the total measured losses. On average, measured losses were slightly less than predicted for the Louetta HPC beams, almost equal to predicted for the San Angelo Eastbound HPC beams, and slightly greater than predicted for the San Angelo Westbound non-HPC beams. Note that the incremental time-step predictions include the same estimated pre-release losses as the total measured losses.

Total losses predicted as part of the actual beam designs were much higher than the total measured losses for the Louetta HPC and San Angelo Westbound non-HPC beams. These beams were designed using TxDOT's PSTRS14 design program [130], which calculates losses from the *AASHTO Standard Specifications* [3] equations for individual loss components. Losses before release are also not considered by the program, which implies an even larger difference between the measured and calculated losses than suggested by the values in Table 7.9.

Total losses were computed during the actual design of the San Angelo Eastbound HPC beams using the ADAPT [13] computer program, which uses a time-step approach for the calculation of losses. The losses shown in Table 7.9 are the average losses computed from the upper and lower bound creep and shrinkage designs, which are explained in Section 2.3.3. Very similar pre-release losses were assumed during the design as those added to the measured losses, so the values can be directly compared. Losses calculated during design were slightly lower than measured losses for all of these beams, but overall there was good agreement. Note that the actual creep and shrinkage properties of the

beam concrete, as measured during companion specimen tests, were used in the design computations. However, the measured modulus of elasticity for the beam concrete was not used in the actual designs, which may account for the most of the difference between these design calculated losses and the measured losses.

Surprisingly, the *AASHTO LRFD* [1] refined lump-sum estimates of total losses based on design parameters showed good agreement with the measured losses for both the Louetta HPC and San Angelo Eastbound HPC beams. The elastic shortening losses were generally overpredicted and the time-dependent losses were predicted very accurately for these HPC beams. However, the overprediction of elastic shortening losses was compensated for by the lack of consideration of pre-release losses. For the San Angelo Westbound non-HPC beams, the time-dependent losses were also overpredicted substantially, such that the total loss estimates were significantly greater than the total measured losses. This trend can be directly attributed to the very low creep exhibited by the concrete used for the non-HPC beams.

Losses computed using the *AAHSTO LRFD* [1] individual component equations resulted in an extreme overprediction of the actual losses for all beams in this study, despite the lack of consideration of pre-release losses in this method. Total losses of up to 732.7 MPa (106.27 ksi) were predicted for the San Angelo Eastbound HPC beams using design parameters. These calculated losses are almost double the measured losses and equate to more than half of the initial jacking stress. Losses computed using the *LRFD* individual component equations with measured parameters still resulted in extreme overpredictions of the actual losses, although the calculated losses were slightly closer to the measured losses.

Losses computed using the *PCI Design Handbook* [108] component equations with design parameters also resulted in overpredictions of the total losses. However, the calculated losses using this method are much closer in magnitude to the measured losses than the losses calculated using the *AASHTO LRFD* component equations with design parameters. Still, the losses are overestimated by as much as 50 percent even though pre-release losses are not considered. Calculations based on the *PCI* equations using measured parameters showed good agreement with the measured losses for the Louetta HPC and San Angelo Westbound non-HPC beams, although the consideration of pre-release losses would result in an overprediction of the measured losses. For the San Angelo Eastbound HPC beams, the calculated losses based on measured parameters still

overpredicted the measured losses, even without the consideration of losses before release.

7.4.3 Discussion

The magnitudes of the total measured losses for the beams in this study show that very large prestress forces can be used in HPC without the undesired consequence of extremely high prestress losses. The total losses in the most highly stressed San Angelo Eastbound HPC beams did not exceed 414 MPa (60 ksi). While this value does not represent a significant threshold or limit per se, it should be clear that total losses much in excess of this value will result in inefficient beam designs. It may thus be concluded that the losses in these beams were high, but not excessive. Had the same design been used with a concrete having lower stiffness (modulus of elasticity) or higher creep, total losses would certainly have been excessive.

On the other hand, total measured losses for the Louetta HPC beams were all less than 310 MPa (45 ksi), and were less than 276 MPa (40 ksi) on average. These losses are more typical of losses for conventional prestressed concrete highway bridge beams. The four beams in which long-term measurements were successfully recorded were not quite as heavily stressed as the San Angelo Eastbound HPC beams, and had a design concrete strength of 80.0 MPa (11,600 psi) as opposed to 89.6 to 96.5 MPa (13,000 to 14,000 psi) for the San Angelo Eastbound HPC beams. Even if the modulus were lower or the creep were higher, total losses in these beams likely would have been acceptable. Total losses in the Westbound non-HPC beams were also very reasonable, which is a reflection of the relatively high stiffness and low creep exhibited by the concrete used in these beams. Even though the concrete was not designated HPC, it has many properties quite similar to those of HPC.

There are two basic issues associated with the estimation of prestress losses during design. The first is the adequacy of the method used for the calculations, and the second is the satisfactory knowledge or estimation of the material properties for the beam. Each of these aspects are important and will thus be discussed in the subsequent paragraphs. The calculations of losses using both design and measured properties in the previous section helps to separate these two issues in a logical sense.

If the material properties are known to a good degree of accuracy, then the method used to predict losses should provide a reasonably accurate result. The incremental time-step method suggested by many throughout the literature is generally considered to have a relatively high level of accuracy if good material property data is used in the calculations. The values listed in Table 7.9 verify this conclusion, as the time-step method described in Appendix G resulted in good predictions of the measured losses. Unfortunately, the time-step approach is more suited to analysis rather than design, and cannot easily be used by hand. The time-step approach should be utilized if deflection calculations are also being performed using the approach, but simpler design methods are still needed for the estimation of total prestress losses.

Lump-sum estimates are much easier to use, but are probably too simple to cover all possible designs using HPC. The *AASHTO LRFD* [1] time-dependent lump-sum estimate provided a reasonably accurate prediction of the time-dependent losses for the HPC designs in this study, but actually overestimated the losses for the non-HPC designs. The accuracy and applicability of this method, however, cannot be established without field data from several other bridges, and broad generalizations must not be made at this time. The *LRFD* lump-sum estimate should certainly provide some improvement over older lump-sum estimates that do not consider concrete strength and include elastic shortening. Still, it is the opinion of the author that lump-sum estimates are simply too basic for use with HPC beam designs, which are much more sensitive to the actual material properties than conventional designs.

The component methods of calculation for losses have several advantages, including the fact that they are relatively simple to apply, are well-known and commonly used, and are descriptive methods (i.e. distinguish the separate sources of loss to some extent). However, the assumptions used for simplification in the *AASHTO LRFD* [1] and *PCI Design Handbook* [108] make these methods (without modifications) rather useless for HPC designs. As discussed in Section 7.4.2, total losses calculated using these methods substantially overpredicted the measured losses for HPC beams in this study, regardless of whether design or measured parameters were used.

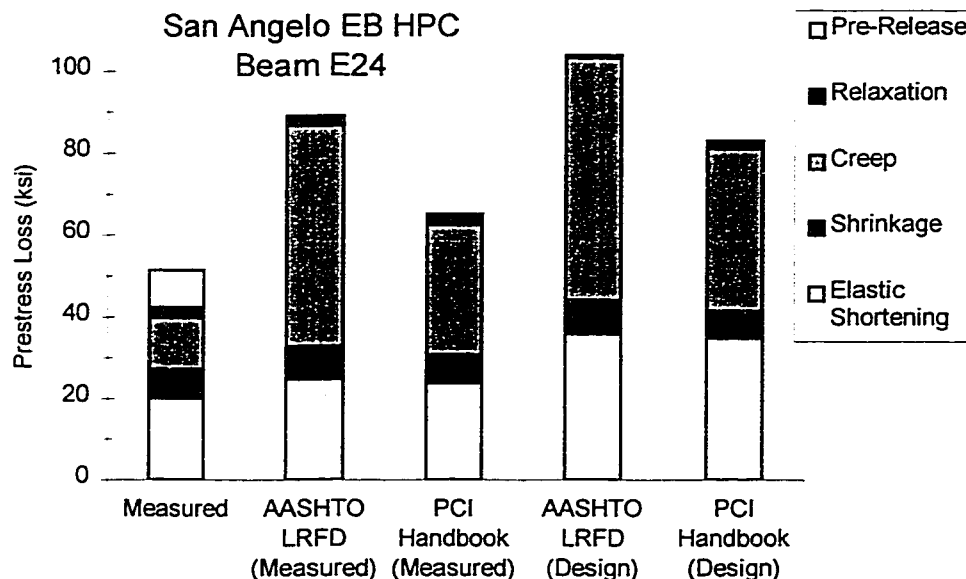


Figure 7.8 - Components of Measured and Predicted Losses for Beam E24

A comparison of the individual components of loss calculated using these methods is shown in Figure 7.8 for San Angelo HPC Beam E24. Clearly, the two main components of loss in these highly-stressed beams are elastic shortening and creep. With both the *LRFD* and *PCI* methods, the elastic shortening losses were substantially overpredicted when design properties were used but were only slightly overpredicted when measured parameters were used. The obvious difference is in the modulus of elasticity of the concrete. It is clear that if the modulus of elasticity is known reasonably well, then the elastic shortening loss can be predicted to an acceptable level of accuracy. This conclusion was also discussed in Section 7.3.3.

The trends are clearly different for the loss due to creep. The creep losses are overestimated to an extreme degree because the *LRFD* and *PCI* methods do not model the creep behavior of HPC properly. While the overestimation is a bit less extreme when measured parameters are used, there is no doubt that the difference is still unacceptable. This indicates that the methods themselves are simply too rigid with respect to their simplifications for creep, even if the elastic strains (and stresses) are estimated accurately.

In the *LRFD* expression for creep loss, multipliers of 12 and 7 are applied to the calculated elastic stresses to represent the product of the modular ratio and long-term creep

coefficient. For the beams in this research program, the first coefficient should be significantly lower than 12. Using measured modulus of elasticity and creep data (with appropriate corrections for volume-to-surface ratio and average relative humidity), this coefficient should be approximately 4 for the Louetta and San Angelo Eastbound HPC beams, and 3 for the San Angelo Westbound non-HPC beams. Slightly lower coefficients would apply to the term corresponding to applied loads (i.e. second term), although the reduction would not be very large for HPC because the loading age effect should be reduced for the more mature concrete at early ages.

The *PCI* method has the advantage of being somewhat more transparent than the *LFRD* expressions, as the actual modular ratio is used in the expression rather than being lumped into an arbitrary coefficient. This allows for a more accurate prediction of the creep loss if the modulus of elasticity is known or estimated accurately. Still, the use of $K_{\text{cr}}=2.0$ for the creep multiplier overestimates the creep for HPC and results in high calculated losses. Considering the approximate effects of volume-to-surface ratio and average relative humidity and the measurements from the creep tests discussed in Section 4.5, this coefficient should be more in the range of 1.0 for the Louetta and San Angelo Eastbound HPC beams and 0.6 for the San Angelo Westbound non-HPC beams.

The strength of the *PCI Design Handbook* method is in its transparency, at least with respect to the modular ratio. If the suggested value of 2.0 for K_{cr} is ignored, the expressions are also more transparent with regard to the creep coefficient. Creep and elastic shortening losses should then both be calculated with a reasonable degree of accuracy if the modulus of elasticity and creep coefficient are known. The creep multiplier K_{cr} should consider not only the long-term creep coefficient, but must be adjusted for the effects of volume-to-surface ratio and relative humidity. In the absence of established relationships from measurements, modifications for these effects can be applied using the ACI 209 [8] equations. These equations are presented in Section 4.5.1.

A similar approach can be taken with the shrinkage loss, as the assumed long-term shrinkage value of $550 \mu\epsilon$ can be replaced with the value determined from tests on companion specimens. (Note that the coefficient of 8.2×10^{-6} in the *PCI* shrinkage equation shown in Table 7.7 is essentially equal to the strain of 550×10^{-6} multiplied by 1.5). If such a replacement is used, appropriate considerations must again be made regarding the effect of volume-to-surface ratio and average relative humidity. If the “measured” shrinkage has been converted to the field conditions by the ACI 209 method described in Section 4.6.1 or

another approach, then the terms in the *PCI* equation for volume-to-surface ratio and average relative humidity should obviously be deleted. Because the magnitude of the relaxation loss component is so small, there is really no justification for changing this term and the *PCI* equation is recommended as is. Thermal losses before release should also be considered, and a term corresponding to the measurements discussed in Section 7.2 should thus be added to the total loss. Losses due to relaxation before release also must be added to the total loss. Losses from shrinkage *before* release should also theoretically be considered at the appropriate time (before release), but can be assumed to be incorporated into the total shrinkage loss.

The recommended modified method is summarized in Table 7.11. Using measured creep, shrinkage, and modulus of elasticity data for the concrete used in the beams in this study, losses were estimated using the recommended method. The computed losses for each beam are listed in the last column of Table 7.9, and can be seen to show good agreement with the measured losses. Thus, the recommended method can be used as a similar, yet more general, approach compared to the *PCI and LRFD* component methods, and should provide a very good estimate of the total losses if measured properties are known.

Obviously, the major difficulty when using these methods is in the accurate determination of material properties. Unfortunately, there is not yet a large enough database on the modulus of elasticity, creep, and shrinkage properties of HPC such that reliable expressions for the estimation of these properties have been developed. For example, it was shown in Section 7.3 that using Equation 4.4 to estimate the modulus of elasticity for HPC could result in a large error in the prediction of elastic shortening losses.

Until enough data has been collected to develop reliable expressions for the estimations of these material properties, trial batching and past experience must be utilized as much as possible. Ideally, these important properties would be measured for each HPC concrete mix used in prestressing plants, but it is rather unlikely that many of these parameters will be known during design at the present time. At the very least, the modulus of elasticity should be measured on all HPC mixes since both the elastic shortening and creep losses are dependent on this property. It is somewhat more unrealistic to expect creep data to be obtained for all HPC mixes, but some reduction relative to conventional values for creep coefficients should be used to model the reduced creep for HPC.

Table 7.11 - Suggested Equations for Calculation of Total Losses by Components

	Suggested Component Loss Equations	Notes
$\Delta f_{ps,ES}$ El. Shortening	$\frac{E_{ps}}{E_{ci}} \cdot f_{cgp}$	$f_{s0} = .90 \cdot f_{sj}$
$\Delta f_{ps,SH}$ Shrinkage	$\epsilon_{sh}^* \cdot E_{ps}$	ϵ_{sh}^* adjusted by any common method to beam V/S ratio and avg. jobsite RH
$\Delta f_{ps,CR}$ Creep	$K_{cr} \cdot \left(\frac{E_{ps}}{E_c} \right) \cdot (f_{cgp} - f_{cdp})$	K_{cr} adjusted by any common method to beam V/S ratio and avg. jobsite RH
$\Delta f_{ps,RE}$ Relaxation	$[K_{re} - J \cdot (\Delta f_{ps,ES} + \Delta f_{ps,SH} + \Delta f_{ps,CR})] \cdot C$	$K_{re} = 5.0$, $J = 0.04$, $C = 1.00$ for low-relaxation Grade 270 strand stressed initially to $0.75 \cdot f_{su}$
$\Delta f_{ps,PR}$ Pre-Release (Relaxation + Thermal)	$\frac{\log(24 \cdot t_0)}{.45} \cdot \left[\frac{f_{sj}}{f_{sy}} - 0.55 \right] \cdot f_{sj}$ + $\frac{1}{3} \cdot E_{ps} \cdot \alpha_{ps} \cdot (T_{peak-hydration} - T_{stressing})$	Temperatures should be estimated from past experience. (ΔT was about 60 °F for HPC beams in this study.)
<p>All losses in units of ksi. 1 ksi = 6.895 MPa 1 in. = 25.4 mm °F = °C*(1.8) +32 f_{cgp} = stress in concrete at c.g. of pretensioned strands at release (due to prestress and self-weight), ksi; f_{cdp} = stress in concrete at c.g. of pretensioned strands due to applied loads (not acting at release), ksi; E_{ps} = modulus of elasticity of prestressing steel, ksi; E_{ci} = modulus of elasticity of concrete at release, ksi; E_c = modulus of elasticity of concrete at 28 days, ksi; f_{sj} = strand stress at jacking, ksi; f_{s0} = strand stress just after release, ksi; f_{su} = ultimate strength of the strand, ksi; f_{sy} = yield strength of the strand, ksi; t_0 = time in days between jacking and release</p>		

For HPC mixes in Texas made of similar constituent materials as those in this research program, the creep and shrinkage characteristics presented in Section 4.5 and Section 4.6 based on measurements in this research program should be used in lieu of conventional concrete characteristics. Obviously, much more research and many more material tests are needed to determine how representative these values are of all HPC, but the use of the data obtained in this research program should be more representative of HPC than traditional values determined from tests on conventional concrete.

Even when the values for these important material properties are measured, there will always be some variation in the properties for the actual concrete in the member. The sensitivity of HPC designs, as a result of the large prestress forces and loads associated with these designs, will probably result in larger variations of losses in HPC beams than in conventional concrete beams. These variations in losses may or may not present a problem in terms of stresses, but at the very least the designer must be aware of these potential variations. The effect of this increased sensitivity on deflection behavior is discussed in Chapter 8.

7.5 Summary and Conclusions

The following observations were made in this chapter regarding Prestress Losses Before Release:

- 1) Prestress losses measured between stressing and casting for five San Angelo Eastbound HPC beam pours ranged from - 9.5 to 33.0 MPa (- 1.38 to 4.79 ksi), with an average of 9.9 MPa (1.43 ksi). These losses were measured directly using a load cell placed at the dead end bulkhead.
- 2) The measured losses between stressing and casting were lower than the relaxation and thermal losses predicted analytically using measured times and strand temperatures. The lower measured losses are probably due to some unrecorded relaxation loss occurring before the first measurements in addition to friction at the intermediate bulkheads along the bed.
- 3) Initial jacking stresses averaged 1358 MPa (197.05 ksi) for these 15 mm (0.6 in.) diameter stands, which is 2.7 percent lower than the nominal jacking stress of 1396 MPa (202.5 ksi). These initial forces were probably low for the same reasons mentioned above (regarding the lower than predicted measured losses before casting.)
- 4) Losses cannot be measured directly after casting using only a load cell at the bulkhead. However, using the analytical strand model presented in Section 7.2.2, these force measurements can be used along with measured strand temperatures to *estimate*

the prestress loss occurring between casting and release. Much more research is needed to establish the accuracy of this model.

- 5) Based on the measurements from the load cells at the bulkheads and temperatures of the strands, losses between casting and release of 17.9 to 58.7 MPa (2.59 to 8.52 ksi) were estimated using the analytical model described in Section 7.2.2. The average estimated loss was 33.1 MPa (4.80 ksi), and about two-thirds of the loss was attributed to temperature effects. This average thermal loss corresponds to a strain change associated with a temperature increase of 11 °C (20 °F).
- 6) For calculations throughout this research program, total pre-release losses of 4.5, 4.0, and 3.5 percent of the nominal jacking stress were assumed for the Louetta HPC, San Angelo Eastbound HPC, and San Angelo Westbound HPC beams, respectively.

The following observations were made in this chapter regarding Elastic Shortening at Release of Pretensioned Strands:

- 1) Average measured elastic shortening losses were 123.8, 121.2, and 92.5 MPa (17.96, 17.58, and 13.41 ksi) for the Louetta HPC, San Angelo Eastbound HPC, and San Angelo Westbound non-HPC beams, respectively. As a percentage of the nominal jacking stress, these average losses are 8.87, 8.68, and 6.62 percent, respectively. The higher losses for the HPC beams are a direct result of higher prestress forces, since the measured moduli of elasticity for the various beam groups were similar.
- 2) For most beams, especially the San Angelo Eastbound HPC beams, the measured elastic shortening losses were higher than predicted using the transformed section and measured modulus of elasticity. The average ratio of measured to predicted losses by this method was 1.02, 1.25, and 1.11 for the Louetta HPC, San Angelo Eastbound HPC, and San Angelo Westbound HPC beams, respectively. For three individual beams, this ratio was greater than 1.38.
- 3) Restraint against shortening of the beams prior to release was probably the primary reason that measured losses were higher than predicted (using the exact method). The release of this restraint as the prestress was transferred to the concrete would have caused measured strains, and thus losses, to appear artificially high.

- 4) Differences between the actual modulus of elasticity and the values determined from companion specimen tests also could have led to differences between measured and predicted losses. However, the observed differences imply that for most beams the actual modulus would have been lower than the measured modulus, and this trend is generally contradicted by other measurements in this research program.
- 5) Elastic shortening losses are strongly influenced by the modulus of elasticity of the concrete, as evidenced by the direct relationship in Equation 7.12 and the large differences in the predicted losses using the approximate method with an estimated modulus (from Equation 4.2 or Equation 4.4) and the approximate method with the measured modulus.

The following observations were made in this chapter regarding Total Prestress Losses:

- 1) Total measured prestress losses in beams, taken from readings in the Spring of 1998 after the completion of jobsite construction, averaged 267.3, 376.8, and 228.0 MPa (38.76, 54.65, and 33.07 ksi) for the Louetta HPC, San Angelo Eastbound HPC, and San Angelo Westbound HPC beams, respectively. These losses include estimated pre-release losses based on the observations in Section 7.2.
- 2) For all beams, elastic shortening accounted for the largest component of the total measured loss, and the combined time-dependent loss due to creep and shrinkage was less than elastic shortening. Pre-release losses accounted for up to 25 percent of the total losses.
- 3) The incremental time-step approach using measured concrete material properties and the actual construction schedule showed good agreement with the total measured losses. Predicted losses were slightly higher than measured losses in the Louetta HPC beams, about equal to measured losses in the San Angelo Eastbound HPC beams, and slightly greater than predicted in the San Angelo Westbound non-HPC beams.
- 4) Total losses computed using PSTRS14 [130] during the actual beam designs were significantly higher than the measured losses for the Louetta HPC beams and San Angelo Westbound non-HPC beams. For the San Angelo Eastbound HPC beams, the losses calculated during the actual beam designs using ADAPT [13] were slightly lower

than the measured total losses, but overall the predicted losses were acceptable for these beams.

- 5) The *AASHTO LRFD* [1] time-dependent lump-sum estimates of loss calculated using design properties showed relatively good agreement with the measured time-dependent losses. Elastic shortening losses were overpredicted using design properties, however, and pre-release losses were not considered with this method.
- 6) Calculated losses using the *AASHTO LRFD* [1] and *PCI Design Handbook* [108] component equations resulted in total losses drastically larger than the measured losses for all beams, indicating that these methods should not be used for HPC without modifications. The methods are too restrictive in terms of simplifying assumptions that are based on the properties of conventional concrete. In general, both elastic shortening and creep losses were substantially overpredicted with these methods, especially when design properties were used.
- 7) Losses predicted using the modified component method described in Table 7.11 show good agreement with the measured total losses when calculations are based on measured creep, shrinkage, and modulus of elasticity values determined in this research program.

7.6 Recommendations

The following recommendations are made on the basis of the information presented in this chapter regarding Prestress Losses Before Release:

The measurements in this study imply that prestress losses occur prior to release as a result of relaxation, thermal effects, and shrinkage. Standard methods can be used to consider relaxation and shrinkage losses. However, the losses occurring *before* release as a result of these effects should be acknowledged at the appropriate time stage (i.e. before release) since these losses will affect the initial prestress force. Thermal losses also appear to occur before release and are influenced to some degree by the high hydration

temperatures developed in HPC beams. As a rough estimate, it is recommended that thermal losses be calculated using approximately one-third of the difference between the temperature at stressing and the peak hydration temperature (at the level of the strand). Since these temperatures will never be known during design, it is recommended that this temperature difference be taken as approximately 33 °C (60 °F) on the basis of this research alone.

Obviously, much more research is needed with regard to prestress losses before release. A simple analytical model that attempts to approximate the highly complex behavior in prestressed concrete beams before release was proposed in Section 7.2.2. Measurements on several future beams, especially those constructed using HPC, are needed to establish the accuracy of this simple model.

The following recommendations are made on the basis of the information presented in this chapter regarding Elastic Shortening at Release of Pretensioned Strands:

The approximate method for calculation of elastic shortening losses in pretensioned beams, given in Equation 7.14 and based on gross section properties, is acceptable for designs with HPC. However, accurate prediction of elastic shortening losses can only be made if the modulus of elasticity is known reasonably well. Furthermore, it must be noted that elastic shortening losses in HPC designs will be extremely large if the modulus of elasticity is not sufficiently high, as a direct result of the large prestress forces used in such designs. If elastic shortening losses are high, it is reasonable to assume that time-dependent losses will be high as well. If necessary, a minimum modulus of elasticity should be specified as part of the contract documents to ensure that concrete with adequate stiffness is used.

Due to the importance of modulus of elasticity in reducing losses in HPC beams, as well as for accurate prediction of losses, trial batching should be performed whenever possible to determine the modulus. At a minimum, designers should rely on past experience with similar concrete mixes, especially those with the same aggregate. The use of standard equations for modulus of elasticity, such as Equation 4.2 and Equation 4.4, should not be expected to give accurate estimates of the modulus of elasticity for all concretes.

The following recommendations are made on the basis of the information presented in this chapter regarding Total Prestress Losses:

In light of the fact that the component loss equations presented in the *PCI Design Handbook* [108] and the *AASHTO LRFD Specifications* [1] (and the similar equations found in the *AASHTO Standard Specifications* [3]) do not provide adequate estimates of losses for HPC beams, the modified component equations presented in Table 7.11 should be used for the prediction of losses in future HPC members. The main difficulty in using these more general equations is in the estimation of material properties. In particular, the modulus of elasticity and creep must be known to a reasonable degree of accuracy if the losses are to be estimated sufficiently.

At this time, there is not a large enough database of material property data on HPC to develop *reliable* expressions for the estimation of these material properties. Until such expressions are available, trial batching and past experience must be used in order to obtain accurate estimates for these properties. Unfortunately, losses in HPC beams will be very sensitive to these properties because of the relatively large prestress forces and loads typically associated with these beams. The modulus of elasticity should be measured on trial batches and adjustments made to the concrete mix if the modulus of measured modulus of elasticity differs significantly from the estimated values. It is also recommended that a required modulus of elasticity be specified on contract documents and fabrication drawings, since the beam concrete *must* have adequate stiffness in order to avoid excessive losses with HPC designs.

It is somewhat more unrealistic to expect creep to be measured for every concrete mix, so approximations may have to be made in design. The creep parameters measured for the concrete mixes in this study, which were presented in Section 4.5, should be used for HPC mixes in Texas composed of similar constituent materials in similar proportions. If these particular values are not used, the lower creep typical of HPC must be considered in some fashion.

8 CHAPTER EIGHT: CAMBER AND DEFLECTION

8.1 Introduction

8.1.1 General

Camber and deflection behavior of prestressed beams must be considered during the design and construction of highway bridges. While deflection considerations do not affect ultimate strength, they play an important role in the serviceability and constructability of such structures. Ideally, highway bridges under full dead load would be nearly level or exhibit a slight upward camber. Excessive camber or deflection under full dead load can result in an uneven riding surface. Excessive deflection may also cause ordinary citizens to perceive the structure to be unsafe. It is therefore important that deflection behavior be considered, and predicted with at least a reasonable degree of accuracy, in the design of highway bridge structures.

Excessive beam camber prior to construction of the deck can lead to difficulties in satisfying minimum deck thickness requirements at midspan. Similarly, inadequate camber can cause problems in obtaining desired grade elevations. Extra deck concrete may be required near midspan to make up for a camber deficit in beams, but this extra concrete will lead to a further increase in deflection. Camber differences among adjacent beams in a span can also result in difficulties in obtaining desired grade elevations.

Camber and deflection are caused by a variety of sources in prestressed beams for highway bridges. Many sources related to load effects are rather obvious, including the application of prestress, member self-weight, weight of the bridge deck, and superimposed dead loads (such as guardrails and deck surfacing). Each of these sources will cause an elastic camber or deflection, as well as a time-dependent change in camber or deflection associated with creep. The situation is further complicated because some of these effects are interrelated. For example, the prestress force will change over time as a result of prestress loss. There is camber component due to the initial elastic effect of prestressing, a

time-dependent growth in camber associated with prestress due to creep, and a time-dependent deflection due to the loss (or gain) of prestress force.

Some sources are temporary, and thus lead to an elastic component of camber or deflection but not a time-dependent component. Such sources include live loads and thermal gradients in the composite bridge. Other sources may also exist, including differential shrinkage between the cast-in-place deck slab and beams, and early-age thermal and shrinkage effects in beams before release of prestress. These sources may or may not be significant, depending on a variety of factors, and are typically not considered in design. In general, *any* effect that causes a strain gradient (curvature) over the depth of the member will cause a change in the deflection behavior. The source of the strain gradient need not be load-related.

Camber and deflection are affected by several material properties and structural parameters. Modulus of elasticity, unit weight, and creep of concrete all influence the magnitude of camber and deflection. The moments of inertia of the beam and composite cross-section also affect the magnitudes of various camber and deflection components. Beam spacing, deck thickness, beam cross-section, prestress force, and prestress eccentricity are some of the important structural parameters that must be known for accurate prediction of deflection behavior.

In general, each elastic component of camber or deflection can be related to the curvature or strain gradient at some point (or points) along the member. This relation is shown in Equation 8.1, where the coefficient k represents the shape of the curvature diagram along the member:

$$\Delta = k\phi \cdot \frac{L^2}{EI} = \frac{f(L^2, L^3, \text{ or } L^4)}{EI}$$

Equation 8.1

For the sources of camber and deflection discussed in the preceding paragraphs, the curvature will generally be uniform, linear, or parabolic along the length of the member. As a result, the deflection will be related to the square, cube, or fourth power of the span length. This relationship holds for time-dependent behavior as well, if such behavior is analyzed as multiples of the elastic curvatures.

The relationship given in Equation 8.1 has some important consequences for designs with HPC. When HPC is implemented to accommodate larger girder spacing, but span lengths are not increased, each camber or deflection component can be expected to be higher than for typical designs by a proportional amount. For example, if girder spacing is 50% larger than "typical" (and the same cross-section is used), then the deflection due to deck loads may be expected to be about 50% larger as a result of the increased spacing. However, this increase is offset by the potentially higher modulus of elasticity and lower creep coefficients exhibited by many high performance concretes.

If HPC is implemented in design such that span lengths are increased, there is a completely different effect. Every component of camber or deflection, no matter what the source, is magnified as an increase in the square, cube, or fourth power of the span length. For instance, increasing the span length by 25 percent, say from 30.5 m (100 ft.) to 38.1 m (125 ft.), increases the magnitude of each component of camber or deflection by 56, 95, or 144 percent (depending on whether the term is related to the square, cube, or fourth power of the span length). While the increased stiffness and reduced creep of many HPC's will offset this increase to a small extent, it is clear that the sensitivity of beams with very high span-to-depth ratios is greatly magnified.

The previous discussion was intended to show the effect of span lengths, and does not consider the effects of other changes in design as a result of using HPC. As discussed in Chapter 1, higher prestress forces are essential for HPC designs, and more camber due to prestress can thus be expected in such designs. Still, the important quantity for design is the *net* camber or deflection due to *all* components. There is no doubt that as each individual term is increased in magnitude, accurate prediction of the algebraic sum of all components becomes much more difficult. This sensitivity concept will be addressed throughout the various sections of this chapter.

This chapter presents a comparison of measured and predicted camber and deflection behaviors for all instrumented beams. A complete measured deflection history was obtained on a total of 26 beams, including twelve Louetta HPC U-beams, ten San Angelo Eastbound HPC beams, and four San Angelo Westbound non-HPC beams. Measurements were obtained on a few other beams in selected cases, as discussed in Section 3.4.3. Camber at release of pretensioning is discussed first, followed by time-dependent growth of camber in beams during storage at the precast plant. Camber and deflection due to other elastic components is then examined. Finally, time-dependent

camber and deflection under full dead load is discussed, and comparisons are made to predictions from time-dependent models.

As in Chapters 6 and 7, predictions are typically computed using two approaches. The first approach involves the use of standard design assumptions and design-based properties. The second method is a more refined method considering actual measured material properties, transformed section properties, etc. These two methods allow for an examination of both the prediction model itself, as well as its sensitivity to assumptions typically used in design. Parameters used in the two types of models are listed for each beam in Appendix F.

8.1.2 Corrections to Field Measurements of Camber and Deflection

Two systems were used for measurement of camber and deflection: the tensioned-wire system and the precise surveying system. The tensioned-wire system is described in Section 3.2.2.6, and the precise surveying system is described in Section 3.2.2.7. Each of these systems provided reliable data. However, a few corrections must be made to the raw measurements such that meaningful comparisons with predicted behavior can be made. Three basic types of corrections are described in this section. Each of these corrections was performed using an analytical procedure based on measured parameters.

The first correction applies only for certain measurements, and can be called a *measurement location* correction. Each camber or deflection measurement was intended to be relative to the points along the beam corresponding to the center of bearings in the bridge. As shown in Figure 8.1, measurements could not be taken exactly at these points in two cases, so that a correction to raw data was necessary. For the San Angelo Eastbound HPC Type IV beams, end bolts for the tensioned-wire system could not be placed directly above the center of bearing locations because of the cutouts required to accommodate post-tensioning anchorages. Instead, bolts were placed about 200 mm (8 in.) farther in from the beam end. Thus, camber readings were measured on a slightly shorter span than desired, requiring that the measurement location correction be made. This correction was also necessary when measurements were made on the bottom surface of beams in the completed bridge using the precise surveying system. In this case, elevations exactly at the center of bearing could not be measured, but measurements were instead made at the face

of the pier, typically about 225 mm (9 in.) away. Note that in most cases, the magnitude of this correction tended to be rather small (less than 3.2 mm [0.125 in.]). The only case where the correction became somewhat larger was in the San Angelo bridges, where the vertical grade of about 3% had to be accounted for.

A second correction was necessary for beams stored at the prestressing plant between release and erection. This correction can be referred to as a *support condition* correction, and accounts for the fact that beams were supported at a variety of different span lengths during storage. Beams were typically supported on wood or concrete railroad ties near the beam ends, but not at a location coinciding with the centerline of bearing in the completed bridge. This analytical correction was based on actual support conditions measured by the researchers at the prestressing plant, and allows for comparison of measured data with predictions based on a single span length.

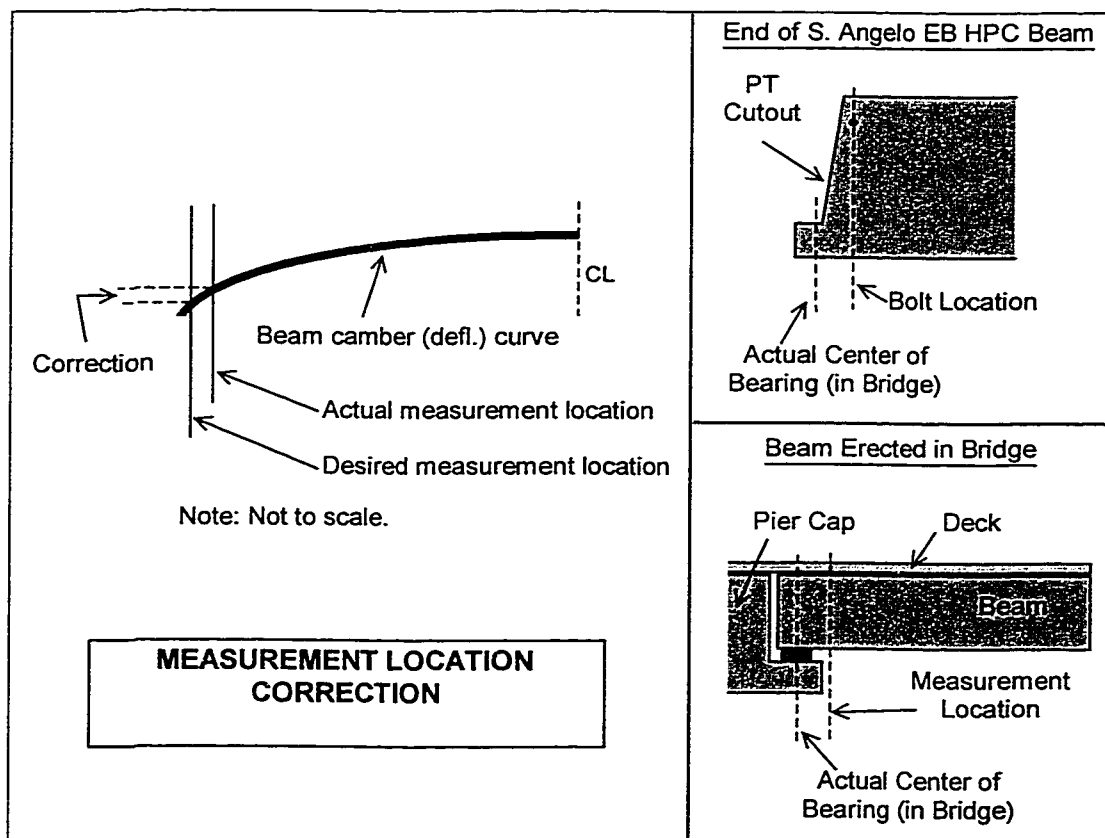


Figure 8.1 - Measurement Location Correction for Camber and Deflection Readings

The third correction was applied to as many measurements as possible, and is a *thermal gradient* correction. This correction accounts for the fluctuations in deflection behavior due to thermal gradients in both the composite bridges and beams in storage. The analytical correction is based on measured thermal data from embedded gauges, and is based on the procedure described in Section 5.4.1. Problems with this analytical correction method are caused by the fact that temperatures are interpolated between measured temperature locations (gauge locations). Especially in beams stored at the prestressing plant, the orientation of beams and the sun can affect such readings. Still, the method represents a reasonable correction for thermal effects in cases where temperature measurements were available. For only a few beams, such temperature measurements were not available and the thermal correction was not applied. These specific cases are identified throughout this chapter. Note that the effect of thermal gradients on the deflection behavior of pretensioned beams in composite bridges was observed in field studies in Texas [69] and Minnesota [139]. However, analytical corrections using measured temperatures were not applied to measured deflections in these studies.

8.2 Camber at Release of Prestress (Pretensioning)

8.2.1 Background

Camber at release of prestress is an important measurement of deformation in prestressed concrete beams. In many respects, the elastic camber at this stage is an informal measure of the level of prestress acting on the member. This measurement corresponds to the first point on the time-dependent deflection (camber) curve for a beam, and all points at larger ages are, to a large degree, a function of the elastic deformation at this stage.

Camber at release is generally considered to be the sum of two components, as shown in Equation 8.2:

$$\Delta_{rel} = \Delta_p - \Delta_{sw}$$

Equation 8.2

The first component Δ_p is due to the eccentricity of the prestressing, and generally causes upward camber. The second component Δ_{sw} is due to the self-weight of the member, and causes a downward deflection.

Each of these terms can be computed by considering the curvature along the length of the beam, as given by the individual terms in Equation 6.7. Predictions for the upward camber component due to eccentric prestress can be developed for specific layouts of prestress, and the effects of draping and debonding should be considered (although debonding can usually be neglected if it is present only at the very ends of the beam). The midspan upward camber due to eccentric prestress for a beam with straight strands (and no debonding) is given in Equation 8.3:

$$\Delta_p = \frac{P_0 e L^2}{8EI}$$

Equation 8.3

Note that this simple equation neglects any change in prestress force along the length of the member (due to changes in elastic shortening losses). Equations for other very simple layouts can be found in the *PCI Design Handbook* [108].

The downward deflection at midspan due to self-weight of the beam can usually be predicted by Equation 8.4, which assumes the beam weight to be uniformly distributed along the length of the member:

$$\Delta_{sw} = \frac{5w_{self-wt} L^4}{384EI}$$

Equation 8.4

Variations on this general case, including the effects of diaphragms in U-beams, can be predicted using standard equations for deflections under concentrated or distributed loads.

It is important to note that the self-weight deflection term given in Equation 8.4 is a function of the fourth power of the span length, while the eccentric prestress camber given in Equation 8.4 is only a function of the square of the span length. This relationship is typical for most prestressed concrete highway bridge girders, and means that the self-weight term increases at a fast rate as span lengths are increased. It can be shown that for typical designs with very long span-to-depth ratios, the increase in magnitude of the self-weight term may be greater than the increased magnitude of the prestress term (which increases with the square of the length and increased prestress force) [57]. The result is that net release cambers for very long span-to-depth ratios may actually decrease as spans are increased. Since the dead load deflections (under loads other than the beam self-weight) would be higher, it is quite possible that excessive sag (downward deflection) under full dead load would be present in designs with very large span-to-depth ratios.

8.2.2 Measurements

Midspan camber at release was measured on a total of 26 beams, including twelve Louetta HPC beams, ten San Angelo Eastbound HPC beams, and four San Angelo Westbound non-HPC beams. The tensioned-wire system, which is described in Section 3.2.2.6, was used for release camber measurements on all beams. A baseline (zero deflection) reading was recorded just prior to release, and another measurement was recorded immediately after release. Thermal gradient corrections were applied to measured beam cambers as discussed in Section 8.1.2. Measurement location corrections were also applied where applicable, namely on the San Angelo Eastbound HPC beams.

Measured release cambers are shown in Figure 8.2 and Figure 8.3 for Louetta and San Angelo beams, respectively. Actual camber measurements (including measurement location corrections) and thermally corrected measurements are shown to indicate the effect of thermal gradients. Each of these measurements is also listed in Table 8.1. Note that in most cases, a positive thermal gradient was present at release, such that the thermally corrected camber is lower than the actual measured camber. In a few Louetta U-beams, however, a negative gradient was actually present at release, such that the thermally corrected camber was higher than the actual measured camber. The maximum thermal correction at release was 13 mm (0.51 in.), in Beams E24, E26, and E33.

Measured thermally corrected cambers in Louetta U-beams ranged from 46.5 to 80.5 mm (1.83 to 3.17 in.). (Note that actual measured cambers in the two beams where thermal corrections were not made, Beams N23 and S26, were slightly outside of this range at 45.0 and 84.6 mm [1.77 and 3.33 in.], respectively.) Measured thermally corrected cambers in San Angelo Eastbound HPC beams were substantially smaller and ranged from -6.6 to 39.6 mm (-0.26 to 1.52 in.). Although lighter per unit length, many of these beams are substantially longer than the Louetta HPC beams, and they were not fully prestressed at this stage. Prestress force from an additional 20 to 26 post-tensioned strands was applied at a later age. Measured thermally corrected cambers in the San Angelo Westbound non-HPC beams were also quite small and ranged from 13.5 to 24.9 mm (0.53 to 0.98 in.). These beams were not post-tensioned at a later age, and therefore exhibited very little upward camber under full prestress.

Although there were variations in measured camber between identical and nearly identical beams, the release camber in companion beams was generally quite close. In most cases, identical beams exhibited less than 2.5 mm (0.10 in.) difference in camber at release. In only two cases was the variation in release camber among identical beams greater than 5.1 mm (0.20 in.). Note that identical beams are beams that are identical (or exhibit *very slight* variations) in span length, cross-section, and prestressing layout, and are cast during the same beam pour.

Predicted midspan release cambers are also shown in Figure 8.2 and Figure 8.3, for Louetta and San Angelo beams, respectively, and are listed in Table 8.1. Two types of predictions were calculated for each beam, one based on typical *design* assumptions, and one based on *measured* parameters. In particular, the *design* approach used gross section properties, a modulus of elasticity calculated from Equation 4.2 or 4.4, and a standard assumed unit weight for concrete. The refined measurement-based prediction was based on transformed section properties, a measured modulus of elasticity from companion cylinders, and a measured unit weight of concrete. The refined approach also considered a potential loss of prestress before release, based on the observations discussed in Section 7.2, and considered the effects of debonding at the ends of beams. These differences are summarized in Table 8.2, and the parameters used in each analysis are listed in Appendix F for each beam.

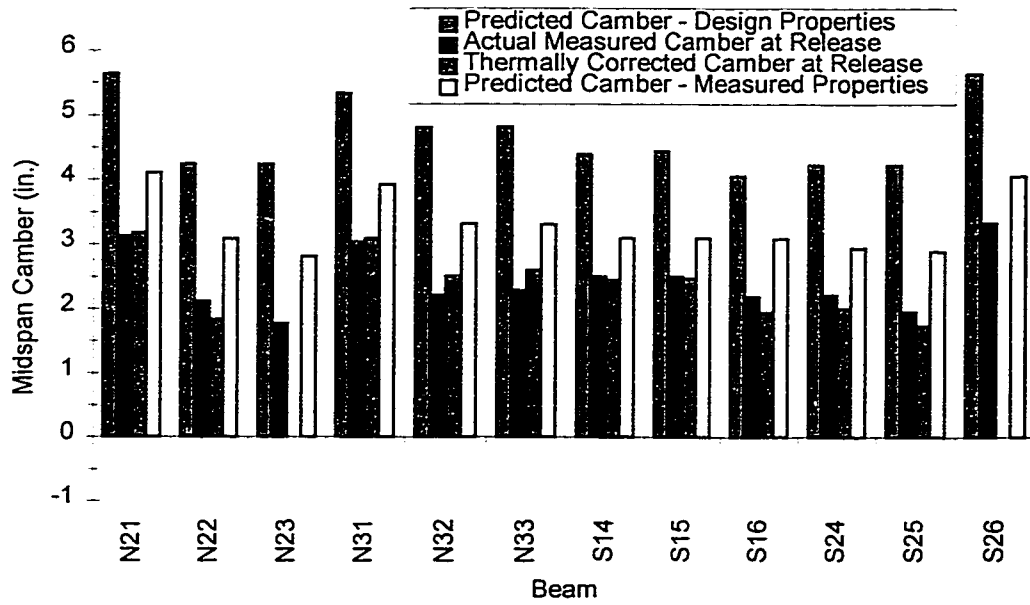


Figure 8.2 - Measured and Predicted Midspan Release Camber (Louetta)

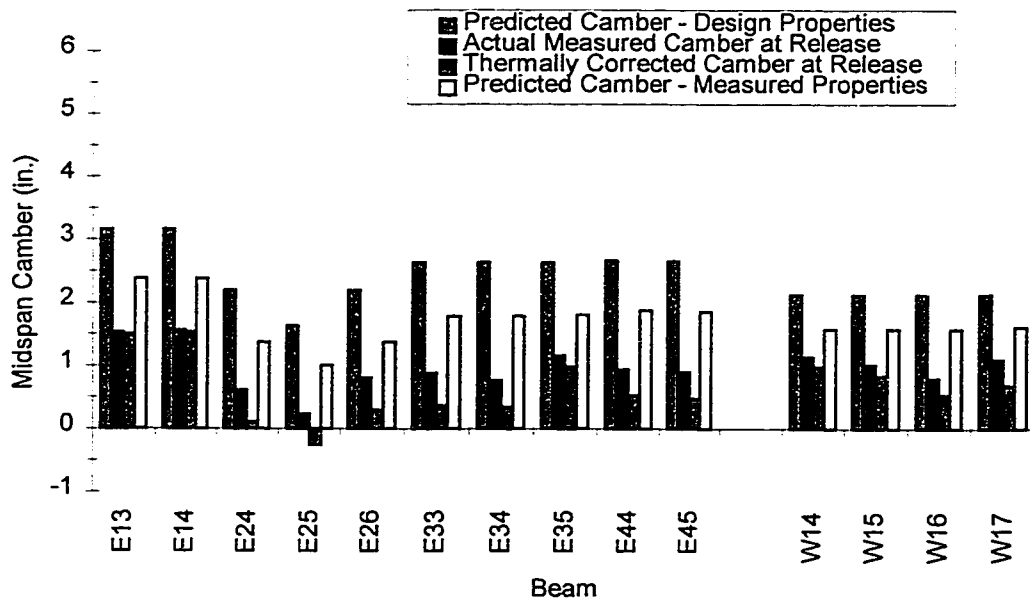


Figure 8.3 - Measured and Predicted Midspan Release Camber (San Angelo)

Table 8.1 - Summary of Measured and Predicted Midspan Release Cambers

Beam	Measured Release Camber		Predicted Release Camber		
	Actual	Thermally Corrected	"Design" Parameters	"Measured" Parameters	PSTRS14 / ADAPT †
N21	3.12	3.17	5.64	4.11	N/A
N22	2.11	1.83	4.24	3.08	N/A
N23	1.77	N/A #	4.24	2.81	N/A
N31	3.03	3.08	5.33	3.92	N/A
N32	2.20	2.51	4.80	3.32	N/A
N33	2.28	2.60	4.81	3.31	N/A
S14	2.50	2.44	4.39	3.09	N/A
S15	2.50	2.46	4.44	3.09	N/A
S16	2.18	1.94	4.06	3.08	N/A
S24	2.21	2.00	4.23	2.94	N/A
S25	1.95	1.74	4.23	2.89	N/A
S26	3.33	N/A #	5.64	4.06	N/A
E13	1.52	1.49	3.16	2.38	1.94
E14	1.55	1.52	3.16	2.38	1.94
E24	0.61	0.10	2.19	1.37	1.07
E25	0.23	-0.26	1.63	1.00	0.70
E26	0.80	0.29	2.19	1.37	1.07
E33	0.87	0.36	2.63	1.78	1.44
E34	0.76	0.34	2.63	1.78	1.44
E35	1.15	0.98	2.63	1.80	1.44
E44	0.94	0.52	2.66	1.87	1.47
E45	0.89	0.47	2.65	1.85	1.47
W14	1.13	0.98	2.12	1.57	N/A
W15	1.01	0.83	2.12	1.57	N/A
W16	0.79	0.53	2.12	1.57	N/A
W17	1.09	0.68	2.12	1.60	N/A

Note: All camber measurements in inches. 1 in. = 25.4 mm
Positive values represent upward camber.
† From actual beam designs. Note that PSTRS14 does not provide a prediction of initial elastic camber at release.
No thermal correction applied.

Table 8.2 - Summary of Methods Used for Prediction of Midspan Release Camber

Parameter(s)	“Design” Analysis	“Measured” Analysis
Section Properties	Gross section properties	Transformed section properties
Prestress Force / Loss	No loss assumed before release. Elastic shortening loss calculated by approximate method given in <i>AASHTO LRFD Specifications</i> [1] (see Section 7.2).	3.5 to 4.5% loss assumed before release based on measurements in Section 7.2. Elastic shortening loss not added because exact analysis using transformed section properties was used.
Beam Self-Weight	Based on gross beam area and assumed 150 pcf (3.29 kg/m ³).	Based on gross beam area and measured unit weight, with approx. weight of steel included.
Modulus of Elasticity	Eq. 4.2 (non-HPC) or Eq. 4.4 (HPC). (Required for calculation of elastic shortening and curvature.)	Based on tests of companion specimens. (Required for calculation of curvature and transformed section properties.)

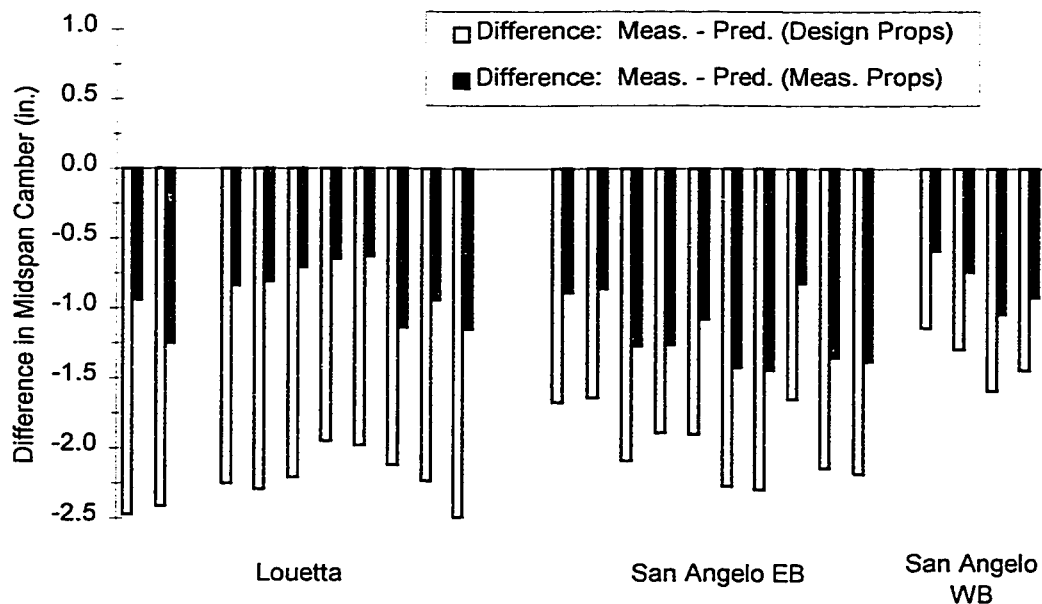


Figure 8.4 - Difference in Measured and Predicted Midspan Release Camber

Top of each bar represents predicted upward camber due to prestress.
 Length of each bar represents predicted downward deflection due to self-weight.
 Bottom of each bar represents net predicted camber at release.
 Predictions based on measured parameters.

X Measured Camber (no thermal correction)
 + Measured Camber
 - - - - - Sum of Individual Terms

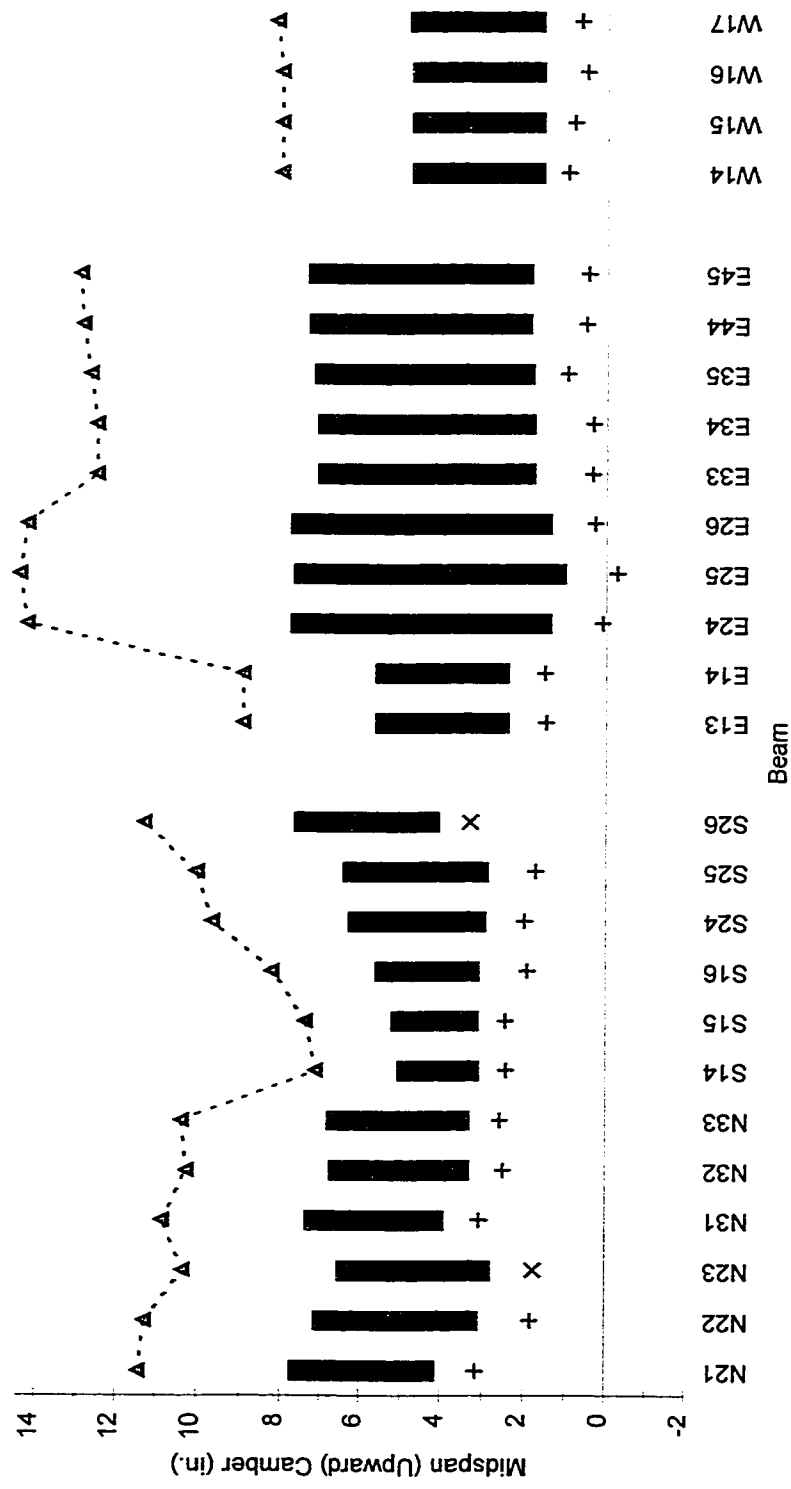


Figure 8.5 - Measured Release Camber and Predicted Release Camber Shown as Algebraic Sum of Two Components

Table 8.3 - Approximate Error in Prediction of Camber at Release

Beam	Predicted Release Camber (Measured Props.)			Measured Release Camber	% Error (Equation 8.5)
	Δ_p	$\Delta_{self-wt.}$	Δ_{rel}		
<i>Louetta Northbound and Southbound HPC Beams</i>					
N21	7.77	3.66	4.11	3.17	8.22%
N22	7.18	4.10	3.08	1.83	11.08%
N23	6.58	3.77	2.81	1.77 #	N/A #
N31	7.39	3.47	3.92	3.08	7.73%
N32	6.79	3.48	3.31	2.51	7.89%
N33	6.85	3.54	3.31	2.60	6.83%
S14	5.11	2.02	3.09	2.44	9.12%
S15	5.25	2.15	3.10	2.46	8.51%
S16	5.66	2.58	3.08	1.94	13.83%
S24	6.31	3.37	2.94	2.00	9.71%
S25	6.47	3.58	2.89	1.74	11.44%
S26	7.69	3.63	4.06	3.33 #	N/A #
<i>San Angelo Eastbound HPC Beams</i>					
E13	5.67	3.29	2.38	1.49	9.93%
E14	5.67	3.29	2.38	1.52	9.60%
E24	7.80	6.43	1.37	0.10	8.92%
E25	7.72	6.71	1.01	-0.26	8.73%
E26	7.80	6.43	1.37	0.29	7.59%
E33	7.14	5.37	1.77	0.36	11.35%
E34	7.14	5.37	1.77	0.34	11.51%
E35	7.24	5.44	1.80	0.98	6.47%
E44	7.37	5.50	1.87	0.52	10.49%
E45	7.40	5.54	1.86	0.47	10.66%
<i>San Angelo Westbound Non-HPC Beams</i>					
W14	4.82	3.24	1.58	0.98	7.32%
W15	4.82	3.24	1.58	0.83	9.18%
W16	4.82	3.24	1.58	0.53	12.90%
W17	4.89	3.29	1.60	0.68	11.25%
Average Error for All Beams					9.60%
Note: All camber and deflection measurements in inches. 1 in. = 25.4 mm					
# Not corrected for thermal gradients					

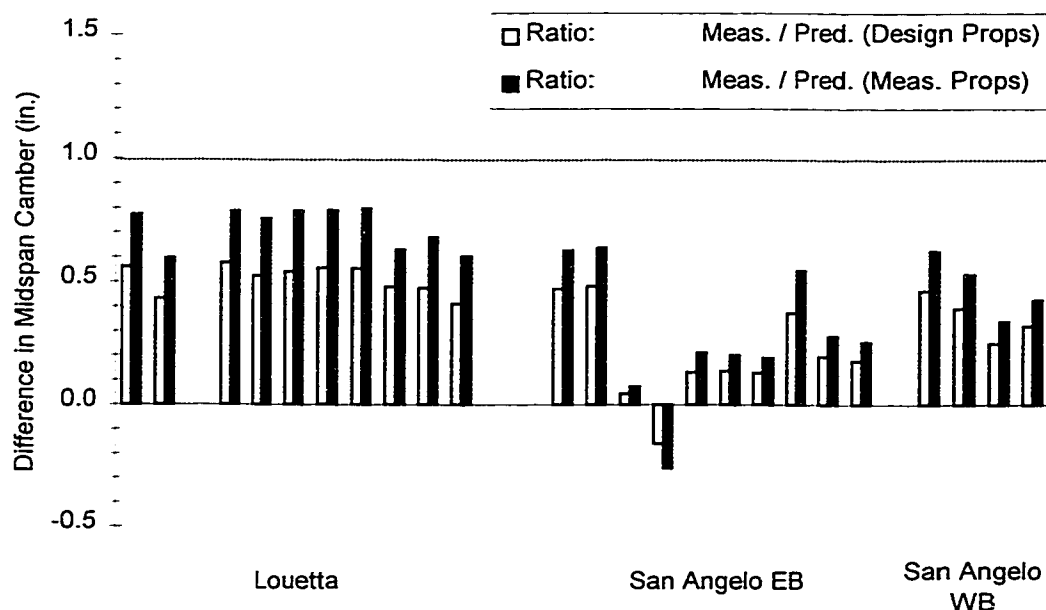


Figure 8.6 - Ratio of Measured to Predicted Release Cambers at Midspan

Note that for each of the 26 beams, the measured camber at release was less than the predicted camber. This trend is true for both the actual measured camber at release and the thermally corrected camber. Furthermore, this trend is true for both *design* and *measured* prediction methods. Possible reasons for the low observed camber at release are discussed in Section 8.2.3.

Values of initial camber at release predicted as part of the actual beam designs are listed in the last column of Table 8.1. Cambers predicted by the ADAPT computer analysis are listed for each of the San Angelo Eastbound HPC beams. In general, the ADAPT analyses predicted slightly less camber than the predictions based on measured parameters. This difference was probably a result of differences in the values used for modulus of elasticity, but could have been due to slight differences in the estimation of other parameters as well. No values are given for the Louetta HPC and San Angelo Westbound non-HPC beams because the TxDOT PSTRS14 design program used by TxDOT does not report the initial camber.

8.2.3 Discussion

The difference between measured thermally corrected release camber and predicted release camber is shown for all beams in Figure 8.4. Measurements are compared to predictions based on both types of prediction methods. It is clear that the design-based approach yielded extremely poor predictions, and overestimated the midspan release camber in all beams. The difference between measured camber and design-based predictions ranged from 41.7 to 63.2 mm (1.64 to 2.49 in.) in Louetta HPC and San Angelo Eastbound HPC beams, and from 29.0 to 40.4 mm (1.14 to 1.59 in.) in San Angelo Westbound non-HPC beams.

The most significant reason for this large magnitude of error is an error in estimation of the modulus of elasticity. The moduli of elasticity estimated by Equation 4.2 and Equation 4.4, which were used by in the design-based prediction, generally differed from the measured moduli of elasticity (from tests on companion specimens) by 15 to 25 percent. In all cases, the measured modulus of elasticity was higher than predicted by the appropriate equation. Errors in estimation of concrete unit weight, which was taken as 3.29 kg/m³ (150 pcf) in the design-based approach, also significantly contributed to the difference between measured and predicted camber. Finally, errors in estimation of prestress force (i.e. loss) and the use of gross-section properties could also have contributed to the total differences in release camber shown in Figure 8.4.

It is clear that the sensitivity of camber predictions for the beams studied in this research program is very high. Since net camber predictions are dependent on the accurate prediction of the *individual* terms in Equation 8.2, they become much more sensitive as the magnitudes of the individual terms increase. For HPC designs, this occurs when span lengths become longer or when prestress forces become higher. The magnitude of the individual components of the net camber (upward component due to eccentric prestress and downward component due to self-weight) for each beam in this study are shown graphically in Figure 8.5 and listed in Table 8.3. Magnitudes of the individual components in the figure and table are based on the refined prediction using measured parameters. The top of each bar in Figure 8.5 represents the predicted upward camber due to prestress. The length of each bar represents the predicted downward deflection due to the self-weight of the beam. The bottom of each bar thus represents the

predicted net midspan camber at release, as calculated using the refined approach with measured parameters.

It can be seen in Figure 8.5 that the magnitudes of the individual components are greater for most HPC beams than for the San Angelo Westbound non-HPC beams. The exceptions are the shorter span HPC beams in Span 1 of the Louetta Southbound bridge and Span 1 of the San Angelo Eastbound bridge. For the longer San Angelo HPC beams in Spans 2, 3, and 4 of the Eastbound bridge, the individual components are extremely high, but also similar in magnitude such that the *net* predicted camber is small. For the Louetta beams, the eccentric prestress component is significantly higher than the self-weight component, such that there is substantial camber predicted at release.

As mentioned previously, the sum of the absolute values of the two components of predicted release camber is a good indication of the sensitivity associated with the prediction. A realistic estimate of the “error” between the measured and predicted cambers must consider the sum of the absolute values of these components rather than their algebraic sum, as shown in Equation 8.5:

$$\% \text{ Error} = \frac{\Delta_{\text{rel, meas(th. corr)}} - \Delta_{\text{rel, pred(meas. prop)}}}{|\Delta_{\text{p, pred(meas, prop)}}| + |\Delta_{\text{self-wt., pred(meas, prop)}}|} \cdot 100\%$$

Equation 8.5

The sums of the absolute values of individual components of release camber for each beam are shown in Figure 8.5, and the errors computed using Equation 8.5 are listed in Table 8.3. For HPC beams, the error ranged from 6.5 percent to 13.8 percent, with an average of 9.6 percent. For the four San Angelo Westbound non-HPC beams, the average error was slightly higher at 10.2 percent. Actual differences between measured and predicted (based on measured parameters) release cambers, which are shown in Figure 8.4, were highest in the San Angelo Eastbound beams, indicating the higher sensitivity for these beams. The average differences for Louetta HPC, San Angelo HPC, and San Angelo non-HPC beams were 23, 30, and 21 mm (0.91, 1.18, and 0.82 in.), respectively.

The average errors of 9.6 percent for HPC beams and 10.2 percent for non-HPC beams are within reason considering the number of factors to which error may be attributed. The seemingly high absolute differences are largely a consequence of the high sensitivity

exhibited by the beams in this study. Still, it is important to note that *all* 26 beams showed less camber than predicted by the refined method. This method considered the measured modulus of elasticity and transformed section properties. Furthermore, the actual concrete unit weight was used in determination of the beam self-weight, and an increase of about 0.29 to 0.73 kN/m (20 to 50 lb./ft.) of beam length was assumed to account for the steel in the section (strands and reinforcement). Prestress losses of 3.5 to 4.5 percent prior to release were also assumed, based on the observations discussed in Section 7.2. Consideration of each of these factors (increased weight and prestress loss prior to release) leads to a decrease in the predicted net camber at release, yet the measured camber is still less than predicted in *every* beam by a significant amount. This trend thus merits a careful examination.

Although the modulus of elasticity obtained from tests on companion specimens was used in the refined predictions of release camber, it is probable that there is some variation in modulus of elasticity between the companion cylinders and the concrete in the actual beam. Any error, however, would tend to affect each term of Equation 8.2 a proportional amount, such that a 10 percent error in modulus of elasticity would cause a 10 percent error in the prediction of net camber. It can be seen in Figure 8.6 that the ratio of measured to predicted camber is highly variable, and in only six beams is it greater than 0.70. The ratio is closer to unity for the beams with a higher net camber, namely the Louetta HPC beams, but is actually less than 0.65 for all San Angelo beams. In other words, if the *only* error were due to estimation of the actual modulus of elasticity, the modulus of elasticity would have to be in error by greater than 35 percent for every San Angelo beam. This is considered to be extremely unlikely, and leads to the conclusion that errors in the estimation of modulus of elasticity cannot be the only source of error.

In order to examine the effects of errors in estimation of prestress force (loss) and member self-weight, the contour plot shown in Figure 8.7 is introduced for Beam S24. In this plot, prestress loss is plotted along the vertical axis and concrete unit weight is plotted along the horizontal axis. Each diagonal line represents the combinations of prestress loss and self-weight that would result in a given magnitude of camber at release, based on the relationships established in Equation 8.2, Equation 8.3, and Equation 8.4. Note that the relatively minor effects of debonding and the additional weight of the U-beam diaphragms have also been considered in this example.

A midspan camber of 51 mm (2.00 in.), after correction for thermal effects at release, was measured in Beam S24. Numerous combinations of prestress loss and unit weight could combine to give this net release camber, and each of these combinations is represented by the diagonal line marked "2.00 in.". For example, a unit weight of 3.60 kg/m³ (164 pcf) and 23 percent total prestress loss at release would result in a net camber of about 51 mm (2.00 in.). Unfortunately, most of the combinations represented by this line seem impossible since the unit weight of the Louetta beam mix was measured to be 3.38 kg/m³ (153.9 pcf) and elastic shortening losses were measured to be within the range of 6 to 10 percent for most beams.

The point corresponding to refined ("measured") prediction discussed in this section is also plotted in Figure 8.7. A net camber at release of 74.7 mm (2.94 in.) was predicted based on 11.58 percent total loss at release (including an assumed 4% prior to release based on the observations of Section 7.2) and a unit weight of 3.49 kg/m³ (158.9 pcf). Note that this unit weight is based on the measured unit weight plus an additional weight corresponding to the steel in the beam. A camber of 83.8 mm (3.30 in.) is predicted when the extra weight of the steel and prestress losses before release are neglected, resulting in an even further discrepancy between measured and predicted values.

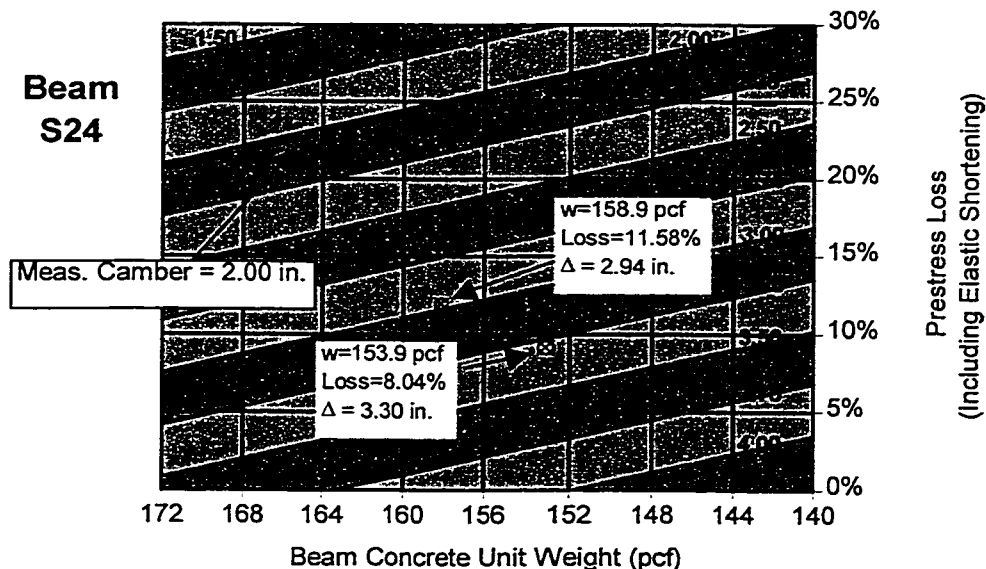


Figure 8.7 - Influence of Unit Weight and Prestress Loss on Release Camber

It should be noted that combinations corresponding to a predicted camber within 20 percent of the measured camber are also highly unlikely. For instance, a predicted camber of 61.0 mm (2.40 in.) might correspond to a prediction where the modulus of elasticity is in error by 20 percent. According to the plot in Figure 8.7, such a combination would require an additional 7 to 8 percent prestress loss above those estimated, or some combination of error in estimation of prestress loss and unit weight. Considering the fact that losses prior to release were already considered and the weight of the steel (strands and reinforcement) in the beam was accounted for, such a combination is considered to be highly unlikely.

Furthermore, this illustrative example is based only on Beam S24, for which there was a deficit of 23.9 mm (0.94 in.) between the measured and predicted camber. This is relatively close to the average deficit for all beams. In approximately one quarter of the beams, the deficit was greater than 31.2 mm (1.25 in.). It should be evident from the preceding discussion that for the beams in this study, this magnitude of difference between measured and predicted cambers cannot be explained simply by errors in prestress loss, self-weight, and modulus of elasticity.

It is therefore implied that another source of deflection might exist at release. As mentioned in Section 8.1.1, any change in curvature, no matter what the source, will result in a deflection response. That is, sources of camber and deflection need not be load-related. The discussions of Section 5.2.3 and Section 6.2.3 established that temperature and strain behavior prior to release is complex. It is quite possible and even probable that a strain gradient of some kind develops during hydration. Depending on when it is formed, such a gradient would have the potential to cause an additional component of the net camber at release. Two main factors, temperature and shrinkage, may contribute to such a strain gradient.

One possible explanation is related to the thermal gradient that develops in beams during hydration. In Section 5.2, it was discussed that temperature gradients were measured over the depths of beams during hydration. In general, the top portions of the beams became significantly hotter than the lower portions. It would be therefore be expected that the top of the beam would shorten more as it cools, since it had reached a higher temperature. If such a strain gradient does develop, it would cause a downward deflection in the cooling beam. The deflection component would be permanent, since it is due to the cooling from a gradient that developed as the beam was forming.

Similarly, there is a greater potential for shrinkage at very early ages at the top of the beam. During fabrication, the top surface is generally exposed to the environment first, before the side forms have been removed from the hardened beam. The bottom surface of the beam is never fully exposed until after release, since it is in contact with the bed liner. It is therefore quite possible that differential shrinkage occurs at very early ages, with the top of the beam shortening more than the bottom. Such a strain gradient would also result in a downward deflection, although it might be expected that such a deflection would be at least partially recoverable as the total shrinkage toward the bottom of the beam tends to catch up with the shrinkage toward the top. Any deflection resulting from an internal shrinkage restraint associated with non-symmetric reinforcement would not be recoverable, however.

Whether the cause of an additional downward component of the net deflection at release is a thermal gradient, differential shrinkage, or some combination of the two, such a component is difficult to see because it is impossible to isolate. Because the beam is fully supported along its length prior to release, this component would not appear until after release, when the effects of the eccentric prestress and member self-weight are also acting. It is quite possible that such a deflection component is present in typical prestressed beams (following the same fabrication methods), but that its magnitude is relatively small since these beams are usually shorter and (possibly) develop lower temperature gradients during hydration.

If the curvature that developed as a result of these effects is *assumed* to be uniform over the length of the beam, then the deflection component Δ_{EAST} (due to Early Age Shrinkage and Thermal effects) could be estimated by:

$$\Delta_{EAST} = \phi_{EAST} \cdot \frac{L^2}{8}$$

Equation 8.6

In Figure 8.8, the difference between measured release camber (after thermal corrections) and release camber predicted using the refined (“measured”) analysis is plotted for all beams in this study as a function of span length. An average curvature ϕ_{EAST} of 0.121 $\mu\epsilon/\text{mm}$ (3.07 $\mu\epsilon/\text{in.}$) was determined using a simple regression analysis. For the beams of the depth in this study (1371 mm [54 in.]), this curvature is equivalent to a linear strain

gradient with a difference in top and bottom fiber strains of $166 \mu\epsilon$. This magnitude is reasonable, considering the strain measurements before release discussed in Section 6.2.

Note the scatter of the points plotted shown in Figure 8.8, indicating that the actual deflection and equivalent curvature due to each of these factors may be highly variable. Of course, the points plotted in the figure are based on the assumption that all other parameters in the camber prediction (modulus of elasticity, prestress loss, unit weight, etc.) are exactly correct. This is clearly a poor assumption, and it is most likely that errors in the estimation of each of these parameters also contribute to the low measured camber.

It should be noted that in a similar field study in Minnesota [139], friction between the beam and the bed liner was observed to affect camber measurements at release. In particular, it was found that the camber was affected by the restraint on the beam at the very ends (where the beam is supporting its own weight) after the beam is released. As a result, the researchers took a set of measurements, lifted the beam completely off the bed, set the beam back down, and took another set of measurements. Differences of 10 to 12 percent of the measured camber were observed to occur between the two sets of readings. For the beams in this study, a second set of readings was not performed after picking the member up and placing it back down on the bed. It should be noted that small pieces of plywood were placed under the beam ends (between the beam and the bed liner) just before release in order to reduce the friction between the beam and the bed liner. This procedure was performed as part of the fabricator's standard operations.

Measured beam cambers just after release (while the beam is still on the bed) and immediately after the beam is placed in storage are compared in Table 8.4 for several beams in this study. Corrections for measured thermal gradients and support conditions during storage were applied to all of the listed measurements, such that in theory the measurements may be directly compared. The effects of creep within the first hour or so after release are not accounted for, however, and may explain some of the difference between the measured values. For the most part these differences were relatively small, but it can be concluded that bed friction could have had a small effect on the measured camber values at release. Clearly however, any such error could not account for more than a very small portion of the differences between measured and predicted camber at release.

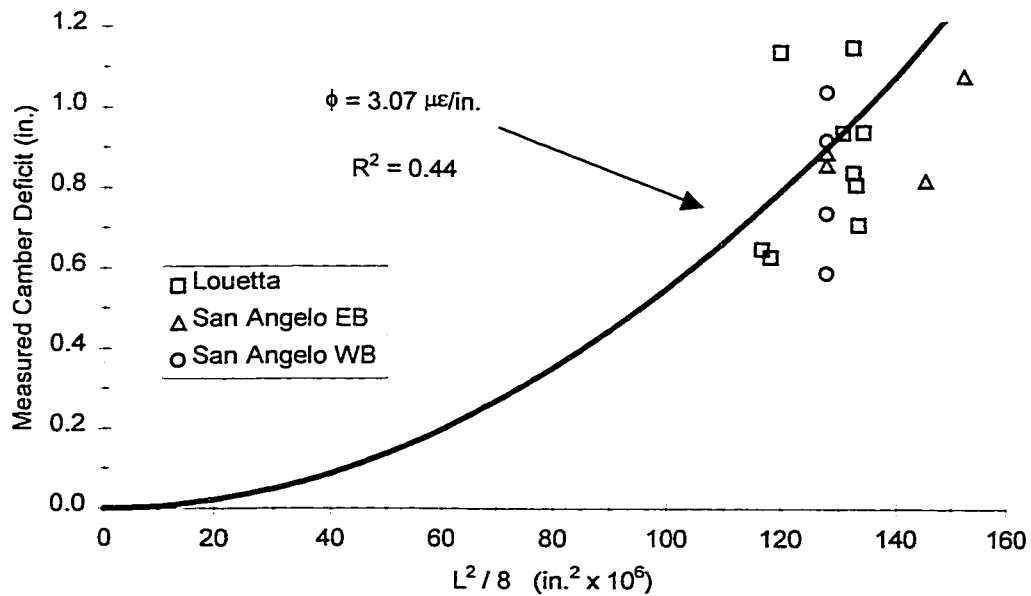


Figure 8.8 - Camber Deficit as a Function of Span Length

Table 8.4 - Measured Camber at Release Before and After Removal to Storage

Beam	Just After Release (on Bed)	After Removal to Storage	Difference
S24	2.00	2.08	+ .08
S25	1.74	1.79	+ .05
S26	3.33	3.52	+ .19
E13	1.49	1.39	- .10
E14	1.52	1.41	- .11
E24	0.10	0.22	+ .12
E25	- 0.36	- 0.26	+ .10
E26	0.29	0.20	- .09
E33	0.36	0.76	+ .40
E34	0.34	0.50	+ .16
E35	0.98	0.89	- .09
E44	0.52	0.77	+ .25
E45	0.47	0.64	+ .17

All values in inches. 1 in. = 25.4 mm
 All values are corrected for thermal effects (except Beam S26) and storage values are corrected for support conditions. See Section 8.1.2.

Most likely, the low release camber observed in the beams in this study is a combination of several factors. These factors include errors in estimation of the modulus of elasticity, unit weight, and prestress losses, and the possible presence of another deflection component related to early-age shrinkage and thermal effects. The sensitivity of camber predictions was also clearly illustrated in this study, even for the four San Angelo Westbound non-HPC beams.

It is recommended that predictions of release camber be performed with as much knowledge regarding material and structural properties as possible. The use of trial batching and the corresponding determination of material properties is recommended, especially for modulus of elasticity and unit weight. When actual determination of these properties is not possible, designers may wish to explore the sensitivity of predictions with respect to specific parameters. Experience from past projects using similar concretes may also help the designer in developing more accurate estimates of material properties than those provided by typical code equations.

The designer must acknowledge the dramatic increase in sensitivity with HPC designs. Longer span lengths and higher prestress forces cause the magnitude of individual components of release camber or deflection to increase significantly, and the accurate prediction of their net algebraic sum becomes much more difficult as a result. Designers should also acknowledge that early-age shrinkage and thermal effects could cause an additional component of downward deflection, depending on hydration temperatures and curing schemes. If a lack of camber is likely to present a problem during construction, the designer should consider including this potential additional downward deflection as an adjustment to the predicted camber at release.

In light of the very low release cambers observed in this study, additional research should be performed to investigate the camber and deflection of HPC and non-HPC beams. In particular, research should focus on determining whether and to what extent hydration temperatures and curing schemes may affect deflection behavior in these beams.

8.3 Time-Dependent Camber Growth in Beams During Storage

8.3.1 Background

For both ordinary reinforced and prestressed concrete beams, there is a time-dependent growth in camber or deflection associated with creep of concrete. Creep tends to increase the magnitude of strain associated with a given sustained stress. Furthermore, if a stress gradient exists in a member, then the creep strains are highest where the stress is highest. This results in a component of camber or deflection associated with the time-dependent curvature. In the interest of simplicity, only the time-dependent camber or deflection associated with those forces acting on the member at release of prestress (i.e. eccentric prestress and member self-weight) is considered in this section. The overall deflection behavior of beams in this study is examined in Section 8.5, including the elastic and time-dependent effects of post-tensioning and placement of the composite deck.

As discussed in Section 6.4, the approximate step-function method proposed by Branson [25] and adopted by ACI Committee 435 [11] can be used to predict the time-dependent deflection behavior of prestressed beams. This method presents a single equation to estimate the net camber or deflection, and can be used in lieu of the more complicated incremental time-step approach in which behavior is broken down into a series of short time intervals. The individual components of camber or deflection at release, which are given in Equation 8.3 and Equation 8.4 for common situations, are magnified to account for the effects of creep. As discussed in Section 6.4, the parameter S_t is introduced to account for the loss of prestress and its effect on the component of camber due to eccentric prestress. The parameter S_t is defined in Equation 6.9. The time-dependent net camber resulting only from prestress and beam self-weight can thus be approximated by Equation 8.7:

$$\Delta_{\text{net}}(t) = \left(\frac{1+S_t}{E_{ci}} \right) \cdot \Delta_p - \left(\frac{1+C_t}{E_{ci}} \right) \cdot \Delta_{sw}$$

Equation 8.7

Note that the sign convention used in Equation 8.7 assumes that positive values represent upward camber and negative values represent downward deflection.

As discussed in Section 6.4, changes in modulus of elasticity are not explicitly accounted for in Equation 8.7, but the creep coefficient inherently includes the time effect on modulus of elasticity if it is defined and determined by the definitions and procedures given in Section 4.5. If the creep coefficient does not include these effects, then the effective modulus approach [11] can be used to account for the time-dependent changes in modulus of elasticity. Equation 8.7 also does not account for deflection components resulting from differential shrinkage strains, whether due to differences in the rate of shrinkage across the depth of the cross-section or due to non-symmetric internal restraint provided by the reinforcement.

While Equation 8.7 does not provide an exact model, it does provide a basis for comparison with measured data, especially when predictions are based on measured properties. Such comparisons provide insight regarding the actual behavior of the beams observed in this research program.

8.3.2 Measurements

Midspan camber was measured at several stages during storage at the prestressing plant for each of the 26 beams. All measurements were made using the tensioned-wire system described in Section 3.2.2.6, and are relative to baseline (zero deflection) readings recorded just before release. Corrections for support conditions during storage were applied to all beams, based on the actual locations of the beam supports measured by the researchers. Thermal gradient corrections were also applied to all beams except Louetta HPC beams N23 and S26, in which temperatures were not measured. These analytical corrections, which are described in Section 8.1.2, allow for easier comparison of time-dependent measurements to the camber predictions. The corrections “convert” the actual raw measurements to conditions of uniform temperature (i.e. no thermal gradient) and full span length (i.e. center-to-center of permanent bearings in the bridge).

An example of the effect of these analytical corrections can be seen in Figure 8.9 for Louetta HPC Beam N31. Raw uncorrected camber measurements are shown in this plot, along with data corrected only for support conditions and data corrected for both support conditions and thermal gradients. The support condition corrections were generally the same for all readings unless the beam supports were moved, and were usually less than

13 mm (0.5 in.) in magnitude. The thermal gradient corrections were much more variable, and could be as high as 20 mm (0.8 in.) in magnitude for readings taken in the middle of the afternoon. The thermal gradient correction was negligible for readings taken during the early-to-mid morning hours. The use of these corrections clearly allows for a much more direct comparison of measured and predicted time-dependent camber, as the fluctuation in camber readings due to thermal effects is minimized.

Time-dependent camber was predicted for all beams using Equation 8.7. Parameters used in the prediction were based on measured values rather than design assumptions. Specifically, modulus of elasticity and unit weight were based on companion specimen tests. The creep coefficients measured for each beam mix, which are listed in Table 4.17, were used with appropriate correction factors for volume-to-surface ratio and average relative humidity. Transformed section properties were also used in the analysis for each beam, with the full prestress force prior to elastic shortening loss (for prediction of the initial elastic camber before time effects). Based on the observations of Section 7.2, the initial prestress force included the assumption of a small loss before release.

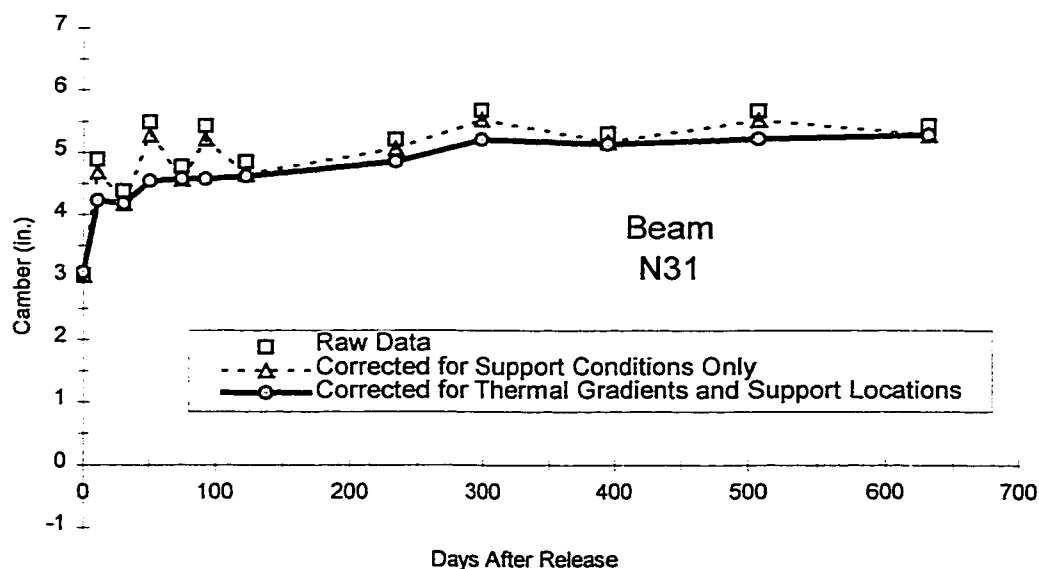


Figure 8.9 - Effect of Analytical Corrections for Support Conditions and Thermal Gradients on Camber Measurements

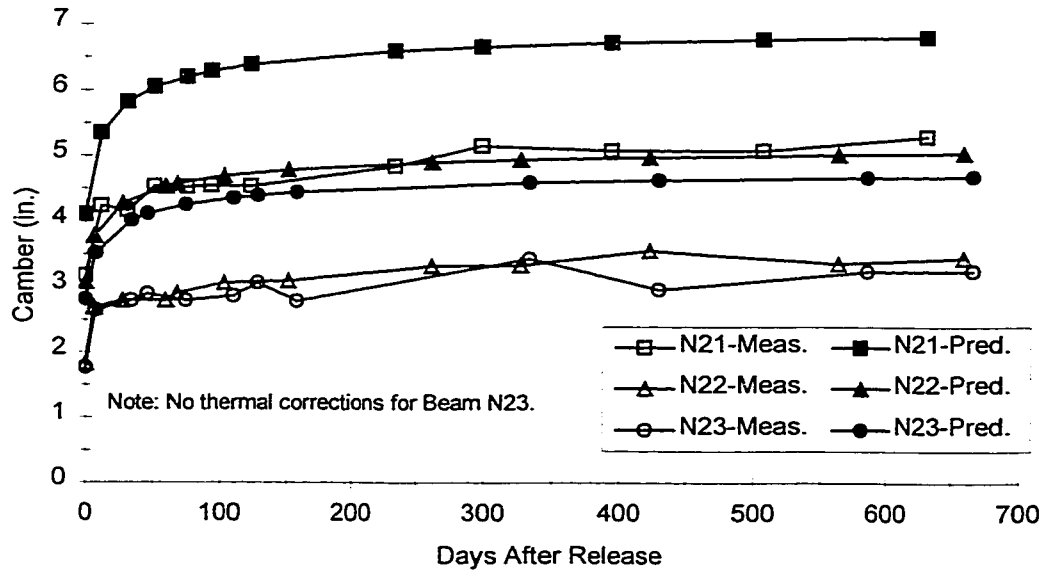


Figure 8.10 - Measured and Predicted Time-Dependent Camber for Beams in Storage (Louetta HPC Northbound Span 2)

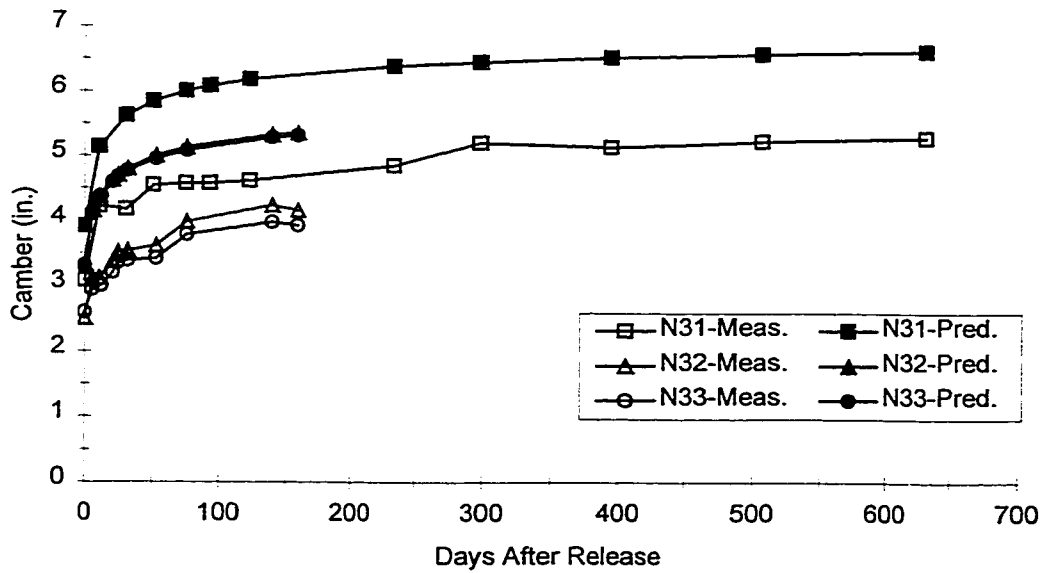


Figure 8.11 - Measured and Predicted Time-Dependent Camber for Beams in Storage (Louetta HPC Northbound Span 3)

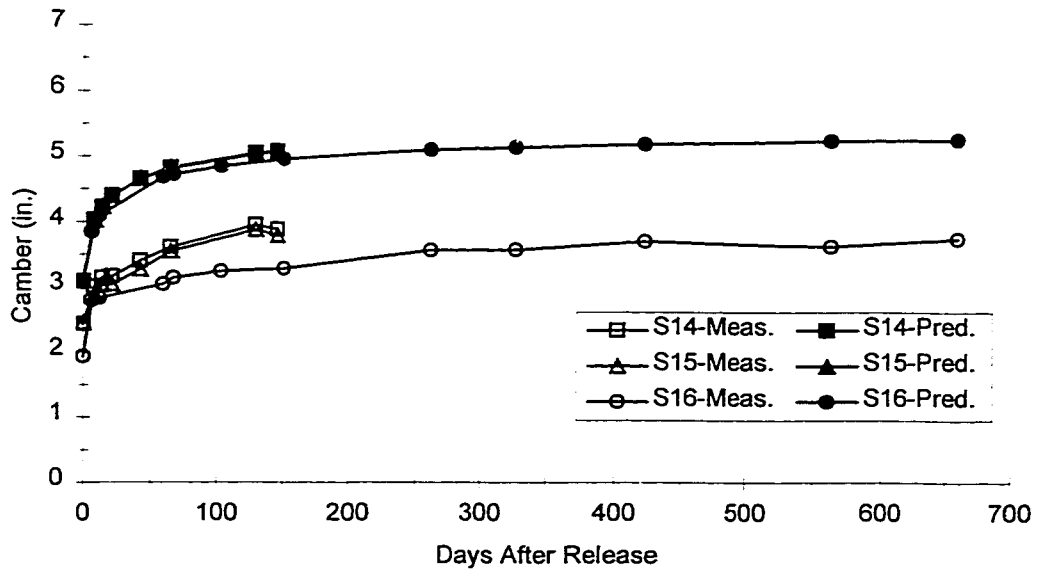


Figure 8.12 - Measured and Predicted Time-Dependent Camber for Beams in Storage (Louetta HPC Southbound Span 1)

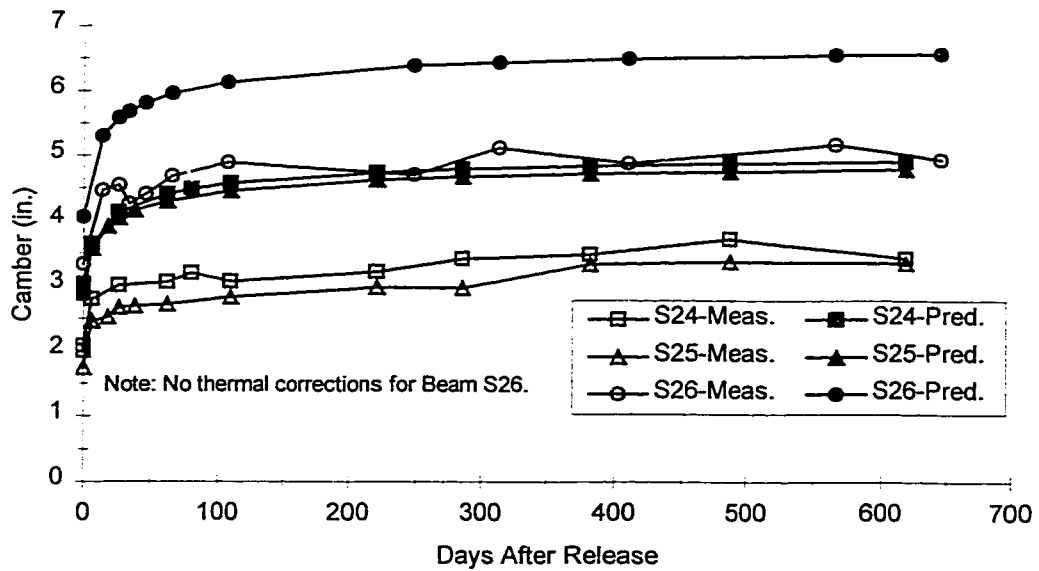


Figure 8.13 - Measured and Predicted Time-Dependent Camber for Beams in Storage (Louetta HPC Southbound Span 2)

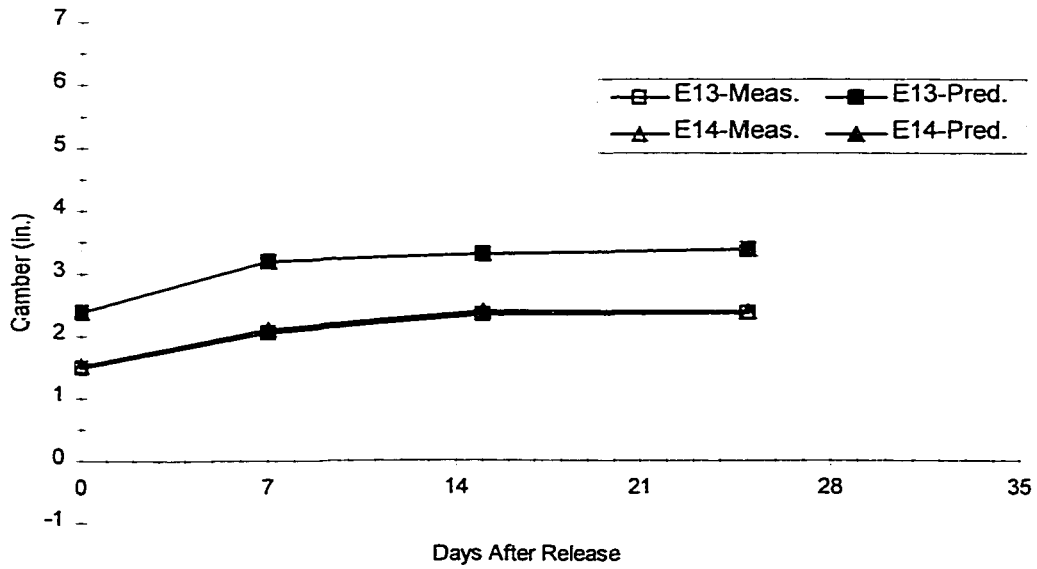


Figure 8.14 - Measured and Predicted Time-Dependent Camber for Beams in Storage (San Angelo HPC Eastbound Span 1)

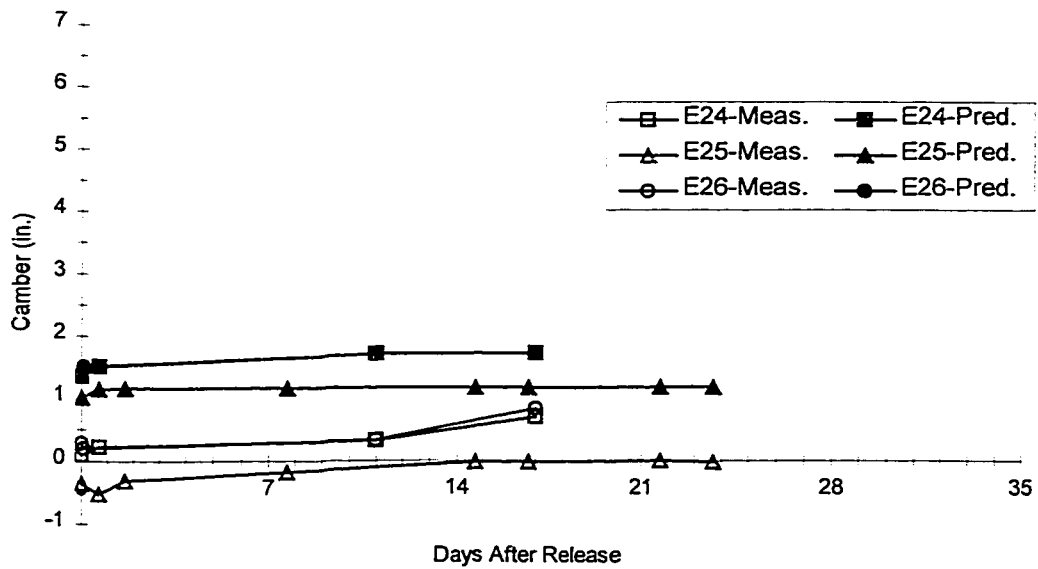


Figure 8.15 - Measured and Predicted Time-Dependent Camber for Beams in Storage (San Angelo HPC Eastbound Span 2)

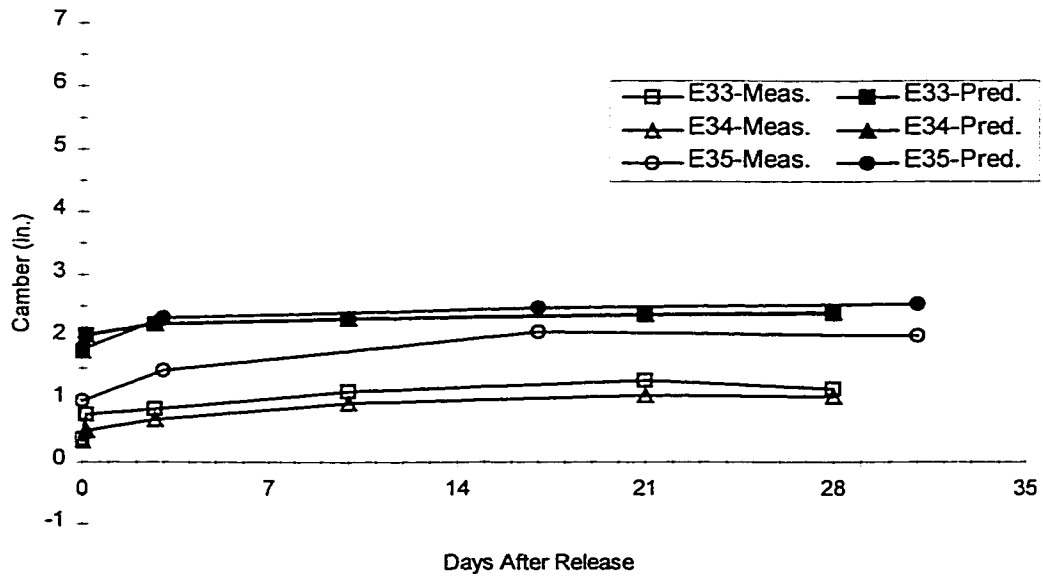


Figure 8.16 - Measured and Predicted Time-Dependent Camber for Beams in Storage (San Angelo HPC Eastbound Span 3)

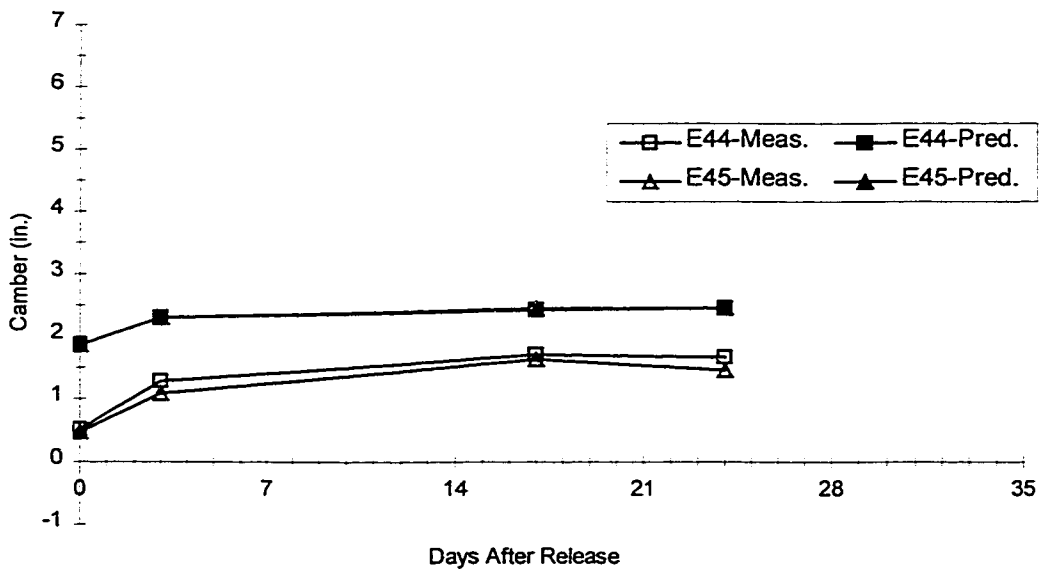


Figure 8.17 - Measured and Predicted Time-Dependent Camber for Beams in Storage (San Angelo HPC Eastbound Span 4)

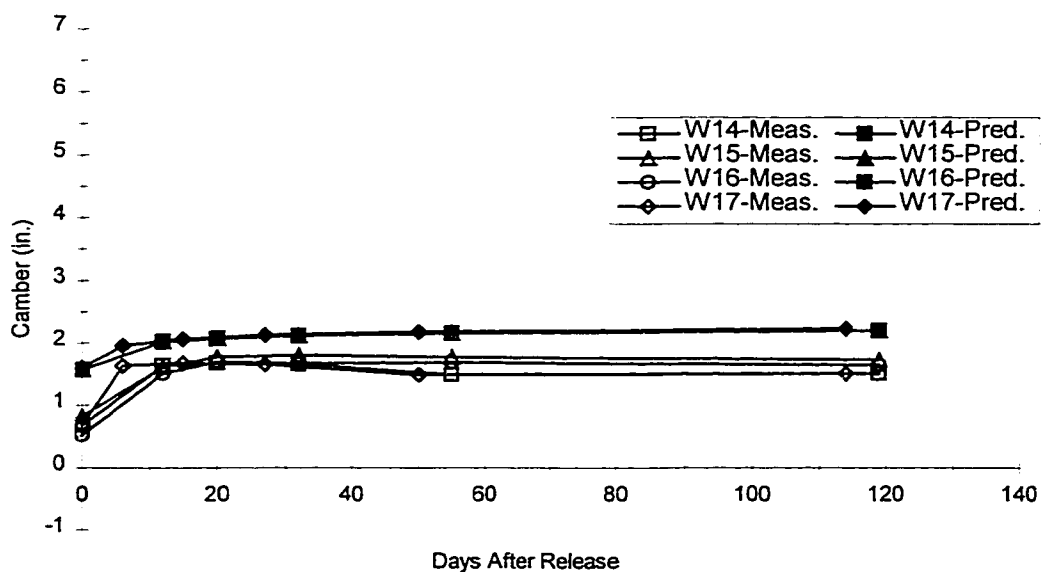


Figure 8.18 - Measured and Predicted Time-Dependent Camber for Beams in Storage (San Angelo Non-HPC Westbound Span 1)

Note that a prediction based on design properties was not performed for each beam because observations regarding trends in the camber behavior of the beams are of primary interest in this section. Furthermore, these additional predictions would have cluttered the plots of measured and predicted data presented in this section. A comparison of predicted time-dependent behavior based on both design and measured properties is presented for selected beams in Section 8.3.3, however, so that the sensitivity of time-dependent camber to material properties can be illustrated. Actual comparisons using design parameters are also presented in Section 8.5 for all beams, where the full time-dependent deflection behavior due to all dead loads is studied.

Measured and predicted time-dependent camber growth during storage are compared for all beams in Figure 8.10 through Figure 8.18. Camber growth during storage is also summarized in Table 8.5. An examination of the plots, which have been organized by span for clarity, shows that companion beams exhibited very similar behavior in almost all cases. For the Louetta HPC beams, this includes the two instrumented interior beams in each span, for which the strand pattern was identical and the span length only slightly

different. (Louetta Beams N21, N31, S16, and S26 are *exterior* beams, and all others shown are *interior* beams.) For the San Angelo beams, this includes all beams in any given span, with the exception of Beam E25 in Span 2 of the Eastbound HPC bridge. This beam was the “test beam” and was cast much earlier than the other beams in that span, with a different layout of prestress.

It can be seen in Figure 8.10 through Figure 8.13 that for the Louetta HPC beams, measured camber growth was similar to predicted camber growth with respect to the shape of the camber-time curves. For all of the Louetta HPC beams, the difference between measured and predicted camber grew with time, and the ratio of measured to predicted camber remained relatively constant over time. For those Louetta beams that remained in storage for over 600 days, camber growth during storage ranged from about 36 to 56 mm (1.4 to 2.2 in.), depending on the magnitude of the elastic camber at release.

As can be seen in Figure 8.14 through Figure 8.17, the behavior was slightly different for the San Angelo Eastbound HPC beams. For these beams, the difference between measured and predicted camber generally decreased slightly or remained relatively constant over the first few weeks in storage. The ratio of measured to predicted camber increased significantly over this period, but this ratio is somewhat less meaningful because of the very small release cambers exhibited by these beams. Note that readings after about the first month in storage are not shown for these beams, since they were post-tensioned at that time, causing the prediction of camber to become more complex.

Measured and predicted camber over the first 120 days in storage is compared in Figure 8.18 for the four San Angelo Westbound non-HPC beams studied in this research program. These beams exhibited a quick increase in camber, of a magnitude substantially higher than predicted, followed by a relatively constant camber throughout the duration of storage. Over the first 120 days in storage, the difference between measured and predicted camber decreased, while the ratio of measured to predicted camber increased. In this sense, the behavior was similar to the behavior of the San Angelo Eastbound HPC beams.

Table 8.5 - Summary of Measured and Predicted Camber Growth in Beams During Storage at the Prestressing Plant

Beam	Days of Data	Camber Growth † (in.)		
		Measured	Predicted	Difference (Meas. - Pred.)
<i>Louetta HPC Beams</i>				
N21	632	2.13	2.70	- 0.57
N22	660	1.62	1.98	- 0.36
N23 #	667	1.48	1.88	- 0.40
N31	632	2.20	2.69	- 0.49
N32	159	1.65	2.43	- 0.78
N33	159	1.33	2.00	- 0.67
S14	146	1.44	1.98	- 0.54
S15	146	1.33	1.98	- 0.65
S16	660	1.80	2.18	- 0.38
S24	619	1.42	1.96	- 0.54
S25	619	1.61	1.91	- 0.30
S26 #	646	1.61	2.52	- 0.91
<i>San Angelo Eastbound HPC Beams</i>				
E13	25	0.87	1.00	- 0.13
E14	25	0.86	1.00	- 0.14
E24	17	0.59	0.35	+ 0.24
E25	24	0.34	0.16	+ 0.18
E26	17	0.54	0.35	+ 0.19
E33	28	0.81	0.59	+ 0.22
E34	28	0.70	0.61	+ 0.09
E35	31	1.04	0.72	+ 0.32
E44	24	1.15	0.60	+ 0.55
E45	24	0.99	0.60	+ 0.39
<i>San Angelo Westbound Non-HPC Beams</i>				
W14	119	0.55	0.63	- 0.08
W15	119	0.90	0.63	+ 0.27
W16	119	1.12	0.63	+ 0.49
W17	114	0.83	0.63	+ 0.20
1 in. = 25.4 mm				
# Not corrected for thermal gradients. † Net camber less initial elastic camber.				

8.3.3 Discussion

The time-dependent growth in camber, defined as the difference between camber at any time during storage and the initial elastic camber, is of primary interest in this section rather than the net camber readings. By examining the growth rather than the cumulative camber, the effects of differences between the measured and predicted camber at release can be reduced. Possible reasons for differences between measured and predicted camber at release are discussed in Section 8.2.3. However, it must always be acknowledged that the growth of camber is inherently related to the initial elastic camber.

It is important to note that observations regarding the time-dependent growth of camber in storage are consistent with the observations related to time-dependent strains discussed in Section 6.4. For the Louetta HPC beams, the time-dependent curvature growth and time-dependent camber growth were both less than expected. For the San Angelo Eastbound HPC beams, on the other hand, both the time-dependent curvature growth and time-dependent camber growth were about equal to or slightly greater than predicted. These similarities between measured strain (curvature) and camber behavior help to validate each type of reading.

Several factors may contribute to differences between measured and predicted camber growth exhibited for the various types of beams. A higher actual modulus of elasticity than determined from tests on companion specimens would result in a lower than predicted camber at release and during storage. Errors in estimation of the actual creep coefficient, or in the correction factors for volume-to-surface ratio and relative humidity, would lead to differences in the rate of camber growth. Of course, errors in the prediction of the initial elastic camber might also directly lead to errors in the prediction of time-dependent camber.

For the Louetta HPC beams, the camber growth was lower than predicted, although the ratio of measured to predicted camber remained relatively constant. Since an error in modulus of elasticity would have approximately the same effect on camber at all times, this trend implies that differences between the actual modulus of elasticity and the modulus of elasticity measured in tests on companion specimens were the primary error. However, because the ratio of measured to predicted camber was greater than 0.75 for only seven of the twelve beams (both at release and at the time of final storage readings), it can probably

be concluded that there are other sources leading to the lower than predicted camber growth. As mentioned previously, differences between the actual creep coefficient and the value determined in companion tests could have had a significant influence.

As a group, the San Angelo Eastbound HPC beams exhibited different behavior than the Louetta HPC beams. Camber growth in these beams was about equal to or slightly greater than predicted. For most of these beams, very little camber growth was actually predicted during storage because of the relatively uniform stress (strain) distribution in these beams at midspan. Any camber growth resulting from a slight (negative) curvature at midspan and a higher (negative) curvature away from midspan should be countered by a deflection associated with the loss of prestress. Despite this, some camber growth was observed in each of these beams over the first month or so in storage. This trend is inconsistent with an underestimation of the actual modulus of elasticity, although an underestimation of the creep coefficient could have contributed to this behavior.

Another possible explanation for the early camber growth in these beams is related to the reasons for low camber at release discussed in Section 8.2. This growth could be associated with the recovery of camber due to differential shrinkage. As noted in Section 6.4, very little (compressive) strain growth was observed at the top fiber in these beams, implying that more shrinkage was occurring toward the bottom of the beam during storage. This differential shrinkage would result in an upward camber, much as the opposite differential shrinkage effect before release (more shrinkage at the top than the bottom) would result in a downward deflection. Because of the very large span-to-depth ratios for these beams, the magnitude of the differential shrinkage would not need to be very large to cause a noticeable increase in camber.

For the San Angelo Westbound non-HPC beams, overall behavior was similar to the behavior for the San Angelo Eastbound HPC beams. More camber growth was observed than predicted in these beams during approximately the first four months in storage. Unfortunately, time-dependent strains were not successfully recorded in any of these four beams (mostly due to cracking at the gauge locations before release and the resulting effect on the baseline readings), so the time-dependent camber behavior cannot be verified by an examination of curvature behavior. It is probable that the same differential shrinkage effect could have caused more camber growth than was predicted. Differences between the actual and measured creep coefficient may also have been a factor, but the

observed behavior was inconsistent with an underestimation of the actual modulus of elasticity.

As for many of the other aspects of structural behavior studied in this research program, it is impossible to positively identify the exact reasons for differences between measured and predicted behavior. This is especially true when the sensitivity of time-dependent deflections to certain parameters is considered. Camber predictions based on both measured and design parameters are shown in Figure 8.19 for three beams, including one Louetta HPC beam, one San Angelo Eastbound HPC beam, and one San Angelo Westbound non-HPC beam. The prediction based on measured parameters has been discussed previously, and uses measured concrete properties from companion tests for creep, modulus of elasticity, and unit weight. The prediction based on design parameters includes the use of Equation 4.2 or Equation 4.4 for modulus of elasticity, an assumed 3.29 kg/m^3 (150 pcf) unit weight for the beam concrete, and the use of the "standard" ACI 209 [8] equation for creep with appropriate correction factors for volume-to-surface ratio and relative humidity. Gross section properties were also used in the *design* prediction.

Different results are clearly provided by the two predictions for each beam. The prediction based on design parameters results in very large cambers relative to the measured predictions, which are already higher than the actual measured camber for each beam. Thus, the predictions based on design properties are in extreme error relative to the actual measured camber for each beam (which are not plotted in Figure 8.19 for clarity). The difference between the *design* and *measured* predictions for each beam is shown in Figure 8.20. Note that there is a substantial difference between the predicted elastic cambers at release, and that the difference for each beam grows significantly over time.

The prediction of time-dependent camber growth is dependent on several important parameters including creep, modulus of elasticity, prestress force (or loss), and self-weight of the beam. In order to examine the sensitivity with respect to each of these parameters, the parameters were individually increased or decreased by a small amount (5 to 10 percent), and the resulting difference in predicted camber computed. The results of this sensitivity analysis are shown in Table 8.6, Table 8.7, and Table 8.8 for Louetta HPC Beam N21, San Angelo Eastbound HPC Beam E35, and San Angelo Westbound non-HPC Beam W17, respectively. The base case for each beam is the *measured* prediction shown in Figure 8.19. Elastic camber and time-dependent camber growth have been separated in

the tables for clarity. A time of 180 days after release was arbitrarily chosen for the time-dependent calculations.

The results of this simple sensitivity analysis show that camber is sensitive to changes in all of the parameters for the HPC designs. In particular, variations in the prestress force and beam self-weight can have a very large impact. This is a direct result of the large magnitudes of the individual camber and deflection components associated with eccentric prestress and beam self-weight. Furthermore, both the elastic and time-dependent camber are affected by variations in these parameters. Note that changes in the prestress force have a larger effect for the Louetta HPC beam, since the prestress forces are higher for these beams (when post-tensioning is not included in the San Angelo beam analysis). The effects of variations in the beam self-weight are larger for the San Angelo HPC beam because of the very long span length.

The HPC designs are less sensitive to creep variations because only the time-dependent growth is affected. The modulus of elasticity affects both the elastic and time-dependent portions of camber, however, and thus has a more significant effect than creep. The modulus of elasticity and creep coefficient clearly have a larger impact on the Louetta HPC beam than on the San Angelo HPC beam, which is a direct result of the higher *net* elastic camber in these beams. The modulus of elasticity and creep coefficient affect the net camber, while the prestress force and self-weight affect the individual components.

The San Angelo Westbound non-HPC beam is clearly much less sensitive to changes in these important parameters. The individual camber and deflection components associated with prestress force and self-weight are much smaller in magnitude for these beams, such that the effect of changes in these two parameters is much less significant. Likewise, the net elastic camber is relatively low, so changes in the creep coefficient and modulus of elasticity do not have a large effect. It should be noted that the measured creep coefficient for this mix (which was used in the "base case" camber prediction) was very small, and that variation relative to a larger creep coefficient would have a larger effect. The effect of such variation would probably still not be very significant.

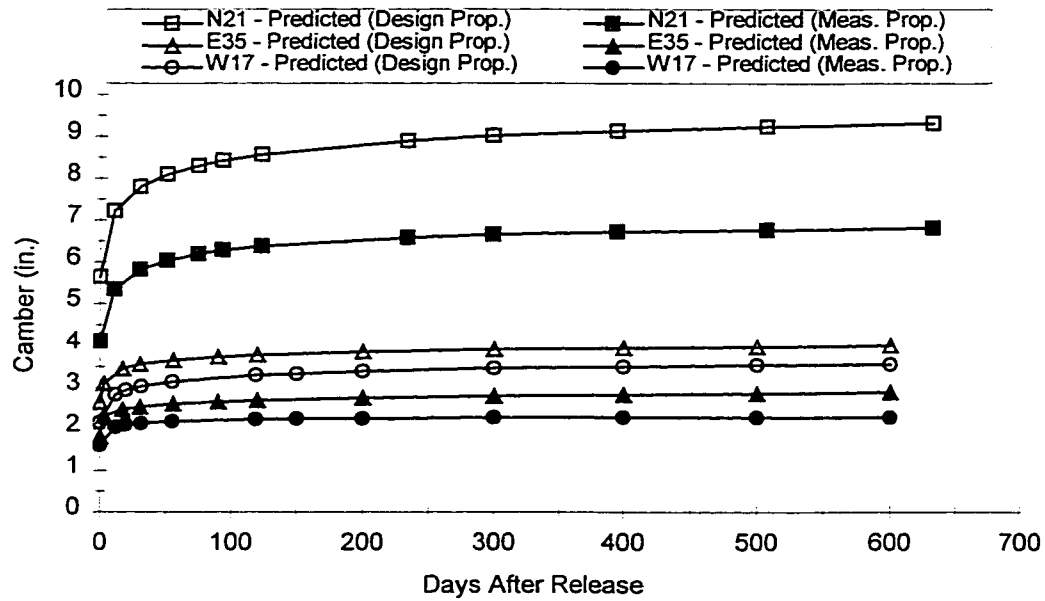


Figure 8.19 - Predicted Camber Based on Design and Measured Parameters for Selected Beams

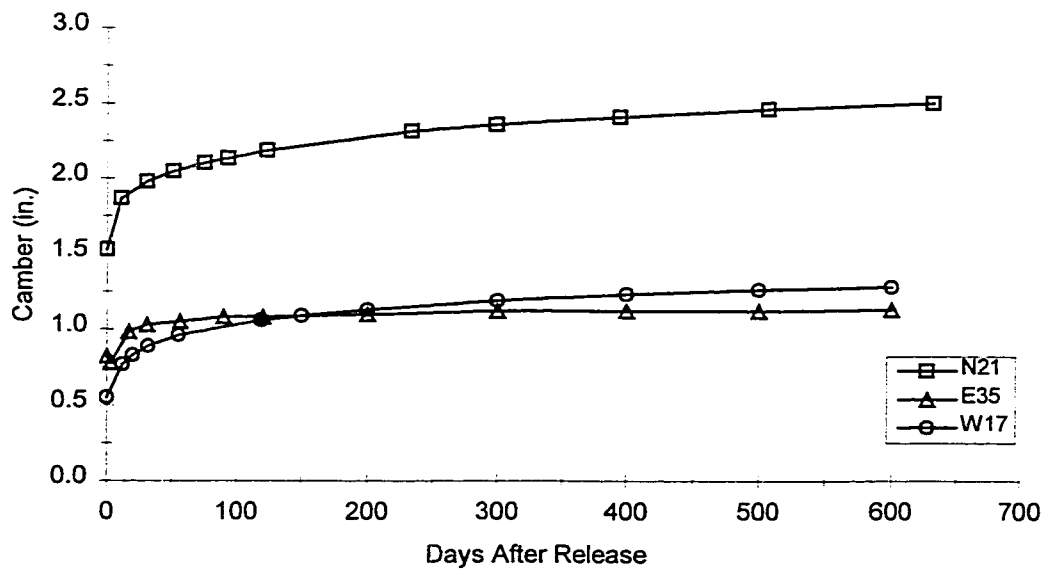


Figure 8.20 - Difference in Predicted Camber Based on Design and Measured Parameters for Selected Beams

Table 8.6 - Sensitivity of Elastic and Time-Dependent Camber to Selected Parameters (Louetta HPC Beam N21)

<i>Louetta Beam N21</i>		Predicted Camber at 180 days (in.)			Change from Base Case (in.)		
		Elastic	Growth	Total	Elastic	Growth	Total
Base Case		4.23	2.47	6.70	N/A	N/A	N/A
Creep Coefficient	+ 10%	4.23	2.73	6.96	0	+ 0.26	+ 0.26
	- 10%	4.23	2.21	6.44	0	- 0.26	- 0.26
Modulus of Elasticity	+ 10%	3.85	2.31	6.16	- 0.38	- 0.16	- 0.54
	- 10%	4.70	2.65	7.35	+ 0.47	+ 0.18	+ 0.65
Prestress Force	+ 5%	4.63	2.75	7.38	+ 0.40	+ 0.28	+ 0.68
	- 5%	3.84	2.19	6.03	- 0.39	- 0.28	- 0.67
Beam Self-Weight	+ 5%	4.06	2.33	6.39	- 0.17	- 0.14	- 0.31
	- 5%	4.41	2.60	7.01	+ 0.18	+ 0.13	+ 0.31

1 in. = 25.4 mm

Table 8.7 - Sensitivity of Elastic and Time-Dependent Camber to Selected Parameters (San Angelo Eastbound HPC Beam E35)

<i>San Angelo EB Beam E35</i>		Predicted Camber at 180 days (in.)			Change from Base Case (in.)		
		Elastic	Growth	Total	Elastic	Growth	Total
Base Case		1.84	0.93	2.77	N/A	N/A	N/A
Creep Coefficient	+ 10%	1.84	1.04	2.88	0	+ 0.11	+ 0.11
	- 10%	1.84	0.82	2.66	0	- 0.11	- 0.11
Modulus of Elasticity	+ 10%	1.67	0.89	2.56	- 0.17	- 0.04	- 0.21
	- 10%	2.04	0.98	3.02	+ 0.20	+ 0.05	+ 0.25
Prestress Force *	+ 5%	2.20	1.19	3.39	+ 0.36	+ 0.26	+ 0.62
	- 5%	1.48	0.69	2.17	- 0.36	- 0.24	- 0.60
Beam Self-Weight	+ 5%	1.56	0.76	2.32	- 0.28	- 0.17	- 0.45
	- 5%	2.11	1.11	3.22	+ 0.27	+ 0.18	+ 0.45

1 in. = 25.4 mm * Does not include post-tensioned strands.

Table 8.8 - Sensitivity of Elastic and Time-Dependent Camber to Selected Parameters (San Angelo Westbound non-HPC Beam W17)

<i>San Angelo WB Beam W17</i>		Predicted Camber at 180 days (in.)			Change from Base Case (in.)		
		Elastic	Growth	Total	Elastic	Growth	Total
Base Case		1.60	0.65	2.25	N/A	N/A	N/A
Creep Coefficient	+ 10%	1.60	0.72	2.32	0	+ 0.07	+ 0.07
	- 10%	1.60	0.61	2.21	0	- 0.04	- 0.04
Modulus of Elasticity	+ 10%	1.45	0.61	2.06	- 0.15	- 0.04	- 0.19
	- 10%	1.77	0.70	2.47	+ 0.17	+ 0.05	+ 0.22
Prestress Force	+ 5%	1.84	0.77	2.61	+ 0.24	+ 0.12	+ 0.36
	- 5%	1.35	0.53	1.88	- 0.25	- 0.12	- 0.37
Beam Self-Weight	+ 5%	1.43	0.57	2.00	- 0.17	- 0.08	- 0.25
	- 5%	1.76	0.73	2.49	+ 0.16	+ 0.08	+ 0.24
1 in. = 25.4 mm							

The net time-dependent camber is ultimately of the most importance (for purposes of discussion in this section), and it can be affected in an advantageous or disadvantageous manner by variations in these four parameters. If parameters vary in certain directions, the effects of these variations may cancel. However, if the effects of variations are in a direction such that the errors are superimposed, then large changes in camber may occur. For example, the net camber at 180 days for the Louetta HPC Beam N21 discussed in this sensitivity study could vary by as much as 48.3 mm (1.90 in.) above or 45.2 mm (1.78 in.) below the value corresponding to the base case. This does not even consider other potential sources that can affect camber and deflection, including those observed in this research program. In particular, differential shrinkage and thermal gradients during hydration can affect the net camber, especially for beams with large span-to-depth ratios.

Designers must therefore recognize the increased sensitivity of camber and deflection behavior for HPC designs. A specific approach is recommended in Section 8.5.3, as camber and deflection behavior due to all loads and other effects is examined. In general, predictions based on design parameters should not be expected to provide much

accuracy for HPC designs. Because of the increased sensitivity and the effects of other potential sources of camber or deflection typically not considered in design, predictions based on measured parameters may also show significant differences relative to the actual camber and deflection behavior in the field.

8.4 Elastic Deflection Responses to Post-Tensioning and Deck Loads

8.4.1 Background

Elastic components of camber and deflection have a very significant effect on the net long-term deflection behavior of prestressed concrete beams. Individual elastic components obviously contribute to the algebraic sum of all camber and deflection terms. However, these elastic components also directly affect the magnitude of the time-dependent creep deflections associated with each elastic component. Therefore, it is extremely important to accurately predict the elastic camber or deflection associated with each applied load or force. In this section, the elastic camber resulting from post-tensioning and the elastic deflection due to the dead load of the composite deck are both examined.

8.4.1.1 Post-Tensioning

As for the prediction of concrete stresses due to post-tensioning, the prediction of elastic beam camber (or deflection) associated with the stressing of post-tensioned tendons requires consideration of several factors. First, the tendon layout along the entire length of the beam must be known. Second, the tendon losses due to friction, anchorage, and elastic shortening (if multiple tendons are used) must be computed at several points along the length of the beam. A full discussion of these losses is presented by Lin and Burns [76], and a summary may be found in Section 6.5.1.1.

Once the losses have been calculated, the elastic camber due to post-tensioning can be computed. Because the tendon profile can take a variety of shapes and because losses due to friction vary greatly along the length of the member, no simple mechanics

formula can be used to predict the elastic camber. Instead, the curvature must be calculated at several points along the length of the member. The camber can then be computed using any mechanics approach, such as the moment-area or conjugate beam methods. Recall that the curvature at any point along the length due to the stress in a single tendon is given by Equation 8.8:

$$\phi_{PT} = - \frac{T_x e_{PT}}{EI}$$

Equation 8.8

The tendon eccentricity e_{PT} is assumed to be positive for tendons below the centroid of the beam, and negative curvatures are assumed to cause upward deflections in simply-supported beams.

To be correct, computations should be performed using the net transformed section. This includes the full beam cross-section with the area of bonded pretensioned strands transformed by the modular ratio, and the removal of any area taken up by the post-tensioning ducts. Alternatively, the net concrete section (strands not transformed) can be utilized, but the elastic loss (or gain) of stress in the bonded pretensioned strands should be considered when this approach is used. Often, gross section properties are used in design for simplification.

8.4.1.2 Deck Loads

Elastic deflections due to deck loads are typically computed using a basic classical mechanics formula. If the load is uniformly distributed along the length of the simply-supported member, then the resulting deflection is computed using Equation 8.9:

$$\Delta_{deck} = -\frac{5}{48} \cdot \frac{M_{max}}{EI} \cdot L^2 = -\frac{5}{384} \cdot \frac{wL^4}{EI}$$

Equation 8.9

M_{max} is the maximum moment at the midspan of the simply-supported member, and negative values for Δ_{deck} represent downward deflections.

Equation 8.9 should result in an accurate prediction of deflection under deck loads if all parameters are known and if the load is truly uniform. However, the load w is seldom known with a great deal of accuracy and is generally not perfectly uniformly distributed. The load is dependent on the thickness of the deck, the unit weight of the deck concrete, and the spacing of beams (i.e. tributary width of deck per beam). Noncomposite transformed beam section properties should be used for unshored construction, and composite transformed section properties for shored construction. As a simplification, however, gross section properties are often used in design.

8.4.2 Measurements

8.4.2.1 Post-Tensioning

Beam camber was measured immediately before and after post-tensioning for ten San Angelo Eastbound HPC beams. Measurements were recorded before stressing of the first (top) tendon and after anchorage of the second (bottom) tendon using the tensioned-wire system. Measurements were corrected for the effects of thermal gradients, as discussed in Section 8.1.2, although these corrections were very small because stressing operations were typically performed in an hour or less.

Measured elastic beam camber due to post-tensioning is shown in Table 8.9 for the ten beams. Predicted cambers based on an analysis using measured parameters are also listed for each beam. The analysis is based on the computation of post-tensioning losses using the method described in Section 6.5.1.1 and 8.4.1.1, and utilizes transformed section properties and the modulus of elasticity measured on companion specimens for each beam. After losses are computed, the camber is calculated by numerically integrating the curvature diagram along the length of the member (i.e. by the moment-area method). Losses and curvatures were calculated at fifty points along the member to increase precision. Tendon layouts were specified on the fabrication drawings, and wobble coefficients, curvature coefficients, and anchorage values were specified by the post-tensioning supplier. These values were taken as 0.00066 /m (0.0002 /ft.), 0.25, and 9.5 mm (0.375 in.), respectively.

The analysis also considered the small elastic shortening loss in the top tendon due to the subsequent stressing of the bottom tendon.

Note that the predicted elastic post-tensioning camber computed as part of the actual beam designs are also listed in the table. These values were computed using a similar procedure to that used in the analysis based on measured parameters, and the losses computed along the length of the member were very comparable for the two analyses. The primary difference is that the modulus of elasticity in the ADAPT designs is a calculated value based on a standard prediction equation, and is not based on measured values from tests on companion specimens.

Measured and predicted elastic cambers due to post-tensioning are also shown in Figure 8.21. For all ten beams, the measured elastic camber was less than predicted. The measured camber was less than the camber predicted by the analysis based on measured parameters by an average of 28 percent. The measured camber was less than the camber calculated as part of the actual beam designs by an average of 12 percent.

Table 8.9 - Measured and Predicted Elastic Camber Due to Post-Tensioning

Beam	Measured Camber	Predicted Camber	
		Analysis Based on Measured Parameters	Actual Design (ADAPT)
E13	1.42	2.10	1.68
E14	1.40	2.10	1.68
E24	2.59	3.57	2.85
E25	2.15	2.95	2.34
E26	2.47	3.57	2.85
E33	2.42	3.27	2.76
E34	2.36	3.27	2.76
E35	2.29	3.25	2.76
E44	2.36	3.22	2.68
E45	2.66	3.23	2.68

Note: all measurements in inches. 1 in. = 25.4 mm

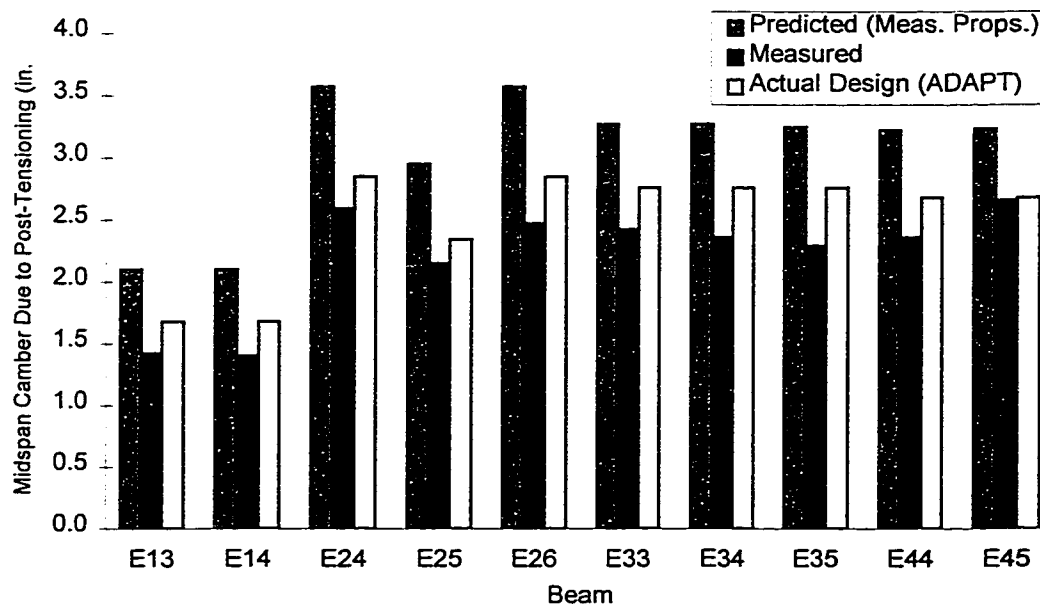


Figure 8.21 - Measured and Predicted Elastic Camber Due to Post-Tensioning

8.4.2.2 Deck Loads

The elastic deflection resulting from placement of the cast-in-place deck was measured for several beams from each bridge using the precise surveying system. Measurements were recorded before any deck concrete had been placed in the span containing the beam, and shortly after all concrete in the span had been placed. Deflections due to deck loads were measured for all but two of the primary instrumented beams, and in a few cases deflections were measured on additional beams so that measurements were recorded for all beams in a single span. All measurements were corrected for the effect of thermal gradients, as described in Section 8.1.2, but these corrections were usually very small because of the effects of deck shading the prestressed concrete beams. Note that thermal gradient corrections at this stage applied only to the beam and not to the composite section, because composite action was not yet developed between the beam and the slab.

Measured elastic beam deflections due to the placement of cast-in-place deck concrete are shown in Table 8.10 and Figure 8.22 for the fourteen Louetta HPC beams studied. Predicted deflections are also shown for comparison. The predicted deflection for each beam is computed using Equation 8.9, and is based on the measured modulus of elasticity from tests on companion specimens, the deck thickness measured during the pour by state inspectors, and the measured unit weight of the deck concrete. Measured beam deflections were less than predicted for all fourteen Louetta HPC beams, with an average difference of 20 percent. Note that deflections computed during the actual designs are not shown because the deck is not separated into layers (precast panels and cast-in-place deck) by the design program.

Table 8.10 - Measured and Predicted Elastic Deflections Due to Placement of the Cast-in-Place Deck (Louetta)

Beam	Measured Deflection	Predicted Deflection	Difference (Meas. - Pred.)	Ratio (Meas. / Pred.)
N21	1.16	1.28	- 0.12	0.91
N22	1.50	1.82	- 0.32	0.82
N23	1.39	1.97	- 0.58	0.71
N31	1.09	1.18	- 0.09	0.93
N32	1.43	1.72	- 0.29	0.83
N33	1.33	1.74	- 0.41	0.77
N34	1.26	1.76	- 0.50	0.72
N35	1.93	2.83	- 0.90	0.68
S14	1.09	1.38	- 0.29	0.79
S15	1.23	1.52	- 0.29	0.81
S16	0.80	1.12	- 0.32	0.71
S24	1.79	2.08	- 0.29	0.86
S25	1.76	2.17	- 0.41	0.81
S26	1.42	1.67	- 0.25	0.85
Average for Louetta HPC Beams			- 0.36	0.80
Note: All deflections in inches. 1 in. = 25.4 mm				

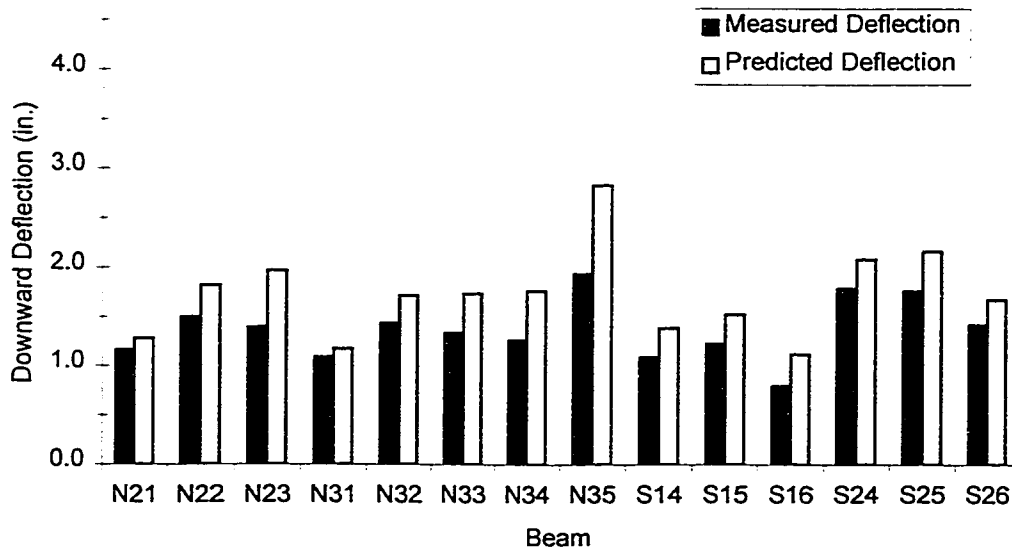


Figure 8.22 - Measured and Predicted Elastic Deflections Due to Placement of the Cast-in-Place Deck (Louetta)

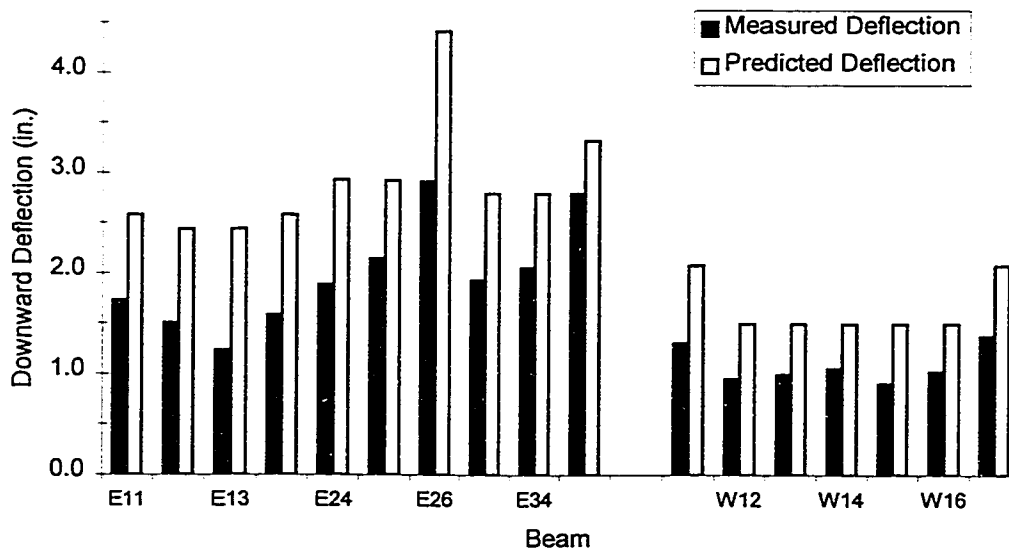


Figure 8.23 - Measured and Predicted Elastic Deflections Due to Placement of the Cast-in-Place Deck (San Angelo)

Table 8.11 - Measured and Predicted Elastic Deflections Due to Placement of the Cast-in-Place Deck (San Angelo)

Beam	Measured Deflection	Predicted Deflection	Difference (Meas. – Pred.)	Ratio (Meas. / Pred.)
E11	1.73	2.58	- 0.85	0.67
E12	1.50	2.44	- 0.94	0.62
E13	1.23	2.44	- 1.21	0.50
E14	1.58	2.58	- 1.00	0.61
E24	1.88	2.93	- 1.05	0.64
E25	2.14	2.92	- 0.78	0.73
E26	2.91	4.41	- 1.50	0.66
E33	1.93	2.79	- 0.86	0.69
E34	2.05	2.79	- 0.74	0.73
E35	2.79	3.32	- 0.53	0.84
Avg. for San Angelo EB HPC Beams			- 0.95	0.67
W11	1.30	2.08	- 0.78	0.63
W12	0.95	1.50	- 0.55	0.63
W13	0.99	1.50	- 0.51	0.66
W14	1.05	1.50	- 0.45	0.70
W15	0.90	1.50	- 0.60	0.60
W16	1.02	1.50	- 0.48	0.68
W17	1.37	2.08	- 0.71	0.66
Avg. for San Angelo WB Non-HPC Beams			- 0.58	0.65
Note: All deflections in inches. 1 in. = 25.4 mm				

Table 8.12 - Measured and Predicted Deflections Due to Total Deck Load

Beam	Measured ¹	Predicted ²	Actual Design ³
Louetta HPC Beams			
N21	2.32	2.26	3.99
N22	2.84	3.23	3.60
N23	2.77	3.49	3.60
N31	2.10	2.07	3.68
N32	2.73	3.03	3.43
N33	2.60	3.07	3.43
S14	2.18	2.39	3.43
S15	2.34	2.57	3.43
S16	1.76	1.88	3.60
S24	3.11	3.41	3.60
S25	3.16	3.54	3.60
S26	2.60	2.72	3.99
San Angelo Eastbound HPC Beams			
E24	4.18	4.96	4.70
E25	4.31	4.95	4.49
E26	4.56	5.42	4.70
E33	4.43	4.96	4.61
E34	4.53	4.96	4.61
E35	4.43	4.40	4.61
San Angelo Westbound non-HPC Beams			
W14	2.21	2.41	2.28
W15	2.05	2.41	2.28
W16	2.15	2.41	2.28
W17	2.33	2.54	2.35
<p>Note: All measurements in inches. 1 in. = 25.4 mm</p> <p>¹ Difference between camber just before precast panel erection and camber just after placement of the cast-in-place deck.</p> <p>² Predicted based on measured parameters. Sum of elastic deflections due to panel erection and elastic deflection due to placement of cast-in-place deck.</p> <p>³ From ADAPT (San Angelo EB) or PSTRS14 (Louetta, San Angelo WB) designs, based on several simplifying assumptions. Represents elastic deflection due to total deck load.</p>			

Measured and predicted elastic deflections due to placement of the cast-in-place deck are shown in Table 8.11 and Figure 8.23 for the 17 San Angelo beams studied. As for the Louetta HPC beams, the measured deflections were substantially less than predicted. For the San Angelo Eastbound HPC beams, the average difference between measured and predicted deflections was 33 percent. For the San Angelo Westbound non-HPC beams, the measured deflections were lower than predicted by an average of 35 percent.

Deflections were not measured immediately before and after the erection of precast deck panels because panel erection usually took place over a period of several days. As a result of this long process, there is a pseudo-elastic deflection in which elastic and time-dependent (creep) responses are intermingled. The measurement of deflections during and after the placement of panels would have necessitated a great amount of additional travel for the researchers, and would have limited value. Measurements of beam camber were, however, recorded on most beams just before panel erection began.

The measurements shown in Table 8.12 are the *total deck placement deflection* for each beam, which can be defined as the difference in the beam camber just before the erection of precast deck panels and just after the placement of the cast-in-place deck. These measurements include the elastic deflections associated with the erection of deck panels and placement of the cast-in-place deck, as well as the creep deflections associated with the erection of precast panels. Measurements are shown for all beams in which camber measurements were made at both of these stages. All values have been corrected for the effect of thermal gradients, as discussed in Section 8.1.2.

Predicted deflections due to the total deck load are also shown in Table 8.12. The prediction method is the same as used for the deflection due to cast-in-place deck loads, except that the weight of the precast panels is also included. Note that only elastic deflections are considered, and that the time-dependent deflection due to creep under the panel loads is not included. Total deck load deflections calculated during the actual beam designs are also shown in the table.

The deflections calculated during the actual beam designs are based on several simplifying design assumptions, assumed deck thicknesses, and assumed material properties. For the San Angelo Eastbound HPC beams, the ADAPT design assumed that the deck load was evenly distributed to all beams in a given span (i.e. no distinction was made between interior and exterior beams). For the Louetta HPC beams, the beam deflections in most exterior beams are based on the full overhang (which was not cast

because of the future widening of the bridges). Furthermore, the Louetta beams were designed in groups to facilitate fabrication, so that the correct span length and spacing are not used in the calculation of each individual beam.

Despite the inclusion of additional time-dependent deflections in the measured values, the measured deflections are less than the predicted total elastic deck deflections for almost every beam. For the Louetta HPC beams, measured deflections were an average of 9 percent less than the predicted deflections and 29 percent less than the design calculated deflections. For both the San Angelo Eastbound HPC beams and San Angelo Westbound non-HPC beams, the measured deflections were lower than the predicted deflections by an average of 11 percent and lower than the design calculated deflections by an average of 5 percent.

8.4.3 Discussion

8.4.3.1 Post-Tensioning

Observations related to measured and predicted elastic camber at post-tensioning are consistent with observations regarding measured and predicted elastic stresses. In particular, measured stress gradients (i.e. curvatures multiplied by the measured modulus on the San Angelo HPC beams were found to be an average of 20 percent less than predicted. Measured elastic cambers were also significantly less than predicted for these beams, with an average difference of 28 percent. The consistency between these two sets of measurements is important, as it serves to validate each of these measurements.

There are two main potential reasons for the lower than predicted camber due to post-tensioning. First, the actual modulus of elasticity of the beam concrete may have been somewhat higher than the modulus of elasticity measured in tests on companion specimens. Any difference in the actual and measured moduli would directly affect the comparison between measured and predicted camber. Furthermore, other types of measurements in this research program have implied a higher actual modulus of elasticity than measured in companion specimen tests. The impact of the modulus of elasticity can be seen clearly in the difference between the predictions using the analysis based on

measured properties and the predictions from the actual beam designs. These analyses showed almost identical losses in the post-tensioning tendons of each beam, but showed different values for the predicted elastic cambers. This difference in camber can directly be attributed to differences in the values used for the modulus of elasticity of the concrete used for the beams.

It is also quite possible that differences between the measured and predicted friction and anchorage losses contributed to the difference between measured and predicted camber. If the actual losses were significantly higher, then the actual camber would tend to be lower. It is impossible to determine the degree to which each of these potential sources affected the difference between measured and predicted camber. Considering the magnitude of the difference (28 percent), however, it is reasonable to assume that both sources contributed to some degree. This conclusion is supported by the fact that measured camber was still lower than predicted in the actual beam designs, in which the value used for modulus of elasticity was substantially higher than the modulus measured in tests on companion specimens.

No modifications to standard design procedures are recommended on the basis of the observations discussed in this section. It should be noted, however that the exact prediction of camber (or deflection) due to post-tensioning can be very difficult because calculations are very dependent on the concrete modulus of elasticity and losses due to friction and anchorage. Since these parameters are usually not known precisely, computed elastic cambers should not be taken as precise values.

8.4.3.2 Deck Loads

Observations regarding measured and predicted elastic deflections due to deck loads are consistent with observations related to measured and predicted stresses due to placement of the cast-in-place deck. Measured elastic deflections were lower than predicted by an average of 20 percent, 33 percent, and 35 percent for the Louetta HPC, San Angelo Eastbound HPC, and San Angelo Westbound non-HPC beams, respectively. Measured stress gradients were lower than predicted by 20 percent in Louetta HPC Beam S15 (the only beam where stresses were measured successfully), and by an average of 33 percent for the San Angelo Eastbound HPC beams. Note the stresses due to placement of

the cast-in-place deck were not successfully measured in the San Angelo Westbound bridge. The general agreement between these two types of measurements helps to validate the results from each type of measurement.

Beam deflections due to the *total* deck load were less than predicted, despite the inclusion of some time-dependent effects in the measured deflections. These results quantitatively support the findings from the measurements of elastic deflections due to only the placement of the cast-in-place bridge decks. However, the comparisons of these measurements to predicted elastic deflections under the total deck load have little overall quantitative value as a result of the inclusion of time-dependent effects.

There are two main potential reasons that measured elastic deflection due to deck loads were lower than predicted. First, the actual modulus of elasticity may have been substantially higher than the modulus of elasticity determined from tests on companion specimens. This conclusion is supported by observations regarding other types of measurements in this research program. Second, variations in the actual deck thickness may have contributed to the low deflections. Even though predictions were based on deck thicknesses measured by state inspectors at selected points of each span, the thickness can be highly variable and lead to variations in the actual deck load. If the actual thickness is 10 percent lower than assumed, say 13 mm (0.5 in.) low in a 127 mm (5.0 in.) deck, then the measured deflections should also be approximately 10 percent lower than predicted.

In all likelihood, both of these factors contributed to the lower than predicted deflections. The fact that measured deflections due to the total deck load were lower than predicted, despite the inclusion of some time-dependent effects in the measurements, implies that deflections due to panel loads only were also low. Because the dimensions of the precast deck panels (and thus panel loads) are usually known with a reasonable degree of certainty, these low deflections are likely caused by a higher modulus of elasticity. However, it is unlikely that the actual modulus of elasticity was 35 percent higher than measured on companion specimens, which is the magnitude of the average difference between the measured and predicted deflections due to cast-in-place deck loads in both of the San Angelo bridges. A 35 percent increase in the modulus of elasticity would imply modulus values in the general range of 55 to 62 GPa (8000 to 9000 ksi), which is more than unlikely. In light of these observations, it is reasonable to assume that variations in *both* the modulus of elasticity and deck thickness had a significant effect on the low elastic deflections due to deck loads.

As for the elastic deflection behavior due to post-tensioning, no changes to standard design procedures are recommended on the basis of measurements discussed in this section. Because of the potentially significant effects of variations in the modulus of elasticity and deck thickness, among other parameters, calculations of elastic beam deflections due to deck loads should not be taken as more than estimates.

8.5 Long-Term Deflection Behavior

8.5.1 Background

Ultimately, it is not the individual components of elastic or time-dependent camber and deflection that are of the most interest during the design and construction of prestressed concrete highway bridges. The net camber due to the combined effects of all components is generally much more significant. As discussed in Section 8.1.1, the net camber after erection of the beams is important because it can influence the placement of the cast-in-place bridge deck. This is especially true for longer span HPC beams, where simple adjustments to the haunch thickness above each beam may not be enough to accommodate large variations in camber, whether such variations are relative to predicted values or between adjacent beams. The long-term net camber or deflection under full dead load is important as a serviceability criterion. Excessive camber or deflection can result in an uneven riding surface or in a poor aesthetic appearance.

Few real guidelines actually exist for camber and deflection of prestressed concrete highway bridge beams under dead load. The *AASHTO Standard Specifications* [3] do not present any requirements or suggest a range of acceptable behavior for camber and deflection under full dead load. In the commentary of the *AASHTO LRFD Specifications* [1], it is stated that control of deflections is permitted but not encouraged, and no suggestions for acceptable dead load deflections are provided.

The current philosophy of the Texas Department of Transportation, as suggested by members of the Bridge Design Division [59] and implied in the manual accompanying the division's PSTRS14 design program [130], is that no downward deflection should be present

under full dead load. In other words, prestressed concrete highway bridge beams should be nearly level or exhibit a slight upward camber under full dead load. This philosophy was utilized in the design of all beams in this study. Note that no upper limit to camber under full dead load is suggested, and that no guidelines exist for the camber at erection of the beams.

Many standard methods have been proposed in the literature to estimate the long-term deflection behavior of prestressed concrete beams. These methods fall into three basic categories: basic multiplier methods, approximate time-step or “advanced” multiplier methods, and incremental time-step methods. These methods vary a great deal in their complexity and accuracy, with the latter methods being the most complex and generally the most accurate.

Basic multiplier methods provide for the calculation of time-dependent camber or deflection as the algebraic sum of multiples of the elastic components of camber or deflection. This approach is similar to the simple deflection multiplier method recommended in the ACI 318 code [7] for time-dependent deflections of reinforced concrete beams. Based on the work of Martin [79], the *PCI Design Handbook* [108] suggests that the net camber at erection and long-term can be estimated by Equation 8.10 and Equation 8.11, respectively:

$$\Delta_{\text{erection}} = 1.80 \cdot \Delta_p - 1.85 \cdot \Delta_{\text{sw}}$$

Equation 8.10

$$\Delta_{\text{long-term}} = 2.20 \cdot \Delta_p - 2.40 \cdot \Delta_{\text{sw}} - 3.00 \cdot \Delta_{\text{sdl}} - 2.30 \cdot \Delta_{\text{cd}}$$

Equation 8.11

Δ_p , Δ_{sw} , Δ_{sdl} , and Δ_{cd} represent the elastic camber or deflection components due to initial prestress, member self-weight, superimposed (noncomposite) dead loads, and the weight of the composite deck (acting on the noncomposite beam section), respectively. Positive values indicate upward camber and negative values indicate downward deflection.

In the development of these multipliers, several assumptions were made regarding typical values for creep, modulus of elasticity, prestress losses, and construction schedule. The multipliers were developed for “typical members” [79,108], which imply normal strength or conventional concrete and span-to-depth ratios of 10 to 20. Clearly, they are not

applicable to HPC beams with large span-to-depth ratio, including those in this research program.

Approximate time-step procedures and "advanced" multiplier methods use the same approach as the basic multiplier method, except that the values of the multipliers themselves are determined as part of the calculations. Once the multipliers have been computed, the long-term camber can be estimated using an algebraic summation of terms like that shown for the basic multiplier method in by Equation 8.10 and Equation 8.11. Branson and Kripanarayanan [27] developed an approximate time-step procedure on this basis that can be applied to a variety of structure types, including prestressed beams with and without composite deck slabs.

Byle and Burns [35] developed a similar method for the computation of time-dependent camber in the Louetta HPC beams monitored in this study. A specific set of multipliers was determined for each beam based on the material properties measured on companion specimens and the actual construction schedule. Kelly et. al. [69] created a simple computer program to determine multipliers for a given set of properties and construction schedule. Both Byle and Kelly found that the advanced multiplier method could predict long-term camber to a reasonable degree of accuracy if the necessary parameters were known and if the elastic camber components were predicted correctly.

More complex incremental time-step procedures have been proposed by many authors and are recommended for use by several committees [11,28,53,75,89,99,104]. These methods of sectional analysis are typically used to simultaneously compute cross-section deformations and loss of prestress. Continuous time functions, such as those recommended by ACI Committee 209 [8], are used to model important material properties, and the strain history of the cross-section is traced in several small incremental time steps. Elastic effects are considered by adding forces at the appropriate times and applying the principles of superposition. These methods are generally considered to be quite accurate, but as with any approach, the correct modeling of time-dependent material properties is essential.

Numerous computer programs have also been developed commercially and in academia for the prediction of time-dependent camber and deflection in prestressed concrete beams. These models involve a number of higher-level approaches such as finite element methods, and are often able to accommodate non-standard conditions and fabrication methods by applying the basic principles of structural mechanics. The main

drawback to these methods is that they often require extensive input data. Considering the variability in deflection behavior of actual structures documented in the literature, these programs are most useful only when the assumptions used in standard methods do not apply. As for all types of structural models for concrete, the output from these computer programs is only as good as the input data used for the modeling of elastic and time-dependent material properties.

8.5.2 Measurements

Camber and deflection measurements continued to be recorded during jobsite construction and service for all 26 beams in which measurements were taken during storage. As discussed in Section 3.2.2.7, the precise surveying method was used to monitor camber after erection for all beams. Whenever possible, corrections for thermal gradients were applied to the measured data, and corrections for end measurement locations were applied where appropriate. Each of these types of corrections is described in Section 8.1.2.

The complete time-dependent camber and deflection history for each beam was also predicted using an incremental time-step analysis based on measured material properties (creep, shrinkage, modulus of elasticity, and unit weight) and the actual construction schedule. Details of this incremental time-step analysis are discussed in Appendix G. Plots of measured and predicted time-dependent camber for each beam may also be found in Appendix G. The time-step analysis used for the predictions was developed by the author for use on a computer spreadsheet, and has the flexibility to model all types of beams used in this research program, including the two stage (pretensioned/post-tensioned) San Angelo Eastbound HPC beams.

Table 8.13 - Measured and Predicted Camber at Erection

Beam	Days After Release	Camber at Erection (in.)		
		Measured	Predicted †	Actual Design ‡
Louetta HPC Beams				
N21	696	5.44	6.42	9.04
N22	724	3.56	4.94	6.58
N23	731	3.34	4.26	6.58
N31	696	5.29	6.16	8.22
N32	221	4.32	5.00	7.42
N33	221	3.98	5.00	7.42
S14	202	3.87	4.91	7.42
S15	202	4.01	4.89	7.42
S16	716	4.02	4.93	6.58
S24	675	3.34	4.57	6.58
S25	675	3.38	4.46	6.58
S26	703	5.16	5.90	9.04
San Angelo Eastbound HPC Beams				
E13	88	N/A #	7.52	6.13
E14	88	N/A #	7.52	6.13
E24	71	6.85	8.25	6.44
E25	413	6.45	6.82	6.25
E26	71	6.36	8.25	6.44
E33	80	6.71	8.20	6.95
E34	80	6.31	8.20	6.95
E35	73	7.33	8.16	6.95
E44	59	7.49	8.21	6.95
E45	59	6.90	8.22	6.95
San Angelo Westbound Non-HPC Beams				
W14	213	1.81	1.95	3.53
W15	213	1.73	1.95	3.53
W16	213	1.65	1.95	3.53
W17	208	1.51	1.98	3.53
1 in. = 25.4 mm				
† Using incremental time-step analysis described in Appendix G.				
‡ Using PSTRS14 or ADAPT, see text for discussion.				
# No measurement before panels were erected.				

Table 8.14 - Measured and Predicted Long-Term Service Camber

Beam	Days After		Long-Term Service Camber (in.)		
	Release	CIP Deck	Measured	Predicted †	Actual Design ‡
<i>Louetta HPC Beams</i>					
N21	961	228	2.87	3.28	5.05
N22	989	228	0.38	0.42	2.97
N23	996	228	0.21	- 0.34	2.97
N31	961	228	2.78	3.32	4.54
N32	486	228	1.15	0.89	3.99
N33	486	228	0.92	0.84	3.99
S14	475	220	1.24	1.66	3.99
S15	475	220	1.15	1.45	3.99
S16	989	220	1.80	2.35	2.97
S24	948	220	- 0.08	0.13	2.97
S25	948	220	- 0.14	- 0.15	2.97
S26	976	220	2.31	2.16	5.05
<i>San Angelo Eastbound HPC Beams</i>					
E13	424	312	2.09	2.60	0.43
E14	424	312	2.42	3.21	0.43
E24	406	299	2.08	2.10	- 0.90
E25	748	299	1.45	0.45	- 1.86
E26	406	299	0.84	1.39	- 0.90
E33	392	285	1.77	2.35	- 0.22
E34	392	285	1.27	2.35	- 0.22
E35	385	285	2.35	2.50	- 0.22
E44	371	261	2.33	2.37	- 0.09
E45	371	261	1.71	2.89	- 0.09
<i>San Angelo Westbound Non-HPC Beams</i>					
W14	773	503	- 1.43	- 1.45	1.15
W15	773	503	- 1.55	- 1.45	1.15
W16	773	503	- 1.51	- 1.45	1.15
W17	768	503	- 2.13	- 1.93	1.15
1 in. = 25.4 mm					
† Using incremental time-step analysis described in Appendix G.					
‡ Using PSTRS14 or ADAPT, see text for discussion.					

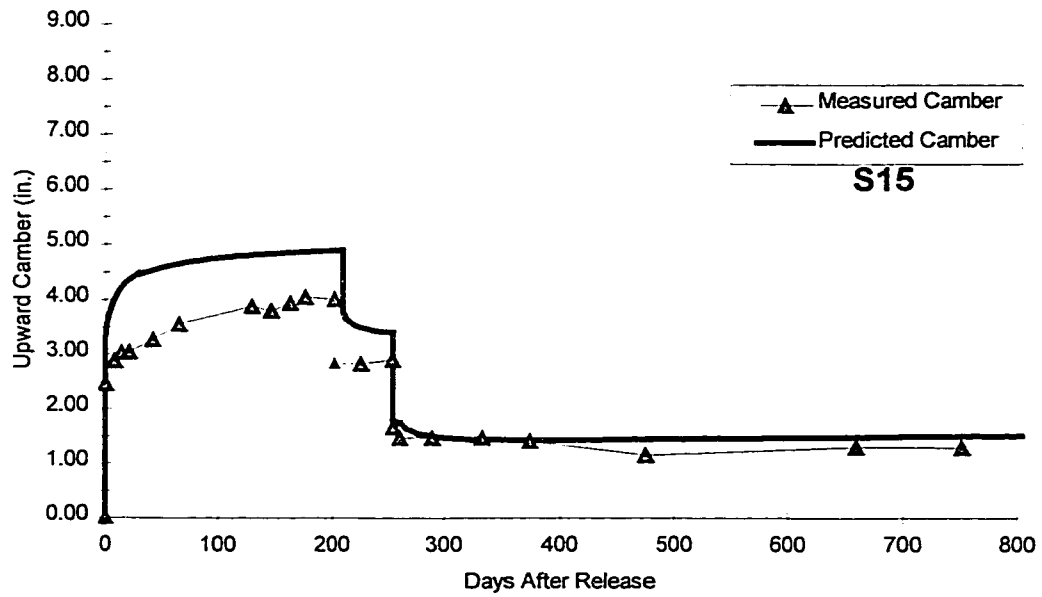


Figure 8.24 - Typical Time-Dependent Camber and Deflection Behavior for a Louetta HPC Beam (Beam S15)

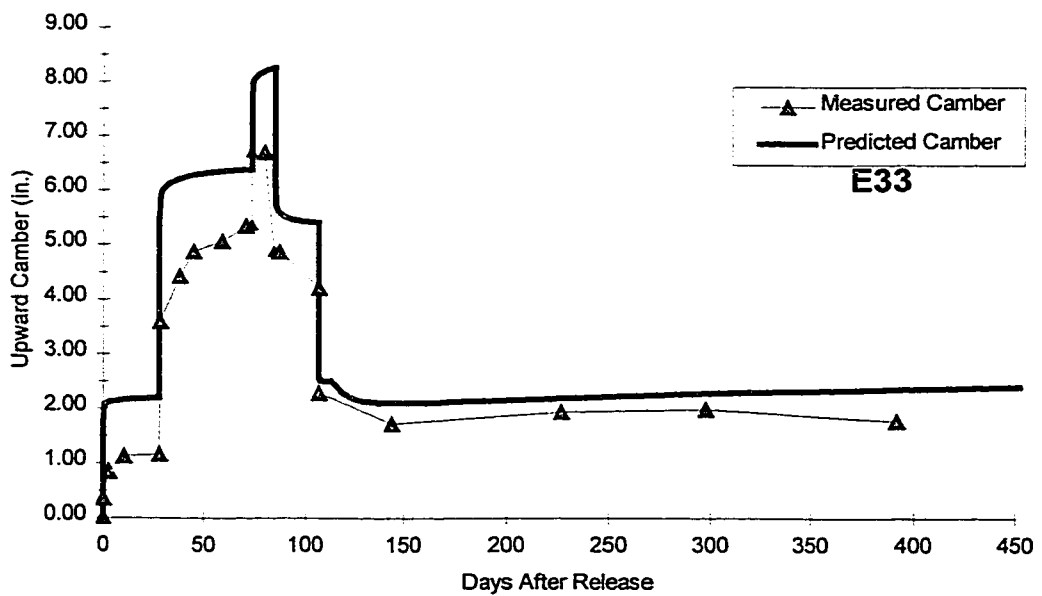


Figure 8.25 - Typical Time-Dependent Camber and Deflection Behavior for a San Angelo Eastbound HPC Beam (Beam E33)

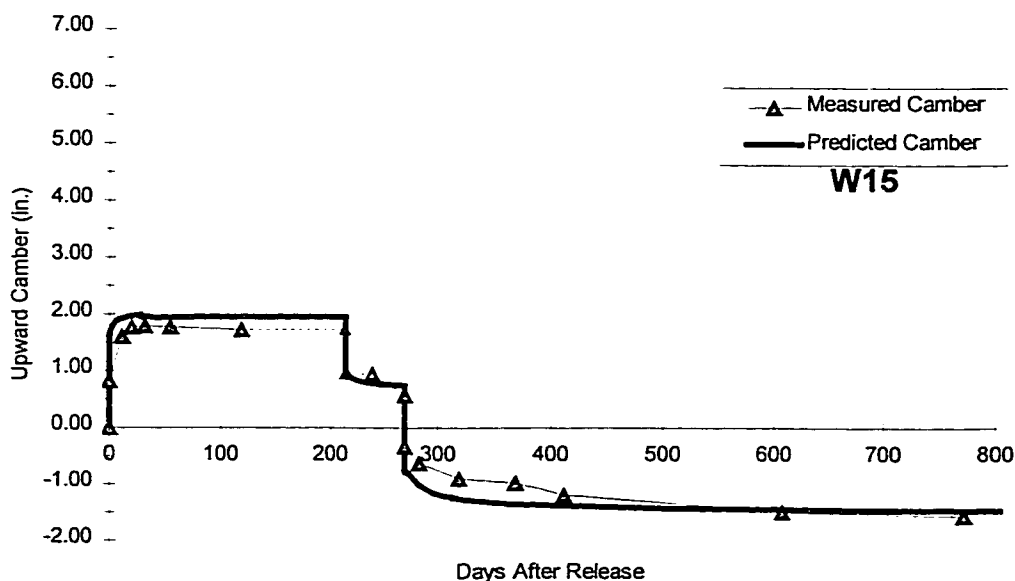


Figure 8.26 - Typical Time-Dependent Camber and Deflection Behavior for a San Angelo Westbound non-HPC Beam (Beam W15)

Measured and predicted camber values at two important stages – erection and long-term (service) – are summarized in Table 8.13 and Table 8.14, respectively, for all 26 beams. Camber computed as part of the actual beam designs is also listed in the tables. For Louetta HPC beams and San Angelo Westbound non-HPC beams, these values were computed using TxDOT's PSTRS14 [130] design program. The program computes time-dependent camber using hyperbolic functions developed by Sinno [34], and specifies a maximum camber at erection since the construction schedule is unknown during design. Long-term (service) camber is not specifically specified in the program output, but can be estimated using the maximum (erection) camber and the calculated elastic deflections under dead loads. Note that the deflection due to the weight of the traffic rail was not included in the values shown in the tables because the rails were never cast on the exterior beams shown in the tables (due to the future widening of the bridges). Measured values listed in the table were recorded before the widening of the bridges. Also note that the Louetta HPC beams were designed in groups to facilitate fabrication, and that a unique camber calculation was not performed for each beam during the design process.

Table 8.15 - Summary of Measured and Predicted Erection and Long-Term Cambers

	Erection			Long-Term Service		
	Lou. HPC	SA EB HPC	SA WB Non-HPC	Lou. HPC	SA EB HPC	SA WB Non-HPC
Measured Camber						
Average	4.14	6.80	1.68	1.22	1.83	- 1.66
Minimum	3.34	6.31	1.51	- 0.14	0.84	- 2.13
Maximum	5.44	7.49	1.81	2.87	2.42	- 1.43
Difference (Measured – Predicted)						
Avg. Absolute Difference ¹	0.98	1.24	0.28	0.29	0.59	0.10
Max. Negative Difference	- 1.38	- 1.89	- 0.47	- 0.55	- 1.18	- 0.20
Max. Positive Difference	N/A	N/A	N/A	0.55	1.00	0.02
Difference (Measured – Actual Design)						
Avg. Absolute Difference ¹	3.26	0.32	1.86	2.57	2.20	2.81
Max. Negative Difference	- 3.88	- 0.64	- 2.02	- 3.11	N/A	- 3.28
Max. Positive Difference	N/A	0.54	N/A	N/A	3.31	N/A
All values in inches. 1 in. = 25.4 mm						
¹ Average of the absolute values of the differences.						

For the San Angelo Eastbound HPC beams, cambers were predicted during the design using the ADAPT computer program [13]. Beam cambers were predicted using an upper and lower bound approach for variations in creep and shrinkage, as discussed in Section 2.3.3. The average for these two values is shown for each beam in the tables, since the upper and lower bound camber values differed by less than 5 mm (0.20 in.) for all beams. The best estimates of creep and shrinkage properties available at the time (from tests on companion specimens conducted as part of this research program) were used as base values. The measured modulus of elasticity was not used in the design calculations. As for predictions using the time-step approach with measured properties, a small prestress loss was assumed to occur before release and an allowance was made for increased self-weight due to the volume of steel (strands) embedded in the beams. Note that all San Angelo Eastbound HPC beams in a span were accommodated by a single design, and that interior and exterior beams were not treated separately.

Typical time-dependent camber and deflection behavior for a Louetta HPC beam is shown in Figure 8.24 for Beam S15. Upward camber was lower than predicted at release and throughout storage at the prestressing plant. Deflections due to the placement of precast deck panels and the cast-in-place deck were substantially lower than predicted for all beams, such that the net long-term service camber was actually reasonably close to the predicted camber. Measured camber at erection for the Louetta HPC beams ranged from 84.8 to 140.7 mm (3.34 to 5.54 in.), and was lower than predicted for all beams. Measured long-term camber at 7 to 8 months after placement of the cast-in-place deck and before the widening of the bridges ranged from - 3.6 mm (- 0.14 in.) (indicating a slight downward deflection) to 72.9 mm (2.87 in.). For Beam S15, shown in Figure 8.24, the measured net camber was 29.2 mm (1.15 in.) and was quite stable as the long-term dead load value.

Typical time-dependent deflection behavior for a San Angelo Eastbound HPC beam is shown in Figure 8.25 for Beam E33. Upward camber was lower than predicted at release and during storage at the prestressing plant, both before and after post-tensioning. After the beams were post-tensioned, however, the camber grew more than predicted because the beams were stored on supports approximately 4 m (13 ft.) from the beam ends (i.e. on a shortened span). The fabricator intentionally used these support conditions to promote camber growth because of the low observed camber at release and before post-tensioning, but this change in support conditions was not modeled in the time-step predictions. After beam erection and after the top strands were cut, the measured camber ranged from 160.3 to 190.2 mm (6.31 to 7.49 in.), but was still substantially lower than predicted for all beams. Deflections due to the placement of precast deck panels and the cast-in-place deck were much lower than predicted, such that the net long-term service camber was much closer to predicted values than the erection camber. Measured long-term camber ranged from 21.3 to 61.5 mm (0.84 to 2.42 in.) at 8 to 10 months after placement of the cast-in-place deck. For Beam E33, shown in Figure 8.25, the measured net camber was 45.0 mm (1.77 in.) and was quite stable as the long-term dead load value.

A plot of the typical time-dependent deflection behavior for a San Angelo Westbound non-HPC beam is shown in Figure 8.26 for Beam W15. Upward camber was significantly less than predicted at release, but increased quickly and generally remained just slightly less than predicted during storage at the prestressing plant. Measured camber at erection (taken from the final readings during storage) ranged from 38.4 to 46.0 mm (1.51 to 1.81 in.) and was slightly less than predicted. Measured deflections due to precast panel

and cast-in-place deck loads were less than predicted, resulting in long-term camber and deflection measurements similar to predicted values. Unfortunately, these beams exhibited a net downward deflection under full dead load within a range of - 36.3 to - 54.1 mm (- 1.43 to - 2.13 in.) (where negative values indicate downward deflections). For Beam W15, shown in Figure 8.26, the measured net downward deflection was - 39.4 mm (-1.55 in.) and was quite stable as the long-term dead load value.

It should also be noted that there was generally good agreement between camber values at erection among beams in a given span. That is, the range of values for erection camber among the beams in a span was generally rather small. No significant problems associated with differential camber among girders in a given span affected the construction of the bridge decks in either the Louetta or San Angelo projects.

A comparison of the differences between measured and predicted cambers at erection and long-term is presented in Table 8.15. For the most part, the measured deflection behavior shows poor correlation with values computed during the actual designs. For all three types of beams, the measured erection and long-term cambers were substantially lower than the cambers estimated during design. As expected, better correlation existed between the measured values and the predictions based on measured parameters, but there is still some degree of variability between the measured and predicted values. It should be noted that the absolute average differences between measured and predicted values were clearly smallest for the San Angelo Westbound non-HPC beams. The average absolute difference between measured and predicted camber was 7.1 and 2.5 mm (0.28 and 0.10 in.), respectively, at erection and long-term. These average differences were 24.9 and 7.4 mm (0.98 and 0.29 in.), respectively for the Louetta HPC beams and 31.5 and 15.0 mm (1.24 and 0.59 in.), respectively, for the San Angelo Eastbound HPC beams.

8.5.3 Discussion

The overall range of long-term measured camber values exhibited by the Louetta HPC and San Angelo Eastbound HPC beams was quite acceptable. None of the HPC beams exhibited significant downward deflection or excessive upward deflection. Although the measured long-term cambers were within the desirable range, it should be noted that this final result is somewhat of a coincidence. All HPC beams exhibited less camber from

release through erection than predicted, but also exhibited less downward deflection due to dead loads. These effects essentially cancelled each other out, resulting in measured cambers that were within the desirable range. Thus, although the net results for HPC beams were quite acceptable, it cannot be said that the actual behavior was as expected.

On the other hand, the San Angelo Westbound non-HPC beams exhibited the undesirable quality of a substantial net downward deflection under full dead load. The downward deflection is not of much significance other than for aesthetic value, and is not large enough to be considered a real serviceability problem. The maximum downward deflection, for Beam W17, is approximately equal to $L/720$. The implication that these beams performed "poorly" (i.e. exhibited a net downward deflection) because they were non-HPC beams is quite misleading. In fact, these beams have properties similar to what might be expected as a worst case scenario (in terms of net camber) for HPC beams. They have a relatively high modulus of elasticity, a high self-weight, and a relatively small prestress force for their span length. Furthermore, the creep of the non-HPC mix used for these beams was actually less than the creep for the HPC mixes. These factors all would lead to a low net camber, and possible downward deflection, under full dead load. It should also be noted that there was much less variation shown for these beams than for the HPC beams. Considering the measured material properties and actual construction schedule, the measured and predicted deflection behavior for these beams was reasonably similar.

As discussed in Section 8.2, Section 8.3, and Section 8.4, several important factors have an influence on camber and deflection. It was shown in Section 8.3.3 that changes in the initial prestress force and dead loads, as well as variations in the modulus of elasticity and creep coefficient, all could substantially influence the elastic and time-dependent components of the net camber at erection or long-term service. Increases in the initial prestress force and the creep coefficient, and decreases in the dead loads and modulus of elasticity, would all lead to a higher net camber. Similarly, variations in the opposite direction would lead to a lower net camber.

Several other factors can also influence the net time-dependent camber in prestressed beams. Variations in the construction schedule can influence the effect of certain time-dependent components of camber or deflection due to creep. Depending on the magnitudes of the individual elastic components, and the rate of creep at early ages, such changes may or may not be significant. The possible presence of a pseudo-elastic deflection component related to early-age shrinkage and thermal effects, as suggested in

Section 8.2.3, may also have an influence on net camber. Differential shrinkage through the depth of the beam over time can have a similar impact. Variations in shrinkage of the composite deck slab may also affect net camber, although the changes in net camber should be relatively small because these effects act on the composite section. Finally, the use of gross section properties as a design simplification can also influence the prediction of net camber.

In order to investigate the effects of variations in these parameters and other factors on the net camber at erection and long-term service, a sensitivity analysis was performed for several designs. Six beam designs were considered, including five from this study and one "typical" design using properties of conventional concrete for a relatively standard design in Texas. Important parameters for each of these designs are listed in Table 8.16. Note that the four HPC beams from this study were selected to represent different implementations of HPC in design. The "typical" design was used as for an additional non-HPC comparison because the San Angelo Westbound beams are in many ways more representative of HPC designs than non-HPC designs, although they do not carry the HPC designation.

Table 8.16 - Important Parameters of the Beam Designs Used in Sensitivity Analysis

	HPC				Non-HPC	
	N21	N33	E13	E24	W14	Typ. ²
Cross-Section Type	U54B	U54A	IV	IV	IV	IV
Span Length (ft.)	134.17	133.40	127.79	152.17	127.79	112.00
Beam Spacing (ft.)	9.99 [#]	12.53	11.00	6.60	5.67	6.00
Design Strength (psi)	13100	11600	13000	14000	7850	6220
Actual Strength ¹ (psi)	14820	13630	13700	14240	10130	-
Modulus of Elasticity ¹ (ksi)	6940	6670	6250	6300	5970	4780
# of Strands	87	64	76	82	52	44
Strand Diameter (in.)	0.6	0.6	0.6	0.6	0.5	0.5

1 in. = 25.4 mm 1 ft. = 0.3048 m 1 psi = 0.006895 MPa 1 ksi = 0.006895 GPa
¹ At 28 days for non-HPC, 56 days for HPC
² Typical design used in Texas with conventional concrete properties.
[#] Beam originally designed for larger tributary deck width of 14.15 ft. including overhang. Spacing shown is based on smaller tributary area before bridge widening.

Table 8.17 - Sensitivity Analysis for Net Camber at Erection and Long-Term Service (Camber Values)

Modification	Erection					Long-Term (1000 days)						
	N21	N33	E13	E24	W14	Typ	N21	N33	E13	E24	W14	Typ
0 Base Prediction	6.42	5.00	7.52	8.25	1.95	2.60	3.27	0.89	2.84	2.33	-1.47	0.14
1 Increase All Initial Prestress Forces (+ 5%)	7.11	5.60	8.19	9.21	2.31	2.99	3.98	1.51	3.54	3.36	-1.10	0.57
2 Decrease All Concrete Dead Loads (- 5%)	6.76	5.32	7.79	8.77	2.20	2.84	3.77	1.43	3.36	3.19	-1.07	0.51
3 Decrease Modulus of Elasticity (-15%)	7.33	5.73	8.68	9.48	2.25	2.96	3.72	1.07	3.40	2.75	-1.67	0.15
4 Increase Ultimate Creep of Beam Concrete (+20%)	6.92	5.38	7.95	8.66	2.07	2.81	3.64	1.13	3.24	2.62	-1.44	0.25
5 Decrease All Initial Prestress Forces (- 5%)	5.72	4.41	6.86	7.29	1.59	2.20	2.57	0.27	2.13	1.29	-1.83	-0.28
6 Increase All Concrete Dead Loads (+ 5%)	6.07	4.68	7.25	7.73	1.69	2.36	2.78	0.36	2.32	1.46	-1.88	-0.23
7 Increase Modulus of Elasticity (+15%)	5.70	4.44	6.64	7.30	1.72	2.31	2.92	0.76	2.42	2.01	-1.31	0.13
8 Decrease Ultimate Creep of Beam Concrete (-20%)	5.90	4.61	7.09	7.83	1.83	2.37	2.89	0.64	2.42	2.02	-1.50	0.02
9 Modifications 1 - 4 Applied Simultaneously	9.17	7.29	10.30	11.74	3.14	3.99	5.60	2.77	5.36	5.40	-0.70	1.25
10 Modifications 5 - 8 Applied Simultaneously	4.39	3.34	5.47	5.70	1.10	1.60	1.60	-0.39	1.04	0.17	-1.98	-0.61
11 Fast Track Construction Schedule ¹	5.64	4.54	7.30	8.05	1.86	2.35	3.18	0.90	2.96	2.53	-1.50	0.41
12 Slow Track Construction Schedule ²	6.39	5.15	7.69	8.18	1.94	2.67	3.23	0.86	2.48	1.81	-1.40	0.15
13 Gross Section Properties Instead of Transformed ³	6.79	5.31	7.59	8.38	2.12	2.78	3.51	0.99	2.25	1.75	-1.18	0.21
14 Early-Age Shrinkage and Temperature Effects ⁴	5.93	4.52	7.08	7.62	1.51	2.26	2.78	0.41	2.40	1.70	-1.91	-0.20

¹ Post-tension, cut top strands, erect panels, erect panels, place C/P deck, and cast rails at 7, 32, 35, 56, & 90 days after release, respectively.
² Post-tension, cut top strands, erect panels, erect panels, place C/P deck, and cast rails at 28, 550, 600, 650, & 750 days after release, respectively.
³ With appropriate adjustments for elastic forces and elastic prestress losses.
⁴ Permanent curvature of 1.50 $\mu\epsilon/in.$ applied to beam section before release.

Table 8.18 - Sensitivity Analysis for Net Camber at Erection and Long-Term Service (Differences from Base Predictions)

Modification	Erection					Long-Term (1000 days)						
	N21	N33	E13	E24	W14	Typ	N21	N33	E13	E24	W14	Typ
0 Base Prediction	0.69	0.60	0.67	0.96	0.36	0.39	0.71	0.62	0.70	1.03	0.37	0.43
1 Increase All Initial Prestress Forces (+ 5%)	0.34	0.32	0.27	0.52	0.25	0.24	0.50	0.54	0.52	0.86	0.40	0.37
2 Decrease All Concrete Dead Loads (- 5%)	0.91	0.73	1.16	1.23	0.30	0.36	0.45	0.18	0.56	0.42	-0.20	0.01
3 Decrease Modulus of Elasticity (-15%)	0.50	0.38	0.43	0.41	0.12	0.21	0.37	0.24	0.40	0.29	0.03	0.11
4 Increase Ultimate Creep of Beam Concrete (+20%)	-0.70	-0.59	-0.66	-0.96	-0.36	-0.40	-0.70	-0.62	-0.71	-1.04	-0.36	-0.42
5 Decrease All Initial Prestress Forces (- 5%)	-0.35	-0.32	-0.27	-0.52	-0.26	-0.24	-0.49	-0.53	-0.52	-0.87	-0.41	-0.37
6 Increase All Concrete Dead Loads (+ 5%)	-0.72	-0.56	-0.88	-0.95	-0.23	-0.29	-0.35	-0.13	-0.42	-0.32	0.16	-0.01
7 Increase Modulus of Elasticity (+15%)	-0.52	-0.39	-0.43	-0.42	-0.12	-0.23	-0.38	-0.25	-0.42	-0.31	-0.03	-0.12
8 Decrease Ultimate Creep of Beam Concrete (-20%)	2.75	2.29	2.78	3.49	1.19	1.39	2.33	1.88	2.52	3.07	0.77	1.11
9 Modifications 1 - 4 Applied Simultaneously	-2.03	-1.66	-2.05	-2.55	-0.85	-1.00	-1.67	-1.28	-1.80	-2.16	-0.51	-0.75
10 Modifications 5 - 8 Applied Simultaneously	-0.78	-0.46	-0.22	-0.20	-0.09	-0.25	-0.09	0.01	0.12	0.20	-0.03	0.27
11 Fast Track Construction Schedule ¹	-0.03	0.15	0.17	-0.07	-0.01	0.07	-0.04	-0.03	-0.36	-0.52	0.07	0.01
12 Slow Track Construction Schedule ²	0.37	0.31	0.07	0.13	0.17	0.18	0.24	0.10	-0.59	-0.58	0.29	0.07
13 Gross Section Properties Instead of Transformed ³	-0.49	-0.48	-0.44	-0.63	-0.44	-0.34	-0.49	-0.48	-0.44	-0.63	-0.44	-0.34
14 Early-Age Shrinkage and Temperature Effects ⁴												

¹ Post-tension, cut top strands, erect panels, place CIP deck, and cast rails at 7, 32, 35, 56, & 90 days after release, respectively.

² Post-tension, cut top strands, erect panels, place CIP deck, and cast rails at 28, 550, 600, 650, & 750 days after release, respectively.

³ With appropriate adjustments for elastic forces and elastic prestress losses.

⁴ Permanent curvature of 1.50 $\mu\epsilon/\text{in.}$ applied to beam section before release.

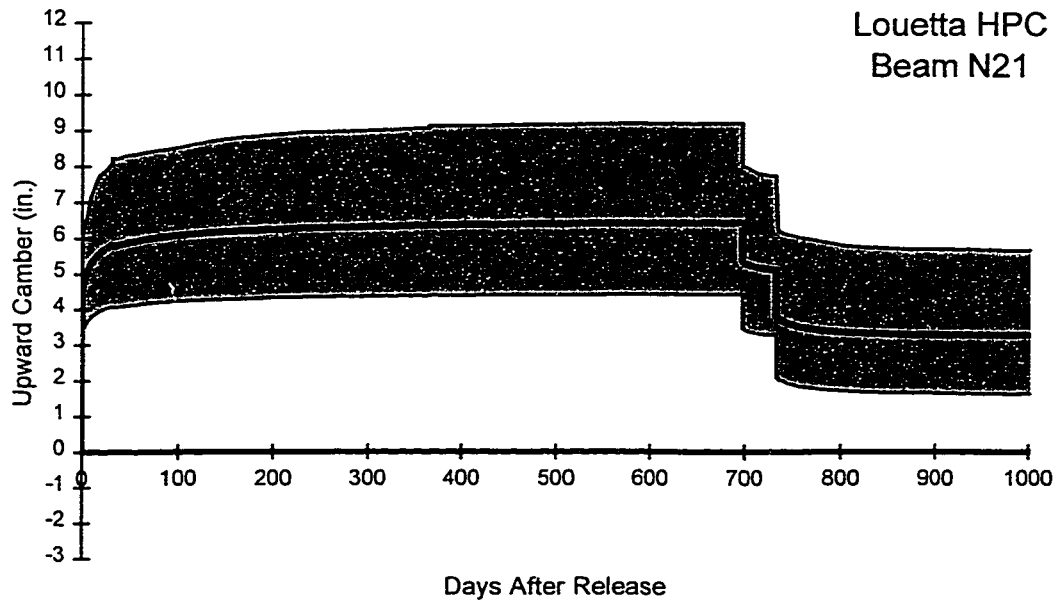


Figure 8.27 - Base Predicted Camber and Upper and Lower Bounds (Beam N21)

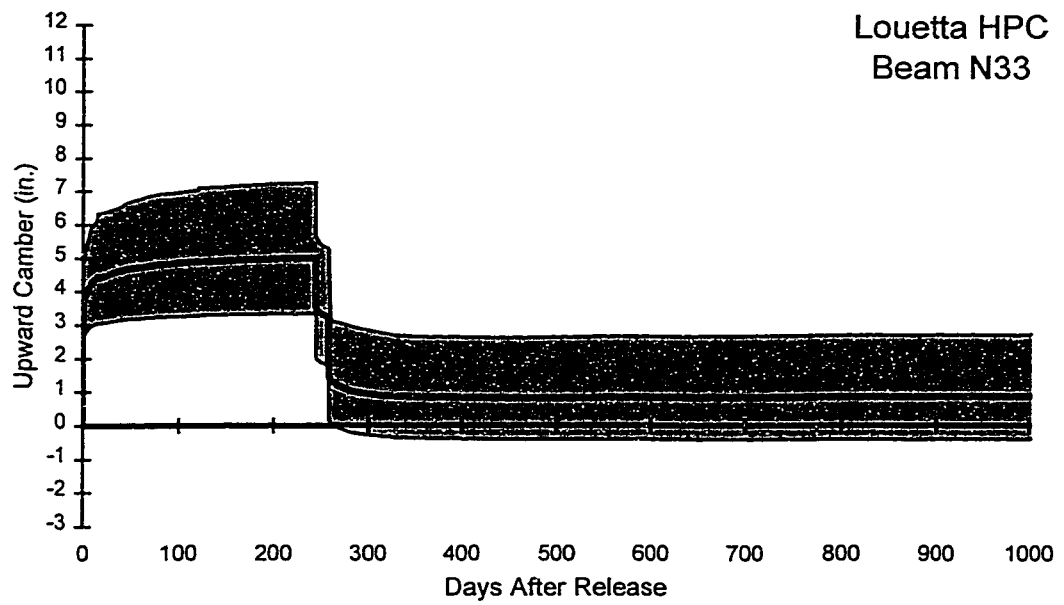


Figure 8.28 - Base Predicted Camber and Upper and Lower Bounds (Beam N33)

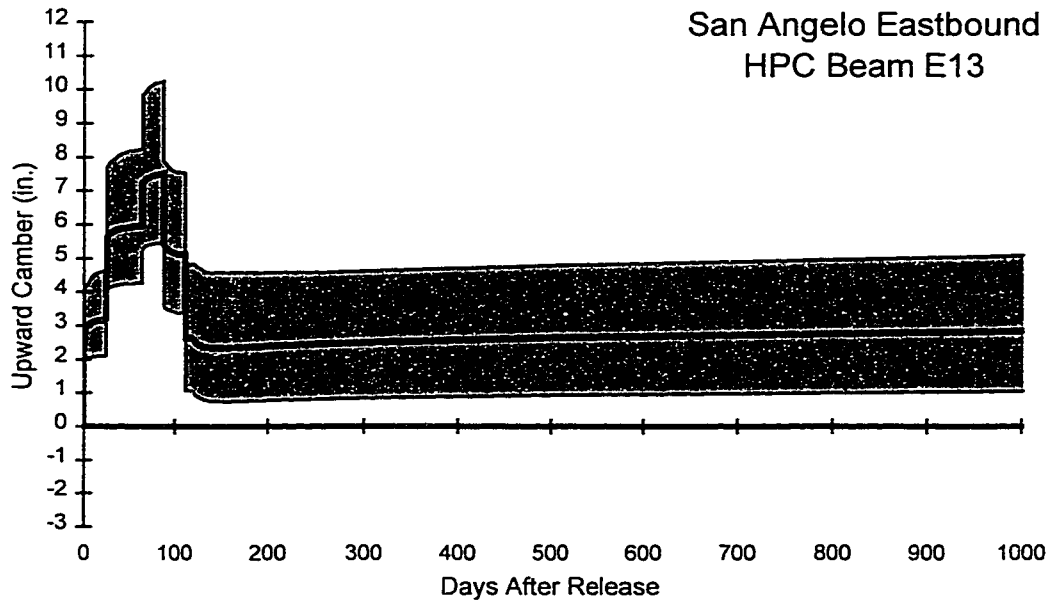


Figure 8.29 - Base Predicted Camber and Upper and Lower Bounds (Beam E13)

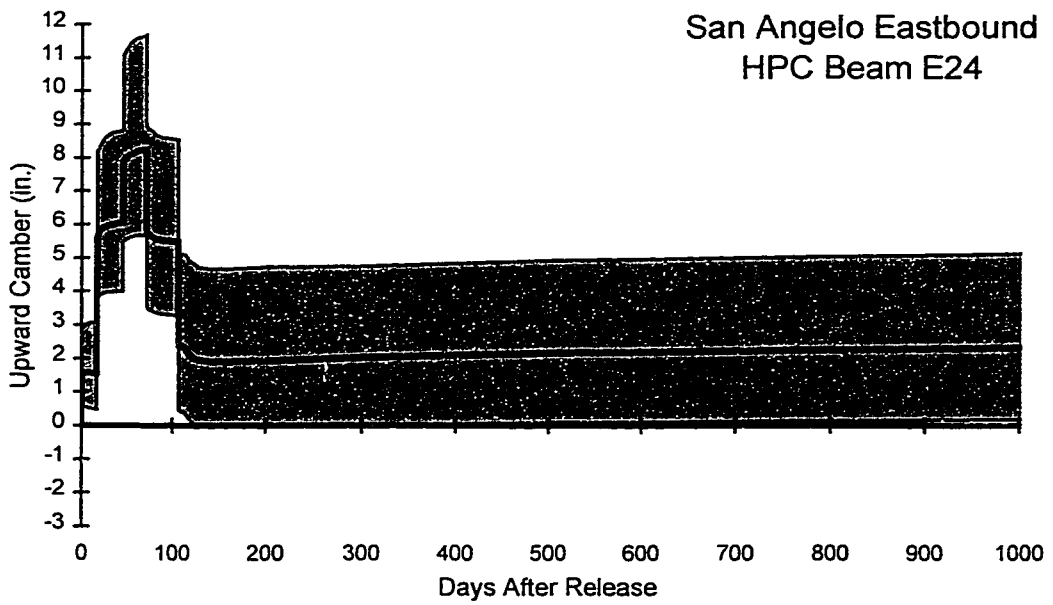


Figure 8.30 - Base Predicted Camber and Upper and Lower Bounds (Beam E24)

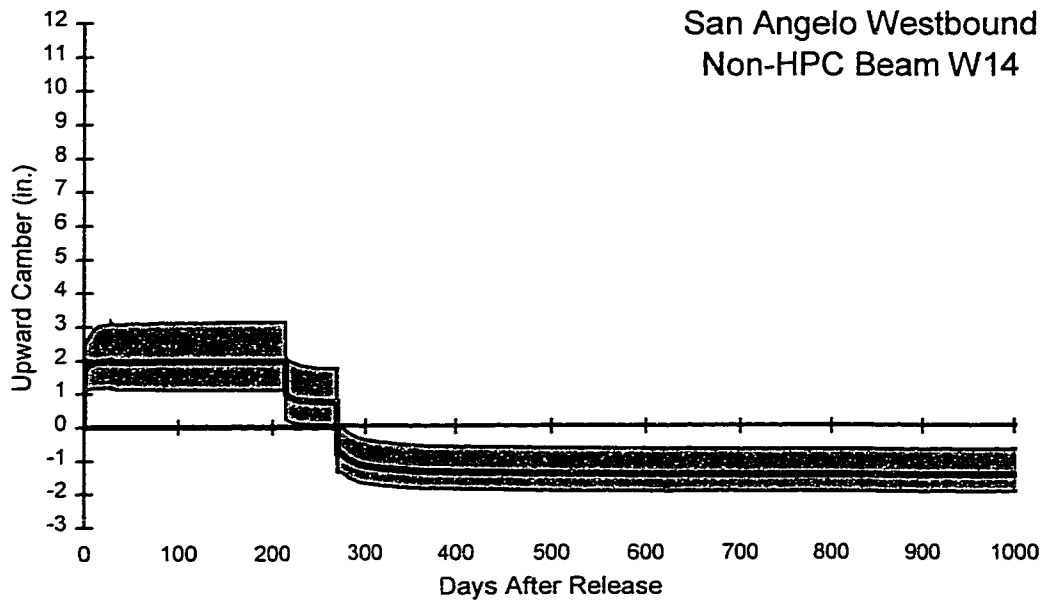


Figure 8.31 - Base Predicted Camber and Upper and Lower Bounds (Beam W14)

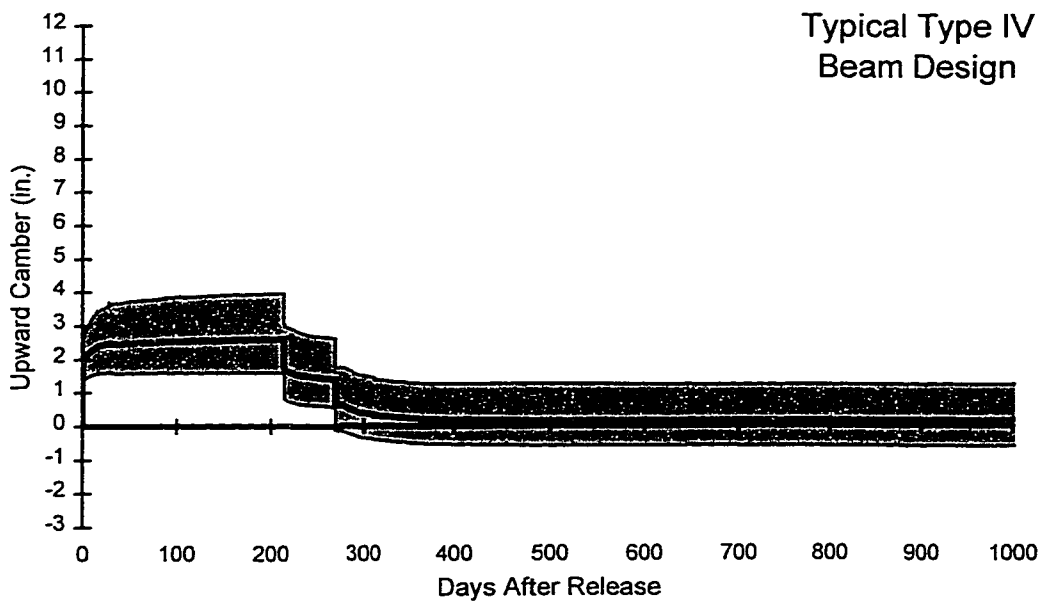


Figure 8.32 - Base Predicted Camber and Upper and Lower Bounds (Typical Conventional Concrete Beam)

The base prediction for each beam corresponds to the actual prediction derived from the incremental time-step analysis for each beam using measured parameters. These values have been presented previously in this section, and are shown in the plots of Appendix G. Several modifications were then applied to each beam individually to determine the effects of specific variations in parameters on the net camber at erection and long-term service for each design. These modifications, and their effects on each beam are listed in Table 8.17 and Table 8.18 and are discussed below. Predicted camber values are listed in Table 8.17 and differences from the base predictions are listed in Table 8.18.

The combined effects of modifications to the most important parameters were also investigated. The initial prestress force, dead loads, modulus of elasticity, and creep coefficient were varied simultaneously in a manner that would produce an upper or lower bound for net camber (based on variations in these four parameters). The plots in Figure 8.27 through Figure 8.32 show the base prediction and upper and lower bounds for each investigated beam design. Net camber predictions at release and long-term service based on this upper and lower bound approach are also listed in Table 8.17 and Table 8.18.

An examination of the values listed in Table 8.18 clearly shows that variations in these four major parameters can have a significant influence on camber for HPC designs. The variations also have an impact on the non-HPC designs, but their impact is not as significant. For the HPC designs, the combined impact of modifying these four parameters can be seen to affect the net camber at erection by up to 88.6 mm (3.49 in.) and the net camber at long-term service (1000 days) by as much as 78.0 mm (3.07 in.).

There are also some clear differences between the long-term camber behavior for the four different HPC designs, however. Beam E24, which utilized very large prestress forces (implemented in a two-stage pretensioned/post-tensioned fabrication process) to accommodate a very large span-to-depth ratio, exhibits the highest camber range at erection and the greatest sensitivity. Using the upper and lower bound approach, the range of possible net camber values at erection is 153.4 mm (6.04 in.) in breadth and the range of possible long-term values is 132.8 mm (5.23 in.) in breadth. By contrast, the ranges of possible camber values for Beam E13 at erection and long-term service are 122.7mm (4.83 in.) and 109.7 mm (4.32 in.) in breadth, respectively. This design implements HPC to accommodate larger beam spacing rather than longer spans, and utilizes slightly less prestress force than the design for Beam E24. The influence of span length on the

sensitivity of camber is clear in this comparison. Regardless, both of these HPC designs show a high degree of sensitivity based on adjustments of these four important parameters.

Louetta Beam N21, which also utilizes very high prestress forces in a Type U54B beam design, shows a similar degree of sensitivity to Beam E13. The ranges of possible camber values at erection and long-term are 121.4 mm (4.78 in.) and 101.6 mm (4.00 in.) in breadth, respectively. The range of net camber values at erection is also lower for Beam N21 than either Beam E13 or Beam E24 as a result of the higher self-weight for the U-beams. Louetta Beam N33, which utilizes significantly less prestress force than Beam N21 to accommodate a smaller beam spacing for a comparable span length (in the original design before widening of the bridges was considered) is somewhat less sensitive to the modifications. The range of camber values at erection and long-term service are 100.3 mm (3.95 in.) and 80.3 mm (3.16 in.) in breadth, respectively for Beam N33. Furthermore, the range of potential camber values at erection and service for this beam are very reasonable. Camber values at erection are generally not too high, and long-term service values range from a tolerable upward camber to a very slight downward deflection.

Camber for the two non-HPC beams is clearly not as sensitive as for the HPC beams. Similar sensitivity is shown for Beam W14 and for the "typical" design. For Beam W14, the range of potential camber values at erection is only 51.8 mm (2.04 in.) in breadth at erection and 32.5 mm (1.28 in.) in breadth at long-term service. For the "typical" design, the range of potential camber values at erection is only 60.7 mm (2.39 in.) in breadth at erection and 47.2 mm (1.86 in.) in breadth at long-term service. These two beams exhibit differing behavior with respect to the magnitude of long-term camber values, however. Beam W14 exhibits a net downward deflection at long-term service for all variations, while the "typical" design exhibits behavior closer to zero camber or deflection. As discussed before, this is a by-product of the fact that Beam W14 has many similarities to a worst-case HPC design since these beams exhibited low creep and a high modulus of elasticity with relatively large span-to-depth ratios (compared to typical designs).

If the above trends are to be put in general terms, camber for HPC designs is clearly more sensitive than for non-HPC designs. The difference in sensitivity appears to be on the order of 2 to 4. In other words, HPC designs are about two to four times more sensitive than non-HPC designs as a result of the efficiency of these designs. There is also a large variation in the sensitivity of HPC designs themselves, with the beams using the highest prestress forces and longest span lengths being the most sensitive.

The construction schedule also can have an influence on the net camber at erection and long-term service. Based on the values listed in Table 8.17 and Table 8.18, it can be seen that the effect at erection is somewhat variable. The primary factors in determining the sensitivity of erection camber to construction schedule are the magnitude of the individual camber and deflection terms and the rate of creep. Because HPC tends to creep at a faster rate at early ages than conventional concrete, the effects of higher individual components are offset for the HPC designs. Erection camber appears to be only slightly more sensitive for the HPC designs in general. The long-term service camber does not appear to be affected significantly for any of the designs.

The effect of using gross section properties in calculations instead of transformed section (or net concrete section) properties is also somewhat variable, and generally not very significant in magnitude. It should be noted that arbitrarily replacing transformed section properties with gross section properties can have a significant effect on calculations, and that the modification discussed here is not based on this incorrect approach. If gross section properties are used in place of transformed section properties, then secondary effects due to elastic changes in strand stresses must be considered in calculations. The modification discussed here, which did not have a very significant impact for the most part, is more of a comparison of the gross section *method* and transformed section *method* than a comparison based on a blind substitution of properties.

Finally, it can be seen that the effects of a potential pseudo-elastic curvature due to early-age shrinkage and thermal effects (of a magnitude equal to about half of that discussed in Section 8.2.3) can have some influence on the net camber. The degree to which these effects may have an influence is directly related to the span length, since a uniform curvature is assumed along the length of the member. These effects can have a significant influence if the curvature and span length are both relatively large. It is difficult to arbitrarily assume the presence of such a curvature for design purposes, but this effect is shown here to indicate that the net camber can be influenced by non-load related effects such as these.

There is clearly some question as to whether camber can be predicted accurately for long HPC prestressed concrete beams. It is widely known that it is very difficult to accurately predict camber and deflection behavior for conventional beams, and based on the observations discussed above, the sensitivity of camber for HPC beams appears to be on the order of two to four times greater than for conventional non-HPC beams.

Furthermore, variations in construction schedule and the possibility of camber and deflection components from non-load related sources increase the difficulty in the prediction of net camber at later ages.

In light of the sensitivity of camber and deflections for HPC designs, the upper and lower bound approach used in the sensitivity analysis for this study should be used during future HPC beam designs. The use of this type of approach is a direct acknowledgement of the sensitivity for these designs, and would serve the purpose of providing the contractor a *range* of possible camber values at erection and long-term. In reality, it serves little purpose to put an estimate of camber on construction documents when there is so little accuracy involved in the estimate – the range of potential values should be stated as well.

Even with this upper and lower bound approach, the accurate assessment of material properties and parameters is important during design. Most importantly, modulus of elasticity and unit weight should be determined from companion tests whenever possible. Trial batching during the design stage, where feasible, can provide good estimates of some of these properties. Furthermore a database must be developed for material properties of various HPC concrete mixes typically used in the fabrication of highway bridge beams, including creep, modulus of elasticity, and unit weight. Such a database would also facilitate the estimation of these important properties, and could potentially lead to more accurate formulae for the prediction of HPC material properties in the absence of specific test data.

The upper and lower bound approach could be used with any method for the prediction of time-dependent behavior that has been proven reasonably accurate and that has the flexibility to accommodate changes in the important parameters. This includes numerous computer programs, incremental time-step analyses, and advanced multiplier methods. Simple multiplier methods, such as the PCI multiplier equations given in Equation 8.10 and Equation 8.11, should never be used for the prediction of net camber in HPC beams because they lack the flexibility to make adjustments in important parameters. Based on the observations of measured and design-calculated camber in this study, it also appears that TxDOT's PSTRS14 design program cannot sufficiently predict the camber and deflection behavior for HPC beams. The program has no capacity for the adjustment of creep parameters, and will therefore significantly overestimate camber for almost all HPC designs.

Specific recommendations are not made here regarding the effects of construction sequence and non-load related camber and deflection components, other than to state that they may potentially influence net camber. These effects are likely to have a greater influence for extremely efficient HPC beam designs with long spans than for conventional designs. Their effects should be investigated on a case-by-case basis, depending on whether they may be of importance. For example, a designer might wish to consider the potential impacts of these effects if net camber without consideration of these effects is likely to be very low.

The current philosophy of “no net deflection under full dead load” is recommended for use in future designs, including those utilizing HPC. This design criterion, although meaningless in terms of ultimate strength, simply reflects sound engineering principles related to serviceability and aesthetics. Considering the sensitivity of HPC designs, it is fortunate that there are no significant repercussions for designs failing to meet this criterion. Still, there is no reasonable basis to ignore serviceability criteria entirely for a prestressed concrete highway bridge structure.

8.6 Summary and Conclusions

The following observations were made in this chapter regarding Camber at Release of Prestress (Pretensioning):

- 1) Thermally-corrected camber measurements at release of pretensioning ranged from 46.5 to 80.5 mm (1.83 to 3.17 in.) for Louetta HPC beams, - 6.6 to 39.6 mm (- 0.26 to 1.52 in.) for San Angelo Eastbound HPC beams, and 13.5 to 24.9 mm (0.53 to 0.98 in.) for San Angelo Westbound non-HPC beams.
- 2) Release cambers measured on identical and nearly identical beams were generally very similar in magnitude.
- 3) For all 26 beams in this study, measured release cambers were lower than predicted release cambers based on either design or measured properties. Differences between measured release cambers and predicted release cambers based on measured properties ranged from 41.7 to 63.2 mm (1.64 to 2.49 in.) for Louetta and San

Angelo Eastbound HPC beams and 29.0 to 40.4 mm (1.14 to 1.59 in.) for San Angelo Westbound non-HPC beams. Differences were substantially larger for *design*-based predictions.

- 4) Differences between measured release camber and predicted release camber based on measured parameters are due in large part to differences between the actual and measured modulus of elasticity for concrete and errors in the refined estimation of the initial prestress force and member self-weight. Still, it appears unlikely that these factors alone could account for some of the large differences.
- 5) It is likely that a curvature due to temperature effects during hydration and differential shrinkage before release also contributed to the lower than predicted net camber at release. These effects may have caused an additional component of downward deflection, which may or may not be recoverable over time.
- 6) The sum of the absolute values of the individual terms comprising the net camber at release is a good indicator of sensitivity. When “errors” in the prediction of release camber (based on measured parameters) are computed on the basis of this absolute sum rather than the algebraic sum of the components, as suggested in Equation 8.5, the average “error” for all beams was 9.6 percent. The HPC designs – especially the San Angelo Eastbound HPC designs – are clearly *very* sensitive as shown by the magnitude of these absolute sums.

The following observations were made in this chapter regarding Time-Dependent Camber Growth in Beams During Storage:

- 1) Support location and thermal gradient corrections discussed in Section 8.1.2 were used rather successfully to compensate for the effects of variable support conditions and temperature fluctuations during storage, and allowed for the meaningful comparison of measured and predicted beam camber. Support location corrections were generally rather small, but thermal gradient corrections were as large as 20 mm (0.8 in.).
- 2) Identical and nearly identical beams generally exhibited similar time-dependent camber growth during storage at the prestressing plant.

- 3) Camber growth during storage was slightly less than predicted for the Louetta HPC beams, about equal to or slightly greater than predicted for the San Angelo Eastbound HPC beams, and greater than predicted for the San Angelo Westbound non-HPC beams. These observations are generally similar to observations related to measured midspan curvature growth during storage discussed in Section 6.4.
- 4) Differences in modulus of elasticity, creep, initial prestress force, and member self-weight can significantly affect the camber growth in beams and accounted for some of the differences in measured and predicted camber growth observed in this study. HPC designs were shown to be particularly sensitive to these parameters.
- 5) The effects of differential shrinkage over time may also have influenced the measured camber growth in the beams of this study.

The following observations were made in this chapter regarding Elastic Deflection Responses to Post-Tensioning and Deck Loads:

- 1) Measured elastic camber due to post-tensioning of the San Angelo Eastbound HPC beams ranged from 35.6 to 67.6 mm (1.40 to 2.66 in.). The measured post-tensioning camber was less than predicted (using measured parameters) by an average of 28 percent, and less than predicted in the actual beam designs by 12 percent. These observations are consistent with observations related to measured curvatures due to post-tensioning discussed in Section 6.4.
- 2) Variations in the modulus of elasticity and friction and anchorage losses are probable reasons for the differences between measured and predicted elastic post-tensioning cambers.
- 3) Measured elastic deflections due to placement of the cast-in-place deck ranged from 20.3 to 49.0 mm (0.80 to 1.93 mm) in the Louetta HPC beams, 31.2 to 73.9 mm (1.23 to 2.79 in.) in the San Angelo Eastbound HPC beams, and 22.9 to 34.8 mm (0.90 to 1.37 in.) in the San Angelo Westbound non-HPC beams.

- 4) For all beams, the measured deflection due to the placement of the cast-in-place deck was lower than predicted using measured parameters. On average, deflections were 20, 33, and 35 percent lower than predicted in the Louetta HPC, San Angelo Eastbound HPC, and San Angelo Westbound HPC beams, respectively. These trends generally agree with the observations related to measured curvatures due to placement of the cast-in-place bridge decks in Section 6.4.
- 5) Differences between measured and predicted deck deflections are due to variations in the concrete modulus of elasticity and deck thickness, even though both of these quantities were based on measured values.
- 6) Measured *total* deck load deflections were 9, 11, and 11 percent lower than predicted using measured parameters for the Louetta HPC, San Angelo Eastbound HPC, and San Angelo Westbound non-HPC beams, respectively. Similarly, the measured total deck deflections were 29, 5, and 5 percent less, respectively, than the total elastic deck deflections calculated during the actual beam designs. These measurements include some extra deflection due to creep after the placement of precast deck panels, but this effect was not considered in the predictions.

The following observations were made in this chapter regarding Long-Term Deflection Behavior:

- 1) Measured net camber at erection ranged from 84.8 to 140.7 mm (3.34 to 5.54 in.) for the Louetta HPC beams, 160.3 to 190.2 mm (6.31 to 7.49 in.) for the San Angelo Eastbound HPC beams, and 38.4 to 46.0 mm (1.51 to 1.81 in.) for the San Angelo Westbound non-HPC beams.
- 2) Measured long-term camber (at least seven months after completion of the cast-in-place bridge decks) ranged from - 3.6 to 72.9 mm (- 0.14 to 2.87in.) for the Louetta HPC beams, 21.3 to 61.5 mm (0.84 to 2.42 in.) for the San Angelo Eastbound HPC beams, and - 36.3 to - 54.1 mm (- 1.43 to - 2.13 in.) for the San Angelo Westbound non-HPC beams.
- 3) These long-term measurements show the desired slight upward deflection for the HPC beams under full dead load, but an undesirable net downward deflection under full

dead load for the San Angelo Westbound non-HPC beams. This downward deflection is largely an aesthetic issue, and is a result of the fact that the non-HPC beam concrete exhibited many properties of HPC, including a relatively high modulus of elasticity and very low creep, despite not carrying the HPC designation.

- 4) In all cases, there was generally good agreement among the beams in a span with respect to the camber at erection. No construction problems in any of the bridges occurred as a result of differential erection camber among the beams in a given span.
- 5) For all beams, there was generally very poor correlation between measured long-term cambers and long-term cambers calculated during the actual beam designs.
- 6) For all beams, there was generally a poor correlation between measured camber and predicted camber (using measured parameters) throughout storage and construction at the jobsite. For long-term camber, there was generally good agreement because of the offsetting effect of lower than predicted elastic dead load deflections. Average absolute differences between measured and predicted long-term camber were 7.4, 15.0, and 2.5 mm (0.29, 0.59, and 0.10 in.) for the Louetta HPC, San Angelo Eastbound HPC, and San Angelo Westbound non-HPC beams, respectively.
- 7) A sensitivity analysis on six beam designs, including five from this study and a conventional beam design, indicated a sensitivity 2 to 4 times greater than the sensitivity of non-HPC designs for long-term camber measurements. The combined effects of reasonable variations in initial prestress force, dead loads, modulus of elasticity, and creep coefficient were determined to affect erection and long-term camber for HPC beams by as much as 88.6 and 78.0 mm (3.49 and 3.07 in.), respectively.
- 8) Among HPC beam designs, beams with the highest prestress forces and longest span lengths were clearly the most sensitive with respect to long-term camber.
- 9) The effect of variations in construction schedule and the use of gross-section properties were more variable and generally not as significant as other factors. For HPC beams, the increased sensitivity to construction schedule resulting from larger individual camber and deflection components is offset by the faster rate of creep at early ages.

8.7 Recommendations

The following recommendations are made on the basis of the information presented in this chapter regarding Camber at Release of Prestress (Pretensioning):

It must be recognized that there is a clear increase in sensitivity for release camber with HPC beam designs. The larger prestress forces and longer spans used in these beams result in much larger magnitudes for the individual components of the net camber at release, and the accurate prediction of this algebraic sum becomes much more difficult. Because of this increased sensitivity, it is of extreme importance that parameters be estimated as accurately as possible if reasonable predictions of release camber are to be made. In particular, the use of trial batching for the determination of modulus of elasticity and unit weight is strongly encouraged for HPC designs. When trial batching is not feasible, designers should rely on past experience with similar concretes.

It may also be wise to acknowledge the possibility of an additional downward component of deflection due to thermal gradients during hydration and differential shrinkage before release. Much more research is needed to determine whether such a component exists in beams outside of this research program, and to determine whether portions of this deflection would be recoverable over time. It is expected that if such a component does exist in other beams, its magnitude may be highly variable. When net downward deflections are expected to be a particular problem, designers may wish to consider the possibility of such a component during design.

The following recommendations are made on the basis of the information presented in this chapter regarding Time-Dependent Camber Growth in Beams During Storage:

No specific changes to standard design procedures are recommended on the basis of the observations in this study, other than to recognize the increased sensitivity of camber growth for HPC designs. Variations in modulus of elasticity and creep may lead to large differences between measured and predicted camber growth for HPC beams. Estimates of the initial prestress force and member self-weight may be as important or even more

important because they affect *both* elastic and time-dependent camber growth. Every effort should be made to estimate these parameters as accurately as possible during design, and measured material properties should be used whenever available. Trial batching may help to determine some of these parameters during the design process, and is thus recommended whenever possible.

The following recommendations are made on the basis of the information presented in this chapter regarding Elastic Deflection Responses to Post-Tensioning and Deck Loads:

No specific changes to standard design procedures are recommended for the calculation of elastic camber and deflection due to post-tensioning and deck loads. The exact magnitude of these deflections depends on many parameters which must be estimated during design, including friction and anchorage losses for post-tensioning tendons, cast-in-place deck thickness, and modulus of elasticity. Since these parameters may not be known to a great degree of accuracy during design, these calculated deflections should never be taken as precise values. Unfortunately, the very long span lengths, beam spacing, and prestress forces used for HPC designs will generally result in an increase in sensitivity for these calculations, and will generally make these calculations even more approximate in nature.

The following recommendations are made on the basis of the information presented in this chapter regarding Long-Term Deflection Behavior:

Regardless of the specific method used for calculation of time-dependent camber and deflection, the upper and lower bound approach described in Section 8.5.3 should be used for all HPC designs. As a direct result of the higher prestress forces and longer spans used with such designs, there is a dramatic increase in the sensitivity of camber predictions (and behavior) at all stages of construction and service. Specifically, a base camber prediction should be performed using the best possible estimates or measurements of material properties and important parameters including initial prestress force, dead loads, modulus of elasticity, and creep coefficient. These parameters should then be varied as recommended in Table 8.19. The *range* of possible camber or deflection values computed should be listed on construction drawings (in addition to the base estimate) so that the

contractor is aware of the potential variations and can make necessary adjustments. Possible effects of variations in construction schedule and non-load related camber and deflection components should be examined on a case-by-case basis and incorporated into this procedure as appropriate. Note that the percentages suggested in the Table 8.19 are based on assumed "reasonable" variations, and should be adjusted if quality control procedures and research suggest that different deviations are more appropriate.

Even when using the upper and lower bound approach for camber calculations, the accurate estimation of material properties is extremely important. Trial batching should be used whenever possible to determine the modulus of elasticity and concrete unit weights. Past experience must also be relied upon heavily. Since it is more unrealistic to expect trial batching to produce measurements for creep, designers must make adjustments to standard estimates for creep that are based on conventional concrete. The measurements obtained in this research program may be used for concretes composed of similar proportions using similar constituent materials, but should not be assumed to be an appropriate model for all HPC. Still, the use of these measured creep values should provide better results than values based on conventional concrete. At a minimum, a lower ultimate creep coefficient should be assumed for HPC.

The TxDOT philosophy of "no net deflection under full dead load" is convenient and should be used in future HPC (and non-HPC) designs. Although deflection behavior has no impact on ultimate strength, this criterion reflects the consideration of serviceability and aesthetics, and should be considered in a proper limit states design. Fortunately, there are no significant repercussions if this criterion is not quite met for a particular bridge during construction, but it should be used as a viable design criteria.

Table 8.19 - Suggested Modifications to Parameters for Upper and Lower Bound Approach to Camber Calculations

Parameter	Upper Bound	Lower Bound
Initial Prestress Force(s)	Increase by 5%	Decrease by 5%
All Dead Loads	Decrease by 5%	Increase by 5%
Modulus of Elasticity of Beam Concrete	Decrease by 15%	Increase by 15%
Ultimate Creep of Beam Concrete	Increase by 20%	Decrease by 20%

9 CHAPTER NINE: STATIC LIVE LOAD TESTS

9.1 Introduction

Static live load tests were conducted on the completed Louetta and San Angelo bridges before the bridges were opened to traffic. These tests essentially involved the placement of heavily loaded trucks in specified positions on each bridge, as shown in Figure 9.1 and Figure 9.2, and the measurement of concrete strains and beam deflections caused by each loading. The primary purpose of the tests was to investigate the overall behavior of these bridges under static live load, including specific items such as the distribution of loads among girders in a span, possible continuity between adjacent spans, and most importantly, the order of magnitude of the responses.

It is important to note that these tests were relatively limited in scope for two reasons. First, tests were entirely *static* in nature because of the time required for both concrete strain and beam deflection measurements. The vibrating wire gauges used for concrete strain measurements required about two seconds per gauge for each measurement. Beam deflections were measured using the precise surveying system and at least ten to fifteen minutes was required for measurements on each span, which eliminated any possibility of dynamic measurements. Second, the number of embedded vibrating wire gauges was limited by the number of channels available on each data acquisition system and the high cost of these gauges. Complete concrete strain measurements were not possible on every beam in every loaded span, although deflections were recorded for all beams in each loaded span. Despite these limitations, the tests were very valuable and provided a large amount of useful data.

Distinct differences exist between the Louetta and San Angelo bridges. As discussed in Chapter 2, the Louetta bridges have highly skewed bent lines, non-parallel beams (i.e. variable beam spacing), and are very wide structures. On the other hand, the San Angelo bridges are more straightforward highway overpass structures, with perpendicular bent lines, constant beam spacing, and a roadway width more typical of most highway overpasses. While this does not make measurements on the San Angelo bridges

more valuable per se, it does make these measurements easier to interpret than those from the Louetta bridge. For this reason, more emphasis is placed on the static live load tests from the "cleaner" San Angelo bridge. Measurements from the Louetta bridges are presented in this chapter, but less detailed conclusions are drawn from these tests because of the difficulty in interpreting the data.

9.2 Loading Arrangements and Test Procedures

The basic principle used in selecting loading arrangements for the static live load tests was to simulate maximum and midspan moments resulting from AASHTO [1,3] HS20-44 truck loads. As shown in Figure 9.3, an HS20-44 truck is a three-axle vehicle with variable axle spacing and a total weight of 320 kN (72 kips). The minimum rear axle spacing of 4.3 m (14 ft.) produces the maximum moment in a simply-supported span. Trucks with these axle spacings were not available to the researchers, so a single HS20-44 truck was instead approximated using two shorter dump trucks. The dump trucks were supplied by the Maintenance Divisions of the Texas Department of Transportation (TxDOT) in Houston and San Angelo, respectively.

Dimensions of the trucks are summarized in Figure 9.3, and axle weights for each truck are listed in Table 9.1. Each truck was loaded to a total (gross) weight of 178 kN (40 kips) within a tolerance of ± 2.2 kN (0.5 kips). This weight is slightly higher than half the weight of an HS20-44 load, which compensates for the larger *total* axle spacing associated with using two dump trucks to simulate a single HS20-44 truck. As can be seen in Figure 9.4 for Loading SE-C (described later in this section), the maximum and midspan moments are similar for an HS20-44 truck load and the simulated test load. There are slight differences in the shear diagrams associated with the differences in total load. (Note that simply-supported spans were assumed in determining loading arrangements. This assumption was eventually proven to be quite valid during the actual tests, as discussed in Section 9.4.)

Within each span, the trucks were always placed in the regions where embedded gauges had been installed previously during the instrumentation program. Furthermore, trucks were generally placed in a position that maximized output for the instrumented beams. This generally led to the trucks being positioned directly above the first interior

beam on the instrumented side of each span. In most cases, one pair of trucks was centered over this beam, but in a few cases two pairs of trucks were placed on either side of the first interior beam. Specific loading arrangements are shown in Figure 9.5 and Figure 9.6 for the San Angelo and Louetta live load tests, respectively. A brief description of each loading arrangement is provided in Table 9.2. Note that because a limited number of trucks were available for the tests, trucks were not placed across the full span to simulate complete loading of the bridge (i.e. all design lanes loaded).

Prior to the beginning of static live load testing on each bridge, exact truck (wheel) locations corresponding to each loading arrangement were marked on the bridge deck. Trucks were then loaded with sand, weighed at the maintenance yard, and driven to the bridge for testing. All deflection measurements were recorded manually using the precise surveying system. Concrete strain measurements were recorded automatically at ten minute intervals by the permanent data acquisition system connected to the gauges, and readings were correlated with the loading arrangements by carefully recording the times of each loading and unloading procedure. Concrete temperature measurements were also automatically recorded at the same times as the concrete strain readings.

For each loading arrangement, two full sets of measurements were required – one set of measurements on the unloaded bridge and one set of measurements with the trucks in position on the bridge deck. Unloaded measurements were recorded at several times throughout the day in order to minimize the effects of temperature gradients. In order to save time and increase the total number of loadings possible within the limited total testing time, unloaded measurements were often used in conjunction with *both* the set of loaded measurements immediately before and the set of loaded measurements immediately after the unloaded reading.

On average, about 45 minutes was required for each loading procedure, including the time required to move trucks into place and the time required to manually record all beam deflection measurements in the appropriate spans. Slightly less time was required for the unloading procedure because the trucks did not have to be moved into place. Figure 9.1 shows test trucks being moved into position during the San Angelo live load tests, and Figure 9.2 shows test trucks positioned in Loading Arrangement LS-B during the Louetta live load tests.



Figure 9.1 - Test Trucks Being Positioned During San Angelo Live Load Tests



Figure 9.2 - Test Trucks Positioned in Louetta Loading Arrangement LS-B

9.3 Measurements

The primary measurements recorded during each live load test loading are presented in this section in tabular form. Primary measurements include midspan beam deflections and midspan curvatures through the depth of selected (composite) beams. Data is first presented for the San Angelo live load tests, and then for the Louetta live load tests. The conclusions drawn from these measurements are discussed in Section 9.4, in terms of specific aspects of behavior that are of interest. Supplementary measurements, such as measurements of deck strains during selected loadings, are discussed in the appropriate parts of that section as necessary.

9.3.1 San Angelo

The primary measurements recorded during the seven loading arrangements of the San Angelo live load tests are presented in Table 9.3 through Table 9.10. Midspan beam deflections measured using the precise surveying system are listed in the tables, and are compared to the suggested *AASHTO* [1,3] live load deflection limit of $L/800$ (where L is the span length). Measured midspan curvatures are also listed in the tables for those selected beams which were instrumented with vibrating wire gauges through the depth of the composite section. The curvature was determined by fitting a regression line through the measured concrete strains at several depths. This procedure was discussed in Section 6.3.2 and is illustrated in Figure 6.7. Plane sections were observed to remain essentially plane in all cases. Note that corrections for temperature gradients were applied to all measured concrete strains, but no correction was applied to beam deflection measurements.

Approximate moments carried by each beam are also listed in the tables. These approximate moments are based on the *measured* midspan deflections and curvatures, and were computed using the calculated composite section properties for each beam. Section properties were calculated using measured moduli of elasticity for the beam and deck concretes, deck thicknesses measured by state inspectors during the deck pours, and an effective flange width for the section based on the provisions of Section 8.10.1 of the *AASHTO Standard Specifications* [3]. The shape of the moment diagram based on the

measured truck loads was used to establish the relationship between midspan deflection and midspan moment. The relationship between midspan curvature and midspan moment is based strictly on the composite section properties.

Total span moments calculated from a structural analysis using the measured truck loads are also listed in the tables for comparison. In theory, the sum of the beam moments calculated using the measured deflections should be equal to this total span moment. Note that simply-supported spans were assumed for all calculations.

9.3.2 Louetta

The primary measurements recorded during the five loading arrangements of the Louetta live load tests are presented in Table 9.11 through Table 9.15. Measured beam deflections are listed for each beam in the loaded spans, and are compared to the suggested *AASHTO* live load deflection limit of $L/800$. Deflections were measured at the midspan of each beam along a skew parallel to the bent lines rather than perpendicular across the span. Measured midspan curvatures are also listed in the tables for Beam S15 and Beam S25, along which most of the loading arrangements were located. Curvatures were determined by fitting a linear regression line to the measured strains at different depths in each U-beam. Curvatures for Beam S15 are the average curvatures determined from the strains in both the East and West webs, while curvatures for Beam S25 are based on measurements in the East web only.

Moments were not computed from the measured deflections and curvatures for the Louetta live load tests because of the effect of the skew. Moments in the skewed bridge are much more complicated than in a perpendicular bridge, and one-way bending cannot be arbitrarily assumed. Furthermore, deflections were not measured on a section perpendicular to the beam lines (which themselves are not actually parallel in the Louetta bridge), but instead were measured along a skew parallel to the bent lines.

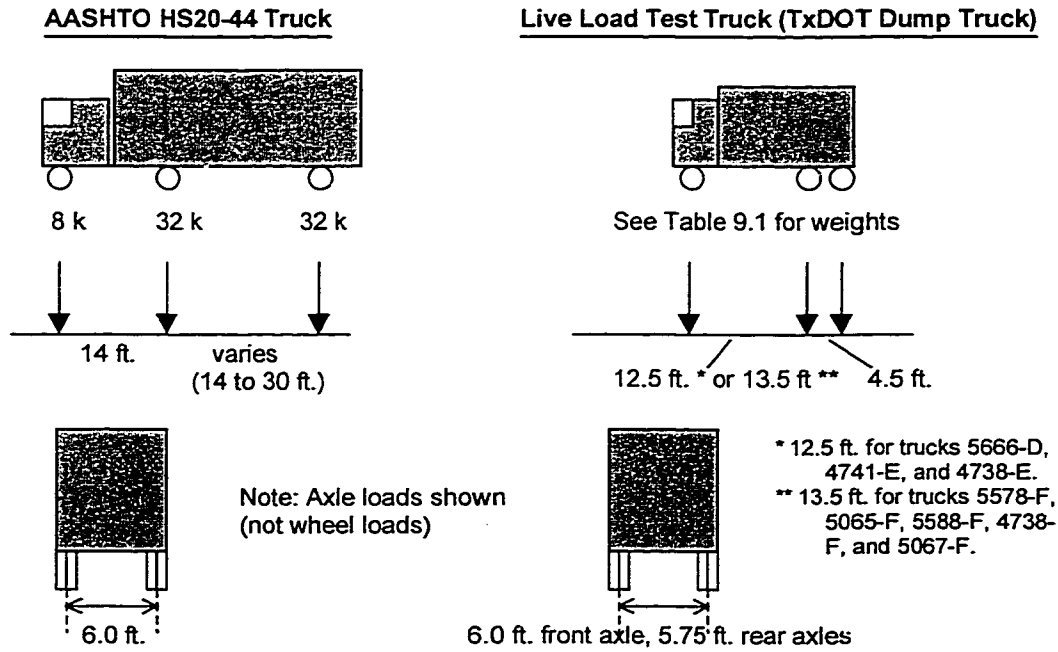


Figure 9.3 - AASHTO HS20-44 Truck and Dump Trucks Used in Live Load Tests

Table 9.1 - Axle Weights for Dump Trucks Used in Live Load Tests

Truck	Front Axle	Middle Rear Axle	Far Rear Axle	Total – Gross Truck Weight
Louetta				
5666-D	10.25	15.45	14.45	40.15
4741-E	11.85	14.25	13.70	39.80
4738-E	11.35	14.50	13.65	39.50
5578-F	10.10	15.30	15.10	40.50
San Angelo				
5065-F	11.24		28.30	39.54
5588-F	11.50		28.30	39.80
4738-F	10.52		29.72	40.24
5067-F	10.00		29.58	39.58

All weights in kips. 1 kip = 4.448 kN
 Note: Individual rear axles not weighed in San Angelo. Rear axles weighed jointly.

Live Load Test Trucks

AASHTO HS20-44 Truck

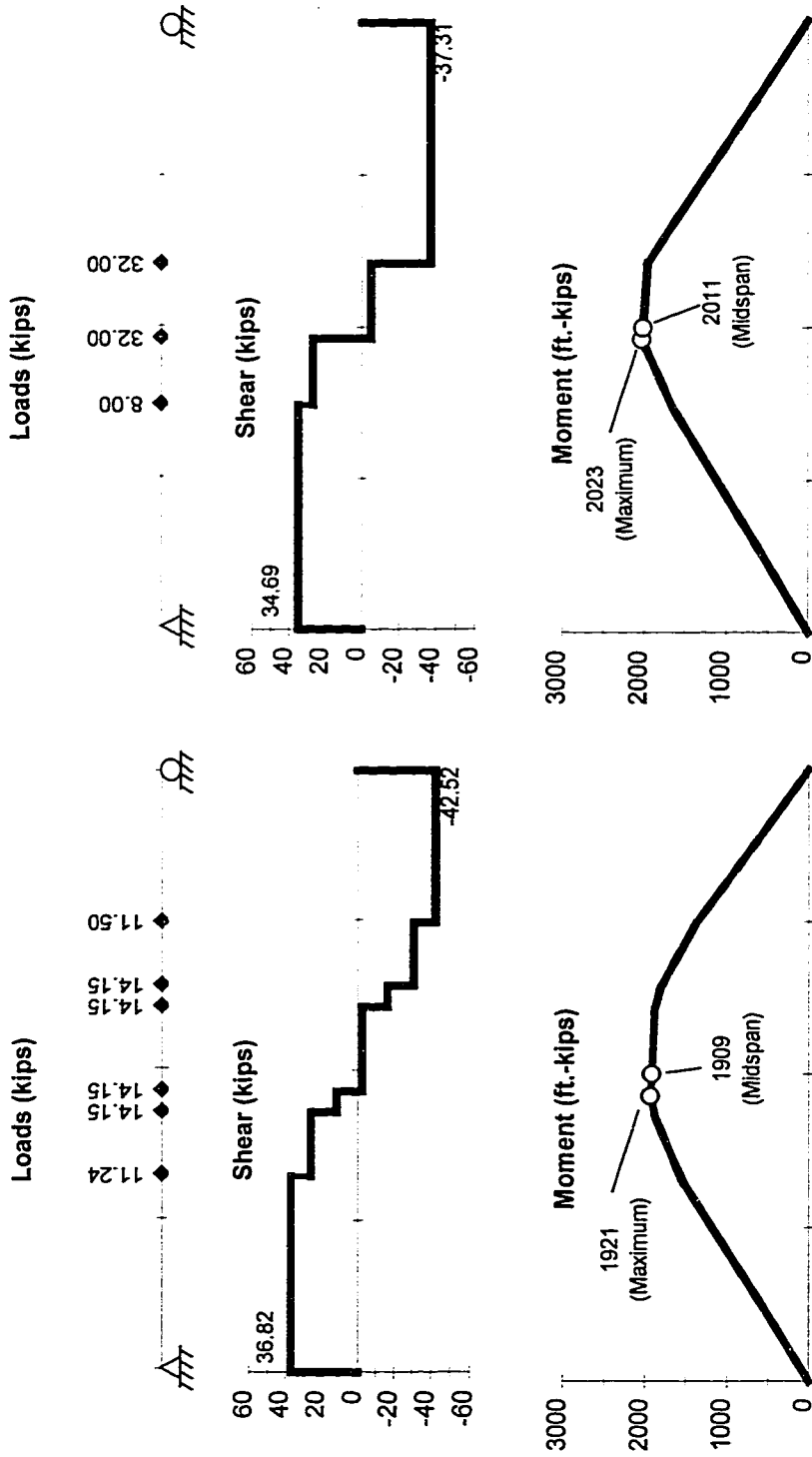


Figure 9.4 - Comparison of Shear and Moment Diagrams for Loading SE-C and an HS20-44 Truck Load (San Angelo Eastbound Bridge, Span 2)

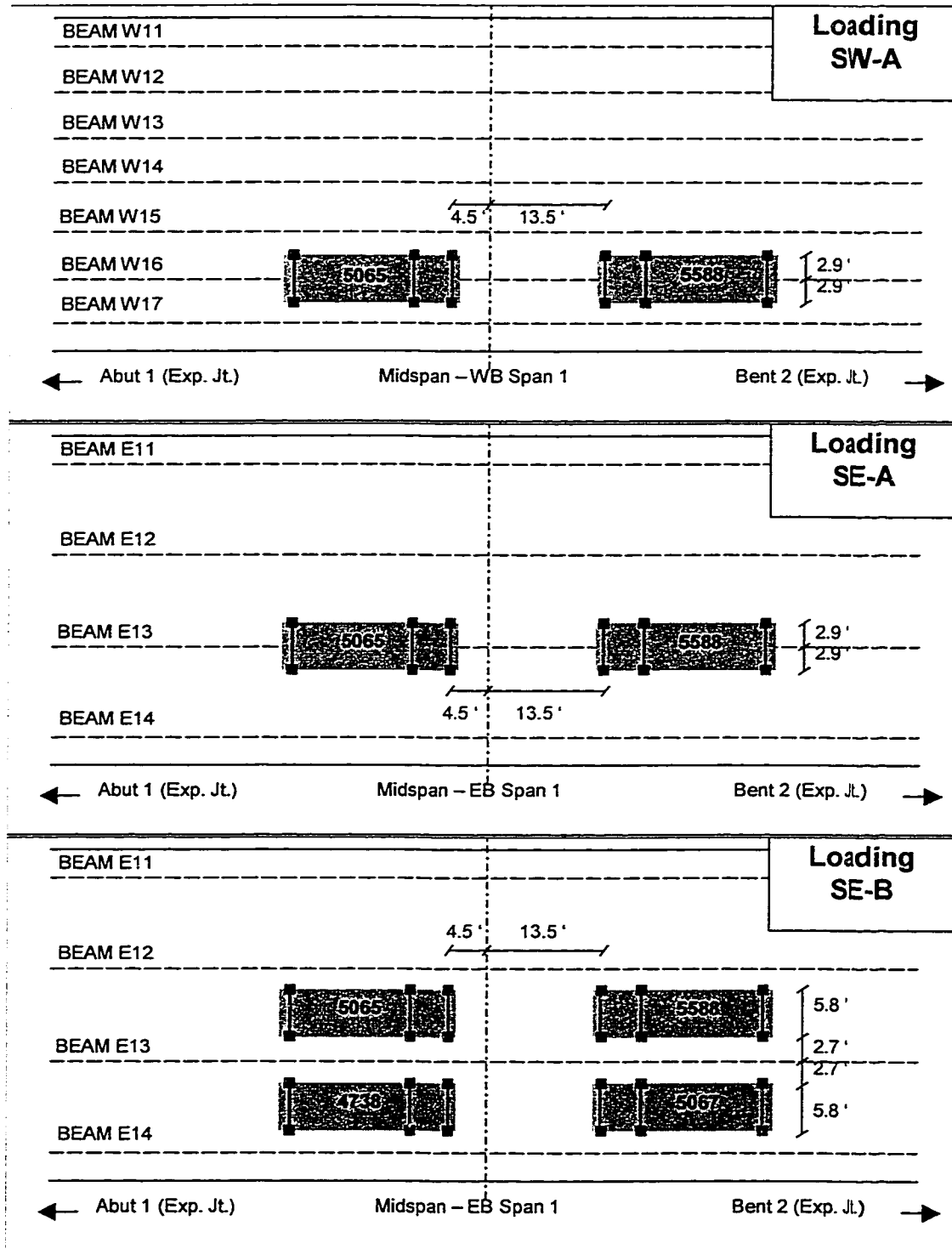


Figure 9.5 - Loading Arrangements for San Angelo Live Load Tests

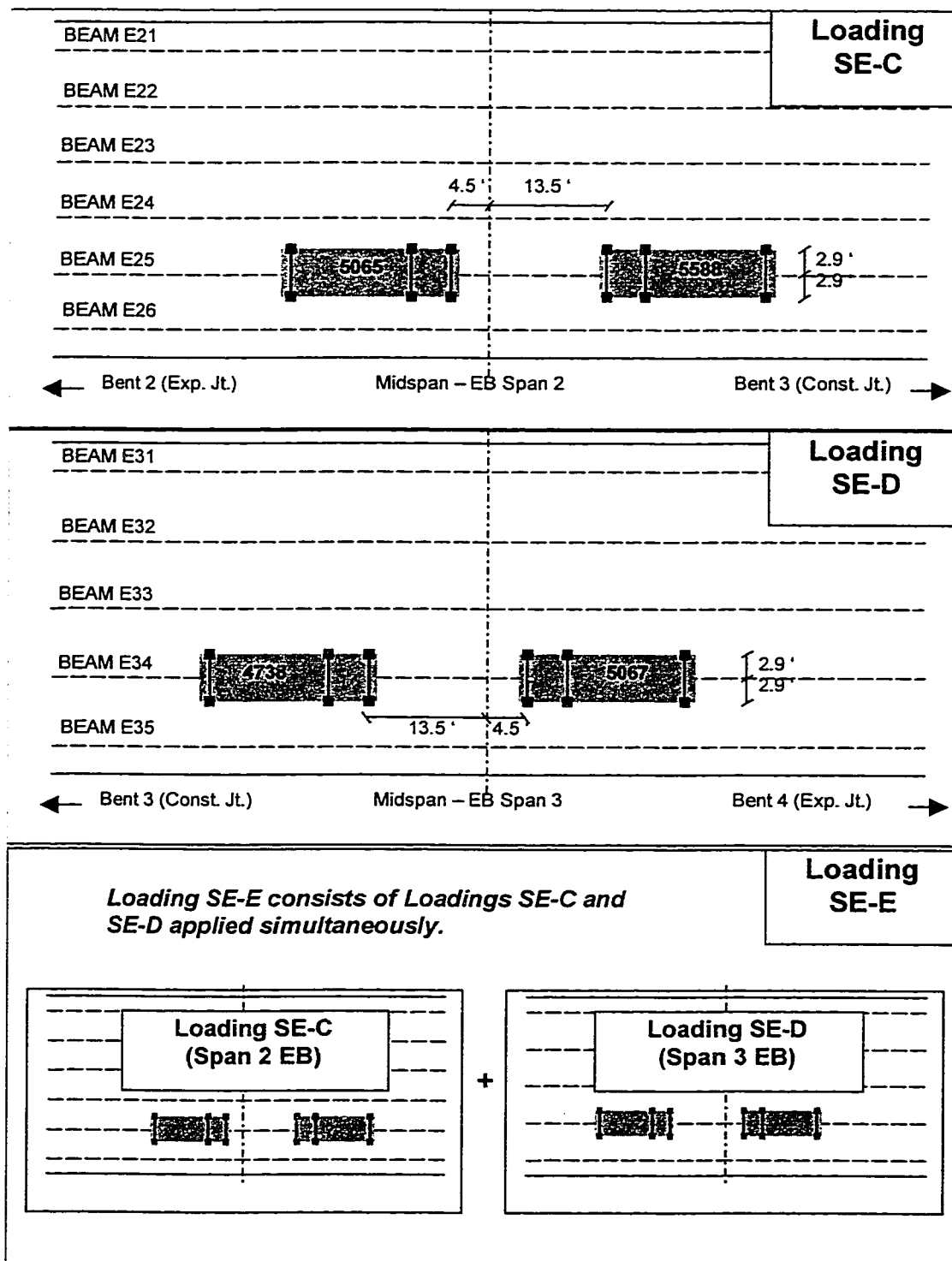


Figure 9.5 (continued) - Loading Arrangements for San Angelo Live Load Tests

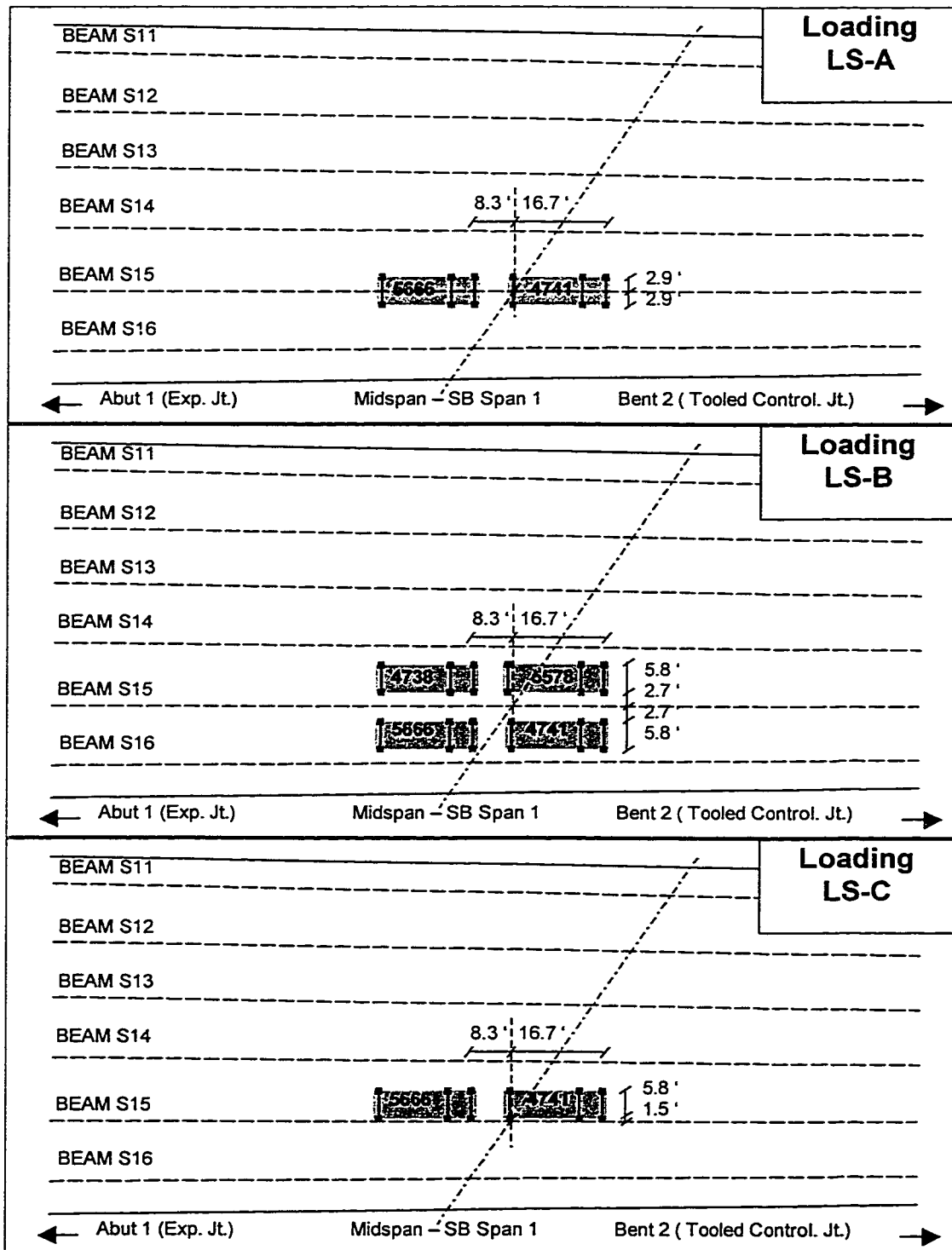
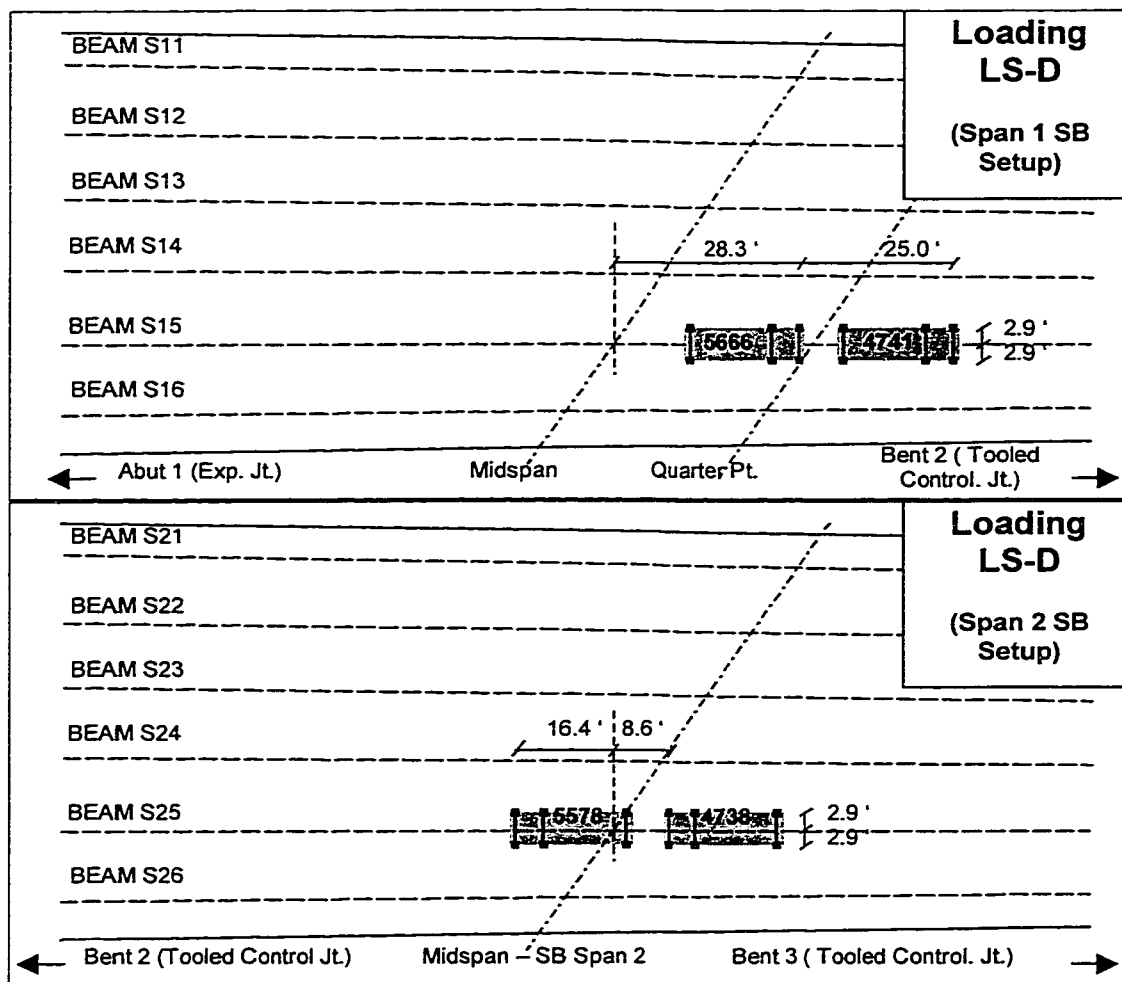


Figure 9.6 - Loading Arrangements for Louetta Live Load Tests



Note: Loading LS-D consists of two trucks with resultant load at quarter point of Beam S15 and two trucks with resultant load at midspan of Beam S25.

Figure 9.6 (continued) - Loading Arrangements for Louetta Live Load Tests

Table 9.2 - Description of Loading Arrangements

<i>San Angelo</i>	
SW-A	One truck pair centered over Beam W16 near midspan of WB Span 1. For general comparison with Loadings SE-A1 and SE-A2.
SE-A1 SE-A2	One truck pair centered over Beam E13 near midspan of EB Span 1. Loading repeated twice at different times during testing.
SE-B	Two truck pairs placed near midspan of EB Span 1. Outer edge of wheel lines for each truck pair at 2.0 ft. from centerline of Beam E13. Intended to produce approximately maximum stress in Beam E13.
SE-C	One truck pair centered over Beam E25 near midspan of EB Span 2.
SE-D	One truck pair centered over Beam E34 near midspan of EB Span 3.
SE-E	Loading SE-C and SE-D applied simultaneously. For investigation of possible continuity across Bent 3.
<i>Louetta</i>	
LS-A1 LS-A2	One truck pair centered over Beam S15 near midspan of SB Span 1 (at Beam S15). Loading repeated twice at different times during testing.
LS-B	Two truck pairs placed near midspan of SB Span 1 (at Beam S15). Outer edge of wheel lines for each truck pair at 2.0 ft. from centerline of Beam S15. Intended to produce approximately maximum stress in Beam S15.
LS-C	One truck pair near midspan of SB Span 1 (at Beam S15). One wheel line centered halfway between Beams S14 and S15, other wheel line above Beam S15.
LS-D	One truck pair with resultant of loads at quarter-point of Beam E15 and one truck pair with resultant of loads at midspan of Beam S25. For investigation of possible continuity across Bent 2. If continuity exists, this loading should produce negative moment at Bent 2 and positive moment at midspan of Span 2.
1 ft. = 0.3048 m	

9.4 Discussion

Specific aspects of the responses observed during the San Angelo and Louetta live load tests are discussed in this section. The general magnitudes of the deflection and curvature responses are discussed first, followed by the distribution of load across a span, continuity, and transverse deck strains. As necessary, additional measurements are briefly presented to complement the main measurements listed in the tables of Section 9.3.

Table 9.3 - Main Live Load Test Measurements (Loading SE-A1)

SAN ANGELO LOADING SE-A1				
Beam	Measured Deflection ¹ (in.)	Measured Curvature ² ($\mu\epsilon$ /in.)	Moment Computed from Deflection (ft.-kips)	Moment Computed from Curvature (ft.-kips)
E11	-0.07		147	
E12	-0.17		384	
E13	-0.31	1.34	701	706
E14	-0.27	1.11	567	544
L/800	-1.97			
Total Computed Moment			1799	
Total Span Moment from Analysis			1875	
1 in. = 25.4 mm 1 ft.-kip = 14.59 kN/m				
¹ Negative values indicate downward deflection. All measurements at midspan.				
² Positive values indicate downward deflection. All measurements at midspan.				

Table 9.4 - Main Live Load Test Measurements (Loading SE-A2)

SAN ANGELO LOADING SE-A2				
Beam	Measured Deflection ¹ (in.)	Measured Curvature ² ($\mu\epsilon$ /in.)	Moment Computed from Deflection (ft.-kips)	Moment Computed from Curvature (ft.-kips)
E11	-0.08		168	
E12	-0.18		407	
E13	-0.33	1.50	746	788
E14	-0.30	1.18	630	579
L/800	-1.97			
Total Computed Moment			1951	
Total Span Moment from Analysis			1875	
1 in. = 25.4 mm 1 ft.-kip = 14.59 kN/m				
¹ Negative values indicate downward deflection. All measurements at midspan.				
² Positive values indicate downward deflection. All measurements at midspan.				

Table 9.5 - Main Live Load Test Measurements (Loading SE-B)

SAN ANGELO LOADING SE-B				
Beam	Measured Deflection ¹ (in.)	Measured Curvature ² ($\mu\epsilon$ /in.)	Moment Computed from Deflection (ft.-kips)	Moment Computed from Curvature (ft.-kips)
E11	-0.21		442	
E12	-0.44		997	
E13	-0.58	2.71	1314	1428
E14	-0.58	2.45	1220	1201
L/800	-1.97			
Total Computed Moment			3973	
Total Span Moment from Analysis			3783	
1 in. = 25.4 mm 1 ft.-kip = 14.59 kN/m				
¹ Negative values indicate downward deflection. All measurements at midspan.				
² Positive values indicate downward deflection. All measurements at midspan.				

Table 9.6 - Main Live Load Test Measurements (Loading SW-A)

SAN ANGELO LOADING SW-A				
Beam	Measured Deflection ¹ (in.)	Measured Curvature ² ($\mu\epsilon$ /in.)	Moment Computed from Deflection (ft.-kips)	Moment Computed from Curvature (ft.-kips)
W11	-0.01		17	
W12	-0.03		48	
W13	-0.08		127	
W14	-0.15		238	
W15	-0.23		366	
W16	-0.30	1.07	484	403
W17	-0.33	1.16	546	448
L/800	-1.97			
Total Computed Moment			1825	
Total Span Moment from Analysis			1875	
1 in. = 25.4 mm 1 ft.-kip = 14.59 kN/m				
¹ Negative values indicate downward deflection. All measurements at midspan.				
² Positive values indicate downward deflection. All measurements at midspan.				

Table 9.7 - Main Live Load Test Measurements (Loading SE-C)

SAN ANGELO LOADING SE-C				
Beam	Measured Deflection ¹ (in.)	Measured Curvature ² ($\mu\epsilon$ /in.)	Moment Computed from Deflection (ft.-kips)	Moment Computed from Curvature (ft.-kips)
E21	- 0.13		203	
E22	- 0.33		483	
E23	- 0.42		615	
E24	- 0.52		762	
E25	- 0.59	1.27	861	602
E26	- 0.65		1014	
L/800	- 2.36			
Total Computed Moment			3938	
Total Span Moment from Analysis			2395	
1 in. = 25.4 mm 1 ft.-kip = 14.59 kN/m				
¹ Negative values indicate downward deflection. All measurements at midspan.				
² Positive values indicate downward deflection. All measurements at midspan.				

Table 9.8 - Main Live Load Test Measurements (Loading SE-D)

SAN ANGELO LOADING SE-D				
Beam	Measured Deflection ¹ (in.)	Measured Curvature ² ($\mu\epsilon$ /in.)	Moment Computed from Deflection (ft.-kips)	Moment Computed from Curvature (ft.-kips)
E31	- 0.08		106	
E32	- 0.22		345	
E33	- 0.35		548	
E34	- 0.37		580	
E35	- 0.40	1.16	532	458
L/800	- 2.25			
Total Computed Moment			2111	
Total Span Moment from Analysis			2287	
1 in. = 25.4 mm 1 ft.-kip = 14.59 kN/m				
¹ Negative values indicate downward deflection. All measurements at midspan.				
² Positive values indicate downward deflection. All measurements at midspan.				

Table 9.9 - Main Live Load Test Measurements (Loading SE-E, Span 2)

SAN ANGELO LOADING SE-E (Span 2)				
Beam	Measured Deflection ¹ (in.)	Measured Curvature ² ($\mu\epsilon$ /in.)	Moment Computed from Deflection (ft.-kips)	Moment Computed from Curvature (ft.-kips)
E21	-0.11		172	
E22	-0.29		425	
E23	-0.38		557	
E24	-0.48		703	
E25	-0.51	1.42	745	671
E26	-0.61		952	
L/800	-2.36			
Total Computed Moment			3552	
Total Span Moment from Analysis			2395	
1 in. = 25.4 mm 1 ft.-kip = 14.59 kN/m				
¹ Negative values indicate downward deflection. All measurements at midspan.				
² Positive values indicate downward deflection. All measurements at midspan.				

Table 9.10 - Main Live Load Test Measurements (Loading SE-E, Span 3)

SAN ANGELO LOADING SE-E (Span 3)				
Beam	Measured Deflection ¹ (in.)	Measured Curvature ² ($\mu\epsilon$ /in.)	Moment Computed from Deflection (ft.-kips)	Moment Computed from Curvature (ft.-kips)
E31	-0.13		173	
E32	-0.19		298	
E33	-0.31		486	
E34	-0.43		674	
E35	-0.47	1.07	626	421
L/800	-2.25			
Total Computed Moment			2255	
Total Span Moment from Analysis			2287	
1 in. = 25.4 mm 1 ft.-kip = 14.59 kN/m				
¹ Negative values indicate downward deflection. All measurements at midspan.				
² Positive values indicate downward deflection. All measurements at midspan.				

Table 9.11 - Main Live Load Test Measurements (Loading LS-A1)

LOUETTA LOADING LS-A1					
Beam (Span 1)	Measured Deflection ¹ (in.)	Measured Curvature ² ($\mu\epsilon/\text{in.}$)	Beam (Span 2)	Measured Deflection ¹ (in.)	Measured Curvature ² ($\mu\epsilon/\text{in.}$)
S11	0.02		S21	- 0.03	
S12	0.10		S22	0.07	
S13	0.04		S23	0.06	
S14	- 0.02		S24	N/A ³	
S15	- 0.10	0.91	S25	N/A ³	- 0.13
S16	- 0.14		S26	N/A ³	
L/800	- 1.82		L/800	- 2.03	

1 in. = 25.4 mm

¹ Negative values indicate downward deflection. All measurements taken at midspan of individual beams (along skew). Average of readings from each web of U-beam.

² Positive values indicate downward deflection. All measurements at midspan.

³ Bad reading

Table 9.12 - Main Live Load Test Measurements (Loading LS-A2)

LOUETTA LOADING LS-A2					
Beam (Span 1)	Measured Deflection ¹ (in.)	Measured Curvature ² ($\mu\epsilon/\text{in.}$)	Beam (Span 2)	Measured Deflection ¹ (in.)	Measured Curvature ² ($\mu\epsilon/\text{in.}$)
S11	0.05		S21	0.03	
S12	0.07		S22	0.03	
S13	0.02		S23	0.04	
S14	- 0.06		S24	0.08	
S15	- 0.12		S25	0.08	
S16	- 0.12		S26	0.07	
L/800	- 1.82		L/800	- 2.03	

1 in. = 25.4 mm

¹ Negative values indicate downward deflection. All measurements taken at midspan of individual beams (along skew). Average of readings from each web of U-beam.

² Positive values indicate downward deflection. All measurements at midspan.

Table 9.13 - Main Live Load Test Measurements (Loading LS-B)

LOUETTA LOADING LS-B					
Beam (Span 1)	Measured Deflection ¹ (in.)	Measured Curvature ² ($\mu\epsilon/\text{in.}$)	Beam (Span 2)	Measured Deflection ¹ (in.)	Measured Curvature ² ($\mu\epsilon/\text{in.}$)
S11	0.07		S21	0.04	
S12	0.08		S22	0.09	
S13	0.01		S23	0.07	
S14	-0.17		S24	0.01	
S15	-0.31	1.75	S25	0.05	-0.04
S16	-0.21		S26	0.04	
L/800	-1.82		L/800	-2.03	

1 in. = 25.4 mm

¹ Negative values indicate downward deflection. All measurements taken at midspan of individual beams (along skew). Average of readings from each web of U-beam.

² Positive values indicate downward deflection. All measurements at midspan.

Table 9.14 - Main Live Load Test Measurements (Loading LS-C)

LOUETTA LOADING LS-C					
Beam (Span 1)	Measured Deflection ¹ (in.)	Measured Curvature ² ($\mu\epsilon/\text{in.}$)	Beam (Span 2)	Measured Deflection ¹ (in.)	Measured Curvature ² ($\mu\epsilon/\text{in.}$)
S11	-0.02		S21	0.05	
S12	-0.02		S22	0.01	
S13	-0.05		S23	0.03	
S14	-0.10		S24	0.00	
S15	-0.14	1.14	S25	0.06	-0.04
S16	-0.07		S26	0.02	
L/800	-1.82		L/800	-2.03	

1 in. = 25.4 mm

¹ Negative values indicate downward deflection. All measurements taken at midspan of individual beams (along skew). Average of readings from each web of U-beam.

² Positive values indicate downward deflection. All measurements at midspan.

Table 9.15 - Main Live Load Test Measurements (Loading LS-D)

LOUETTA LOADING LS-D					
Beam (Span 1)	Measured Deflection ¹ (in.)	Measured Curvature ² ($\mu\epsilon/\text{in.}$)	Beam (Span 2)	Measured Deflection ¹ (in.)	Measured Curvature ² ($\mu\epsilon/\text{in.}$)
S11	0.09		S21	0.06	
S12	0.08		S22	0.05	
S13	0.08		S23	0.04	
S14	- 0.07		S24	- 0.05	
S15	- 0.13	0.50	S25	- 0.11	0.58
S16	- 0.05		S26	- 0.08	
L/800	- 1.82		L/800	- 2.03	
1 in. = 25.4 mm					
¹ Negative values indicate downward deflection. All measurements taken at midspan of individual beams (along skew). Average of readings from each web of U-beam.					
² Positive values indicate downward deflection. All measurements at midspan.					

9.4.1 General Magnitudes of the Deflection and Curvature Responses

The magnitudes of the deflections during each loading of the San Angelo live load tests were relatively small, indicating that the bridges are rather stiff. Despite the very long spans and large beam spacing in the Eastbound Bridge, deflections of no more than 17 mm (0.65 in.) were measured for any of the loadings. All beam deflections were less than 30 percent of the suggested AASHTO [1,3] L/800 limit for live load deflections. Although higher deflections would be expected under full loading across the span and with dynamic (impact) effects included, it is clear that the total deflections would not exceed the AASHTO limit. In fact, beam deflections are likely to be significantly lower than the L/800 limit since additional truck loads would be positioned over the beams which were less heavily loaded during the live load tests. (Note that lane loading actually governs for the very long spans in the San Angelo bridges with lengths greater than about 43 m (140 ft.), but this should not cause a large increase in deflection relative to HS20-44 truck loading across the span and deflections should still be well below the L/800 limit. Live load reduction for multiple loaded lanes would also be beneficial in reducing the total deflections.)

The individual beam deflections measured during Loading SE-A1 and SE-A2 in Span 1 of the San Angelo Eastbound HPC bridge were very similar in magnitude to the individual beam deflections measured during Loading SW-A in Span 1 of the San Angelo Westbound non-HPC bridge. The maximum individual beam deflections for Loading SE-A1, SE-A2, and SW-A were 7.9, 8.4, and 8.4 mm (0.31, 0.33, and 0.33 in.), respectively. These spans have identical total span length, but only four Type IV beams were used in the Eastbound Span 1 while seven Type IV beams were used in the Westbound Span 1. Clearly, this implies that there is not a major impact on live load deflections when HPC is implemented to reduce the number of beams in a span.

The magnitudes of the deflections measured during the Louetta live load tests were also very small. The Louetta Southbound bridge is clearly very stiff, in part due to the high stiffness of the U-beams and in part due to the skewed geometry of the bridge. In fact, the magnitudes of the deflections are difficult to distinguish from the magnitudes of potential measurement errors associated with the tolerance of the precise surveying system and possible thermal gradient effects. Small upward deflections (cambers) were measured for many beams in the unloaded areas of the Louetta bridges for each loading arrangement, indicating the probable presence of thermal effects. Considering the scatter in the deflection measurements for the Louetta live load tests, conclusions should only be drawn regarding the very small magnitude of the deflection responses.

For most San Angelo loading arrangements, there was good agreement between the sum of the beam moments (within a span) calculated from the measured deflections and the total span moment computed during analysis. There was also generally good agreement between the individual beam moments calculated using measured deflections and beam moments calculated using measured curvatures (for those beams in which curvatures were measured). To a large extent, this can be viewed as a verification of the calculated composite section properties.

Only for measurements in Span 2 of the San Angelo Eastbound HPC bridge was there not good correlation between these calculated moments. For this span, the moments calculated from beam deflections appear to be rather high compared to the total span moment computed in the structural analysis and the individual beam moments calculated from measured curvatures. These high values may be due to additional deflections related to thermal gradients (over the time between the loaded measurements and the unloaded

measurements, which were recorded *after* loading and during the afternoon) or due to variations between the actual and calculated composite section properties.

9.4.2 Distribution of Loads

The beam moments calculated from the measured deflections can be used to examine the distribution of loads between the beams in a span during each loading. For all of the loading arrangements in the San Angelo live load tests, there was a substantial distribution of load across the span and all beams carried at least a portion of the total span moment. As a result, a relatively low percentage of the total load was typically carried by the beam over which the test trucks were centered (in loading arrangements using a single truck pair). For example, the percentage of total span moment carried by the first interior beam (over which the test trucks were centered) was only 39, 27, 22, and 27 percent, respectively, for Loadings SE-A1, SE-D, SE-C, and SW-A. In the order stated, these loadings correspond to spans with 4, 5, 6, and 7 beams, respectively, and a total roadway width of 12.2 m (40.0 ft.). Despite the higher fraction of the total span moment carried by the "loaded" beam (39 percent for Loading SE-A1), there was still clearly a good distribution of load in Span 1 of the Eastbound bridge, which has a very large beam spacing of 3.35 m (11.0 ft.). When two truck pairs were positioned with the outer edges of their interior wheel line 0.6 m (2.0 ft.) from the centerline of the first interior beam, as in Loading SE-B, this fraction was reduced to 33 percent of the moment from two truck pairs.

Few major conclusions can be drawn regarding the distribution of load across the beams in the Louetta Southbound bridge. Based on the deflection measurements alone, it appears that the loads positioned over the first interior beam (Beam S15) were resisted primarily by that beam and the adjacent beam on either side (Beams S14 and S16). The beams toward the opposite (unloaded) side of the span actually exhibited a slight upward deflection (camber) during all loading arrangements. This upward deflection (camber) is probably due to thermal gradient effects, but does indicate that there is little, if any, contribution of these beams in resisting the load over Beam S15. The large beam spacing and relatively large stiffness of each U-beam might contribute to this limited "influence area" for each loading. It is also quite likely, however, that the deflection behavior in the span is strongly affected by the skew, so these conclusions must be taken with caution.

9.4.3 Continuity

Specific loading arrangements were selected for the live load tests on each bridge to investigate possible structural continuity across interior bents. The bridge decks in both the Louetta and San Angelo bridges were constructed using “poor-boy” continuity, in which the cast-in-place deck is somewhat continuous over certain bents. The continuity is largely dependent on deck reinforcement across the bent and is not typically counted on during design (i.e. all designs consider spans to be simply-supported for all loads, including live load). This construction method is commonly used in Texas for the construction of decks in precast prestressed girder-and-slab highway bridges.

Two different types of poor-boy joints were utilized in the two bridges. In the Louetta bridge, the deck was cast using a continuous placement of concrete and a tooled control joint was placed at the bent to control cracking. In the San Angelo bridge, each deck span was cast in a different pour and a cold construction joint was located at the bent (with a minimum amount of reinforcement across the joint). In either case, there is no connection between the *beams* in adjacent spans and the beams are supported on elastomeric bearing pads. These bearing pads are generally quite flexible, and accommodate movements of the beams without the development of significant restraint forces.

For the San Angelo bridges, the level of structural continuity can be established largely by examining the main measurements (deflections and curvatures) from Loadings SE-C, SE-D, and SE-E. These loadings correspond to test trucks placed in Span 2, Span 3, and *both* Spans 2 and 3 of the Eastbound bridge, respectively. Spans 2 and 3 are “connected” by poor-boy slab across Bent 3, and expansion joints are located at Bents 2 and 4. Deflections in the beams of Span 2 were almost identical for Loadings SE-C and SE-E (with trucks positioned on Span 2), and deflections in the beams of Span 3 were almost identical for Loadings SE-D and SE-E (with trucks positioned on Span 3). Similarly, there was negligible deflection in Span 2 when Span 3 was loaded and vice versa. If any structural continuity was present, there would at least be some level of load carried over to adjacent spans and deflections would result, but this was clearly not the case. Curvature measurements showed the same trends, with Spans 2 and 3 essentially behaving independently of each other and not as a two-span continuous unit.

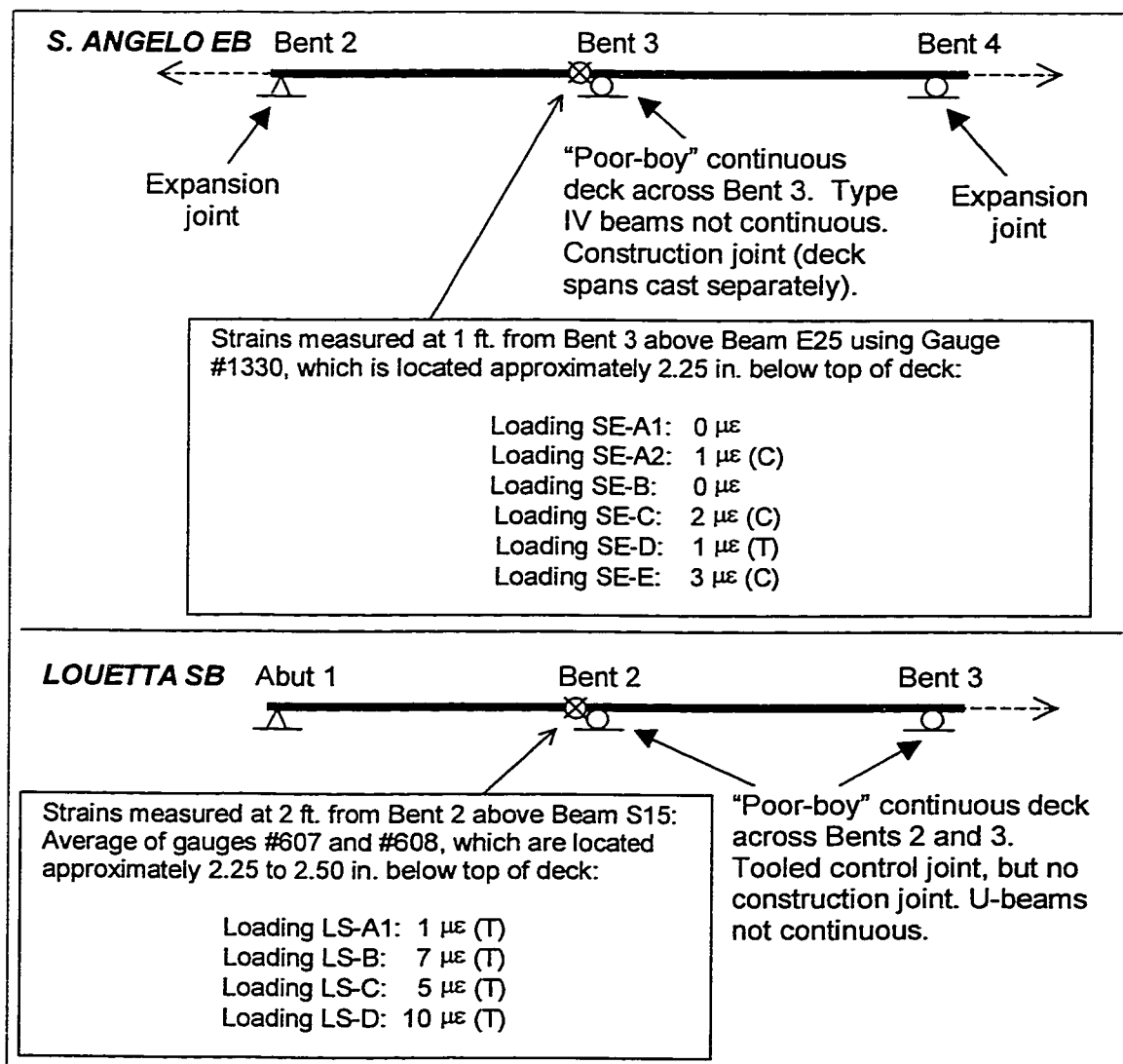


Figure 9.7 - Deck Strain Measurements Near "Poor-Boy" Continuous Bents

Vibrating wire strain gauges placed in the cast-in-place deck of the San Angelo bridge were also used to establish the level of continuity. As shown in Figure 9.7, a gauge was placed very close to the poor-boy construction joint in the cast-in-place deck, approximately 57 mm (2.25 in.) below the top of the deck. Any structural continuity would tend to produce a tensile strain at the level of the gauge, but almost no strain of any orientation was recorded during any of the loading arrangements (after correction for

relatively small temperature fluctuations at the gauge location during each unloading-loading cycle). It can therefore be concluded that no structural continuity is provided by the San Angelo poor-boy joints. These cold construction joints with minimal continuous reinforcement essentially do not provide any mechanism for the transfer of forces across the bent, and the spans behave as if they were simply-supported.

Similar observations were made during the static live load tests on the Louetta Southbound HPC bridge. Vibrating wire gauges placed in the cast-in-place deck near Bent 2 registered very small tensile strains for all loading arrangements, as shown in Figure 9.7, with a maximum strain of $10 \mu\epsilon$ recorded during Loading LS-D. This loading was intended to investigate continuity, and combined trucks positioned near the quarter point of Beam S15 in Span 1 with trucks positioned near midspan of Beam S25 in Span 2. Continuity would lead to a negative moment at the poor-boy joint and tensile strains in the deck at the gauge locations.

Even though tensile strains were recorded at the gauges, their magnitude is very small. This indicates that little force, if any, is transferred across the poor-boy tooled control joint and the bridge thus behaves as if it were simply supported. It is possible that the level of structural continuity across the bent would be somewhat higher if the tooled control joint were not located at the bent, since the concrete deck was poured continuously across the bent, but it is unlikely that there would be a significant impact on stresses and deflections within the spans.

It is also quite possible that some structural continuity would be present if the beam supports were not flexible and allowed for the development of restraint forces. A force couple might then be developed between the support and the deck, and a substantially larger moment could potentially be developed than in the deck slab alone. In both the Louetta and San Angelo bridges, the beams were supported on elastomeric bearing pads, which are quite flexible and do not allow for the development of such forces. In these bridges, any force transferred across the bent is essentially transferred only through the deck slab, and only a very small moment can therefore be developed.

9.5 Summary and Conclusions

The following observations were made in this chapter regarding Static Live Load Tests:

- 1) All beam deflections measured during static live load tests were relatively small in magnitude. No beam deflection was more than 30 percent of the AASHTO [1,3] L/800 live load deflection limit for any loading arrangement. Even if full design live loads (i.e. all design lanes loaded) were applied, it is very likely that deflections would still be substantially below this limit.
- 2) There was no significant difference between the maximum beam deflections recorded during Loadings SE-A1 and SE-A2 in Span 1 of the San Angelo Eastbound HPC bridge and Loading SW-A in Span 1 of the San Angelo Westbound non-HPC bridge. This indicates that the use of HPC to reduce the number of Type IV beams in the span from seven to four had almost no effect on live load deflections.
- 3) There was good distribution of load in the San Angelo bridges, as determined by computing individual beam moments from measured deflections. Although a higher percentage of the total span moment was resisted by each beam in the spans with larger beam spacing, there was still good distribution of load to the unloaded side of the span. In no case did a single beam resist more than 39 percent of the total span moment, even though the truck was centered over that beam.
- 4) In the Louetta Southbound HPC bridge, load did not appear to be transferred all the way across the span. Instead, the beam over which test trucks were centered and the adjacent beams on each side resisted almost all of the load. Behavior in the Louetta bridge may be affected by the large beam spacing, wide total roadway width, and skewed geometry of the bridge, as well as the stiffness of the composite U-beams.
- 5) Based on both strain and deflection measurements, there appears to be no structural continuity across the “poor-boy” construction (deck) joints in the San Angelo bridges. Although there was continuous reinforcement across the joints, deck spans were cast separately such that there was a construction joint at the bents with poor-boy joints. Almost no force appeared to be transferred across these joints.

- 6) There may be a very small transfer of force across the “poor-boy” tooled control joints at the interior bents of the Louetta bridges. Still, it appears that any structural continuity across these joints is essentially negligible. Although the deck in the Louetta bridges was placed continuously, a tooled control joint was placed at each bent. The cracking provoked at these locations reduces the degree of structural continuity across these poor-boy joints to a large extent.
- 7) Some degree of structural continuity might have been developed if beams were not supported on flexible elastomeric bearing pads. Both the Louetta and San Angelo bridges utilized elastomeric bearing pads for the support of beams, and any force transferred across the poor-boy joints was essentially transferred through the deck slab alone.

9.6 Recommendations

The following recommendations are made on the basis of the information presented in this chapter regarding Static Live Load Tests:

No changes to current design procedures are recommended on the basis of the static live load tests discussed in this chapter. The tests were relatively limited in scope and conclusions drawn from them should be taken with caution. It is recommended that “poor-boy” deck continuity be neglected in designs of bridges of this type (assuming the same basic construction procedures and applications of poor-boy continuity as used in the Louetta and San Angelo bridges, including the use of elastomeric bearing pads), since it appears that any structural continuity is negligible. All spans should be treated as simply-supported spans for all loads, including live loads. This recommendation is consistent with the current practice of TxDOT, and does not represent a suggested change to design procedures.

10 CHAPTER TEN: COMPARISON OF THE BRIDGES

10.1 Introduction

One of the most important conclusions in this entire research program is the simple fact that the Louetta Road Overpass and (San Angelo) North Concho River/U.S. 87/S.O.R.R. Overpass represent the successful implementation of high performance concrete in highway bridge structures. HPC was utilized in both projects in the design and construction of an efficient bridge structure, and hopefully a structure with excellent long-term durability and an extended service life. Still, the two bridges represent distinctly different methods of implementing HPC in terms of structural design, and are decidedly different in terms of cross-sections, span lengths, beam spacings, concrete strengths, and other parameters. A critical comparison of the two bridges is invaluable for examining how HPC might *best* be implemented in the design and construction of prestressed concrete highway bridge structures.

This chapter presents such a comparison in terms of several design- and construction-related issues. For the most part, emphasis is on qualitative observations regarding major considerations not addressed in previous chapters. The behavior of each bridge with respect to concrete temperatures, concrete strains (and stresses), prestress losses, and deflection behavior has been discussed in detail in Chapters 5 through 8, respectively, and is not addressed here. Some of the observations from these chapters have been considered in the recommendations at the end of this chapter, however. Materials-related issues, such as concrete placement and quality control issues are also not addressed here, but are covered by Myers and Carrasquillo [88].

Beam fabrication issues are discussed first in this chapter, followed by issues related to handling and stability of the beams. Overall project costs are summarized, and then ultimate strength and ductility are examined briefly. Finally, an overall summary comparing the two bridge projects is presented, and recommendations are made regarding the implementation of HPC in future prestressed highway bridge structures.

10.2 Beam Fabrication Issues

As discussed in Section 1.4.2, the implementation of HPC for prestressed concrete highway girders necessitates the use of higher prestress forces in order to make use of the higher available concrete strengths. These higher prestress forces may require certain adjustments to standard fabrication practices, including the upgrade of existing prestressing bed capacities, the possible use of dual stage (pretension/post-tension) fabrication, and the use of larger diameter strands. All of these considerations were present during the fabrication of HPC girders for one or both of the bridges discussed in this dissertation.

The designs for the Louetta HPC U-beams called for as many as 87 15 mm (0.6 in.) diameter pretensioned strands stressed to an initial stress of 1396 MPa (202.5 ksi). The total initial prestress force for these beams was thus greater than 17 MN (3,800 kips), and few if any prestressing beds in the state of Texas can accommodate such a force. The only bed with such capacity at Texas Concrete Company, the fabricator for the Louetta and San Angelo HPC beams, had a 17.8 MN (4000 kip) capacity but was set up to pour two lines of Type IV beams at a 8.9 MN (2000 kip) capacity for each line [102]. The stressing plates and abutments thus had to be modified to accommodate this high prestressing force, at a total cost of approximately \$100,000. It is clear that such costly upgrades will be necessary if HPC is to become the norm, but these overhead costs can be justified by distributing the cost over many beams. In this particular case, the fabricator now has the capacity to fabricate almost any HPC U-beam.

Similar upgrades to existing prestress beds were required for the original designs of the San Angelo Eastbound HPC beams. The original designs for these beams called for as many as 84 15 mm (0.6 in.) diameter pretensioned strands, with a total initial force of almost 16.5 MN (3,700 kips). Because these designs were for AASHTO Type IV beams, extensive bed modifications would have been necessary to upgrade the aforementioned 17.8 MN (4000 kip) capacity bed to handle a single line of beams. These upgrades also would have cost approximately \$100,000 [102], so the fabricator elected to use a dual stage (pretension/post-tension) option to fabricate the HPC beams. Pretensioning was applied up to the existing bed capacity, and the remaining prestress was applied through post-tensioning within one month after casting. Note that this dual-stage fabrication method is *not* typically used in Texas.

There are obvious advantages and disadvantages to the dual-stage fabrication process used for the San Angelo HPC beams. Advantages include the use of existing stressing hardware without bed modifications, reduced concrete release strength requirements, and possible increased strand efficiency (i.e. eccentricity) by grouping strands into a multi-strand tendon for post-tensioning. Disadvantages include the labor involved in a second stressing operation for each individual beam, and the additional time and cost during fabrication associated with installing post-tensioning ducts and anchorage zone reinforcement to accommodate the post-tensioning forces.

On the basis of the observations in this research program, the benefits of dual-stage fabrication simply did not outweigh the drawbacks. For the fabrication of the San Angelo beams, these additional considerations lengthened the duration of the fabrication cycle for each beam pour to as much as seven days. The typical fabrication cycle at the plant is about two days for Type IV beams and about three days for U-beams. Small reductions in the required release strength and very slight increases in strand efficiency did result, but certainly did not compensate for the delays in the fabrication cycle. Furthermore, any cost to upgrade existing stressing hardware is an overhead cost and can be distributed among many beams, as discussed previously. For the implementation of HPC in future bridge projects, it simply makes more sense to modify the fabrication hardware than to modify the fabrication procedure for every beam.

Other concerns are related more specifically to the use of 15 mm (0.6 in.) strand, which is essential in obtaining the high prestress forces required for HPC designs. Concerns over bond and development have been ongoing and have been examined recently in several studies. Issues related to transfer length are important at the release of pretensioning in HPC beams, but no bond (splitting) cracking was observed at release in the actual bridge beams. In fact, very low transfer lengths were measured on prototype and test beams throughout this research program [23,46,58]. Development length issues do not really apply to the HPC beams in these bridges because of the extremely large span lengths involved.

Some fabricators in Texas have also expressed safety concerns related to draping 15 mm (0.6 in.) diameter strands, although these strands are currently being draped in some states for the fabrication of HPC beams. While this may or may not be a legitimate concern, it should be recognized that debonding could still be used to control release stresses if strands are not draped. In fact, debonding *must* be used in U-beams and many

other trapezoidal sections because these sections cannot accommodate draped strands. Therefore, this concern should not be a problem for future HPC designs.

10.3 Handling Issues

Three basic factors can affect the handling of HPC prestressed beams. The length, weight, and lateral stability of HPC beams may be different than for conventional beams, and may require additional considerations during fabrication and construction. In particular, handling of the beams at the prestressing plant, transportation of the beams from the plant to the jobsite, and erection of the beams at the jobsite all may be affected to some degree. The extent to which current (standard) handling procedures must be modified to accommodate HPC designs will clearly have a strong impact on the future use of HPC for prestressed highway bridge beams.

Lateral stability of prestressed concrete beams is essentially an issue of roll equilibrium, and differs from stability concerns related to members with low torsional rigidity such as steel wide-flange beams. Roll equilibrium is summarized graphically in Figure 10.1. When a prestressed beam is lifted and supported by cables, the beam will have a tendency to rotate about a *roll axis*. The roll axis is the imaginary line passing through the lifting points at each end of the beam, which are usually taken at the top fiber of the section. Slight initial imperfections in the fabricated beam, or effects such as (horizontal) thermal gradients, will cause a small initial movement out of plane. When the beam moves out of plane, it must rotate (about the roll axis) to maintain equilibrium, and this rotation in turn causes an additional out of plane movement because some of the self-weight is transferred from the strong axis to the weak axis. In most cases, a state of equilibrium like that shown in Figure 10.1 will eventually be established, but if the flexural stiffness in the weak direction is low then the beam may continue to rotate and deflect until it fails.

The problem of lateral instability in long, slender prestressed beams lifted by cables has been investigated by Swann and Godden [127] and in a more practical form by Anderson [17] and Mast [80]. The basic principles outlined by Mast also provide the basis for a simplified design approach suggested in the *PCI Design Manual* [108]. Mast showed that at the most fundamental level, lateral stability is essentially a function of the ratio between the distances y_r and \bar{z} , which are defined in Figure 10.1. Both of these

parameters are based on the section properties of the beam; the distance y_r is a function of the section properties about the strong axis, while the distance \bar{z} is a function of the section properties about the weak axis. The length, weight, and modulus of elasticity of the member also affect the parameter \bar{z} , since it is essentially a computed deflection. In simple terms, the higher the ratio of y_r to \bar{z} is, the greater the factor of safety against instability. The lower this ratio becomes, the greater the chance of buckling.

Specific equations for this basic analysis may be found in the paper by Mast [80]. Mast [80] and Anderson [17] also suggested how resistance to lateral instability can be improved. Aside from modifying the beam cross-section and increasing the modulus of elasticity, they suggest three basic methods for increasing the stability of long beams. These methods include raising the roll axis by means of a rigid lifting attachment, moving lifting points inward from the ends of the beam, and providing temporary bracing.

\bar{z} = deflection of beam c.g. about weak axis due to W_y (avg. along span, not max. deflection)
 e_i = initial eccentricity of beam c.g. from roll axis
 y_r = distance from roll axis to c.g. of beam (at lifting point)

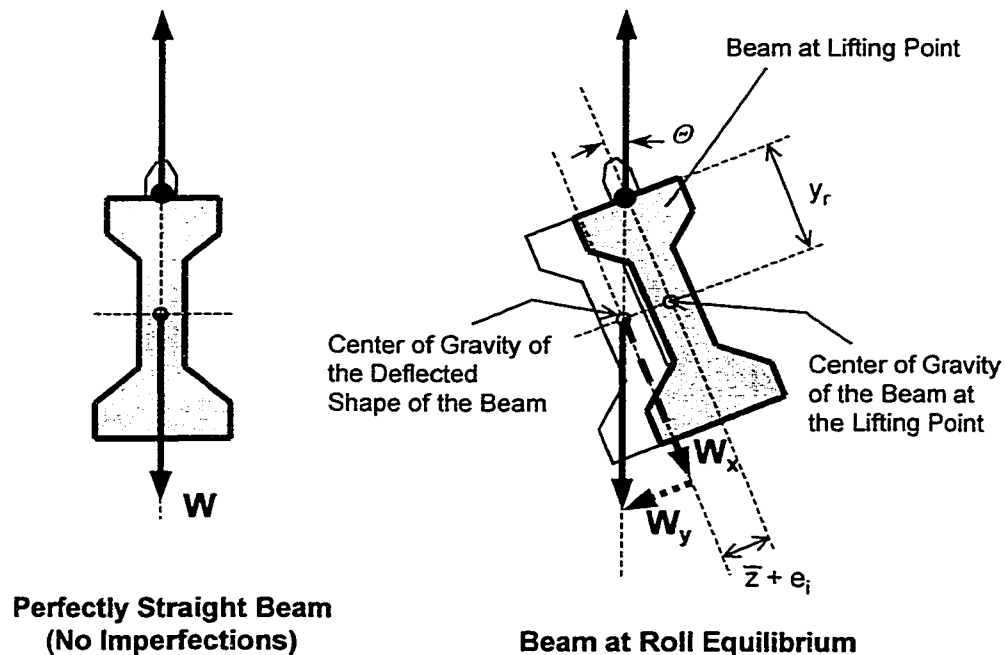


Figure 10.1 - Prestressed Beam at Roll Equilibrium

Mast also investigated the lateral stability of long beams supported from below by elastic supports [81], such as when beams are in storage or being transported. The solution for determining the potential of stability problems for beams in this condition was found to be much different than for beams lifted by cables, and was found to be more a function of the properties of the support than those of the beam itself. Mast found that most prestressed beams were able to undergo a much larger rotation than could be accommodated by ordinary supports such as bearing pads and transportation equipment. A procedure for investigating this stability condition is outlined in the paper by Mast [81]. The procedure is considerably more complex than for beams supported by cables from above.

Mast's recommendations [80,81] were considered by the fabricator for the successful handling of the long San Angelo Eastbound HPC Type IV beams, which had lengths of up to 47 m (153 ft.). As can be seen in Figure 10.2, a rigid lifting frame was utilized during all handling operations at the prestressing plant. This frame was "fixed" to the beam using shims, such that the frame and beam would rotate together about a roll axis much higher than if the beam were lifted by cables alone. The use of this frame was very effective, and the fabricator did not encounter any problems during handling at the plant. All handling operations still required a great deal of care and caution, however.

The rigid lifting frames could not be used for transportation of the beams or the actual erection of the beams at the jobsite. Thus, two other steps were taken to decrease the potential for instability problems. First, the lifting points for cables were moved in to a distance of 4.0 m (13 ft.) from the beam ends. The use of these lifting points reduced the beam deflection about the weak axis, due to any rotation, by shortening the effective span. In addition, six pretensioned strands were incorporated into the top flange of the beam during design. These strands were bonded only over the 6.1 m (20 ft.) at each end of the beam, but were stressed (and thus effective) over the remaining portion of the span until being cut *after* erection. These strands provided an additional temporary precompression in the top flange. Although there were no tensile stresses in the top flange due to prestressing alone (for these particular beam designs), this portion of the beam has the least compression and would experience some tension under roll instability. This temporary prestress thus acted as an additional factor of safety against cracking and failure of the beam.



Figure 10.2 - Use of Rigid Lifting Frame for Handling of San Angelo Eastbound HPC Type IV Beams at Prestressing Plant



Figure 10.3 - Transportation of San Angelo Eastbound HPC Type IV Beams

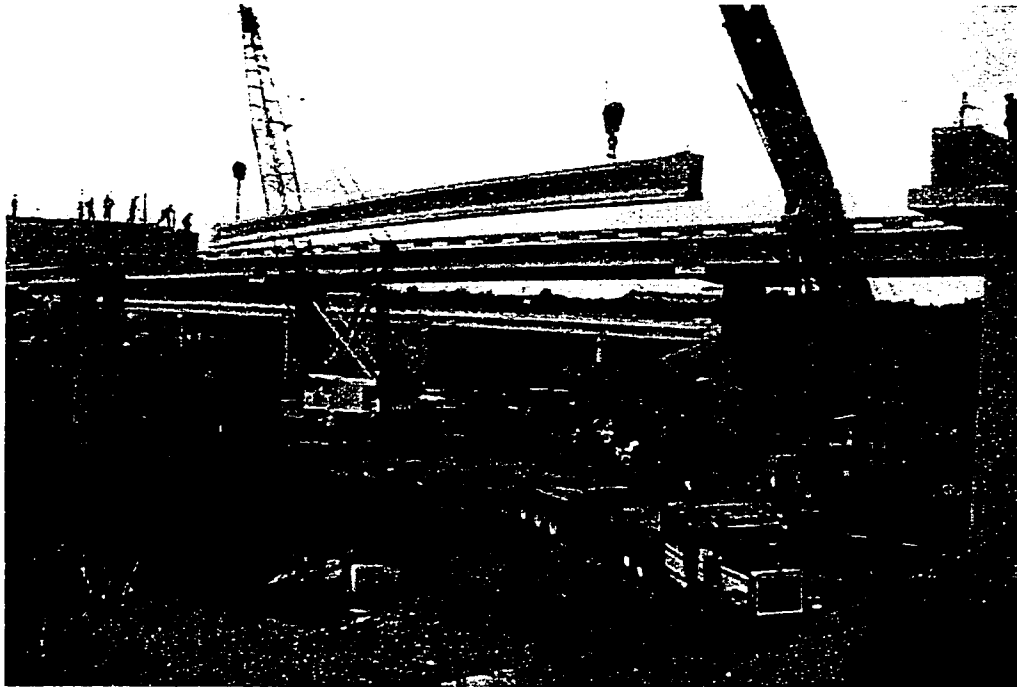


Figure 10.4 - Erection of San Angelo Eastbound HPC Type IV Beams at Jobsite

As with handling of the beams at the prestressing plant, the transportation and erection of the San Angelo Eastbound HPC Type IV beams required extreme care. The transportation and erection of one of these beams can be seen in Figure 10.3 and Figure 10.4, respectively. No problems were encountered during these operations except for the handling of one beam during initial lifting of the beam off the transport rig at the jobsite. This beam underwent a large degree of rotation when lifted using cables and deflected laterally, but was placed back down before it failed. Otherwise, the transportation and erection of these beams went rather smoothly, although the necessary precautions caused these operations to be much slower than for standard projects.

While stability issues had a definite impact on the San Angelo project, they were of no importance for the Louetta project. The Texas U-beam, as discussed in Section 2.2.2, has a very large moment-of-inertia about the y-axis (vertical axis). In fact, the moment of inertia of the U-beam is actually greater about the y-axis than the x-axis. Instability of the individual webs is prevented by the diaphragms cast as part of the beam itself. As a result, no special precautions were required to satisfy stability concerns during the handling of the Louetta U-beams, and transportation and erection operations were not adversely impacted.

Beam length and weight are also issues in terms of handling aspects that are not related to stability. Transportation of the San Angelo Eastbound HPC Type IV beams required numerous special considerations because of the extremely long lengths of these beams. The fabricator had to obtain special permitting, use special hauling rigs, and search for a route along which these beams could be transported from Victoria to San Angelo, Texas. Likewise, there were special considerations for the transportation of the Louetta HPC U-beams, although these concerns were primarily based on weight and the shipping distance was shorter. Special permits were required to ship these beams, and additional axles were required on hauling rigs to distribute the large weight of the beams.

Additionally, the increased weight of all HPC beams in the two projects, especially the Louetta HPC U-beams, had to be accommodated by special considerations during erection. The large beam weights require crane capacities much larger than for many standard projects. This was not a problem during the construction of the Louetta Road Overpass in Houston, since the bridge is located within a major metropolitan area where the equipment was available. However, the weight of the San Angelo HPC beams, in combination with the increased lifting heights required for beam erection in this bridge, meant that cranes with increased capacity had to be brought in from well outside San Angelo. This caused a substantial delay during the actual day(s) of beam erection, and was a substantial additional expense for the contractor.

10.4 Project Costs

High performance concrete bridges are expected to have a construction cost less than that of most similar conventional concrete bridges and a life-cycle cost substantially less than conventional concrete bridges. The reduced initial cost comes from more efficient structural designs, while the reduced life-cycle costs result from longer service lives and reduced maintenance. Although life-cycle costs will take several years to determine for the Louetta and San Angelo bridges, preliminary construction costs for the two bridges are available because jobsite construction is complete. These preliminary construction costs are summarized by Ralls [112], and are listed in Table 10.1.

Table 10.1 - Cost Summary for Louetta and San Angelo Bridge Projects

	Louetta		San Angelo	
	Louetta HPC Bridges (Northbound and Southbound)	Conventional Concrete Bridges on Same Highway Project	Eastbound HPC Bridge	Westbound Non-HPC Bridge
Unit Bridge Costs (per sq. ft. of deck)	\$24.09	\$23.61	\$47.39	\$40.91
% Difference	+2%	-	+16%	-
Beam Costs (per lineal ft.) *	\$100	\$100	\$186	\$90
1 ft. = 0.3048 m				
All costs reported by Ralls [112].				
* Beam costs for Louetta are based on bid including all beams, HPC and non-HPC. Beam costs for San Angelo are based on approximations using information supplied by fabricator and contractor. Bid cost for all San Angelo beams = \$115 per lineal ft.				

The data in Table 10.1 are based on as-bid costs for each bridge. Because the Eastbound HPC and Westbound non-HPC bridges of the San Angelo project were essentially part of a single bid, additional information was acquired from the contractors and fabricators by Ralls to estimate the actual total costs for each bridge. Based on this information, the approximate unit bridge costs (for the entire structure) were \$510 and \$440 per m² (\$47.39 and \$40.91 per ft.²) for the San Angelo Eastbound HPC and San Angelo Westbound non-HPC bridges, respectively. This represents an increase of approximately 16 percent when costs of the HPC bridge are compared to costs of the non-HPC bridge. Ralls [112] also notes that an approximate calculation for a fictitious conventional concrete bridge using the actual length and roadway width for the Eastbound HPC bridge resulted in only a 2 percent difference in cost from the Westbound bridge.

Clearly, there was an increase in cost for the HPC bridge, which can be attributed to the relative inexperience of the contractor with HPC and significantly higher beam costs. Although the Eastbound HPC and Westbound non-HPC beams were bid jointly at a cost of \$377 per lineal m (\$115 per lineal ft.), Ralls estimates that the actual costs were approximately \$220, \$295, and \$610 per lineal m (\$67, \$90, and \$186 per lineal ft.) for the

Texas Type B, non-HPC Type IV, and HPC Type IV beams, respectively. (Texas Type B beams were used in the ramp structures at the far end of the project, but not in the main spans.) The cost of the HPC Type IV beams was thus more than twice the cost of the conventional concrete Type IV beams, which can be attributed to the fabrication and stability considerations for these beams discussed in Section 10.2 and Section 10.3. There was also a concern about the potential impact to the project if even one of these beams failed during transportation or erection, and this may have impacted the actual bid cost for these beams.

The as-bid unit cost for the Louetta Road Overpass was only \$259 per m² (\$24.09 per ft.²), which is substantially less than the cost for either of the San Angelo bridges. This cost is also only 2 percent greater than the average cost of twelve conventional concrete U-beam bridges constructed as part of the same highway improvement project as the Louetta bridge, which averaged \$254 per m² (\$23.61 per ft.²). This is not meant to infer that U-beam bridges are tremendously cheaper than most I-beam bridges in Texas, only that the Louetta bridge was similar in cost to most prestressed concrete highway bridges in Texas and that the San Angelo bridges were *both* more expensive. During the time period in which these projects were constructed, the average unit cost for typical prestressed concrete I-beam bridges was \$291 per m² (\$27 per ft.²), which is slightly higher than the average cost for a Texas U-beam bridge.

Beams for the Louetta bridge and the other twelve conventional concrete bridges that Louetta was a part of were all bid together, and Ralls was unable to isolate the cost of the Louetta HPC beams from this lumped estimate. The as-bid cost for all U-beams on the entire project was \$328 per lineal m (\$100 per lineal ft.), which is substantially less than the average of \$394 per lineal m (\$120 per lineal ft.) for all U-beam projects in Texas at the time. This clearly implies that there was not a significant increase in cost resulting from the use of HPC in the Louetta beams.

10.5 Ultimate Strength and Ductility

As discussed in Section 1.4.2, ultimate strength requirements are typically easily satisfied for HPC members. Still, a comparison of the Louetta and San Angelo HPC bridges would not be complete without a brief examination of the strength and ductility behavior of

the sections used in these bridges. Therefore, a moment-curvature analysis was performed for one composite section from each bridge using the principles of strain compatibility. The results of these analyses provide important information regarding the total capacity of these HPC composite beam sections, as well as information regarding the probable mode of failure at full capacity.

The moment-curvature analyses were based on the approach outlined by Burns [34]. The starting point of each analysis was assumed to be the condition with full dead load acting on the structure (except for *non-composite* superimposed dead loads). All loads are assumed to act on the non-composite beam section prior to the starting point, and all subsequent loads are assumed to act on the composite section. All prestressing steel was lumped together at the c.g. of all strands, and an effective steel stress of 1103 MPa (160 ksi) was assumed at the starting point of the analysis. Note that this assumption is a rough average based on the measured prestress losses discussed in Chapter 7, and affects the cracking moment but not the ultimate strength of the section.

Other simplifications used in the analyses include the conservative assumption that all nonprestressed reinforcement in the deck slab could be neglected. The minimal nonprestressed reinforcement in the beams was also neglected. Nominal design material properties (i.e. compressive strength and modulus of elasticity) were used in the analysis, and the flexural strength of the beam concrete was assumed to be 10 times the square root of the compressive strength to reflect the increased tensile strength of HPC [39]. Failure was assumed to occur at a top fiber compressive strain in the deck of 0.003.

Constitutive relationships used in the analyses are summarized in Figure 10.5, and are based on the recommendations of Castrodale et. al. [40] for strain compatibility analyses using high strength concrete. A bilinear stress-strain relationship was assumed for the HPC beam concrete, and the constitutive relationship proposed by Burns [34] was used to model the concrete in the deck slabs. The constitutive equation for the prestressing steel is the Menegotto and Pinto equation, with coefficients proposed by Castrodale et. al. [40].

The composite cross-sections used for the analyses are also shown in Figure 10.5. The moment-curvature plots based on the strain compatibility analysis are shown in Figure 10.6 and Figure 10.7, respectively, for Louetta Beam N21 and San Angelo Beam E24. The ultimate capacities for each section are summarized in Table 10.2, and are compared to moment capacities computed using the *AASHTO Standard Specifications* [3] and *LRFD Specifications* [1] equations for nominal flexural capacity.

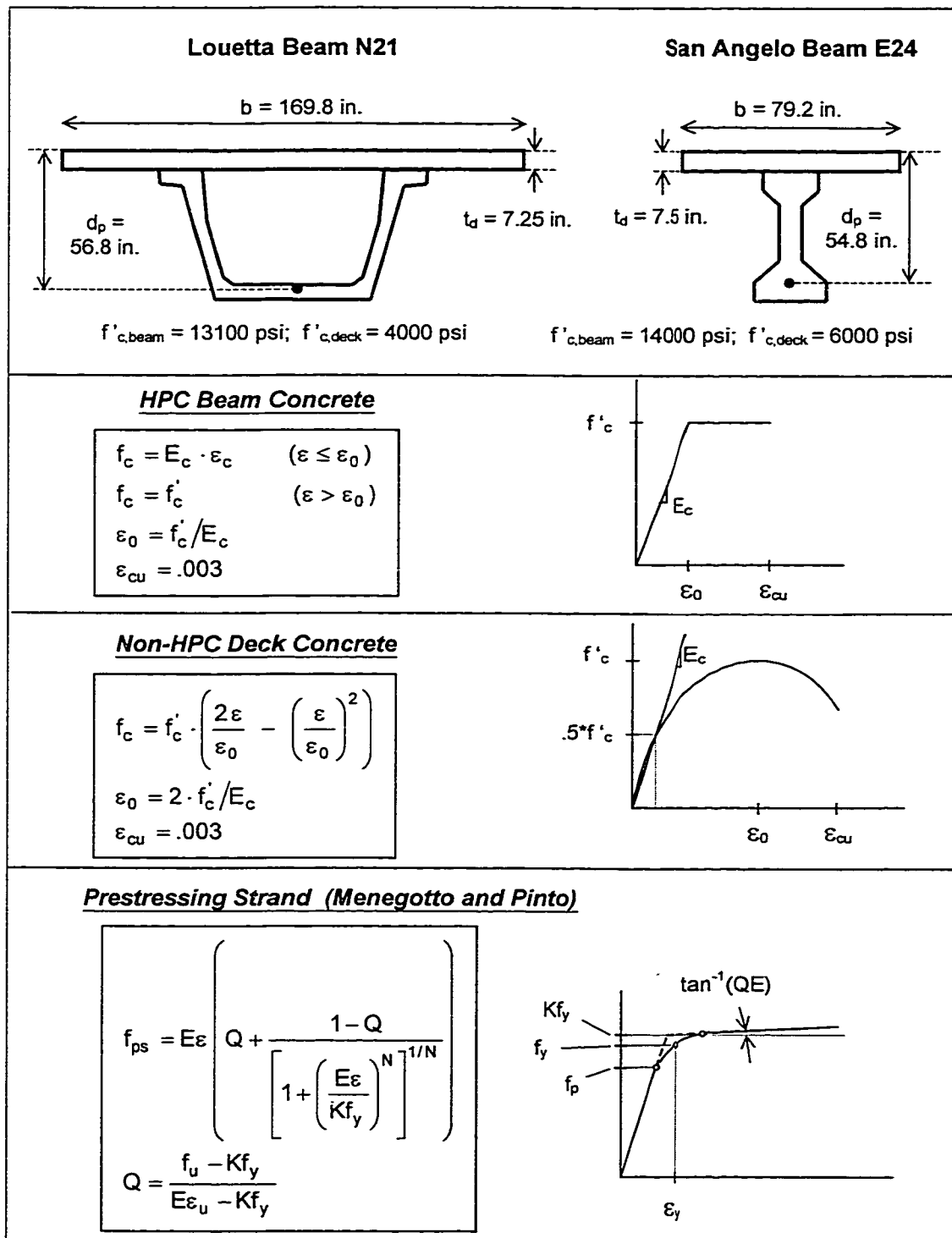


Figure 10.5 - Composite Sections and Constitutive Relationships for Strain Compatibility Analyses

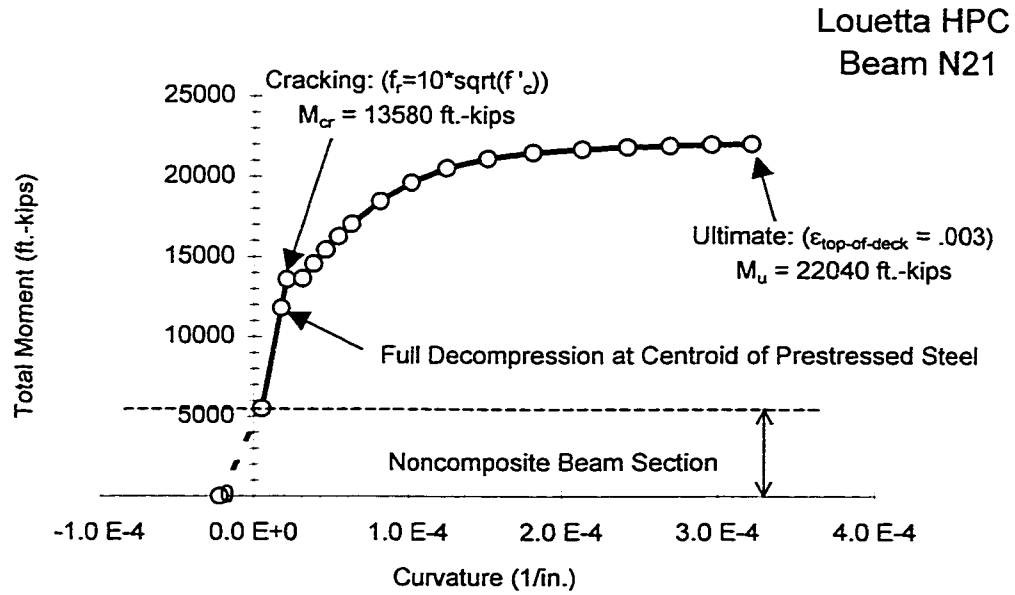


Figure 10.6 - Moment Curvature Relationship for Louetta Beam N21 Based on Strain Compatibility Analysis

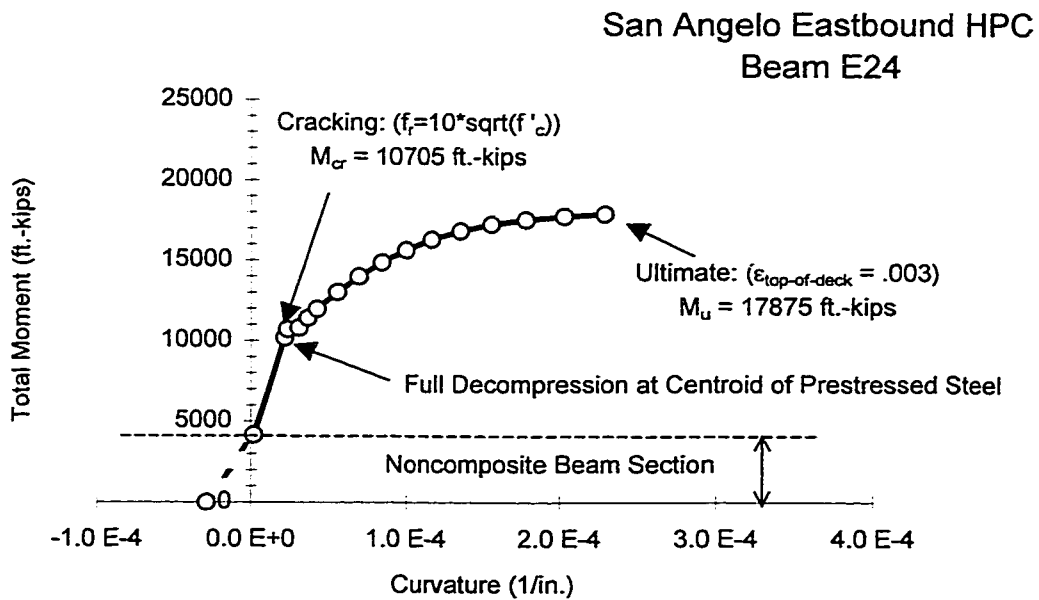


Figure 10.7 - Moment Curvature Relationship for San Angelo Beam E24 Based on Strain Compatibility Analysis

Table 10.2 - Ultimate Strength and Ductility Comparison for a Louetta HPC Beam and a San Angelo HPC Beam

	Louetta Beam N21 (Type U54)	San Angelo Beam E24 (Type IV)
Total Unfactored Moment $M_{DL} + M_{LL+I}$	8750	6160
Total Factored Moment (AASHTO Std. Specs [3]) $1.3*[M_{DL} + (1.67*M_{LL+I})]$	13930	9570
Total Factored Moment (AASHTO LRFD Specs [1]) $1.25*M_{DL} + 1.75*M_{LL+I}$	12400	8600
Calculated ϕM_n (AASHTO Std. Specs [3], $\phi=1.0$)	21210	16390 *
Calculated ϕM_n (AASHTO LRFD Specs [1], $\phi=1.0$)	19860	13980 *
Calculated M_n (Strain Compatibility Analysis)	22040	17880
$M_n / M_{cracking}$ (Strain Compatibility Analysis)	1.62	1.67
Depth of NA at Failure (Strain Compatibility Analysis)	11.5 in.	15.9 in.
Steel Strain at Failure (Strain Compatibility Analysis)	2.07 %	1.52 %
All moments in ft.-kips 1 ft.-kip = 1.356 kN-m 1 in. = 25.4 mm		
* Over-reinforced flange section per code. Moment capacity reduced using provisions in code commentary.		

The ultimate strength determined from the moment-curvature analyses for each of the two composite beam sections is more than adequate when compared to the factored moments using the load factors of either the *AASHTO Standard Specifications* [3] or the *AASHTO LRFD Specifications* [1]. Compared to the total unfactored (service) moments, these composite sections have a factor of safety in the range of 2.5 to 2.9 against collapse. Clearly, these composite sections have adequate flexural capacity, and are substantially overdesigned with respect to the strength limit state alone.

Ultimate strengths based on the moment-curvature analyses were also greater than the strength capacities calculated using *AASHTO* [1,3] code equations. The difference in these strengths is based primarily on the fact that both sections are flanged sections at ultimate (i.e. neutral axis is in the beam), and that the *AASHTO* equations do not specifically consider the higher concrete strength in the beams (compared to the deck). As suggested by Castrodale et. al. [40], use of the more general *ACI 318* [7] equivalent rectangular stress

block approach would result in more accurate estimation of the flexural capacity since different concrete strengths can be used for the deck and beam.

Differences between the calculated moment capacities using the *AASHTO Standard* and *LRFD* equations, as shown in Table 10.2, result primarily from the different treatment of the equivalent rectangular stress block in the flanged portion of the composite section. This slight difference between the codes is discussed in more detail in the *Commentary of the AASHTO LRFD Specifications* [1]. Also note that capacities are reduced for San Angelo Eastbound Beam E24 when using the *AASHTO* code equations, because this beam is over-reinforced according to code equations. Despite this reduction, the code-based calculations suggest that the beam has ample flexural capacity to carry the required factored load moment.

Although the general trends related to ultimate strength are similar for the two beams, there are slight differences related to the ductility of the two sections. Based on the moment-curvature analysis, Louetta Beam N21 exhibits good ductile behavior. The beam is a flanged section at ultimate with a neutral axis depth of 292 mm (11.5 in.). The ratio of the ultimate to cracking moment is 1.62, such that there is a very large reserve capacity after cracking. The elongation of the prestressed steel at failure is 2.07%, which is not extremely large but is well beyond yield. Furthermore, the simplifying assumptions used in the analysis tend to decrease the ductility of the section. The actual deck is probably higher in strength and somewhat thicker than the nominal deck thickness, and the deck reinforcement was neglected. If these effects were considered, the neutral axis would be substantially higher at failure and the section would be even more ductile.

For San Angelo Beam E24, behavior was slightly less ductile according to the moment-curvature analysis. This beam is also a flanged section at failure, but has a larger neutral axis depth of 404 mm (15.9 in.). Steel elongation is also somewhat smaller than for the composite Louetta U-beam, and is 1.52% at failure. Still, there is an extremely large amount of reserve strength after cracking, and the ratio of ultimate to cracking moment is 1.67. While the consideration of effects neglected in the simplifying assumptions would also increase the ductility for this section, it should be noted that the use of a 27.6 MPa (4000 psi) deck would have a rather significant influence on ductility. The use of this more standard deck concrete strength would result in a significant reduction in both strength and ductility for the section, to the point where there may be less warning of an impending failure

than for Louetta Beam N21. Still, it is important to note that there is more than adequate reserve capacity compared to the factored loads.

In summary, it can thus be concluded that strength will almost never control the design of HPC beams because of the extremely high reinforcement quantities for such beams. It is unlikely that the ultimate capacity, or even the cracking moment for these beams would ever be approached, in the service loading expected for the structure. Still, because these beams are being considered for 75 to 100 year service lives, it is impossible to truly know what loads the structure may be required to resist during its lifetime. In this sense, ductility is still an important consideration despite the tremendous flexural capacities of these beams.

Based on the limited observations regarding these moment-curvature analysis, it would appear that the flexural behavior of the Louetta U-beams is more ductile in general. At the basic level, it is clear that the primary factor influencing the ductility in these *composite* beams is the width of the deck slab (per beam), unless higher strength concrete is used in the deck. It may therefore be concluded that using HPC to increase beam spacing, for either U- or I- shaped beams, will result in more desirable ductile behavior than using HPC to increase span lengths. Likewise, the use of the Texas U-beam should automatically result in beam spacings with sufficient width to ensure ductile behavior.

10.6 Summary and Recommendations

The two bridges which were monitored during this research program represent different implementations of HPC in highway bridge structures. A brief summary of the overall behavior trends is presented in this section, in terms of a comparison of certain aspects of the Louetta and San Angelo bridges. Final recommendations for the implementation of HPC in future bridges are then presented based on the overall set of observations in this research program. Note that these recommendations consider only structural efficiency and feasibility, but the most beneficial implementation of HPC may clearly be for durability and result in a much longer service life for the structure. These aspects are discussed in more detail by Myers and Carrasquillo [88].

The recommendations in this section are separated into two basic comparisons. The use of the Texas U-beam and the AASHTO Type IV beam are discussed first. The implementation of HPC for longer spans and larger girder spacing is discussed second. As these comparisons are made, it is still important to note that both bridges in this research program were ultimately constructed *successfully*. These comparisons are intended to identify the best implementations of HPC for future highway bridge structures, based on the observations in this research program.

10.6.1 Texas U54 Beam vs. AASHTO Type IV Beam

In many respects, the Texas U-beam is simply an ideal cross-section for the implementation of HPC in highway bridge structures. The U-beam is a significantly larger section compared to other cross-sections of the same depth, and can thus accommodate the higher prestress forces associated with HPC designs. Furthermore, Ralls et. al. [113] demonstrated that the structural efficiency of the U-beam clearly overcomes its larger self-weight. Similar observations were reported in Section 2.2.2 of this dissertation.

Throughout this research program, the larger section properties of the U-beam have been shown to stabilize behavior when compared to the AASHTO Type IV section. This is a very important factor when the overall sensitivity of all aspects of structural behavior for efficient HPC designs is considered. In other words, the larger, stiffer U-beam helped to “dampen” some of the sensitivity associated with longer span lengths and larger girder spacing. Prestress losses for the Louetta HPC U-beams were quite reasonable in magnitude. Although deflection behavior was sensitive for the Louetta U-beams, it was generally more predictable than for the San Angelo HPC Type IV beams.

The AASHTO Type IV section was also utilized successfully with HPC in the San Angelo bridge, but prestress losses were high (although not excessive) and deflection behavior was quite sensitive. Still, the most critical limiting factor for the use of this cross-section in future HPC bridges will be issues related to stability. The strong potential for instability problems with the very long AASHTO Type IV beams required special considerations during handling and ultimately drove up costs for the San Angelo HPC bridge. Calculations also show that certain composite sections utilizing HPC in AASHTO Type IV beams with low deck concrete strengths and small girder spacing could result in

designs with less ductility, although HPC beams in general have a tremendous amount of extra flexural capacity.

On the basis of these observations, it is recommended that the Texas U-beam be used extensively in future HPC projects. The AASHTO Type IV beam can also be used successfully in future bridges, especially those with span lengths of less than 41 m (135 ft.), but many considerations may make the use of this section less economical and less structurally efficient than the U-beam.

10.6.2 Long Spans vs. Larger Girder Spacing

In Section 1.4.2, long spans and larger girder spacing were identified as the primary benefits of increased structural efficiency for HPC designs. Shallower girder depths were also mentioned as a possible application of HPC, but were not a part of the HPC bridges in this study. Throughout this research program, a marked increase in sensitivity for all aspects of structural behavior was observed for HPC beams with very long spans. Deflection behavior was more variable for longer span beams because the individual components of camber and deflection were larger. Similarly, non-load related effects such as thermal gradients had a larger influence on deflection.

Handling issues were also a much larger concern for the very long beams in the San Angelo Eastbound HPC bridge. In fact, there were essentially no special handling concerns other than the increased weight during transportation for the HPC and non-HPC beams in the Louetta and San Angelo bridges that did not have the longest span lengths (over 44 m [145 ft.]). The special handling consideration for the longest San Angelo beams resulted in a direct cost increase, which negated much of the economic benefit resulting from the use of HPC.

Thus, a practical span limit of 41 m (135 ft.) is recommended for future HPC and non-HPC designs using 1370 mm (54 in.) deep sections, including both the Texas U54 and AASHTO Type IV sections. This limit is based on both the observations of this research program, as well as past experience in Texas. Alternatively, a limiting span-to-depth ratio of 30 is recommended for beam sections of other depths, although additional research is needed to examine the actual behavior of beams with different depths. The construction of the San Angelo Eastbound HPC bridge has shown that a bridge can be constructed

successfully if this proposed limit is exceeded. However, several special considerations may be required and increased construction costs may result.

Furthermore, the primary focus for the implementation of HPC in future highway bridges should be the use of larger girder spacing. A great cost savings would surely result if fewer girders are utilized per span since there would be fewer girders to fabricate, fewer girders to transport, and fewer girders to erect. Furthermore, when precast prestressed deck panels are used, a reduction in girders will directly result in a reduction of the number of deck panels. Because all of these results can be obtained without the drawbacks associated with longer spans, it is be clear that a direct economic benefit should result when HPC is utilized to increase girder spacing.

11 CHAPTER ELEVEN: SUMMARY AND CONCLUSIONS

11.1 General

The most important observations of this research program are summarized briefly in this chapter. In general, the findings of this research program were summarized in detail at the end of each major chapter. Thus, only the most important conclusions are listed here. These conclusions are followed by a brief comment on the major trends observed for HPC structural members in this research program, and a short list of future research needs.

11.2 Summary of Most Important Findings

The following are the most important findings from this research program:

- 1) Two prestressed concrete highway bridges were successfully constructed in Texas using high performance concrete. Concrete with required compressive strengths of up to 61 MPa (8800 psi) at release and 97 MPa (14,000 psi) at 56 days was used successfully at a prestressing plant in the fabrication of beams for these bridges.
- 2) Concerns indirectly resulting from the use of HPC, especially handling issues, caused the San Angelo bridge to be more difficult and expensive to construct than the Louetta bridge.
- 3) The Texas U-beam is strongly recommended for extensive use in future HPC bridges. The U-beam is an efficient cross-section that is able to accommodate the large prestress forces required for HPC designs, and has increased stiffness compared to other cross-sections of the same depth. Lateral stability is also not a concern with the Texas U-beam.

- 4) The AASHTO Type IV beam can also be used successfully in future HPC highway bridges, although it is a less structurally efficient cross-section than the Texas U54 beam. There are also more practical limitations involved with the use of Type IV beams, especially related to handling issues.
- 5) The use of larger beam spacing should be the primary focus for the future implementation of HPC in highway bridge structures. The use of larger beam spacing would result in fewer beams to fabricate, transport, and erect, without the need for special consideration of practical issues such as stability during handling. Furthermore, the use of larger beam spacing would typically result in a reduced number of precast deck panels.
- 6) A practical span limit of 41 m (135 ft.) is recommended for precast 1372 mm (54 in.) deep beam sections based on handling issues, especially for AASHTO Type IV beams. Longer span lengths can be accommodated using this girder depth if necessary, but special considerations will be required for handling of such beams. An increase in sensitivity of prestress losses and deformations (strains and deflections) to material properties and other parameters should also be expected above this practical span limit.
- 7) Measured prestress losses for the all beams in this study were generally in the range of 207 to 414 MPa (30 to 60 ksi), or 20 to 30 percent of the nominal jacking stress. Losses averaged 377 MPa (54.65 ksi) or 27.0 percent in the San Angelo Eastbound HPC bridge, and were generally higher than losses in the Louetta HPC bridge, which averaged 267 MPa (38.76 ksi) or 19.1 percent. Losses were lower for the beams in the San Angelo Westbound non-HPC bridge, where the average loss was 228 MPa (33.07 ksi) or 16.3 percent.
- 8) The simplified AASHTO [1] and PCI [108] equations for prestress losses are not appropriate for HPC. A modified general form of these component methods was proposed, but it is largely dependent on the accurate estimation of material properties.
- 9) The long-term deflection behavior of the HPC beams was as desired – all HPC beams exhibited a small upward camber under full dead load in the composite bridge. Errors in deflection predictions cancelled out, and the total long-term deflections were satisfactory. The non-HPC beams in the San Angelo Westbound bridge actually exhibit a slight downward deflection under full dead load. This net downward deflection is a

result of the concrete used in these beams exhibiting many properties of HPC and the beams utilizing relatively low levels of prestress (compared to the HPC beams).

- 10) Long-term deflection behavior was extremely sensitive for the HPC beams in this study. Small variations in material properties and prestress losses can have a significant impact on deflection behavior for these beams. An upper and lower bound method is recommended for deflection calculations for HPC beams.
- 11) For all 26 beams in this study, measured camber at the release of pretensioned strands was significantly less than predicted using measured parameters. This trend may be due in part to the effect of thermal gradients during hydration and differential shrinkage before release.
- 12) For the HPC mixes in this study, both creep and shrinkage were found to be largely dependent on the amount of mix water. For HPC used in this project, creep was less than the ACI 209 [8] "standard" values and generally lower than the creep for non-HPC mixes used in this project. Shrinkage for the HPC mixes was also found to be less than the ACI 209 "standard" values, but there was no clear trend with respect to differences between the HPC and non-HPC mixes in this study.
- 13) Behavior during hydration had a significant impact on several measurements made during this research program, including concrete strains, prestress losses, and beam deflections.
- 14) Measured concrete strains (stresses) and beam deflections due to post-tensioning and the placement of the cast-in-place bridge decks were substantially less than predicted for all beams in this study.
- 15) Deflection measurements during the static live load tests indicate that both the Louetta and San Angelo bridges are very stiff, despite the use of HPC for longer spans and larger girder spacing.
- 16) Thermal gradients in composite and noncomposite HPC beams had a significant influence on behavior, especially measured deflections and concrete strains in the deck.
- 17) Although the shapes were similar, the design positive thermal gradients suggested by NCHRP 276 [65] and *AASHTO LRFD* [1] underestimated the temperatures measured at two depths in the composite deck. The design and measured negative

gradients showed good agreement with respect to the magnitude of the deck temperatures at two depths in the composite deck, but there was a difference in the shape of the negative gradient below the deck. Slight modifications to these design gradients are suggested based on the measurements in this research program. Because temperature measurements were not recorded at the very top of the deck, there is not sufficient justification for modification of the deck surface temperature recommended in the existing code gradients.

- 18) Hydration temperatures for beams in this study were generally rather high, and significant cracking was observed before release because these beams were restrained from shortening as they cooled (by the prestressing bed). This type of cracking should be avoided by releasing the prestress for these beams as soon as possible after the required release strength is obtained and side forms are stripped. Significant vertical thermal gradients were also observed in the beams during hydration.
- 19) The extreme average bridge temperatures suggested in the *AASHTO Standard* [3] and *LRFD* [1] specifications did not accurately reflect the extreme average bridge temperatures measured in this study. A simple equation was proposed that should more accurately estimate the extreme bridge temperatures *at a specific geographical location*.
- 20) Vibrating wire strain gauges worked very well for long-term measurements in the field, and are recommended for use in future projects. Bonded resistance strain gauges proved to be unreliable and are not recommended for future field projects where long-term measurements are desired.
- 21) Both the tensioned wire and precise surveying systems worked well and are recommended for use in future instrumentation projects. Each system has specific advantages and disadvantages relative to the other system.

11.3 Major Trends

For all highway bridges, including those constructed using HPC, prestress losses and deflection behavior must be estimated to at least a reasonable degree of accuracy. If prestress losses are underestimated, then there is a potential for allowable stresses to be

exceeded under full service load and cracking may occur. On the other hand, if prestress losses are overestimated during the design process, then the structure may be substantially overdesigned and a significant loss of structural efficiency will occur. If camber and deflection is underestimated or overestimated, then a long-term serviceability problem may result.

Unfortunately, the use of HPC can make the accurate estimation of prestress losses and deflection behavior more difficult because of the increased sensitivity associated with these designs. Throughout this study, it has been noted that the general structural behavior of HPC bridges is very sensitive as a direct result of the increase in structural efficiency for HPC designs as compared to conventional concrete designs. In particular, HPC designs are more sensitive to variations in material properties and other design parameters including the magnitudes of prestress forces and all dead loads. For this reason, care must be exercised in designing HPC structures, and designers must be aware of the increased sensitivity.

In reality, it may not be possible to accurately predict the behavior of HPC highway bridge structures, unless certain material properties, especially the modulus of elasticity and ultimate creep, are estimated adequately during the design process. Because there is already some inherent variability in all concrete material properties, variations resulting from simplifying design assumptions must be eliminated to the greatest extent possible. Eventually, there should be enough knowledge about the material properties of different high performance concretes such that reasonable prediction methods for HPC material properties will be available. Until such time, it is critical that there be some level of continuity between the design and construction phases for HPC structures with respect to the knowledge of material properties. This can be accomplished to some extent by trial batching and by reliance on past experience. A range of acceptable modulus of elasticity and ultimate creep values should also be specified on the contract documents for HPC designs in order to assure that there is some agreement between the design material properties and the material properties of the actual concrete used in the structure.

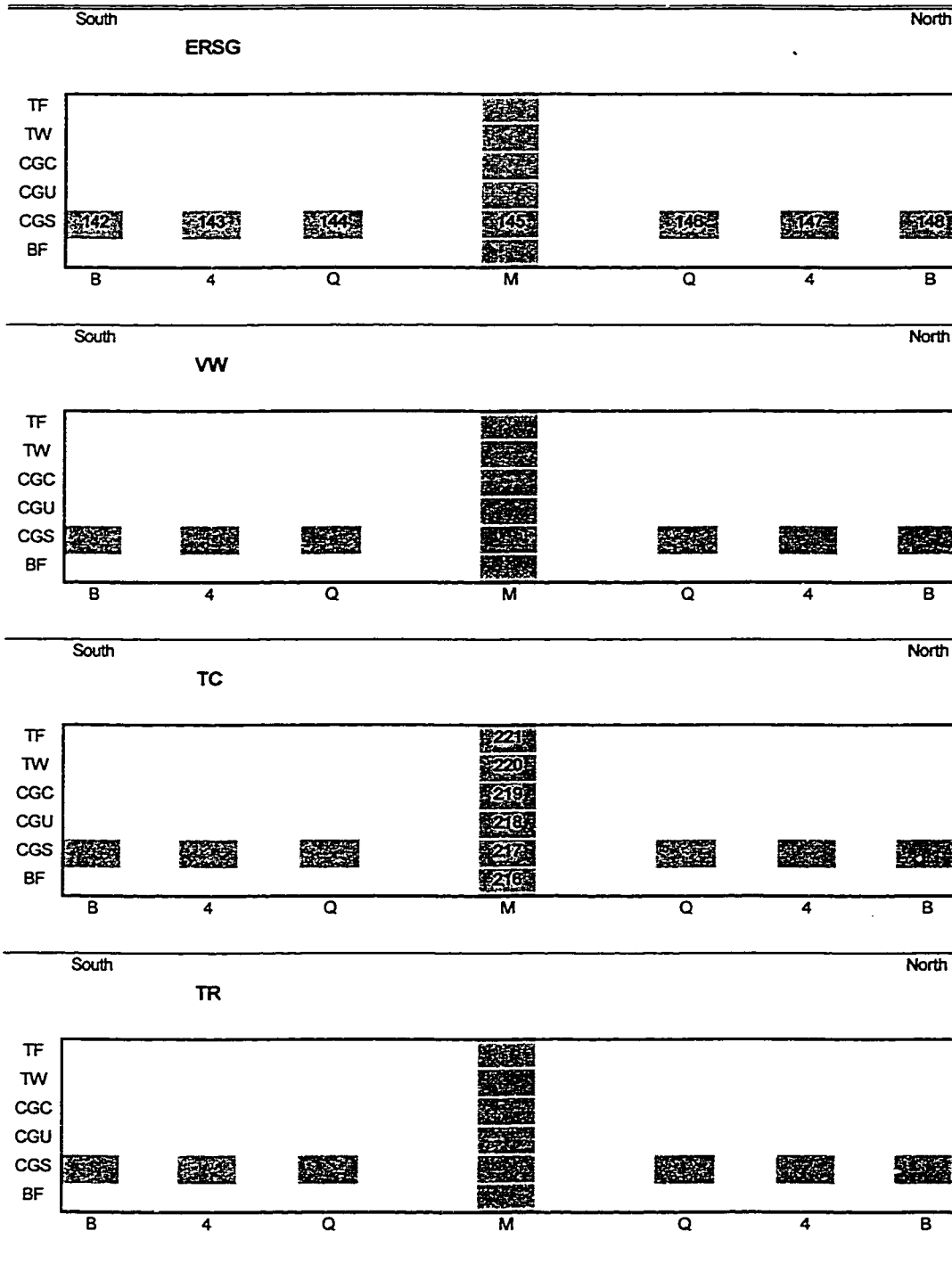
11.4 Recommendations for Future Research

Additional research is needed in the following major areas:

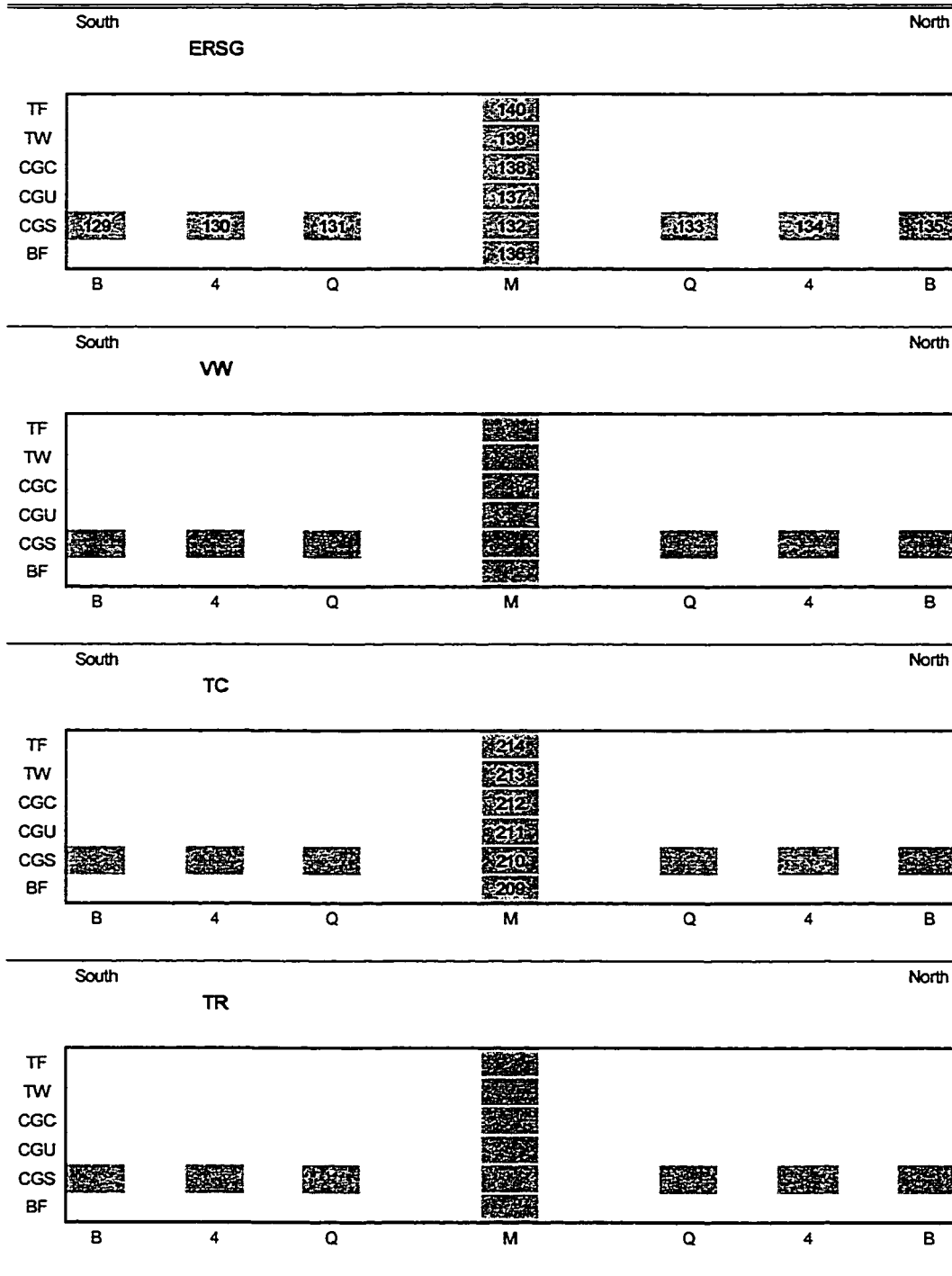
- 1) Additional bridges should be instrumented to investigate behavior of HPC structures with different structural configurations. Emphasis should be placed on measurement of prestress losses and beam deflections.
- 2) A database must be developed for the material properties of different HPC mixes, especially for modulus of elasticity and creep. Databases should be developed at local, regional, national, and international levels. Once such a database is developed, more approximate calculation procedures for prestress losses and camber (deflection) *may* be possible.
- 3) Additional measurements of bridge temperatures in Texas and other areas are necessary, especially if HPC is to be utilized in continuous bridges or with shored construction. In such structures, thermal gradients may cause high stresses. Measurements should be compared with existing design thermal gradients and extreme bridge temperatures, as well as those recommended in this research program.
- 4) Much more research is needed on the behavior of prestressed concrete beams during hydration (i.e. before release). The observations in this research program indicate that behavior at this stage can have a significant influence on concrete strains, prestress losses, and deflection behavior.

**APPENDIX A: SKETCHES DEPICTING GAUGE LOCATIONS FOR
INSTRUMENTATION OF THE LOUETTA ROAD OVERPASS**

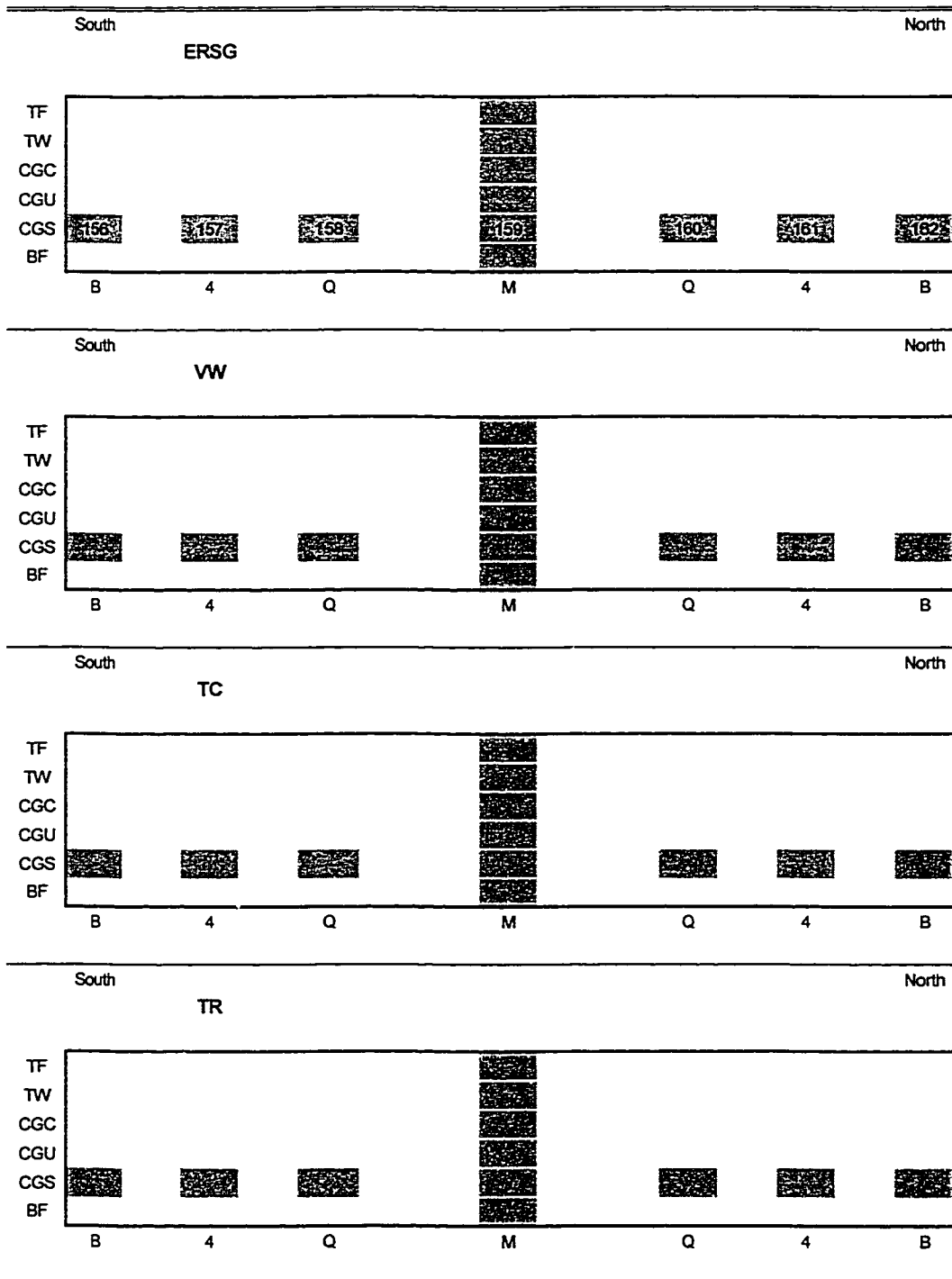
Louetta Beam N21 - East Web



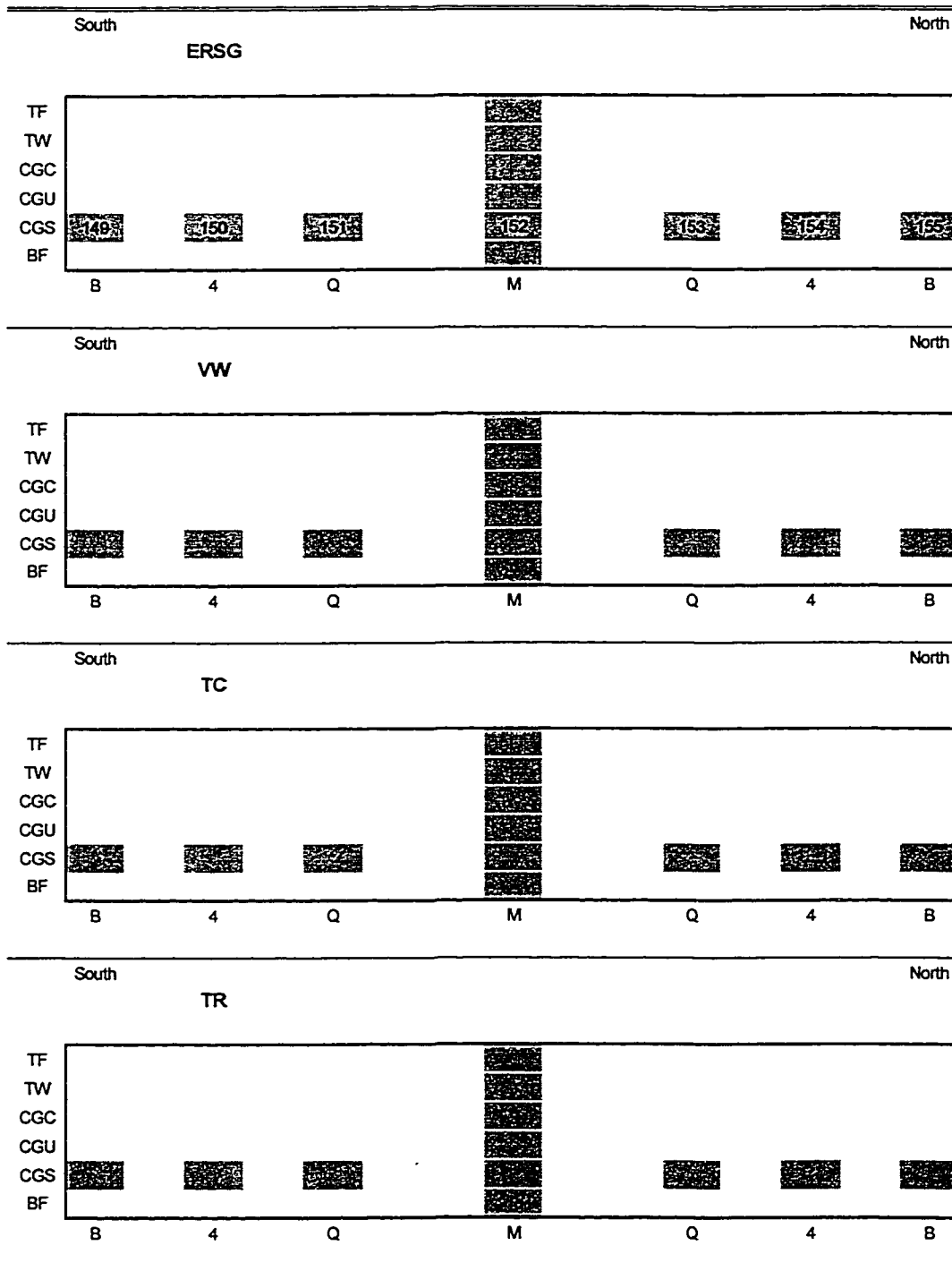
Louetta Beam N21 - West Web



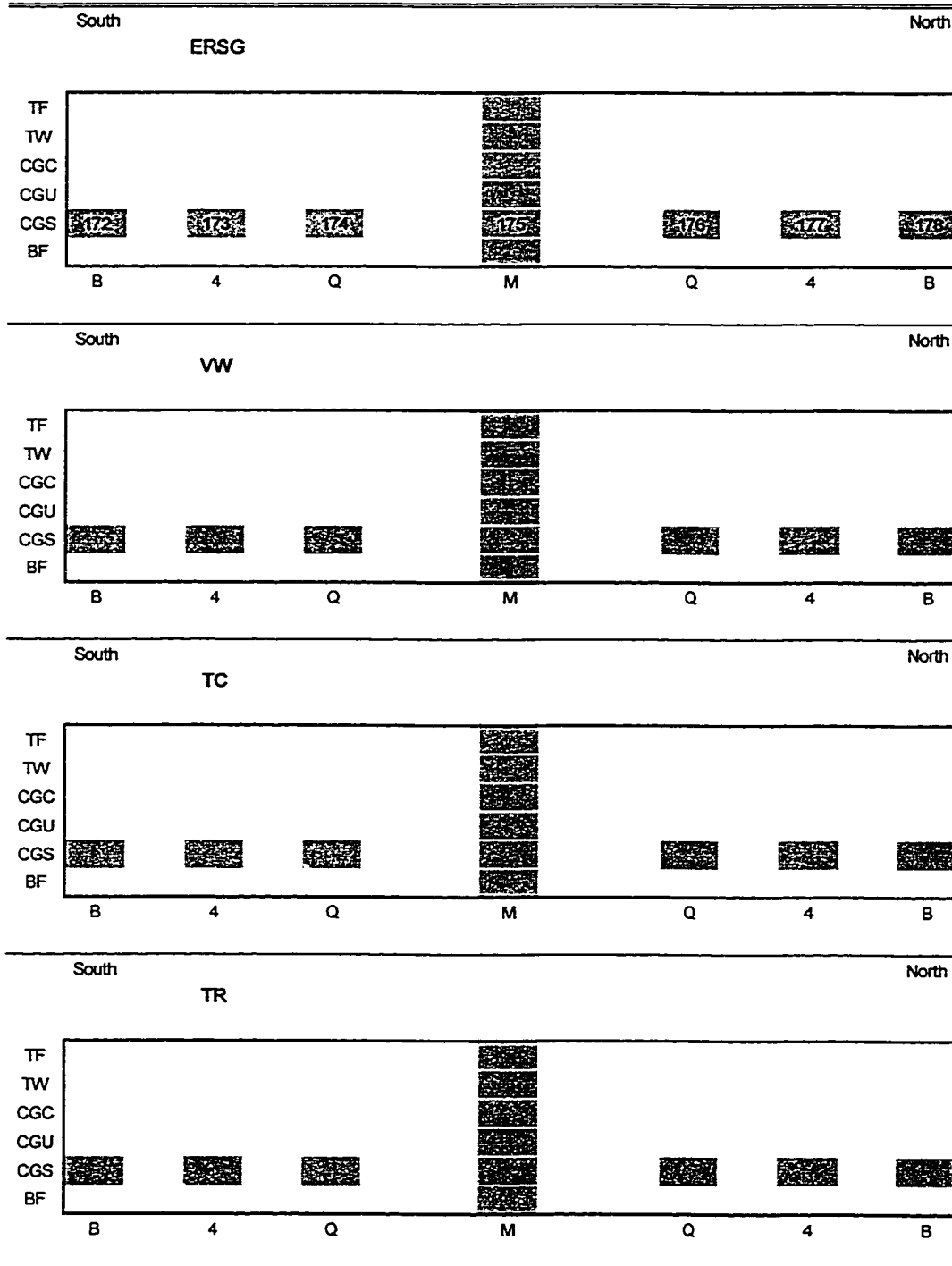
Louetta Beam N22 - East Web



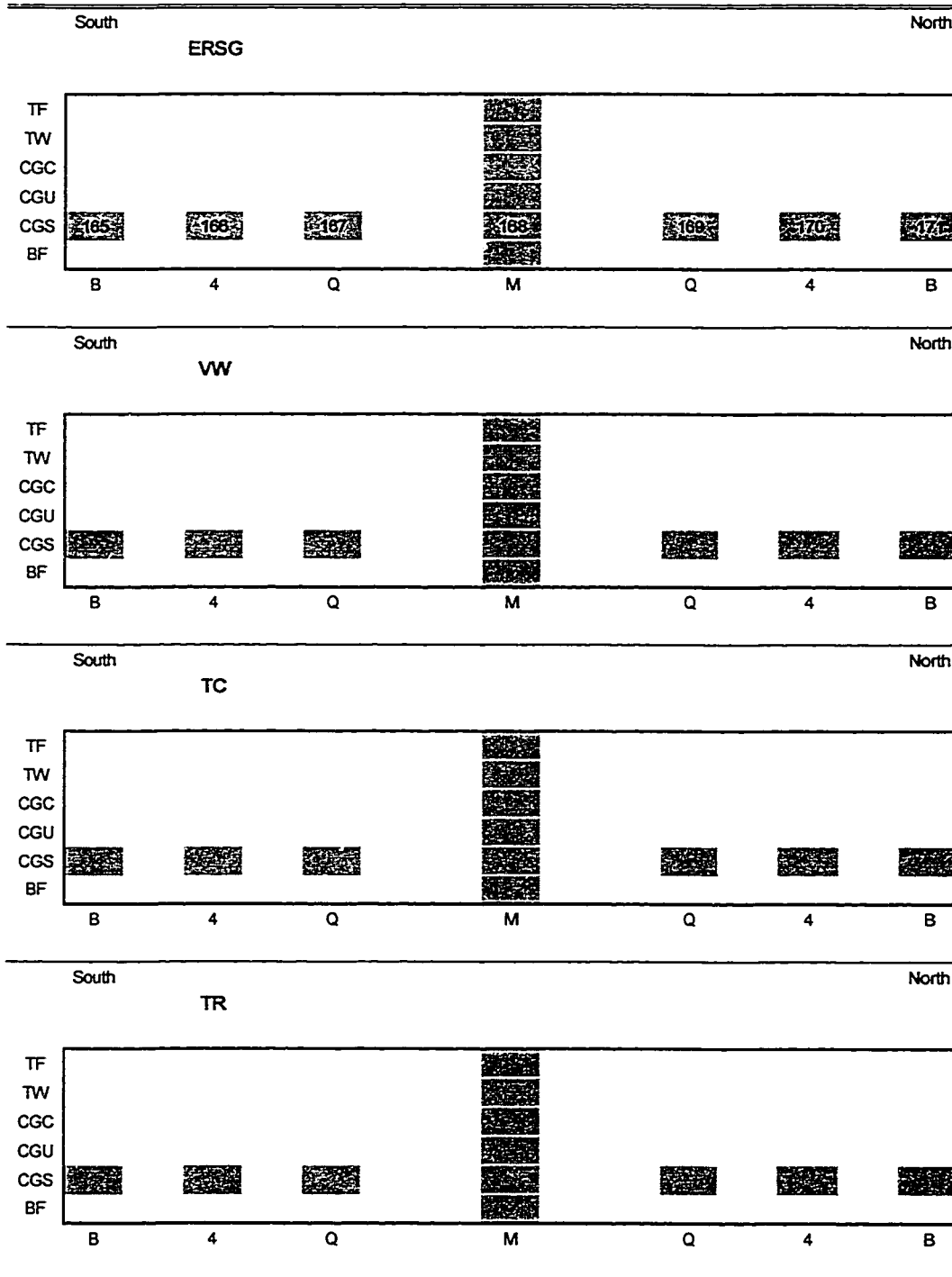
Louetta Beam N22 - West Web



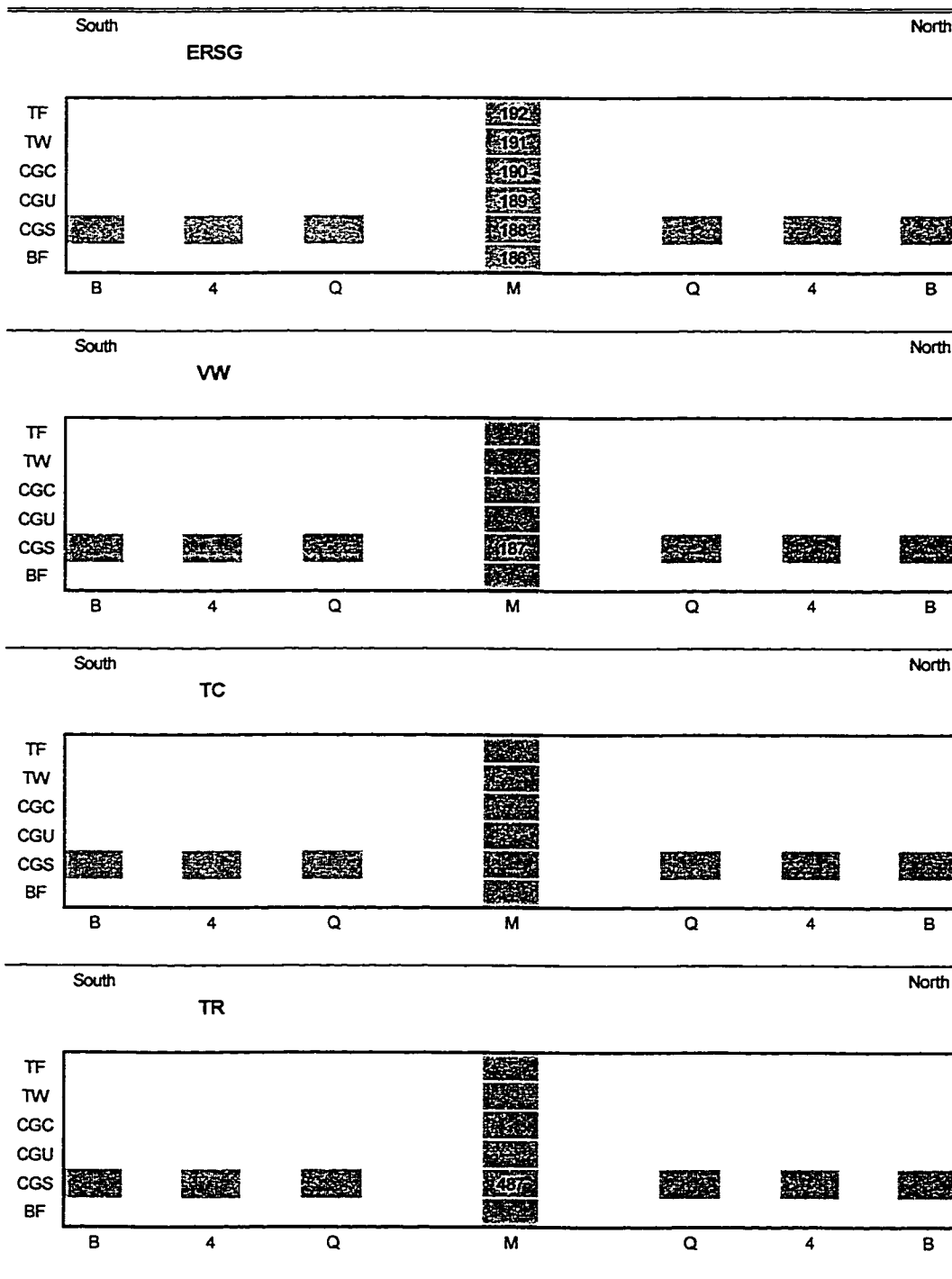
Louetta Beam N31 - East Web



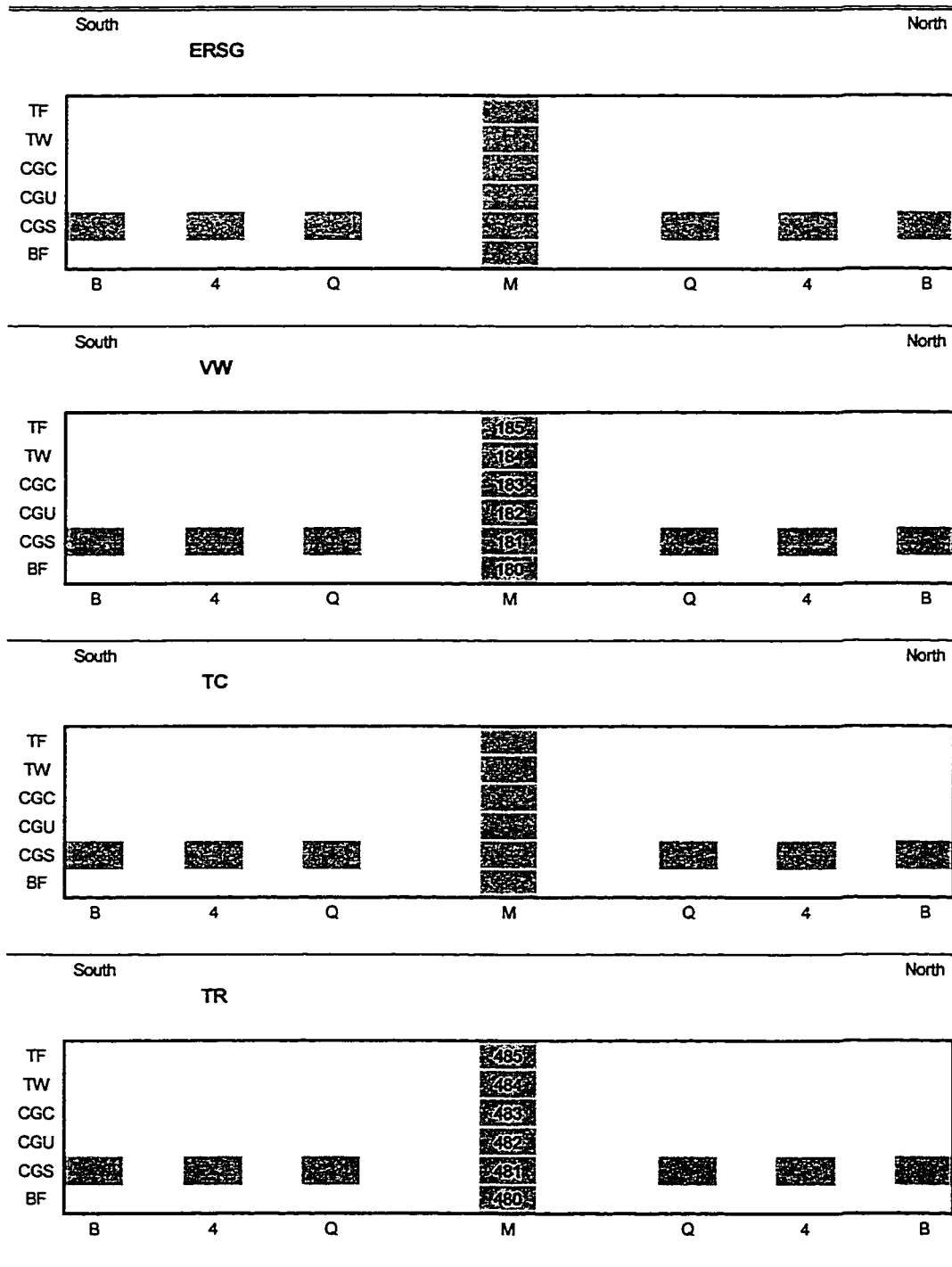
Louetta Beam N31 - West Web



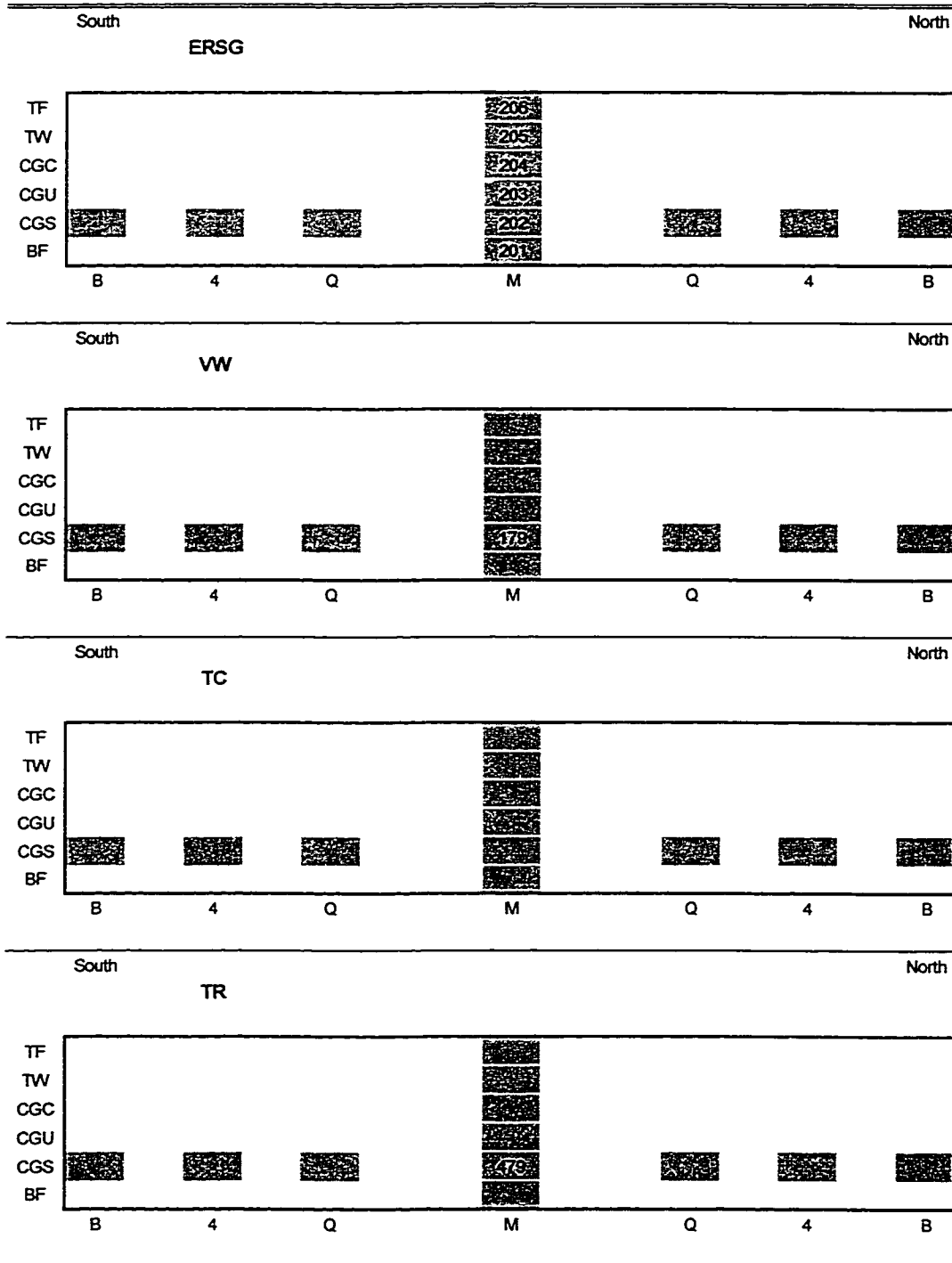
Louetta Beam N32 - East Web



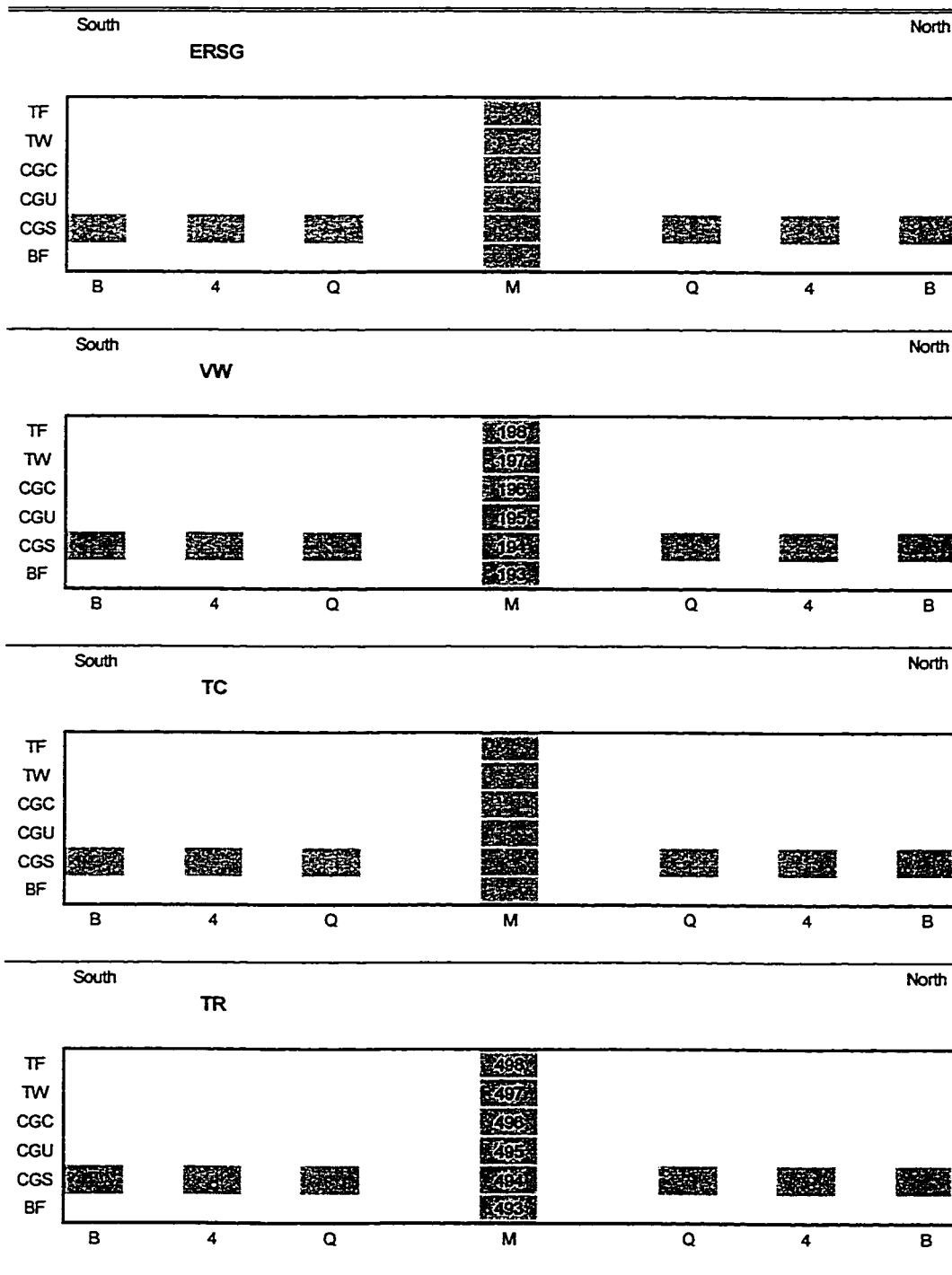
Louetta Beam N32 - West Web



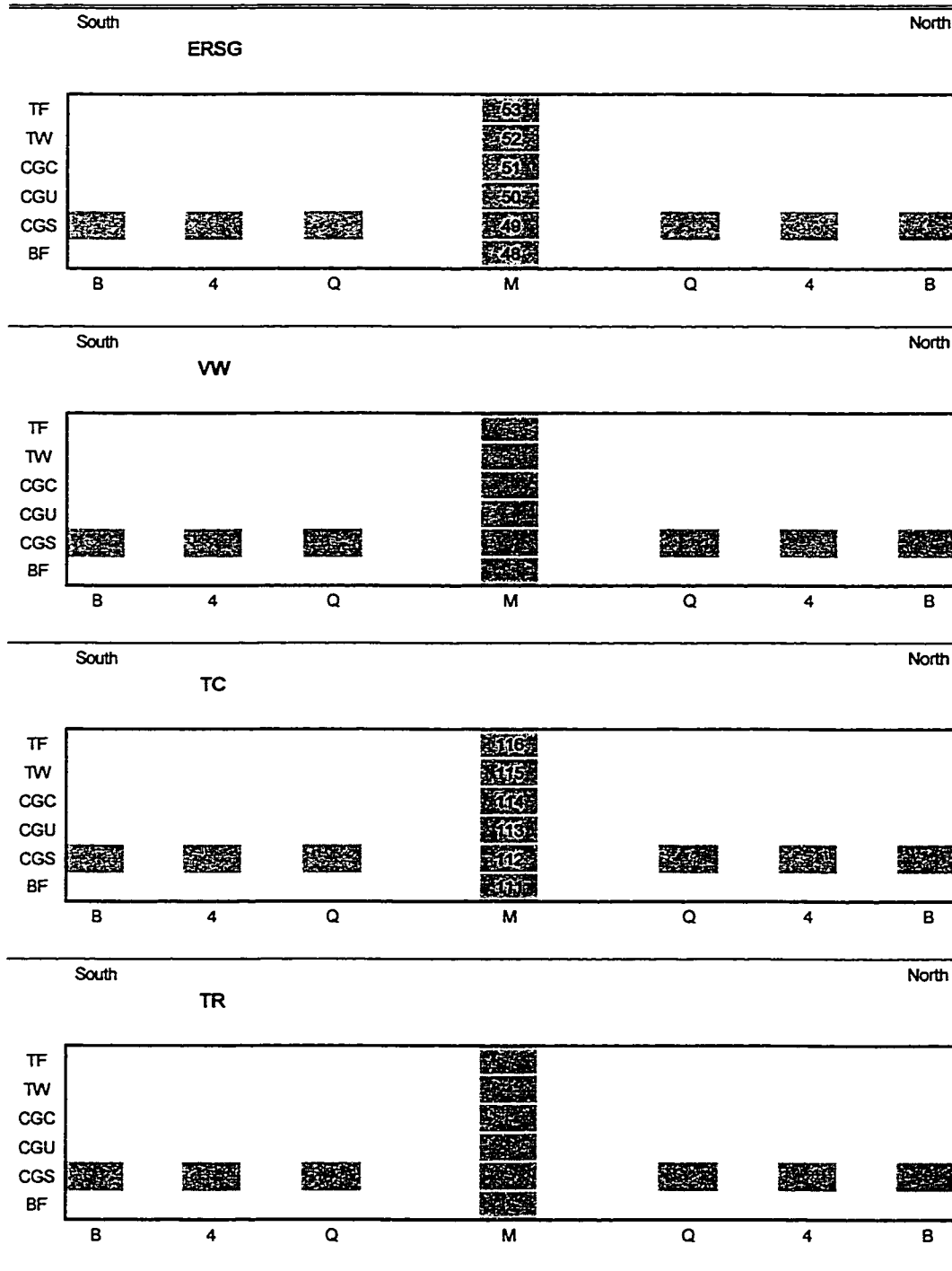
Louetta Beam N33 - East Web



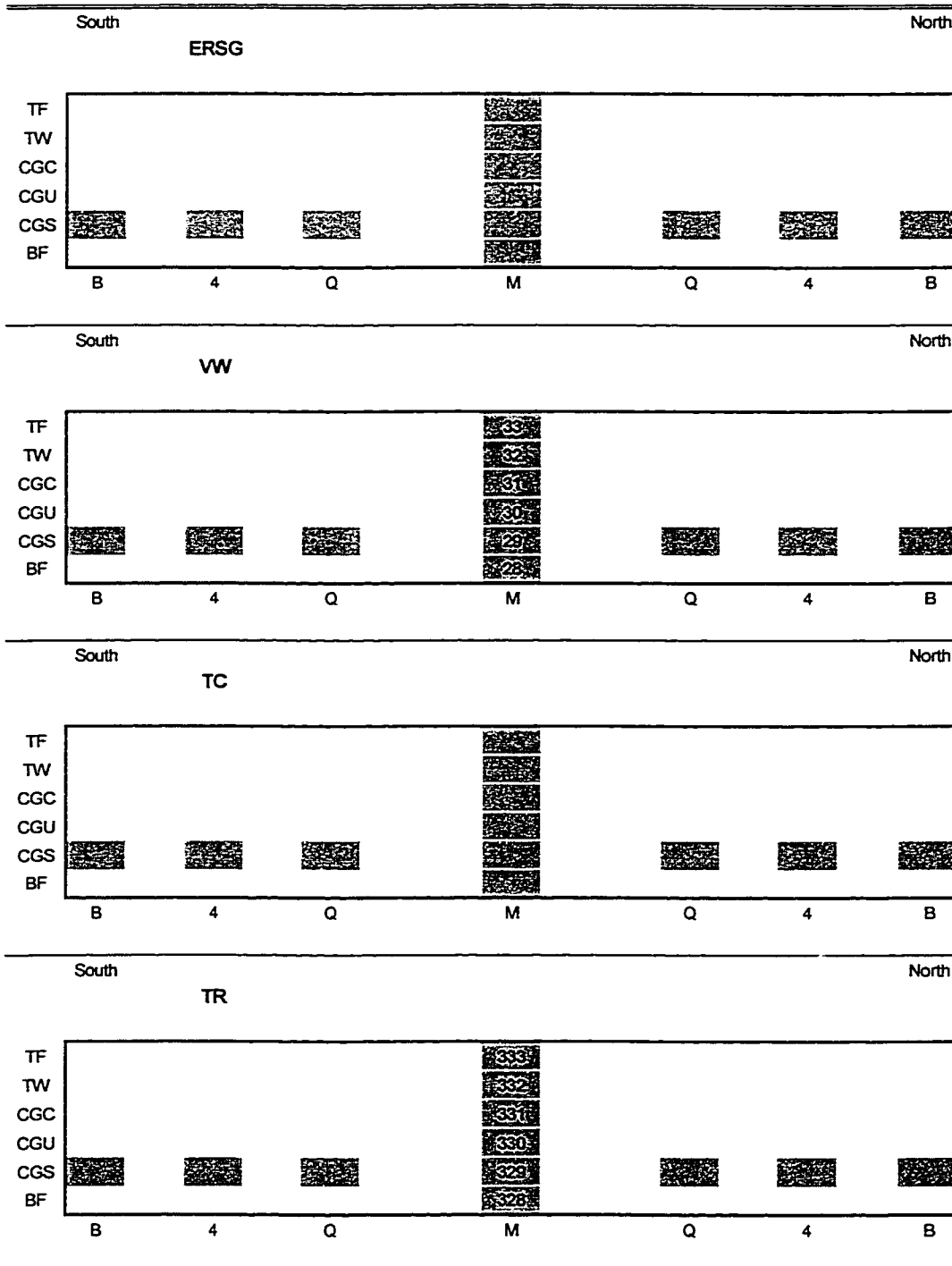
Louetta Beam N33 - West Web



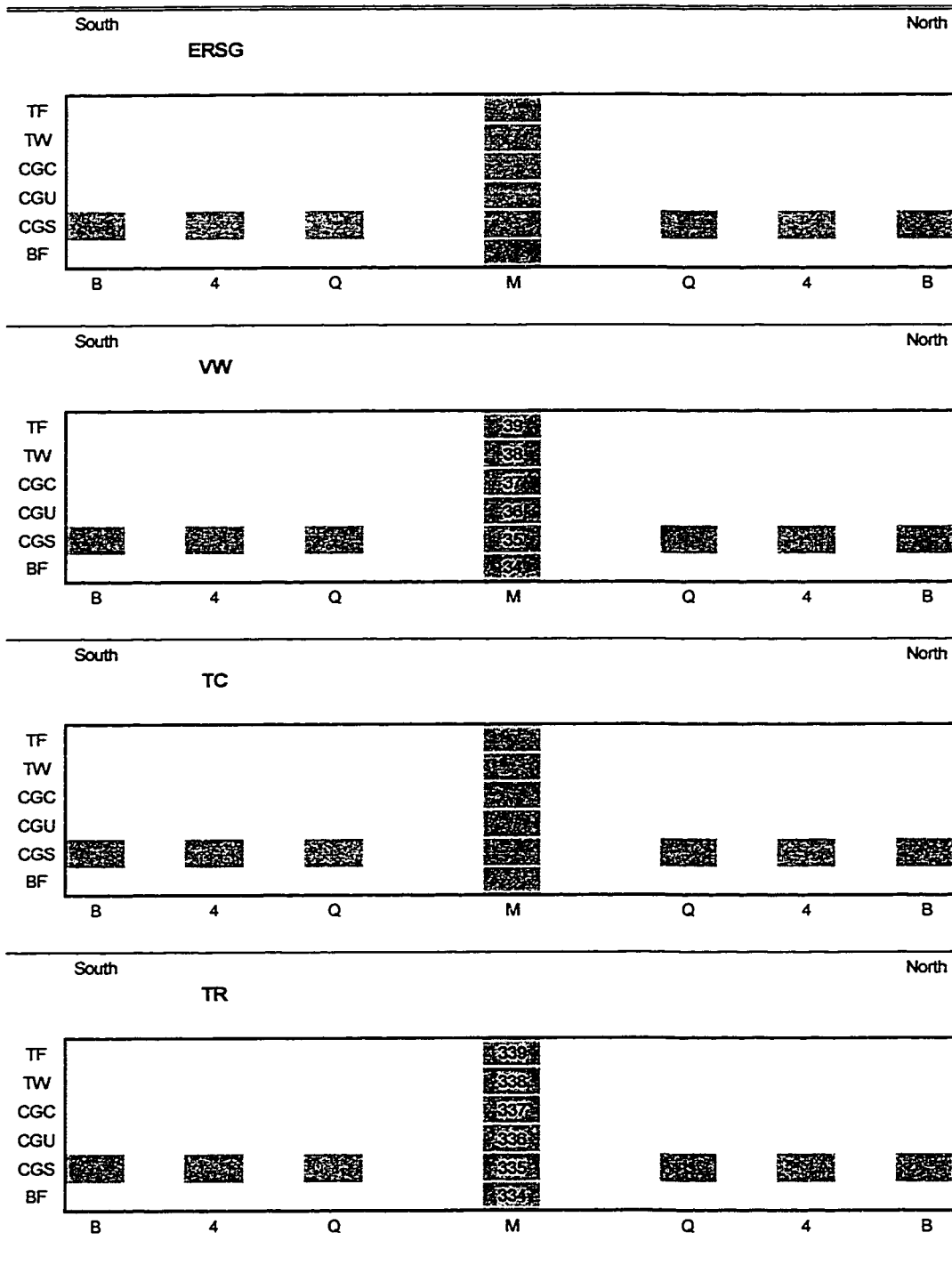
Louetta Beam S14 - East Web



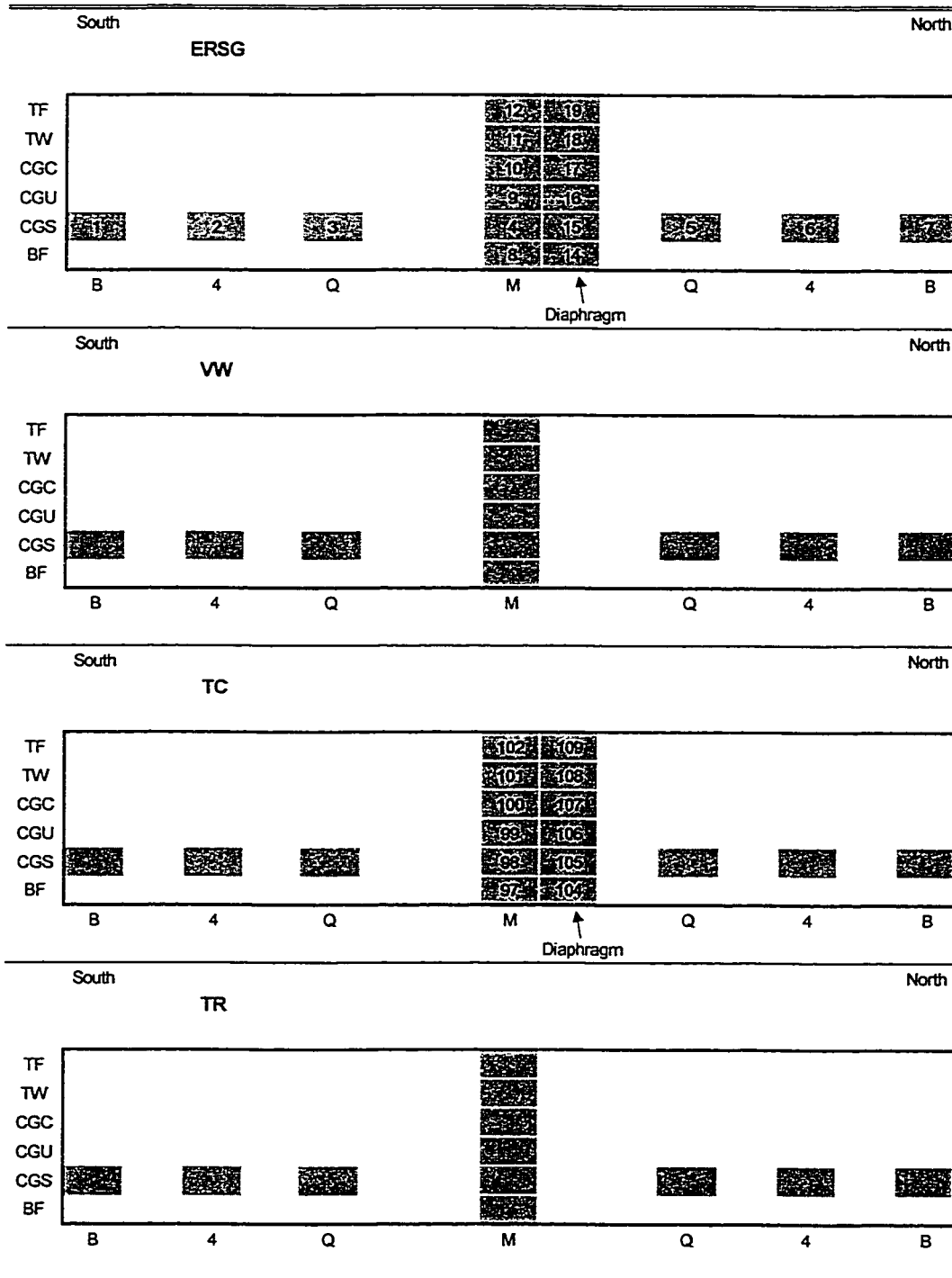
Louetta Beam S15 - East Web



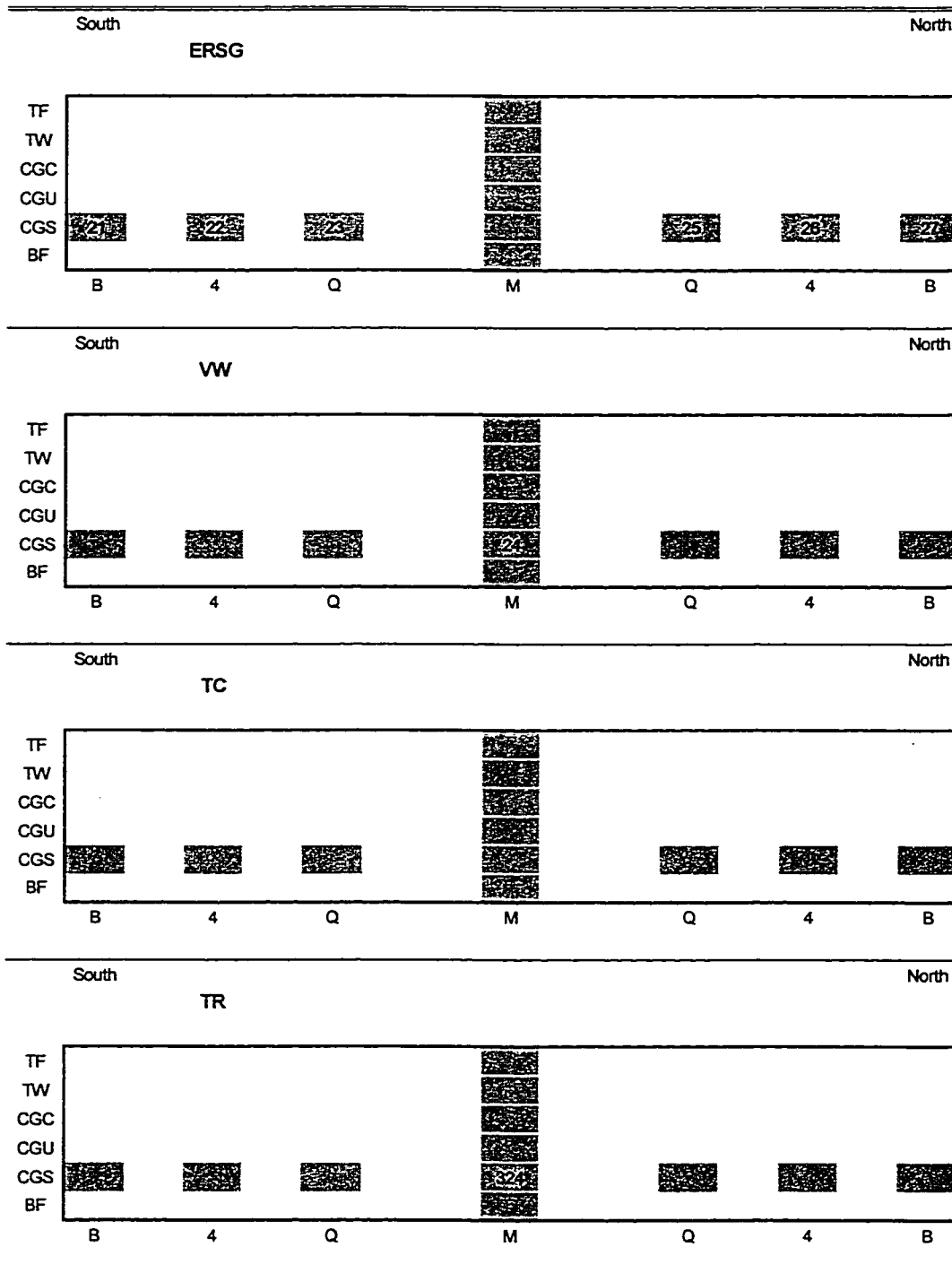
Louetta Beam S15 - West Web



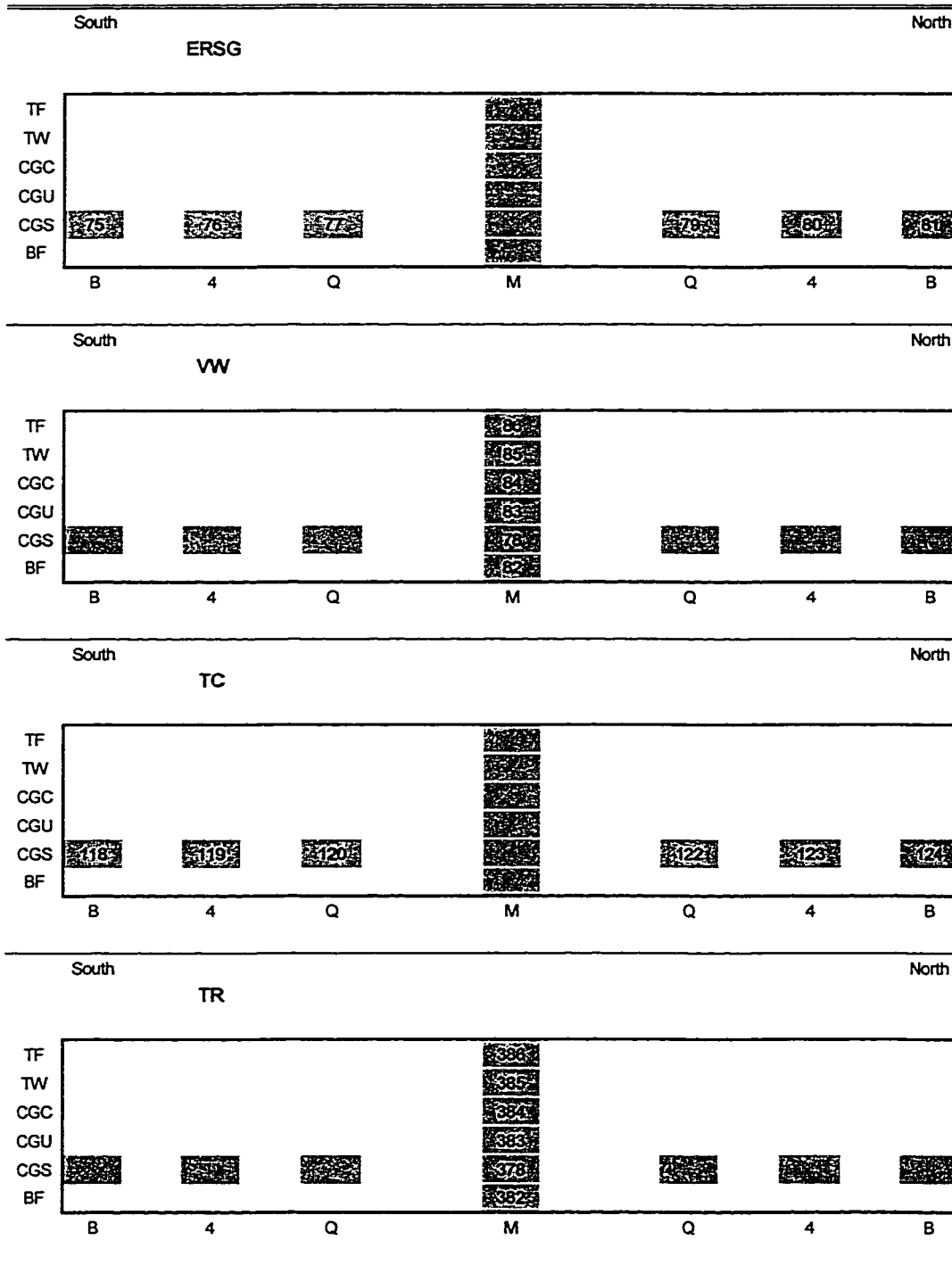
Louetta Beam S16 - East Web



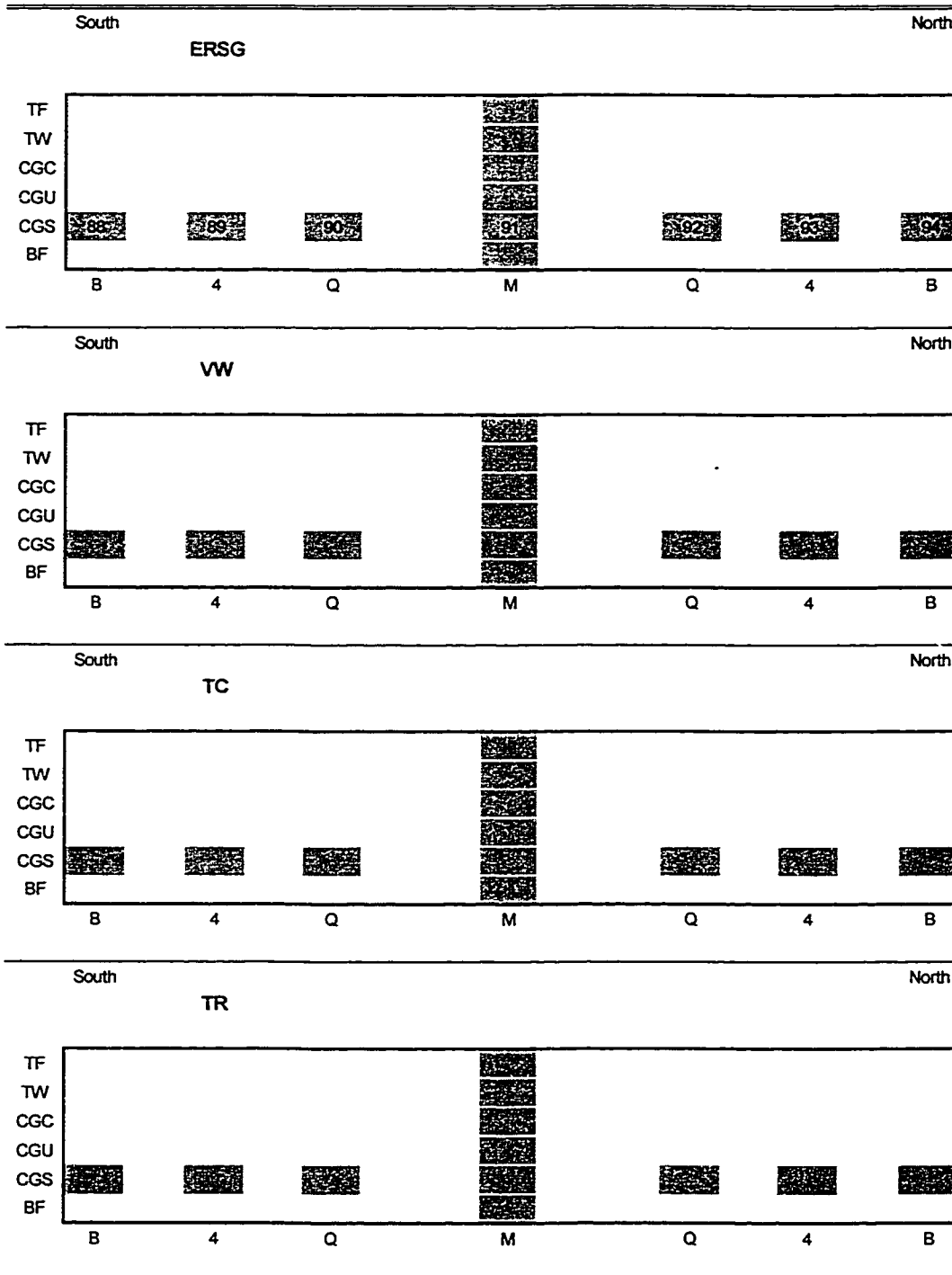
Louetta Beam S16 - West Web



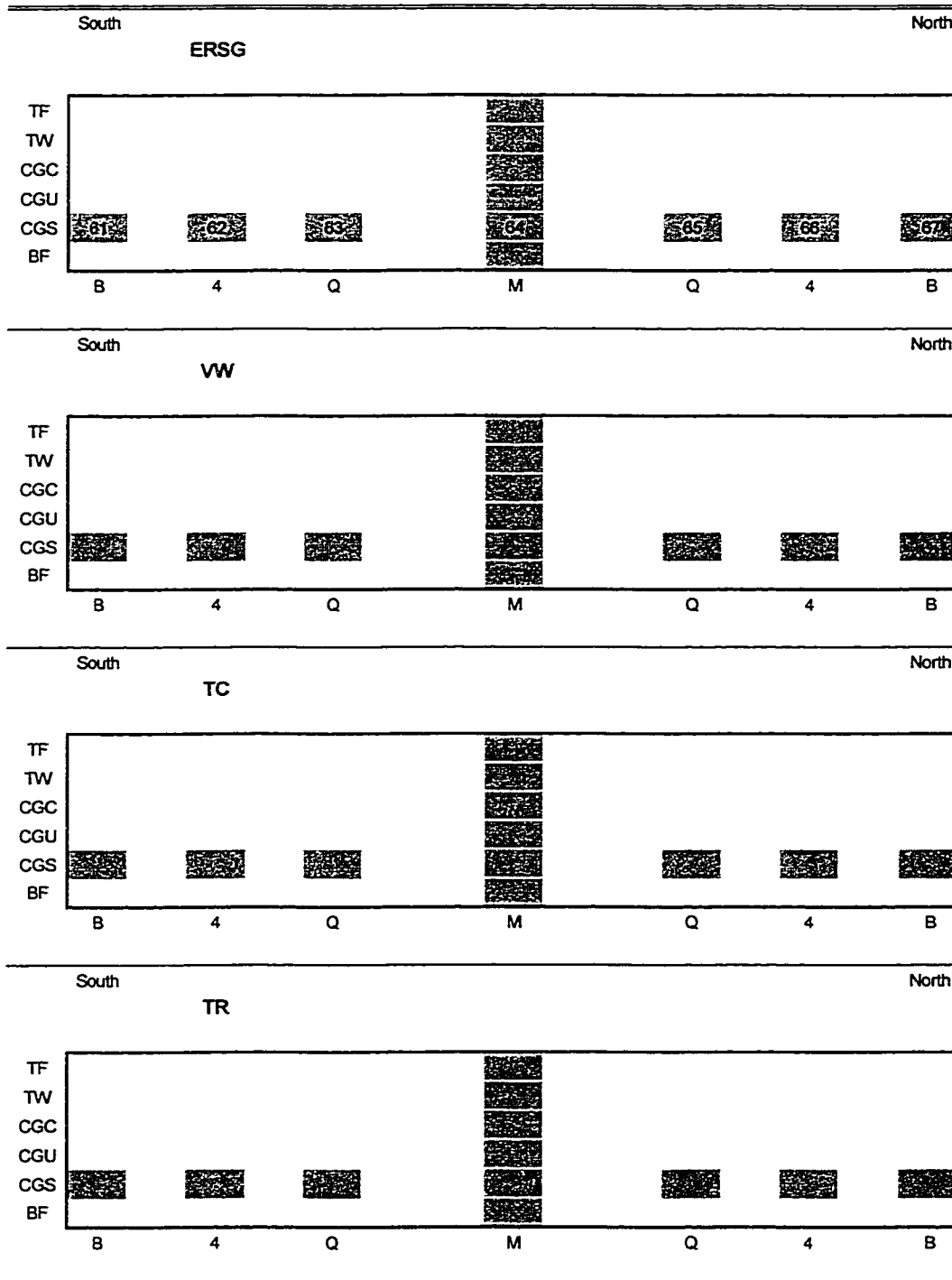
Louetta Beam S25 - East Web



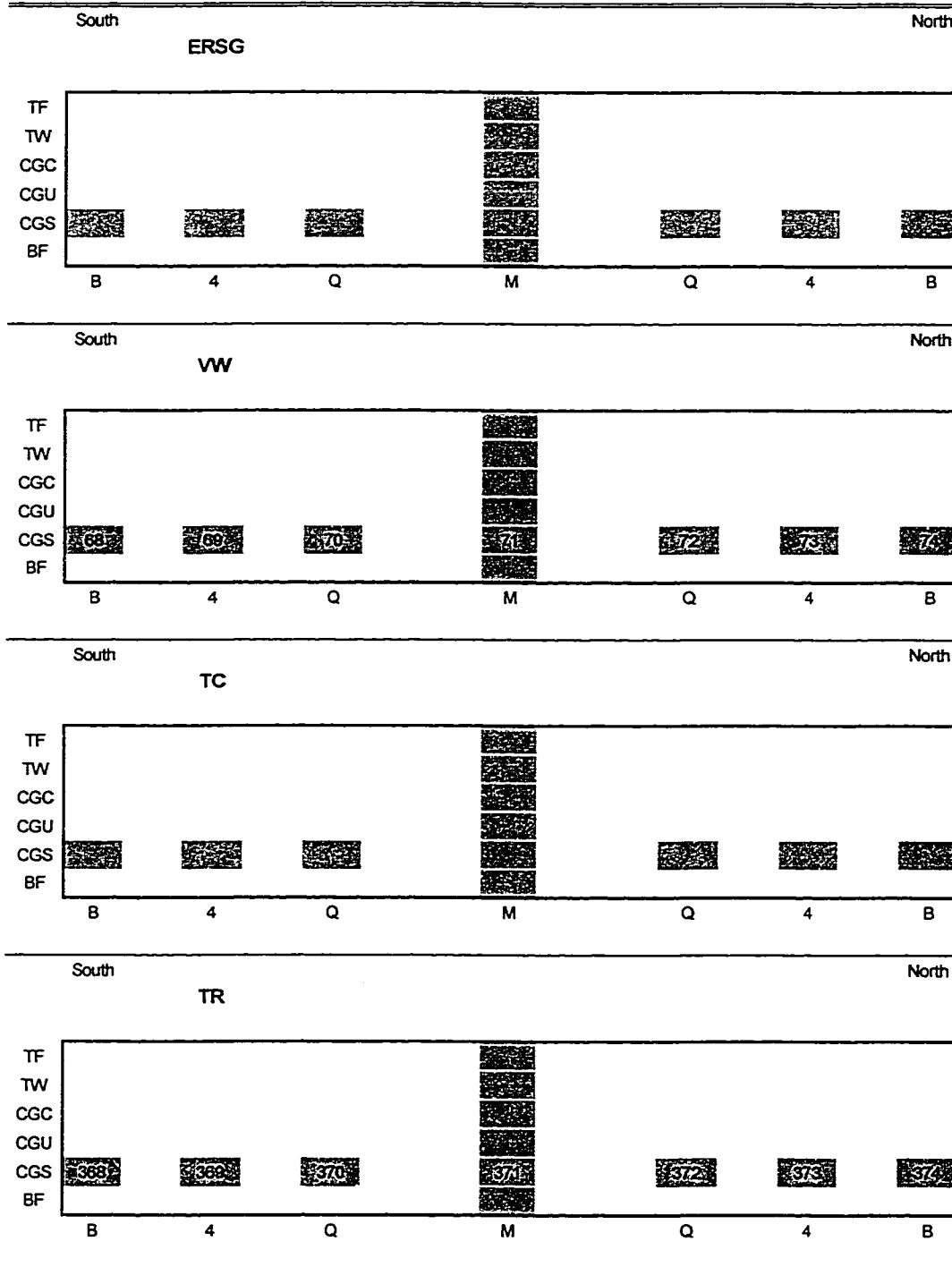
Louetta Beam S25 - West Web

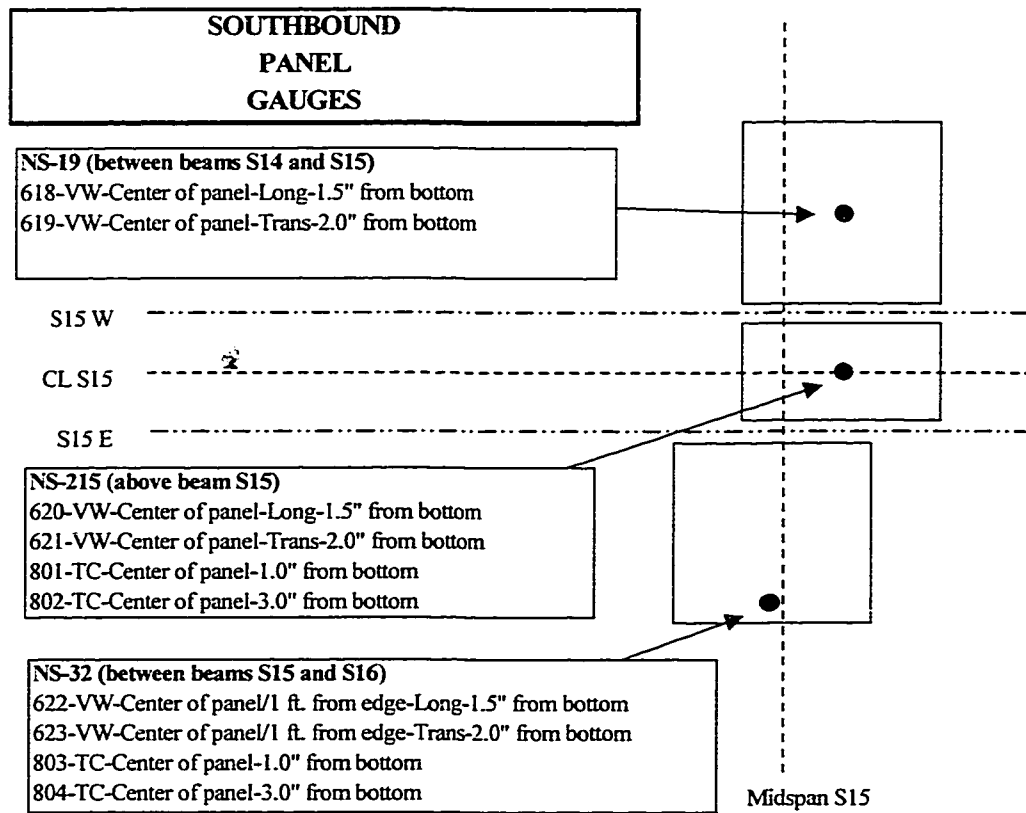


Louetta Beam S26 - East Web



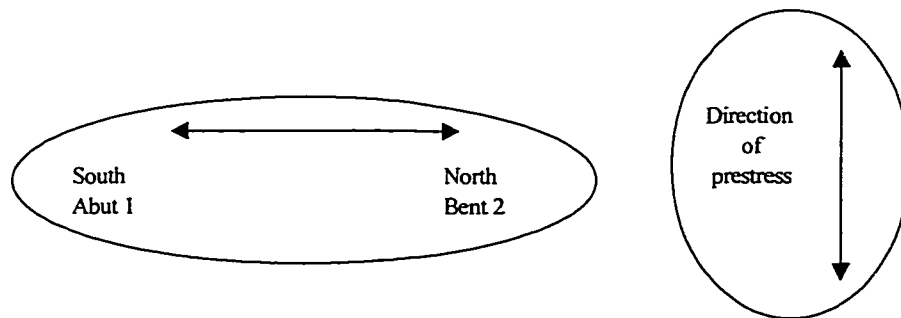
Louetta Beam S26 - West Web

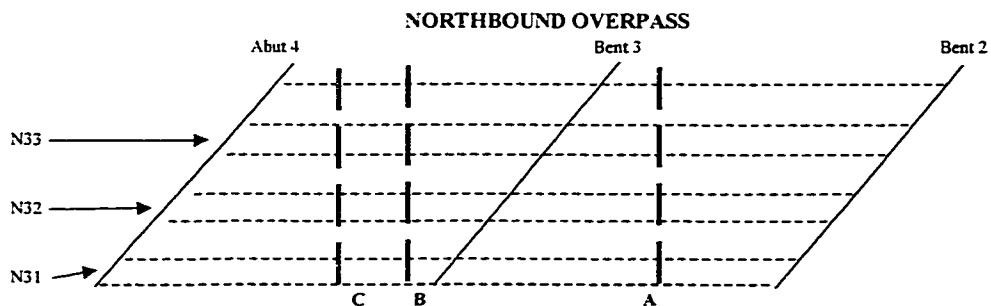




Longitudinal VW (across strands) is 1.5 in. from bottom of panel
 Transverse VW (along strands) is 2.0 in. from bottom of panel

Thermocouples are placed at 1.0 and 3.0 in. from bottom of panel





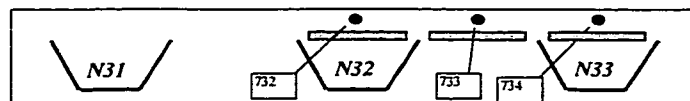
600's = VW
 700's = ERSG
 800's = TC

Thermocouples above panels layered at approximately 1/2" and 2" above top of panel
 All other gauges layered at approximately 1 1/2" below top of panel and 2" above top of panel
 Design thickness of CIP deck = 3 3/4"

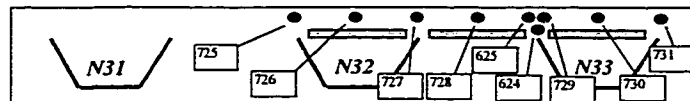
A
 Midspan of N21
 Thermocouples



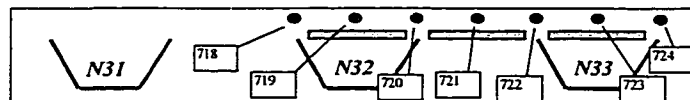
B
 Midspan of N33
 Transverse Gauges



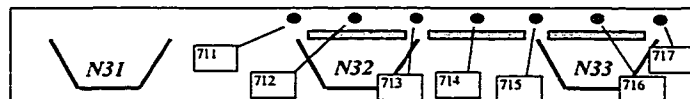
B
 Midspan of N33
 Longitudinal Gauges

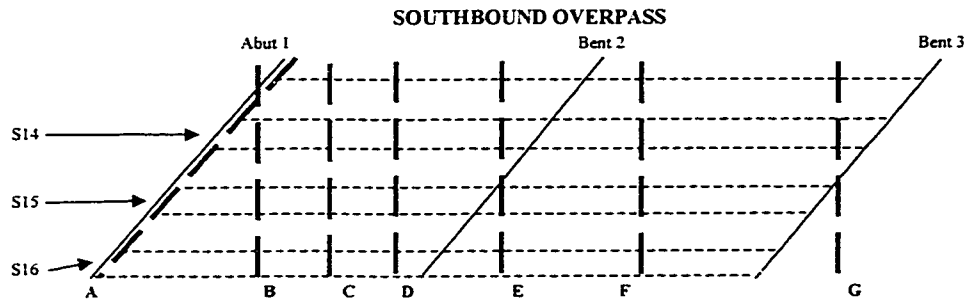


C
 Midspan of N32
 Transverse Gauges



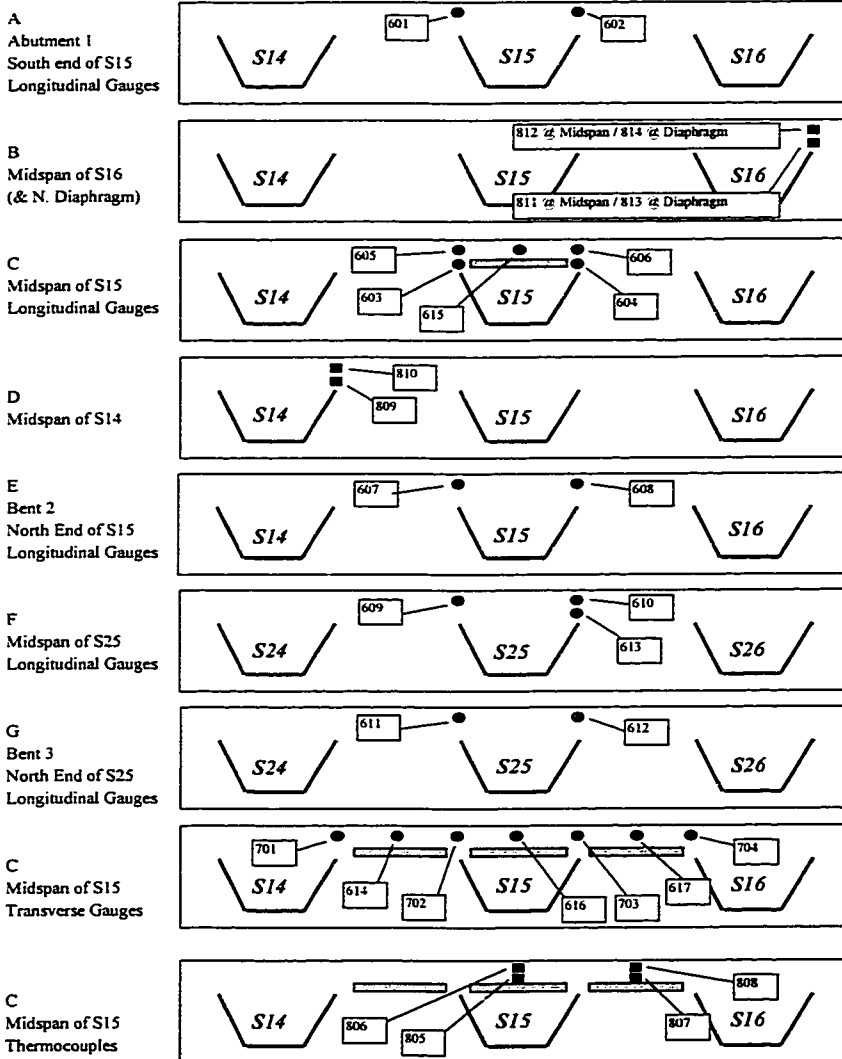
C
 Midspan of N32
 Longitudinal Gauges





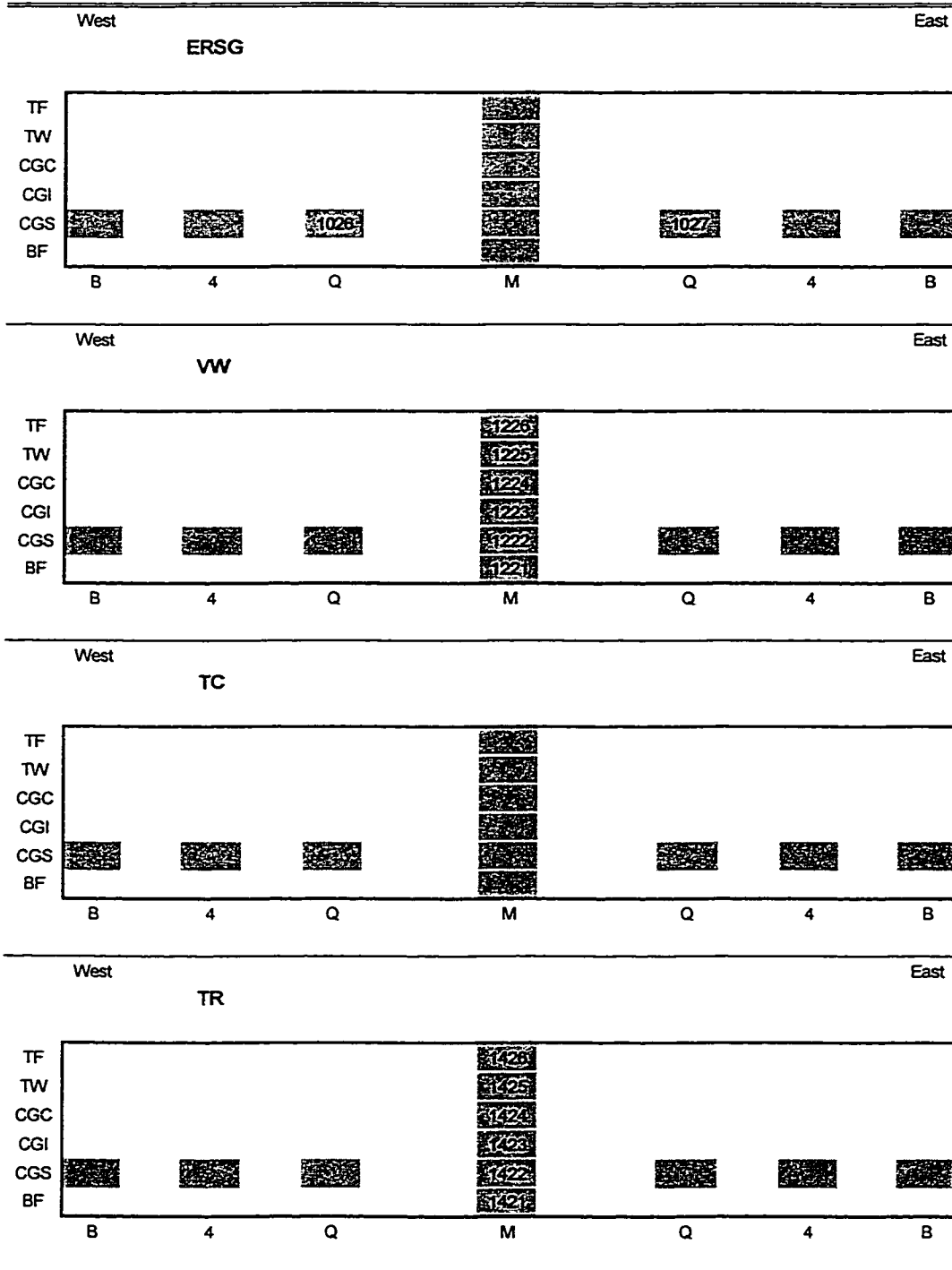
600's = VW
 700's = ERSG
 800's = TC

Thermocouples above panels layered at approximately 1/2" and 2" above top of panel
 All other gauges layered at approximately 1 1/2" below top of panel and 2" above top of panel
 Actual gauge depths measured in field from top of panel and top of beam
 Design thickness of CIP deck = 3 3/4"

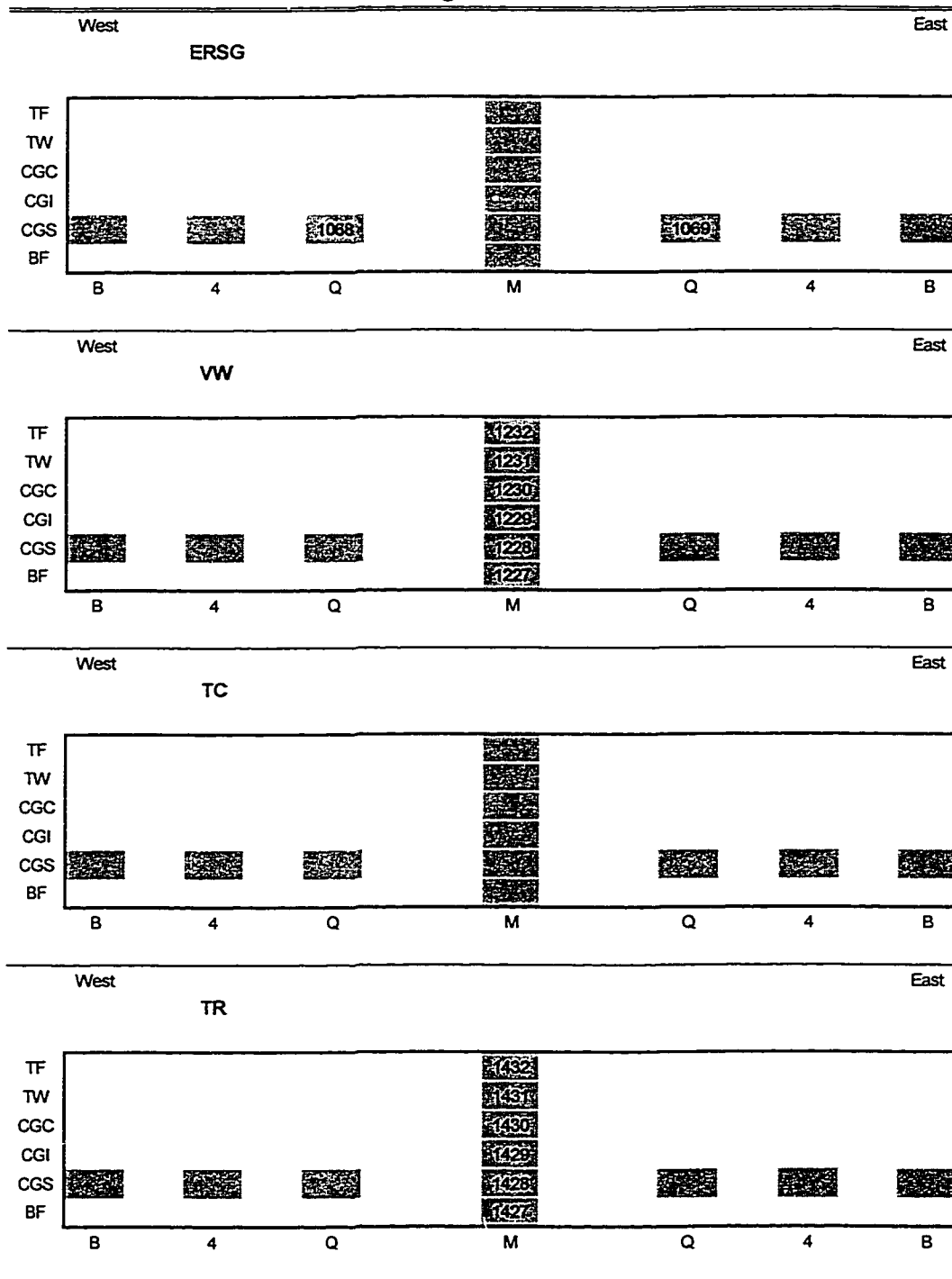


**APPENDIX B: SKETCHES DEPICTING GAUGE LOCATIONS FOR
INSTRUMENTATION OF THE N. CONCHO RIVER/U.S. 87/S.O.R.R.
OVERPASS**

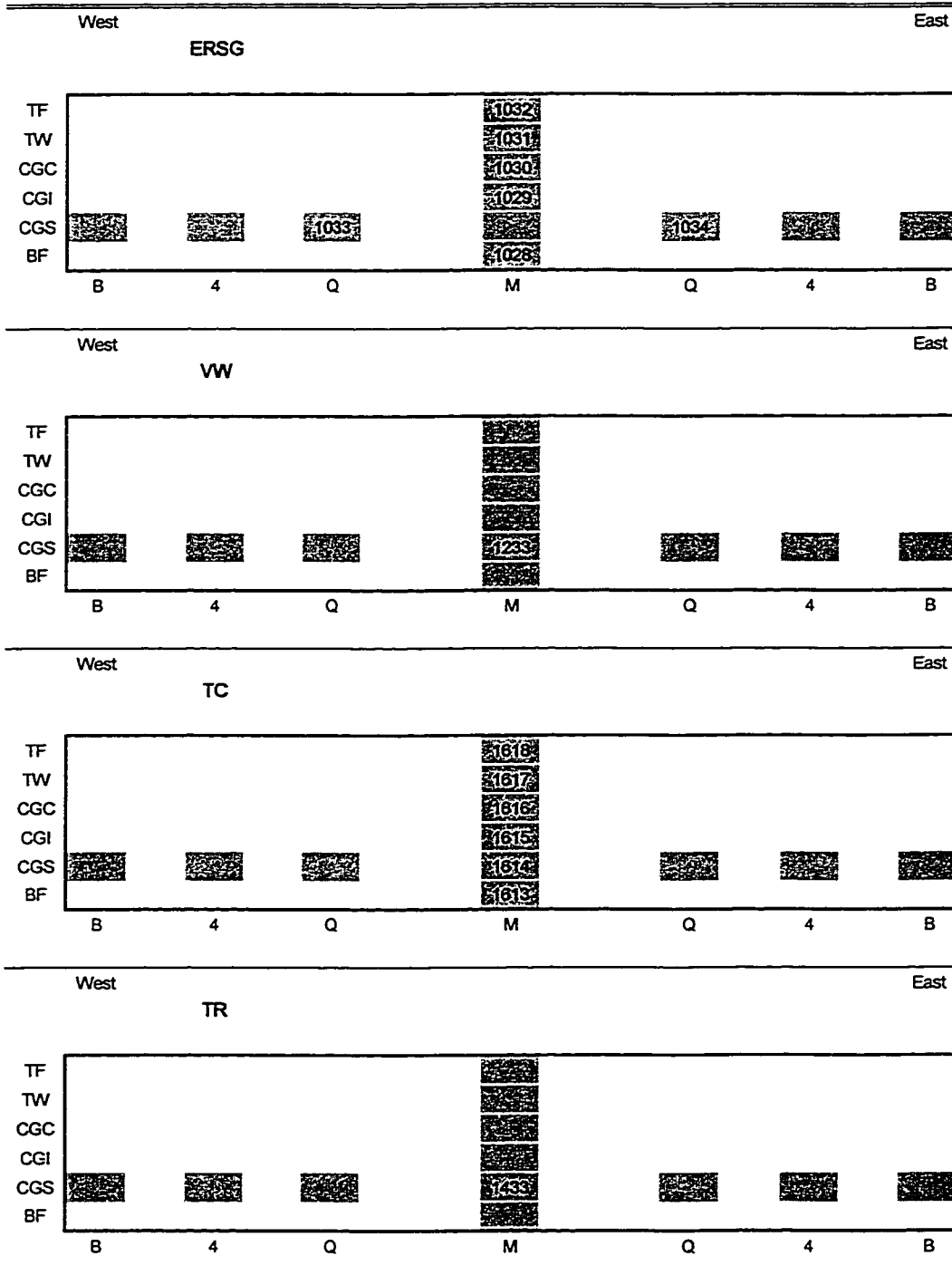
San Angelo Beam E13



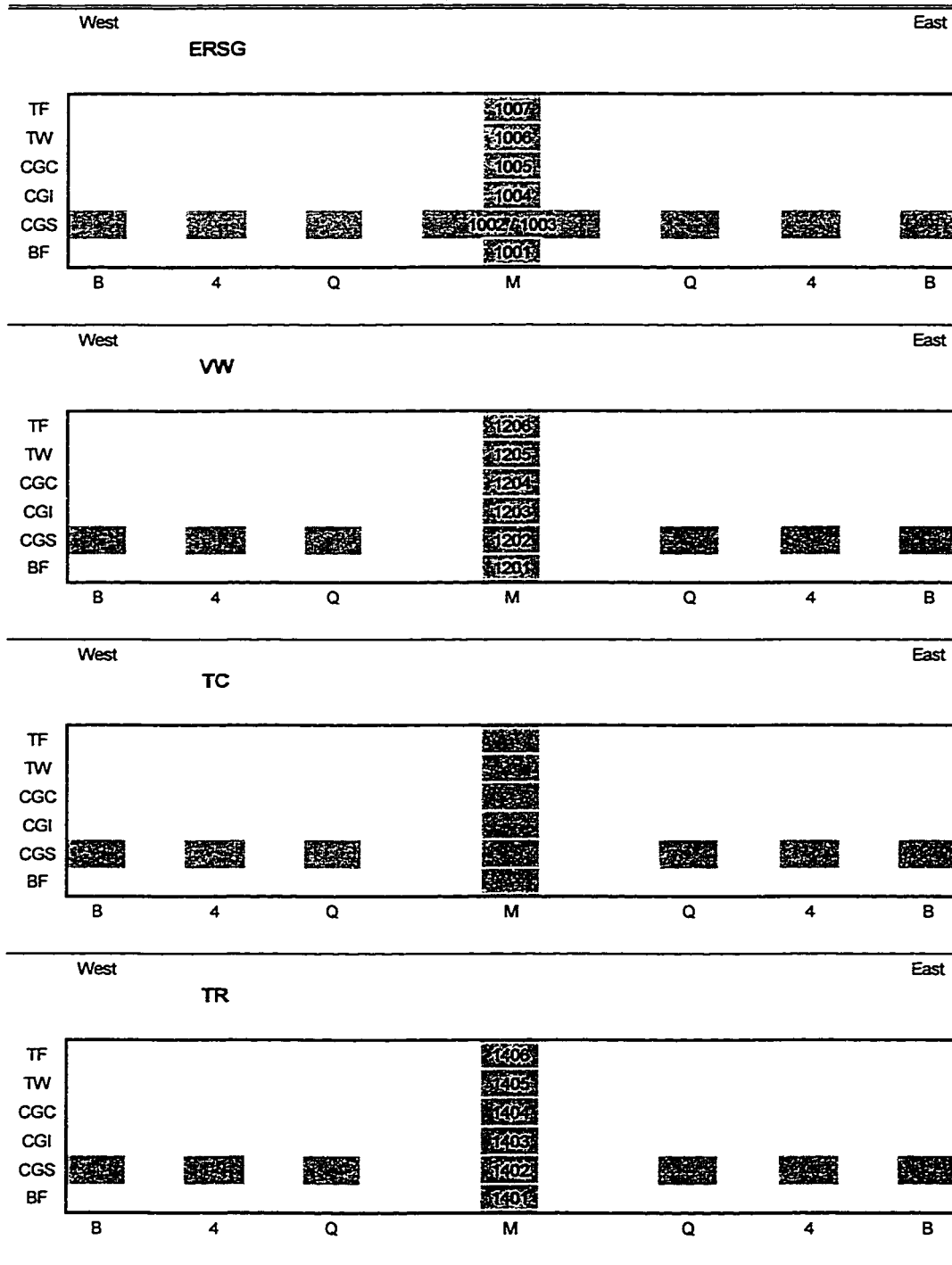
San Angelo Beam E14



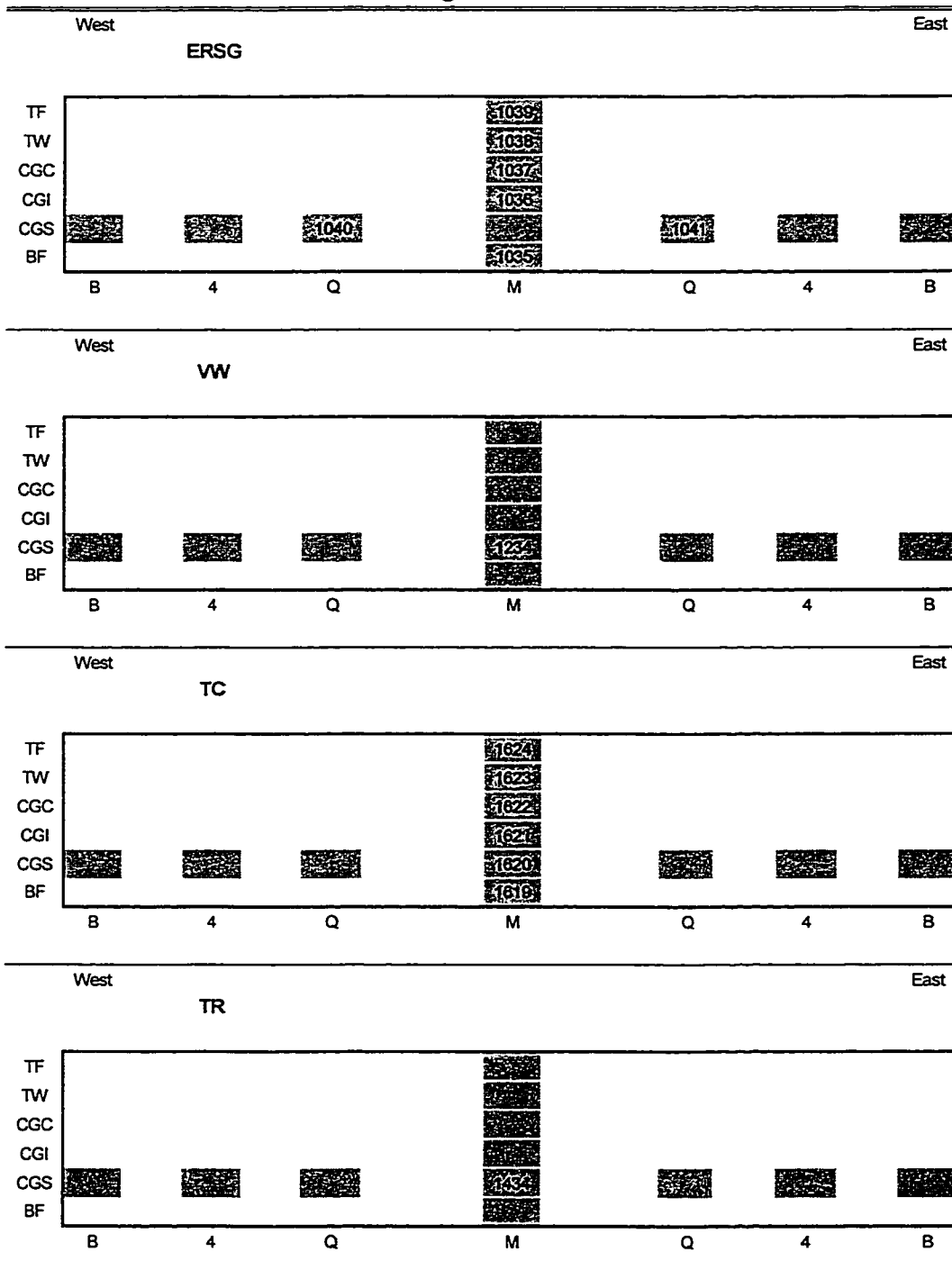
San Angelo Beam E24



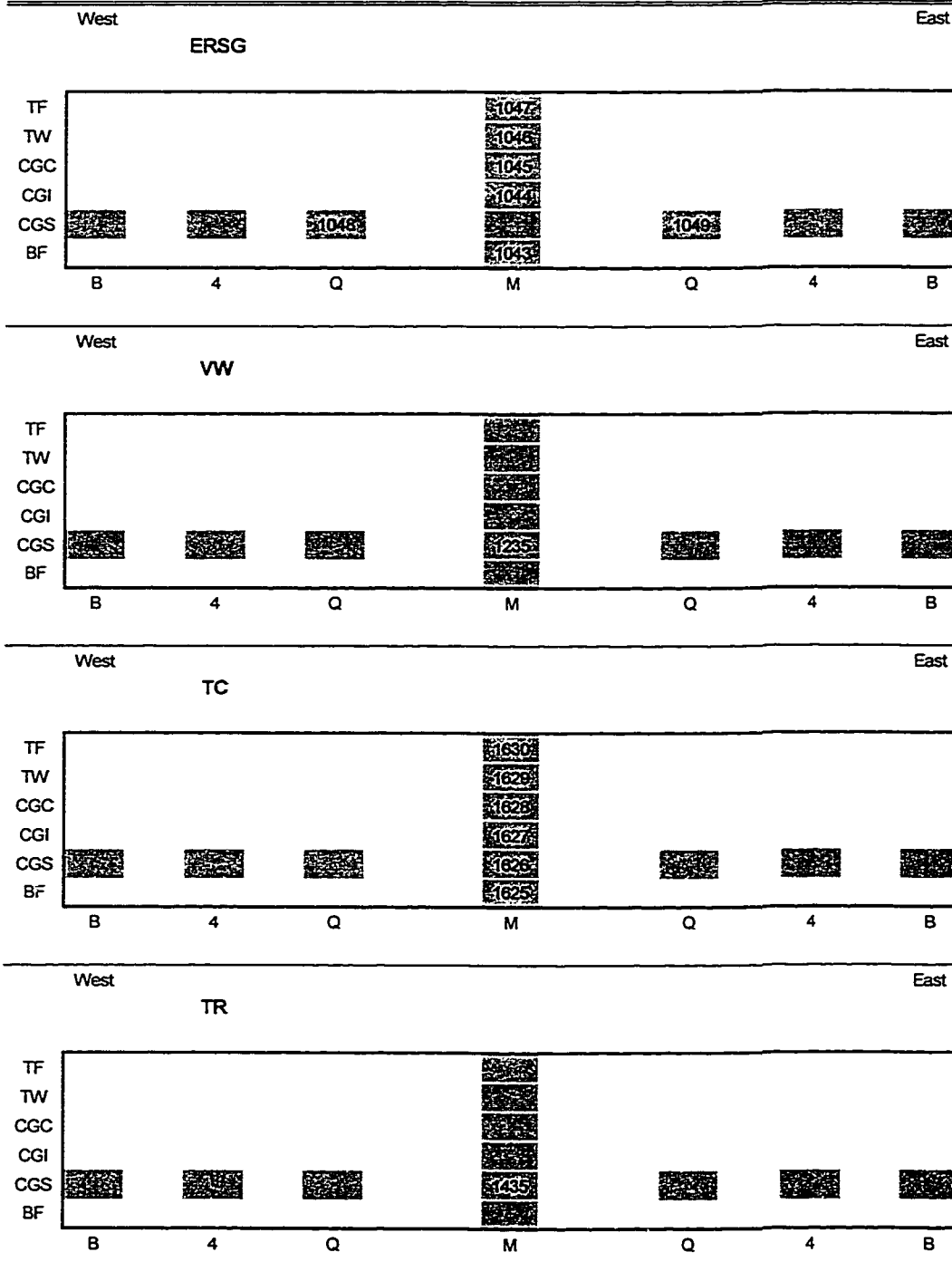
San Angelo Beam E25



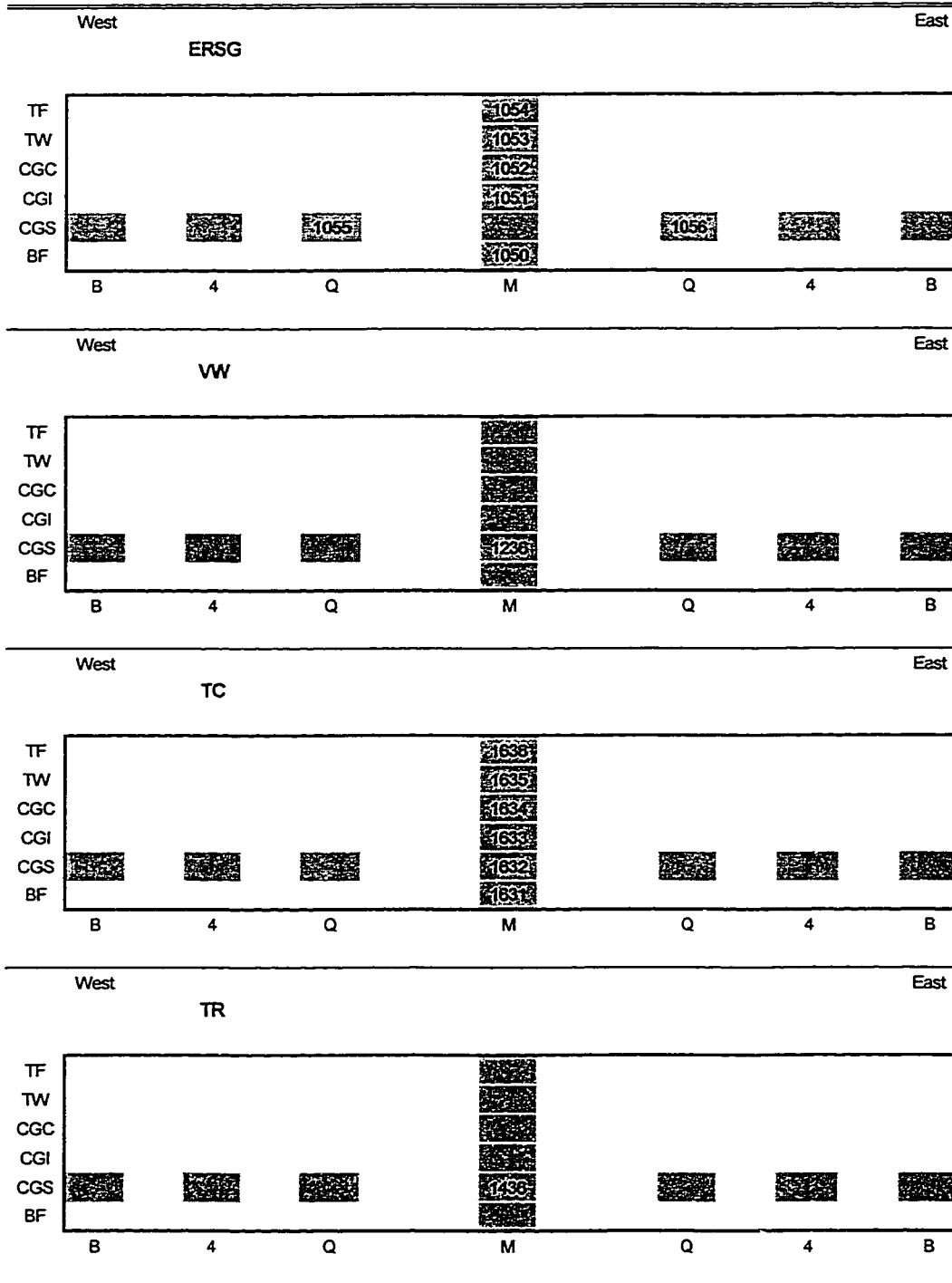
San Angelo Beam E26



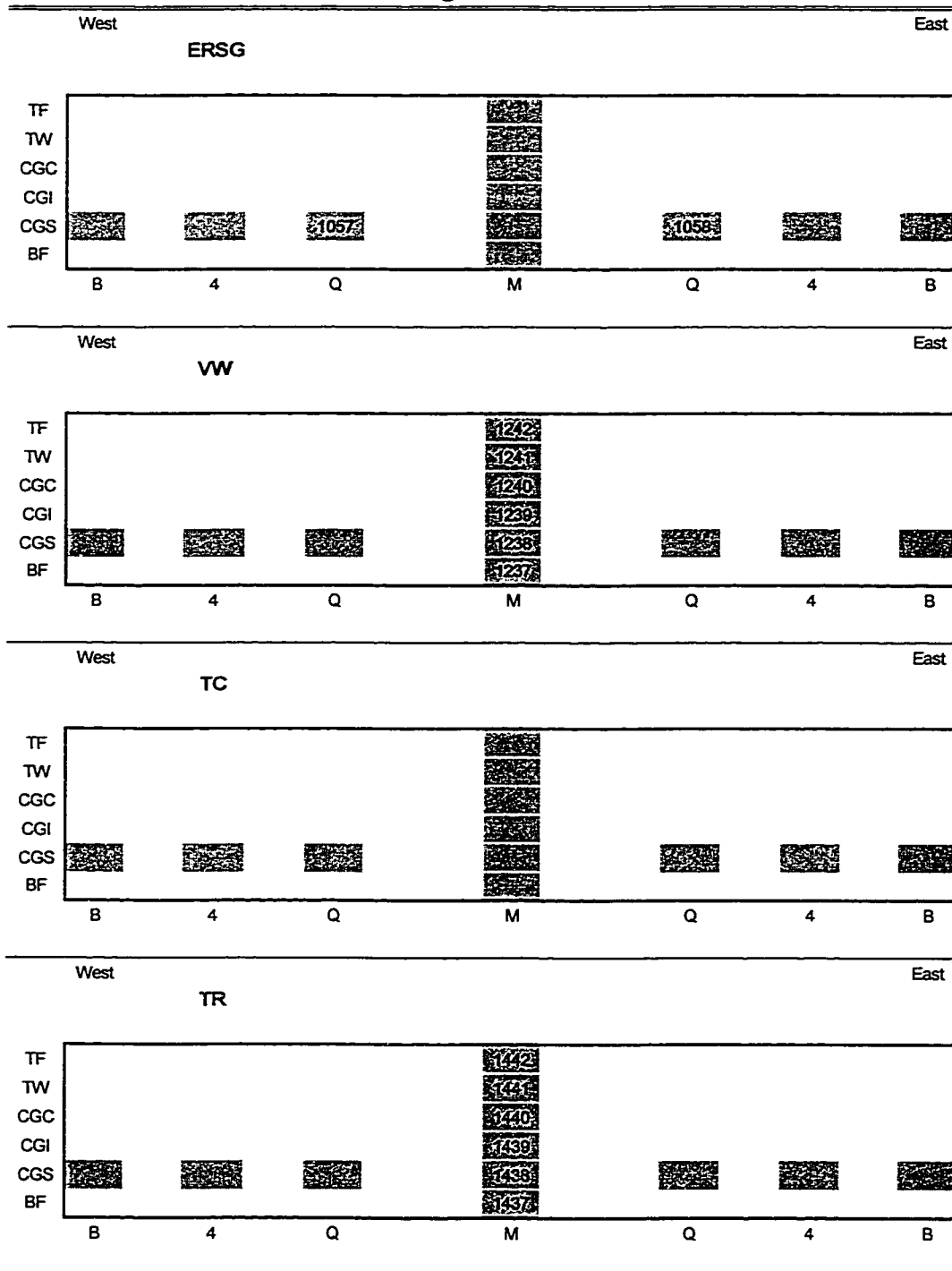
San Angelo Beam E33



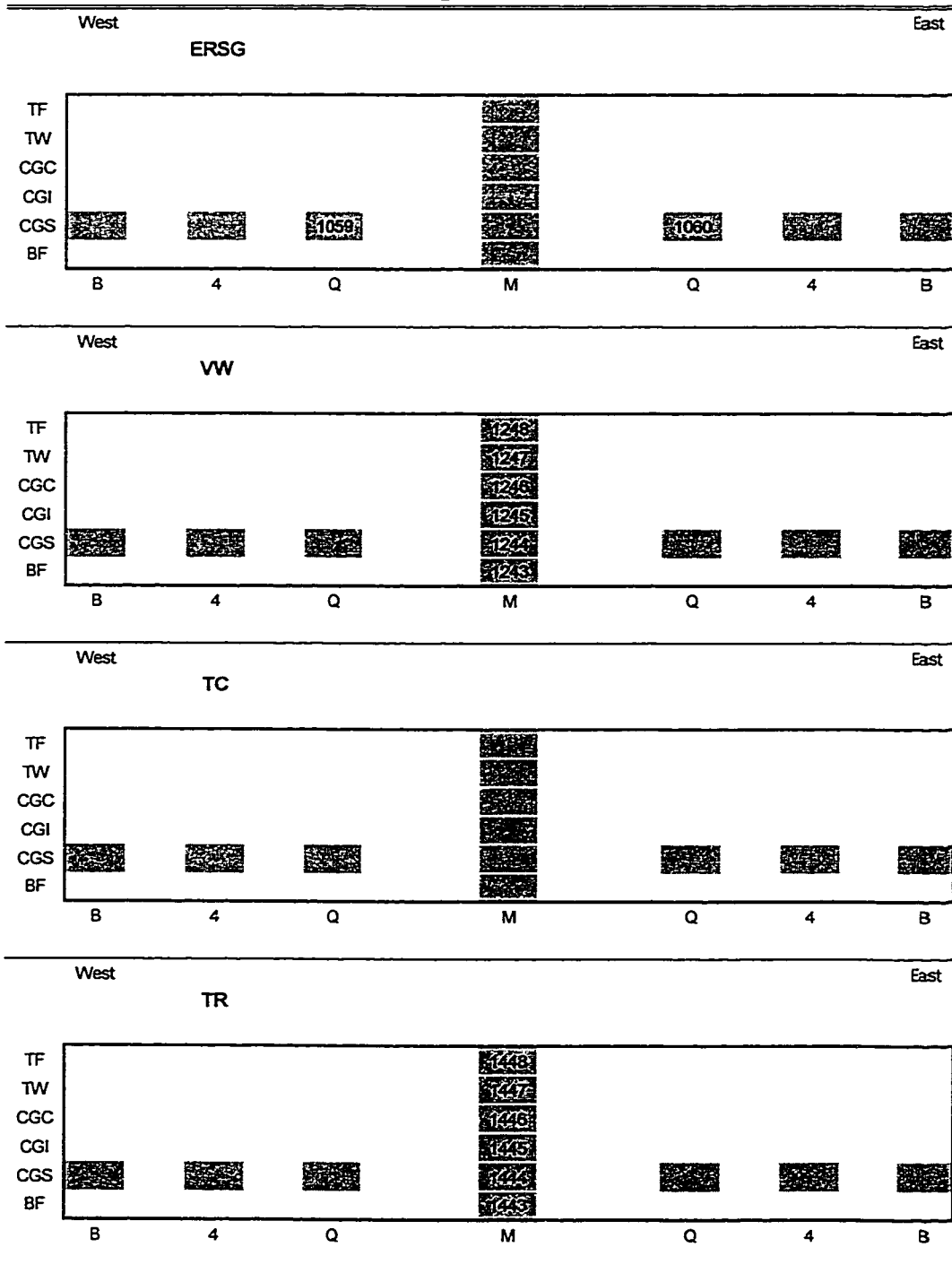
San Angelo Beam E34



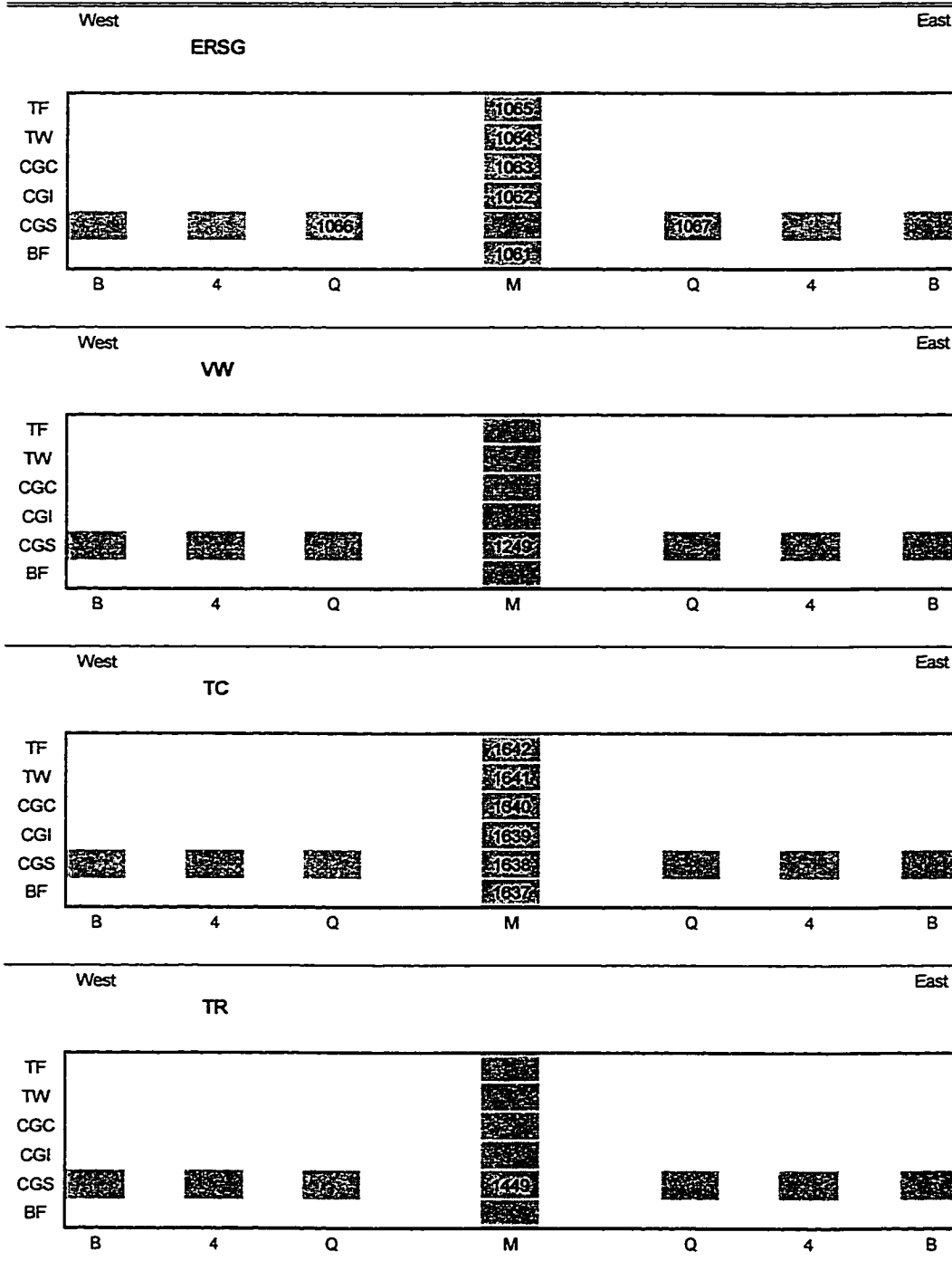
San Angelo Beam E35



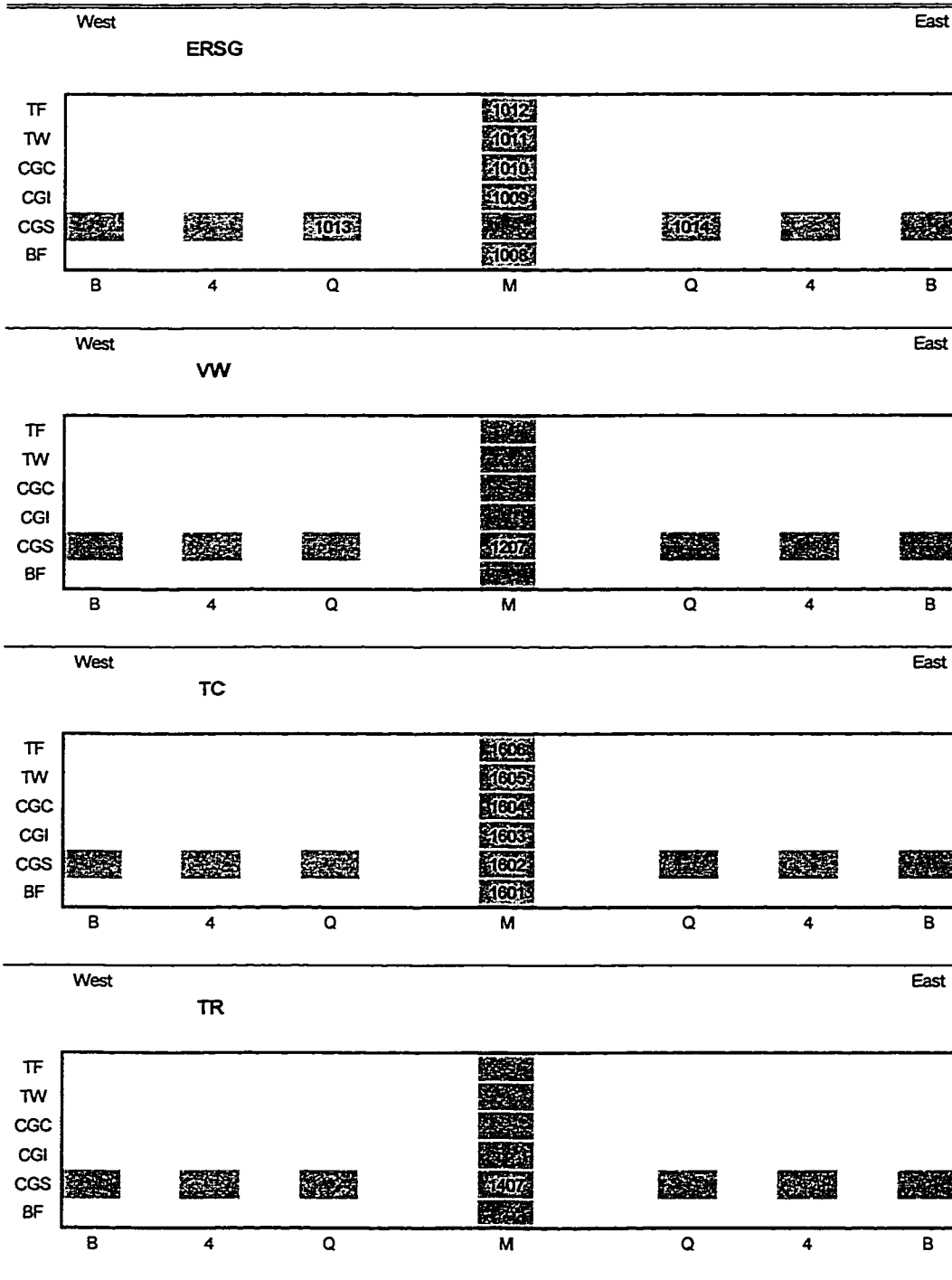
San Angelo Beam E44



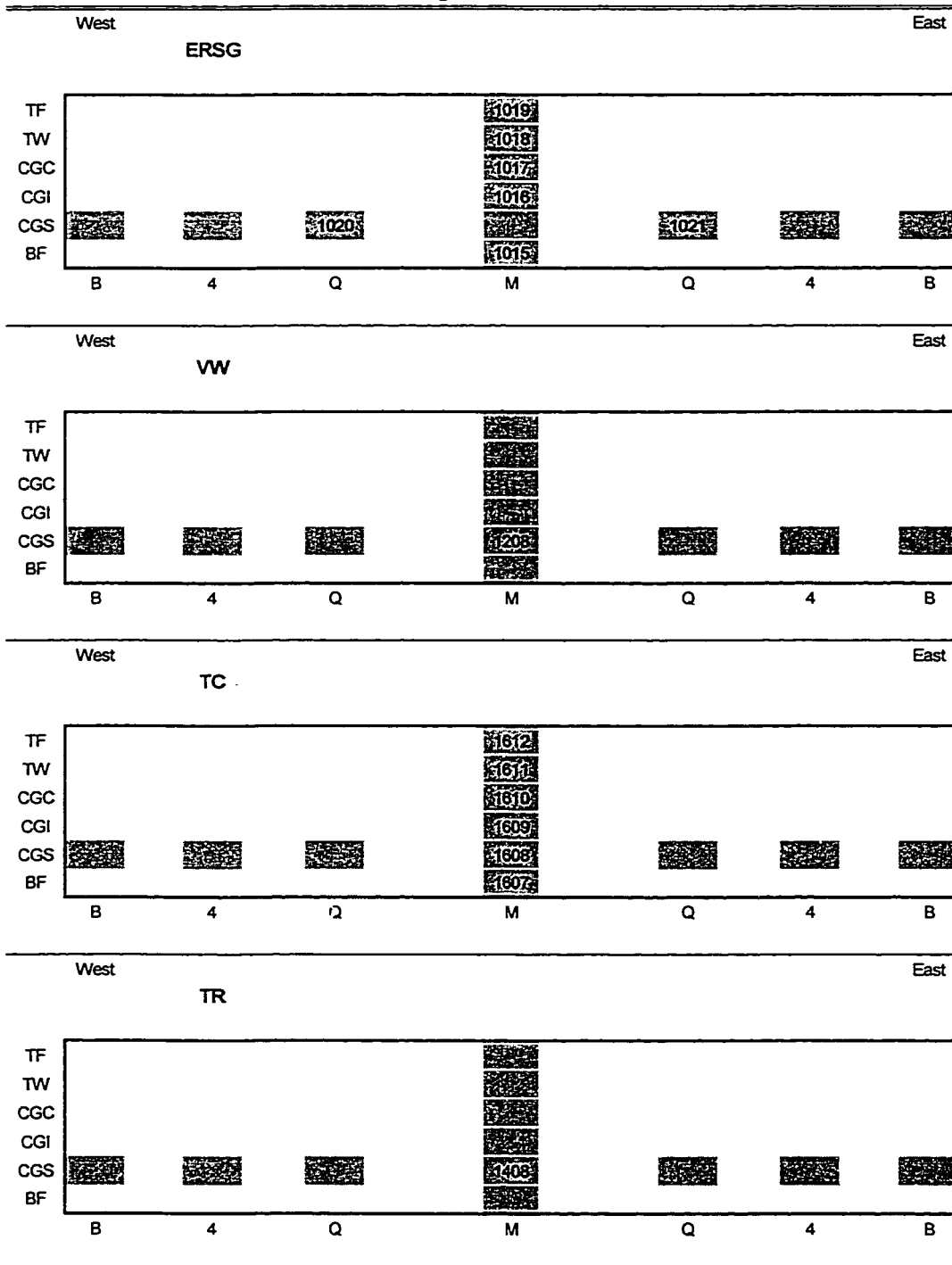
San Angelo Beam E45



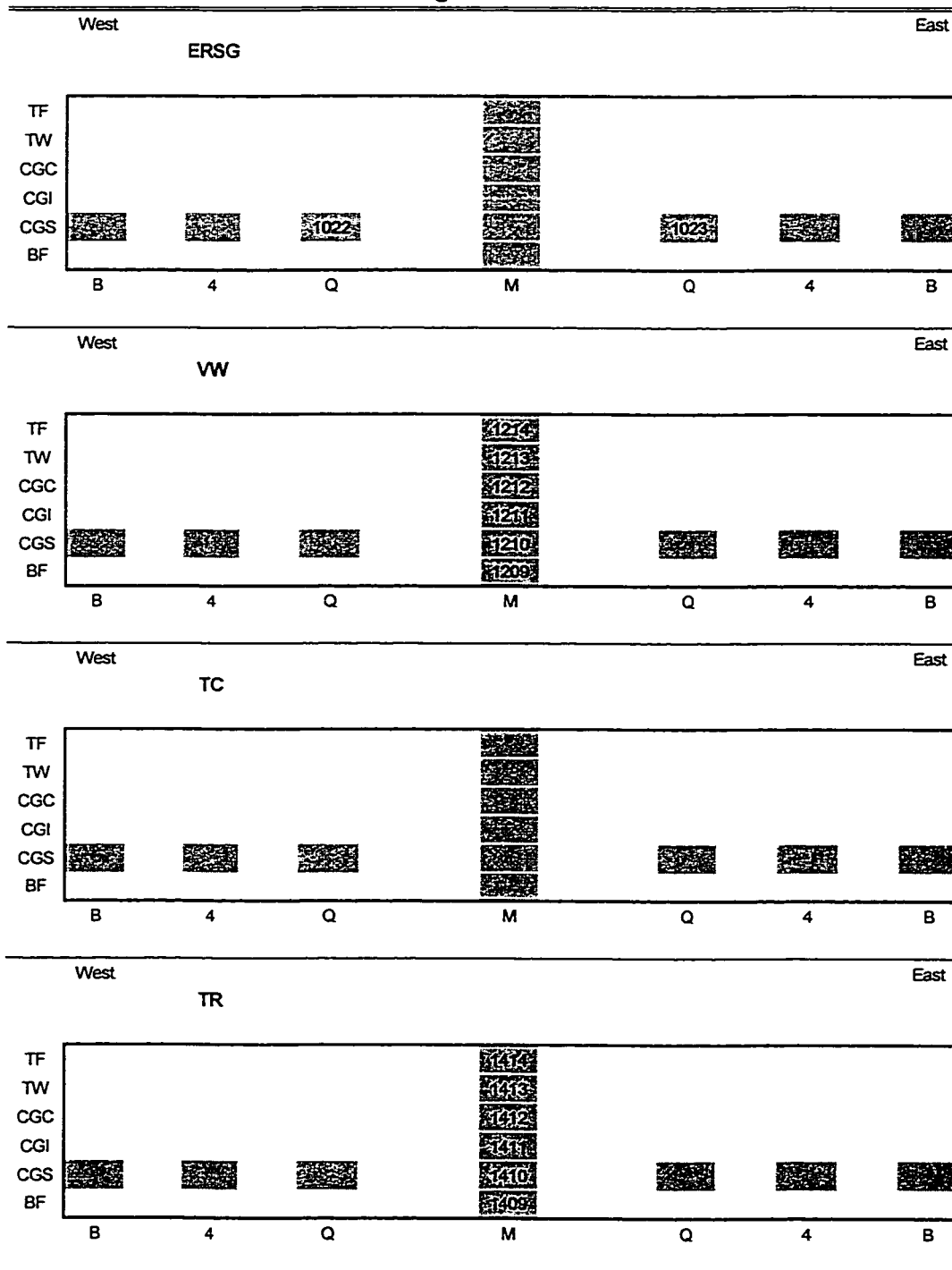
San Angelo Beam W14



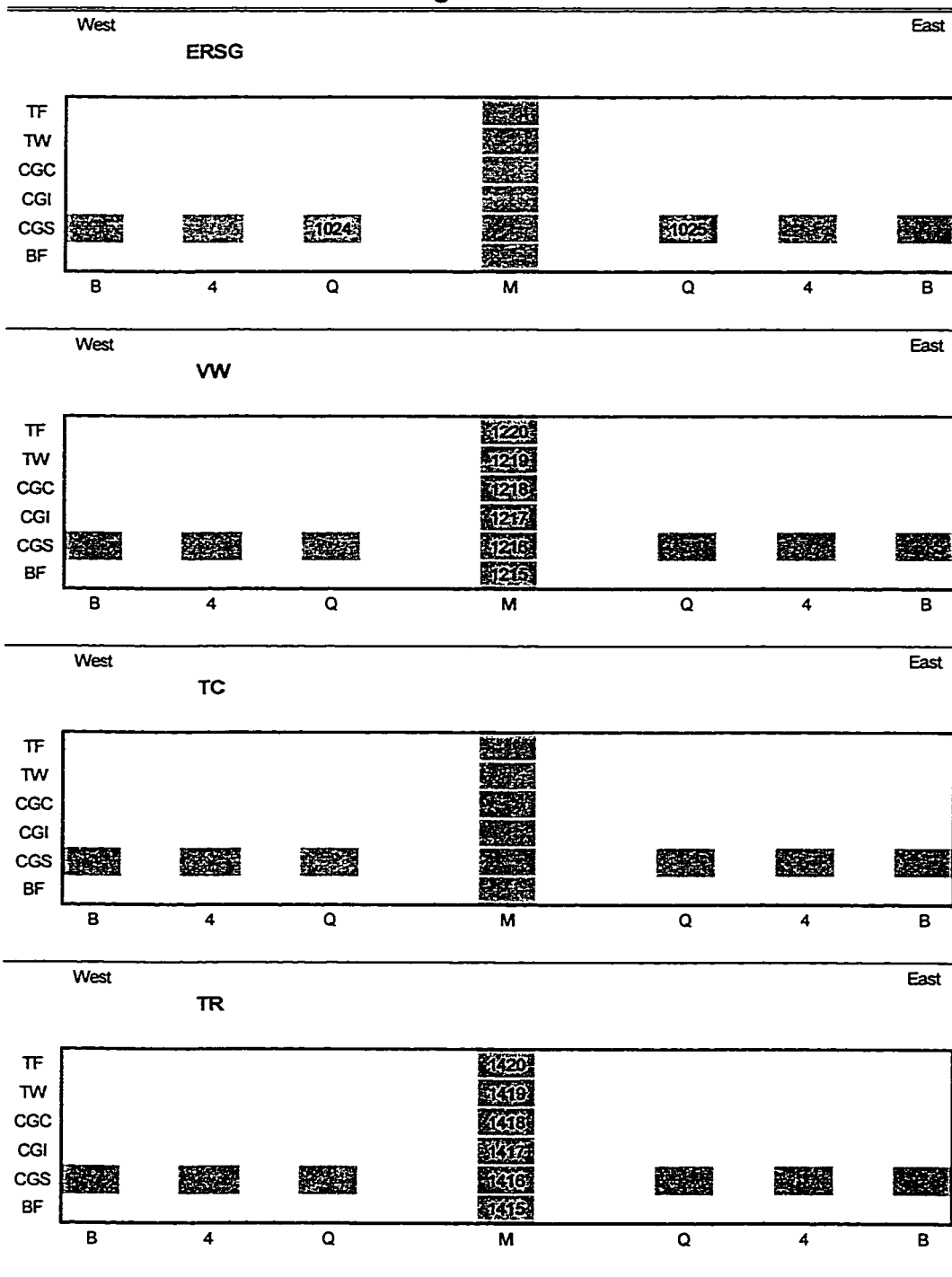
San Angelo Beam W15

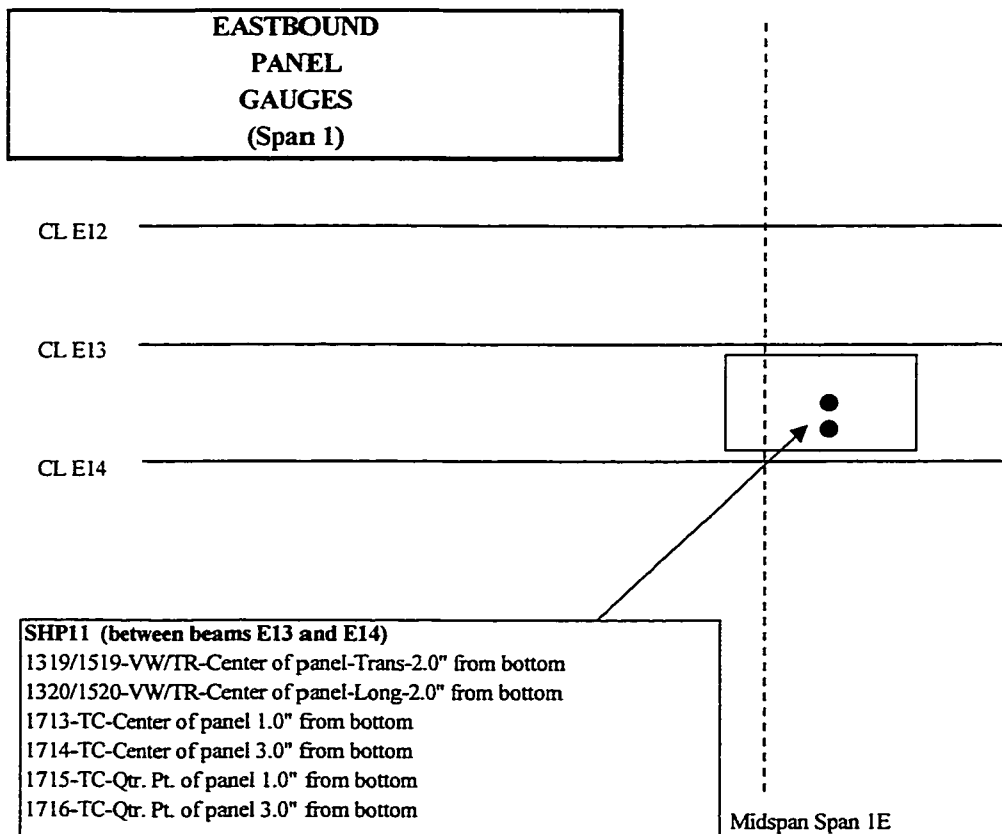


San Angelo Beam W16



San Angelo Beam W17

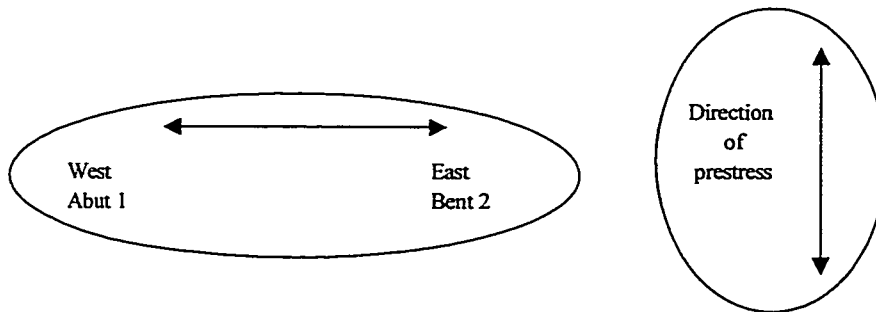


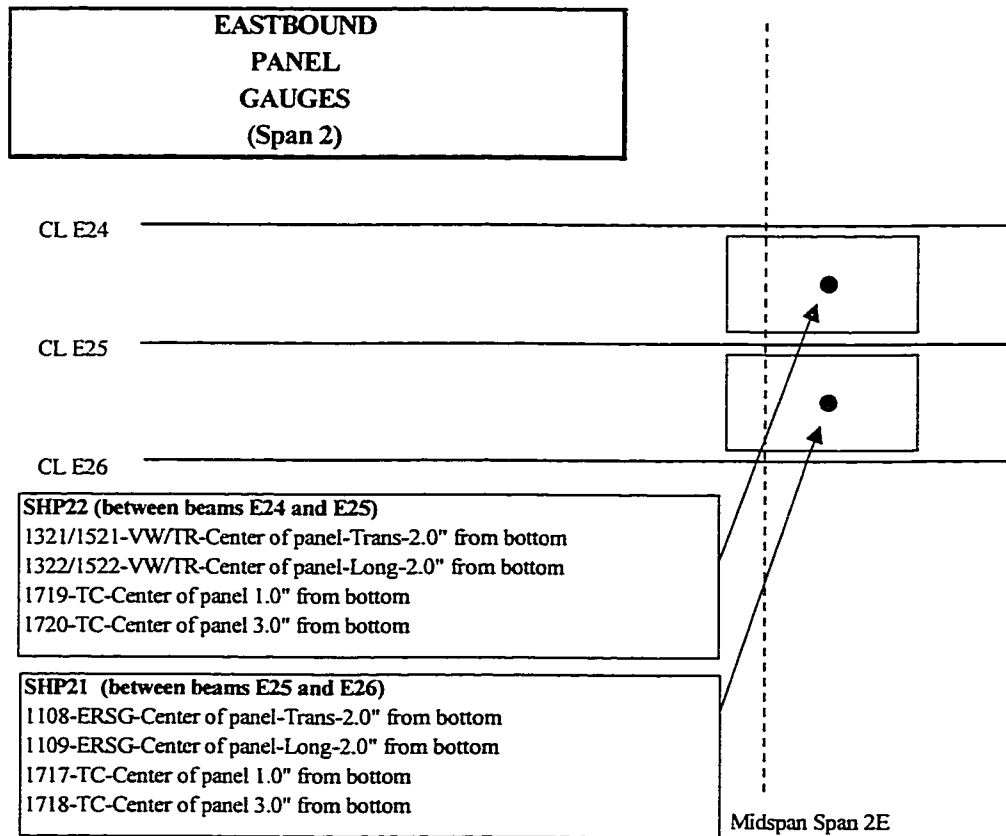


Longitudinal VW (across strands) is 2.0 in. from bottom of panel
 Transverse VW (along strands) is 2.0 in. from bottom of panel

Thermocouples are placed at 1.0 and 3.0 in. from bottom of panel

Panel dimensions are 8 ft. by 10.3 ft. (96 in. by 123.6 in.)

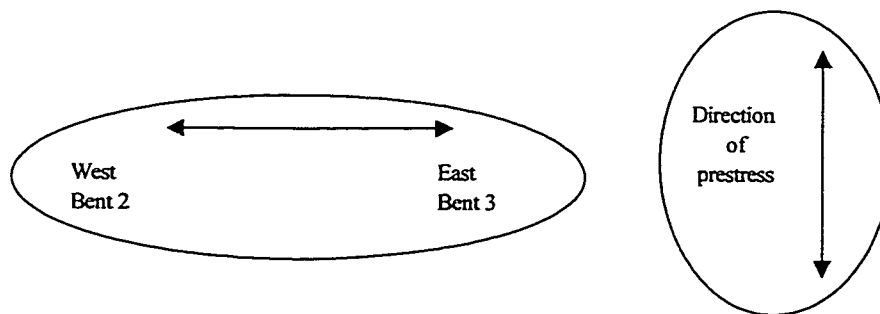


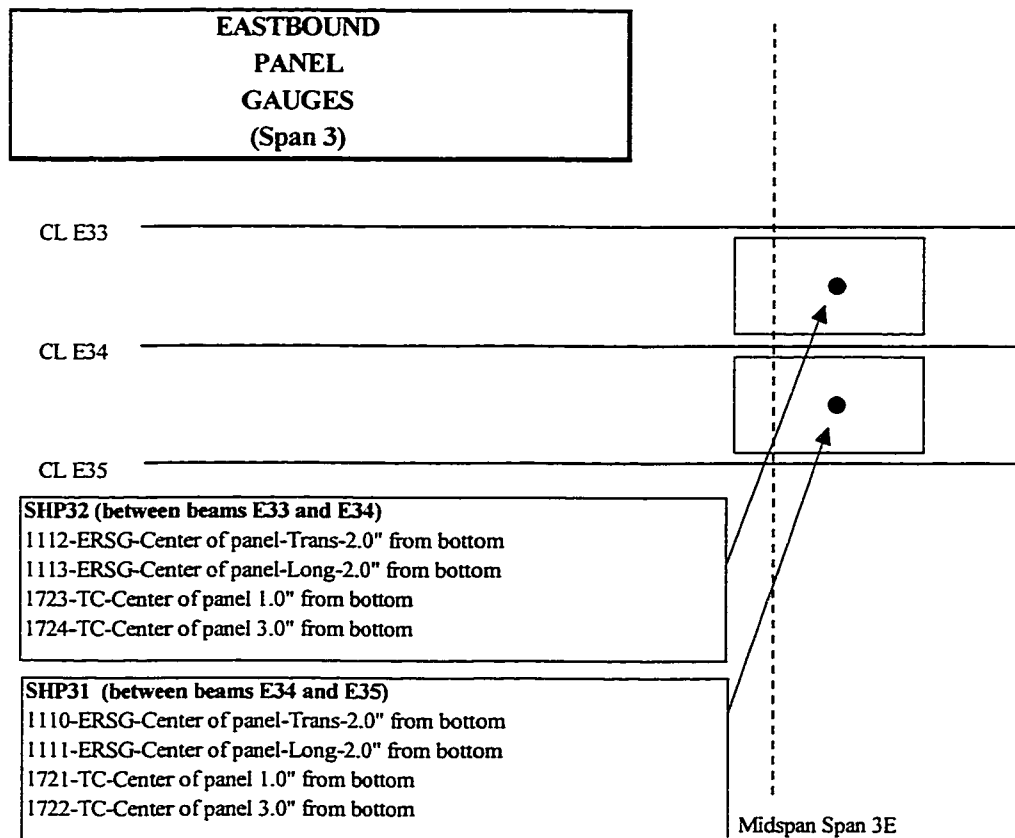


Longitudinal VW (across strands) is 2.0 in. from bottom of panel
 Transverse VW (along strands) is 2.0 in. from bottom of panel

Thermocouples are placed at 1.0 and 3.0 in. from bottom of panel

Panel dimensions are 8 ft. by 5.8 ft. (96 in. by 69.6 in.)

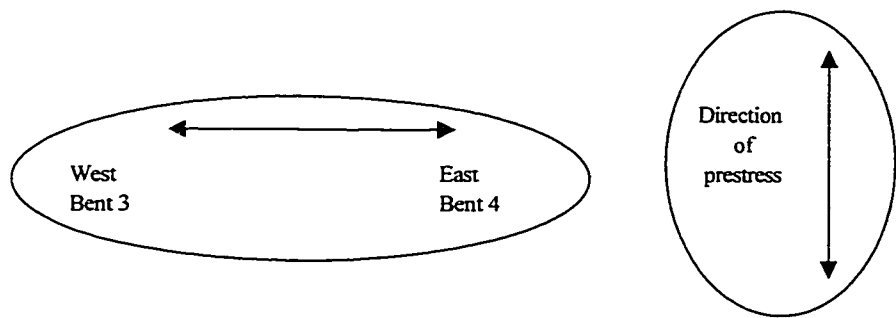


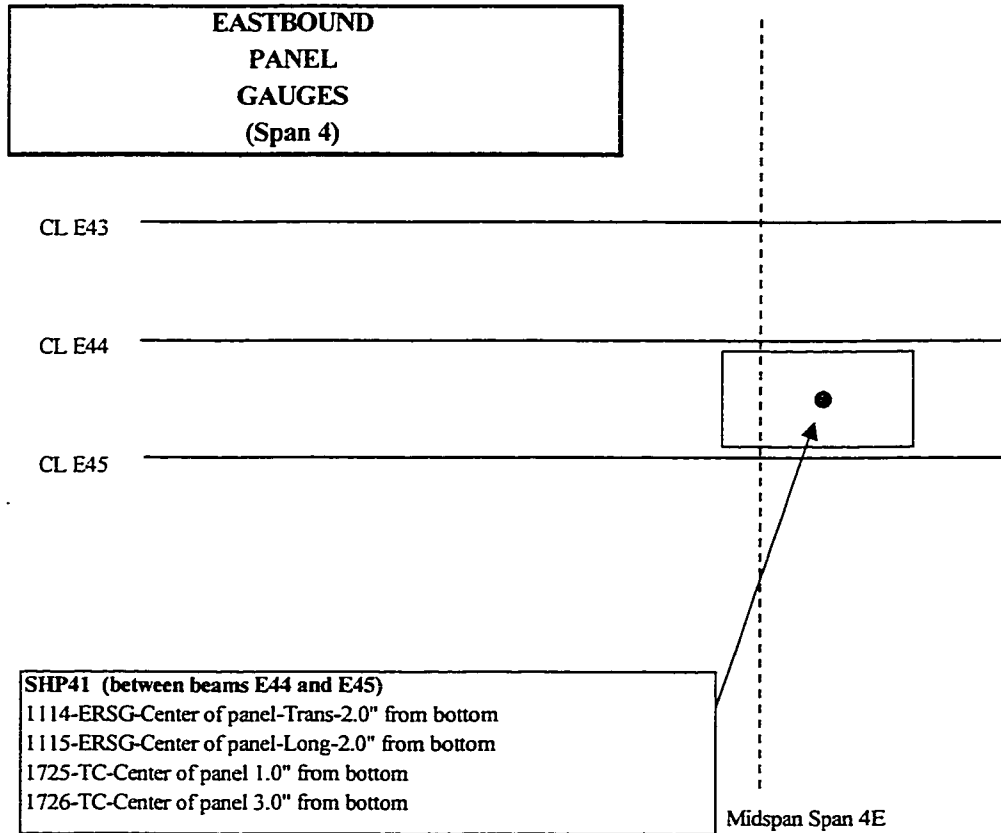


Longitudinal VW (across strands) is 2.0 in. from bottom of panel
 Transverse VW (along strands) is 2.0 in. from bottom of panel

Thermocouples are placed at 1.0 and 3.0 in. from bottom of panel

Panel dimensions are 8 ft. by 7.5 ft. (96 in. by 90 in.)

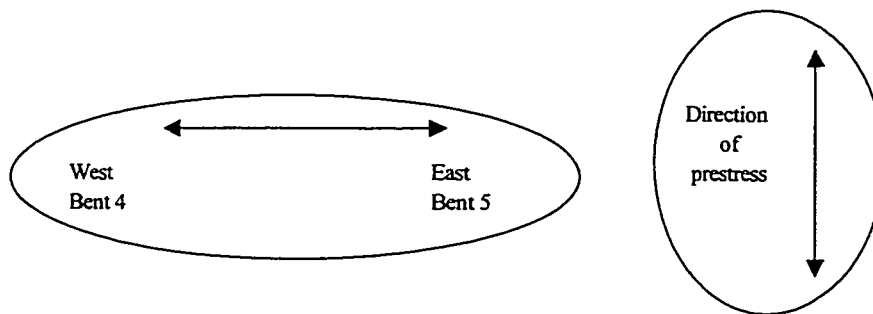


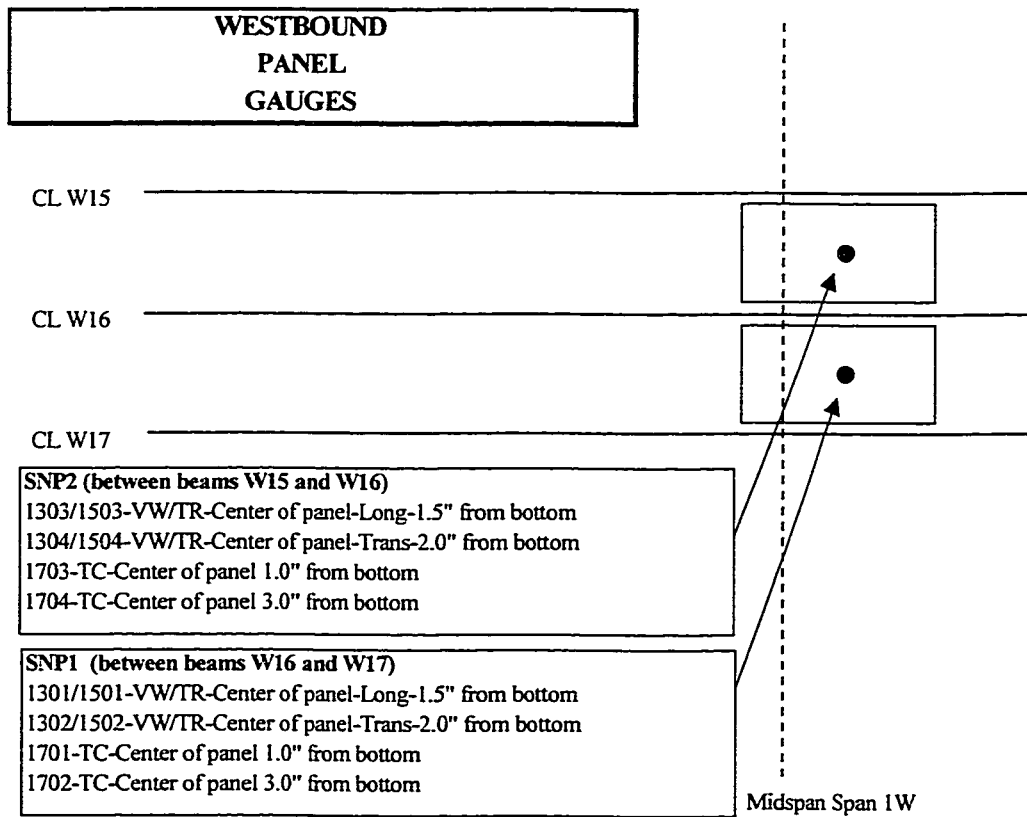


Longitudinal VW (across strands) is 2.0 in. from bottom of panel
 Transverse VW (along strands) is 2.0 in. from bottom of panel

Thermocouples are placed at 1.0 and 3.0 in. from bottom of panel

Panel dimensions are 8 ft. by 7.5 ft. (96 in. by 90 in.)

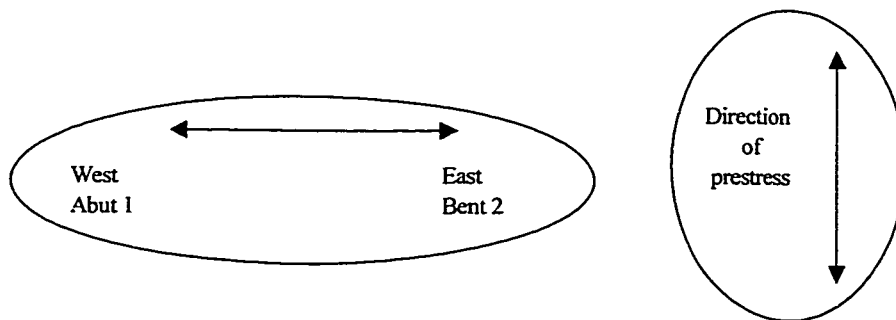




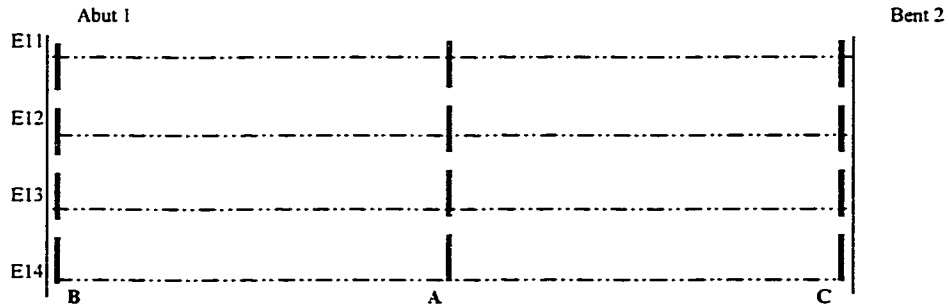
Longitudinal VW (across strands) is 1.5 in. from bottom of panel
 Transverse VW (along strands) is 2.0 in. from bottom of panel

Thermocouples are placed at 1.0 and 3.0 in. from bottom of panel

Panel dimensions are 8 ft. by 4.9 ft. (96 in. by 58.8 in.)
 Offset of center of panels to midspan is approx. 2.5 ft. (30 in.)



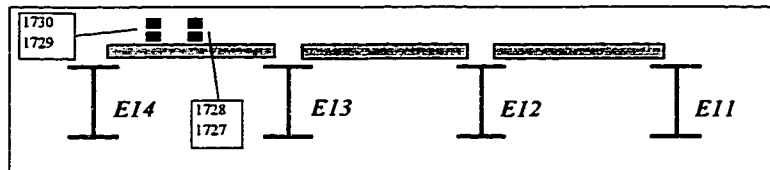
EASTBOUND OVERPASS (Span 1)



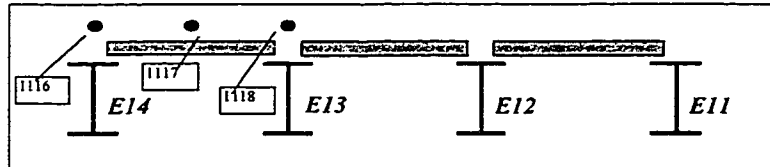
1100's = ERSG
 1300's = VW
 1500's = TR
 1700's = TC

Thermocouples above panels layered at approximately 1" and 2" above top of panel
 All other gauges layered at approx. 1 3/4" below top of panel and 1 3/4" above top of panel
 Actual gauge depths measured in field from top of panel and top of beam
 Design thickness of CIP deck = 3 1/2"

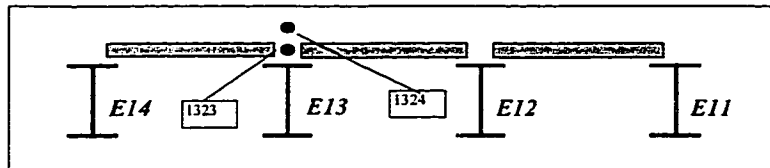
A
 Midspan
 Thermocouples



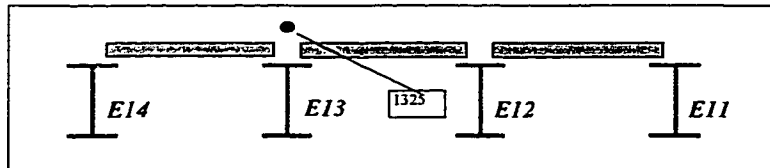
A
 Midspan
 Transverse
 ERSG Gauges



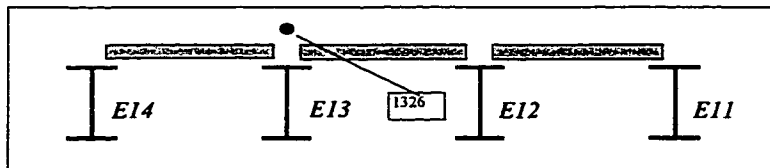
A
 Midspan
 Longitudinal
 VW Gauges



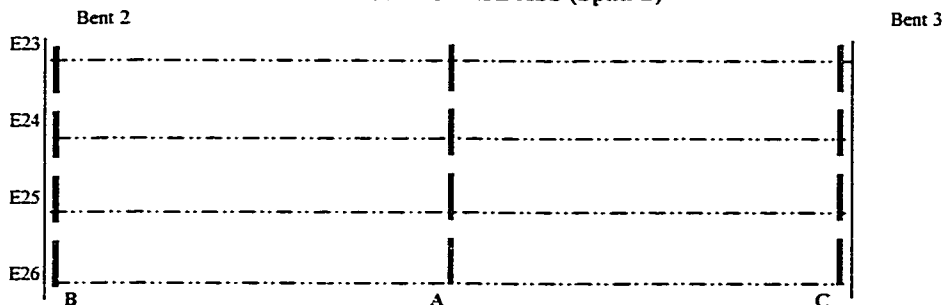
B
 Abut 1
 Longitudinal
 VW Gauges



C
 Bent 2
 Longitudinal
 VW Gauges



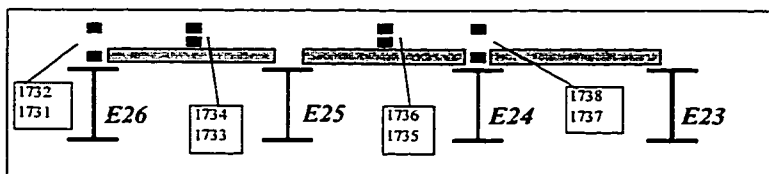
EASTBOUND OVERPASS (Span 2)



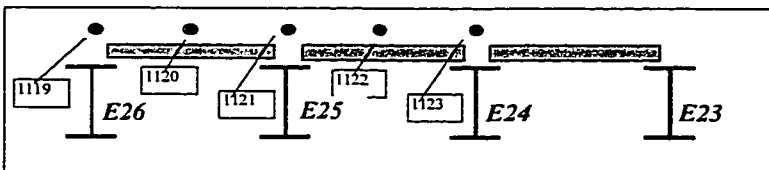
1100's = ERSG
 1300's = VW
 1500's = TR
 1700's = TC

Thermocouples above panels layered at approximately 1" and 2" above top of panel
 All other gauges layered at approx. 1 3/4" below top of panel and 1 3/4" above top of panel
 Actual gauge depths measured in field from top of panel and top of beam
 Design thickness of CIP deck = 3 1/2"

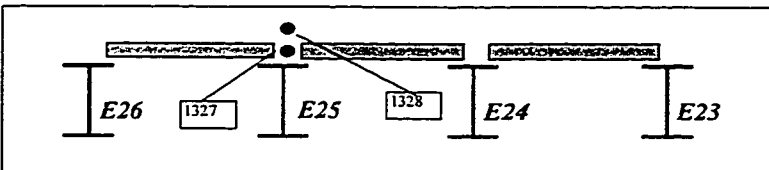
A
 Midspan
 Thermocouples



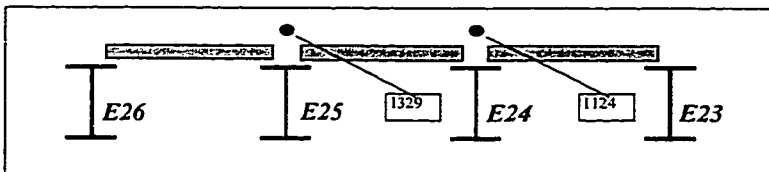
A
 Midspan
 Transverse
 ERSG Gauges



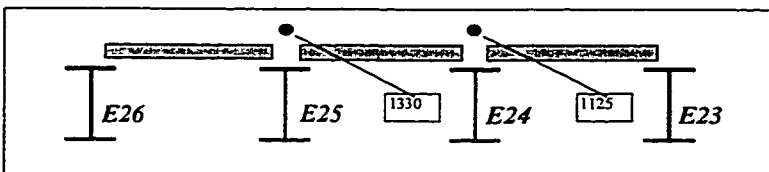
A
 Midspan
 Longitudinal
 VW Gauges



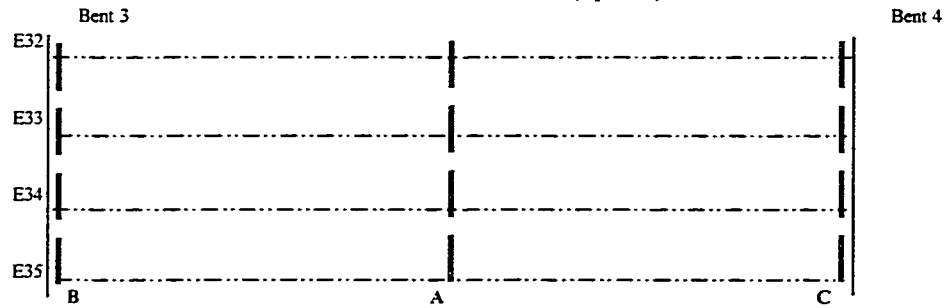
B
 Bent 2
 Longitudinal
 VW/ERSG Gauges



C
 Bent 3
 Longitudinal
 VW/ERSG Gauges



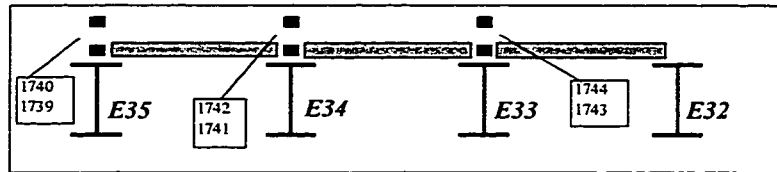
EASTBOUND OVERPASS (Span 3)



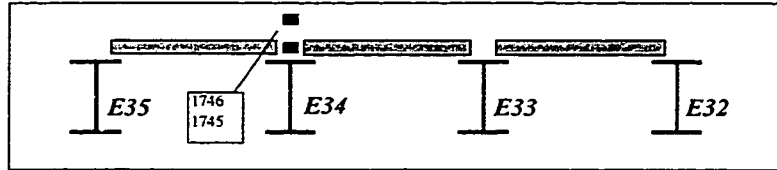
1100's = ERSG
 1300's = VW
 1500's = TR
 1700's = TC

Thermocouples above panels layered at approximately 1" and 2" above top of panel
 All other gauges layered at approx. 1 3/4" below top of panel and 1 3/4" above top of panel
 Actual gauge depths measured in field from top of panel and top of beam
 Design thickness of CIP deck = 3 1/2"

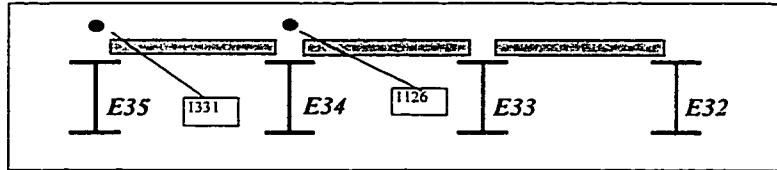
A
 Midspan
 Thermocouples



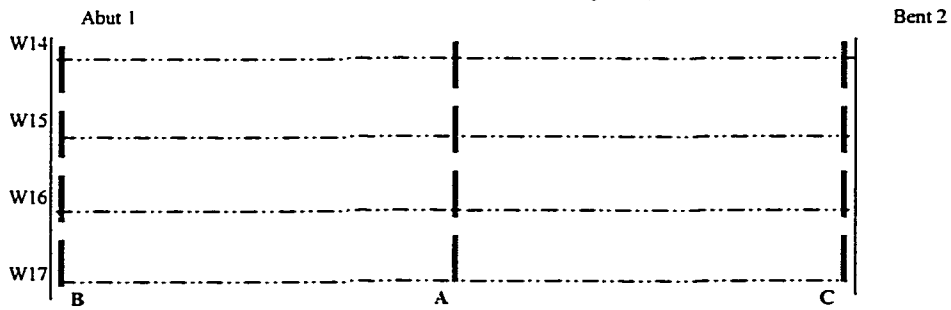
C
 Bent 4
 Thermocouples



A
 Midspan
 Longitudinal
 VW/ERSG Gauges



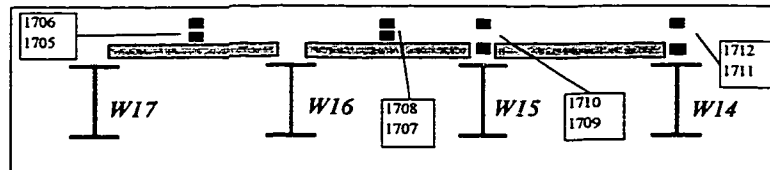
WESTBOUND OVERPASS (Span 1)



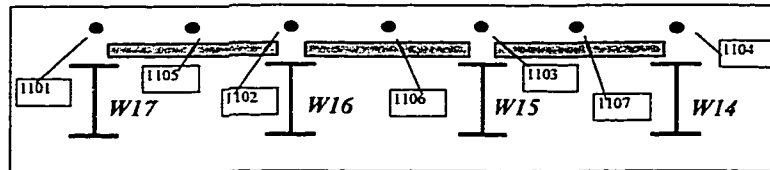
1100's = ERSG
1300's = VW
1500's = TR
1700's = TC

Thermocouples above panels layered at approximately 1" and 2" above top of panel
All other gauges layered at approx. 1 3/4" below top of panel and 1 3/4" above top of panel
Actual gauge depths measured in field from top of panel and top of beam
Design thickness of CIP deck = 3 1/2"

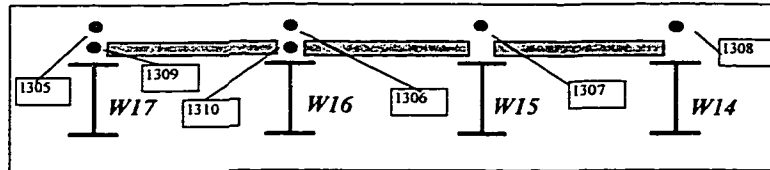
A
Midspan
Thermocouples



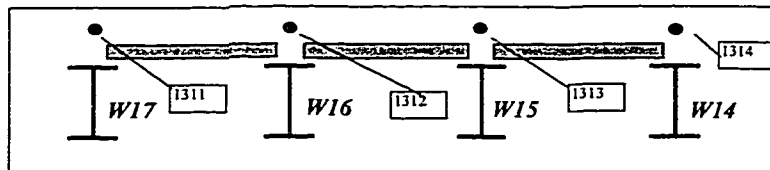
A
Midspan
Transverse
ERSG Gauges



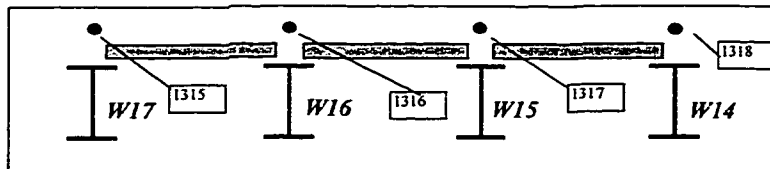
A
Midspan
Longitudinal
VW Gauges



B
Abut 1
Longitudinal
VW Gauges



C
Bent 2
Longitudinal
VW Gauges



APPENDIX C: MEASURED CAST-IN-PLACE DECK GAUGE DEPTHS

Louetta Northbound Bridge

Theoretical CIP Deck Thickness = 3.75 in.

Note: Actual gauge locations NOT measured. Distances are based on theoretical location of deck reinforcement and assumption of a 1.5 in. haunch. Actual CIP thickness measured by TxDOT field engineers.

Type	Gauge #	Distance Above Panel	Distance Above Beam	Distance Below Top of Deck	Actual CIP Thickness
VW	624	-2.00	3.00	5.75	3.75
	625	1.50	6.50	2.25	3.75
ERSG	711	1.75	6.75	2.00	3.75
	712	1.75	6.75	2.00	3.75
	713	1.75	6.75	2.00	3.75
	714	1.75	6.75	2.00	3.75
	715	1.75	6.75	2.00	3.75
	716	1.75	6.75	2.00	3.75
	717	1.75	6.75	2.00	3.75
	718	1.75	6.75	2.00	3.75
	719	1.75	6.75	2.00	3.75
	720	1.75	6.75	2.00	3.75
	721	1.75	6.75	2.00	3.75
	722	1.75	6.75	2.00	3.75
	723	1.75	6.75	2.00	3.75
	724	1.75	6.75	2.00	3.75
	725	1.75	6.75	2.00	3.75
	726	1.75	6.75	2.00	3.75
	727	1.75	6.75	2.00	3.75
	728	1.75	6.75	2.00	3.75
	729	1.75	6.75	2.00	3.75
	TC	815	-1.50	3.50	5.50
816		2.00	7.00	2.00	4.00
817		-1.50	3.50	5.50	4.00
818		2.00	7.00	2.00	4.00

Louetta Southbound Bridge

Theoretical CIP Deck Thickness = 3.75 in.

Note: Actual gauge locations measured in field relative to beams and panels.
Distances below top of deck are based on calculation using CIP deck thickness measured by TxDOT field engineers.

Type	Gauge #	Distance Above Panel	Distance Above Beam	Distance Below Top of Deck	Actual CIP Thickness
VW	601	2.00	7.00	2.50	4.50
	602	2.25	7.25	2.25	4.50
	603	-1.50	3.50	5.75	4.25
	604	-1.25	3.75	5.50	4.25
	605	1.75	6.75	2.25	4.00
	606	2.00	7.00	2.25	4.25
	607	1.75	6.75	2.50	4.25
	608	2.00	7.00	2.25	4.25
	609	1.75	6.75	2.75	4.50
	610	2.00	7.00	2.50	4.50
	611	2.00	7.00	2.50	4.50
	612	2.00	7.00	2.50	4.50
	613	-1.50	3.50	6.00	4.50
	614	2.00	7.00	2.00	4.00
	615	1.75	6.75	2.50	4.25
	616	2.00	7.00	2.25	4.25
	617	2.00	7.00	2.25	4.25
ERSG	701	1.25	6.25	2.75	4.00
	702	1.50	6.50	2.75	4.25
	703	1.50	6.50	2.75	4.25
	704	1.00	6.00	3.25	4.25
TC	805	0.50	5.50	3.75	4.25
	806	2.00	7.00	2.25	4.25
	807	0.50	5.50	3.75	4.25
	808	2.00	7.00	2.25	4.25
	809	-1.75	3.25	5.75	4.00
	810	1.75	6.75	2.25	4.00
	811	-1.75	3.25	5.75	4.00
	812	1.75	6.75	2.25	4.00
	813	-1.25	3.75	5.25	4.00
	814	1.75	6.75	2.25	4.00

San Angelo Eastbound Bridge

Theoretical CIP Deck Thickness = 3.50 in.

Note: Actual gauge locations measured in field relative to beams and panels.
Distances below top of deck are based on calculation using CIP deck thickness measured by TxDOT field engineers.

Type	Gauge #	Distance Above Panel	Distance Above Beam	Distance Below Top of Deck	Actual CIP Thickness
VW	1323	-2.00	5.00	6.50	4.50
	1324	2.25	9.25	2.25	4.50
	1325	2.50	9.50	2.25	4.75
	1326	2.00	9.00	2.25	4.25
	1327	-2.00	5.50	6.00	4.00
	1328	1.75	9.25	2.25	4.00
	1329	2.75	9.50	1.25	4.00
	1330	1.75	9.50	2.25	4.00
	1331	2.00	6.50	2.00	4.00
ERSG	1116	2.00	7.50	2.50	4.50
	1117	2.00	8.25	2.50	4.50
	1118	2.00	9.00	2.50	4.50
	1119	1.50	9.00	3.00	4.50
	1120	1.50	9.00	2.50	4.00
	1121	1.50	9.00	2.50	4.00
	1122	1.50	9.00	2.50	4.00
	1123	1.50	9.00	2.50	4.00
	1124	2.25	9.00	1.75	4.00
	1125	1.75	9.50	2.25	4.00
1126	2.00	8.25	2.00	4.00	
TC	1727	1.00	7.25	3.50	4.50
	1728	2.25	8.50	2.25	4.50
	1729	1.00	7.00	3.50	4.50
	1730	2.25	8.25	2.25	4.50
	1731	-1.75	5.75	6.25	4.50
	1732	1.75	9.25	2.75	4.50
	1733	0.75	8.25	3.25	4.00
	1734	1.75	9.25	2.25	4.00
	1735	0.75	8.25	3.25	4.00
	1736	1.75	9.25	2.25	4.00
	1737	-1.75	5.75	5.75	4.00
	1738	1.75	9.25	2.25	4.00
	1739	-2.00	2.50	6.00	4.00
	1740	2.25	6.75	1.75	4.00
	1741	-2.00	4.25	6.00	4.00
	1742	2.25	8.50	1.75	4.00
	1743	-2.00	4.25	6.00	4.00
	1744	2.25	8.50	1.75	4.00
1745	-1.50	4.75	5.50	4.00	
1746	2.00	8.25	2.00	4.00	

San Angelo Westbound Bridge

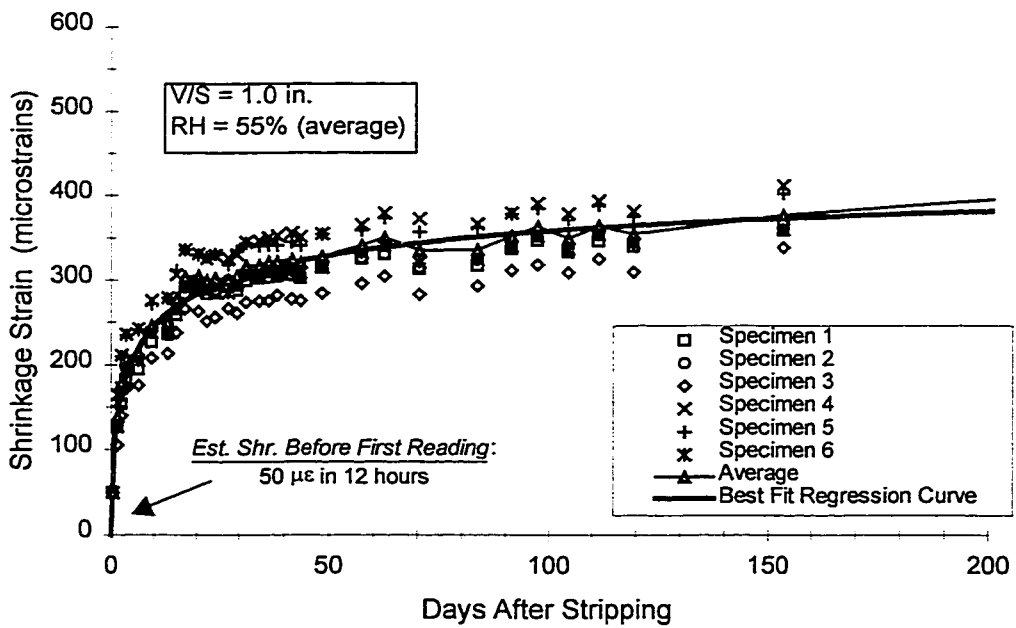
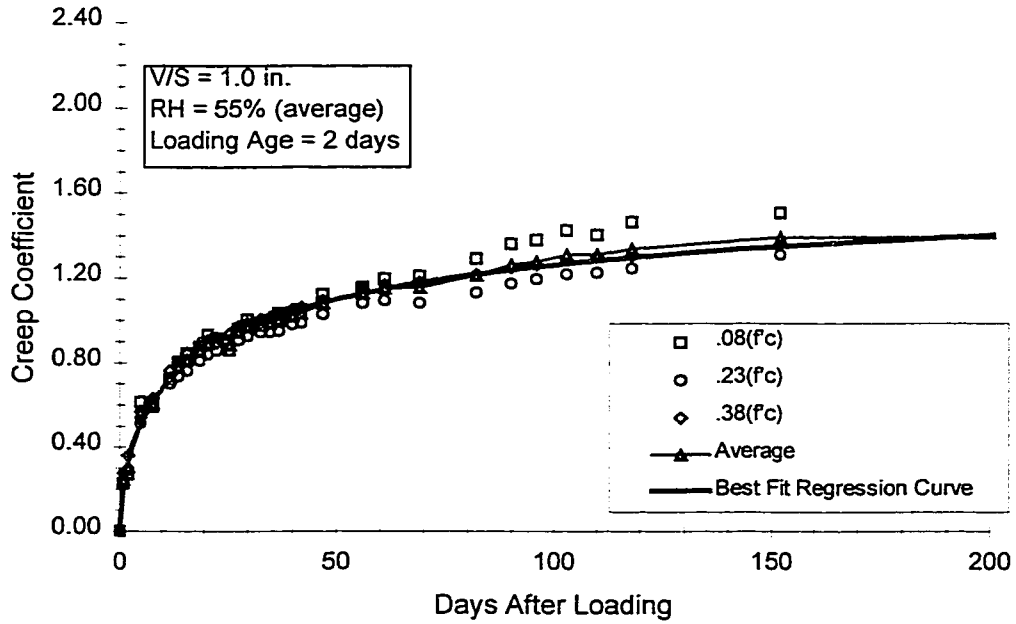
Theoretical CIP Deck Thickness = 3.50 in.

Note: Actual gauge locations measured in field relative to beams and panels.
Distances below top of deck are based on calculation using CIP deck thickness measured by TxDOT field engineers.

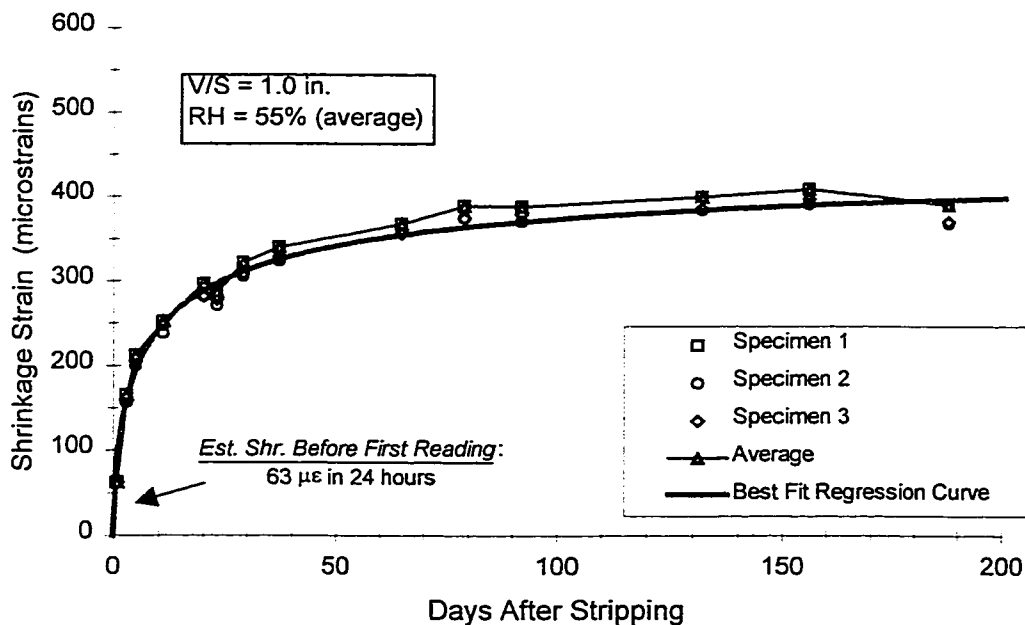
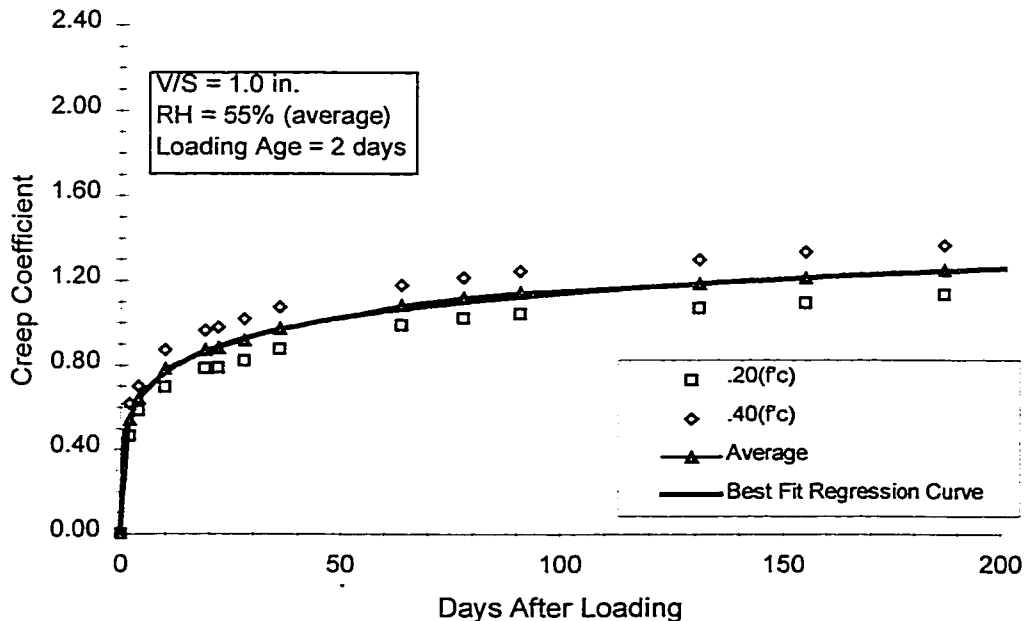
Type	Gauge #	Distance Above Panel	Distance Above Beam	Distance Below Top of Deck	Actual CIP Thickness
VW	1305	3.25	8.75	2.00	5.25
	1306	3.25	8.75	2.00	5.25
	1307	3.00	8.50	2.00	5.00
	1308	3.00	8.50	2.00	5.00
	1309	-1.50	4.00	6.75	5.25
	1310	-1.50	4.00	6.75	5.25
	1311	2.75	8.25	2.75	5.50
	1312	2.75	8.25	2.75	5.50
	1313	3.00	8.50	2.50	5.50
	1314	3.00	8.50	2.50	5.50
	1315	3.00	8.50	2.25	5.25
	1316	2.75	8.25	2.50	5.25
	1317	3.00	8.50	2.25	5.25
1318	3.00	8.50	2.25	5.25	
ERSG	1101	3.00	8.50	2.25	5.25
	1102	2.50	8.00	2.75	5.25
	1103	2.50	8.00	2.75	5.25
	1104	2.50	8.00	2.75	5.25
	1105	3.00	8.50	2.25	5.25
	1106	3.00	8.50	2.25	5.25
	1107	2.75	8.25	2.50	5.25
TC	1705	1.50	7.00	3.75	5.25
	1706	3.00	8.50	2.25	5.25
	1707	1.75	7.25	3.25	5.00
	1708	3.00	8.50	2.00	5.00
	1709	-2.00	3.50	6.75	4.75
	1710	2.75	8.25	2.00	4.75
	1711	-1.75	3.75	6.50	4.75
	1712	2.75	8.25	2.00	4.75

APPENDIX D: CREEP AND SHRINKAGE PLOTS

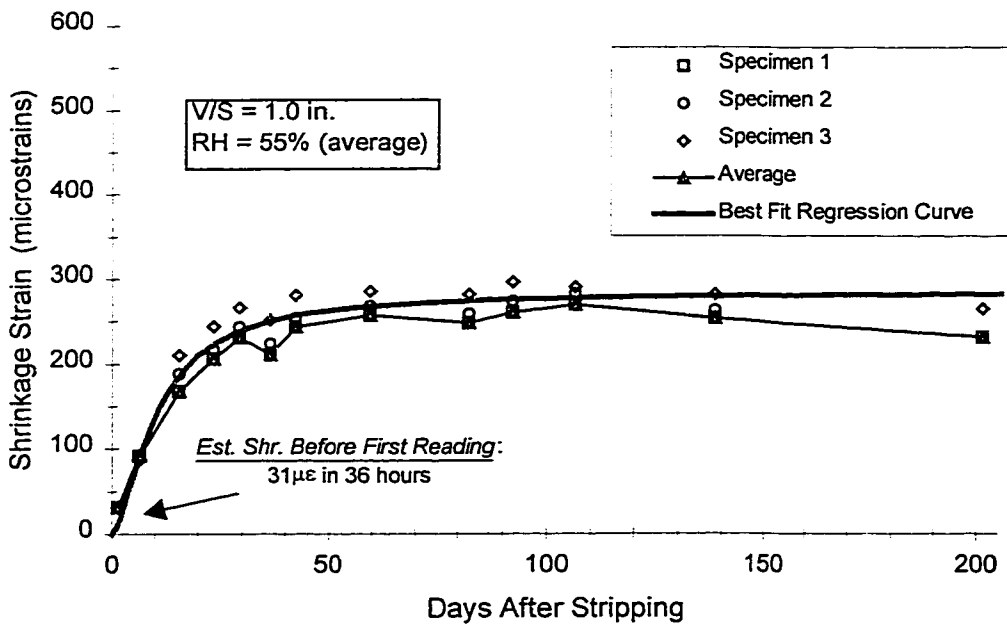
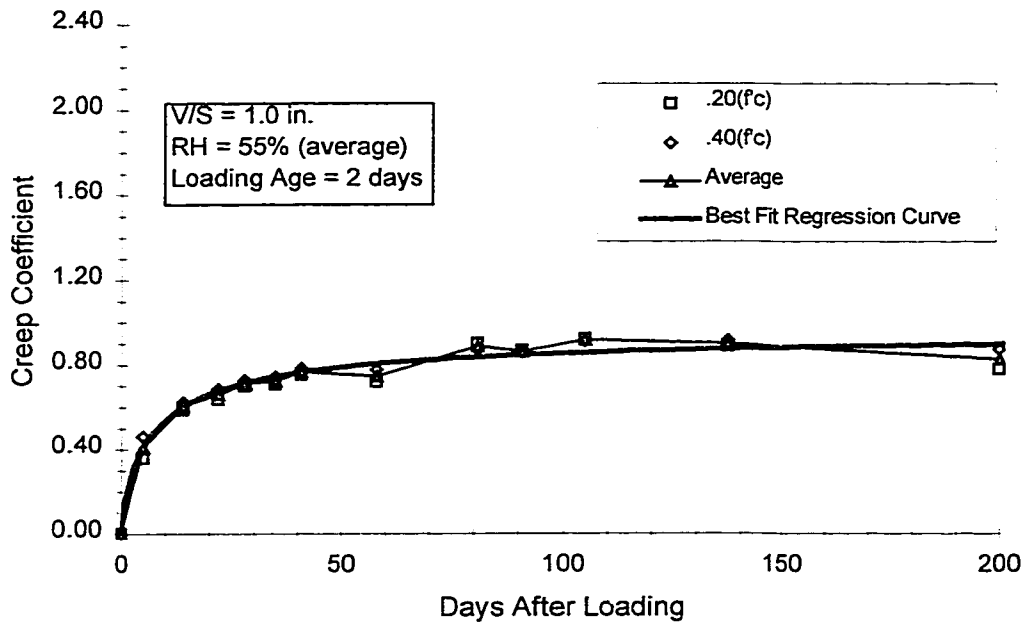
Louetta NB/SB HPC Prestressed Beams



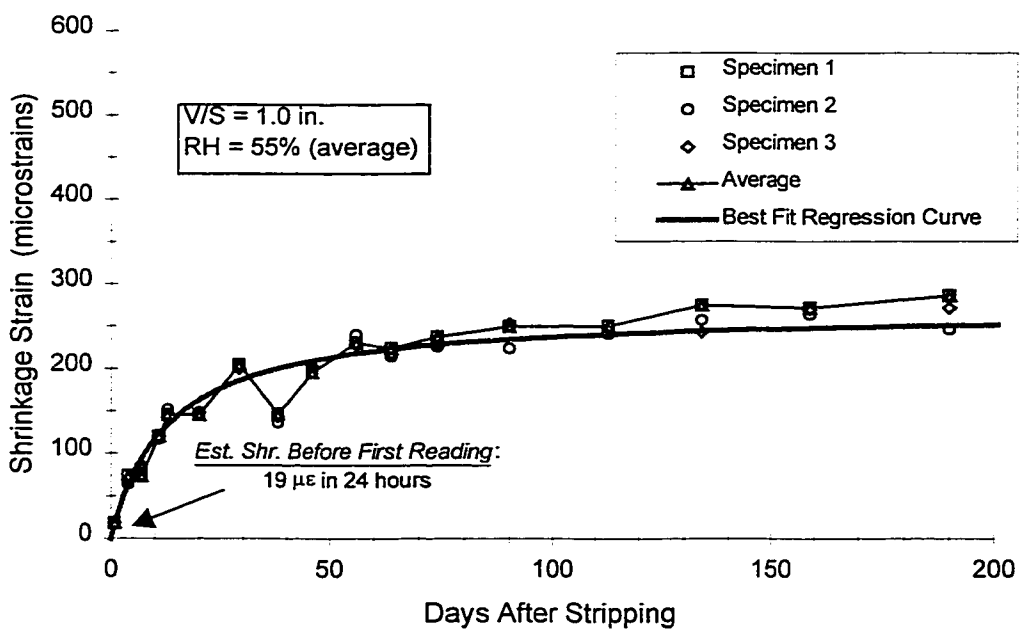
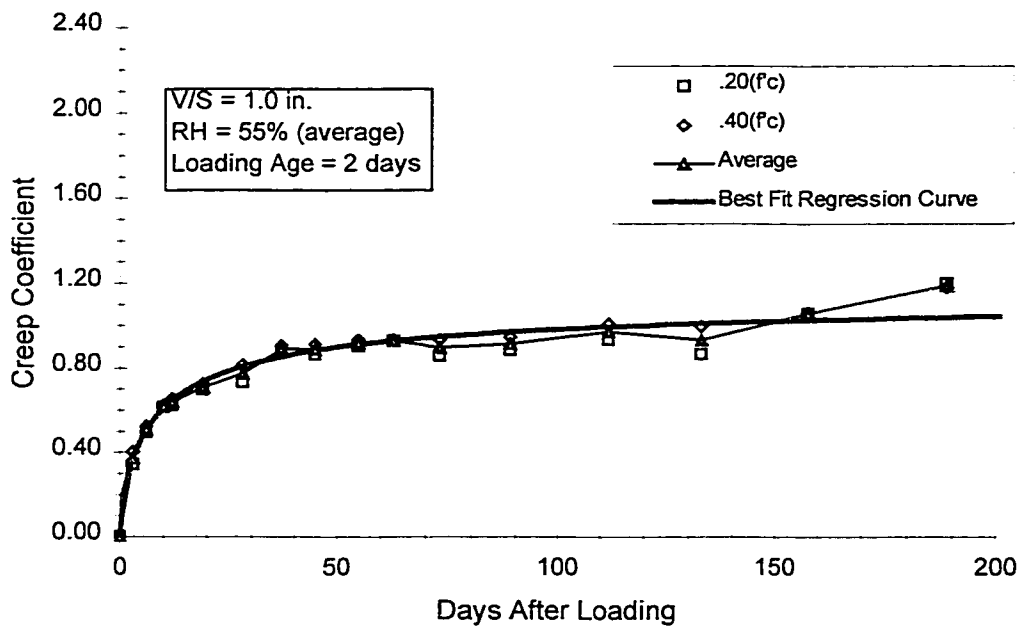
San Angelo EB HPC Prestressed Beams



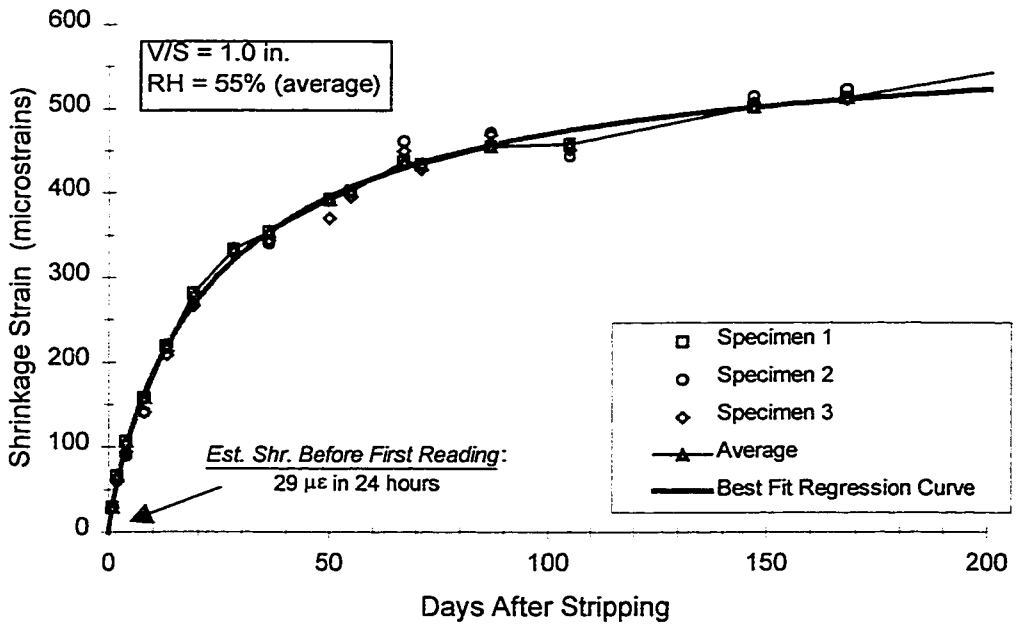
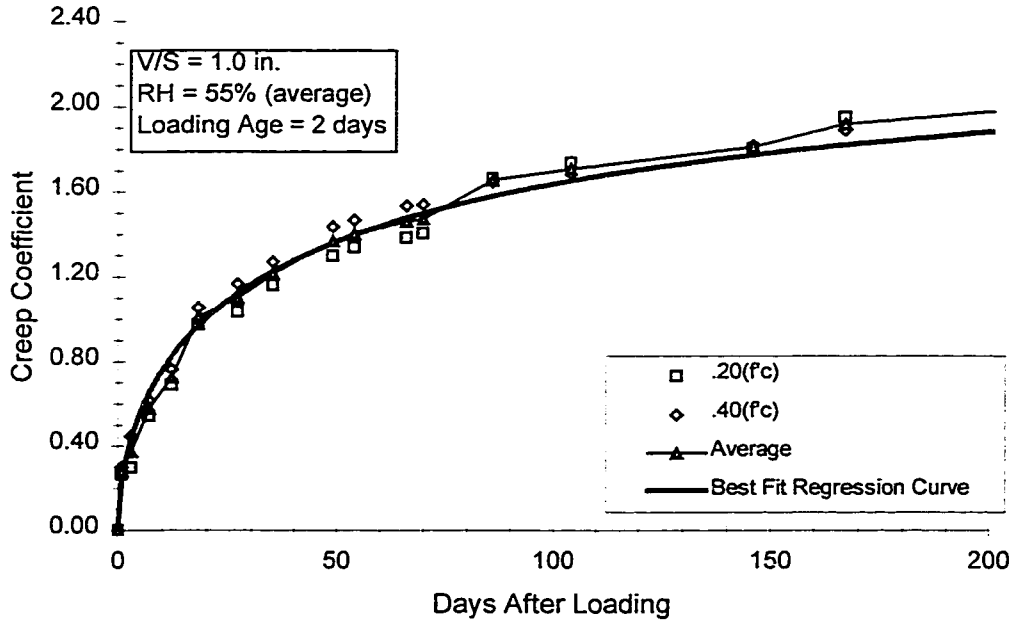
San Angelo WB Non-HPC Prestressed Beams



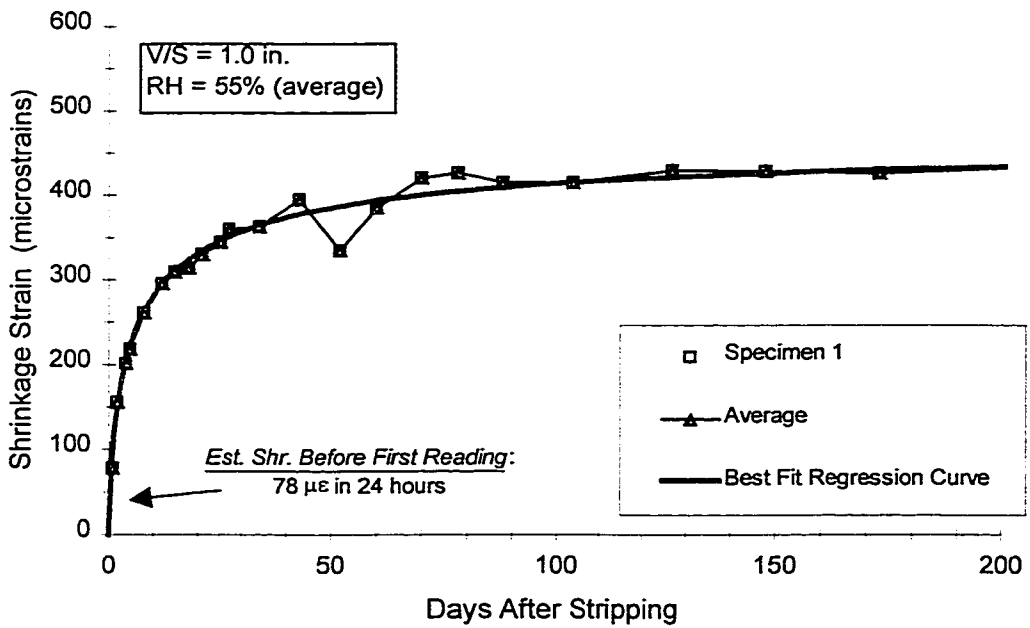
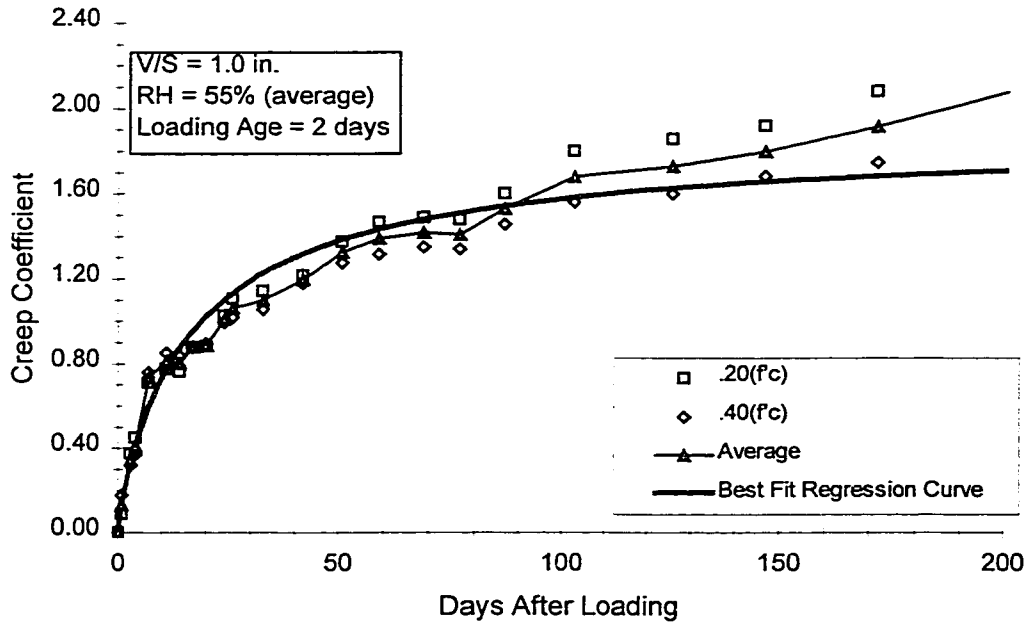
Louetta NB/SB HPC Precast Deck Panels



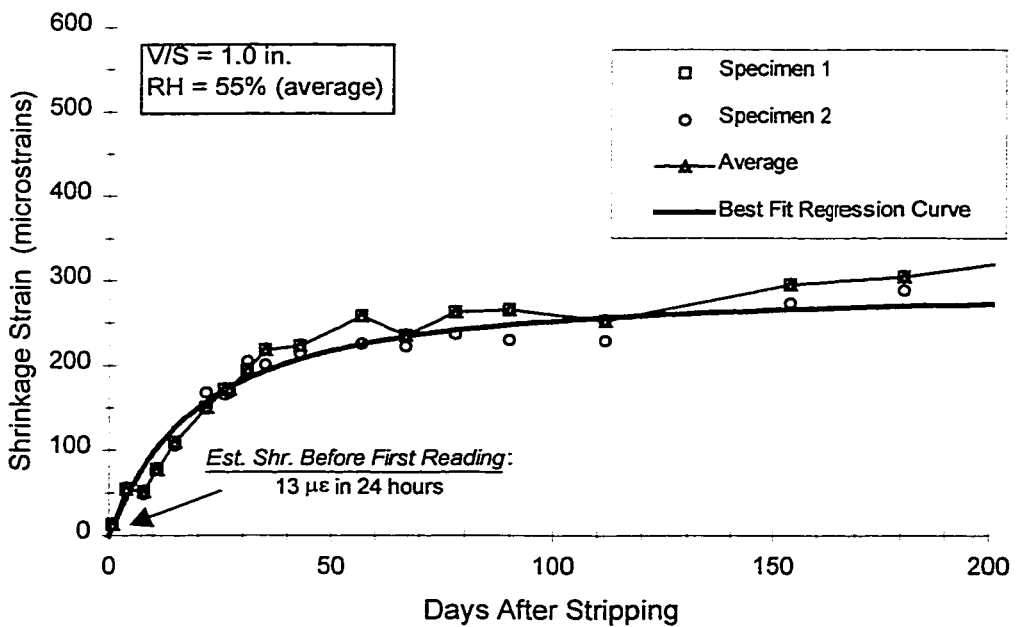
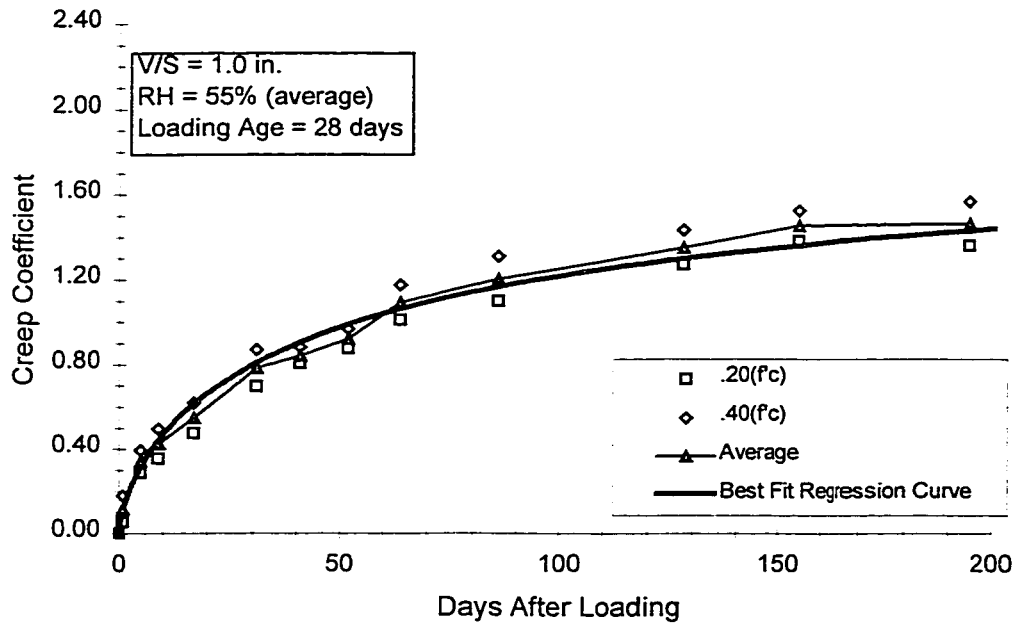
San Angelo EB HPC Precast Deck Panels



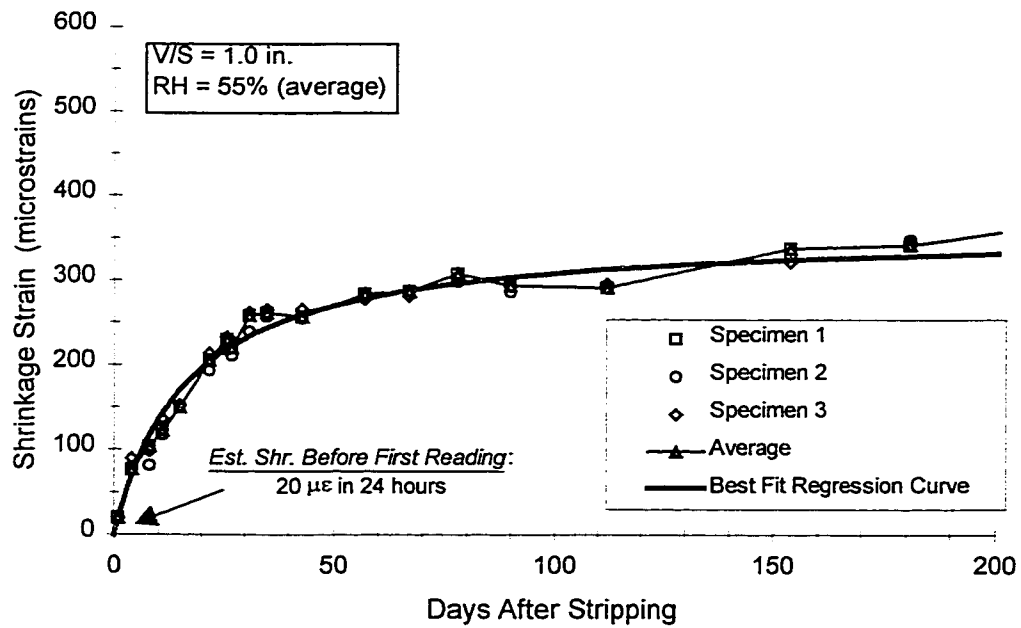
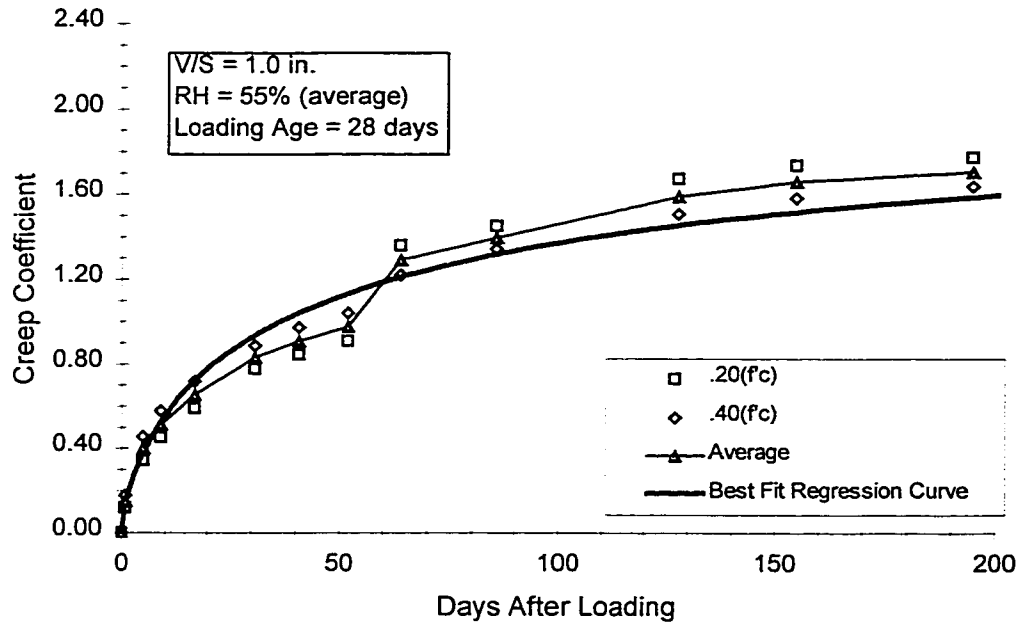
San Angelo WB Non-HPC Precast Deck Panels



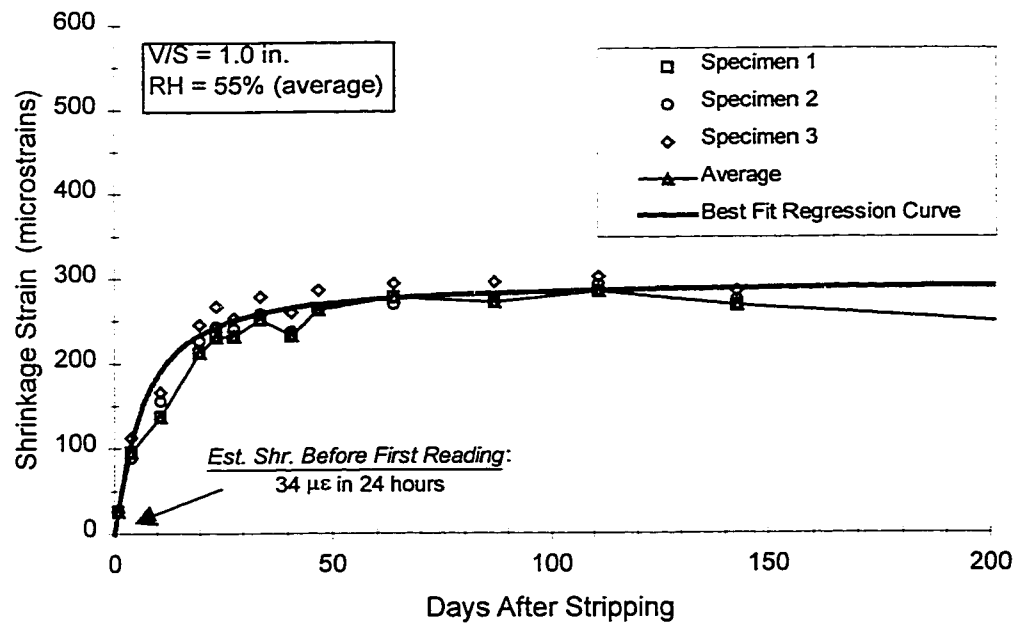
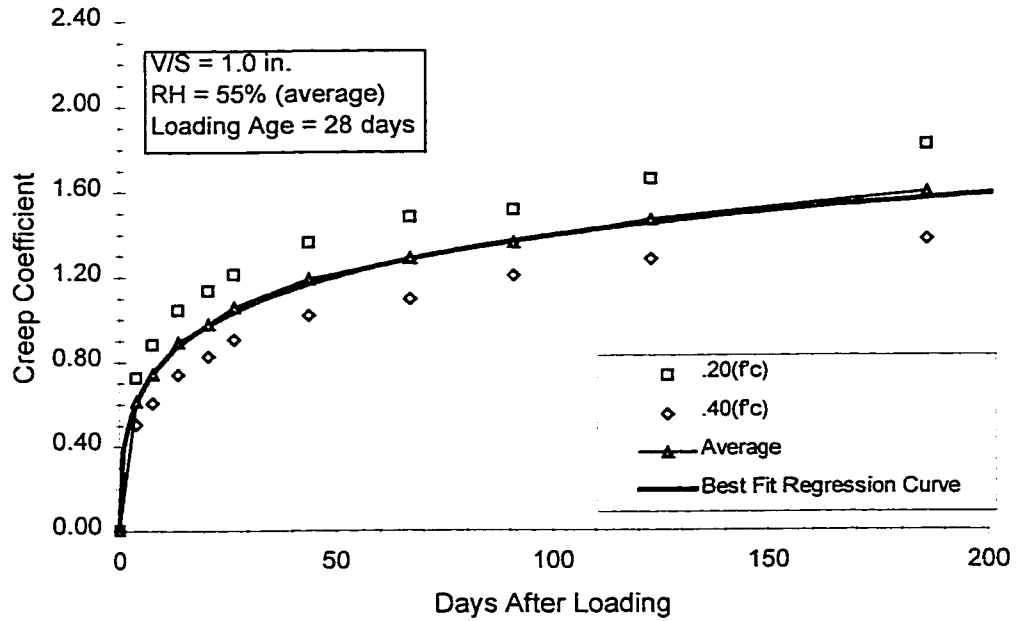
Louetta NB HPC Cast-in-Place Deck



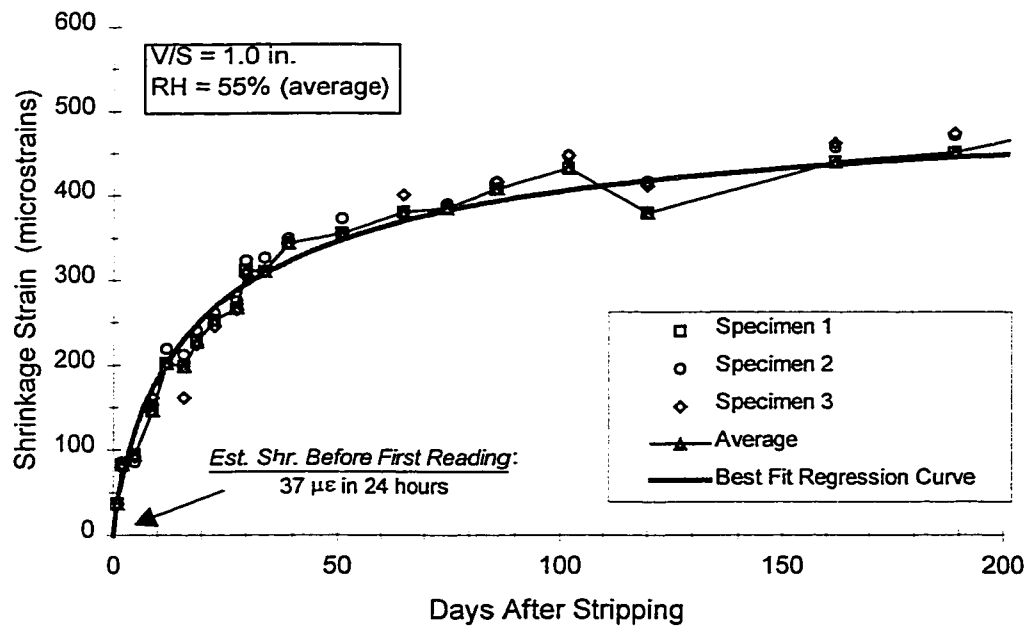
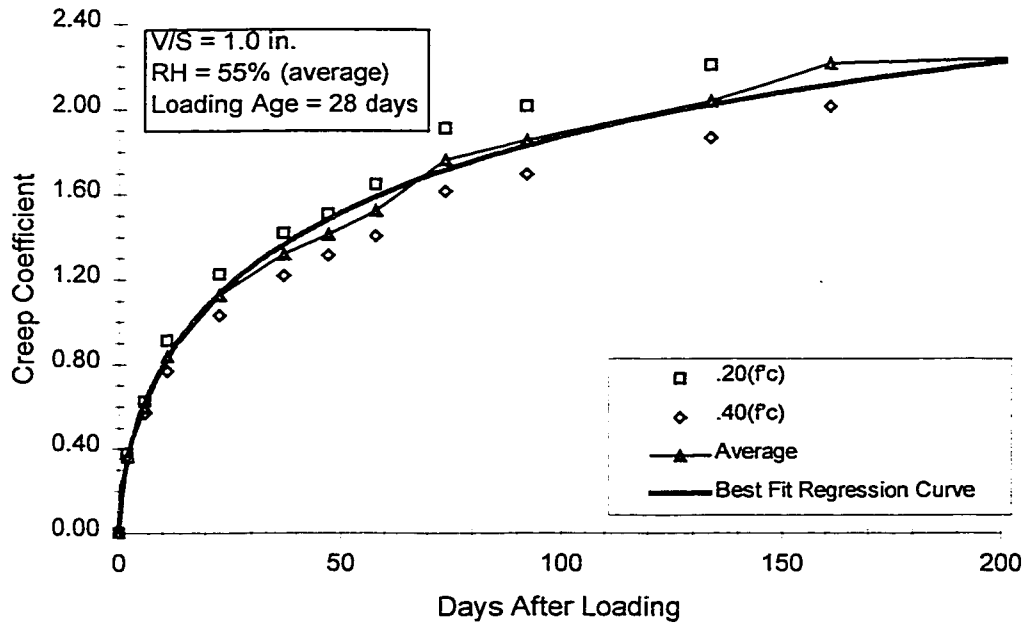
Louetta SB HPC Cast-in-Place Deck



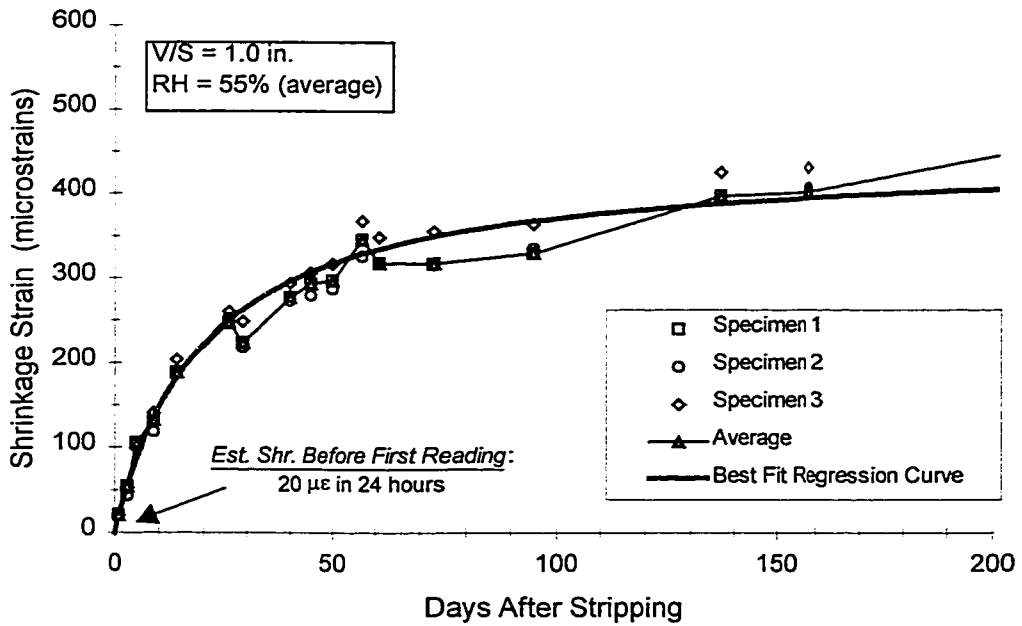
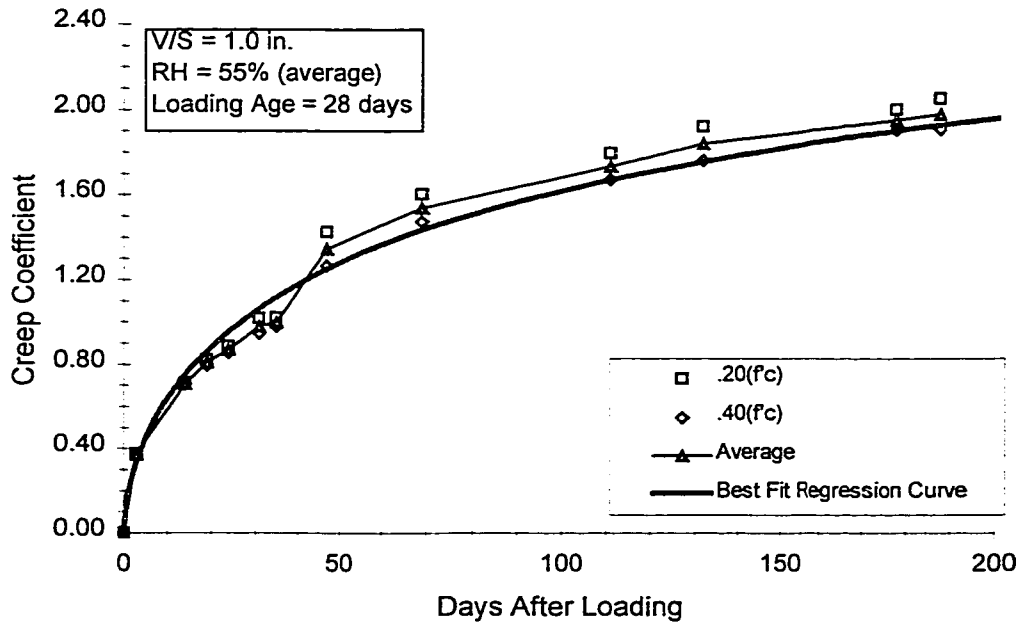
San Angelo EB HPC Class K Cast-in-Place Deck



San Angelo WB HPC Modified Class S Cast-in-Place Deck

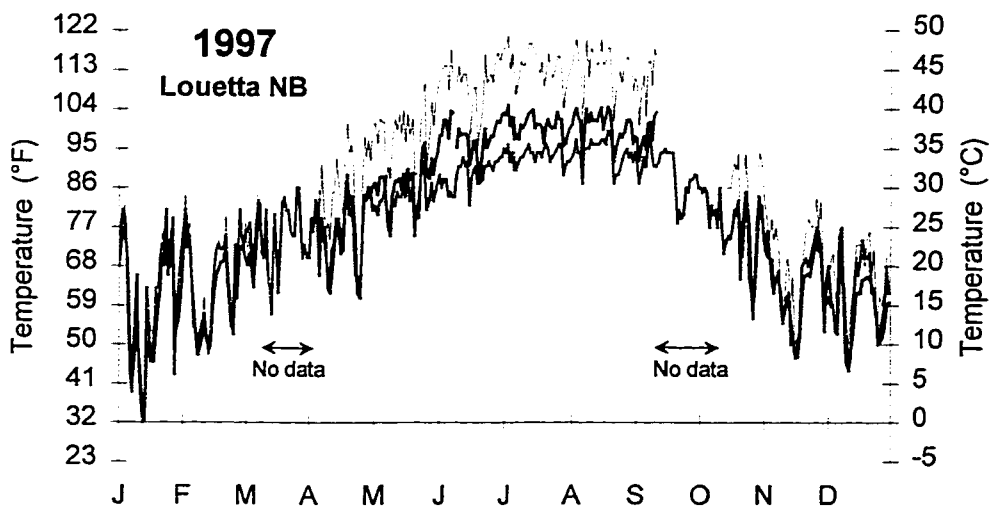


San Angelo WB Non-HPC Standard Class S Cast-in-Place Deck



**APPENDIX E: EXTREME BRIDGE TEMPERATURE AND THERMAL
GRADIENT PLOTS**

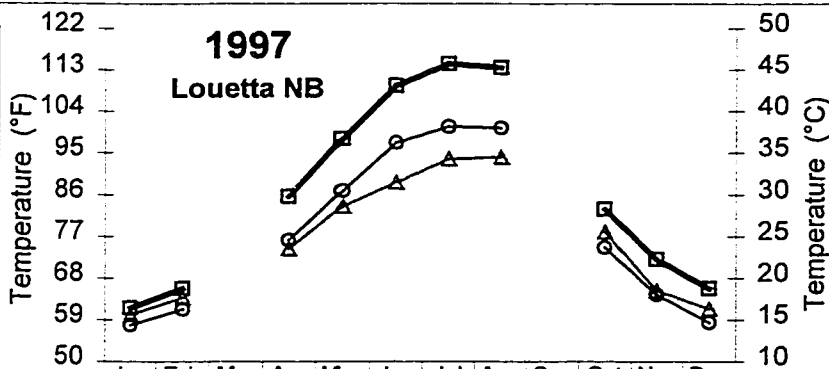
Louetta Northbound – Composite Beam N33
Maximum Bridge Temperatures



— Max. Deck Temp. — Max. Average Bridge Temp. — Max. Ambient Temp.

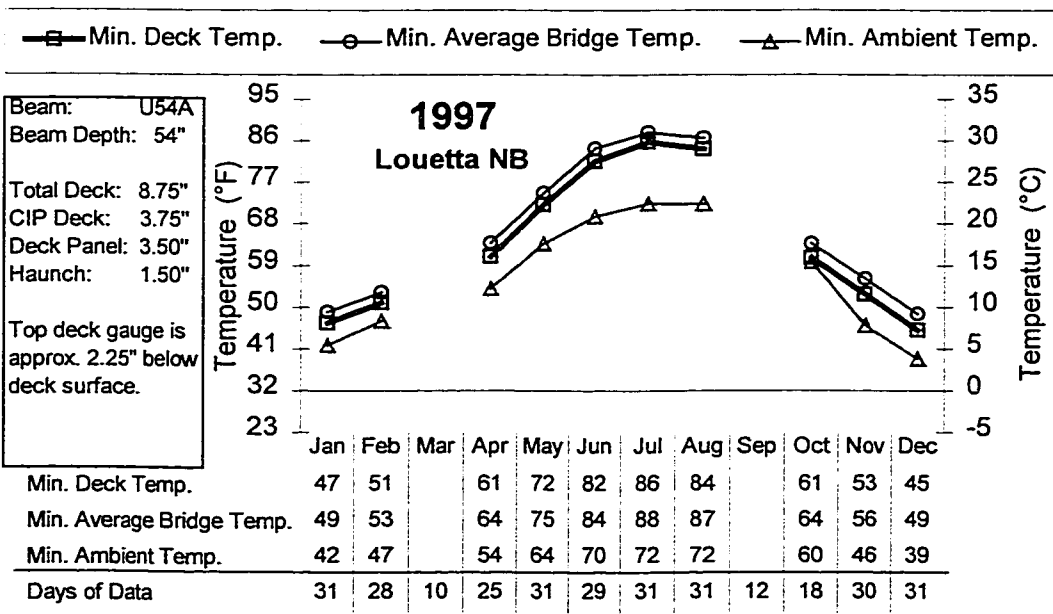
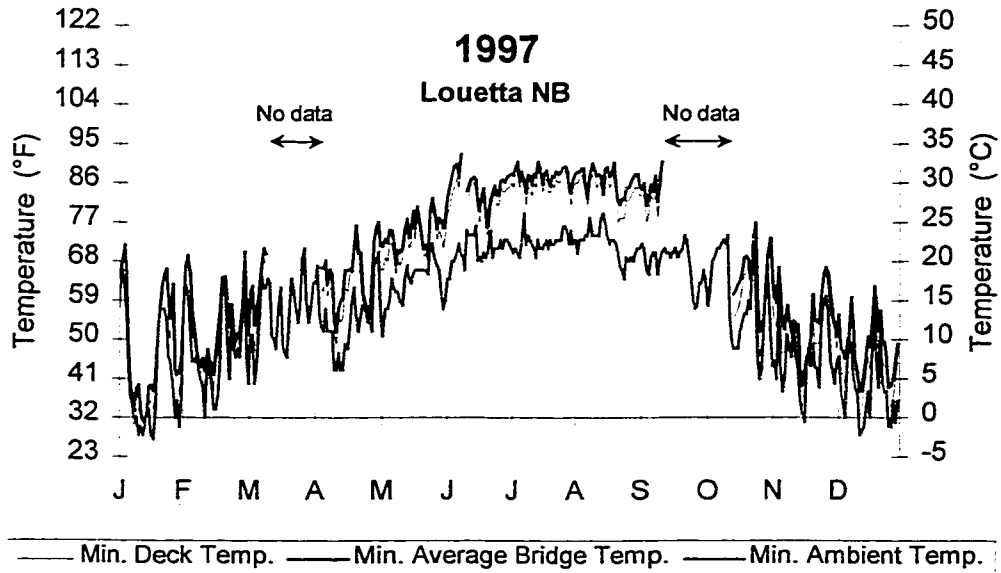
■ Max. Deck Temp. ○ Max. Average Bridge Temp. ▲ Max. Ambient Temp.

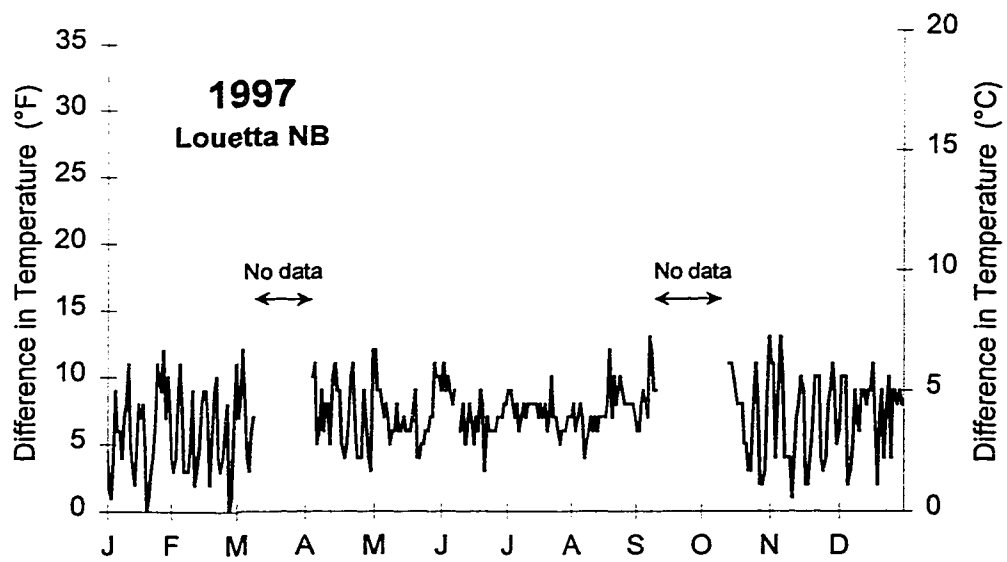
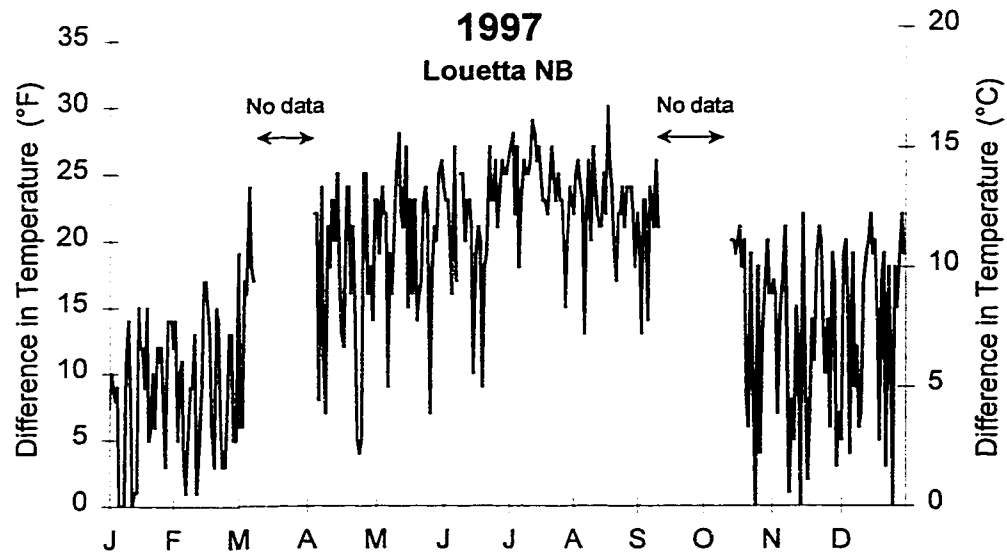
Beam: U54A
 Beam Depth: 54"
 Total Deck: 8.75"
 CIP Deck: 3.75"
 Deck Panel: 3.50"
 Haunch: 1.50"
 Top deck gauge is approx. 2.25" below deck surface.



	Jan	Feb	Mar	Apr	May	Jun	Jul	Aug	Sep	Oct	Nov	Dec
Max. Deck Temp.	61	66		86	98	110	114	113		83	72	66
Max. Average Bridge Temp.	58	61		76	87	97	101	100		75	64	58
Max. Ambient Temp.	60	64		74	83	89	94	94		78	65	61
Days of Data	31	28	10	25	31	29	31	31	12	18	30	31

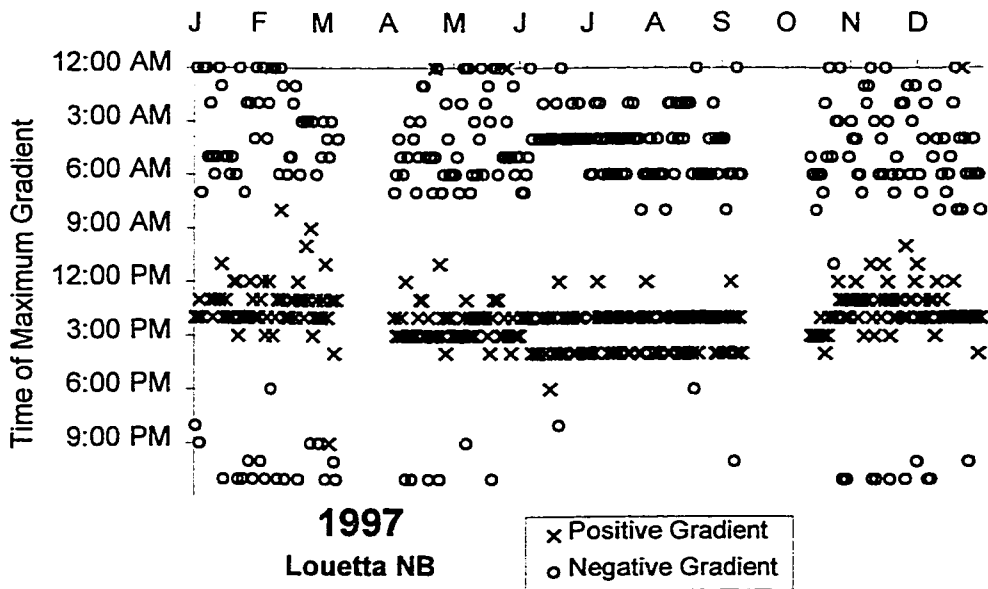
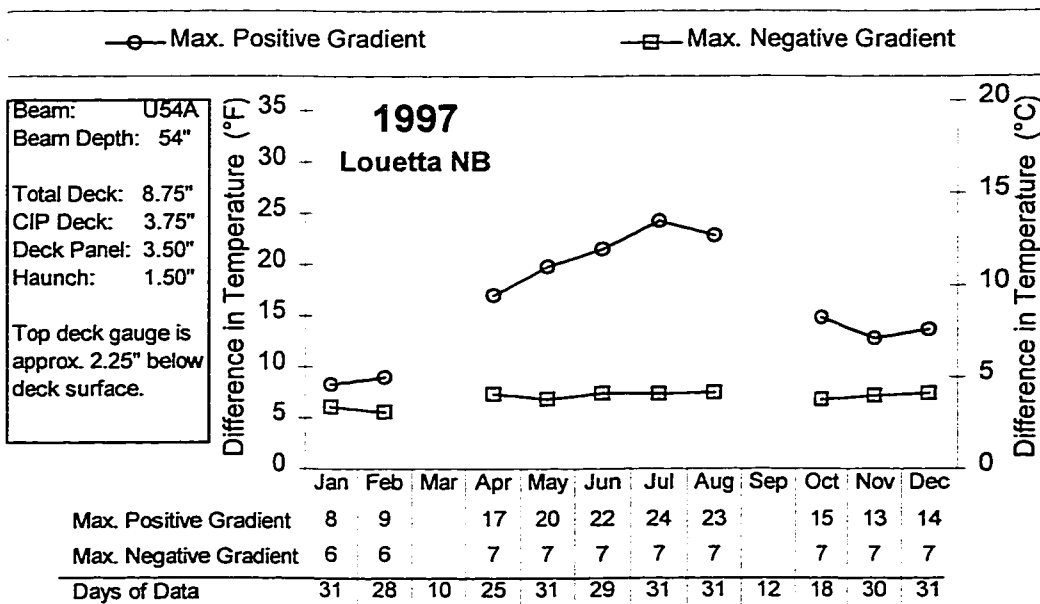
Louetta Northbound – Composite Beam N33
Minimum Bridge Temperatures



Louetta Northbound – Composite Beam N33**Thermal Gradients**

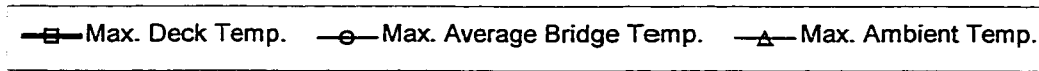
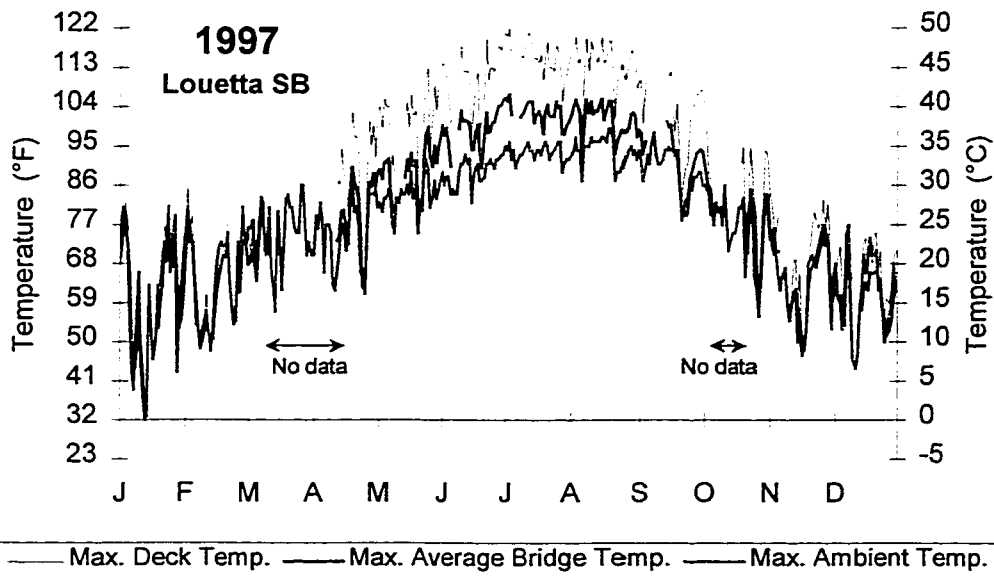
Louetta Northbound – Composite Beam N33

Thermal Gradients

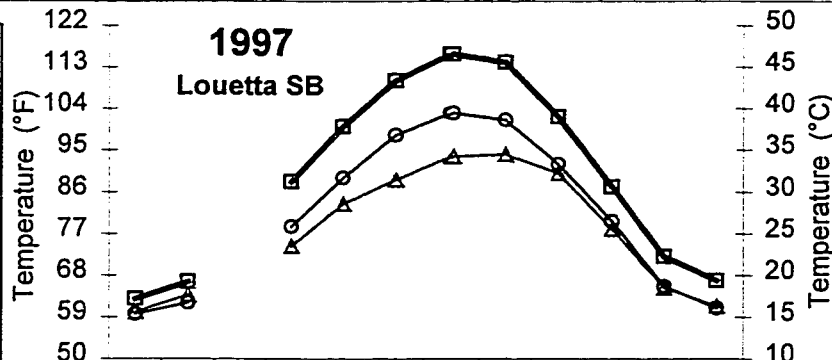


Louetta Southbound – Composite Beam S14

Maximum Bridge Temperatures

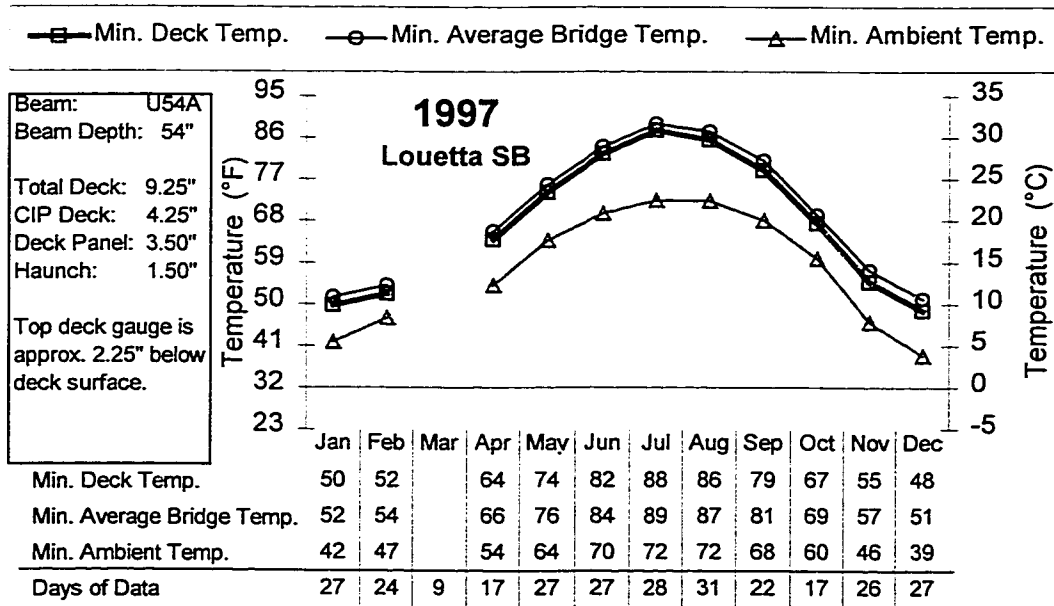
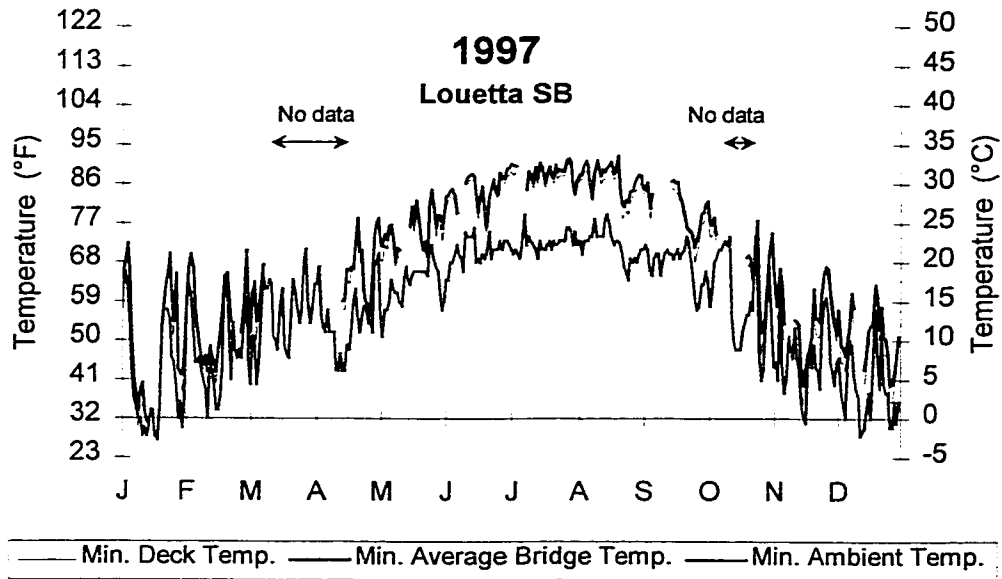


Beam: U54A
 Beam Depth: 54"
 Total Deck: 9.25"
 CIP Deck: 4.25"
 Deck Panel: 3.50"
 Haunch: 1.50"
 Top deck gauge is approx. 2.25" below deck surface.



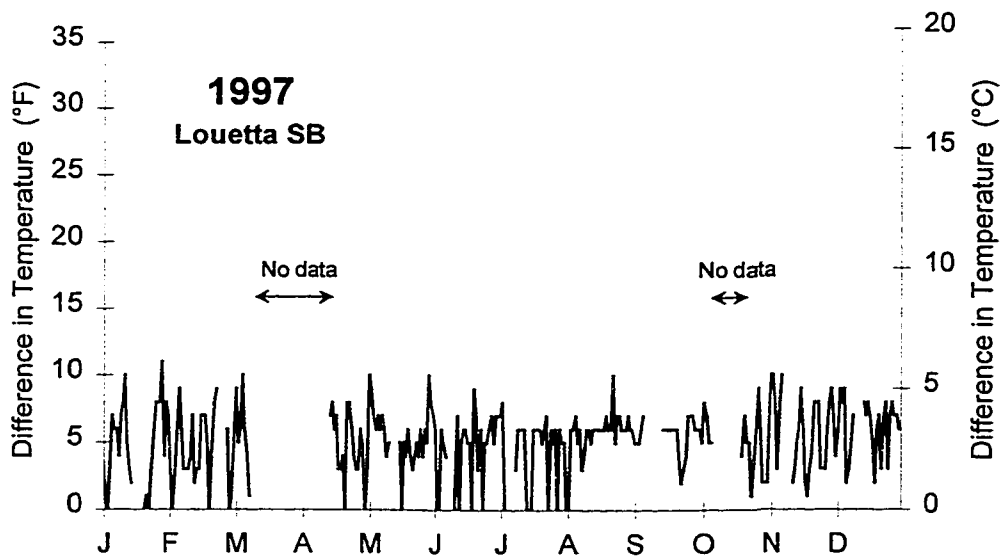
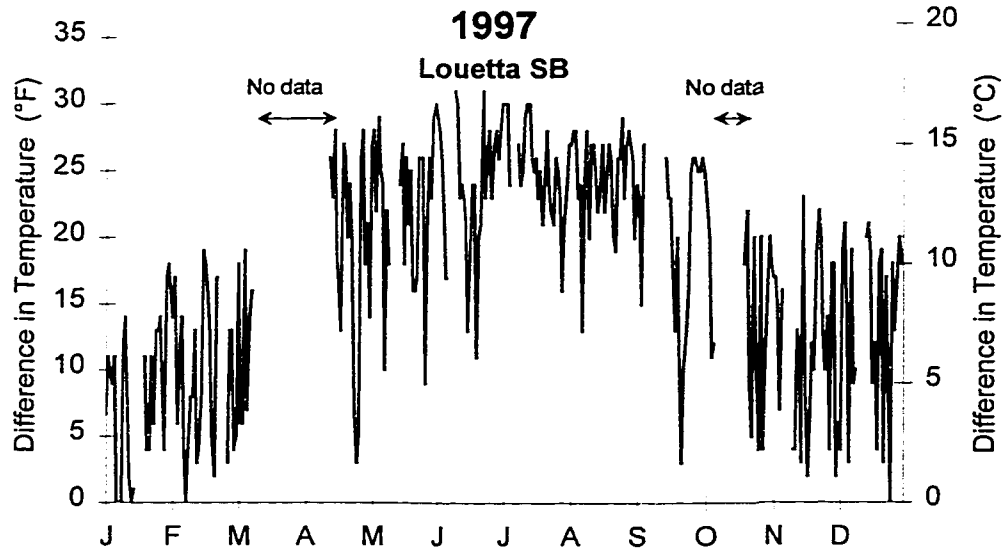
	Jan	Feb	Mar	Apr	May	Jun	Jul	Aug	Sep	Oct	Nov	Dec
Max. Deck Temp.	63	67		88	100	110	116	114	102	87	72	67
Max. Average Bridge Temp.	60	62		79	89	98	103	102	92	80	66	61
Max. Ambient Temp.	60	64		74	83	89	94	94	90	78	65	61
Days of Data	27	24	9	17	27	27	28	31	22	17	26	27

Louetta Southbound – Composite Beam S14
Minimum Bridge Temperatures



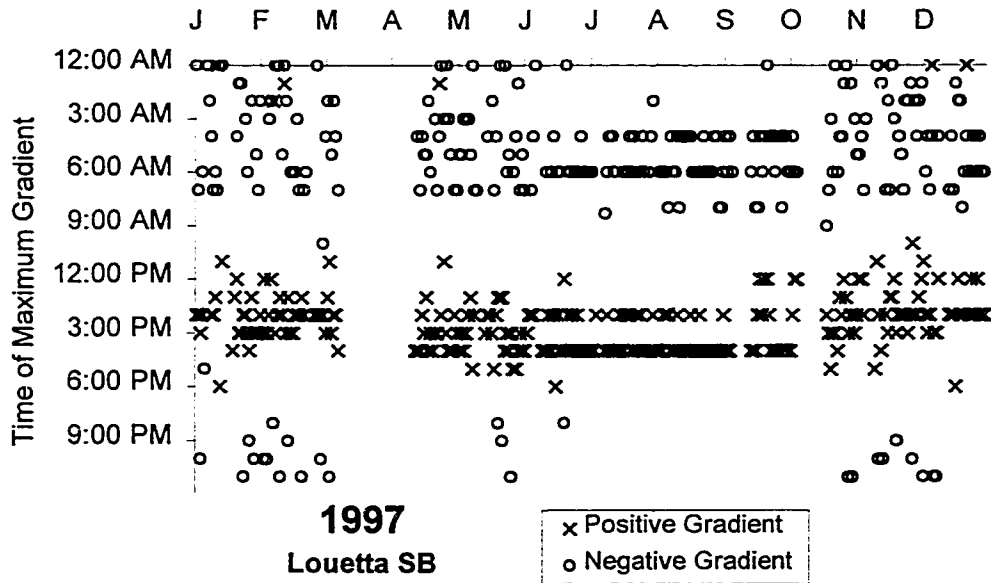
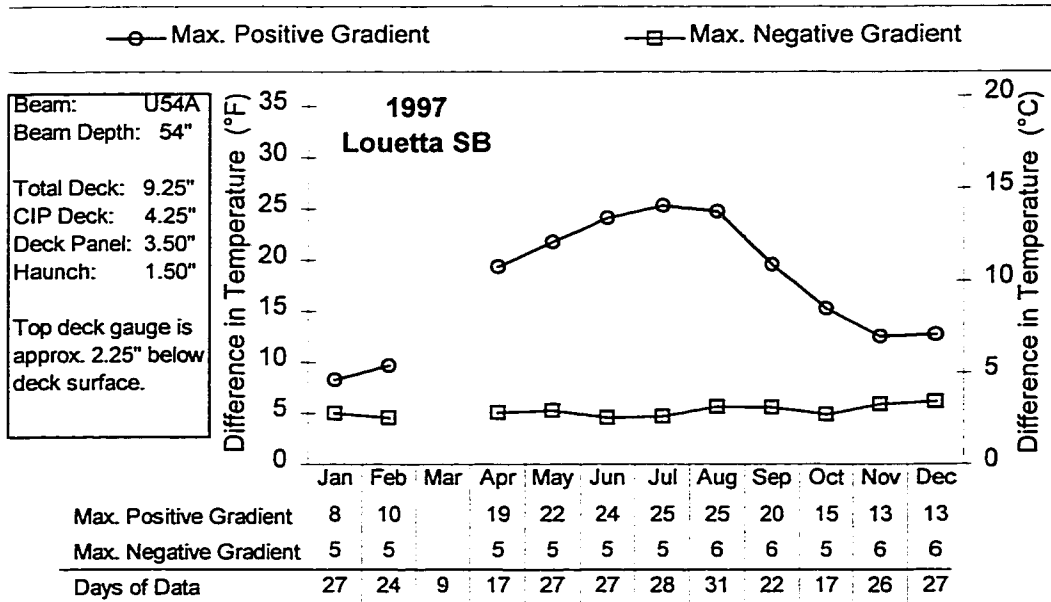
Louetta Southbound – Composite Beam S14

Thermal Gradients

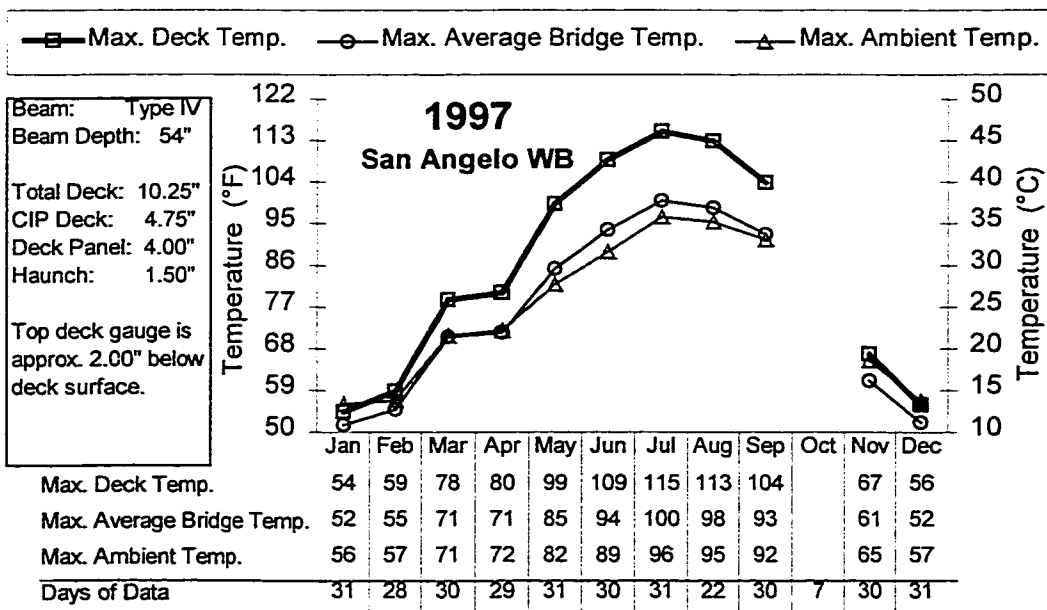
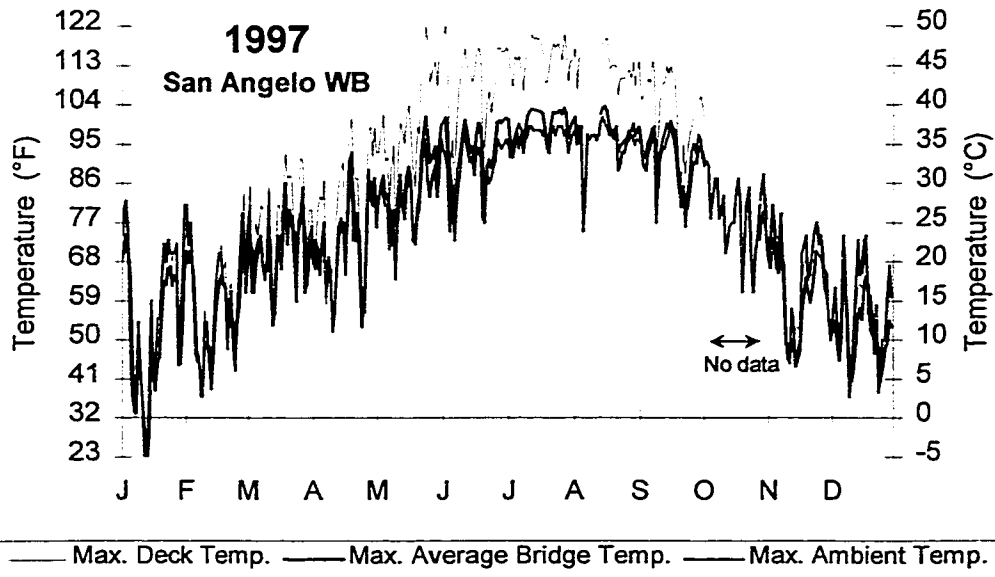


Louetta Southbound – Composite Beam S14

Thermal Gradients

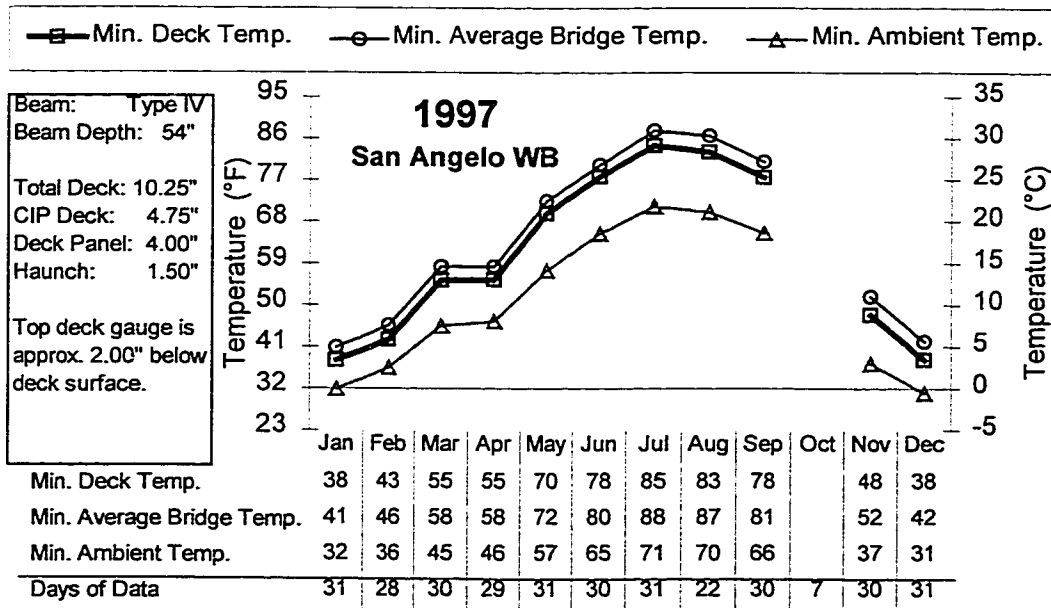
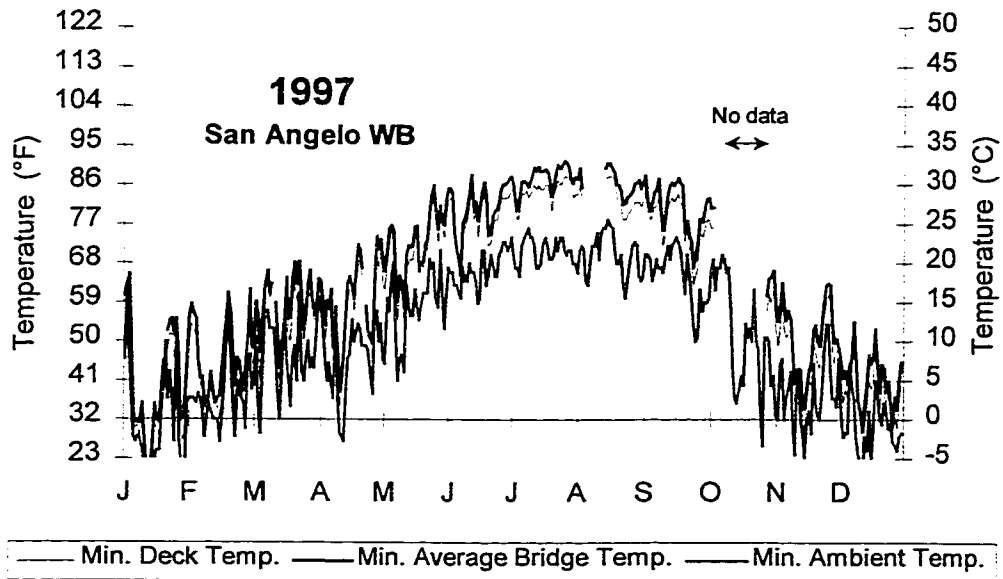


San Angelo Westbound – Composite Beam W15
Maximum Bridge Temperatures



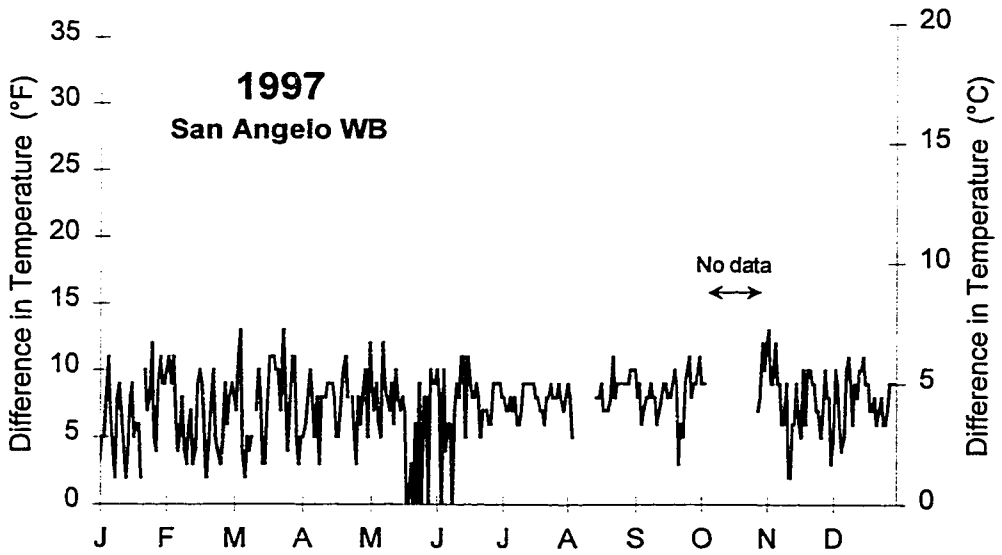
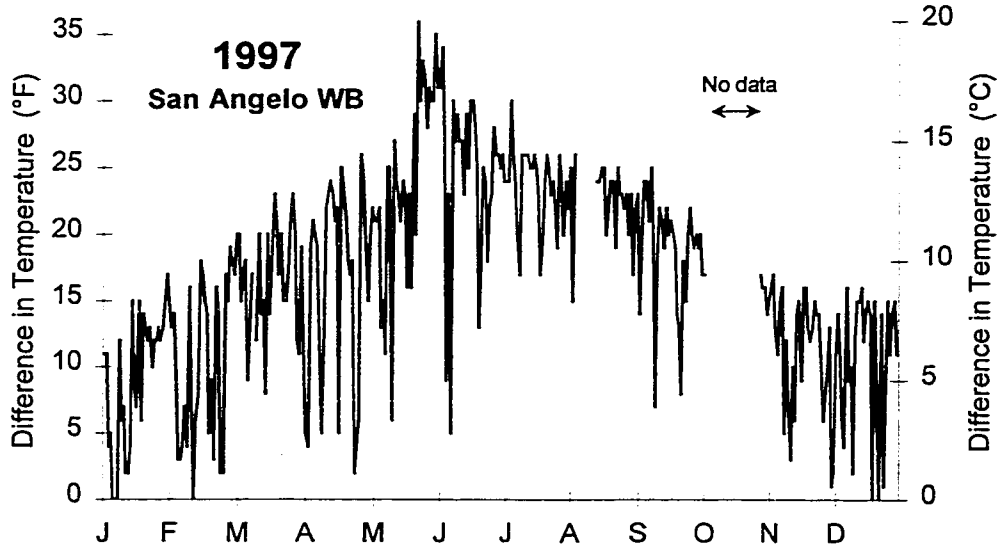
San Angelo Westbound – Composite Beam W15

Minimum Bridge Temperatures



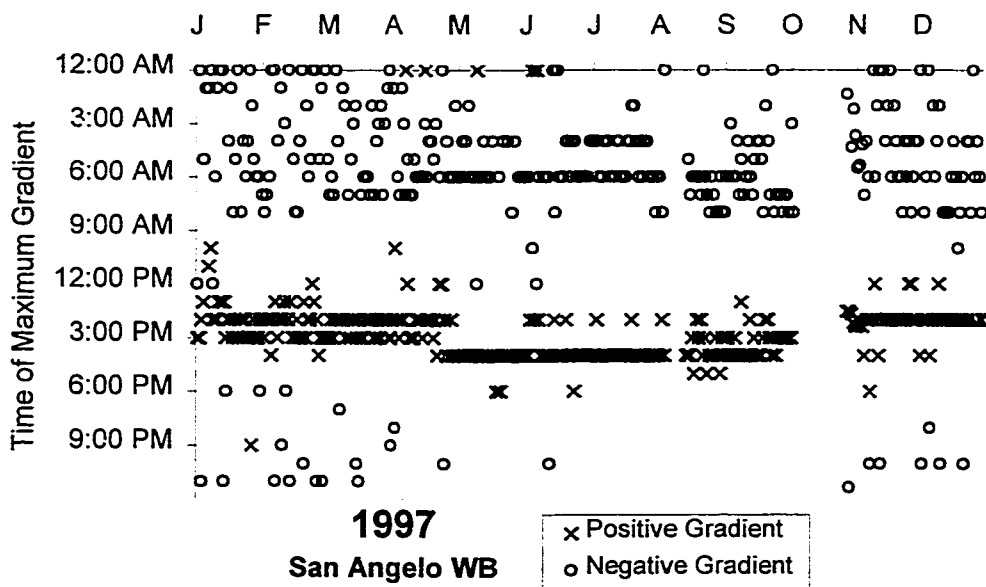
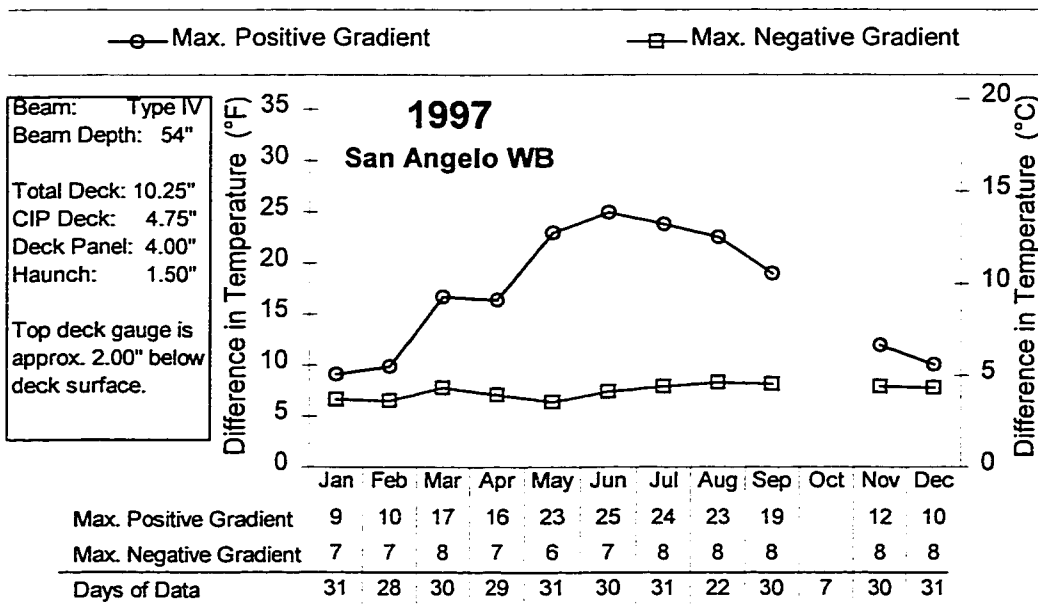
San Angelo Westbound – Composite Beam W15

Thermal Gradients



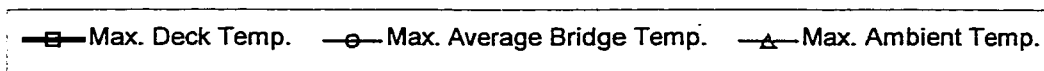
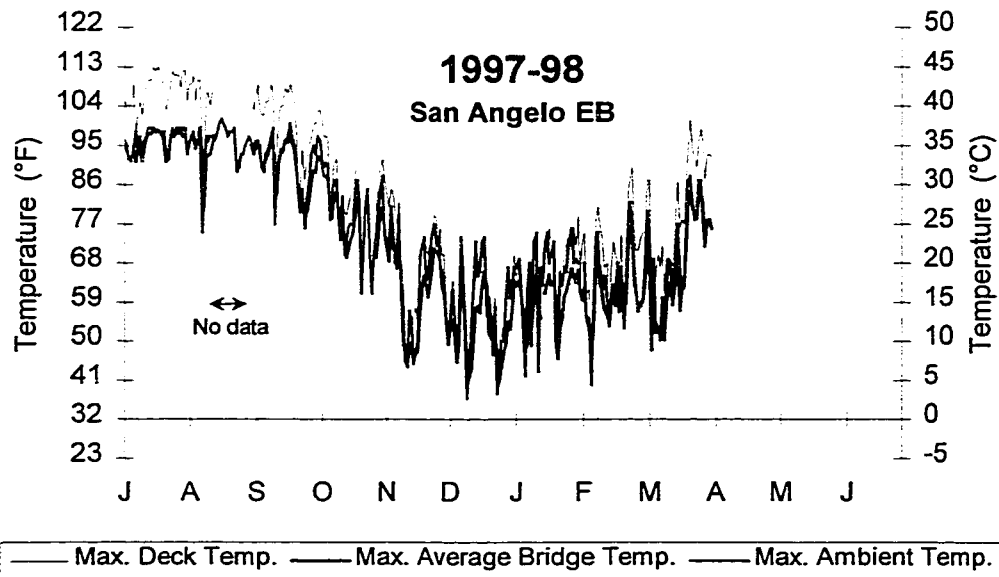
San Angelo Westbound – Composite Beam W15

Thermal Gradients

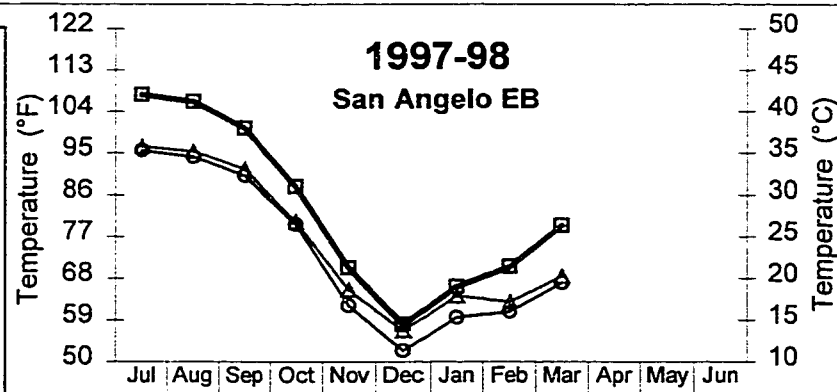


San Angelo Eastbound – Composite Beam E25

Maximum Bridge Temperatures



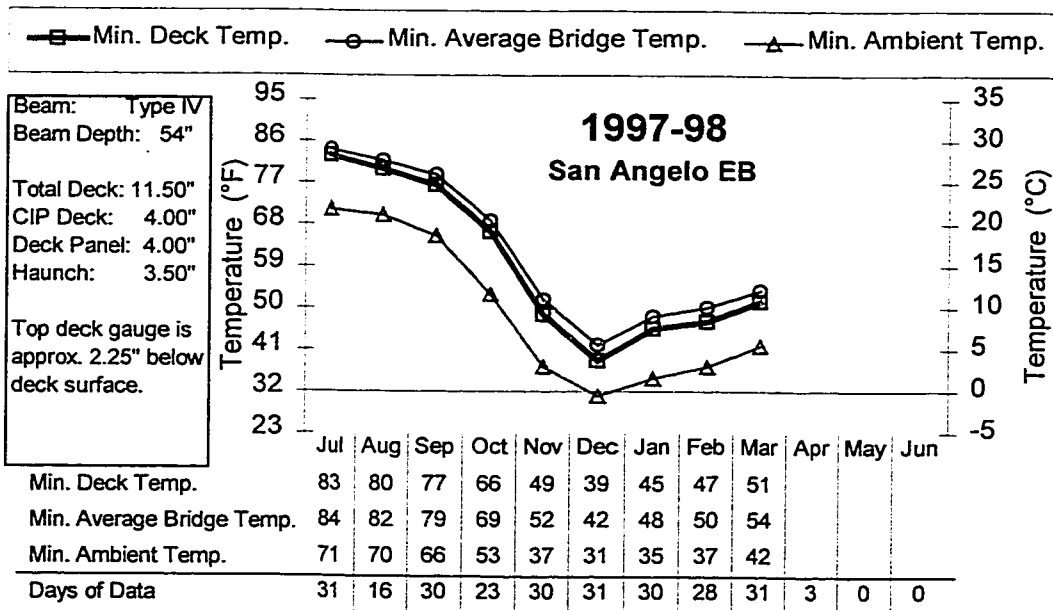
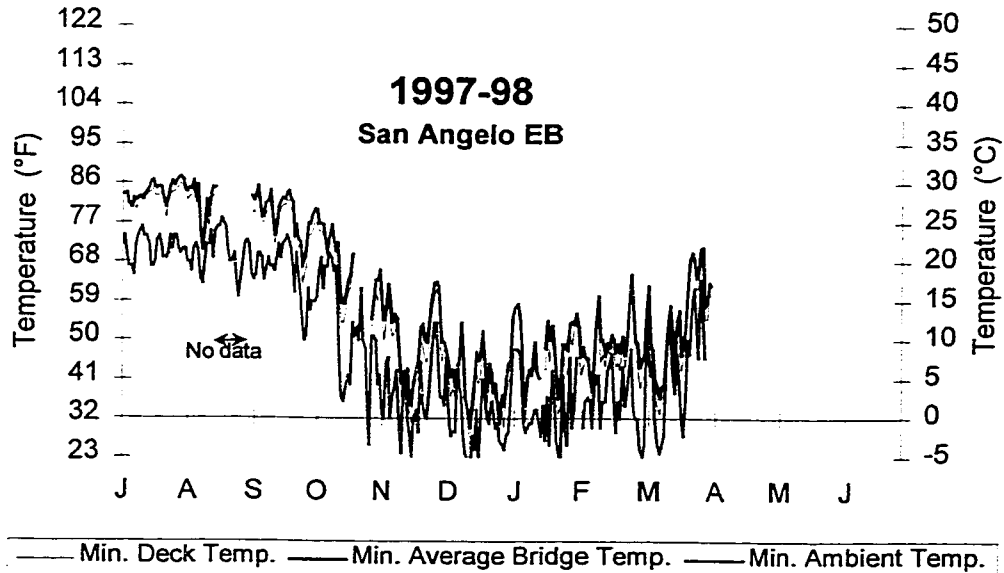
Beam: Type IV
 Beam Depth: 54"
 Total Deck: 11.50"
 CIP Deck: 4.00"
 Deck Panel: 4.00"
 Haunch: 3.50"
 Top deck gauge is approx. 2.25" below deck surface.



	Jul	Aug	Sep	Oct	Nov	Dec	Jan	Feb	Mar	Apr	May	Jun
Max. Deck Temp.	108	106	100	88	70	58	66	70	79			
Max. Average Bridge Temp.	96	94	90	80	62	52	60	61	67			
Max. Ambient Temp.	96	95	92	80	65	57	64	63	68			
Days of Data	31	16	30	23	30	31	30	28	31	3	0	0

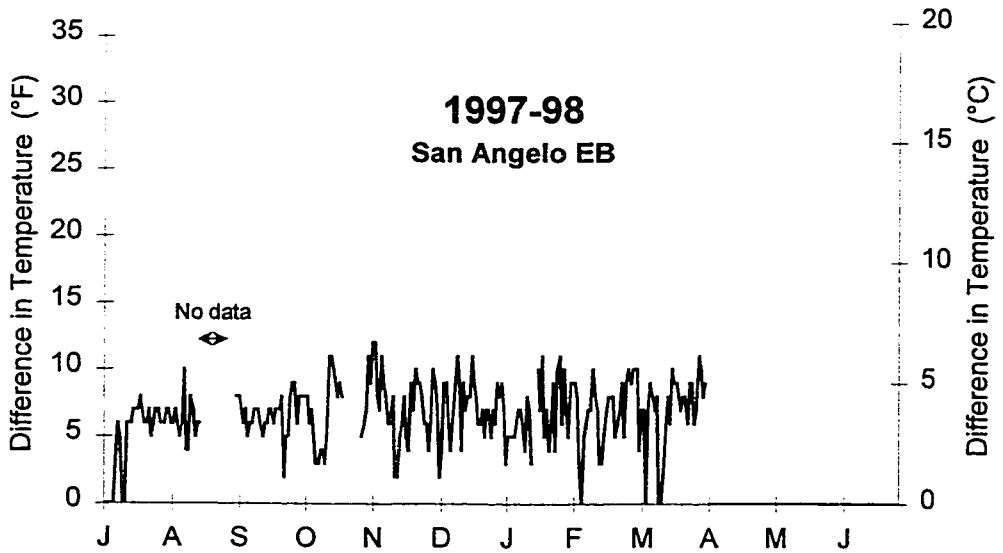
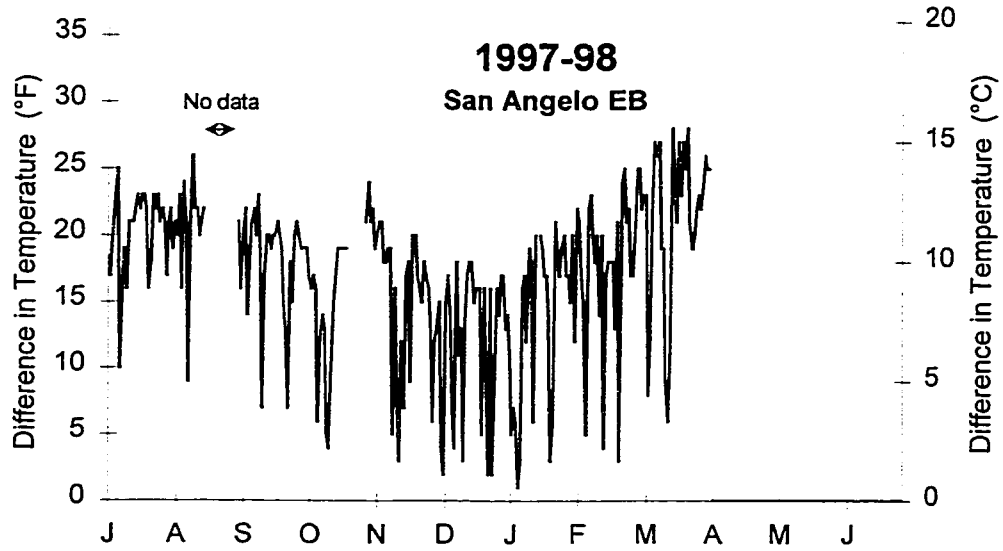
San Angelo Eastbound – Composite Beam E25

Minimum Bridge Temperatures



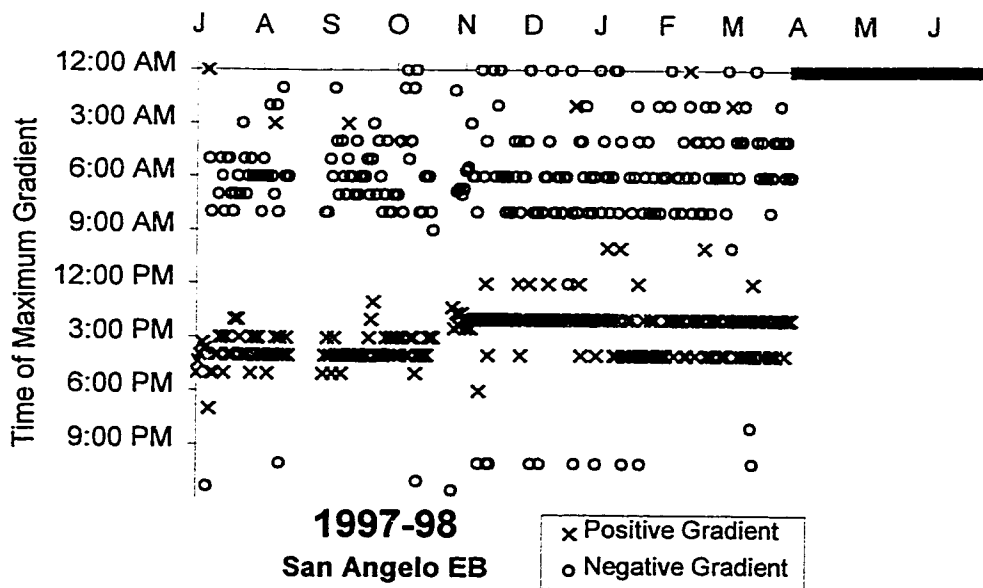
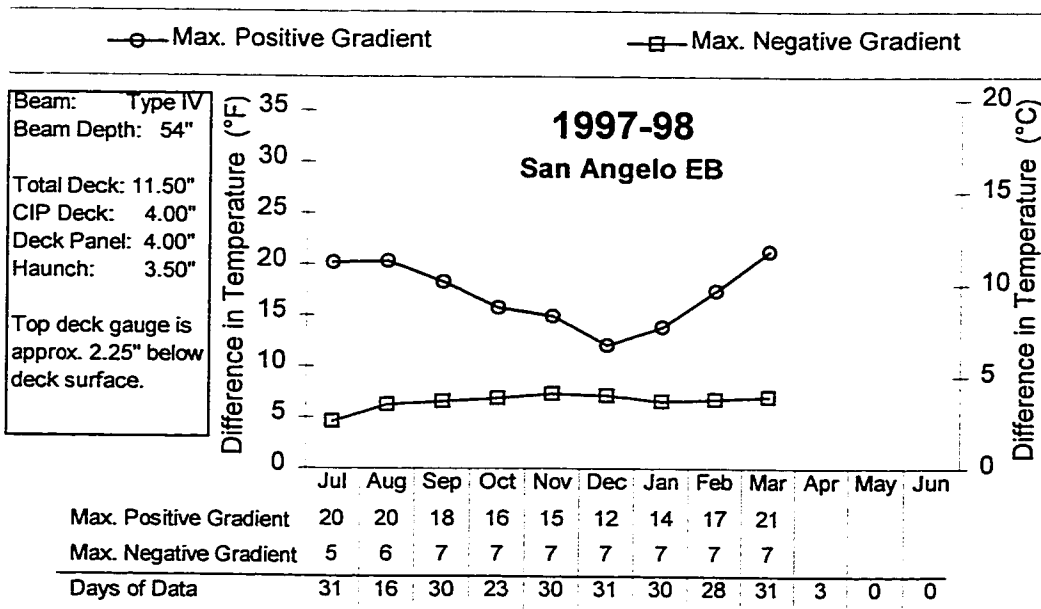
San Angelo Eastbound – Composite Beam E25

Thermal Gradients



San Angelo Eastbound – Composite Beam E25

Thermal Gradients



**APPENDIX F: IMPORTANT PARAMETERS AND CONSTRUCTION
SCHEDULES**

	Parameter	Design	Measured
Material Properties	$f_{ci, beam}$	Specified design strength	Measured strength from SC data at release
	$f_{c, beam}$	Specified design strength	Measured strength from MC data at 28d for non-HPC, 56d for HPC.
	$f_{c, panels}$	Specified design strength	Measured strength from MC data at 28d for non-HPC, 56d for HPC.
	$f_{c, CIP deck}$	Specified design strength	Measured strength from MC data at 28d for non-HPC, 56d for HPC.
	$E_{ci, beam}$	$33 * \rho^{1.5} * (f_c)^{0.5}$ for non-HPC, $1,000,000 + 40,000 * (f_c)^{0.5}$ for HPC	Based on strength vs. modulus regression equations developed for each specific mix.
	$E_{c, beam}$	$33 * \rho^{1.5} * (f_c)^{0.5}$ for non-HPC, $1,000,000 + 40,000 * (f_c)^{0.5}$ for HPC	Based on strength vs. modulus regression equations developed for each specific mix.
	$E_{c, panels}$	$33 * \rho^{1.5} * (f_c)^{0.5}$ for non-HPC, $1,000,000 + 40,000 * (f_c)^{0.5}$ for HPC	Based on strength vs. modulus regression equations developed for each specific mix.
	$E_{c, CIP deck}$	$33 * \rho^{1.5} * (f_c)^{0.5}$ for non-HPC, $1,000,000 + 40,000 * (f_c)^{0.5}$ for HPC	Based on strength vs. modulus regression equations developed for each specific mix.
	ρ_{beam}	Assume unit weight = 150 pcf	Measured unit weight for each mix
	ρ_{panels}	N/A - Deck assumed to be homogeneous	Measured unit weight for each mix
$\rho_{CIP deck}$	Assume unit weight = 150 pcf	Measured unit weight for each mix	
Structural Layout and Geometry	L (beam)	Length specified in drawings	Length specified in drawings
	L (ctr-to-ctr bearings)	Length specified in drawings	Length specified in drawings
	Beam spacing	Width specified in drawings. Calculated as avg. of perpendicular dist. to adjacent beams for non-parallel beams	Width specified in drawings. Calculated as avg. of perpendicular dist. to adjacent beams for non-parallel beams
	Effective deck width	Calculated according to <i>AASHTO Standard Specs</i> Sec. 8.10.1	Calculated according to <i>AASHTO Standard Specs</i> Sec. 8.10.1
	Width of haunch	N/A - haunch ignored	Width calculated as width of beam top flange less two fiberboard widths (assumed to be 2 in. each)
	Gap Betw. Panels	N/A - deck assumed to be homogeneous	Approximate width as specified on drawings.
	Thickness of Haunch	N/A - haunch ignored	Average thickness as measured in field by researchers
	Thickness of Panels	N/A - deck assumed to be homogeneous	Thickness as specified in drawings
	Thickness of CIP Deck	Total deck thickness as specified in drawings	Average CIP thickness as measured in field by inspectors

Section Properties	$A_{\text{beam (release)}}$	Calculated using gross section properties	Calculated using transformed section properties. Uses E_c
	$I_{\text{beam (release)}}$	Calculated using gross section properties	Calculated using transformed section properties. Uses E_c
	$y_{\text{bot,beam (release)}}$	Calculated using gross section properties	Calculated using transformed section properties. Uses E_c
	A_{beam}	Calculated using gross section properties (same as above)	Calculated using transformed section properties. Uses E_c
	I_{beam}	Calculated using gross section properties (same as above)	Calculated using transformed section properties. Uses E_c
	$y_{\text{bot,beam}}$	Calculated using gross section properties (same as above)	Calculated using transformed section properties. Uses E_c
	$A_{\text{composite}}$	Calculated using above dimensions for section geometry. Gross section properties.	Calculated using above dimensions for section geometry. Transformed section properties.
	$I_{\text{composite}}$	Calculated using above dimensions for section geometry. Gross section properties.	Calculated using above dimensions for section geometry. Transformed section properties.
	$y_{\text{bot,composite}}$	Calculated using above dimensions for section geometry. Gross section properties.	Calculated using above dimensions for section geometry. Transformed section properties.
Dead Loads and Midspan Moments	$W_{\text{beam self-wt.}}$	Calculated using gross section area and unit weight as assumed above.	Calculated using actual concrete area plus actual steel area. (i.e. add'l weight of steel accounted for.)
	W_{panels}	N/A - deck assumed to be homogeneous	Calculated using section geometry and panel unit weight as described above.
	$W_{\text{CIP deck}}$	Calculated using section geometry and deck unit weight as described above.	Calculated using section geometry and CIP deck unit weight as described above.
	$W_{\text{composite DL (incl. rail)}}$	Based on uniform composite DL, due to rail, assumed for actual design of beams. Rail assumed to be distributed evenly to all beams	Based on uniform composite DL, due to rail, assumed for actual design of beams. Rail assumed to be distributed to exterior beams only.
	$M_{\text{beam self-wt.}}$	Calculated from uniform distributed load as $wL^2/8$	Calculated from uniform distributed load as $wL^2/8$
	M_{panels}	N/A - deck assumed to be homogeneous	Calculated from uniform distributed load as $wL^2/8$
	$M_{\text{CIP deck}}$	Calculated from uniform distributed load as $wL^2/8$	Calculated from uniform distributed load as $wL^2/8$
	$M_{\text{composite DL (incl. rail)}}$	Calculated from uniform distributed load as $wL^2/8$	Calculated from uniform distributed load as $wL^2/8$

Beam(s) N21

	Parameter	Unit	Design	Measured
Material Properties	$f_{ci, beam}$	psi	8800	10890
	$f_{c, beam}$	psi	13100	14820
	$f_{c, panels}$	psi	8000	9040
	$f_{c, CIP deck}$	psi	4000	5700
	$E_{ci, beam}$	ksi	4750	6020
	$E_{c, beam}$	ksi	5580	6940
	$E_{c, panels}$	ksi	4580	5500
	$E_{c, CIP deck}$	ksi	3530	4490
	ρ_{beam}	pcf	150	153.9
	ρ_{panels}	pcf	150	149.9
	$\rho_{CIP deck}$	pcf	150	143.2
Structural Layout and Geometry	L (beam)	ft.	135.26	135.26
	L (center-to-center bearings)	ft.	134.17	134.17
	Beam spacing	in.	119.9	119.9
	Effective deck width	in.	119.9	119.9
	Width of haunch	in.	0	17.625
	Gap between Panels	in.	0	11.625
	Thickness of Haunch	in.	0	1.5
	Thickness of Panels	in.	0	3.5
	Thickness of CIP Deck	in.	7.25	3.75
Section Properties	A beam (release)	in. ²	1121	1190
	I beam (release)	in. ⁴	404230	425430
	y bot,beam (release)	in.	22.48	21.43
	A beam	in. ²	1121	1178
	I beam	in. ⁴	404230	422030
	y bot,beam	in.	22.48	21.60
	A composite	in. ²	1671	1813
	I composite	in. ⁴	862340	1041490
	y bot,composite	in.	34.05	34.64
Dead Loads and Midspan Moments	W beam self-wt.	kip/ft.	1.168	1.245
	W panels	kip/ft.	0	0.394
	W CIP deck	kip/ft.	0.905	0.514
	W composite DL (incl. rail)	kip/ft.	0.132	0.330
	M beam self-wt.	ft.-kips	2628	2901
	M panels	ft.-kips	0	888
	M CIP deck	ft.-kips	2038	1156
	M composite DL (incl. rail)	ft.-kips	297	743

Beam(s) N22

	Parameter	Unit	Design	Measured
Material Properties	$f_{ci, beam}$	psi	7700	8710
	$f'_{c, beam}$	psi	11600	13290
	$f'_{c, panels}$	psi	8000	9040
	$f'_{c, CIP deck}$	psi	4000	5700
	$E_{ci, beam}$	ksi	4510	5440
	$E_{c, beam}$	ksi	5310	6600
	$E_{c, panels}$	ksi	4580	5500
	$E_{c, CIP deck}$	ksi	3530	4490
	ρ_{beam}	pcf	150	153.9
	ρ_{panels}	pcf	150	149.9
	$\rho_{CIP deck}$	pcf	150	143.2
	Structural Layout and Geometry	L (beam)	ft.	135.83
L (center-to-center bearings)		ft.	134.74	134.74
Beam spacing		in.	159.5	159.5
Effective deck width		in.	159.5	159.5
Width of haunch		in.	0	23.5
Gap between Panels		in.	0	14.625
Thickness of Haunch		in.	0	1.5
Thickness of Panels		in.	0	3.5
Thickness of CIP Deck	in.	7.25	3.75	
Section Properties	$A_{beam (release)}$	in. ²	1121	1182
	$I_{beam (release)}$	in. ⁴	404230	424660
	$y_{bot, beam (release)}$	in.	22.48	21.51
	A_{beam}	in. ²	1121	1169
	I_{beam}	in. ⁴	404230	420380
	$y_{bot, beam}$	in.	22.48	21.71
	$A_{composite}$	in. ²	1890	2057
	$I_{composite}$	in. ⁴	970860	1185370
$y_{bot, composite}$	in.	36.78	37.75	
Dead Loads and Midspan Moments	$W_{beam self-wt.}$	kip/ft.	1.168	1.237
	W_{panels}	kip/ft.	0	0.528
	$W_{CIP deck}$	kip/ft.	1.205	0.681
	$W_{composite DL (incl. rail)}$	kip/ft.	0.132	0.000
	$M_{beam self-wt.}$	ft.-kips	2650	2902
	M_{panels}	ft.-kips	0	1198
	$M_{CIP deck}$	ft.-kips	2734	1545
	$M_{composite DL (incl. rail)}$	ft.-kips	300	0

Beam(s)		N23		
	Parameter	Unit	Design	Measured
Material Properties	$f_{ci, beam}$	psi	7700	11070
	$f_{c, beam}$	psi	11600	11500
	$f_{c, panels}$	psi	8000	9040
	$f_{c, CIP deck}$	psi	4000	5700
	$E_{ci, beam}$	ksi	4510	6060
	$E_{c, beam}$	ksi	5310	6170
	$E_{c, panels}$	ksi	4580	5500
	$E_{c, CIP deck}$	ksi	3530	4490
	ρ_{beam}	pcf	150	153.9
	ρ_{panels}	pcf	150	149.9
	$\rho_{CIP deck}$	pcf	150	143.2
Structural Layout and Geometry	L (beam)	ft.	136.41	136.41
	L (center-to-center bearings)	ft.	135.32	135.32
	Beam spacing	in.	158.8	158.8
	Effective deck width	in.	158.8	158.8
	Width of haunch	in.	0	23.5
	Gap between Panels	in.	0	14.625
	Thickness of Haunch	in.	0	1.5
	Thickness of Panels	in.	0	3.5
Thickness of CIP Deck	in.	7.25	3.75	
Section Properties	$A_{beam (release)}$	in. ²	1121	1174
	$I_{beam (release)}$	in. ⁴	404230	422180
	$y_{bot, beam (release)}$	in.	22.48	21.63
	A_{beam}	in. ²	1121	1173
	I_{beam}	in. ⁴	404230	421790
	$y_{bot, beam}$	in.	22.48	21.65
	$A_{composite}$	in. ²	1886	2119
	$I_{composite}$	in. ⁴	969380	1220840
$y_{bot, composite}$	in.	36.74	38.25	
Dead Loads and Midspan Moments	$W_{beam self-wt.}$	kip/ft.	1.168	1.237
	W_{panels}	kip/ft.	0	0.525
	$W_{CIP deck}$	kip/ft.	1.199	0.678
	$W_{composite DL (incl. rail)}$	kip/ft.	0.132	0.000
	$M_{beam self-wt.}$	ft.-kips	2673	2936
	M_{panels}	ft.-kips	0	1202
	$M_{CIP deck}$	ft.-kips	2745	1552
	$M_{composite DL (incl. rail)}$	ft.-kips	302	0

Beam(s) N31

	Parameter	Unit	Design	Measured
Material Properties	$f_{ci, beam}$	psi	8800	10890
	$f_{c, beam}$	psi	13100	14820
	$f_{c, panels}$	psi	8000	9040
	$f_{c, CIP deck}$	psi	4000	5700
	$E_{ci, beam}$	ksi	4750	6020
	$E_{c, beam}$	ksi	5580	6940
	$E_{c, panels}$	ksi	4580	5500
	$E_{c, CIP deck}$	ksi	3530	4490
	ρ_{beam}	pcf	150	153.9
	ρ_{panels}	pcf	150	149.9
	$\rho_{CIP deck}$	pcf	150	143.2
	Structural Layout and Geometry	L (beam)	ft.	133.67
L (center-to-center bearings)		ft.	132.38	132.38
Beam spacing		in.	115.6	115.6
Effective deck width		in.	115.6	115.6
Width of haunch		in.	0	17.625
Gap between Panels		in.	0	11.625
Thickness of Haunch		in.	0	1.5
Thickness of Panels		in.	0	3.5
Thickness of CIP Deck		in.	7.25	3.75
Section Properties	$A_{beam (release)}$	in. ²	1121	1187
	$I_{beam (release)}$	in. ⁴	404230	425010
	$y_{bot, beam (release)}$	in.	22.48	21.47
	A_{beam}	in. ²	1121	1176
	I_{beam}	in. ⁴	404230	421670
	$y_{bot, beam}$	in.	22.48	21.63
	$A_{composite}$	in. ²	1651	1788
	$I_{composite}$	in. ⁴	851150	1026210
$y_{bot, composite}$	in.	33.76	34.37	
Dead Loads and Midspan Moments	$W_{beam self-wt.}$	kip/ft.	1.168	1.245
	W_{panels}	kip/ft.	0	0.379
	$W_{CIP deck}$	kip/ft.	0.873	0.498
	$W_{composite DL (incl. rail)}$	kip/ft.	0.132	0.330
	$M_{beam self-wt.}$	ft.-kips	2558	2818
	M_{panels}	ft.-kips	0	830
	$M_{CIP deck}$	ft.-kips	1912	1091
	$M_{composite DL (incl. rail)}$	ft.-kips	289	723

Beam(s) N32

	Parameter	Unit	Design	Measured
Material Properties	$P_{ci, beam}$	psi	7700	10470
	$P_{c, beam}$	psi	11600	13630
	$P_{c, panels}$	psi	8000	9040
	$P_{c, CIP deck}$	psi	4000	5700
	$E_{ci, beam}$	ksi	4510	5910
	$E_{c, beam}$	ksi	5310	6670
	$E_{c, panels}$	ksi	4580	5500
	$E_{c, CIP deck}$	ksi	3530	4490
	ρ_{beam}	pcf	150	153.9
	ρ_{panels}	pcf	150	149.9
	$\rho_{CIP deck}$	pcf	150	143.2
Structural Layout and Geometry	L (beam)	ft.	134.18	134.18
	L (center-to-center bearings)	ft.	132.89	132.89
	Beam spacing	in.	151.0	151.0
	Effective deck width	in.	151.0	151.0
	Width of haunch	in.	0	23.5
	Gap between Panels	in.	0	14.625
	Thickness of Haunch	in.	0	1.5
	Thickness of Panels	in.	0	3.5
	Thickness of CIP Deck	in.	7.25	3.75
Section Properties	$A_{beam (release)}$	in. ²	1025	1077
	$I_{beam (release)}$	in. ⁴	380420	400060
	$y_{bot, beam (release)}$	in.	23.88	22.92
	A_{beam}	in. ²	1025	1069
	I_{beam}	in. ⁴	380420	397340
	$y_{bot, beam}$	in.	23.88	23.05
	$A_{composite}$	in. ²	1753	1902
	$I_{composite}$	in. ⁴	868240	1065960
$y_{bot, composite}$	in.	37.89	38.72	
Dead Loads and Midspan Moments	$W_{beam self-wt.}$	kip/ft.	1.068	1.132
	W_{panels}	kip/ft.	0	0.497
	$W_{CIP deck}$	kip/ft.	1.140	0.649
	$W_{composite DL (incl. rail)}$	kip/ft.	0.132	0.000
	$M_{beam self-wt.}$	ft.-kips	2357	2592
	M_{panels}	ft.-kips	0	1097
	$M_{CIP deck}$	ft.-kips	2517	1433
	$M_{composite DL (incl. rail)}$	ft.-kips	291	0

Beam(s) N33

	Parameter	Unit	Design	Measured
Material Properties	$f_{ci, beam}$	psi	7700	10470
	$f_{c, beam}$	psi	11600	13630
	$f_{c, panels}$	psi	8000	9040
	$f_{c, CIP deck}$	psi	4000	5700
	$E_{ci, beam}$	ksi	4510	5910
	$E_{c, beam}$	ksi	5310	6670
	$E_{c, panels}$	ksi	4580	5500
	$E_{c, CIP deck}$	ksi	3530	4490
	ρ_{beam}	pcf	150	153.9
	ρ_{panels}	pcf	150	149.9
	$\rho_{CIP deck}$	pcf	150	143.2
	Structural Layout and Geometry	L (beam)	ft.	134.70
L (center-to-center bearings)		ft.	133.40	133.40
Beam spacing		in.	150.4	150.4
Effective deck width		in.	150.4	150.4
Width of haunch		in.	0	23.5
Gap between Panels		in.	0	14.625
Thickness of Haunch		in.	0	1.5
Thickness of Panels		in.	0	3.5
Thickness of CIP Deck		in.	7.25	3.75
Section Properties	$A_{beam (release)}$	in. ²	1025	1077
	$I_{beam (release)}$	in. ⁴	380420	400060
	$y_{bot,beam (release)}$	in.	23.88	22.92
	A_{beam}	in. ²	1025	1069
	I_{beam}	in. ⁴	380420	397340
	$y_{bot,beam}$	in.	23.88	23.05
	$A_{composite}$	in. ²	1750	1899
	$I_{composite}$	in. ⁴	867100	1064710
$y_{bot,composite}$	in.	37.86	38.69	
Dead Loads and Midspan Moments	$W_{beam self-wt.}$	kip/ft.	1.068	1.132
	W_{panels}	kip/ft.	0	0.495
	$W_{CIP deck}$	kip/ft.	1.136	0.647
	$W_{composite DL (incl. rail)}$	kip/ft.	0.132	0.000
	$M_{beam self-wt.}$	ft.-kips	2375	2619
	M_{panels}	ft.-kips	0	1100
	$M_{CIP deck}$	ft.-kips	2526	1438
	$M_{composite DL (incl. rail)}$	ft.-kips	294	0

Beam(s) S14

	Parameter	Unit	Design	Measured	
Material Properties	$f_{ci, beam}$	psi	7700	10990	
	$f_{c, beam}$	psi	11600	14320	
	$f_{c, panels}$	psi	8000	9040	
	$f_{c, CIP deck}$	psi	8000	9100	
	$E_{ci, beam}$	ksi	4510	6040	
	$E_{c, beam}$	ksi	5310	6830	
	$E_{c, panels}$	ksi	4580	5500	
	$E_{c, CIP deck}$	ksi	4580	4920	
	ρ_{beam}	pcf	150	153.9	
	ρ_{panels}	pcf	150	149.9	
	$\rho_{CIP deck}$	pcf	150	150.2	
	Structural Layout and Geometry	L (beam)	ft.	117.91	117.91
		L (center-to-center bearings)	ft.	116.62	116.62
Beam spacing		in.	194.4	194.4	
Effective deck width		in.	183.0	186.0	
Width of haunch		in.	0	23.5	
Gap between Panels		in.	0	14.625	
Thickness of Haunch		in.	0	1.5	
Thickness of Panels		in.	0	3.5	
Thickness of CIP Deck		in.	7.25	4.0	
Section Properties	A _{beam (release)}	in. ²	1025	1076	
	I _{beam (release)}	in. ³	380420	399550	
	y _{bot,beam (release)}	in.	23.88	22.94	
	A _{beam}	in. ²	1025	1068	
	I _{beam}	in. ³	380420	396850	
	y _{bot,beam}	in.	23.88	23.08	
	A _{composite}	in. ²	2169	2149	
	I _{composite}	in. ³	1001140	1169040	
	y _{bot,composite}	in.	41.68	41.17	
Dead Loads and Midspan Moments	W _{beam self-wt.}	kip/ft.	1.068	1.132	
	W _{panels}	kip/ft.	0	0.655	
	W _{CIP deck}	kip/ft.	1.468	0.901	
	W _{composite DL (incl. rail)}	kip/ft.	0.110	0.000	
	M _{beam self-wt.}	ft.-kips	1815	1996	
	M _{panels}	ft.-kips	0	1114	
	M _{CIP deck}	ft.-kips	2496	1532	
	M _{composite DL (incl. rail)}	ft.-kips	187	0	

Beam(s)		S15		
	Parameter	Unit	Design	Measured
Material Properties	$f_{ci, beam}$	psi	7700	10990
	$f_{c, beam}$	psi	11600	14320
	$f_{c, panels}$	psi	8000	9040
	$f_{c, CIP deck}$	psi	8000	9100
	$E_{ci, beam}$	ksi	4510	6040
	$E_{c, beam}$	ksi	5310	6830
	$E_{c, panels}$	ksi	4580	5500
	$E_{c, CIP deck}$	ksi	4580	4920
	ρ_{beam}	pcf	150	153.9
	ρ_{panels}	pcf	150	149.9
	$\rho_{CIP deck}$	pcf	150	150.2
	Structural Layout and Geometry	L (beam)	ft.	119.44
L (center-to-center bearings)		ft.	118.15	118.15
Beam spacing		in.	192.0	192.0
Effective deck width		in.	183.0	189.0
Width of haunch		in.	0	23.5
Gap between Panels		in.	0	14.625
Thickness of Haunch		in.	0	1.5
Thickness of Panels		in.	0	3.5
	Thickness of CIP Deck	in.	7.25	4.25
Section Properties	$A_{beam (release)}$	in. ²	1025	1076
	$I_{beam (release)}$	in. ⁴	380420	399550
	$y_{bot, beam (release)}$	in.	23.88	22.94
	A_{beam}	in. ²	1025	1068
	I_{beam}	in. ⁴	380420	396850
	$y_{bot, beam}$	in.	23.88	23.08
	$A_{composite}$	in. ²	2169	2200
	$I_{composite}$	in. ⁴	1001140	1190870
	$y_{bot, composite}$	in.	41.68	41.65
Dead Loads and Midspan Moments	$W_{beam self-wt.}$	kip/ft.	1.068	1.132
	W_{panels}	kip/ft.	0	0.646
	$W_{CIP deck}$	kip/ft.	1.450	0.941
	$W_{composite DL (incl. rail)}$	kip/ft.	0.110	0.000
	$M_{beam self-wt.}$	ft.-kips	1863	2072
	M_{panels}	ft.-kips	0	1128
	$M_{CIP deck}$	ft.-kips	2530	1642
	$M_{composite DL (incl. rail)}$	ft.-kips	192	0

Beam(s)		S16		
	Parameter	Unit	Design	Measured
Material Properties	$f_{ci, beam}$	psi	7700	8710
	$f_{c, beam}$	psi	11600	13290
	$f_{c, panels}$	psi	8000	9040
	$f_{c, CIP deck}$	psi	8000	9100
	$E_{ci, beam}$	ksi	4510	5440
	$E_{c, beam}$	ksi	5310	6600
	$E_{c, panels}$	ksi	4580	5500
	$E_{c, CIP deck}$	ksi	4580	4920
	ρ_{beam}	pcf	150	153.9
	ρ_{panels}	pcf	150	149.9
	$\rho_{CIP deck}$	pcf	150	150.2
Structural Layout and Geometry	L (beam)	ft.	121.02	121.02
	L (center-to-center bearings)	ft.	119.71	119.71
	Beam spacing	in.	136.1	136.1
	Effective deck width	in.	131.6	134.6
	Width of haunch	in.	0	17.625
	Gap between Panels	in.	0	11.625
	Thickness of Haunch	in.	0	1.5
	Thickness of Panels	in.	0	3.5
Thickness of CIP Deck	in.	7.25	4.25	
Section Properties	$A_{beam (release)}$	in. ²	1121	1182
	$I_{beam (release)}$	in. ⁴	404230	424660
	$Y_{bot, beam (release)}$	in.	22.48	21.51
	A_{beam}	in. ²	1121	1169
	I_{beam}	in. ⁴	404230	420380
	$Y_{bot, beam}$	in.	22.48	21.71
	$A_{composite}$	in. ²	1944	2004
	$I_{composite}$	in. ⁴	994000	1161420
$Y_{bot, composite}$	in.	37.36	37.32	
Dead Loads and Midspan Moments	$W_{beam self-wt.}$	kip/ft.	1.168	1.237
	W_{panels}	kip/ft.	0	0.454
	$W_{CIP deck}$	kip/ft.	1.028	0.673
	$W_{composite DL (incl. rail)}$	kip/ft.	0.110	0.330
	$M_{beam self-wt.}$	ft.-kips	2092	2315
	M_{panels}	ft.-kips	0	812
	$M_{CIP deck}$	ft.-kips	1841	1206
$M_{composite DL (incl. rail)}$	ft.-kips	197	591	

Beam(s) S24

	Parameter	Unit	Design	Measured	
Material Properties	$f_{ci, beam}$	psi	7700	10320	
	$f_{c, beam}$	psi	11600	13410	
	$f_{c, panels}$	psi	8000	9040	
	$f_{c, CIP deck}$	psi	8000	9100	
	$E_{ci, beam}$	ksi	4510	5870	
	$E_{c, beam}$	ksi	5310	6620	
	$E_{c, panels}$	ksi	4580	5500	
	$E_{c, CIP deck}$	ksi	4580	4920	
	ρ_{beam}	pcf	150	153.9	
	ρ_{panels}	pcf	150	149.9	
	$\rho_{CIP deck}$	pcf	150	150.2	
	Structural Layout and Geometry	L (beam)	ft.	131.75	131.75
		L (center-to-center bearings)	ft.	130.66	130.66
Beam spacing		in.	169.2	169.2	
Effective deck width		in.	169.2	169.2	
Width of haunch		in.	0	23.5	
Gap between Panels		in.	0	14.625	
Thickness of Haunch		in.	0	1.5	
Thickness of Panels		in.	0	3.5	
Thickness of CIP Deck		in.	7.25	4.5	
Section Properties	$A_{beam (release)}$	in. ²	1121	1177	
	$I_{beam (release)}$	in. ⁴	404230	422890	
	$y_{bot, beam (release)}$	in.	22.48	21.59	
	A_{beam}	in. ²	1121	1169	
	I_{beam}	in. ⁴	404230	420320	
	$y_{bot, beam}$	in.	22.48	21.71	
	$A_{composite}$	in. ²	2179	2248	
	$I_{composite}$	in. ⁴	1081180	1291320	
	$y_{bot, composite}$	in.	39.54	39.76	
Dead Loads and Midspan Moments	$W_{beam self-wt.}$	kip/ft.	1.168	1.237	
	W_{panels}	kip/ft.	0	0.563	
	$W_{CIP deck}$	kip/ft.	1.278	0.884	
	$W_{composite DL (incl. rail)}$	kip/ft.	0.110	0.000	
	$M_{beam self-wt.}$	ft.-kips	2492	2729	
	M_{panels}	ft.-kips	0	1202	
	$M_{CIP deck}$	ft.-kips	2727	1887	
	$M_{composite DL (incl. rail)}$	ft.-kips	235	0	

Beam(s)

S25

	Parameter	Unit	Design	Measured
Material Properties	$f_{ci, beam}$	psi	7700	10320
	$f_{c, beam}$	psi	11600	13410
	$f_{c, panels}$	psi	8000	9040
	$f_{c, CIP deck}$	psi	8000	9100
	$E_{ci, beam}$	ksi	4510	5870
	$E_{c, beam}$	ksi	5310	6620
	$E_{c, panels}$	ksi	4580	5500
	$E_{c, CIP deck}$	ksi	4580	4920
	ρ_{beam}	pcf	150	153.9
	ρ_{panels}	pcf	150	149.9
	$\rho_{CIP deck}$	pcf	150	150.2
	Structural Layout and Geometry	L (beam)	ft.	133.40
L (center-to-center bearings)		ft.	132.31	132.31
Beam spacing		in.	167.0	167.0
Effective deck width		in.	167.0	167.0
Width of haunch		in.	0	23.5
Gap between Panels		in.	0	14.625
Thickness of Haunch		in.	0	1.5
Thickness of Panels		in.	0	3.5
Thickness of CIP Deck	in.	7.25	4.5	
Section Properties	A _{beam (release)}	in. ²	1121	1177
	I _{beam (release)}	in. ⁴	404230	422890
	y _{bot,beam (release)}	in.	22.48	21.59
	A _{beam}	in. ²	1121	1169
	I _{beam}	in. ⁴	404230	420320
	y _{bot,beam}	in.	22.48	21.71
	A _{composite}	in. ²	2165	2235
	I _{composite}	in. ⁴	1076590	1285910
	y _{bot,composite}	in.	39.43	39.64
Dead Loads and Midspan Moments	W _{beam self-wt.}	kip/ft.	1.168	1.237
	W _{panels}	kip/ft.	0	0.555
	W _{CIP deck}	kip/ft.	1.261	0.874
	W _{composite DL (incl. rail)}	kip/ft.	0.110	0.000
	M _{beam self-wt.}	ft.-kips	2555	2824
	M _{panels}	ft.-kips	0	1215
	M _{CIP deck}	ft.-kips	2760	1913
	M _{composite DL (incl. rail)}	ft.-kips	241	0

Beam(s) S26

	Parameter	Unit	Design	Measured	
Material Properties	$f_{ci, beam}$	psi	8800	11100	
	$f_{c, beam}$	psi	13100	13560	
	$f_{c, panels}$	psi	8000	9040	
	$f_{c, CIP deck}$	psi	8000	9100	
	$E_{ci, beam}$	ksi	4750	6070	
	$E_{c, beam}$	ksi	5580	6660	
	$E_{c, panels}$	ksi	4580	5500	
	$E_{c, CIP deck}$	ksi	4580	4920	
	ρ_{beam}	pcf	150	153.9	
	ρ_{panels}	pcf	150	149.9	
	$\rho_{CIP deck}$	pcf	150	150.2	
	Structural Layout and Geometry	L (beam)	ft.	135.09	135.09
		L (center-to-center bearings)	ft.	134.00	134.00
Beam spacing		in.	123.6	123.6	
Effective deck width		in.	123.6	123.6	
Width of haunch		in.	0	17.625	
Gap between Panels		in.	0	11.625	
Thickness of Haunch		in.	0	1.5	
Thickness of Panels		in.	0	3.5	
Thickness of CIP Deck		in.	7.25	4.5	
Section Properties	$A_{beam (release)}$	in. ²	1121	1189	
	$I_{beam (release)}$	in. ⁴	404230	425220	
	$y_{bot, beam (release)}$	in.	22.48	21.44	
	A_{beam}	in. ²	1121	1182	
	I_{beam}	in. ⁴	404230	422970	
	$y_{bot, beam}$	in.	22.48	21.55	
	$A_{composite}$	in. ²	1857	1966	
	$I_{composite}$	in. ⁴	956010	1150510	
	$y_{bot, composite}$	in.	36.40	36.61	
Dead Loads and Midspan Moments	$W_{beam self-wt.}$	kip/ft.	1.168	1.247	
	W_{panels}	kip/ft.	0	0.408	
	$W_{CIP deck}$	kip/ft.	0.933	0.650	
	$W_{composite DL (incl. rail)}$	kip/ft.	0.110	0.330	
	$M_{beam self-wt.}$	ft.-kips	2621	2909	
	M_{panels}	ft.-kips	0	916	
	$M_{CIP deck}$	ft.-kips	2095	1459	
	$M_{composite DL (incl. rail)}$	ft.-kips	247	741	

Beam(s) E13

	Parameter	Unit	Design	Measured	
Material Properties	$f_{ci, beam}$	psi	8100	10780	
	$f'_{c, beam}$	psi	13000	13700	
	$f'_{c, panels}$	psi	6000	10100	
	$f'_{c, CIP deck}$	psi	6000	7290	
	$E_{ci, beam}$	ksi	4600	6010	
	$E_{c, beam}$	ksi	5560	6250	
	$E_{c, panels}$	ksi	4100	4970	
	$E_{c, CIP deck}$	ksi	4100	5300	
	ρ_{beam}	pcf	150	152.9	
	ρ_{panels}	pcf	150	150.9	
	$\rho_{CIP deck}$	pcf	150	149.4	
	Structural Layout and Geometry	L (beam)	ft.	128.95	128.95
		L (center-to-center bearings)	ft.	127.79	127.79
Beam spacing		in.	132.0	132.0	
Effective deck width		in.	110.0	122.0	
Width of haunch		in.	0	16.00	
Gap between Panels		in.	0	9.00	
Thickness of Haunch		in.	0	3.0	
Thickness of Panels		in.	0	4.0	
Thickness of CIP Deck	in.	7.5	4.5		
Section Properties	A _{beam (release)}	in. ²	789	821	
	I _{beam (release)}	in. ⁴	260400	263380	
	y _{bot,beam (release)}	in.	24.73	24.30	
	A _{beam}	in. ²	789	842	
	I _{beam}	in. ⁴	260400	276990	
	y _{bot,beam}	in.	24.73	23.58	
	A _{composite}	in. ²	1397	1738	
	I _{composite}	in. ⁴	637780	1011790	
	y _{bot,composite}	in.	39.11	42.90	
Dead Loads and Midspan Moments	W _{beam self-wt.}	kip/ft.	0.822	0.869	
	W _{panels}	kip/ft.	0	0.516	
	W _{CIP deck}	kip/ft.	1.031	0.703	
	W _{composite DL (incl. rail)}	kip/ft.	0.097	0.000	
	M _{beam self-wt.}	ft.-kips	1678	1773	
	M _{panels}	ft.-kips	0	1052	
	M _{CIP deck}	ft.-kips	2105	1436	
	M _{composite DL (incl. rail)}	ft.-kips	198	0	

Beam(s)		E14			
	Parameter	Unit	Design	Measured	
Material Properties	$f_{ci, beam}$	psi	8100	10780	
	$f_{c, beam}$	psi	13000	13700	
	$f_{c, panels}$	psi	6000	10100	
	$f_{c, CIP deck}$	psi	6000	7290	
	$E_{ci, beam}$	ksi	4600	6010	
	$E_{c, beam}$	ksi	5560	6250	
	$E_{c, panels}$	ksi	4100	4970	
	$E_{c, CIP deck}$	ksi	4100	5300	
	ρ_{beam}	pcf	150	152.9	
	ρ_{panels}	pcf	150	150.9	
	$\rho_{CIP deck}$	pcf	150	149.4	
	Structural Layout and Geometry	L (beam)	ft.	128.95	128.95
		L (center-to-center bearings)	ft.	127.79	127.79
Beam spacing		in.	108.0	108.0	
Effective deck width		in.	97.0	103.0	
Width of haunch		in.	0	18.00	
Gap between Panels		in.	0	46.50	
Thickness of Haunch		in.	0	2.5	
Thickness of Panels		in.	0	4.0	
Thickness of CIP Deck		in.	7.5	4.5	
Section Properties	$A_{beam (release)}$	in. ²	789	821	
	$I_{beam (release)}$	in. ⁴	260400	263380	
	$y_{bot, beam (release)}$	in.	24.73	24.30	
	A_{beam}	in. ²	789	842	
	I_{beam}	in. ⁴	260400	276990	
	$y_{bot, beam}$	in.	24.73	23.58	
	$A_{composite}$	in. ²	1326	1611	
	$I_{composite}$	in. ⁴	611100	939480	
	$y_{bot, composite}$	in.	38.09	41.21	
Dead Loads and Midspan Moments	$W_{beam self-wt.}$	kip/ft.	0.822	0.869	
	W_{panels}	kip/ft.	0	0.258	
	$W_{CIP deck}$	kip/ft.	0.844	0.744	
	$W_{composite DL (incl. rail)}$	kip/ft.	0.097	0.194	
	$M_{beam self-wt.}$	ft.-kips	1678	1773	
	M_{panels}	ft.-kips	0	526	
	$M_{CIP deck}$	ft.-kips	1722	1518	
	$M_{composite DL (incl. rail)}$	ft.-kips	198	396	

Beam(s) E24

	Parameter	Unit	Design	Measured
Material Properties	$f_{ci, beam}$	psi	8000	13070
	$f_{c, beam}$	psi	14000	14240
	$f_{c, panels}$	psi	6000	10100
	$f_{c, CIP deck}$	psi	6000	8420
	$E_{ci, beam}$	ksi	4580	6200
	$E_{c, beam}$	ksi	5730	6300
	$E_{c, panels}$	ksi	4100	4970
	$E_{c, CIP deck}$	ksi	4100	5490
	ρ_{beam}	pcf	150	152.9
	ρ_{panels}	pcf	150	150.9
	$\rho_{CIP deck}$	pcf	150	149.4
	Structural Layout and Geometry	L (beam)	ft.	153.34
L (center-to-center bearings)		ft.	152.17	152.17
Beam spacing		in.	79.2	79.2
Effective deck width		in.	79.2	79.2
Width of haunch		in.	0	16.00
Gap between Panels		in.	0	9.00
Thickness of Haunch		in.	0	3.5
Thickness of Panels		in.	0	4.0
Thickness of CIP Deck		in.	7.5	4.0
Section Properties	$A_{beam (release)}$	in. ²	789	819
	$I_{beam (release)}$	in. ⁴	260400	263080
	$y_{bot, beam (release)}$	in.	24.73	24.33
	A_{beam}	in. ²	789	846
	I_{beam}	in. ⁴	260400	277600
	$y_{bot, beam}$	in.	24.73	23.52
	$A_{composite}$	in. ²	1214	1424
	$I_{composite}$	in. ⁴	563570	904250
	$y_{bot, composite}$	in.	36.29	38.77
Dead Loads and Midspan Moments	$W_{beam self-wt.}$	kip/ft.	0.822	0.869
	W_{panels}	kip/ft.	0	0.294
	$W_{CIP deck}$	kip/ft.	0.619	0.424
	$W_{composite DL (incl. rail)}$	kip/ft.	0.065	0.000
	$M_{beam self-wt.}$	ft.-kips	2379	2515
	M_{panels}	ft.-kips	0	852
	$M_{CIP deck}$	ft.-kips	1791	1228
	$M_{composite DL (incl. rail)}$	ft.-kips	188	0

Beam(s) E25

	Parameter	Unit	Design	Measured
Material Properties	$f_{ci, beam}$	psi	8100	9790
	$f_{c, beam}$	psi	13500	14830
	$f_{c, panels}$	psi	6000	10100
	$f_{c, CIP deck}$	psi	6000	8420
	$E_{ci, beam}$	ksi	4600	5920
	$E_{c, beam}$	ksi	5650	6340
	$E_{c, panels}$	ksi	4100	4970
	$E_{c, CIP deck}$	ksi	4100	5490
	ρ_{beam}	pcf	150	152.9
	ρ_{panels}	pcf	150	150.9
	$\rho_{CIP deck}$	pcf	150	149.4
Structural Layout and Geometry	L (beam)	ft.	153.34	153.34
	L (center-to-center bearings)	ft.	152.17	152.17
	Beam spacing	in.	79.2	79.2
	Effective deck width	in.	79.2	79.2
	Width of haunch	in.	0	16.00
	Gap between Panels	in.	0	9.00
	Thickness of Haunch	in.	0	3.5
	Thickness of Panels	in.	0	4.0
	Thickness of CIP Deck	in.	7.5	4.0
Section Properties	$A_{beam (release)}$	in. ²	789	818
	$I_{beam (release)}$	in. ⁴	260400	263120
	$y_{bot, beam (release)}$	in.	24.73	24.34
	A_{beam}	in. ²	789	838
	I_{beam}	in. ⁴	260400	276510
	$y_{bot, beam}$	in.	24.73	23.64
	$A_{composite}$	in. ²	1220	1412
	$I_{composite}$	in. ⁴	566350	895740
	$y_{bot, composite}$	in.	36.40	38.87
Dead Loads and Midspan Moments	$W_{beam self-wt.}$	kip/ft.	0.822	0.867
	W_{panels}	kip/ft.	0	0.294
	$W_{CIP deck}$	kip/ft.	0.619	0.424
	$W_{composite DL (incl. rail)}$	kip/ft.	0.065	0.000
	$M_{beam self-wt.}$	ft.-kips	2379	2509
	M_{panels}	ft.-kips	0	852
	$M_{CIP deck}$	ft.-kips	1791	1228
	$M_{composite DL (incl. rail)}$	ft.-kips	188	0

Beam(s)		E26		
	Parameter	Unit	Design	Measured
Material Properties	$f_{ci, beam}$	psi	8000	13070
	$f_{c, beam}$	psi	14000	14240
	$f_{c, panels}$	psi	6000	10100
	$f_{c, CIP deck}$	psi	6000	8420
	$E_{ci, beam}$	ksi	4580	6200
	$E_{c, beam}$	ksi	5730	6300
	$E_{c, panels}$	ksi	4100	4970
	$E_{c, CIP deck}$	ksi	4100	5490
	ρ_{beam}	pcf	150	152.9
	ρ_{panels}	pcf	150	150.9
	$\rho_{CIP deck}$	pcf	150	149.4
	Structural Layout and Geometry	L (beam)	ft.	153.34
L (center-to-center bearings)		ft.	152.17	152.17
Beam spacing		in.	81.6	81.6
Effective deck width		in.	81.6	81.6
Width of haunch		in.	0	18.00
Gap between Panels		in.	0	46.50
Thickness of Haunch		in.	0	3.5
Thickness of Panels		in.	0	4.0
Thickness of CIP Deck	in.	7.5	4.5	
Section Properties	A _{beam (release)}	in. ²	789	819
	I _{beam (release)}	in. ⁴	260400	263080
	y _{bot,beam (release)}	in.	24.73	24.33
	A _{beam}	in. ²	789	846
	I _{beam}	in. ⁴	260400	277600
	y _{bot,beam}	in.	24.73	23.52
	A _{composite}	in. ²	1227	1494
	I _{composite}	in. ⁴	569500	962960
	y _{bot,composite}	in.	36.52	39.90
Dead Loads and Midspan Moments	W _{beam self-wt.}	kip/ft.	0.822	0.869
	W _{panels}	kip/ft.	0	0.147
	W _{CIP deck}	kip/ft.	0.638	0.639
	W _{composite DL (incl. rail)}	kip/ft.	0.065	0.194
	M _{beam self-wt.}	ft.-kips	2379	2515
	M _{panels}	ft.-kips	0	426
	M _{CIP deck}	ft.-kips	1845	1850
	M _{composite DL (incl. rail)}	ft.-kips	188	562

Beam(s)		E33			
	Parameter	Unit	Design	Measured	
Material Properties	$f_{ci, beam}$	psi	8000	12390	
	$f_{c, beam}$	psi	13800	13750	
	$f_{c, panels}$	psi	6000	10100	
	$f_{c, CIP deck}$	psi	6000	9060	
	$E_{ci, beam}$	ksi	4580	6150	
	$E_{c, beam}$	ksi	5700	6260	
	$E_{c, panels}$	ksi	4100	4970	
	$E_{c, CIP deck}$	ksi	4100	5590	
	ρ_{beam}	pcf	150	152.9	
	ρ_{panels}	pcf	150	150.9	
	$\rho_{CIP deck}$	pcf	150	149.4	
	Structural Layout and Geometry	L (beam)	ft.	146.32	146.32
L (center-to-center bearings)		ft.	145.17	145.17	
Beam spacing		in.	99.0	99.0	
Effective deck width		in.	99.0	99.0	
Width of haunch		in.	0	16.00	
Gap between Panels		in.	0	9.00	
Thickness of Haunch		in.	0	2.25	
Thickness of Panels		in.	0	4.0	
Thickness of CIP Deck		in.	7.5	4.0	
Section Properties	$A_{beam (release)}$	in. ²	789	819	
	$I_{beam (release)}$	in. ⁴	260400	263160	
	$y_{bot, beam (release)}$	in.	24.73	24.32	
	A_{beam}	in. ²	789	846	
	I_{beam}	in. ⁴	260400	277740	
	$y_{bot, beam}$	in.	24.73	23.51	
	$A_{composite}$	in. ²	1323	1550	
	$I_{composite}$	in. ⁴	610160	887500	
	$y_{bot, composite}$	in.	38.06	40.13	
Dead Loads and Midspan Moments	$W_{beam self-wt.}$	kip/ft.	0.822	0.869	
	W_{panels}	kip/ft.	0	0.377	
	$W_{CIP deck}$	kip/ft.	0.773	0.486	
	$W_{composite DL (incl. rail)}$	kip/ft.	0.078	0.000	
	$M_{beam self-wt.}$	ft.-kips	2165	2289	
	M_{panels}	ft.-kips	0	994	
	$M_{CIP deck}$	ft.-kips	2037	1279	
	$M_{composite DL (incl. rail)}$	ft.-kips	205	0	

Beam(s) E34

	Parameter	Unit	Design	Measured
Material Properties	$f_{c, \text{ beam}}$	psi	8000	12390
	$f_{c, \text{ beam}}$	psi	13800	13750
	$f_{c, \text{ panels}}$	psi	6000	10100
	$f_{c, \text{ CIP deck}}$	psi	6000	9060
	$E_{c, \text{ beam}}$	ksi	4580	6150
	$E_{c, \text{ beam}}$	ksi	5700	6260
	$E_{c, \text{ panels}}$	ksi	4100	4970
	$E_{c, \text{ CIP deck}}$	ksi	4100	5590
	$\rho_{\text{ beam}}$	pcf	150	152.9
	$\rho_{\text{ panels}}$	pcf	150	150.9
	$\rho_{\text{ CIP deck}}$	pcf	150	149.4
	Structural Layout and Geometry	L (beam)	ft.	146.32
L (center-to-center bearings)		ft.	145.17	145.17
Beam spacing		in.	99.0	99.0
Effective deck width		in.	99.0	99.0
Width of haunch		in.	0	16.00
Gap between Panels		in.	0	9.00
Thickness of Haunch		in.	0	2.25
Thickness of Panels		in.	0	4.0
Thickness of CIP Deck		in.	7.5	4.0
Section Properties	$A_{\text{ beam (release)}}$	in. ²	789	819
	$I_{\text{ beam (release)}}$	in. ⁴	260400	263160
	$y_{\text{ bot, beam (release)}}$	in.	24.73	24.32
	$A_{\text{ beam}}$	in. ²	789	846
	$I_{\text{ beam}}$	in. ⁴	260400	277740
	$y_{\text{ bot, beam}}$	in.	24.73	23.51
	$A_{\text{ composite}}$	in. ²	1323	1550
	$I_{\text{ composite}}$	in. ⁴	610160	887500
	$y_{\text{ bot, composite}}$	in.	38.06	40.13
Dead Loads and Midspan Moments	$W_{\text{ beam self-wt.}}$	kip/ft.	0.822	0.869
	$W_{\text{ panels}}$	kip/ft.	0	0.377
	$W_{\text{ CIP deck}}$	kip/ft.	0.773	0.486
	$W_{\text{ composite DL (incl. rail)}}$	kip/ft.	0.078	0.000
	$M_{\text{ beam self-wt.}}$	ft.-kips	2165	2289
	$M_{\text{ panels}}$	ft.-kips	0	994
	$M_{\text{ CIP deck}}$	ft.-kips	2037	1279
	$M_{\text{ composite DL (incl. rail)}}$	ft.-kips	205	0

Beam(s)		E35		
	Parameter	Unit	Design	Measured
Material Properties	$f_{ci, beam}$	psi	8000	11340
	$f_{c, beam}$	psi	13800	14490
	$f_{c, panels}$	psi	6000	10100
	$f_{c, CIP deck}$	psi	6000	9060
	$E_{ci, beam}$	ksi	4580	6060
	$E_{c, beam}$	ksi	5700	6310
	$E_{c, panels}$	ksi	4100	4970
	$E_{c, CIP deck}$	ksi	4100	5590
	ρ_{beam}	pcf	150	152.9
	ρ_{panels}	pcf	150	150.9
	$\rho_{CIP deck}$	pcf	150	149.4
	Structural Layout and Geometry	L (beam)	ft.	146.32
L (center-to-center bearings)		ft.	145.17	145.17
Beam spacing		in.	91.6	91.6
Effective deck width		in.	91.6	91.6
Width of haunch		in.	0	18.00
Gap between Panels		in.	0	46.50
Thickness of Haunch		in.	0	0.5
Thickness of Panels		in.	0	4.0
Thickness of CIP Deck		in.	7.5	4.0
Section Properties	$A_{beam (release)}$	in. ²	789	820
	$I_{beam (release)}$	in. ⁴	260400	263300
	$Y_{bot, beam (release)}$	in.	24.73	24.31
	A_{beam}	in. ²	789	846
	I_{beam}	in. ⁴	260400	277570
	$Y_{bot, beam}$	in.	24.73	23.52
	$A_{composite}$	in. ²	1283	1485
	$I_{composite}$	in. ⁴	594010	748130
$Y_{bot, composite}$	in.	37.45	38.58	
Dead Loads and Midspan Moments	$W_{beam self-wt.}$	kip/ft.	0.822	0.869
	W_{panels}	kip/ft.	0	0.189
	$W_{CIP deck}$	kip/ft.	0.716	0.582
	$W_{composite DL (incl. rail)}$	kip/ft.	0.078	0.194
	$M_{beam self-wt.}$	ft.-kips	2165	2289
	M_{panels}	ft.-kips	0	498
	$M_{CIP deck}$	ft.-kips	1885	1534
	$M_{composite DL (incl. rail)}$	ft.-kips	205	511

Beam(s)		E44		
	Parameter	Unit	Design	Measured
Material Properties	$f'_{ci, beam}$	psi	8000	9390
	$f'_{c, beam}$	psi	13700	14550
	$f'_{c, panels}$	psi	6000	10100
	$f'_{c, CIP deck}$	psi	6000	7550
	$E_{ci, beam}$	ksi	4580	5880
	$E_{c, beam}$	ksi	5680	6320
	$E_{c, panels}$	ksi	4100	4970
	$E_{c, CIP deck}$	ksi	4100	5340
	ρ_{beam}	pcf	150	152.9
	ρ_{panels}	pcf	150	150.9
	$\rho_{CIP deck}$	pcf	150	149.4
Structural Layout and Geometry	L (beam)	ft.	145.67	145.67
	L (center-to-center bearings)	ft.	144.52	144.52
	Beam spacing	in.	99.0	99.0
	Effective deck width	in.	99.0	99.0
	Width of haunch	in.	0	16.00
	Gap between Panels	in.	0	9.00
	Thickness of Haunch	in.	0	2.25
	Thickness of Panels	in.	0	4.0
Thickness of CIP Deck	in.	7.5	4.0	
Section Properties	$A_{beam (release)}$	in. ²	789	822
	$I_{beam (release)}$	in. ⁴	260400	263590
	$y_{bot,beam (release)}$	in.	24.73	24.28
	A_{beam}	in. ²	789	846
	I_{beam}	in. ⁴	260400	277540
	$y_{bot,beam}$	in.	24.73	23.52
	$A_{composite}$	in. ²	1325	1524
	$I_{composite}$	in. ⁴	610900	870190
$y_{bot,composite}$	in.	38.09	39.80	
Dead Loads and Midspan Moments	$W_{beam self-wt.}$	kip/ft.	0.822	0.869
	W_{panels}	kip/ft.	0	0.377
	$W_{CIP deck}$	kip/ft.	0.773	0.486
	$W_{composite DL (incl. rail)}$	kip/ft.	0.078	0.000
	$M_{beam self-wt.}$	ft.-kips	2146	2268
	M_{panels}	ft.-kips	0	985
	$M_{CIP deck}$	ft.-kips	2019	1268
	$M_{composite DL (incl. rail)}$	ft.-kips	204	0

Beam(s)		E45		
	Parameter	Unit	Design	Measured
Material Properties	$f_{ci, beam}$	psi	8000	9390
	$f_{c, beam}$	psi	13700	14550
	$f_{c, panels}$	psi	6000	10100
	$f_{c, CIP deck}$	psi	6000	7550
	$E_{ci, beam}$	ksi	4580	5880
	$E_{c, beam}$	ksi	5680	6320
	$E_{c, panels}$	ksi	4100	4970
	$E_{c, CIP deck}$	ksi	4100	5340
	ρ_{beam}	pcf	150	152.9
	ρ_{panels}	pcf	150	150.9
	$\rho_{CIP deck}$	pcf	150	149.4
Structural Layout and Geometry	L (beam)	ft.	145.94	145.94
	L (center-to-center bearings)	ft.	144.79	144.79
	Beam spacing	in.	91.6	91.6
	Effective deck width	in.	91.6	91.6
	Width of haunch	in.	0	18.00
	Gap between Panels	in.	0	46.50
	Thickness of Haunch	in.	0	2.25
	Thickness of Panels	in.	0	4.0
	Thickness of CIP Deck	in.	7.5	4.0
Section Properties	$A_{beam (release)}$	in. ²	789	822
	$I_{beam (release)}$	in. ⁴	260400	263590
	$y_{bot, beam (release)}$	in.	24.73	24.28
	A_{beam}	in. ²	789	846
	I_{beam}	in. ⁴	260400	277540
	$y_{bot, beam}$	in.	24.73	23.52
	$A_{composite}$	in. ²	1285	1488
	$I_{composite}$	in. ⁴	594740	863200
	$y_{bot, composite}$	in.	37.47	39.28
Dead Loads and Midspan Moments	$W_{beam self-wt.}$	kip/ft.	0.822	0.869
	W_{panels}	kip/ft.	0	0.189
	$W_{CIP deck}$	kip/ft.	0.716	0.615
	$W_{composite DL (incl. rail)}$	kip/ft.	0.078	0.194
	$M_{beam self-wt.}$	ft.-kips	2154	2277
	M_{panels}	ft.-kips	0	495
	$M_{CIP deck}$	ft.-kips	1875	1612
	$M_{composite DL (incl. rail)}$	ft.-kips	204	508

Beam(s) W14

	Parameter	Unit	Design	Measured
Material Properties	$f_{ci, beam}$	psi	5770	8560
	$f_{c, beam}$	psi	7850	10130
	$f_{c, panels}$	psi	5000	8250
	$f_{c, CIP deck}$	psi	4000	6120
	$E_{ci, beam}$	ksi	4610	5720
	$E_{c, beam}$	ksi	5370	5970
	$E_{c, panels}$	ksi	4290	4790
	$E_{c, CIP deck}$	ksi	3530	5120
	ρ_{beam}	pcf	150	149.3
	ρ_{panels}	pcf	150	150.7
	$\rho_{CIP deck}$	pcf	150	145.3
	Structural Layout and Geometry	L (beam)	ft.	128.96
L (center-to-center bearings)		ft.	127.79	127.79
Beam spacing		in.	68.0	68.0
Effective deck width		in.	68.0	68.0
Width of haunch		in.	0	16.00
Gap between Panels		in.	0	9.00
Thickness of Haunch		in.	0	1.5
Thickness of Panels		in.	0	4.0
Thickness of CIP Deck		in.	7.5	5.0
Section Properties	$A_{beam (release)}$	in. ²	789	820
	$I_{beam (release)}$	in. ⁴	260400	271470
	$y_{bot, beam (release)}$	in.	24.73	24.00
	A_{beam}	in. ²	789	818
	I_{beam}	in. ⁴	260400	270910
	$y_{bot, beam}$	in.	24.73	24.04
	$A_{composite}$	in. ²	1124	1363
	$I_{composite}$	in. ⁴	518500	744720
	$y_{bot, composite}$	in.	34.58	37.81
Dead Loads and Midspan Moments	$W_{beam self-wt.}$	kip/ft.	0.822	0.839
	W_{panels}	kip/ft.	0	0.247
	$W_{CIP deck}$	kip/ft.	0.531	0.404
	$W_{composite DL (incl. rail)}$	kip/ft.	0.055	0.000
	$M_{beam self-wt.}$	ft.-kips	1678	1713
	M_{panels}	ft.-kips	0	504
	$M_{CIP deck}$	ft.-kips	1084	824
	$M_{composite DL (incl. rail)}$	ft.-kips	112	0

Beam(s) W15

	Parameter	Unit	Design	Measured
Material Properties	$f_{ci, beam}$	psi	5770	8560
	$f_{c, beam}$	psi	7850	10130
	$f_{c, panels}$	psi	5000	8250
	$f_{c, CIP deck}$	psi	4000	6120
	$E_{ci, beam}$	ksi	4610	5720
	$E_{c, beam}$	ksi	5370	5970
	$E_{c, panels}$	ksi	4290	4790
	$E_{c, CIP deck}$	ksi	3530	5120
	ρ_{beam}	pcf	150	149.3
	ρ_{panels}	pcf	150	150.7
	$\rho_{CIP deck}$	pcf	150	145.3
	Structural Layout and Geometry	L (beam)	ft.	128.96
L (center-to-center bearings)		ft.	127.79	127.79
Beam spacing		in.	68.0	68.0
Effective deck width		in.	68.0	68.0
Width of haunch		in.	0	16.00
Gap between Panels		in.	0	9.00
Thickness of Haunch		in.	0	1.5
Thickness of Panels		in.	0	4.0
Thickness of CIP Deck		in.	7.5	5.0
Section Properties	$A_{beam (release)}$	in. ²	789	820
	$I_{beam (release)}$	in. ⁴	260400	271470
	$y_{bot, beam (release)}$	in.	24.73	24.00
	A_{beam}	in. ²	789	818
	I_{beam}	in. ⁴	260400	270910
	$y_{bot, beam}$	in.	24.73	24.04
	$A_{composite}$	in. ²	1124	1363
	$I_{composite}$	in. ⁴	518500	744720
	$y_{bot, composite}$	in.	34.58	37.81
Dead Loads and Midspan Moments	$W_{beam self-wt.}$	kip/ft.	0.822	0.839
	W_{panels}	kip/ft.	0	0.247
	$W_{CIP deck}$	kip/ft.	0.531	0.404
	$W_{composite DL (incl. rail)}$	kip/ft.	0.055	0.000
	$M_{beam self-wt.}$	ft.-kips	1678	1713
	M_{panels}	ft.-kips	0	504
	$M_{CIP deck}$	ft.-kips	1084	824
	$M_{composite DL (incl. rail)}$	ft.-kips	112	0

Beam(s) W16

	Parameter	Unit	Design	Measured
Material Properties	$f_{ci, beam}$	psi	5770	8560
	$f_{c, beam}$	psi	7850	10130
	$f_{c, panels}$	psi	5000	8250
	$f_{c, CIP deck}$	psi	4000	6120
	$E_{ci, beam}$	ksi	4610	5720
	$E_{c, beam}$	ksi	5370	5970
	$E_{c, panels}$	ksi	4290	4790
	$E_{c, CIP deck}$	ksi	3530	5120
	ρ_{beam}	pcf	150	149.3
	ρ_{panels}	pcf	150	150.7
	$\rho_{CIP deck}$	pcf	150	145.3
	Structural Layout and Geometry	L (beam)	ft.	128.96
L (center-to-center bearings)		ft.	127.79	127.79
Beam spacing		in.	68.0	68.0
Effective deck width		in.	68.0	68.0
Width of haunch		in.	0	16.00
Gap between Panels		in.	0	9.00
Thickness of Haunch		in.	0	1.5
Thickness of Panels		in.	0	4.0
Thickness of CIP Deck		in.	7.5	5.0
Section Properties	$A_{beam (release)}$	in. ²	789	820
	$I_{beam (release)}$	in. ⁴	260400	271470
	$y_{bot, beam (release)}$	in.	24.73	24.00
	A_{beam}	in. ²	789	818
	I_{beam}	in. ⁴	260400	270910
	$y_{bot, beam}$	in.	24.73	24.04
	$A_{composite}$	in. ²	1124	1378
	$I_{composite}$	in. ⁴	518500	755020
	$y_{bot, composite}$	in.	34.58	38.10
Dead Loads and Midspan Moments	$W_{beam self-wt.}$	kip/ft.	0.822	0.839
	W_{panels}	kip/ft.	0	0.247
	$W_{CIP deck}$	kip/ft.	0.531	0.404
	$W_{composite DL (incl. rail)}$	kip/ft.	0.055	0.000
	$M_{beam self-wt.}$	ft.-kips	1678	1713
	M_{panels}	ft.-kips	0	504
	$M_{CIP deck}$	ft.-kips	1084	824
	$M_{composite DL (incl. rail)}$	ft.-kips	112	0

Beam(s)		W17		
	Parameter	Unit	Design	Measured
Material Properties	$f_{ci, beam}$	psi	5770	8060
	$f_{c, beam}$	psi	7850	10260
	$f_{c, panels}$	psi	5000	8250
	$f_{c, CIP deck}$	psi	4000	6120
	$E_{ci, beam}$	ksi	4610	5630
	$E_{c, beam}$	ksi	5370	5990
	$E_{c, panels}$	ksi	4290	4790
	$E_{c, CIP deck}$	ksi	3530	5120
	ρ_{beam}	pcf	150	149.3
	ρ_{panels}	pcf	150	150.7
	$\rho_{CIP deck}$	pcf	150	145.3
	Structural Layout and Geometry	L (beam)	ft.	128.96
L (center-to-center bearings)		ft.	127.79	127.79
Beam spacing		in.	70.1	70.1
Effective deck width		in.	70.1	70.1
Width of haunch		in.	0	18.00
Gap between Panels		in.	0	40.50
Thickness of Haunch		in.	0	1.5
Thickness of Panels		in.	0	4.0
Thickness of CIP Deck		in.	7.5	5.25
Section Properties	$A_{beam (release)}$	in. ²	789	821
	$I_{beam (release)}$	in. ⁴	260400	271690
	$y_{bot, beam (release)}$	in.	24.73	23.99
	A_{beam}	in. ²	789	818
	I_{beam}	in. ⁴	260400	270890
	$y_{bot, beam}$	in.	24.73	24.04
	$A_{composite}$	in. ²	1135	1401
	$I_{composite}$	in. ⁴	524060	771880
	$y_{bot, composite}$	in.	34.79	38.45
Dead Loads and Midspan Moments	$W_{beam self-wt.}$	kip/ft.	0.822	0.839
	W_{panels}	kip/ft.	0	0.124
	$W_{CIP deck}$	kip/ft.	0.548	0.562
	$W_{composite DL (incl. rail)}$	kip/ft.	0.055	0.194
	$M_{beam self-wt.}$	ft.-kips	1678	1713
	M_{panels}	ft.-kips	0	253
	$M_{CIP deck}$	ft.-kips	1118	1147
	$M_{composite DL (incl. rail)}$	ft.-kips	112	396

Beam(s)	N22
Section Type	U54B
Strand Size	0.6 in.
# of Strands (Pretensioned)	68
cgs of Pretensioned Strands	3.72 in.
# of Post-tensioned Strands	0

Cast (Beam Concrete Placed)	9/30/94 10:30 AM
Forms Stripped	10/1/94 8:30 AM
Released	10/1/94 1:00 PM
Post-tensioned	N/A
Erected	7/25/96
Panels Placed	9/26/96
Deck Cast	10/31/96
Rails Cast	6/24/97

Notes	
-------	--

Beam(s)	N23
Section Type	U54B
Strand Size	0.6 in.
# of Strands (Pretensioned)	68
cgs of Pretensioned Strands	3.72 in.
# of Post-tensioned Strands	0

Cast (Beam Concrete Placed)	9/23/94 2:30 PM
Forms Stripped	9/24/94 9:30 AM
Released	9/24/94 3:00 PM
Post-tensioned	N/A
Erected	7/25/96
Panels Placed	9/26/96
Deck Cast	10/31/96
Rails Cast	6/24/97

Notes	
-------	--

Beam(s)	N32
Section Type	U54A
Strand Size	0.6 in.
# of Strands (Pretensioned)	64
cgs of Pretensioned Strands	3.94 in.
# of Post-tensioned Strands	0

Cast (Beam Concrete Placed)	2/15/96 9:00 AM
Forms Stripped	2/16/96 8:00 AM
Released	2/16/96 4:30 PM
Post-tensioned	N/A
Erected	7/25/96
Panels Placed	10/17/96
Deck Cast	10/31/96
Rails Cast	6/24/97

Notes	
-------	--

Beam(s)	N33
Section Type	U54A
Strand Size	0.6 in.
# of Strands (Pretensioned)	64
cgs of Pretensioned Strands	3.94 in.
# of Post-tensioned Strands	0

Cast (Beam Concrete Placed)	2/15/96 9:00 AM
Forms Stripped	2/16/96 8:00 AM
Released	2/16/96 4:30 PM
Post-tensioned	N/A
Erected	7/25/96
Panels Placed	10/17/96
Deck Cast	10/31/96
Rails Cast	6/24/97

Notes	
-------	--

Beam(s)	N21
Section Type	U54B
Strand Size	0.6 in.
# of Strands (Pretensioned)	87
cgs of Pretensioned Strands	4.41 in.
# of Post-tensioned Strands	0

Cast (Beam Concrete Placed)	10/28/94 9:00 AM
Forms Stripped	10/29/94 8:00 AM
Released	10/29/94 2:30 PM
Post-tensioned	N/A
Erected	7/25/96
Panels Placed	9/26/96
Deck Cast	10/31/96
Rails Cast	6/24/97

Notes	
-------	--

Beam(s)	N31
Section Type	U54B
Strand Size	0.6 in.
# of Strands (Pretensioned)	83
cgs of Pretensioned Strands	4.19 in.
# of Post-tensioned Strands	0

Cast (Beam Concrete Placed)	10/28/94 8:30 AM
Forms Stripped	10/29/94 8:00 AM
Released	10/29/94 2:30 PM
Post-tensioned	N/A
Erected	7/25/96
Panels Placed	10/17/96
Deck Cast	10/31/96
Rails Cast	6/24/97

Notes	
-------	--

Beam(s)	S14
Section Type	U54A
Strand Size	0.6 in.
# of Strands (Pretensioned)	64
cgs of Pretensioned Strands	3.94 in.
# of Post-tensioned Strands	0

Cast (Beam Concrete Placed)	2/26/96 10:30 AM
Forms Stripped	2/27/96 9:00 AM
Released	2/27/96 4:00 PM
Post-tensioned	N/A
Erected	7/26/96
Panels Placed	9/24/96
Deck Cast	11/8/96
Rails Cast	6/24/97

Notes	
-------	--

Beam(s)	S15
Section Type	U54A
Strand Size	0.6 in.
# of Strands (Pretensioned)	64
cgs of Pretensioned Strands	3.94 in.
# of Post-tensioned Strands	0

Cast (Beam Concrete Placed)	2/26/96 10:30 AM
Forms Stripped	2/27/96 9:00 AM
Released	2/27/96 4:00 PM
Post-tensioned	N/A
Erected	7/26/96
Panels Placed	9/24/96
Deck Cast	11/8/96
Rails Cast	6/24/97

Notes	
-------	--

Beam(s)	S24
Section Type	U54B
Strand Size	0.6 in.
# of Strands (Pretensioned)	68
cgs of Pretensioned Strands	3.72 in.
# of Post-tensioned Strands	0

Cast (Beam Concrete Placed)	11/10/94 10:00 AM
Forms Stripped	11/11/94 8:00 AM
Released	11/11/94 2:00 PM
Post-tensioned	N/A
Erected	7/26/96
Panels Placed	9/24/96
Deck Cast	11/8/96
Rails Cast	6/24/97

Notes	
-------	--

Beam(s)	S25
Section Type	U54B
Strand Size	0.6 in.
# of Strands (Pretensioned)	68
cgs of Pretensioned Strands	3.72 in.
# of Post-tensioned Strands	0

Cast (Beam Concrete Placed)	11/10/94 10:00 AM
Forms Stripped	11/11/94 8:00 AM
Released	11/11/94 2:00 PM
Post-tensioned	N/A
Erected	7/26/96
Panels Placed	9/24/96
Deck Cast	11/8/96
Rails Cast	6/24/97

Notes	
-------	--

Beam(s)	S16
Section Type	U54B
Strand Size	0.6 in.
# of Strands (Pretensioned)	68
cgs of Pretensioned Strands	3.72 in.
# of Post-tensioned Strands	0

Cast (Beam Concrete Placed)	9/30/94 9:30 AM
Forms Stripped	10/1/94 8:30 AM
Released	10/1/94 1:00 PM
Post-tensioned	N/A
Erected	7/26/96
Panels Placed	9/24/96
Deck Cast	11/8/96
Rails Cast	6/24/97

Notes	
-------	--

Beam(s)	S26
Section Type	U54B
Strand Size	0.6 in.
# of Strands (Pretensioned)	87
cgs of Pretensioned Strands	4.41 in.
# of Post-tensioned Strands	0

Cast (Beam Concrete Placed)	10/7/94 10:00 AM
Forms Stripped	10/14/94 8:00 AM
Released	10/14/94 1:00 PM
Post-tensioned	N/A
Erected	7/26/96
Panels Placed	9/24/96
Deck Cast	11/8/96
Rails Cast	6/24/97

Notes	Released at 7 days. Cured under tarp prior to release.
-------	--

Beam(s) E13

Section Type	IV
Strand Size	0.6 in.
# of Strands (Pretensioned)	50 *
cgs of Pretensioned Strands	6.40 in. **
# of Post-tensioned Strands	20

Cast (Beam Concrete Placed)	2/19/97 11:30 AM
Forms Stripped	2/20/97 8:30 AM
Released	2/20/97 3:30 PM
Post-tensioned	3/17/97
Erected	4/25/97
Panels Placed	5/18/97
Deck Cast	6/12/97
Rails Cast	7/2/97

Notes	* does not include six top strands ** cgs of all pretensioned strands = 11.29 in.
-------	--

Beam(s) E14

Section Type	IV
Strand Size	0.6 in.
# of Strands (Pretensioned)	50 *
cgs of Pretensioned Strands	6.40 in. **
# of Post-tensioned Strands	20

Cast (Beam Concrete Placed)	2/19/97 11:30 AM
Forms Stripped	2/20/97 8:30 AM
Released	2/20/97 3:30 PM
Post-tensioned	3/17/97
Erected	4/25/97
Panels Placed	5/18/97
Deck Cast	6/12/97
Rails Cast	7/2/97

Notes	* does not include six top strands ** cgs of all pretensioned strands = 11.29 in.
-------	--

Beam(s)	E24
Section Type	IV
Strand Size	0.6 in.
# of Strands (Pretensioned)	50 *
cgs of Pretensioned Strands	6.40 in. **
# of Post-tensioned Strands	26

Cast (Beam Concrete Placed)	3/8/97 9:00 AM
Forms Stripped	3/10/97 8:00 AM
Released	3/10/97 2:00 PM
Post-tensioned	3/27/97
Erected	4/24/97
Panels Placed	5/20/97
Deck Cast	6/25/97
Rails Cast	7/16/97

Notes	* does not include six top strands ** cgs of all pretensioned strands = 11.29 in.
-------	--

Beam(s)	E26
Section Type	IV
Strand Size	0.6 in.
# of Strands (Pretensioned)	50 *
cgs of Pretensioned Strands	6.40 in. **
# of Post-tensioned Strands	26

Cast (Beam Concrete Placed)	3/8/97 9:00 AM
Forms Stripped	3/10/97 8:00 AM
Released	3/10/97 2:00 PM
Post-tensioned	3/27/97
Erected	4/24/97
Panels Placed	5/20/97
Deck Cast	6/25/97
Rails Cast	7/16/97

Notes	* does not include six top strands ** cgs of all pretensioned strands = 11.29 in.
-------	--

Beam(s)	E25
Section Type	IV
Strand Size	0.6 in.
# of Strands (Pretensioned)	46 *
cgs of Pretensioned Strands	5.83 in. **
# of Post-tensioned Strands	20

Cast (Beam Concrete Placed)	4/1/96 9:00 AM
Forms Stripped	4/2/96 8:30 AM
Released	4/2/96 2:30 PM
Post-tensioned	4/26/96
Erected	4/24/97
Panels Placed	5/20/97
Deck Cast	6/25/97
Rails Cast	7/16/97

Notes	* does not include six top strands ** cgs of all pretensioned strands = 11.15 in.
-------	--

Beam(s)	E35
Section Type	IV
Strand Size	0.6 in.
# of Strands (Pretensioned)	50 *
cgs of Pretensioned Strands	6.40 in. **
# of Post-tensioned Strands	26

Cast (Beam Concrete Placed)	3/29/97 12:00 PM
Forms Stripped	3/31/97 8:30 AM
Released	3/31/97 2:00 PM
Post-tensioned	5/1/97
Erected	6/5/97
Panels Placed	6/16/97
Deck Cast	7/9/97
Rails Cast	8/7/97

Notes	* does not include six top strands ** cgs of all pretensioned strands = 11.29 in.
-------	--

Beam(s)	E33
Section Type	IV
Strand Size	0.6 in.
# of Strands (Pretensioned)	50 *
cgs of Pretensioned Strands	6.40 in. **
# of Post-tensioned Strands	26

Cast (Beam Concrete Placed)	3/22/97 11:00 AM
Forms Stripped	3/24/97 9:00 AM
Released	3/24/97 3:00 PM
Post-tensioned	4/21/97
Erected	6/5/97
Panels Placed	6/16/97
Deck Cast	7/9/97
Rails Cast	8/7/97

Notes	* does not include six top strands ** cgs of all pretensioned strands = 11.29 in.
-------	--

Beam(s)	E34
Section Type	IV
Strand Size	0.6 in.
# of Strands (Pretensioned)	50 *
cgs of Pretensioned Strands	6.40 in. **
# of Post-tensioned Strands	26

Cast (Beam Concrete Placed)	3/22/97 11:00 AM
Forms Stripped	3/24/97 9:00 AM
Released	3/24/97 3:00 PM
Post-tensioned	4/21/97
Erected	6/5/97
Panels Placed	6/16/97
Deck Cast	7/9/97
Rails Cast	8/7/97

Notes	* does not include six top strands ** cgs of all pretensioned strands = 11.29 in.
-------	--

Beam(s)	E44
Section Type	IV
Strand Size	0.6 in.
# of Strands (Pretensioned)	50 *
cgs of Pretensioned Strands	6.40 in. **
# of Post-tensioned Strands	26

Cast (Beam Concrete Placed)	4/12/97 9:00 AM
Forms Stripped	4/14/97 7:30 AM
Released	4/14/97 12:00 PM
Post-tensioned	5/8/97
Erected	6/5/97
Panels Placed	6/16/97
Deck Cast	7/2/97
Rails Cast	8/14/97

Notes	* does not include six top strands ** cgs of all pretensioned strands = 11.29 in.
-------	--

Beam(s)	E45
Section Type	IV
Strand Size	0.6 in.
# of Strands (Pretensioned)	50 *
cgs of Pretensioned Strands	6.40 in. **
# of Post-tensioned Strands	26

Cast (Beam Concrete Placed)	4/12/97 9:00 AM
Forms Stripped	4/14/97 7:30 AM
Released	4/14/97 12:00 PM
Post-tensioned	5/8/97
Erected	6/5/97
Panels Placed	6/16/97
Deck Cast	7/2/97
Rails Cast	8/14/97

Notes	* does not include six top strands ** cgs of all pretensioned strands = 11.29 in.
-------	--

Beam(s) W14

Section Type	IV
Strand Size	0.5 in.
# of Strands (Pretensioned)	52
cgs of Pretensioned Strands	5.46 in.
# of Post-tensioned Strands	0

Cast (Beam Concrete Placed)	3/7/96 10:00 AM
Forms Stripped	3/8/96 8:30 AM
Released	3/8/96 4:30 PM
Post-tensioned	N/A
Erected	10/5/96
Panels Placed	10/8/96
Deck Cast	12/3/96
Rails Cast	1/15/97

Notes	
-------	--

Beam(s) W15

Section Type	IV
Strand Size	0.5 in.
# of Strands (Pretensioned)	52
cgs of Pretensioned Strands	5.46 in.
# of Post-tensioned Strands	0

Cast (Beam Concrete Placed)	3/7/96 10:00 AM
Forms Stripped	3/8/96 8:30 AM
Released	3/8/96 4:30 PM
Post-tensioned	N/A
Erected	10/5/96
Panels Placed	10/8/96
Deck Cast	12/3/96
Rails Cast	1/15/97

Notes	
-------	--

Beam(s)	W16
---------	-----

Section Type	IV
Strand Size	0.5 in.
# of Strands (Pretensioned)	52
cgs of Pretensioned Strands	5.46 in.
# of Post-tensioned Strands	0

Cast (Beam Concrete Placed)	3/7/96 10:00 AM
Forms Stripped	3/8/96 8:30 AM
Released	3/8/96 4:30 PM
Post-tensioned	N/A
Erected	10/5/96
Panels Placed	10/8/96
Deck Cast	12/3/96
Rails Cast	1/15/97

Notes	
-------	--

Beam(s)	W17
---------	-----

Section Type	IV
Strand Size	0.5 in.
# of Strands (Pretensioned)	52
cgs of Pretensioned Strands	5.46 in.
# of Post-tensioned Strands	0

Cast (Beam Concrete Placed)	3/12/96 1:30 PM
Forms Stripped	3/13/96 7:30 AM
Released	3/13/96 1:30 PM
Post-tensioned	N/A
Erected	10/5/96
Panels Placed	10/8/96
Deck Cast	12/3/96
Rails Cast	1/15/97

Notes	
-------	--

**APPENDIX G: PLOTS OF LONG-TERM CAMBER AND PRESTRESS
LOSS**

Incremental Time-Step Model

An incremental time-step model was developed for the prediction of long-term camber and prestress loss in the beams monitored during this research study. The model was developed and programmed for use on a computer spreadsheet, and is loosely based on the general procedure outlined by Libby [86]. The spreadsheet is similar to a time-step spreadsheet developed by Byle and Burns [45] for analysis of the Louetta HPC beams in an earlier part of this research program, but is more general and can be used to model the more complex San Angelo beams. In particular, the model can accommodate the use of post-tensioning tendons in addition to pretensioned strands, and can model the effects of cutting the top strands after beam erection. Although the spreadsheet itself is complicated, its use facilitates the manipulation of parameters without the necessity of adjusting lengthy input files for each beam.

The model is based on elastic bending theory (i.e. plane sections remain plane) and can be used to analyze behavior at a single cross-section. Superposition of elastic and time-dependent stresses and strains is assumed to hold, and the effects from each type of force or applied load are computed separately. This includes forces due to pretensioning, post-tensioning, self-weight of the member, placement of the precast deck panels, placement of the cast-in-place deck, and placement of the traffic rails (or other superimposed load) on the composite section.

During each incremental time-step, cross-section deformations (i.e. axial strain and curvature) that result from time-dependent creep and shrinkage deformations are computed. The creep superposition method, which is described in the literature [127], is used for the modeling of time-dependent creep deformations when loads are removed. This is only of great importance for the cutting of the top strands, since they are the only temporary force acting on the member that is considered in the analyses. Elastic forces and loads are applied in time steps of zero duration. The effects of composite action after placement of the bridge deck are modeled by computing deformations in the beam and slab separately, as if there was no composite action, and then forcing strain compatibility by applying a force to each at the beam-slab interface.

Stresses in each group of prestressed reinforcement – bottom flange (main) pretensioned strands, top flange pretensioned strands, and each post-tensioning tendon –

are computed and maintained separately. The prestress force from each group is assumed to be applied to the concrete section at the centroid of the strand group or tendon. Losses in each group due to creep and shrinkage deformations of the cross-section, and due to the relaxation of steel, are computed during each time-interval. The remaining stress at the end of the interval is assumed to be the stress at the beginning of each subsequent interval. Pseudo-elastic effects on the cross-section due to the loss (or gain) of prestress in each strand group or tendon during an interval are treated by applying equivalent forces to the cross-section at the end of that interval.

One of the main simplifications used in the analysis pertains to the computation of camber and deflection. In theory, deformations should be computed at several sections along the length of the member, and the curvature diagram along the length of the member should be numerically integrated to find the camber or deflection. Instead, deformations are only computed at the midspan section of the simply-supported beams, and each component of camber or deflection is related to a multiple of the midspan curvature. This *effective curvature* was computed for each component of camber or deflection based on the shape of the curvature diagram under the corresponding elastic force. The effective curvature for each type of prestress force is a function of the strand or tendon pattern along the length of the member, and the effects of debonding, draping, and post-tensioning tendon layouts can be approximated using this approach. For the beams in this study, these effects were calculated exactly for the elastic response, and assumed to be constant throughout the time-dependent behavior.

Essentially, this simplification is assuming only that the *shape* of the curvature diagram due to each source of force or load remains the same over time. This would be true if prestress losses did not vary along the length of the member. Still, this approach should not result in a major loss of accuracy because midspan curvatures are computed exactly, and the curvatures at sections near midspan contribute much more to the deflection of a simply-supported member than the curvatures near the beam ends.

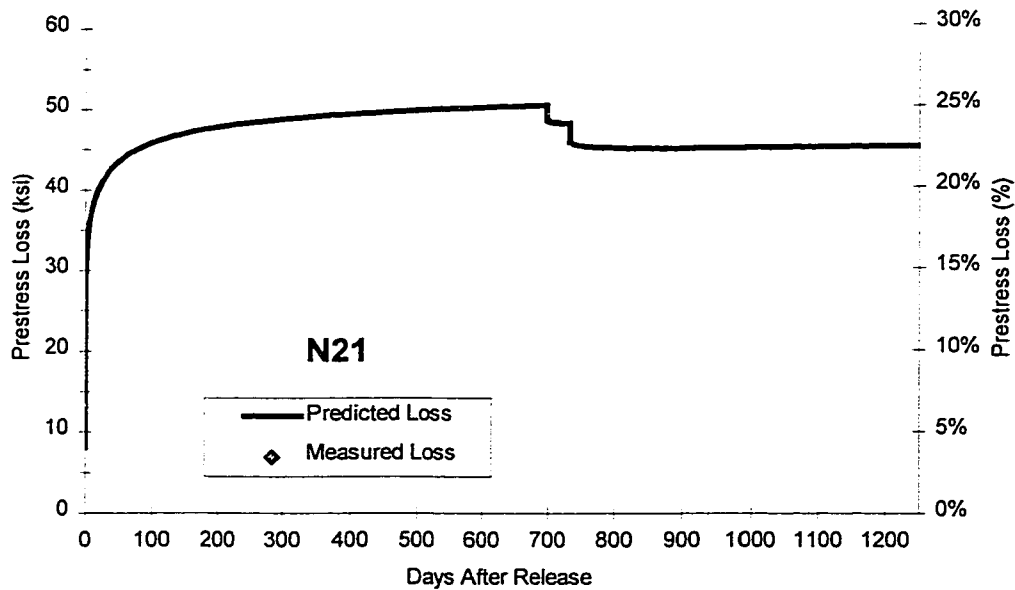
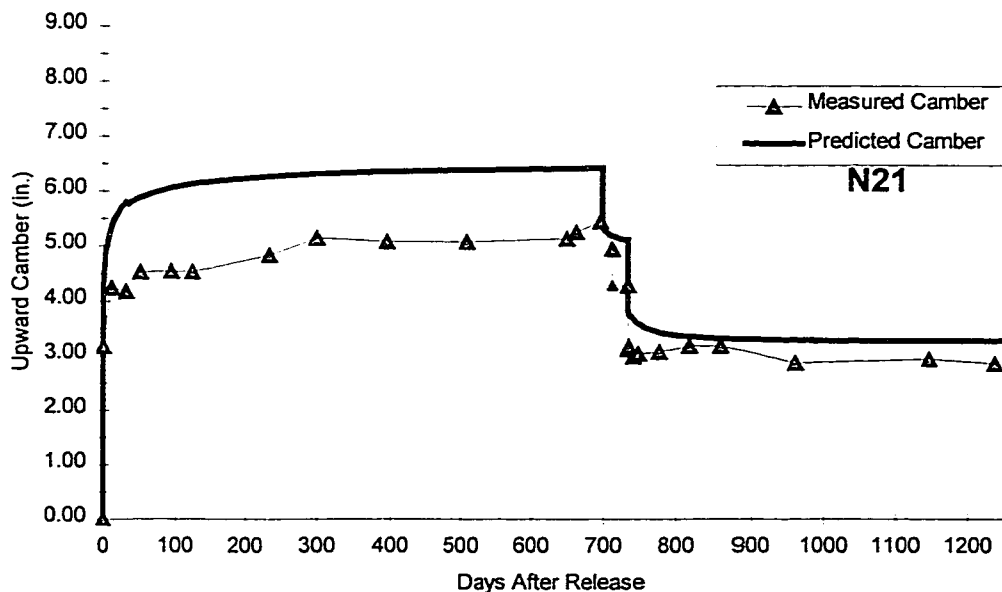
Measured material properties, determined from tests on companion specimens, were used in the analyses for each beam. The creep-time, shrinkage-time, strength-time, and modulus-strength relationships developed for each beam or concrete mix in Chapter 4 were used to continuously model the beam concrete properties at all times. Shrinkage of the cast-in-place deck slab was modeled in the same manner. Appropriate creep and

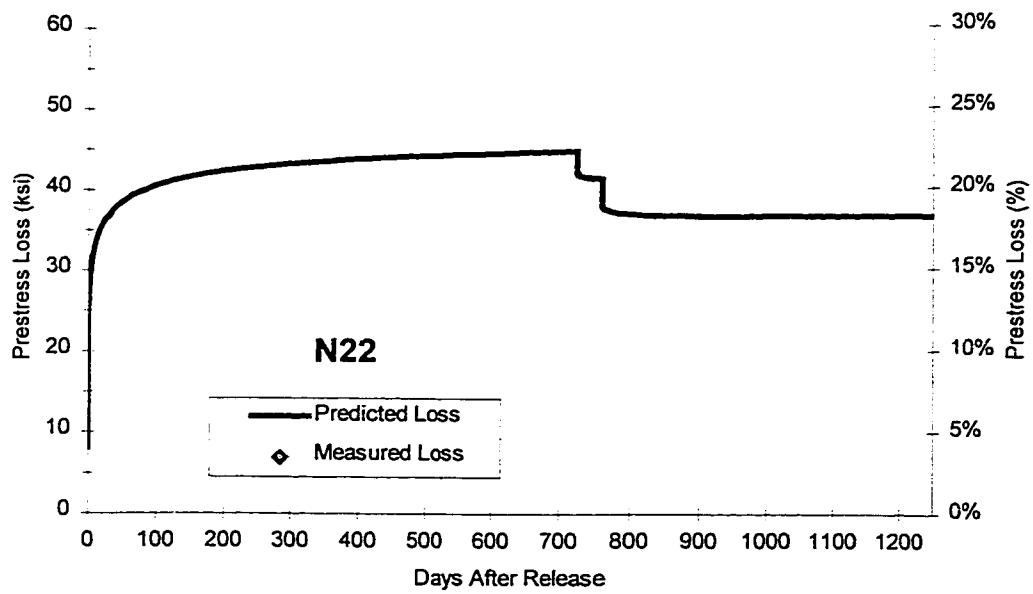
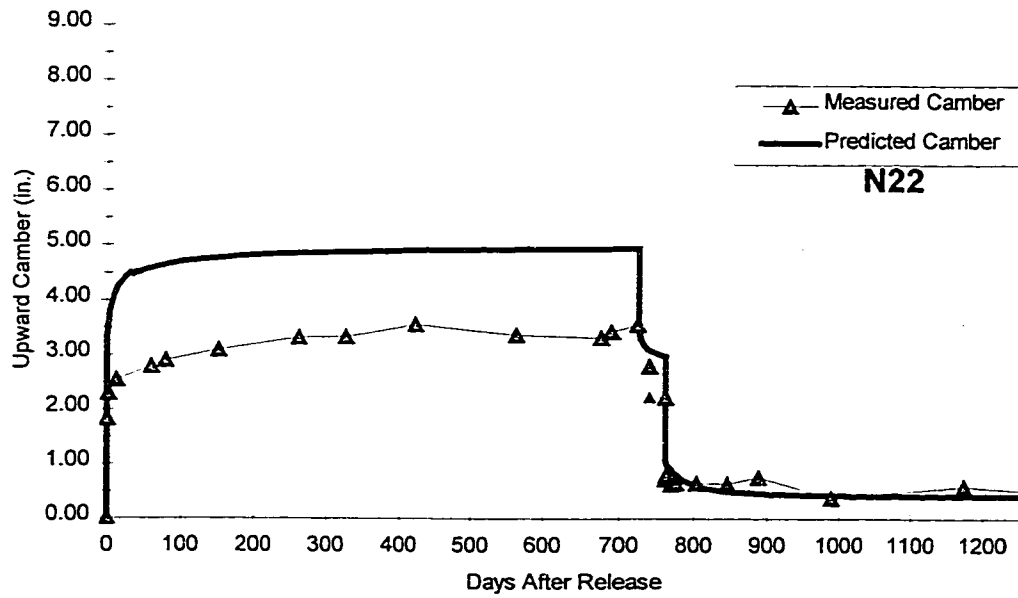
shrinkage correction factors were applied for volume-to-surface ratio, average relative humidity, and loading age using the ACI 209 [68] multipliers. The volume-to-surface ratios of U54A beams, U54B beams, Type IV beams, and cast-in-place deck slabs were taken as 2.89, 3.19, 4.74, and the average thickness of the slab, respectively. Average relative humidities were assumed to be 75 percent for Houston (Louetta) and 60 percent for San Angelo. (Average relative humidity at the prestressing plant in Victoria was also assumed to be 75 percent.)

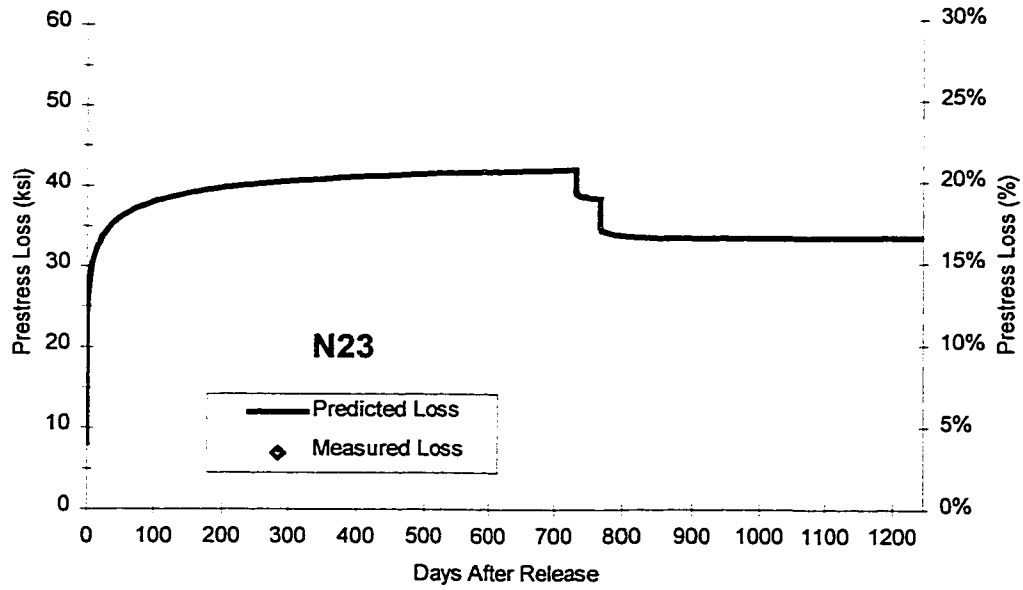
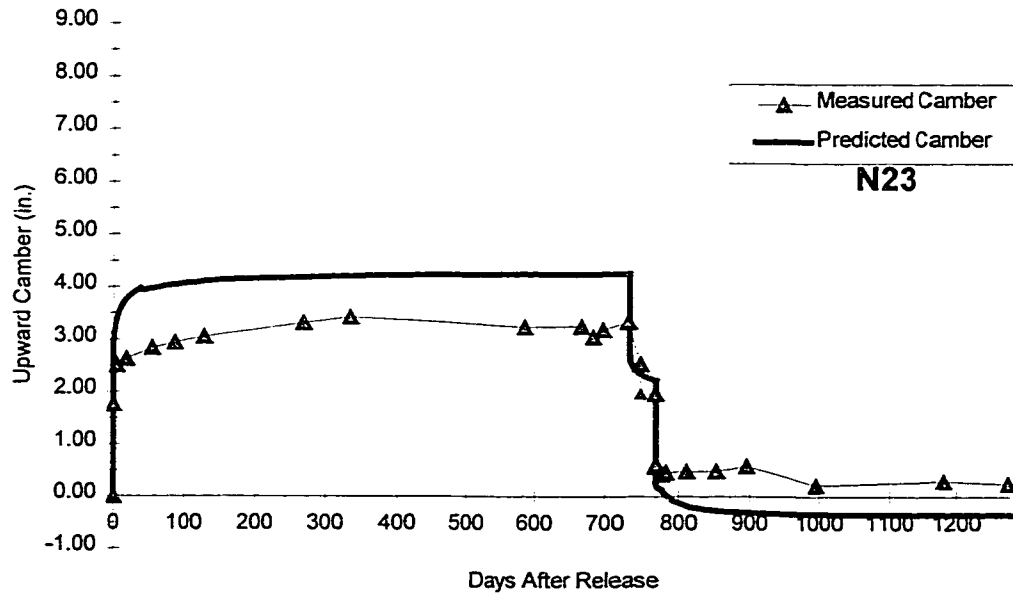
Transformed section properties and the actual construction schedules were used for each analysis. Loads were based on measured concrete unit weights, and the weight of the beams was increased slightly to account for the large volume of steel present (i.e. prestressing strands). A loss of 3.5 to 4.5 percent was assumed to occur before release for all beams, based on the observations in Section 7.2. Parameters used in the analysis for each beam are listed in Appendix F.

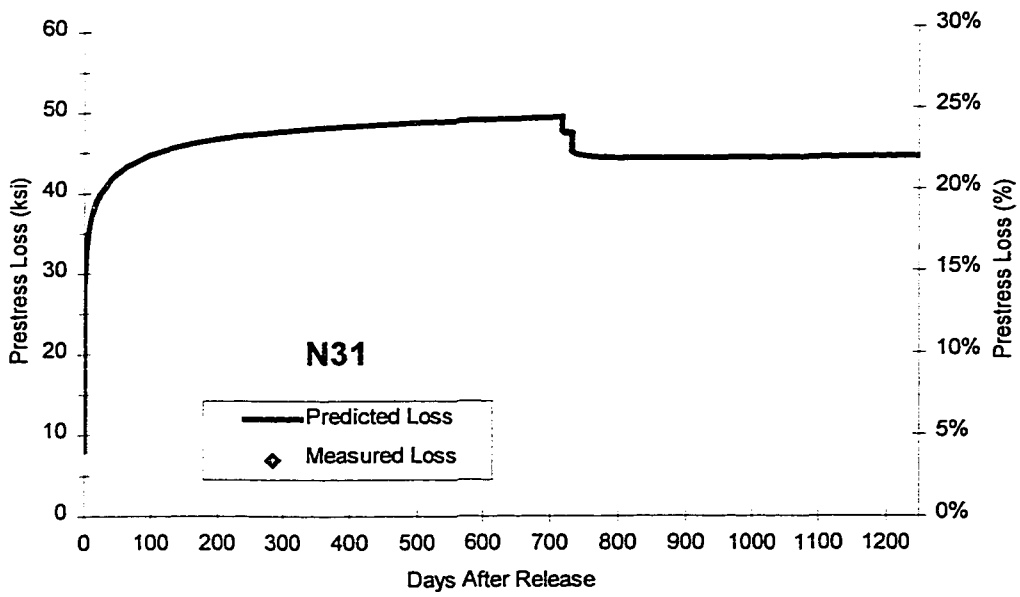
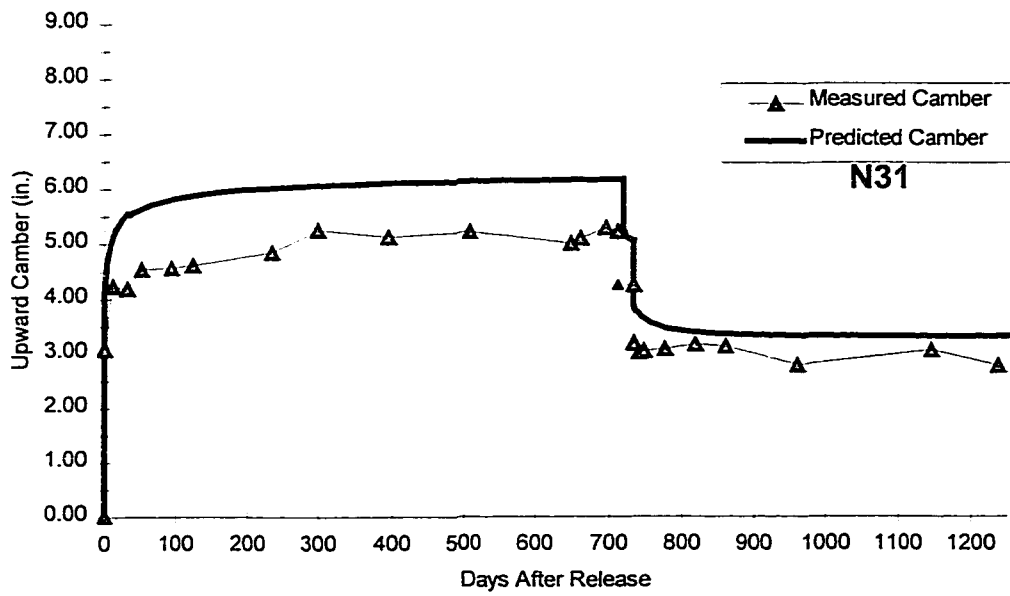
Plots of Measured and Predicted Camber and Prestress Loss

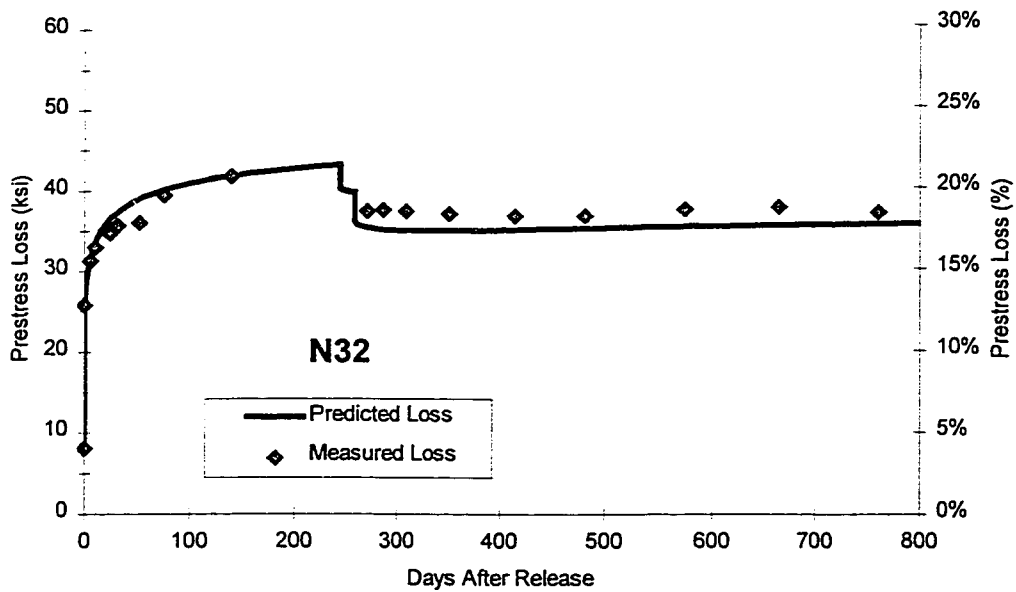
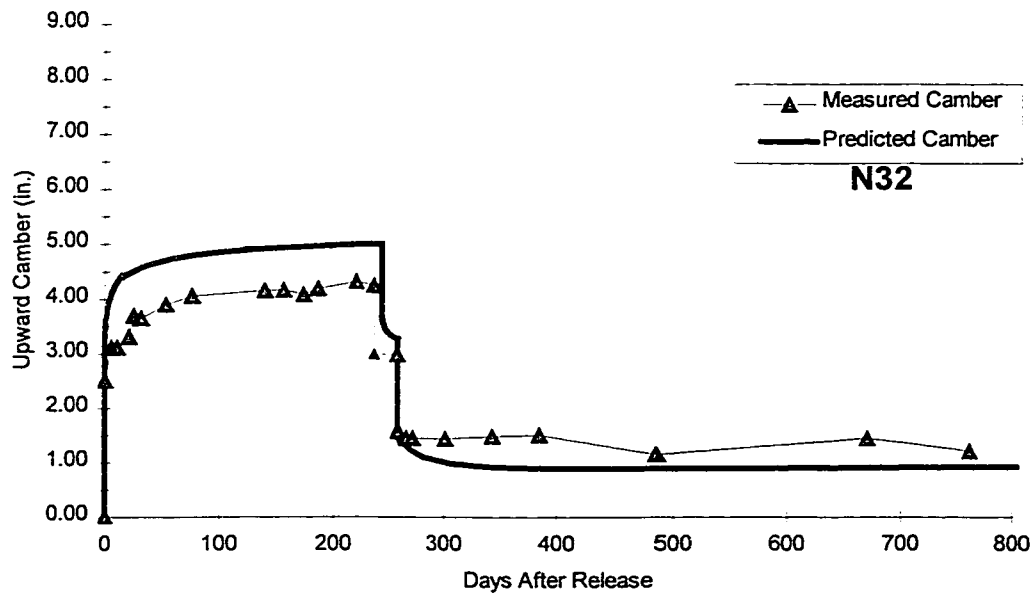
Plots of measured and predicted time-dependent camber and prestress loss are shown in the following pages for each beam. As appropriate, measured camber values have been corrected for support conditions and end measurement locations using the method discussed in Section 8.1.2. Thermal gradient corrections have been applied to all measurements where temperature data was available. Plots of measured prestress loss have been adjusted to account for the approximate loss before release, and computed losses due to steel relaxation have also been added in to the measured data. All measurements shown were obtained from durable vibrating wire gauges, and have been corrected for uniform temperature movements. These adjustments are discussed in Section 7.1.2.

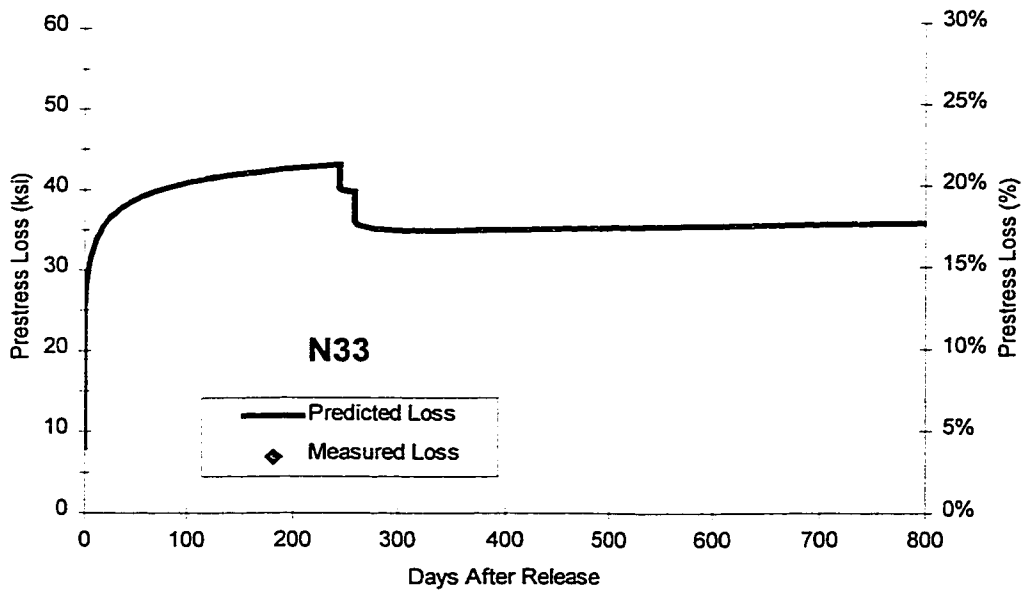
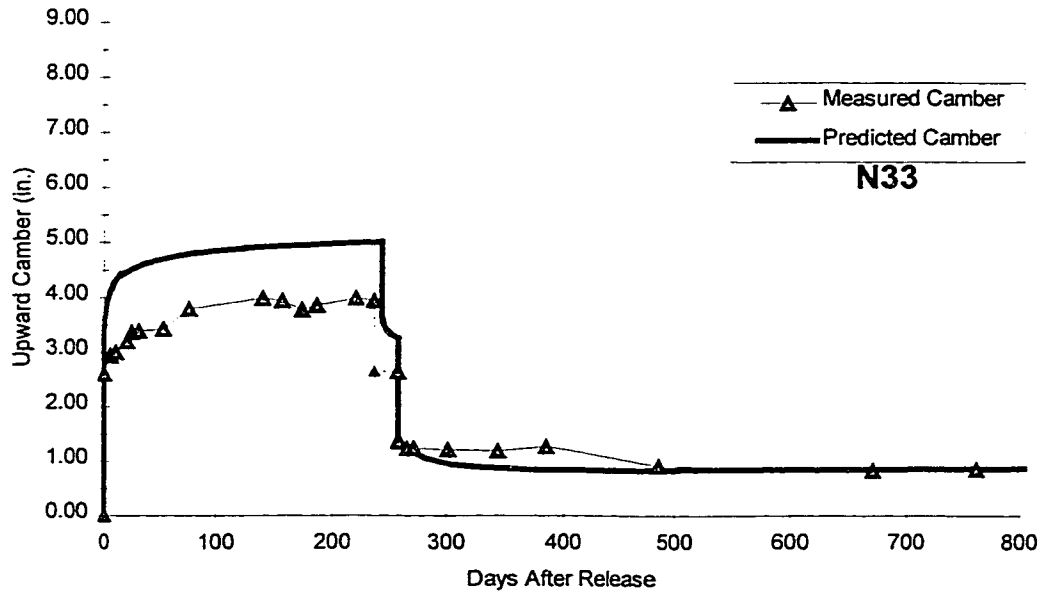


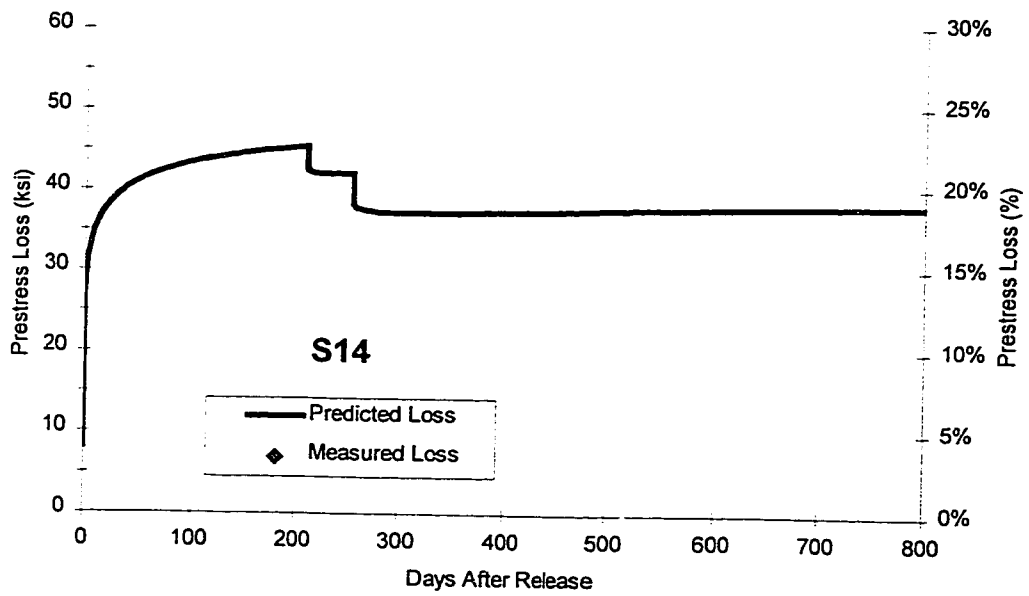
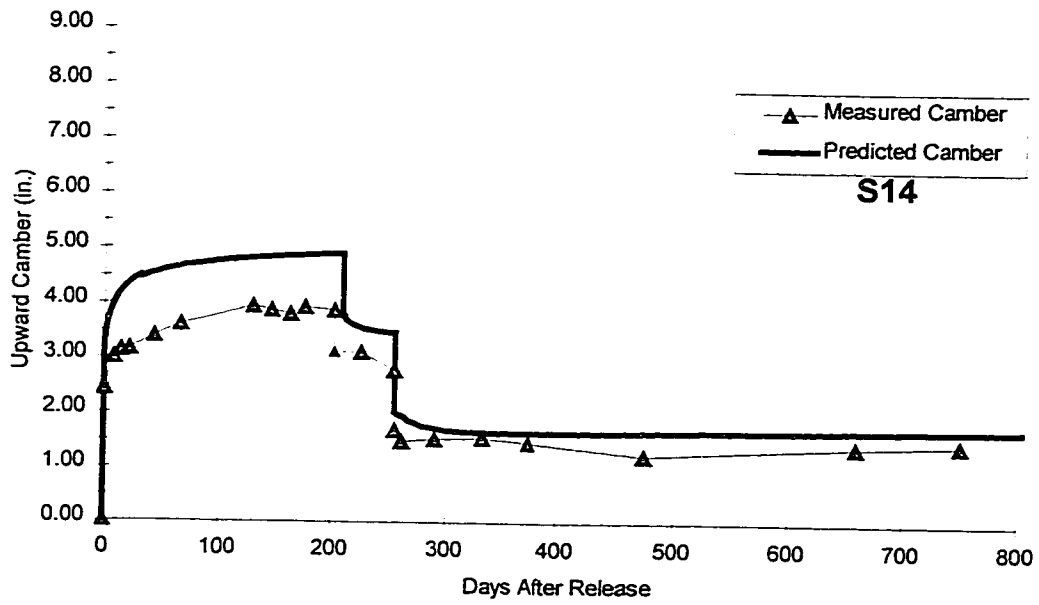


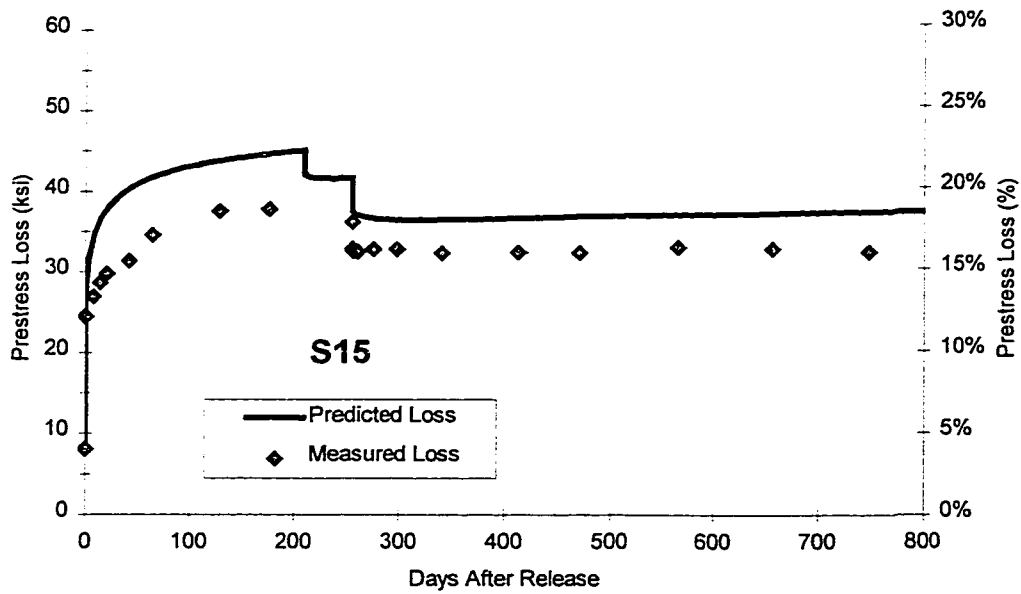
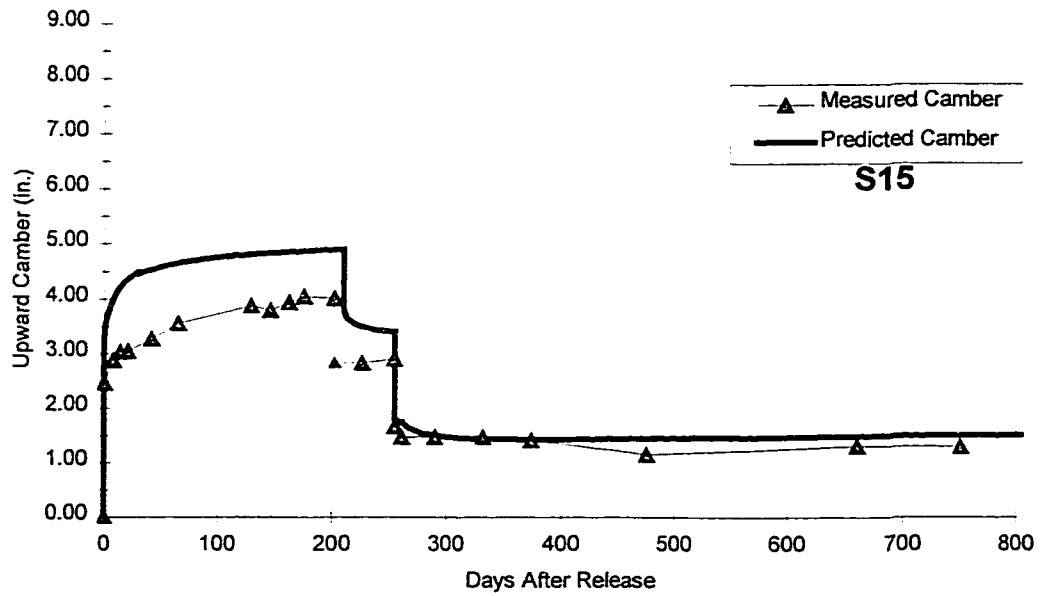


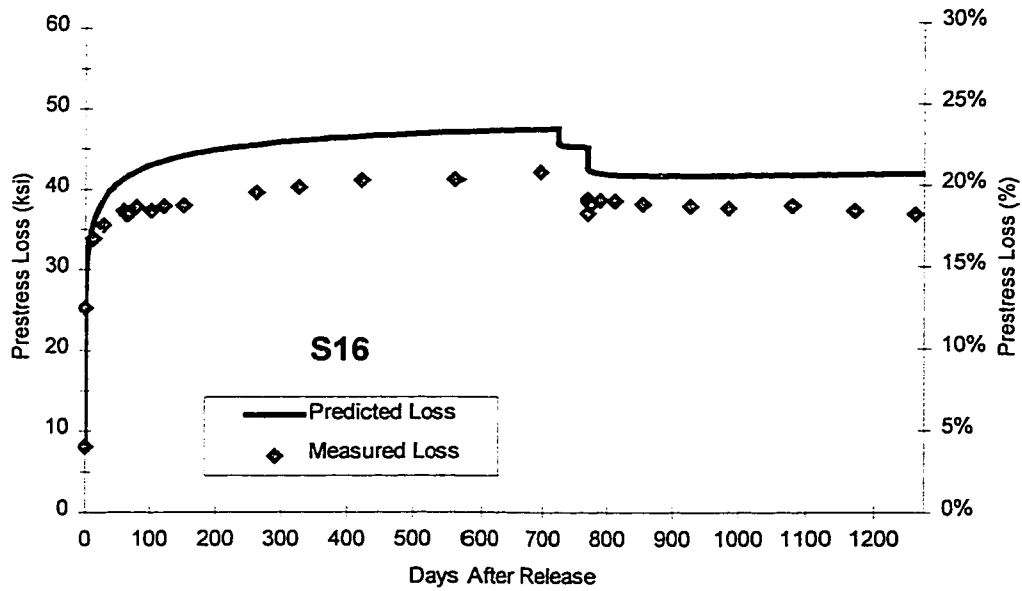
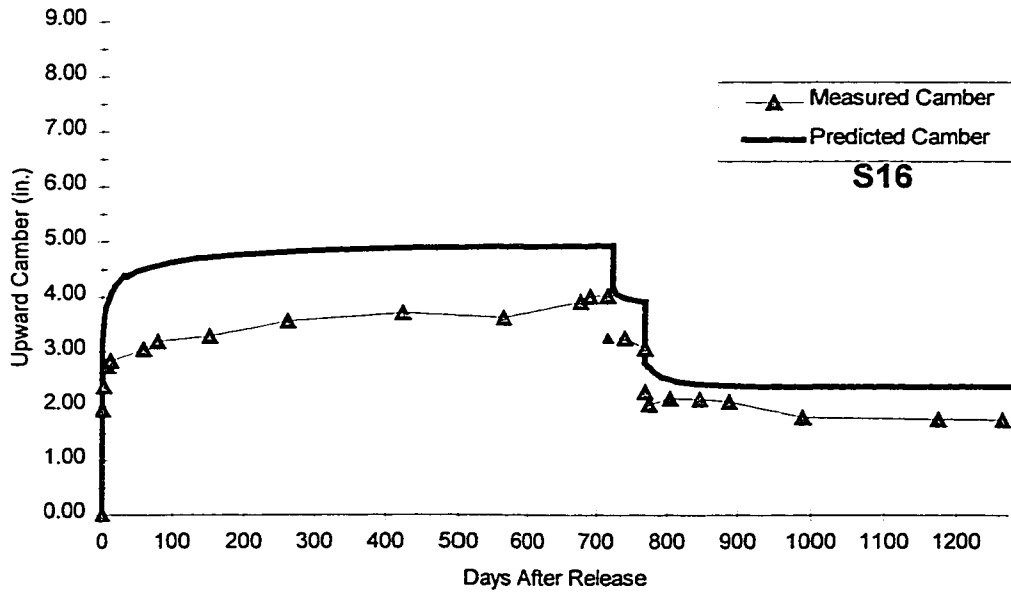


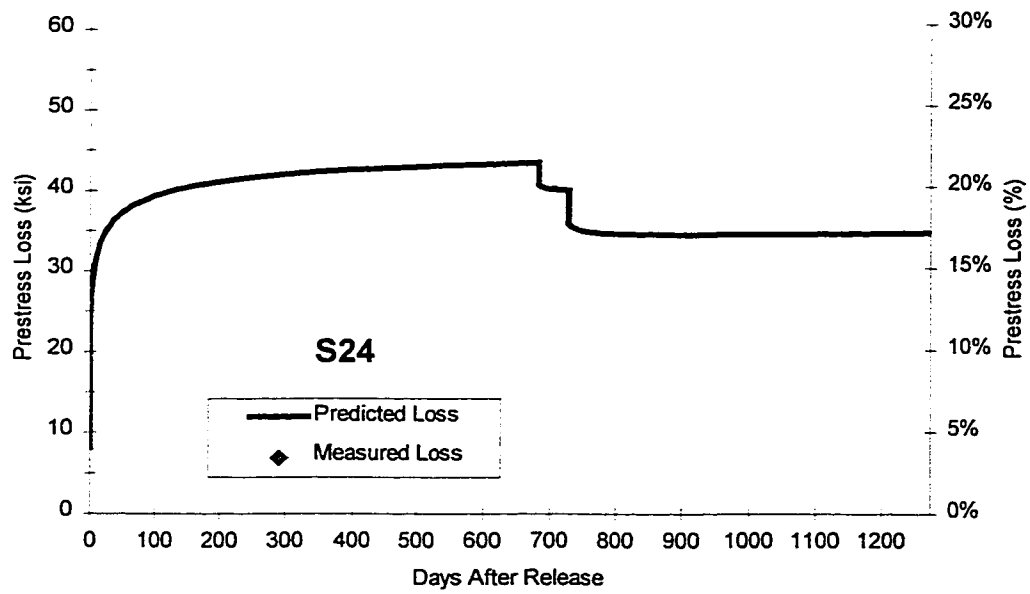
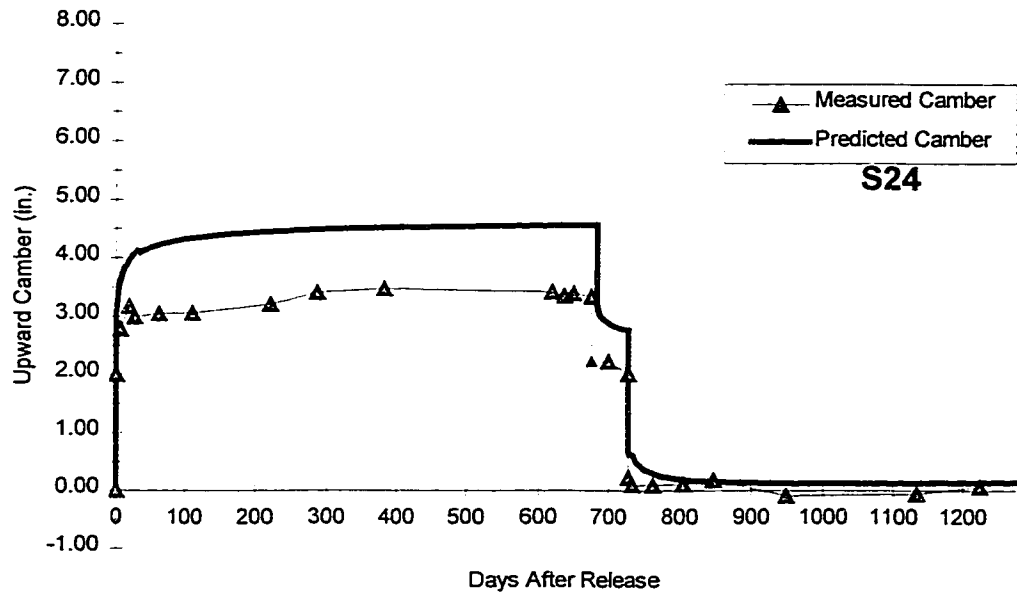


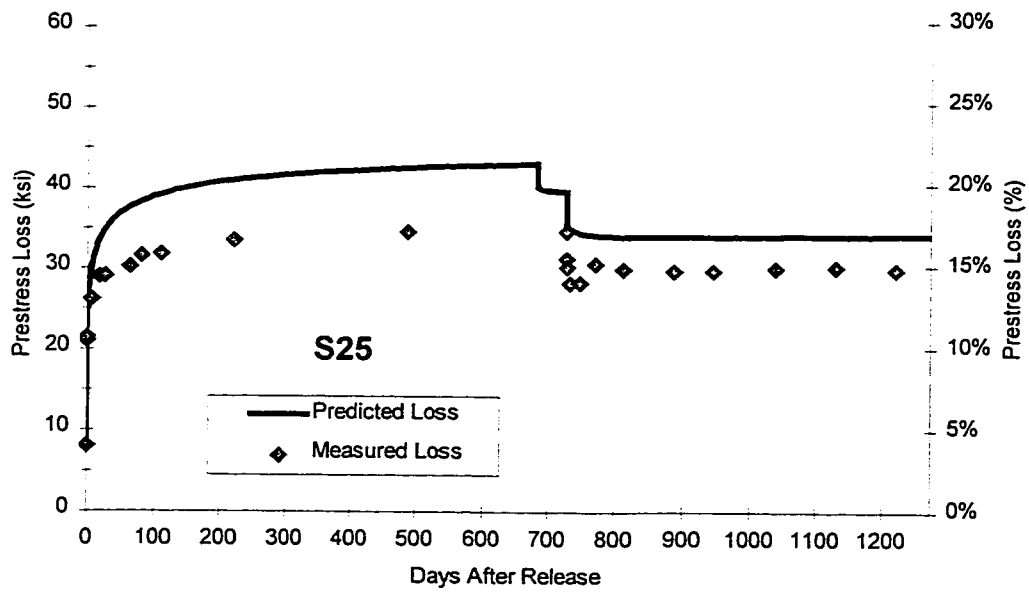
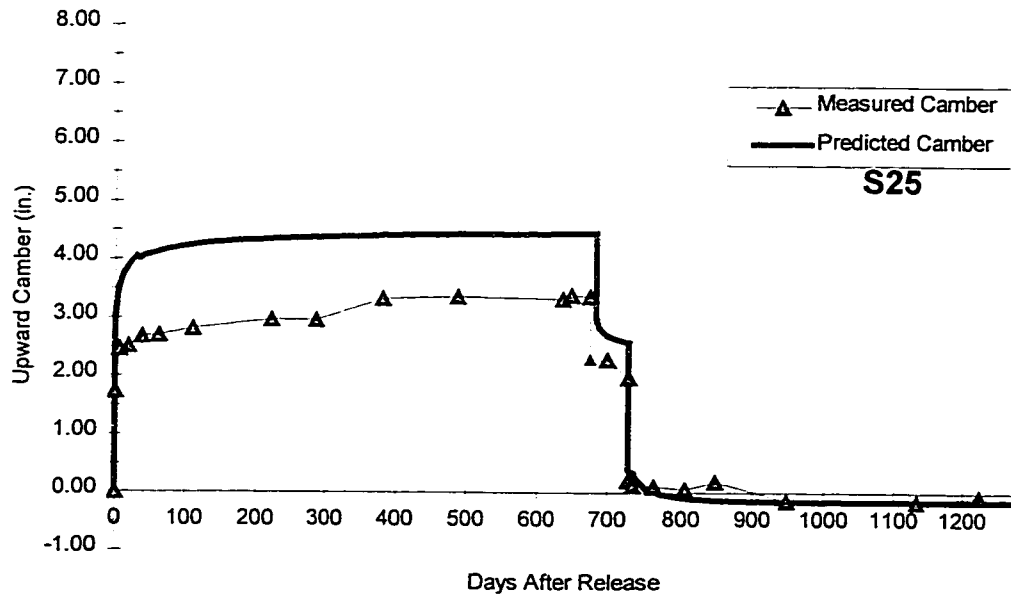


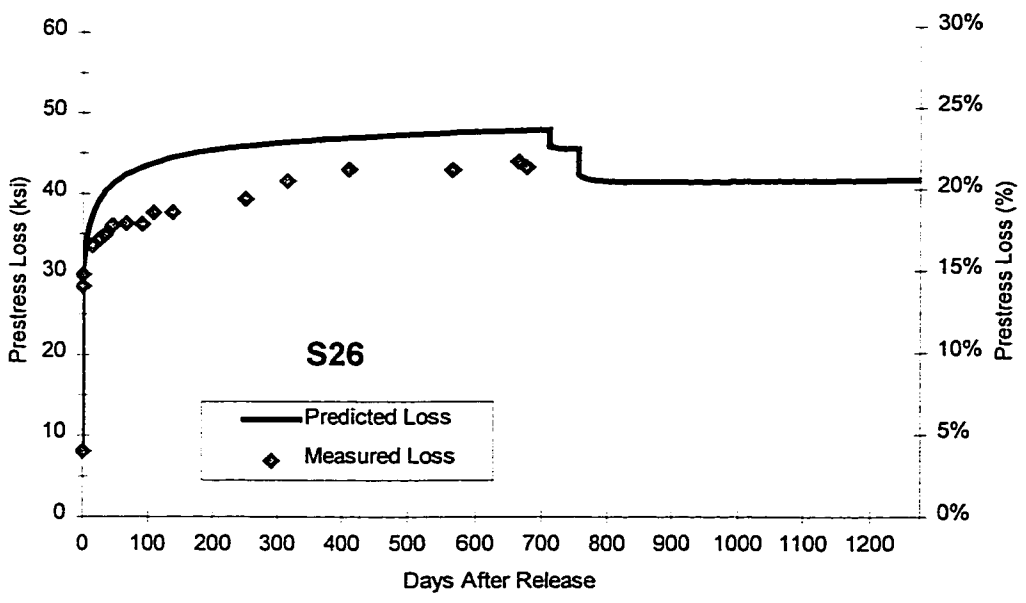
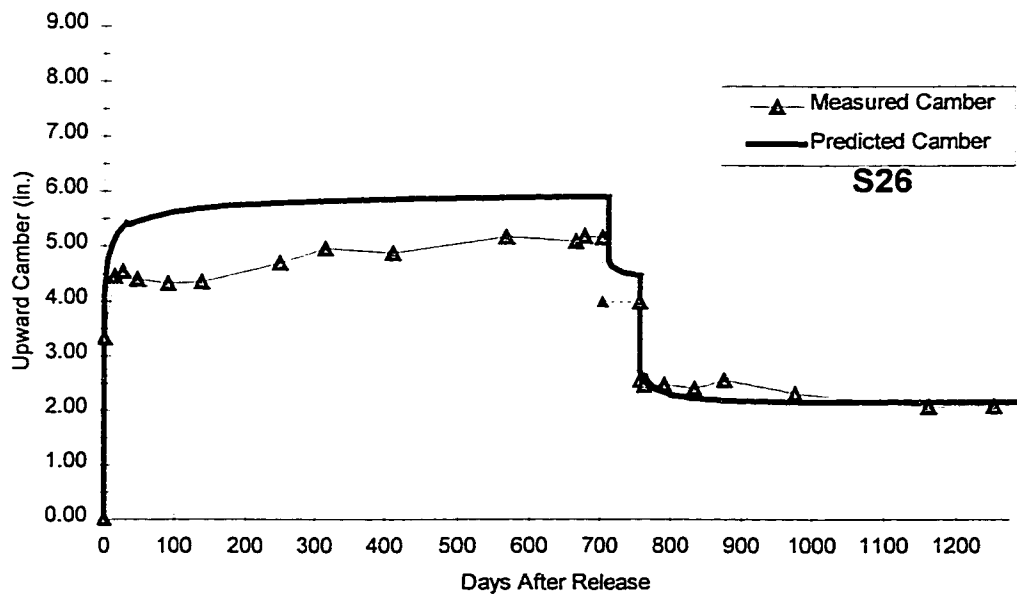


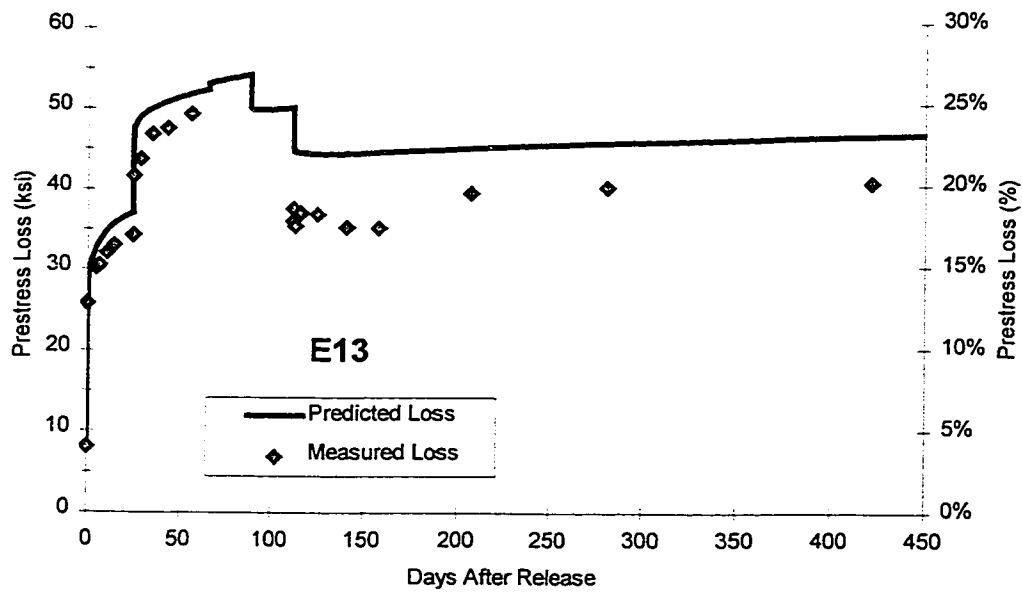
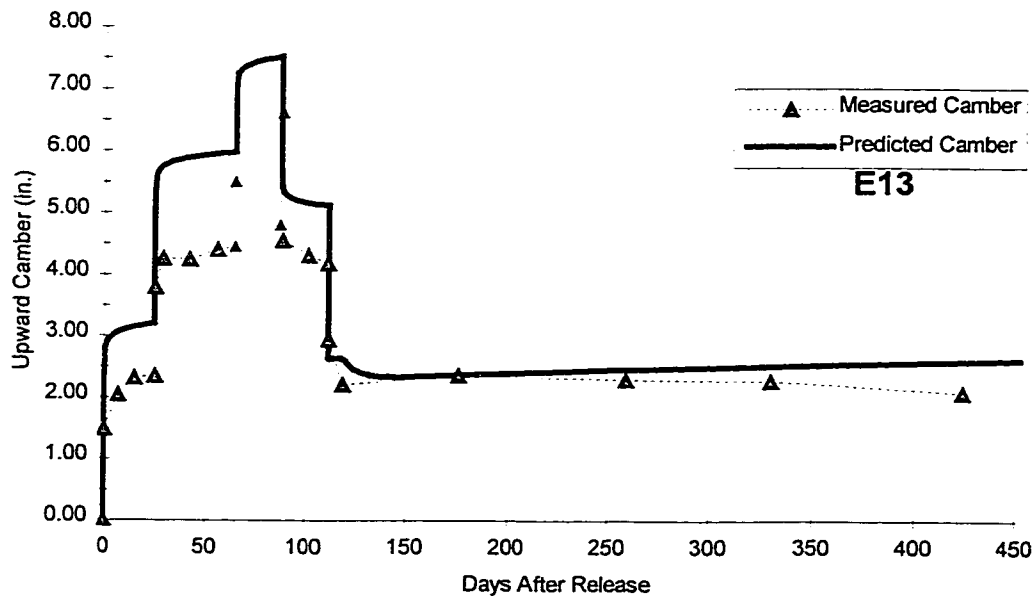


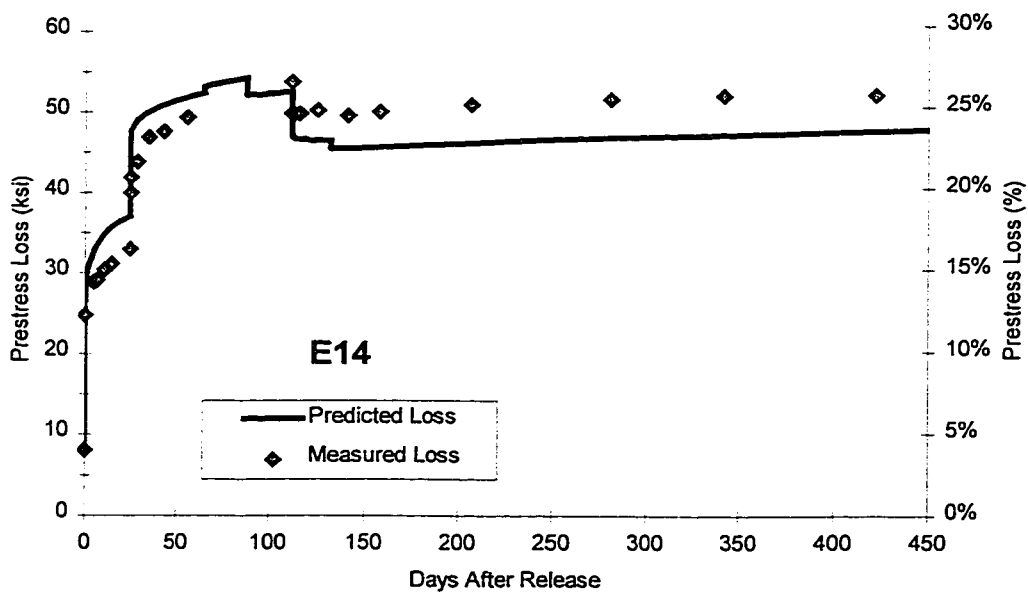
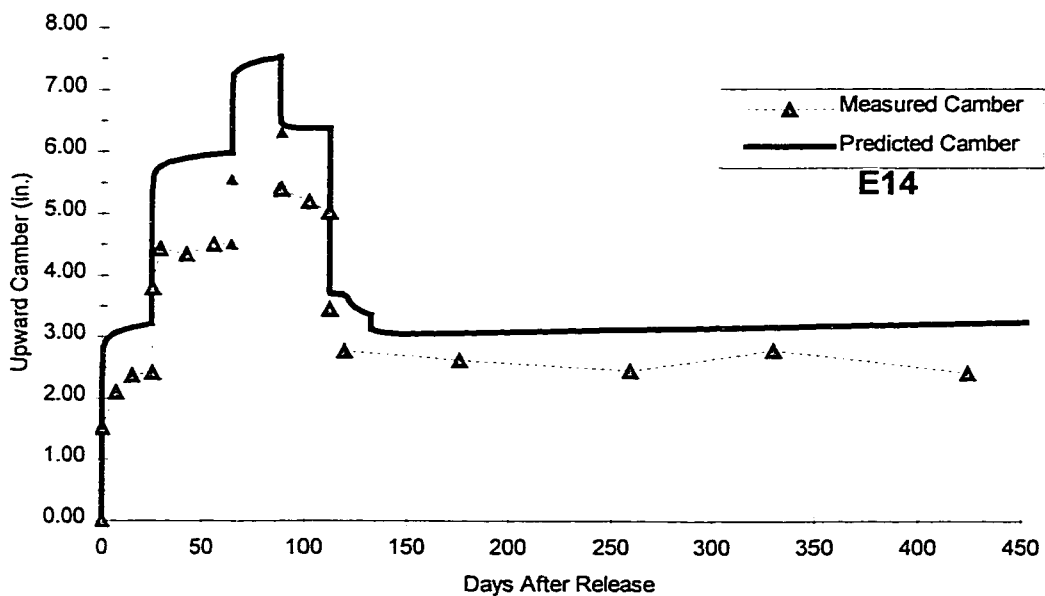


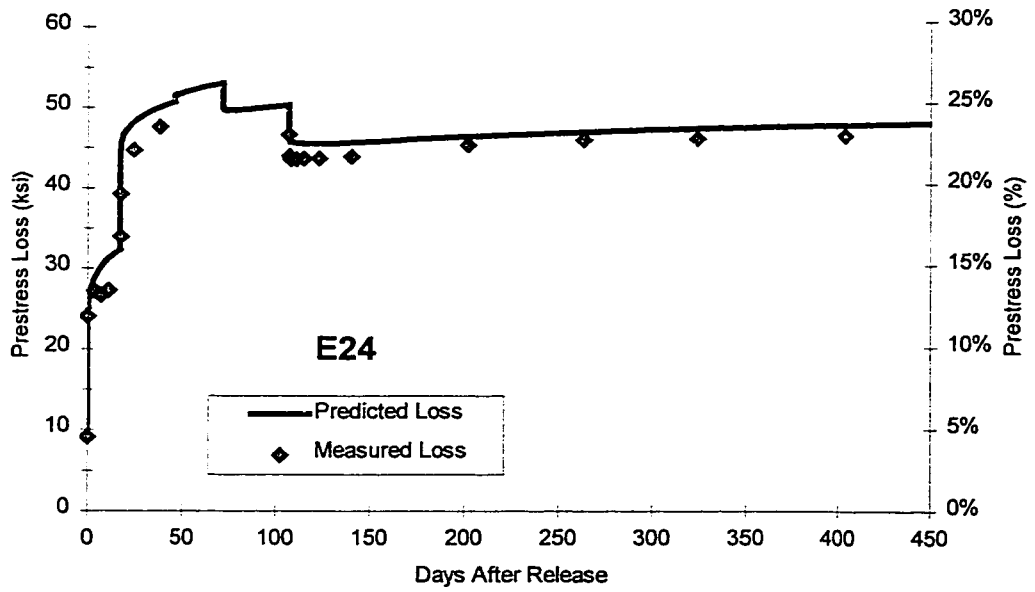
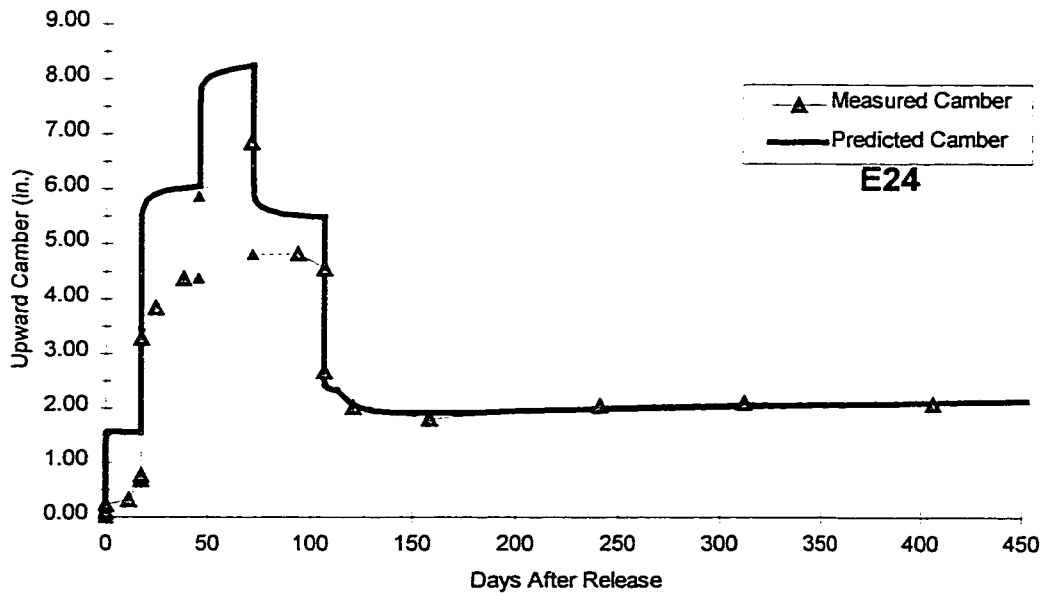


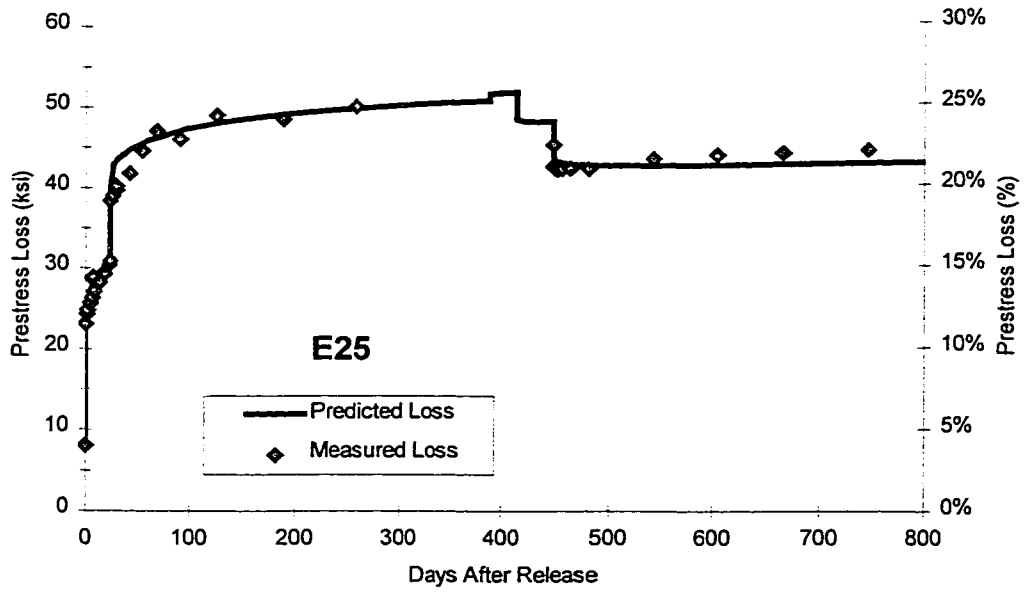
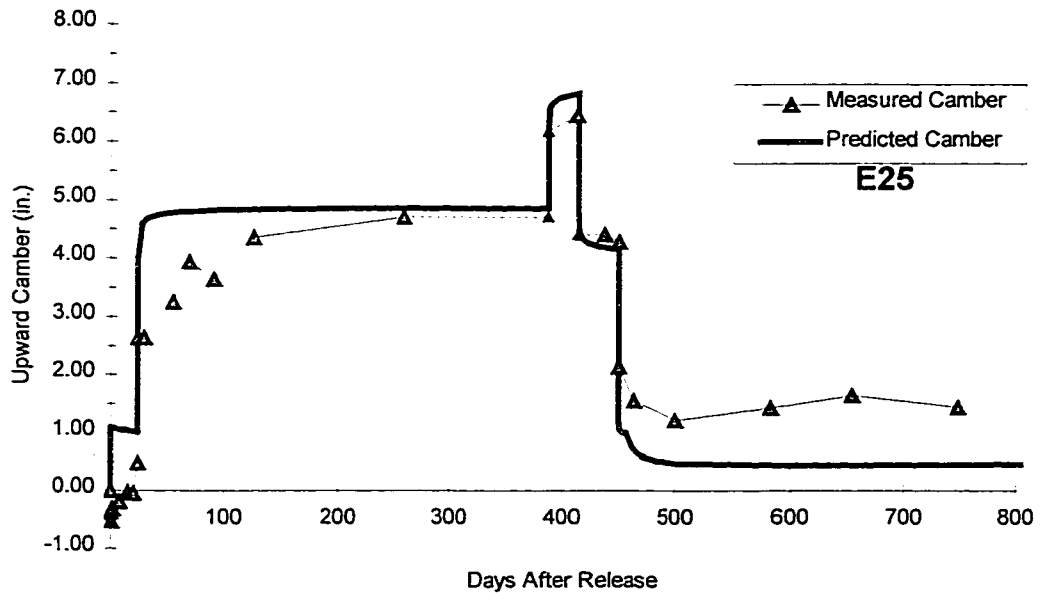


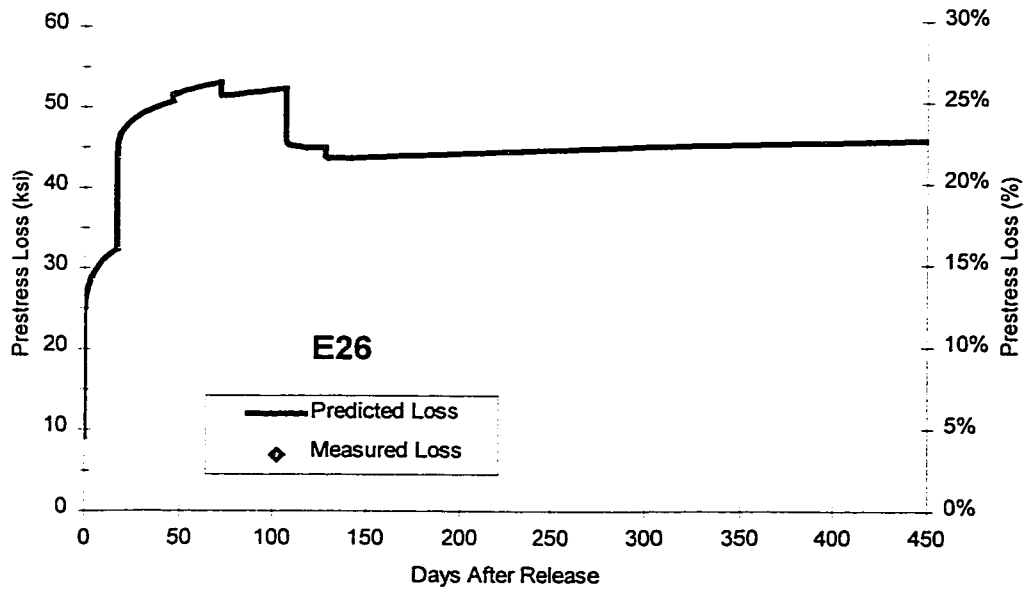
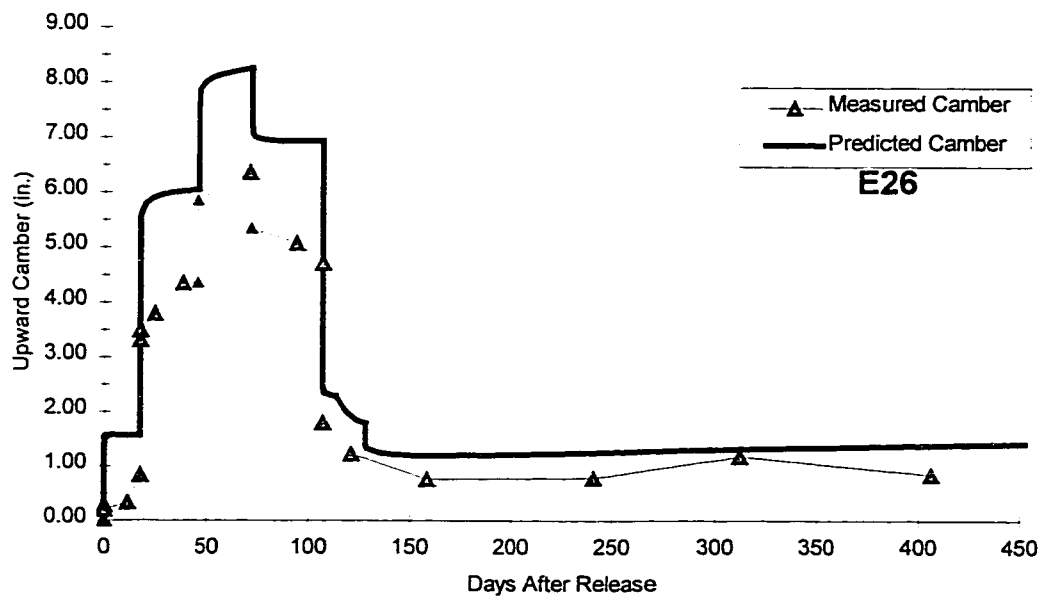


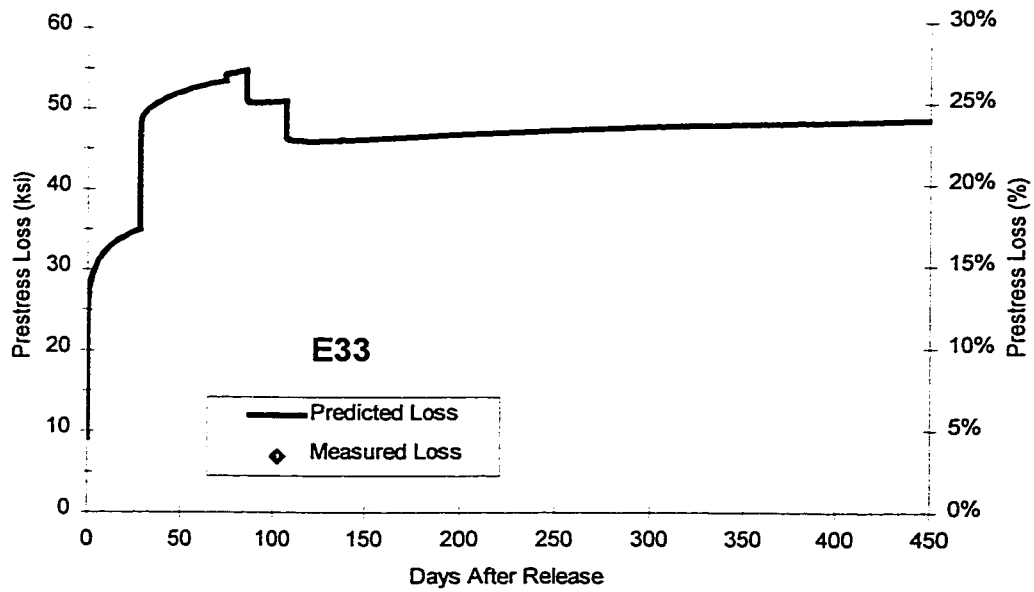
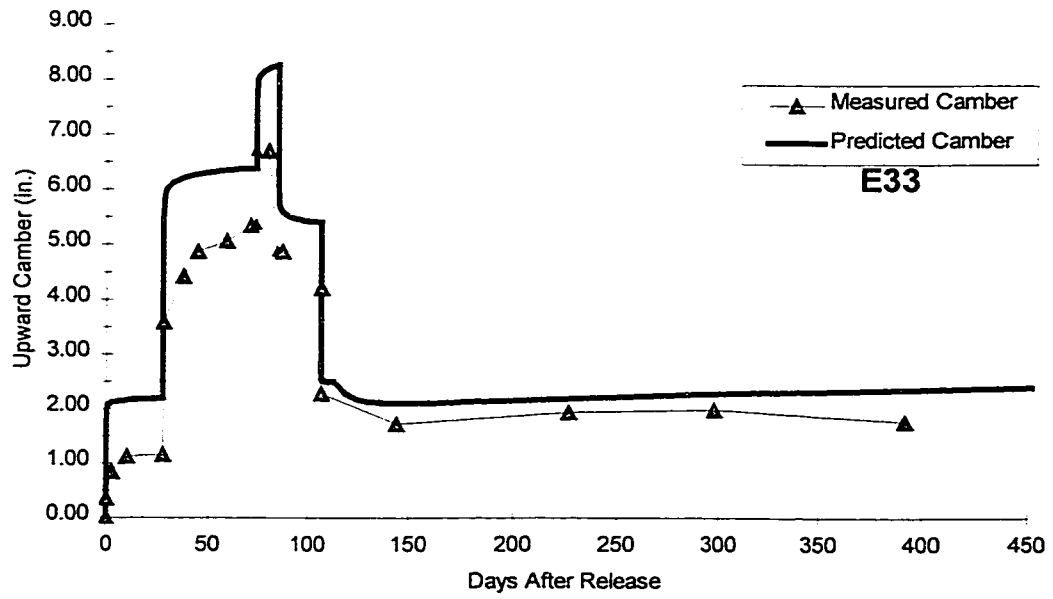


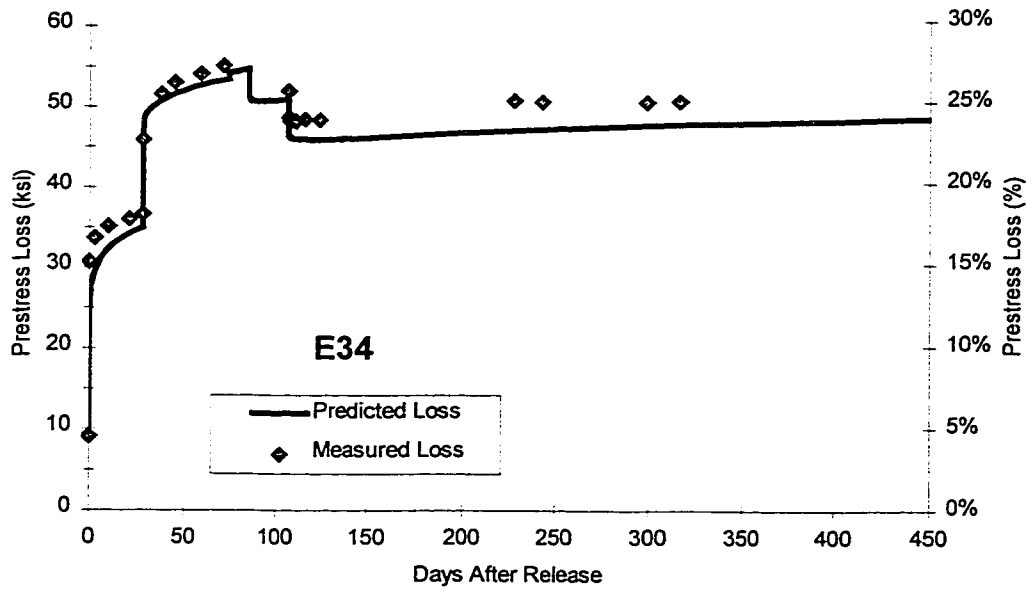
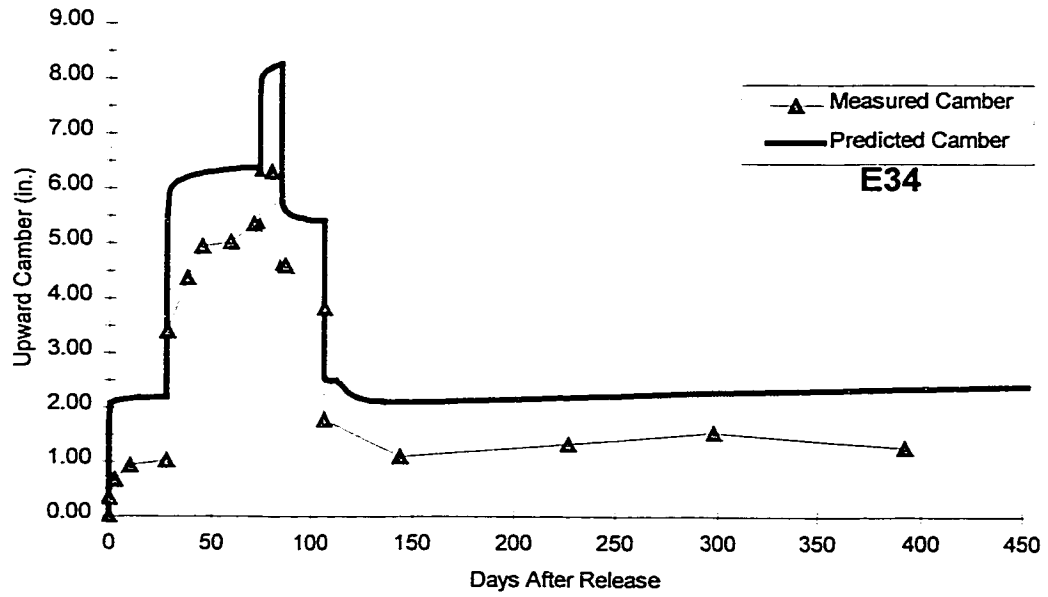


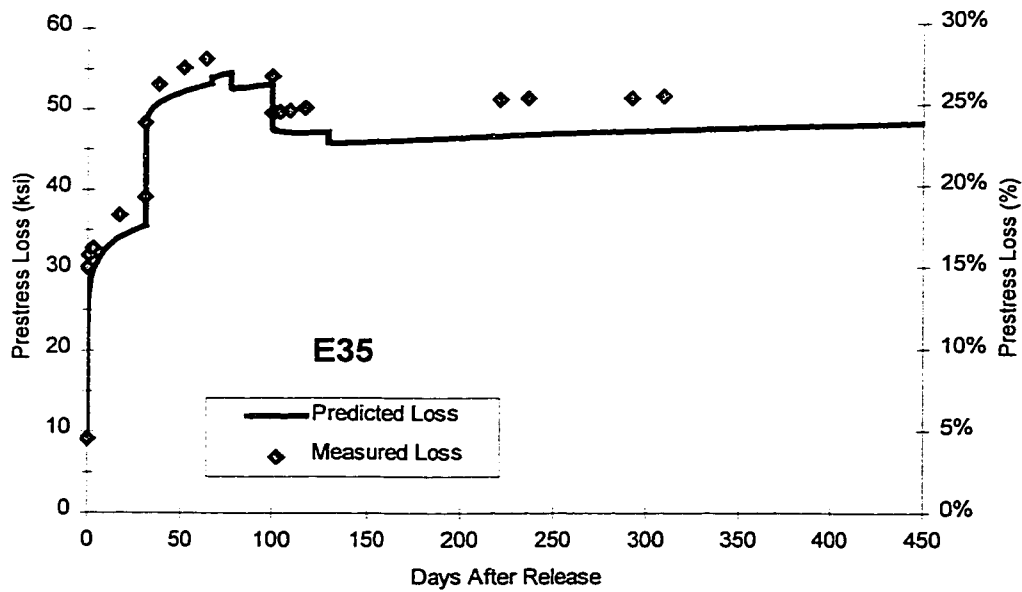
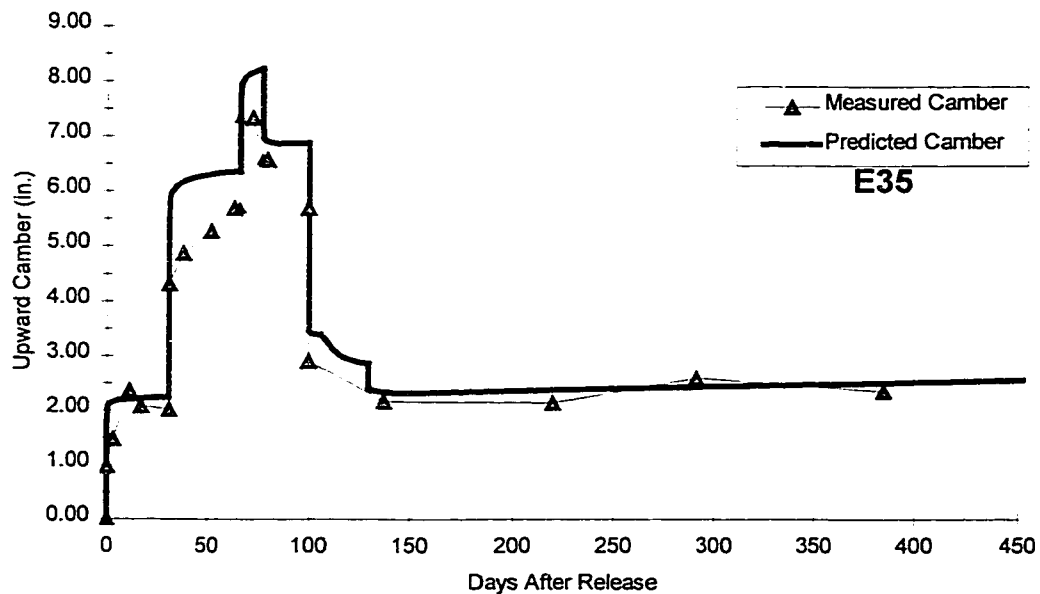


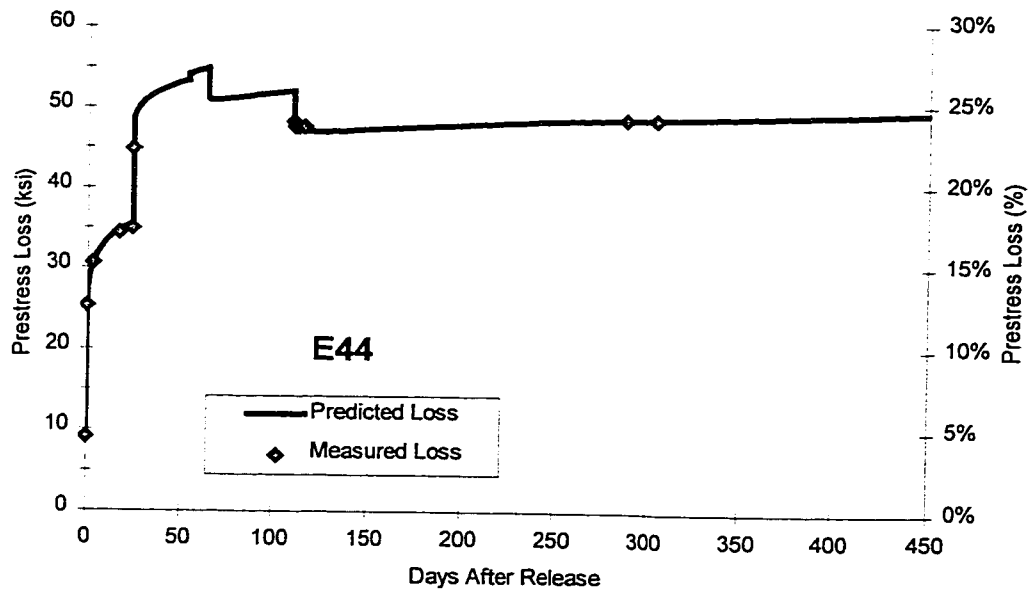
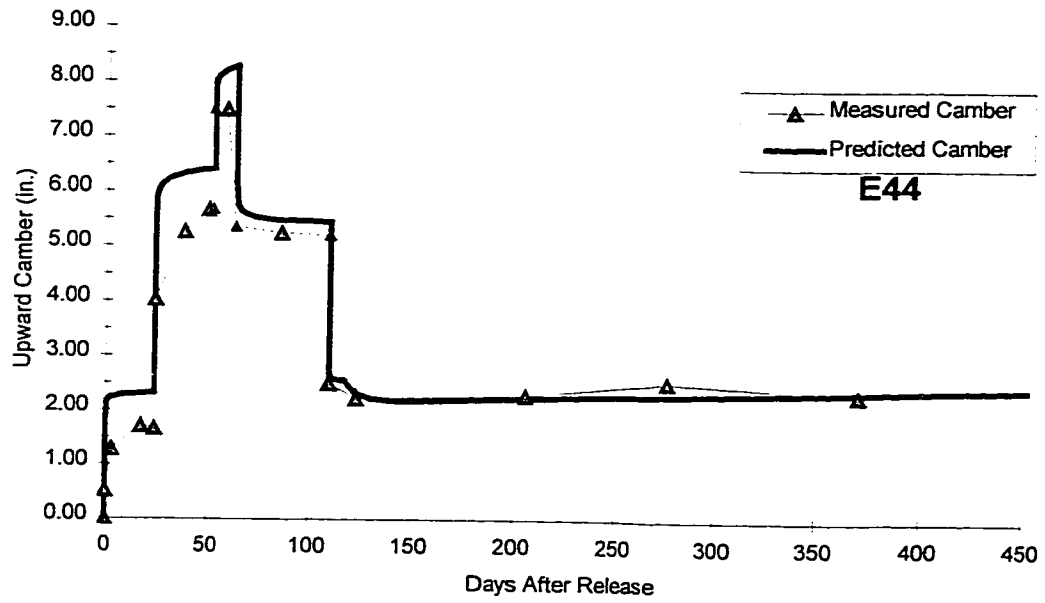


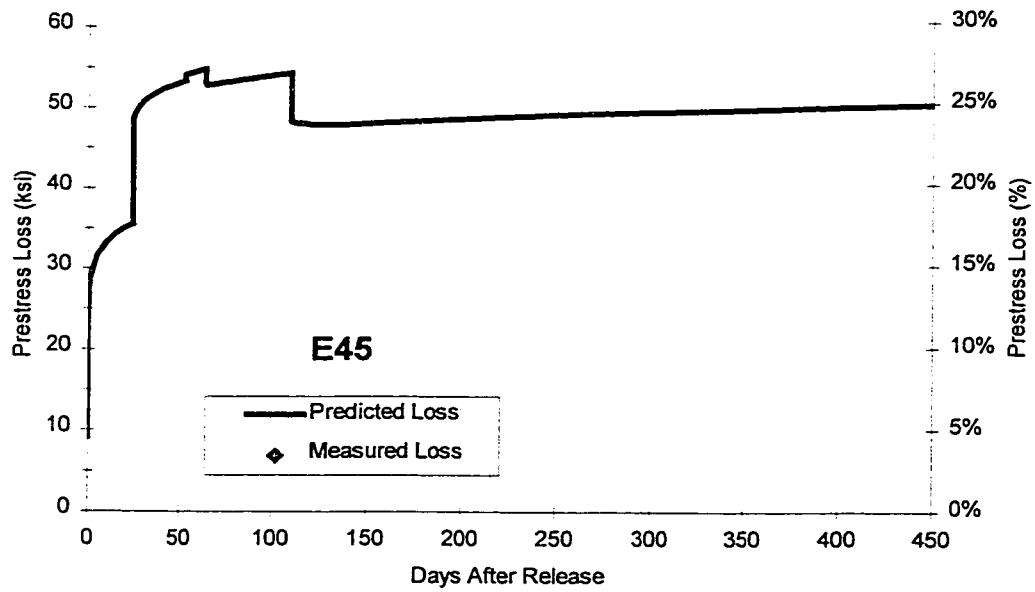
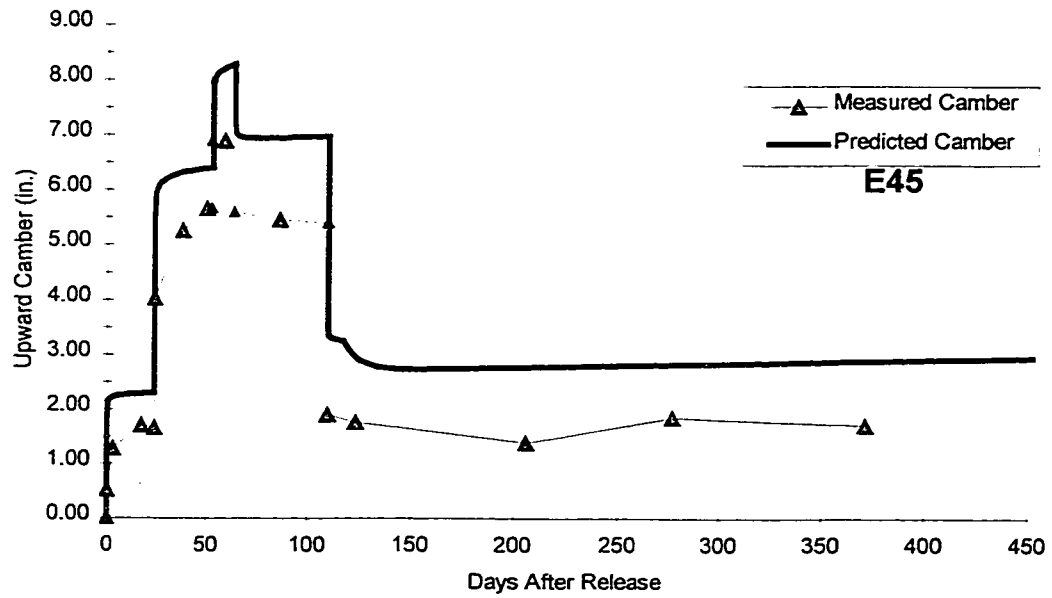


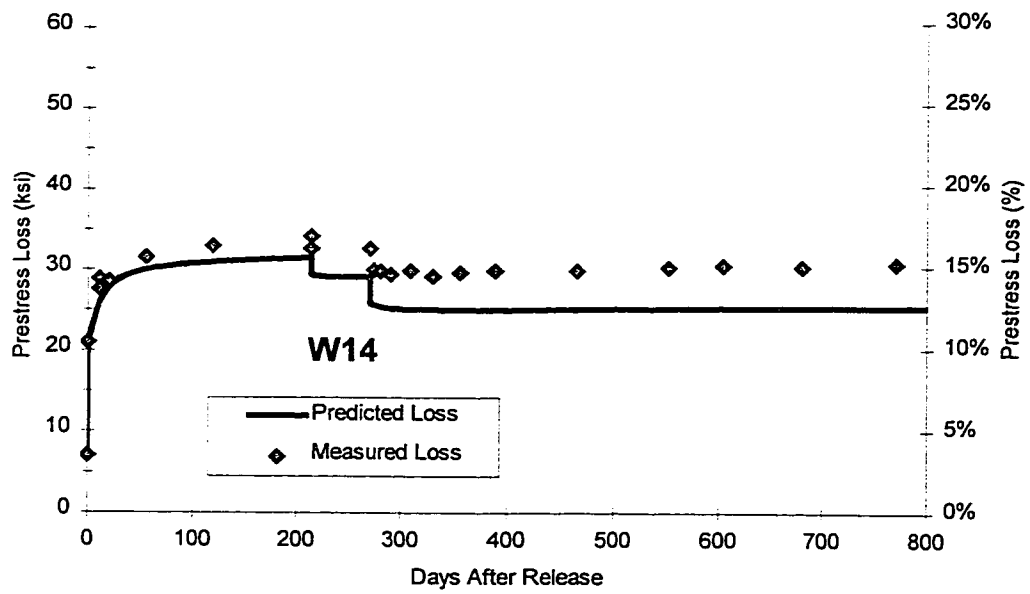
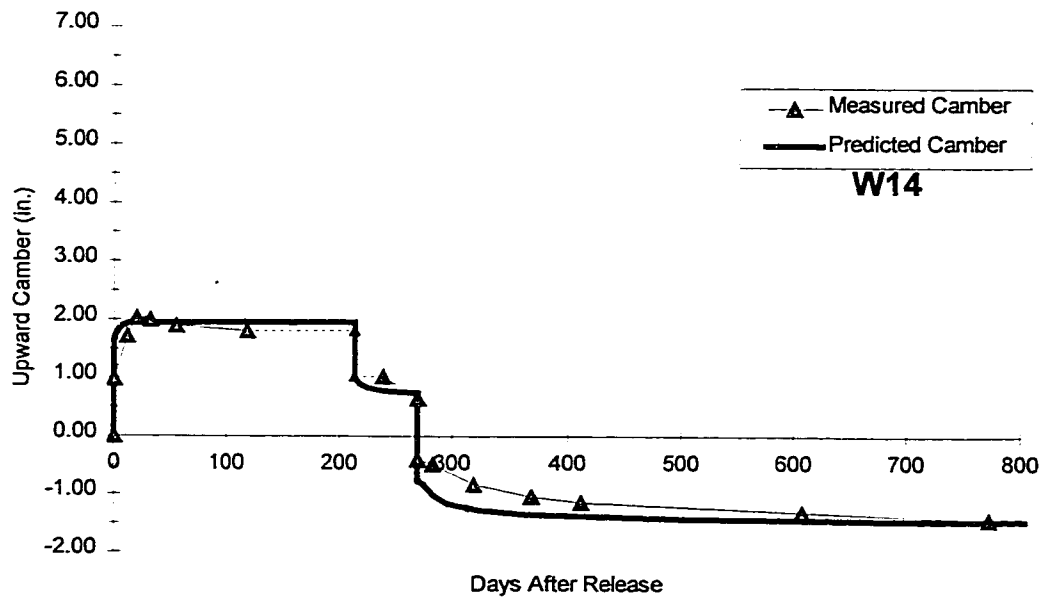


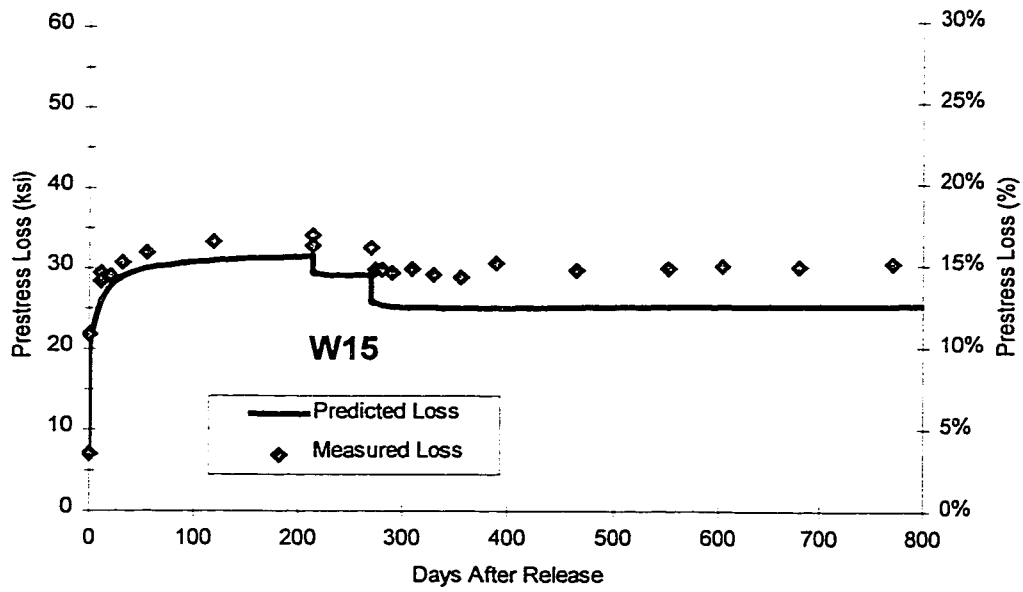
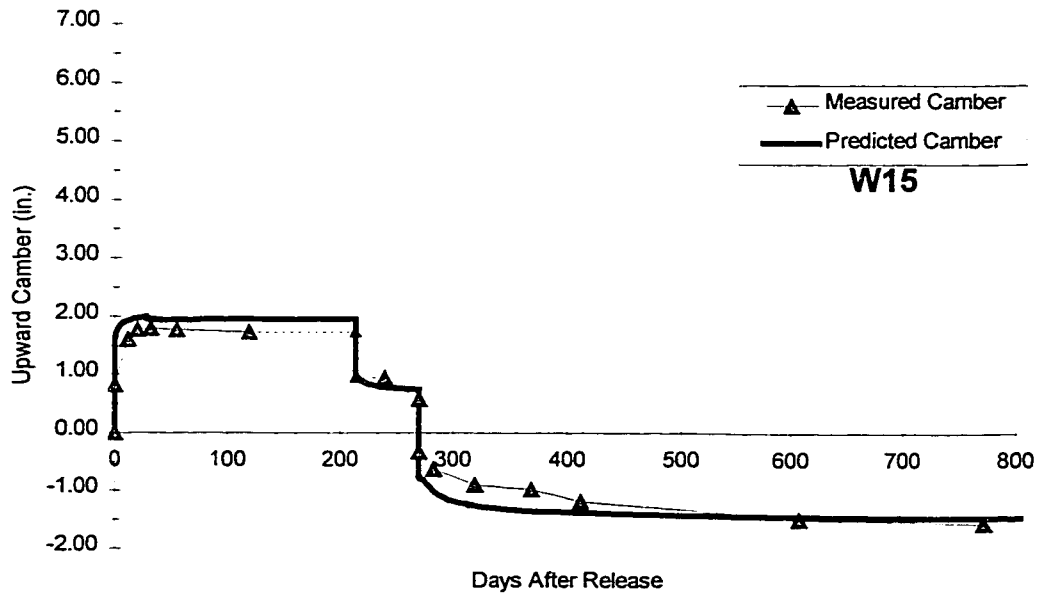


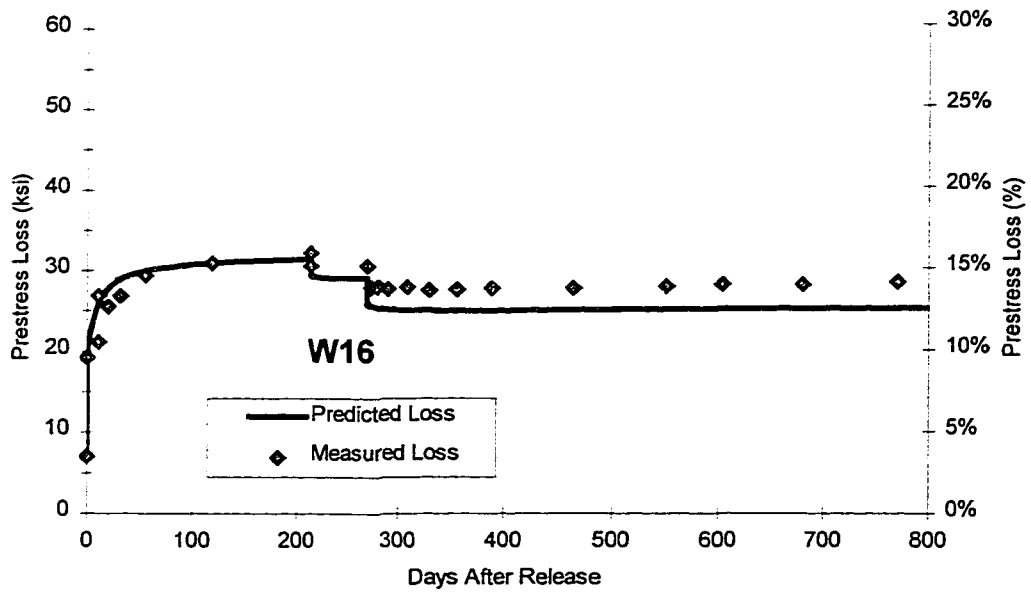
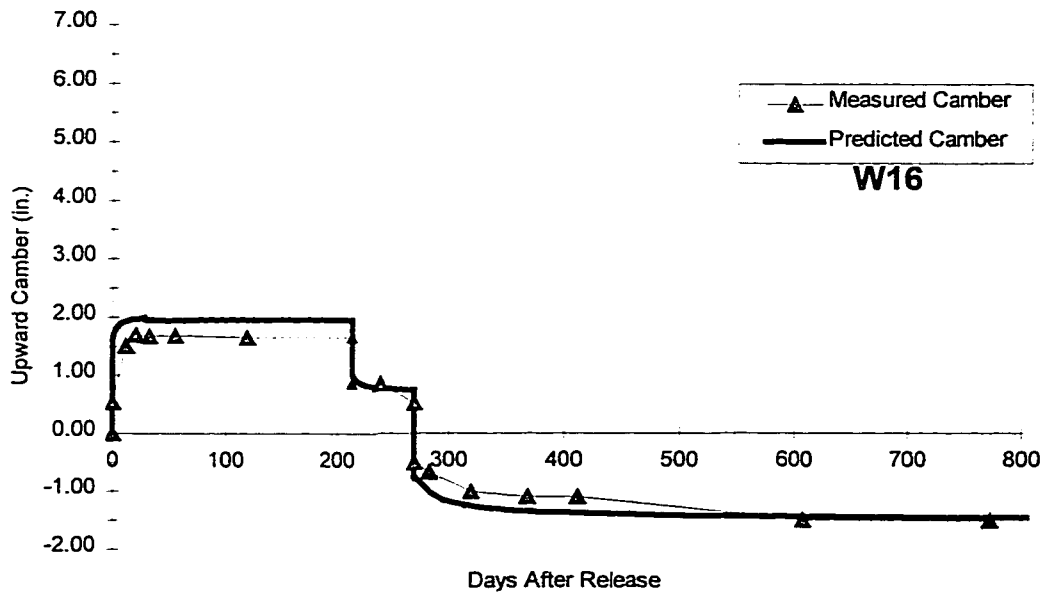


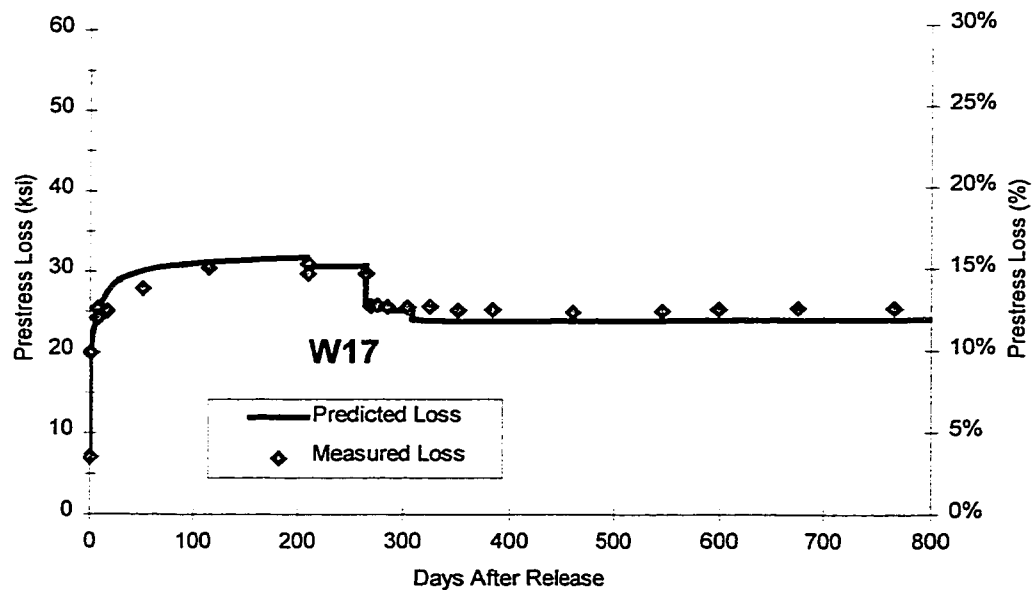
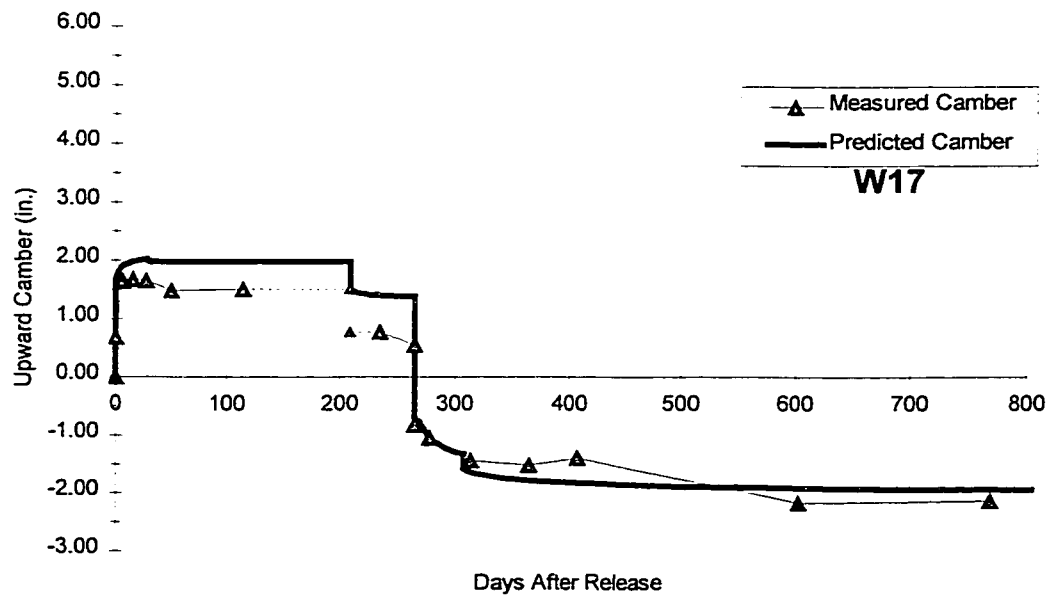












**APPENDIX H: PRESTRESS LOSS MEASUREMENTS AND
CALCULATIONS FOR INDIVIDUAL BEAMS**

Measured prestress losses and losses calculated by several methods are presented in this appendix for each beam in terms of the individual components of loss. A few general notes related to each of these methods are provided below:

- Nominal jacking stress = 1396 MPa (202.5 ksi) for all beams
- For explanation of “design” and “measured” parameters, see Table 7.10

Measured Losses:

- Pre-release losses (PR) estimated based on observations from Section 7.2
- Elastic shortening (ES), creep, and shrinkage (CR+SH) losses measured using vibrating wire gauges.
- Creep and shrinkage component includes compensation for measured elastic change in prestress due to superimposed loads.

Incremental Time-Step Method:

- See beginning of Appendix G for discussion of assumptions used with this method.
- Losses not separated into components

Actual Beam Designs (Louetta HPC and San Angelo Westbound non-HPC):

- Losses calculated by *AASHTO Standard Specifications* [32] component equations using TxDOT's PSTRS14 [50] design program.
- Design-assumed properties

Actual Beam Designs (San Angelo Eastbound HPC):

- Losses calculated by time-step method using ADAPT [55] computer program.
- Losses shown are average of upper and lower bound calculations described in Section 2.3.3.
- Pre-release losses assumed during design.

AASHTO LRFD [79] Lump-Sum Method:

- Elastic shortening (ES) losses computed using design parameters.

- Time-dependent lump-sum estimates (SH+CR+RE) based on Equation 7.15 or Equation 7.16 using design concrete strength.

AASHTO LRFD [79] Component Equations Method:

- Component equations listed in Table 7.7 for elastic shortening (ES), shrinkage (SH), creep (CR), and relaxation (RE).
- No separate consideration of pre-release losses, although relaxation (RE) component includes relaxation before release.

PCI Design Handbook [124] Component Equations Method:

- Component equations listed in Table 7.7 for elastic shortening (ES), shrinkage (SH), creep (CR), and relaxation (RE).
- No consideration of pre-release losses.

Suggested Component Equations Method:

- Component equations listed in Table 7.11 for elastic shortening (ES), shrinkage (SH), creep (CR), relaxation (RE), and pre-release losses (PR).

Measured Prestress Losses

Beam	Days After Release	Loss Components (ksi)				Total Loss (ksi)	Total Loss (% of f _{jack})
		PR	ES	CR+SH *	RE		
Louetta HPC Beams							
N32	761	8.10	17.75	14.47	2.78	43.11	21.29
S15	748	8.10	16.38	10.61	2.77	37.86	18.70
S16	1262	8.10	17.16	11.93	3.06	40.26	19.88
S25	1221	8.10	12.96	9.70	3.04	33.81	16.70
Average		8.10	16.07	11.68	2.92	38.76	19.14
San Angelo Eastbound HPC Beams							
E13	422	8.10	25.03	15.02	2.46	50.61	24.99
E14	422	8.10	24.58	22.10	2.46	57.24	28.27
E24	404	9.11	20.19	19.78	2.43	51.51	25.44
E25	746	8.10	22.46	18.63	2.77	51.95	25.66
E34	316	9.11	30.86	15.17	2.30	57.43	28.36
E35	309	9.11	30.52	16.26	2.28	58.17	28.73
E44	305	9.11	26.15	18.09	2.28	55.63	27.47
Average		8.68	25.68	17.86	2.42	54.65	26.99
San Angelo Westbound Non-HPC Beams							
W14	771	7.09	13.94	10.84	2.79	34.67	17.12
W15	771	7.09	14.73	9.81	2.79	34.41	16.99
W16	771	7.09	12.18	10.62	2.79	32.68	16.14
W17	766	7.09	12.80	7.84	2.79	30.51	15.07
Average		7.09	13.41	9.78	2.79	33.07	16.33
1 ksi = 6.895 MPa * Includes compensation for measured elastic change in stress due to superimposed dead load See general notes at beginning of Appendix H. PR: Pre-release (See Section 7.2); ES: Elastic Shortening; CR: Creep; SH: Shrinkage; RE: Relaxation							

Losses Predicted by the Incremental Time-Step Method

Beam	Total Loss (ksi)	Total Loss (% of f_{jack})
<i>Louetta HPC Beams</i>		
N32	42.30	20.89
S15	44.36	21.91
S16	46.32	22.87
S25	40.99	20.24
Average	43.49	21.48
<i>San Angelo Eastbound HPC Beams</i>		
E13	54.48	26.90
E14	54.76	27.04
E24	54.17	26.75
E25	49.74	24.56
E34	54.79	27.06
E35	54.73	27.03
E44	55.70	27.51
Average	54.05	26.69
<i>San Angelo Westbound Non-HPC Beams</i>		
W14	30.52	15.07
W15	30.52	15.07
W16	30.52	15.07
W17	30.49	15.06
Average	30.51	15.07
<p>1 ksi = 6.895 MPa</p> <p>* Includes compensation for measured elastic change in stress due to superimposed dead load</p> <p>See general notes at beginning of Appendix H.</p> <p>PR: Pre-release (See Section 7.2); ES: Elastic Shortening; CR: Creep; SH: Shrinkage; RE: Relaxation</p>		

Losses Calculated as Part of Actual Beam Designs

Beam	Total Loss (ksi)	Total Loss (% of f_{jack})
<i>Louetta HPC Beams (PSTRS14)</i>		
N32	57.79	28.54
S15	57.79	28.54
S16	52.99	26.17
S25	52.99	26.17
Average	55.39	27.36
<i>San Angelo Eastbound HPC Beams (ADAPT)</i>		
E13	49.36	24.38
E14	49.36	24.38
E24	49.83	24.61
E25	42.26	20.87
E34	50.85	25.11
E35	50.85	25.11
E44	51.01	25.19
Average	49.07	24.23
<i>San Angelo Westbound Non-HPC Beams (PSTRS14)</i>		
W14	47.91	23.66
W15	47.91	23.66
W16	47.91	23.66
W17	47.91	23.66
Average	47.91	23.66
<p>1 ksi = 6.895 MPa</p> <p>* Includes compensation for measured elastic change in stress due to superimposed dead load</p> <p>See general notes at beginning of Appendix H.</p> <p>PR: Pre-release (See Section 7.2); ES: Elastic Shortening; CR: Creep; SH: Shrinkage; RE: Relaxation</p>		

**Losses Predicted by the AASHTO LRFD Time-Dependent Lump Sum (Based on
Design Parameters Including Design Concrete Strength)**

Beam	Design Concrete Strength (psi)	Loss Components (ksi)		Total Loss (ksi)	Total Loss (% of f_{jack})
		ES	SH+CR+RE		
<i>Louetta HPC Beams (PSTRS14)</i>					
N32	11600	23.72	15.00	38.72	19.12
S15	11600	25.65	15.00	40.65	20.07
S16	11600	23.29	15.00	38.29	18.91
S25	11600	21.68	15.00	36.68	18.11
Average		23.59	15.00	38.59	19.05
<i>San Angelo Eastbound HPC Beams (ADAPT)</i>					
E13	13000	35.98	21.23	57.21	28.25
E14	13000	35.98	21.23	57.21	28.25
E24	14000	36.03	20.40	56.43	27.87
E25	13500	30.69	20.81	51.50	25.43
E34	13800	37.10	20.57	57.67	28.48
E35	13800	37.10	20.57	57.67	28.48
E44	13700	37.20	20.65	57.85	28.57
Average		35.73	20.78	56.51	27.90
<i>San Angelo Westbound Non-HPC Beams (PSTRS14)</i>					
W14	7850	15.55	25.47	41.02	20.26
W15	7850	15.55	25.47	41.02	20.26
W16	7850	15.55	25.47	41.02	20.26
W17	7850	15.55	25.47	41.02	20.26
Average		15.55	25.47	41.02	20.26
1 ksi = 6.895 MPa					
* Includes compensation for measured elastic change in stress due to superimposed dead load					
See general notes at beginning of Appendix H.					
PR: Pre-release (See Section 7.2); ES: Elastic Shortening; CR: Creep; SH: Shrinkage; RE: Relaxation					

Losses Predicted by the AASHTO LRFD Method (Design Parameters)

Beam	Loss Components (ksi)				Total Loss (ksi)	Total Loss (% of f _{jack})
	ES	SH	CR	RE		
<i>Louetta HPC Beams</i>						
N32	23.72	5.75	33.82	3.76	67.05	33.11
S15	25.65	5.75	37.84	3.29	72.53	35.82
S16	23.29	5.75	37.27	3.61	69.92	34.53
S25	21.68	5.75	30.48	4.21	62.12	30.68
Average	23.59	5.75	34.85	3.72	67.91	33.53
<i>San Angelo Eastbound HPC Beams</i>						
E13	35.98	8.00	57.64	0.73	102.35	50.54
E14	35.98	8.00	59.89	0.59	104.46	51.59
E24	36.03	8.00	59.30	0.63	103.96	51.34
E25	30.69	8.00	48.72	1.90	89.31	44.10
E34	37.10	8.00	59.89	0.46	105.45	52.07
E35	37.10	8.00	60.77	0.40	106.27	52.48
E44	37.20	8.00	60.20	0.43	105.83	52.26
Average	35.73	8.00	58.06	0.73	102.52	50.63
<i>San Angelo Westbound Non-HPC Beams</i>						
W14	15.55	8.00	23.45	4.91	51.91	25.63
W15	15.55	8.00	23.45	4.91	51.91	25.63
W16	15.55	8.00	23.45	4.91	51.91	25.63
W17	15.55	8.00	23.24	4.92	51.71	25.54
Average	15.55	8.00	23.40	4.91	51.86	25.61
<p>1 ksi = 6.895 MPa</p> <p>* Includes compensation for measured elastic change in stress due to superimposed dead load</p> <p>See general notes at beginning of Appendix H.</p> <p>PR: Pre-release (See Section 7.2); ES: Elastic Shortening; CR: Creep; SH: Shrinkage; RE: Relaxation</p>						

Losses Predicted by the AASHTO LRFD Method (Measured Parameters)

Beam	Loss Components (ksi)				Total Loss (ksi)	Total Loss (% of f_{jack})
	ES	SH	CR	RE		
<i>Louetta HPC Beams</i>						
N32	16.23	5.75	30.89	4.84	57.71	28.50
S15	17.33	5.75	33.63	4.54	61.25	30.25
S16	17.47	5.75	32.04	4.62	59.88	29.57
S25	14.99	5.75	26.47	5.25	52.46	25.91
Average	16.51	5.75	30.76	4.81	57.83	28.56
<i>San Angelo Eastbound HPC Beams</i>						
E13	25.76	8.00	52.15	2.28	88.19	43.55
E14	25.76	8.00	53.44	2.20	89.40	44.15
E24	24.80	8.00	54.00	2.29	89.09	44.00
E25	22.16	8.00	43.95	3.21	77.32	38.18
E34	25.80	8.00	55.00	2.11	90.91	44.89
E35	26.14	8.00	54.45	2.10	90.69	44.79
E44	26.92	8.00	55.01	1.97	91.90	45.38
Average	25.33	8.00	52.57	2.31	88.21	43.56
<i>San Angelo Westbound Non-HPC Beams</i>						
W14	11.48	8.00	20.48	5.58	45.54	22.49
W15	11.48	8.00	20.48	5.58	45.54	22.49
W16	11.48	8.00	20.48	5.58	45.54	22.49
W17	11.66	8.00	18.65	5.67	43.98	21.72
Average	11.53	8.00	20.02	5.60	45.15	22.30
<p>1 ksi = 6.895 MPa</p> <p>* Includes compensation for measured elastic change in stress due to superimposed dead load</p> <p>See general notes at beginning of Appendix H.</p> <p>PR: Pre-release (See Section 7.2); ES: Elastic Shortening; CR: Creep; SH: Shrinkage; RE: Relaxation</p>						

Losses Predicted by the PCI Design Handbook Method (Design Parameters)

Beam	Loss Components (ksi)				Total Loss (ksi)	Total Loss (% of f_{jack})
	ES	SH	CR	RE		
<i>Louetta HPC Beams</i>						
N32	22.55	4.75	20.17	3.10	50.57	24.97
S15	24.48	4.75	23.88	2.88	55.99	27.65
S16	22.20	4.64	26.05	2.89	55.78	27.55
S25	20.59	4.64	17.76	3.28	46.27	22.85
Average	22.46	4.70	21.97	3.04	52.15	25.75
<i>San Angelo Eastbound HPC Beams</i>						
E13	34.84	6.57	38.52	1.80	81.73	40.36
E14	34.84	6.57	41.76	1.67	84.84	41.90
E24	34.89	6.57	39.81	1.75	83.02	41.00
E25	29.61	6.57	31.53	2.29	70.00	34.57
E34	35.96	6.57	39.63	1.71	83.87	41.42
E35	35.96	6.57	40.87	1.66	85.06	42.00
E44	36.05	6.57	40.09	1.69	84.40	41.68
Average	34.59	6.57	38.89	1.80	81.85	40.42
<i>San Angelo Westbound Non-HPC Beams</i>						
W14	14.67	6.57	14.36	3.58	39.18	19.35
W15	14.67	6.57	14.36	3.58	39.18	19.35
W16	14.67	6.57	14.36	3.58	39.18	19.35
W17	14.67	6.57	14.04	3.59	38.87	19.20
Average	14.67	6.57	14.28	3.58	39.10	19.31
<p>1 ksi = 6.895 MPa</p> <p>* Includes compensation for measured elastic change in stress due to superimposed dead load</p> <p>See general notes at beginning of Appendix H.</p> <p>PR: Pre-release (See Section 7.2); ES: Elastic Shortening; CR: Creep; SH: Shrinkage; RE: Relaxation</p>						

Losses Predicted by the PCI Design Handbook Method (Measured Parameters)

Beam	Loss Components (ksi)				Total Loss (ksi)	Total Loss (% of f_{jack})
	ES	SH	CR	RE		
<i>Louetta HPC Beams</i>						
N32	15.41	4.75	15.04	3.59	38.79	19.16
S15	16.52	4.75	16.07	3.51	40.85	20.17
S16	16.64	4.64	16.89	3.47	41.64	20.56
S25	14.22	4.64	11.63	3.78	34.27	16.92
Average	15.70	4.70	14.91	3.59	38.89	19.20
<i>San Angelo Eastbound HPC Beams</i>						
E13	24.93	6.57	29.76	2.55	63.81	31.51
E14	24.93	6.57	31.42	2.48	65.40	32.30
E24	23.99	6.57	32.11	2.49	65.16	32.18
E25	21.36	6.57	24.39	2.91	55.23	27.27
E34	24.99	6.57	32.48	2.44	66.48	32.83
E35	25.32	6.57	31.58	2.46	65.93	32.56
E44	26.08	6.57	32.27	2.40	67.32	33.24
Average	24.51	6.57	30.57	2.53	64.19	31.70
<i>San Angelo Westbound Non-HPC Beams</i>						
W14	10.82	6.57	10.48	3.89	31.76	15.68
W15	10.82	6.57	10.48	3.89	31.76	15.68
W16	10.82	6.57	10.48	3.89	31.76	15.68
W17	11.00	6.57	8.00	3.98	29.55	14.59
Average	10.87	6.57	9.86	3.91	31.21	15.41
<p>1 ksi = 6.895 MPa</p> <p>* Includes compensation for measured elastic change in stress due to superimposed dead load</p> <p>See general notes at beginning of Appendix H.</p> <p>PR: Pre-release (See Section 7.2); ES: Elastic Shortening; CR: Creep; SH: Shrinkage; RE: Relaxation</p>						

**Losses Predicted by the Suggested Method in Table 7.11 (Measured Parameters
Including Modulus, Creep, and Shrinkage Values)**

Beam	Loss Components (ksi)					Total Loss (ksi)	Total Loss (% of f_{jack})
	PR	ES	SH	CR	RE		
<i>Louetta HPC Beams</i>							
N32	6.01	15.41	7.14	7.67	3.79	40.02	19.76
S15	6.01	16.52	7.14	8.20	3.73	41.60	20.54
S16	6.01	16.64	6.92	8.36	3.72	41.65	20.57
S25	6.01	14.22	6.92	5.76	3.92	36.83	18.19
Average	6.01	15.70	7.03	7.50	3.79	40.03	19.77
<i>San Angelo Eastbound HPC Beams</i>							
E13	6.01	24.93	7.28	14.14	3.15	55.51	27.41
E14	6.01	24.93	7.28	14.93	3.12	56.27	27.79
E24	6.01	23.99	7.28	15.25	3.14	55.67	27.49
E25	6.01	21.36	7.28	11.59	3.39	49.63	24.51
E34	6.01	24.99	7.28	15.43	3.09	56.80	28.05
E35	6.01	25.32	7.28	15.00	3.10	56.71	28.00
E44	6.01	26.08	7.28	15.33	3.05	57.75	28.52
Average	6.01	24.51	7.28	14.52	3.15	55.48	27.40
<i>San Angelo Westbound Non-HPC Beams</i>							
W14	5.73	10.82	4.79	3.09	4.25	28.68	14.16
W15	5.73	10.82	4.79	3.09	4.25	28.68	14.16
W16	5.73	10.82	4.79	3.09	4.25	28.68	14.16
W17	5.73	11.00	4.79	2.36	4.27	28.15	13.90
Average	5.73	10.87	4.79	2.91	4.26	28.55	14.10
1 ksi = 6.895 MPa * Includes compensation for measured elastic change in stress due to superimposed dead load See general notes at beginning of Appendix H. PR: Pre-release (See Section 7.2); ES: Elastic Shortening; CR: Creep; SH: Shrinkage; RE: Relaxation							

BIBLIOGRAPHY

1. American Association of State Highway and Transportation Officials, *AASHTO LRFD Bridge Design Specifications*, First Edition, 1994.
2. American Association of State Highway and Transportation Officials, *Guide Specifications for Design and Construction of Segmental Concrete Bridges*, Proposed Second Edition, 1998.
3. American Association of State Highway and Transportation Officials, *Standard Specifications for Highway Bridges*, Sixteenth Edition, 1996.
4. American Association of State Highway and Transportation Officials, *Standard Specifications for Highway Bridges*, Fifteenth Edition, 1992.
5. American Association of State Highway and Transportation Officials, *Standard Specifications for Highway Bridges*, Fourteenth Edition, 1989.
6. American Association of State Highway and Transportation Officials, *Standard Specifications for Highway Bridges*, Eleventh Edition (Interim Specifications), 1975.
7. American Concrete Institute, *Building Code Requirements for Structural Concrete (and Commentary)*, ACI 318-95/318R-95, Detroit, 1995.
8. ACI Committee 209, "Prediction of Creep, Shrinkage, and Temperature Effects in Concrete Structures," ACI 209R-92, American Concrete Institute, Detroit, 1992.
9. ACI Committee 211, "Guide for Selecting Proportions for High-Strength Concrete with Portland Cement and Fly Ash," ACI 211.4R-93, American Concrete Institute, Detroit, 1993.
10. ACI Committee 363, "State-of-the-Art Report on High-Strength Concrete," ACI 363R-92, American Concrete Institute, Detroit, 1992.
11. ACI Committee 435, "Control of Deflection in Concrete Structures," ACI 435R-95, American Concrete Institute, Detroit, 1995.

12. ACI TAC Subcommittee on High Performance Concrete, *High Performance Concrete in Severe Environments*, ACI SP-140, American Concrete Institute, Detroit, 1993, preface.
13. ADAPT Corporation, ADAPT-ABI, ADAPT-Bridge Incremental Structural Concrete Software System, Version 2.00, 1996.
14. Ahmad, S. H., and Shah, S. P., "Structural Properties of High Strength Concrete and its Implications for Precast Prestressed Concrete," *PCI Journal*, November/December 1985, Vol. 30, No. 6, pp. 92-119.
15. Aitcin, P.-C., and Mehta, P. K., "Effect of Coarse Aggregate Characteristics on Mechanical Properties of High-Strength Concrete," *ACI Materials Journal*, March/April 1990, Vol. 87, No. 2.
16. Aitcin, P.-C., Laplante, P., and Bedard, C., "Development and Experimental Use of 90 MPa (13,000 psi) Field Concrete," *High-Strength Concrete*, ACI SP-87, American Concrete Institute, Detroit, 1985, pp. 51-70.
17. Anderson, A. R., "Lateral Stability of Long Prestressed Concrete Beams," *PCI Journal*, May/June 1971, Vol. 16, No. 3, pp. 7-9.
18. Arrellaga, J., *Instrumentation Systems for Post-Tensioned Segmental Box Girder Bridges*, Masters Thesis, The University of Texas at Austin, Austin, Texas, 1991.
19. American Society for Testing and Materials, "Standard Practice for Making and Curing Concrete Test Specimens in the Field," ASTM C31-91, ASTM, West Conshohocken, Pennsylvania, 1991.
20. American Society for Testing and Materials, "Standard Test Method for Compressive Strength of Cylindrical Concrete Specimens," ASTM C39-93a, ASTM, West Conshohocken, Pennsylvania, 1993.
21. American Society for Testing and Materials, "Standard Test Method for Creep of Concrete in Compression," ASTM C512-87(1992)e1, ASTM, West Conshohocken, Pennsylvania, 1992.
22. American Society for Testing and Materials, "Standard Test Method for Static Modulus of Elasticity and Poisson's Ratio of Concrete in Compression," ASTM C469-94, ASTM, West Conshohocken, Pennsylvania, 1994.
23. Barrios, A. O., Burns, N. H., and Carrasquillo, R. L., *Behavior of High Strength Concrete Pretensioned Girders During Transfer of Prestressing Forces*, Research

Report 580-1, Center for Transportation Research, The University of Texas at Austin, Austin, Texas, 1996 (awaiting final publication).

24. Bazant, Z. P. and Panula, L., "Creep and Shrinkage Characterization for Analyzing Prestressed Concrete Structures," *PCI Journal*, May/June 1980, Vol. 15, No. 3, pp. 87-122.
25. Branson, D. E., *Deformation of Concrete Structures*, McGraw-Hill, New York, 1977.
26. Branson, D. E. and Christiason, M. L., "Time-Dependent Concrete Properties Related to Design – Strength and Elastic Properties, Creep, and Shrinkage," ACI Special Publication SP-27, *Creep, Shrinkage, and Temperature Effects in Concrete Structures*, American Concrete Institute, Detroit, 1971.
27. Branson, D. E. and Kripanarayanan, K. M., "Loss of Prestress, Camber, and Deflection of Non-composite and Composite Prestressed Concrete Structures," *PCI Journal*, September/October 1971, Vol. 16, No. 5, pp. 22-52.
28. Branson, D. E. and Ozell, A. M., "Camber in Prestressed Concrete Beams," *ACI Journal (Proceedings)*, June 1961, Vol. 57, No. 12, pp. 1549-1574.
29. British Standards Institute, *British Standard BS5400, Steel, Concrete, and Composite Bridges, Part 2*, 1978.
30. Brooks, J. J. and Neville, A., "Creep and Shrinkage of Concrete as Affected by Admixtures and Cement Replacement Materials," *Creep and Shrinkage of Concrete: Effect of Materials and Environment*, ACI SP 135, American Concrete Institute, Detroit, 1992, pp. 19-36.
31. Bruce, R. N., Martin, B. R., Russell, H. G., and Roller, J. J., *Feasibility Evaluation of Utilizing High-Strength Concrete in Design and Construction of Highway Bridge Structures*, Report No. 282, Louisiana Transportation Research Center, Baton Rouge, Louisiana, 1994.
32. Buckner, C. D., *An Analysis of Transfer and Development Lengths for Prestressed Concrete Structures*, Publication No. FHWA-RD-94-049, Federal Highway Administration, McLean, Virginia, 1994.
33. Burdette, E. G., Deatherage, J. H., and Chew, C. K., "Development Length and lateral Spacing Requirements of Prestressing Strand for Prestressed Concrete Bridge Girders," *PCI Journal*, January/February 1994, Vol. 39, No. 1, pp. 70-83.

34. Burns, N. H., "Moment Curvature Relationships for Partially Prestressed Concrete Beams," *PCI Journal*, February 1964, Vol. 9, No. 1, pp. 52-63.
35. Byle, K. A., Burns, N. H., and Carrasquillo, R. L., *Time-Dependent Deformation Behavior of Prestressed High Performance Concrete Bridge Beams*, Research Report 580-6, Center for Transportation Research, The University of Texas at Austin, Austin, Texas, 1998 (awaiting final publication).
36. Campbell Scientific, Inc., PC208, Software Package for Campbell Scientific Dataloggers, 1992.
37. Carlton, M. and Carrasquillo, R. L., *Quality Control of High Performance Concrete for Highway Bridges*, Research Report 580-3, Center for Transportation Research, The University of Texas at Austin, Austin, Texas, 1997 (awaiting final publication).
38. Carpenter, J. E., "Applications of High-Strength Concrete for Highway Bridges," *Public Roads*, September 1980, Vol. 44, No. 2, pp. 76-83.
39. Carrasquillo, R. L., Nilson, A. H., and Slate, F. O., "Properties of High Strength Concrete Subject to Short-Term Loads," *ACI Journal*, May/June 1981, Vol. 78, No. 3, pp. 171-179.
40. Castrodale, R. W., Kreger, M. E., and Burns, N. H., *A Study of Pretensioned High-Strength Concrete Girders in Highway Bridges — Design Considerations*, Research Report 381-4F, Center for Transportation Research, The University of Texas at Austin, Austin, Texas, 1988.
41. Cetin, A. and Carrasquillo, R. L., *Effect of Accelerated Heat Curing and Mix Characteristics on the Heat Development and Mechanical Properties of High Performance Concrete*, Research Report 580-4, Center for Transportation Research, The University of Texas at Austin, Austin, Texas, 1997 (awaiting final publication).
42. Colaco, J. P., "75-Story Texas Commerce Plaza, Houston — The Use of High-Strength Concrete," *High Strength Concrete*, ACI SP-87, American Concrete Institute, Detroit, 1985, pp. 1-8.
43. Comité Euro-International du Béton (CEB), *CEB-FIP International Recommendations for the Design and Construction of Concrete Structures*, Paris-London, 1970.
44. Comité Euro-International du Béton (CEB), *CEB-FIP Model Code 1990*, Final Draft, Lausanne, 1991.

45. Cook, J. E., "Research and Application of High-Strength Concrete: 10,000 psi Concrete," *Concrete International*, October 1989, Vol. 11, No. 10, pp. 67-75.
46. Cordova, C. R., Burns, N. H., Carrasquillo, R. L., and Fowler, D. W., *Transfer and Development Length of 0.6-Inch Diameter Prestressing Strand at Two-Inch Spacing in Fully Bonded High Strength and Normal Strength Concrete Composite Texas Type C Beams*, Research Report 580-3, Center for Transportation Research, The University of Texas at Austin, Austin, Texas, 1998 (currently under revision - awaiting final publication).
47. Drake, K. D., "High-Strength Concrete in Seattle," *High-Strength Concrete*, ACI SP-87, American Concrete Institute, Detroit, 1985, pp. 21-34.
48. Durning, T. A. and Rear, K. B., "Braker Lane Bridge — High Strength Concrete in Prestressed Bridge Girders," *PCI Journal*, May/June 1993, Vol. 38, No. 3, pp. 46-51.
49. El Hindy, E., Miao, B., Chaallal, O., and Aitcin, P.-C., "Drying Shrinkage of Ready-Mixed High Performance Concrete," *ACI Materials Journal*, May/June 1994, Vol. 91, No. 3, pp. 300-305.
50. Emerson, M., *Bridge Temperatures for Settling Bearings and Expansion Joints*, TRRL Supplemental Report 479, Department of transport, Berkshire, England, 1979.
51. Farrington, E. W., Burns, N. H., and Carrasquillo, R. L., *Creep and Shrinkage of High Performance Concrete*, Research Report 580-5, Center for Transportation Research, The University of Texas at Austin, Austin, Texas, 1997 (awaiting final publication).
52. French, C. Shield, C., and Ahlborn, T., "Tests of Two High Performance Concrete Prestressed Bridge Girders," *Proceedings of the PCI/FHWA International Symposium on High Performance Concrete*, Prestressed/Precast Concrete Institute, Chicago, 1997, pp. 394-405.
53. Ghali, A. and Favre, R., *Concrete Structures, Stresses and Deformations*, Chapman Hall, London, 1986.
54. Gilbert, R. I., *Time Effects in Concrete Structures*, Elsevier Science Publishers, Amsterdam, 1988.
55. Goodspeed, C. H., Vanikar, S., and Cook, R. A., "High-Performance Concrete Defined for Highway Structures," *Concrete International*, February 1996, Vol. 18, No. 2, pp. 62-67.

56. Gross, S. P., SORTDTA1, Data Manipulation and Reduction Program for Use With Custom Data Acquisition Systems in the Texas HPC Bridge Instrumentation Projects, Version 1.0, 1994.
57. Gross, S. P. and Burns, N. H., "Deflection of Long-Span High Performance Concrete Girders," *Proceedings of the ASCE Texas Section Spring 1998 Meeting, ASCE Texas Section*, Austin, Texas, 1998.
58. Gross, S. P. and Burns, N. H., *Transfer and Development Length of 15.2 mm (0.6 in.) Diameter Prestressing Strand in High Performance Concrete: Results of the Hoblitzell-Buckner Beam Tests*, Research Report 580-2, Center for Transportation Research, The University of Texas at Austin, Austin, Texas, 1997 (awaiting final publication).
59. Group discussion involving May Lou Ralls, TxDOT, Ned Burns and Shawn Gross, The University of Texas at Austin, Burson Patton, Texas Concrete Company, and Lisa Carter Powell, P.E. Structural Consultants on April 2, 1996.
60. Guyon, Y., *Prestressed Concrete*, John Wiley and Sons, New York, 1953.
61. Hansen, T. C. and Mattock, A. H., "Influence of Size and Shape of Member on the Shrinkage and Creep of Concrete," *ACI Journal*, February 1966, Vol. 63, No. 2, pp. 267-289.
62. Hanson, J. A., "Prestress Loss as Affected by Type of Curing," *PCI Journal*, April 1964, Vol. 9, No. 2, pp. 69-93.
63. Huang, T., "Study of Prestress Losses Conducted by Lehigh University," *PCI Journal*, September/October 1982, Vol. 27, No. 5, pp. 48-61.
64. "Hybrid girder in cable-stay debut," *Engineering News Record*, November 15, 1984, pp. 32-36.
65. Imbsen, R. A., Vandershof, D. E., Schamber, R. A., and Nutt, R. V., *Thermal Effects in Concrete Bridge Superstructures*, NCHRP Report No. 276, Transportation Research Board, Washington, D.C., September 1985.
66. Jobse, H. J. and Moustafa, S. E., "Applications of High Strength Concrete for Highway Bridges," *PCI Journal*, May/June 1984, Vol. 29, No. 3, pp. 44-73.
67. Joint FIP-CEB Working Group on High Strength Concrete, *High Strength Concrete: State of the Art Report*, CEB Bulletin No. 197 (FIP SR 90/1), Federation Internationale de la Prescontrainte, London, 1990.

68. Kaar, P. H., Hanson, N. W., and Capell, H. T., "Stress-Strain Characteristics of High-Strength Concrete," *Proceedings of the Douglas McHenry International Symposium on Concrete and Concrete Structures*, ACI SP-55, American Concrete Institute, Detroit, 1978, pp. 161-185.
69. Kelly, D. J., Bradberry, T. E., and J. E. Breen, *Time Dependent Deflections of Pretensioned Beams*, Research Report No. 381-1, Center for Transportation Research, The University of Texas at Austin, 1987.
70. Klieger, P., *Some Aspects of Durability and Volume Change of Concrete for Prestressing*, Research Development Bulletin 118, Portland Cement Association, Skokie, Illinois, 1960.
71. Kosmatka, S. H. and Panarese, W. C., *Design and Control of Concrete Mixtures*, Portland Cement Association, Skokie, Illinois, Thirteenth Edition, 1988.
72. Lachemi, M., Lessard, M., and P.-C. Aitcin, "Early-Age Temperature Developments in a High-Performance Concrete Viaduct," *High-Strength Concrete: An International Perspective*, ACI SP-167, American Concrete Institute, Detroit, 1996, pp. 149-174.
73. Lane, S. N., "Development Length of Prestressing Strand," *Public Roads*, September 1990, Vol. 54, No. 2, pp. 200-205.
74. Lester, B. and Tadros, G., "Northumberland Strait Crossing: Design Development of Precast Prestressed Bridge Structure," *PCI Journal*, September/October 1995, Vol. 40, No. 5, pp. 32-44.
75. Libby, J. R., *Modern Prestressed Concrete*, Fourth Edition, Van Nostrand Reinhold, New York, 1990.
76. Lin, T. Y., and Burns, N. H., *Design of Prestressed Concrete Structures*, John Wiley and Sons, New York, 1981.
77. Ludlum, D. M., *National Audobon Society Field Guide to North American Weather*, Knopf, Inc., 1991.
78. Malier, Y., Brzillier, D., and Roi, S., "The Bridge of Joigny," *Concrete International*, May 1991, Vol. 13, No. 5, pp. 40-42.
79. Martin, L. D., "A Rational Method for Estimating Camber and Deflection in Precast Prestressed Members," *PCI Journal*, January/February 1977, Vol. 22, No. 1, pp. 100-108.

80. Mast, R. F., "Lateral Stability of Long Prestressed Concrete Beams – Part 1," *PCI Journal*, January/February 1989, Vol. 34, No. 1, pp. 34-53.
81. Mast, R. F., "Lateral Stability of Long Prestressed Concrete Beams – Part 2," *PCI Journal*, January/February 1993, Vol. 38, No. 1, pp. 70-88.
82. McDonald, D., "Development of a Simplified Code Procedure for the Prediction of Shrinkage and Creep," *Creep and Shrinkage of Concrete – Proceedings of the Fifth International RILEM Symposium*, International Union of Testing and Research Laboratories for Materials and Structures (RILEM), Cambridge, 1993.
83. Mindess, S. and Young, J. F., *Concrete*, Prentice-Hall, Englewood Cliffs, New Jersey, 1981.
84. Mitchell, D., Cook, W. D., Khan, A. A., and Tham, T., "Influence of High Strength Concrete on Transfer and Development Length of Pretensioning Strand," *PCI Journal*, May/June 1993, Vol. 38, No. 3, pp. 52-66.
85. Moreno, J., "225 W. Wacker Drive," *Concrete International*, January 1990, Vol. 12, No. 1, pp. 35-39.
86. "Mountain View Road Bridge," *PCI Journal*, March/April 1984, Vol. 29, No. 2, pp. 148-151.
87. Muller, H. S., "New Prediction Models for Creep and Shrinkage of Concrete," *Creep and Shrinkage of Concrete: Effect of Materials and Environment*, ACI SP 135, American Concrete Institute, Detroit, 1992, pp. 1-18.
88. Myers, J. J. and Carrasquillo, R. L., *Production and Quality Control of High Performance Concrete in Texas Bridge Structures*, Research Report 580/589-1, Center for Transportation Research, The University of Texas at Austin, Austin, Texas, 1998 (under review).
89. Naaman, A. E., *Prestressed Concrete Analysis and Design – Fundamentals*, McGraw-Hill, New York, 1982.
90. Naaman, A. E. and Hamza, A. M., "Prestress Losses in Partially Prestressed High Strength Concrete Beams," *PCI Journal*, June/July 1993, Vol. 38, No. 3, pp. 98-114.
91. National Climatic Data Center, internet site on World Wide Web, www.ncdc.noaa.gov

92. National Oceanic and Atmospheric Administration, internet site on World Wide Web, www.noaa.gov
93. Nasser, K. W. and Al-Manaseer, A. A., "Creep of Concrete Containing Fly Ash and Superplasticizer at Different Stress/Strength Ratios," *ACI Journal*, July/August 1986, Vol. 83, No. 4, pp. 668-673.
94. Nawy, E. G., *Fundamentals of High Strength High Performance Concrete*, Longman Group, Essex, England, 1996.
95. Neville, A. M., *Properties of Concrete*, Third Edition, Pitman Publishing, London, 1981
96. Neville, A. M. and Brooks, J. J., *Concrete Technology*, Revised Edition, Longman Scientific, Essex, England, 1990.
97. Neville, A. M., Dilger, W. H., and Brooks, J. J., *Creep of Plain and Structural Concrete*, Longman Group, 1983.
98. Ngab, A. S., Nilson, A. H., and Slate, F. O., "Shrinkage and Creep of High Strength Concrete," *ACI Journal*, July/August 1981, Vol. 78, No. 4, pp. 255-261.
99. Nilson, A. H., *Design of Prestressed Concrete*, John Wiley and Sons, New York, 1987.
100. Nilson, A. H. and Winter, G., *Design of Concrete Structures*, Eleventh Edition, McGraw-Hill, New York, 1991.
101. Parrot, L. J., "The Properties of High-Strength Concrete," Technical Report No. 42.417, Cement and Concrete Association, Wexham Springs, 1969.
102. Patton, B., "Fabrication of Prestressed Concrete Beams for Two High Performance Concrete Bridge Projects in Texas," *Proceedings of the PCI/FHWA International Symposium on High Performance Concrete*, Prestressed/Precast Concrete Institute, Chicago, 1997, pp. 488-503.
103. Pauw, A., "Static Modulus of Elasticity of Concrete as Affected by Density," *ACI Journal (Proceedings)*, December 1960, Vol. 57, No. 6, pp. 679-688.
104. PCI Committee on Prestress Losses, "Recommendations for Estimating Prestress Losses," *PCI Journal*, July/August 1975, Vol. 20, No. 4, pp. 43-75.

105. Perenchio, W. F. and Klieger, P., "Some Physical Properties of High-Strength Concrete," Research and Development Bulletin No. RD056.01T, Portland Cement Association, Skokie, 1978.
106. Potgieter, I. C. and Gamble, W. L., "Nonlinear Temperature Distributions in Bridges at Different Locations in the United States," *PCI Journal*, July/August 1989, Vol 34, No. 4, pp. 80-103.
107. Powell, L. C., "Design and Analysis of Pretensioned Post-Tensioned Long-Span High Performance Concrete I-Beams," *Proceedings of the PCI/FHWA International Symposium on High Performance Concrete*, Prestressed/Precast Concrete Institute, Chicago, 1997, pp. 504-514.
108. Precast/Prestressed Concrete Institute, *PCI Design Handbook*, Fourth Edition, Chicago, 1992.
109. Priestley, M. J. N., "Design of Concrete Bridges for Temperature Gradients," *ACI Journal*, May 1978, Vol. 75, No. 5, pp. 209-217.
110. "Put that in your pipe and cure it," *Engineering News Record*, February 16, 1989, pp. 44-53.
111. Radolli, M. and Green, R., "Thermal Stresses in Concrete Bridge Superstructures Under Summer Conditions," *Transportation Research Record*, Transportation Research Board, No. 547, 1975, pp. 23-36.
112. Ralls, M. L., "Texas High-Performance Concrete Bridges – How Much Do They Cost?," *Concrete International*, March 1998, Vol. 20, No. 3, pp. 71-74.
113. Ralls, M. L., Ybanez, L., and Panak, J. J., "The New Texas U-Beam Bridges: An Aesthetic and Economical Design Solution," *PCI Journal*, September/October 1993, Vol. 38, No. 5, pp. 20-29.
114. Reynolds, J. C. and Emanuel, J. H., "Thermal Stresses and Movements in Bridges," *Journal of the Structural Division (ASCE)*, American Society of Civil Engineers, January 1974, Vol. 100, No. ST1, pp. 63-78.
115. Russell, B. W., "Impact of High Strength Concrete on the Design and Construction of Pretensioned Girder Bridges," *PCI Journal*, July/August 1994, Vol. 39, No. 4, pp. 76-89.
116. Russell, B. W. and Burns, N. H., *Design Guidelines for Transfer, Development, and Debonding of Large Diameter Seven Wire Strands in Pretensioned Concrete Girders*,

Research Report 1210-5F, Center for Transportation Research, The University of Texas at Austin, 1993.

117. Russell, H. G., "High-Strength Concrete in Bridges – History and Challenges," *Proceedings of the PCI/FHWA International Symposium on High Performance Concrete*, Prestressed/Precast Concrete Institute, Chicago, 1997, pp. 27-38.
118. Russell, H. G., *Implementation Program on High Performance Concrete: Guidelines for Instrumentation of Bridges*, Publication No. FHWA-SA-96-075, Federal Highway Administration, Washington, D.C., 1996.
119. Russell, H. G., Volz, J. S., and Bruce, R. N., *Optimized Sections for High-Strength Concrete Bridge Girders*, Publication No. FHWA-RD-95-180, Federal Highway Administration, McLean, Virginia, 1997.
120. Sennour, M. L. and Carrasquillo, R. L., *Creep and Shrinkage Properties in Concrete Containing Fly Ash*, Research Report 481-6, Center for Transportation Research, The University of Texas at Austin, Austin, Texas, 1989.
121. Shah, S.P. and Ahmad, S. H., *High Performance Concrete: Properties and Applications*, McGraw-Hill, New York, 1994.
122. Sinno, R., *The Time-Dependent Deflections of Prestressed Concrete Bridge Beams*, Ph.D. Dissertation, Texas A&M University, College Station, Texas, 1968.
123. Smadi, M. M., Slate, F. O., and Nilson, A. H., "Shrinkage and Creep of High-, Medium-, and Low-Strength Concretes, Including Overloads," *ACI Materials Journal*, May/June 1987, Vol. 84, No. 3, pp. 224-234.
124. "Stayed girder reaches a record with simplicity," *Engineering News Record*, May 22, 1986, pp. 26-28.
125. "Stronger concrete," *Engineering News Record*, June 8, 1982, p. 12.
126. Swamy, R. N. and Anand, K. L., "Shrinkage and Creep Properties of High Strength Structural Concrete," *Civil Engineering and Public Works Review (London)*, October 1973, Vol. 68, No. 807, pp. 859-868.
127. Swann, R. A. and Godden, W. G., "The Lateral Buckling of Concrete Beams Lifted by Cables," *The Structural Engineer*, January 1966, Vol. 44, No.1, pp. 21-33.

128. Tadros, M. K., Ghali, A., and Dilger, W. H., "Time-Dependent Prestress Loss and Deflection in Prestressed Concrete Members," *PCI Journal*, May/June 1975, Vol. 20, No. 3, pp. 86-98.
129. "Tall concrete buildings come of age," *Engineering News Record*, November 30, 1989, pp.25-27.
130. Texas Department of Transportation, PSTRS14, Prestressed Concrete Beam Design/Analysis Program, Version 3.20, 1991.
131. Texas Department of Transportation, *Standard Specifications for Construction of Highways, Streets, and Bridges*, Eighth Edition, 1993.
132. Thornton, C. T., Mohamad, H., Hungspruke, U., and Joseph, L., "High Strength Concrete for High Rise Towers," *Proceedings of the ACI International Conference on High-Performance Concrete, Singapore, 1994*, ACI SP-149, American Concrete Institute, Detroit, 1994, pp. 769-784.
133. Touma, W. E., "Permeability of High Performance Concrete: Rapid Chloride Ion Test vs. Chloride Ponding Test," unpublished Master's Thesis, The University of Texas at Austin, 1997.
134. "Tower Road Bridge," *PCI Journal*, March/April 1984, Vol. 29, No. 2, pp. 144-147.
135. "Tower touches few bases," *Engineering News Record*, June 16, 1983, pp. 24-25.
136. Troxell, G. E., Davis, H. E., and Kelly, J. W., *Composition and Properties of Concrete*, Second Edition, McGraw-Hill, New York, 1968.
137. "Up and away to a world record," *Engineering News Record*, September 19, 1994, pp. 76-82.
138. Williams, J., *The USA Today Weather Almanac 1995*, Gannett, New York, 1994.
139. Woolf, D. and French, C. E., *A Camber Study of Mn/DOT Prestressed Concrete I-Girders*, Final Report No. 1998-08, Center for Transportation Studies, The University of Minnesota, 1998.
140. Yuan, R. L., Ragab, M., Hill, R. E., and Cook, J. E., "Evaluation of Core Strength in High Strength Concrete," *Concrete International*, May 1991, Vol. 13, No. 5, pp. 30-34.

141. Zia, P., "State-of-the-Art of HPC: An International Perspective," *Proceedings of the PCI/FHWA International Symposium on High Performance Concrete, Prestressed/Precast Concrete Institute, Chicago, 1997*, pp. 49-59.
142. Zia, P., Ahmad, S. H., and Leming, M. L., *High Performance Concretes: A State-of-the-Art Report (1989-1994)*, Federal Highway Administration, McLean, Virginia, 1996 (available via internet only).
143. Zia, P., Leming, M. L., and S. H. Ahmad, *High Performance Concretes: A State-of-the-Art Report*, SHRP-C/FR-91-103, Strategic Highway Research Program, National Research Council, Washington, D.C., 1991.
144. Zia, P., Preston, H. K., Scott, N. L., and Workman, E. B., "Estimating Prestress Losses," *Concrete International*, June 1979, Vol. 1, No. 6, pp. 32-38.
145. Zia, P., Schemmel, J. J., and Tallman, T. E., *Structural Applications of High-Strength Concrete*, Report No. FHWA/NC/89-006, North Carolina Center for Transportation Engineering Studies, North Carolina State University, Raleigh, North Carolina, 1989.

VITA

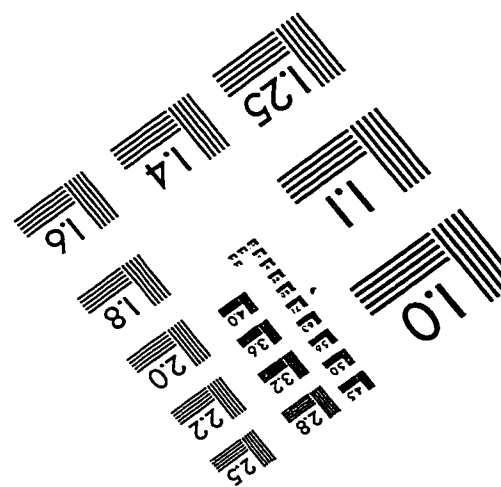
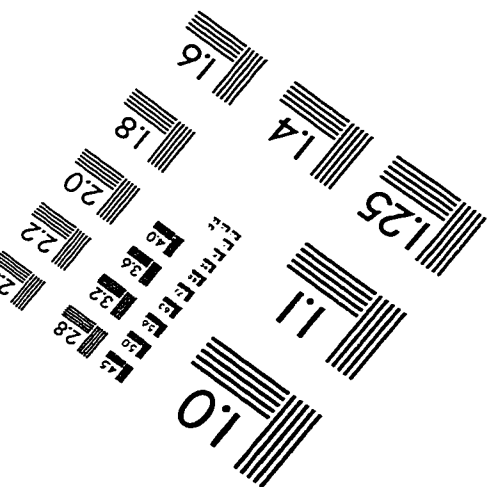
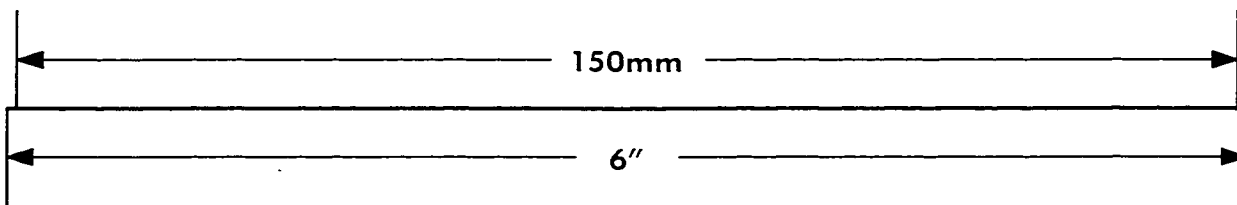
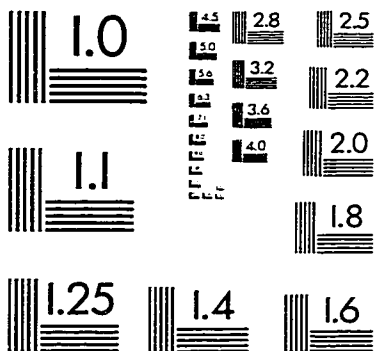
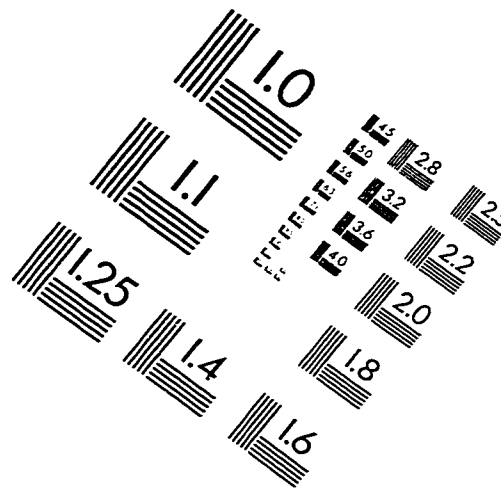
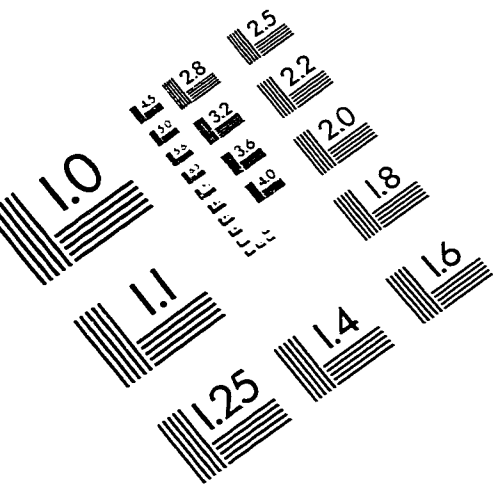
Shawn Patrick Gross was born in Hialeah, Florida on June 13, 1972, the son of Patricia Ann Dolan and Richard Wilson Gross. After earning valedictory honors at Miami Springs Senior High School in Miami Springs, Florida in May 1989, he entered Tulane University in New Orleans, Louisiana on a Deans' Honor Scholarship. He received a Bachelor of Science in Engineering degree from Tulane in May 1993.

In August 1993, he enrolled at The University of Texas at Austin under a Thrust 2000 Fellowship from the College of Engineering. He earned a Master of Science in Engineering in May 1995, and began study toward a Doctor of Philosophy in Civil Engineering immediately thereafter. Upon completion of this degree, he was employed as an Assistant Professor of Civil and Environmental Engineering at Villanova University in Villanova, Pennsylvania.

Permanent Address: 178 DeLeon Drive, Miami Springs, Florida, 33166

This dissertation was typed by the author.

IMAGE EVALUATION TEST TARGET (QA-3)



APPLIED IMAGE, Inc
1653 East Main Street
Rochester, NY 14609 USA
Phone: 716/482-0300
Fax: 716/288-5989

© 1993, Applied Image, Inc., All Rights Reserved